Two-way coupling between potential and viscous flows for a marine application

Young-Myung Choi

THESE DE DOCTORAT DE

L'ÉCOLE CENTRALE DE NANTES
COMUE UNIVERSITE BRETAGNE LOIRE

ECOLE DOCTORALE N° 602
Sciences pour l'Ingénieur
Spécialité : Mécanique des Milieux Fluides

Par
Young-Myung CHOI

Two-way Coupling between Potential and Viscous Flows for a Marine Application

Thèse présentée et soutenue à Nantes, le 21 Novembre 2019

Unité de recherche : Laboratoire de recherche en Hydrodynamique, Énergétique et Environnement Atmosphérique, CNRS UMR 6598

Rapporteurs avant soutenance :

Odd Magnus Faltinsen	Professeur, Université Norvégienne de Science et Technologie
Andrea Di Mascio	Professeur, Université de l'Aquila, Italie

Composition du Jury :

Président :	Jean-Yves Billard	Professeur des universités, École Navale, BCRM de Brest
Examinateurs :	Sime Malenica	Directeur adjoint de la recherche, Docteur, Bureau Veritas, Puteaux
	Ermina Begovic	Professeur associé, Université de Naples Federico II, Italie
	Pierre-Emmanuel Guillerm	Expert sénior hydrodynamique, Docteur, Naval Group, Lanester
Dir. de thèse :	Pierre Ferrant	Professeur des universités, École Centrale de Nantes
Co-encadrant :	Benjamin Bouscasse	Chargé de recherche, École Centrale de Nantes

Doctoral Thesis

Two-way Coupling between Potential and Viscous Flows for a Marine Application

by

Young-Myung Choi

École Centrale de Nantes

Nantes, 2019

Acknowledgements

While I am finalizing my thesis, I realize that I am honestly fortunate to have met good people who were willing to help me. Thanks to them, I could finalize my thesis during my stay in Ecole Centrale de Nantes. I truly have learned a lot from them not only for research but for living as a good man.

First of all, I am very grateful to Prof. Odd Magnus Faltinsen at the Norwegian University of Science and Technology and Prof. Andrea Di Mascio at the Università degli Studi dell'Aquila for accepting being reviewers of my thesis. Also, I would like to express my gratitude to Prof. Jean-Yves Billard at the Ecole Navale for accepting the president of jury members. And I would like to express my sincere thank to Prof. Ermina Begovic at the University of Naples Federico II, Dr. Pierre-Emmanuel Guillerm at Naval Group and Dr. Šime Malanica in Bureau Veritas for being the jury member.

I am deeply grateful to Prof. Pierre Ferrant, my supervisor for not only giving me the opportunity to study on this subject but also being a great advisor. I am sincerely appreciated for his consistent support to work and discussion on the topic. Whenever I asked old pieces of literature or programs, he always tried to find them on his shelf or asked someone to help me.

I would express my thanks to Dr. Benjamin Bouscasse and Dr. Lionel Gentaz, my co-supervisors. I could discuss with them on my topic whenever I have difficulty. They are always opened to discuss and it was very helpful. They organized my diverging research and read my manuscript for the first time. Even though there are uncountable mistypes and wrong grammar, they are very patient to read my poor manuscript. Thanks to their efforts, the manuscript is well organized and significantly improved. Furthermore, Dr. Benjamin Bouscasse helped me living in France.

I would like to thank researchers in Ecole Centrale de Nantes. I was glad to discuss with Dr. Alain Clément, who retired Ecole Centrale de Nantes last year. When I stuck in the problem of calculating the time domain Green function, he shared his clever insight on this topic. I am also pleased to work with Prof. Guillaume Ducrozet. When I have difficulties with the HOS wave theory, he advised me on how to generate good waves. I am also very thankful to Prof. David Le Touzé on his consistent support on my topic. Whenever I brought some numerical results, he figured out the missing points and encouraged me to work on deeply.

I would like to express my sincere gratitude to the colleagues in Ecole Centrale de Nantes. I was always pleased to work with Dr. Zhaobin Li and Young Jun Kim and Théo Descamps. Discussion with them was always helpful to work on OpenFOAM. Especially, I benefited from the work by Dr. Zhaobin Li for multi-phase SWENSE. I am also thanks to Dr. Chunmei Xie, Dr. Wenjin Cao, Dr. Yang Zhang and Zhenrong Jing for all discussions, dinners and fun.

I would like to express my sincere appreciation to Dr. Šime Malenica in Bureau Veritas. He recommended me as a doctoral student of Ecole Centrale de Nantes and suggested my research topic. He had provided me literature to set a direction of my thesis and advised my research topic. Moreover, he sincerely has taken care of me for living in France and encouraged me to

focus on the research. I could learn many things from him how to live as a good researcher and the humble attitude to the other.

I would like also to thank Dr. Xiao-Bo Chen in Bureau Veritas. After he had returned to the headquarter in Paris, I could discuss with him on the potential flow, especially for elementary functions. He gladly sent me a research note before publication and it was very helpful to my research. I am also appreciated to Dr. Sopheak Seng and Dr. Charles Monroy in Bureau Veritas. They also provided a well-developed OpenFOAM package, `foamStar`, to be used in my research. When I have a problem with OpenFOAM, they also advised me to develop the code in the right way.

I would like to thank Prof. Hrvoje Jasak, Dr. Vuko Vukčević and Dr. Inno Gatin from University of Zagreb. They also gladly provided me a well-coordinated OpenFOAM package, `NavalHydro`. Thanks to their efforts, there was no difficulty regarding the implementation of the viscous flow solver. Without their devotion to this package, I am quite sure that I could not finalize my work. Especially, I am very appreciated to Dr. Vuko Vukčević for discussion. His insight on the numerical procedure and CFD was always surprising.

I would like to express my sincere thanks to Prof. Sun Hong Kwon, my previous supervisor during my master course, and Mr. Yun-Suk Chung in Bureau Veritas Korea. They recommended me to be a doctoral student in France. They have supported and encouraged me to start a doctoral course and I am very appreciated for their efforts.

I would like to thank Dr. Jang Young Chung at Pusan National University and Prof. Jun Soo Park at Kyungnam University and Prof. Young-Jun Yang at Dongmyeong University. They were my previous colleagues from Pusan National University. Whenever I contacted them, they show grateful cheers to me.

I would like to thank Dr. Sa Young Hong and Dr. Kyung-Hwan Kim in Korea Research Institute of Ships and Ocean engineering (KRISO) and Prof. Bo Woo Nam in Seoul National University. They were supervisors when I had worked in KRISO as a replacement of military service. I could learn a lot from them and they encouraged me to start doctoral course.

The financial support from the Chaire Hydrodynamique et Structure Marines CENTRALE NANTES - BUREAU VERITAS should be acknowledged.

I would like to express my warmest thanks to my family. They show their consistent support during my stay in France. Lastly, I am also very thanks to my friends: Hwan Lee, Gian Jung, Wookjae Choi and Juyoung Jung for cheering me up whenever I contacted them.

Contents

List of Figures

List of Tables

Nomenclature

Calligraphy letters

$\mathcal{C}_{mn}$	Fourier-Laguerre coefficients of normal fluid velocity on matching surface
$\mathcal{E}_n$	Fourier coefficients of wave elevation multiplied by g on matching waterline
$\mathcal{F}$	Waterline elementary functions
$\mathcal{H}_I$	Pressure jump used for Ghost Fluid Method
$\mathcal{I}$	Some integrals used for evaluation of semi-infinite integral
$\mathcal{L}_m(-sz)$	Laguerre functions
$\mathcal{R}$	Source term in Green function
$\mathcal{R}^*$	Image source term in Green function
$\mathcal{S}$	Surface elementary functions
$\mathcal{U}_{pn}$	Fourier-Laguerre coefficients of fluid velocity at field point
$\mathcal{W}_{mn}$	Fourier-Laguerre coefficients of tangential fluid velocity on matching surface
$\mathcal{Z}_{mp}^{(i)}(s;k), \mathcal{Z}_p^{(4)}(s;k)$	Vertical integral functions

Latin letters

$\mathbf{s}_f$	Face surface vector
Δt	Time difference, time step
Δx	Cell length
Δz	Cell height
$\frac{1}{r_1}$	Source term in Green function
$\frac{1}{r_2}$	Image source term in Green function
$\mathbf{g}$	Gravitational acceleration
$\mathbf{n}$	Normal unit vector
$\mathbf{S}$	Source terms
$\mathbf{t}$	Tangential unit vector
$\mathbf{u}$	Fluid velocity
$\mathbf{v}$	Fluid rotational velocity
$\mathbf{w}$	Fluid tangential velocity
A	Wave amplitude

a	Source point coordinates, Cylinder radius
a_N	Off-diagonal coefficient of discretized matrix
a_P	Diagonal coefficient of discretized matrix
a_{NP}	Upper off-diagonal coefficient for owner cell P and neighbor cell N
a_{PN}	Lower off-diagonal coefficient for owner cell P and neighbor cell N
$b_{ij}^{(p)}$	Basis spline function with respect to order p
c_p	Wave phase velocity
C_{mn}	Fourier-Laguerre coefficients
d	Distance from nearest interface face
D_n	Fourier coefficients
F	Wave term in Green function, Acting force on the body
F_f	Flux at face f
G	Green function
g	Magnitude of gravitational acceleration
H	Wave height, Wave term in Green function
h	Water depth
H_s	Significant wave height of irregular waves
k	Wavenumber
N	Neighbor cell index
P	Owner cell index
p	Pressure
Q_P	Source coefficient for discretized matrix for owner cell P
s	Wavenumber parameter used for Laguerre function
T	Wave period
T_p	Peak period of irregular waves
V	Cell volume
w	Weight function, tangential velocity components
w^d	Dynamic weight function
CFD	Computational Fluid Dynamics
Co	Courant-Friedrichs-Lewy number (CFL Number)
EFD	Experimental Fluid Dynamics

Re	Reynolds number
Greek letters	
α	Volume Of Fluid (VOF)
$\boldsymbol{\tau}$	Stress tensor
$\mathbf{x} = (r, \theta, z)$	Field point in circular cylindrical coordinates
$\mathbf{x} = (x, y, z)$	Field point in cartesian coordinates
$\boldsymbol{\xi} = (\xi, \eta, \zeta)$	Source point in cartesian coordinates
$\boldsymbol{\xi} = (a, \theta', \zeta)$	Source point in circular cylindrical coordinates
δ	Boundary layer thickness
$\Delta\theta$	Phase difference
δ_{mn}	Kronecker delta function
γ	Peak enhancement factor used for JONSWAP wave spectrum
κ_R	Reflection coefficient
λ	Wavelength
λ_f^{limit}	Flux limiter at face f
λ_f	Dimensionless distance parameter defining interface location by Level-set function
μ	Fluid kinematic viscosity
ν	Fluid dynamic viscosity
ν_{eddy}	Eddy viscosity used for wave breaking model in HOS
ω	Wave frequency
Φ	Velocity potential
ϕ	Velocity potential in frequency domain
Φ_C	Complementary velocity potential
Φ_I	Incident wave velocity potential
ψ	Level-set function
ψ_C	Complementary Level-set function
Ψ_I	Incident wave stream function for regular wave
ψ_I	Stream function in frequency domain, Incident wave Level-set function
ρ	Fluid density
Ξ	Wave elevation

ξ	Nondimensionalized coordinates for weight function, Source point coordinates

Operators

$\hat{\mathbf{q}} = (q^x, q^y, -q^z)$	Operator multiplying minus one (-1) on vertical vector component, q^z
$[\![q]\!]$	Jump operator, $[\![q]\!] = q_a - q_w$, representing the difference across the interface, q_a and q_w are quantities in air and water, respectively
$\nabla_\xi = \left(\frac{\partial}{\partial \xi}, \frac{\partial}{\partial \eta}, \frac{\partial}{\partial \zeta}\right)$	Source point gradient in cartesian coordinates
$\nabla_\xi = \left(\frac{\partial}{\partial a}, \frac{\partial}{\partial \theta'}, \frac{\partial}{\partial \zeta}\right)$	Source point gradient in circular cylindrical coordinates
$\nabla_x = \left(\frac{\partial}{\partial r}, \frac{\partial}{\partial \theta}, \frac{\partial}{\partial z}\right)$	Field point gradient in circular cylindrical coordinates
$\nabla_x = \left(\frac{\partial}{\partial x}, \frac{\partial}{\partial y}, \frac{\partial}{\partial z}\right)$	Field point gradient in cartesian coordinates
$\{q\}^e$	Explicit finite volume (FV) discretization
$\{q\}^i$	Implicit finite volume (FV) discretization

Superscripts

q^a	a-component of vector $\mathbf{q}$
$q^{\theta'}$	θ'-component of vector $\mathbf{q}$
q^η	η-component of vector $\mathbf{q}$
q^ξ	ξ-component of vector $\mathbf{q}$
q^ζ	ζ-component of vector $\mathbf{q}$
q^x	x-component of vector $\mathbf{q}$
q^y	y-component of vector $\mathbf{q}$
q^z	z-component of vector $\mathbf{q}$
$q^{(m)}$	The harmonic order, Perturbation order, Kind of function

Subscripts

$(q)_N$	The value at neighbor cell center (N)
$(q)_P$	The value at owner cell center (P)
$q_\eta = \frac{\partial q}{\partial \eta}$	Partial derivative with respect to source point cartesian coordinate η
$q_\xi = \frac{\partial q}{\partial \xi}$	Partial derivative with respect to source point cartesian coordinate ξ
$q_\zeta = \frac{\partial q}{\partial \zeta}$	Partial derivative with respect to source point cartesian/cylindrical coordinate ζ
$q_a = \frac{\partial q}{\partial a}$	Partial derivative with respect to field point cartesian coordinate a
$q_n = \nabla_\xi q \cdot \mathbf{n}$	Normal gradient component

$q_x = \frac{\partial q}{\partial x}$	Partial derivative with respect to field point cartesian coordinate x
$q_y = \frac{\partial q}{\partial y}$	Partial derivative with respect to field point cartesian coordinate y
$q_z = \frac{\partial q}{\partial z}$	Partial derivative with respect to field point cartesian/cylindrical coordinate z
$q_{\theta'} = \frac{\partial q}{\partial \theta'}$	Partial derivative with respect to field point cartesian coordinate θ'
q_C	Complementary wave flow
q_I	Incident wave flow

1 Introduction

1.1 Numerical modeling of wave-structure interaction

The wave-structure interaction is a major concern for naval architecture and ocean engineering. The ships and offshore platforms, which have an expected lifetime of 25 years or so, are exposed to ocean environment where the typical wave periods are in the range of 6-25s. They experience billions of oscillations during their lifetime, therefore it is essential to estimate the forces acting on those structure and their motions.

The hydrodynamic forces are of various kinds from simple hydrostatic loads to very complex wave impacts and the complexity of the mathematical model is relevant to achieve accuracy. Some transfer function as the motion Response Amplitude Operators (RAOs) are very well and quickly computed with linear potential flow, whereas extreme response or extreme loads could be influenced by nonlinear features or even multiphase flow and consequently a more complex and dedicated model is necessary, often based on Navier Stokes equations, with or without turbulence model.

The behavior of bodies in waves is possible to compute analytically for a limited number of geometrical shapes and with strong assumptions on the hydrodynamic model, specifically the linearization of the free surface and body boundary conditions. Real ships and offshore platforms have complex geometries and the wave structure interaction phenomena can be assessed by conducting experiments or by solving numerically the chosen mathematical model. Performing experiments is a good methodology to get real-time data and to emulate complex natural phenomena, however there are numerous limitations as scaling effects, the facility, the data acquisition and overall costs. This explains why the numerical analysis is often attractive, though the cost and the complexity of the computation can also be large. In the present research, the objective is to use complex models but to limit the computational costs in simulating the wave structure interaction problem. This is done by coupling different types of hydrodynamic models which have different levels of assumptions.

Two mathematical models are commonly used in naval and ocean engineering fields nowadays, that can be stated as potential flow and viscous flow models, the former being derived with hypothesis imposed on the latter.

Potential flow models are derived from the assumption of incompressible, inviscid fluid and irrotational flow. The most common numerical algorithms are based on the boundary integral equation which transforms a three-dimensional (3D) computational domain into two-dimensional (2D) domain. 3D problems are reformulated along the body surface with the introduction of a Green function satisfying all the boundary conditions except body boundary condition. This methodology is used in the naval and offshore fields to compute Linear Transfer Function (LTF), Quadratic Transfer Function (QTF), radiation forces (added mass and radiation damping) and motion Response Amplitude Operators (RAOs) of a floating/fixed body subject to waves. However, potential flow based solvers cannot model vorticity, viscosity, turbulence and wave breaking

phenomenon, making them less attractive for computing the drag resistance of ships, maneuvering, roll damping and gap resonance. In addition, the algorithm complexity and the numerical cost increase when the nonlinearity of the free surface and the body perturbation need to be accounted.

Viscous flow models are more and more used in wave-structure interaction problems to overcome the limitations of the potential flow model thanks to the increase of computational resources. Viscous flow models are generally derived from the Navier Stokes equations and the assumption of Newtonian fluid. A 3D computational grid is required to solve the equations numerically. The size of the grid depends generally of several parameters and specifically from the Reynolds number for a typical marine computation. Turbulence models can be used to reduce the number of nodes, Reynolds averaged Navier-Stokes equations (RANSE) are commonly used to solve a highly nonlinear phenomena including viscosity, vorticity and turbulent effects. Though the numerical computation of the free surface motions in viscous flows has also its challenges, the simulation of wave run-up, green water, and extreme bow slamming events are more and more conducted. Performing long simulations with floating or fixed body, as example in irregular waves for the typical duration of 3 hours is still very expensive and unpractical for engineering companies.

Those two different flow models have each advantages and drawbacks for simulating wave-structure interaction. The coupling of potential and viscous flows in wave-structure interaction problem has started in the early 1990s to take the benefits of those two different models. The viscous model needs a large computational effort and it is not suitable to model propagating waves to the far-field. Meanwhile, the potential flow model is regarded as good for wave propagation. Therefore, the propagating waves in the far-field region of the domain with viscous flow can potentially be improved by using a potential flow model, as depicted in figure 1.1.

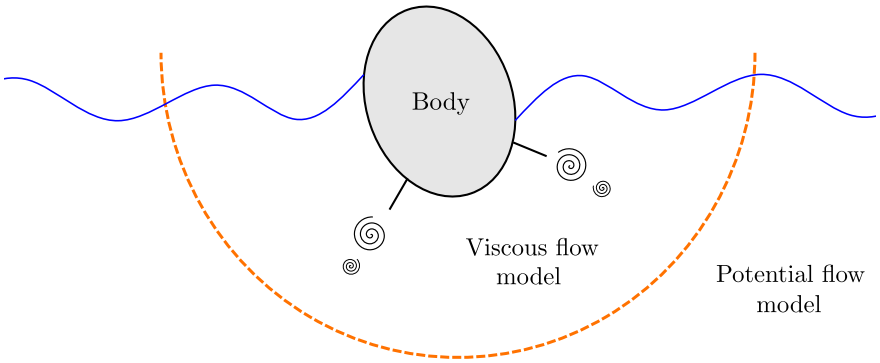

Figure 1.1. The concept of coupling between two flows in wave-structure interaction problem.

The reduction of the computational domain dedicated to the viscous flow decreases the computational burden. The key is that this reduction does not increases the wave reflections on the boundary and that the computational cost to solve the potential flow does not compensate what has been gained. This is the reason why in this thesis the speed of the potential flow algorithm has been accounted for and object of dedicated studies.

Two flow models are based on different assumptions that raise many questions in a sense of physical meaning. However, the coupling between potential and viscous flow models is attractive and has a strength on both efficiency and accuracy.

1.2 Previous and related researches

1.2.1 Potential flow

In potential flow, Boundary Element Method (BEM) is widely used for numerical simulations. It is classified into two methods which depends on the selection of the fundamental solution: the Rankine method and the solution using the free surface Green function.

Rankine panel method uses a simple source as the fundamental solution. It provides a flexibility in treating boundary conditions, and calculating singularities is simple. However, the boundary surface where singularities are located should cover the whole fluid domain and a panelling over the free surface is necessary. As a result, the computational effort increases due to the need to solve a large and fully populated linear system. Recently, it has often been applied with nonlinear free surface and body boundary conditions which appear in problems of ship with forward speed in waves and of wave-structure interaction in high wave. Dawson (1977) showed that this methodology gives a fairly good result for a ship with forward speed. After his work, Nakos (1990) introduced a B-spline shape function for panel connectivity and investigated numerical dispersion, dissipation, and stability. Raven (1995) compared the different numerical implementation of nonlinear free surface boundary condition. This methodology was applied in the time domain by Kring (1994). Recently, Kim et al. (2011) used this method in the principle of weak scattering already introduced by Pawlowski (1992).

The method using the free surface Green function, which satisfies a linearized free surface condition with sea bottom and radiation conditions, is the second category of BEM. With a linearized boundary condition, the integral equation is only discretized on the mean position of the body. Therefore, a small computational effort is necessary to solve a linear system of relatively small size. However, the algorithms for the computation of the Green functions are complex. The mathematical representation of the wave Green function is well summarized in the book of Wehausen and Laitone (1960). Typically, the wave Green function involves an infinite integral with singularity which makes its numerical evaluation difficult. Therefore, most of associated research works have focused on the efficient computation of Green functions. Newman (1985); Telste and Noblesse (1986); Chen (1991); Newman (1992) suggested several numerical algorithms by applying different approximations depending on nondimensional variables for numerical efficiency. Recently, Xie et al. (2018) summarized the single-integral type of wave Green function in the frequency domain and compared the precision and computational cost of various available numerical algorithms. A different perspective on the deep water wave Green function has been proposed by Clément (1998). He showed that the time domain wave Green function is a solution of 4-th order Ordinary Differential Equation (ODE), and he identified that the frequency domain wave Green function satisfies a second order ODE by applying Fourier transform (Clément, 2013).

Clément (1998) used a 4-th order Runge-Kutta time integration to solve the 4-th order ODE of the time domain Green function. Later, Chuang et al. (2007) introduced a time-marching Frobenius method to solve the ODE analytically. Recently, Bingham (2016) compared the efficiency of the numerical algorithms calculating the time domain wave Green function. A good summary of existing ordinary differential equations in both time and frequency domain with respect to spatial and temporal variables can be found in Xie (2019).

The panel discretization along the boundary surface is a concern in BEM. Linear potential codes for a diffraction-radiation problem in frequency domain, such as WAMIT by Lee (1995), HydroStar by Chen (2004), Aquaplus by Delhommeau (1989) and Nemoh by Babarit and Delhommeau (2015), are based on constant panel method. Kim (2011) used a linear panel method to solve the hydroelasticity problem of floating body. For a precise computation of wave drift forces, corresponding to second-order problem, Hong et al. (2005) applied a Higher-Order BEM (HOBEM) and validated with experiments.

Other numerical approaches than BEM are applicable for potential flows. Bai and Yeung (1974) solved the free surface problem by Finite Element Method (FEM) for 2D problem. Later, Bai (1981); Bai et al. (1989) extended FEM for 3D free surface flow. Recently, Nam (2015) applied 3D FEM for berthing problem with fully nonlinear free surface and body boundary conditions. The Harmonic Polynomial Cell (HPC) method was proposed by Shao and Faltinsen (2014). Differently from the BEM, these methodologies require the whole 3D computational domain to be discretized into the cells.

The mentioned potential flow models have focused on the evaluation of velocity potential on the boundary surface. Noblesse et al. (1997) introduced a new Poincaré's velocity representation in free surface potential flow to compute the fluid velocity at field points. The original boundary integral equation states that the velocity at field points can be calculated by the surface distribution of sources and dipoles with their strength. In his work, the dipole contribution is transformed into the equivalent source contribution multiplied by the tangential velocity. Therefore, the fluid velocity at any field points can be expressed explicitly by the velocity distribution over the surrounding boundary surfaces. Following his previous work, Noblesse (2001) presented a generic expression for free surface flows and suggested the Poincaré's velocity representations for the cases of soft ($\Phi = 0$) and rigid ($\frac{\partial \Phi}{\partial z} = 0$) free surface, steady forward ship problem, time-harmonic without/with forward speed. Furthermore, he introduced a potential representation which is called weakly singular boundary integral equation by defining a vertically integrated Green function (Noblesse and Yang, 2004). Guillerm (2001) applied Noblesse's representation for the steady forward ship problem by coupling a viscous flow model in the vicinity of the ship and a potential flow model far from the ship.

1.2.2 Viscous flows

Viscous flow models solve Navier-Stokes equations, which are the governing equations of Newtonian fluid. RANSE version of Navier-Stokes equations is frequently used in naval and offshore engineering applications and they can be solved efficiently by decomposing velocities and viscos-

ity into time-averaged and fluctuating parts. These equations are solved numerically, because analytical solutions are rarely available for the nonlinear viscous flows with free surface. The Finite Volume Method (FVM) is commonly used because it satisfies the conservation laws even when the discretized mesh is relatively coarse. FVM discretizes the fluid domain into cells which are small control volumes (CVs) where fluxes comes in and out through the control surfaces. The governing equations are reconstructed in the framework of FVM. The fluid media (water) in marine hydrodynamics is assumed to be incompressible and viscous. Patankar and Spalding (1972) introduced Semi-Implicit Method for Pressure Linked Equations (SIMPLE) algorithm to solve steady-state problems of incompressible viscous fluid. In this algorithm, the pressure correction is introduced to satisfy the continuity equation after solving the momentum equation. Issa (1986) devised Pressure-Implicit with Splitting of Operators (PISO) algorithm, which is an extended version of SIMPLE algorithm, for unsteady problem. In the PISO algorithm, the coupled velocity and pressure are solved by one predictor and two corrector steps.

The numerical modeling of the interface between air and water is also one of the main research topic in marine hydrodynamics. Interface models are categorized into Lagrangian and Eulerian approaches. The Lagrangian approach advects special marker points distributed on the interface, and reconstructs the interface with the distribution of marker points (Harlow and Welch, 1965). The reconstructed interface is considered as sharp and precise, but an extra redistribution procedure is necessary to get a sufficient resolution. Unverdi and Tryggvason (1992) proposed a front-tracking method, transporting marker points in an Eulerian domain. It enables the calculation of an accurate surface curvature and the conservation of a sharp interface. However, an extra redistribution procedure is still necessary to get a sufficient resolution. Furthermore, the complexity increases in the case of wave breaking. Meanwhile, the Eulerian approach uses an indicator function, representing whether a CV is wet or dry by a function value defined at each cell. This approaches are commonly used nowadays, from Harlow and Welch (1965) who proposed a marker and cell method. Other indicator functions, the Volume Of Fluid (VOF) by Hirt and Nichols (1981), the Level-Set (LS) function by Osher and Sethian (1988) and the Phase Function (PF) by Boettinger et al. (2002), have been proposed in the literature and are widely used in many applications. Those methods using indicator functions need however a special attention on treating numerically the convection terms due to its diffusivity.

VOF methods conserve the mass well but suffer from interface smearing and the difficulty on the calculation of the interface curvature. Several convection schemes have been applied to prevent smearing interface and maintain boundedness. Most of convection terms are evaluated by blending the low and high order advection flows with flow limiter, such as HRIC by Muzaferija and Peric (1999), Flux-corrected transport (FCT) by Boris and Book (1973), CICSAM by Ubbink (1997). The multiphase solver in OpenFOAM (`interFoam`) is based on the FCT method which has been extended up to multi-dimensions by Zalesak (1979). The computation procedures are well explained in Damián (2013). As an alternative to algebraic solving techniques, a geometric VOF approach was proposed by Roenby et al. (2016) though it limits the maximum Courant number.

LS function keeps the interface sharp, but mass loss often happens due to its signed distance

(Sussman et al., 1994). Extra computation procedures, re-distancing the level-set, have been applied to improve the accuracy while maintaining the interface sharpness (Chang et al., 1996; Sussman et al., 1998; Di Mascio et al., 2007).

PF method uses a smoothly varying function $\phi \in (-1, 1)$ in computational domain. It also has a mass loss problem like LS function, but the proper choice of phase-function may help the accuracy and boundedness. The use of biased phase function having values between 0 and 1 is adopted to keep the boundedness (Desjardins et al., 2008). Sun and Beckermann (2007) set the phase-function has a hyperbolic curve. The derived PF equation involves the self-adjusting variable controlling interface diffusion.

The quality of wave propagation in the computational domain is important for any wave-structure interaction problem. The numerical dissipation brought by the discretization makes simulations in large domain difficult and the oscillatory behavior of waves calls for a special boundary condition to minimize undesired reflections at the inlet/outlet. Ocean waves have typical periods in the range of 6-25s and travel long distances with very small energy dissipation. Waves with a wavelength of 73.15m ($T = 6.84s$) travel 924 km in a day, with its wave height only diminished by one or two percent because of friction (Lamb, 1945; Joseph, 2006). Nonlinear potential wave models are useful to initialize and generate incident waves. For example, Rienecker and Fenton (1981) used a stream function for fully nonlinear regular waves, and some nonlinear potential models for irregular waves can be found (Ducrozet et al., 2007, 2012; Engsig-Karup et al., 2009).

However, the absorption of waves at the extremities of the domain is still ongoing research. The waves at outlet are a combination of incident waves, body-scattered waves and are also affected by numerical dissipation. Israeli and Orszag (1981) introduced the technique of "damping zone" or "sponge layer" to absorb the waves. A relaxation scheme which blends the computed quantities with a target solution in the sponge layer (also called relaxation zone; blending zone) has been popular recently, see Kim et al. (2012); Jacobsen et al. (2012); Paulsen et al. (2014). As the target flow and weight function can be specified by the user, the wave outlet is relatively easily handled compared to with other methodologies which need a parameter tuning. The relaxation scheme is categorized into implicit and explicit relaxation. The implicit relaxation scheme combines the governing equations and target equations with a spatially distributed weight factor. As a result, source terms appear in the original equations, see Kim et al. (2012); Vukčević (2016). Meanwhile, the explicit relaxation scheme blends the flow values with target values in the relaxation zone after solving the governing equations, see Mayer et al. (1998); Fuhrman (2004); Engsig-Karup (2006); Seng (2012) for example.

1.2.3 Coupling of potential and viscous flows

Navier-Stokes equations are used to state the behaviour of viscous flow. Viscosity effect and rotational flow are considered naturally in governing equations. The potential flow is introduced based on the hypothesis that fluid is incompressible and inviscid and flow is irrotational. Consequently, the coupling between viscous and potential flows is sort of a contradiction. After Prandtl (1904) discovered boundary layer exists only near a body moving through fluid media, it has been

thought that the potential flow model can model the outer fluid region of the boundary layer. However, flow quantities such as fluid velocity and stress considered in viscous and potential flow models are derived in different manner. The coupling between two flow models is considered to be skeptical in view of physics.

The efforts to couple potential and viscous flows in marine hydrodynamics have been investigated from the early 1990s. Fluid viscosity has not been accounted for seriously because viscous effects on the global performance of ship and offshore platform are some times very low and often hard to estimate. The viscous effect is important for specific phenomena such as friction resistance of ship, roll damping, gap resonance, moonpool resonance. Most of the associated research has assumed that the flow quantities of viscous and potential flow models are continuous or have changed the boundary condition to consider viscosity effects.

In this section, previous research on the coupling between viscous and potential flow models in marine hydrodynamics are summarized by categorizing coupling methodology. The way of coupling is defined by transferring the information from one solver to the other. (1) One-way coupling is when an available solution is transferred to the solver, but the available solution is not affected by the solver. (2) Two-way coupling means that each flow solvers delivers the information to the other, and each flow solver is updated from the delivered information. The figure 1.2 shows a schematic view of coupling ways with decomposition.

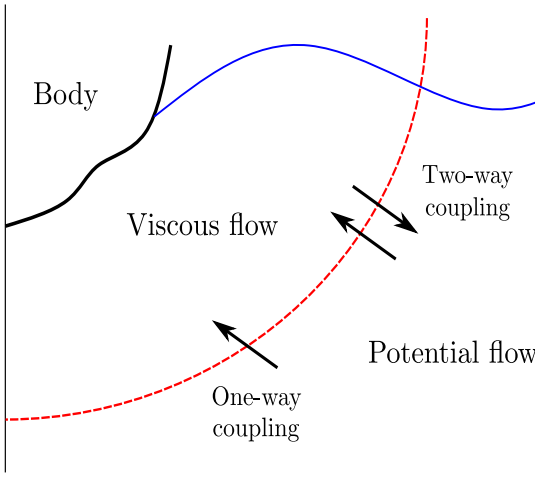

Figure 1.2. Categorization of coupling methodologies by information delivery direction.

In a coupled solver, the computation can be decomposed spatially and/or functionally. The decomposition of total problem can be then categorized into two groups:

- Domain decomposition: The computational domain for each flow is separated or overlapped. Potential and viscous flow models are applied in the separated domains.
- Functional decomposition: The total quantities in viscous flow are decomposed into potential and viscous parts. The governing equations and boundary conditions are changed.

Remark that the domain and functional decompositions are applicable together for one problem.

Domain decomposition

The domain decomposition (DD) splits the computational domain and applies the different flow models that are suitable for concerned phenomenon. In the wave-structure interaction problem, viscous effects and wave nonlinearities are strong in the vicinity of body surface. Even though the generated vortex propagates up to relatively far-field, it is possible to decompose the computational domain into viscous inner sub-domain and potential outer sub-domain. Both two-way and one-way coupling methodologies are applicable with different coupling regions. In the coupling region, the information is delivered from viscous/potential flow to the other. It is usually categorized into direct and overlapped coupling regions. The direct coupling region represents that two flows share one surface (S_d) to deliver each of the flow quantities to the other. The overlapped coupling regions refers to that the information transfer happens at two distinct boundary surfaces (S_o) with distance or the volumic blending zones ($\mathcal{Z}_b$). In the volumic blending zone, the weight function is applied for smooth transition of flow quantities. Therefore, information delivery is done in different places. Figure 1.3 shows direct and overlapped coupling regions.

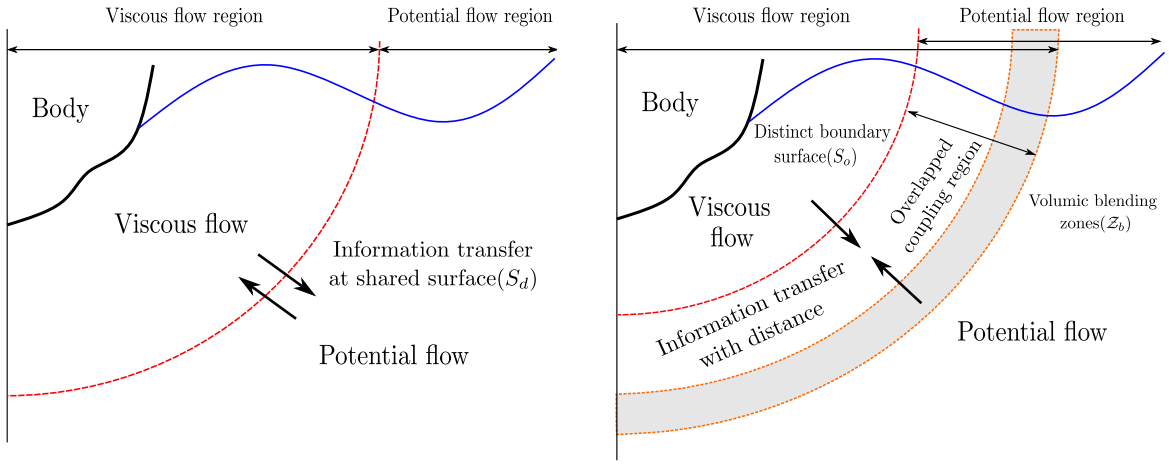

(a) Direct coupling surface

(b) Overlapped coupling region

Figure 1.3. Categorization of coupling methodology by place of information delivery.

Tahara et al. (1992) applied two-way coupling by two distinct boundary surfaces for inviscid and viscous flows, respectively. BEM and FVM are used to solve each flow region, the normal velocity for potential flow and the total velocity for viscous flows being updated at each time step. Campana et al. (1992) used Rankine source BEM and FVM to solve the two-dimensional submerged wings in current with the free surface. The normal velocity for potential flow and the pressure and velocity for viscous flow are imposed as boundary conditions for each flow at direct coupling surface. Later, Campana et al. (1995) applied the two distinct coupling surfaces for the forward speed ship problem and reported that the overlapped region gave a stable simulation. Iafrati and Campana (2003) used FVM for viscous flow in the region near to free surface and BEM for the region body surface to FVM region for the simulation of wave breaking by interaction of current and submerged obstacle. They defined two different coupling techniques, DtN (Dirichlet to Neumann) and NtD (Neumann to Dirichlet), leading to different delivered information. In

the boundary integral equation

$$-4\pi\Phi = \oiint_S \left(G\frac{\partial\Phi}{\partial n} - \Phi\frac{\partial G}{\partial n} \right) dS, \tag{1.1}$$

where Φ is a velocity potential and G is the Green function, DtN update the velocity potential (Φ) on the boundary surface by Bernoulli equation from the obtained pressure in the viscous flow. The Dirichlet boundary condition (Φ) is used to calculate the normal derivatives of velocity potential ($\frac{\partial\Phi}{\partial n}$) along the boundary surface. The velocity calculated from the potential flow is imposed to viscous flow boundary condition. NtD applies a Neumann boundary condition ($\frac{\partial\Phi}{\partial n}$) on the boundary surface by fluid velocity obtained from viscous flow to calculate the velocity potential (Φ). The pressure by Bernoulli's equation is imposed as the boundary condition for viscous flow.

Colicchio et al. (2006) applied the coupling between BEM and FVM with domain decomposition for dam breaking and wave impact problem. Two distinct matching surfaces are used to transfer the velocity, wave elevation or the pressure, and the pressure correction in the viscous flow solver from the obtained potential fluid velocity. They also reported that the overlapped matching surface gives a stable result both in potential and viscous flow solver. Greco et al. (2013) extended up to 3D problem to simulate Green water impact on a deck. To reduce the computational cost of potential flow, Hamilton and Yeung (2011) adopted a cylindrical matching surface and applied the Shell function, which is the surface integrated Green function, to solve potential flow. Fredriksen (2015) limited the viscous flow region near to the corner of two-dimensional moonpool, and attempted to couple velocity and pressure in a segregated numerical algorithm.

A two-way coupling with the linear potential theory based on Poincaré's velocity representation is attempted by Guillerm (2001) for steady forward ship problem. He adopted the overlapped surfaces for both flows and the viscous flow is solved by Finite Difference Method (FDM) with boundary conditions computed by the linear potential flow. As a coupling variable, the normal and tangential velocity is transferred to potential flow, as the boundary condition for viscous flow, the velocity and wave elevation calculated by the potential flow is used. Poincaré's velocity representation for generic free surface flows are given in Noblesse et al. (1997); Noblesse (2001). He suggested the Poincaré's velocity representation for the problems of satisfying free surface conditions $\phi = 0$ and $\frac{\partial\phi}{\partial z} = 0$, steady forward speed, time-harmonic without and with forward speed. After his work on two-way coupling, there has been no more attempt to apply Poincaré's velocity representation for a time-harmonic or unsteady problem.

Two-way coupling solves both flows, consequently the iterations between two flows increase the computational costs. Therefore, one-way coupling is commonly used nowadays by imposing the incident waves as the boundary condition. Chen et al. (2005); Kim et al. (2012); Jacobsen et al. (2012); Paulsen et al. (2014) applied a relaxation/blending scheme in volumic relaxation zones, which relaxing the total flows into incident components. Therefore, the scattering term shall be blended zero smoothly in the relaxation zone. The weight function gives an extra source in relaxation zones, therefore, it generates unnecessary waves in the computation domain (Perić et al., 2018b).

Functional decomposition

The functional decomposition (FD) splits the total solution into potential and viscous flow components in the same computational domain. The governing equations and boundary conditions are reformulated for the quantities of interest. The Helmholtz decomposition theorem states that the total fluid velocity can be decomposed into the irrotational and vortical velocity (Arfken et al., 1995)

$$\mathbf{u} = \mathbf{v} + \nabla\Phi, \tag{1.2}$$

where $\mathbf{v}$ is a rotational velocity and Φ is velocity potential. $\mathbf{v}$ and $\nabla\Phi$ satisfiy the continuity equation

$$\nabla \cdot \mathbf{v} = 0, \qquad \nabla^2\Phi = 0, \tag{1.3}$$

and

$$\nabla \cdot \mathbf{u} = \nabla \cdot \mathbf{v} + \nabla^2\Phi = 0, \qquad \nabla \times \mathbf{u} = \nabla \times \mathbf{v}. \tag{1.4}$$

Based on the Helmholtz decomposition theorem, Kim et al. (2005) proposed a complementary Reynolds Averaged Navier-Stokes Equations(RANSE) that solves the vortical velocity. Potential flow solver calculates the irrotational velocity. Consequently, the Euler terms are cancelled in the momentum equation. They reported that the functional decomposition reduces the computational cost by adopting a coarse grid in the far-field. For the 2D wing problem, Edmund (2012); Rosemurgy (2014) manipulated the body boundary condition for potential flow that the contribution of vortical velocity is taken into account by integrating them within the boundary layer. Following the equation (1.2), the derivative of velocity potential on the body surface is given as

$$\mathbf{u} = 0, \quad \Longleftrightarrow \quad \nabla\Phi = -\mathbf{v}. \tag{1.5}$$

The normal derivative of velocity potential is given in

$$\nabla\Phi \cdot \mathbf{n} = -\mathbf{v} \cdot \mathbf{n}, \tag{1.6}$$

where $\mathbf{n}$ is normal vector at body surface. In a local-orthogonal coordinate system shown in figure 1.4

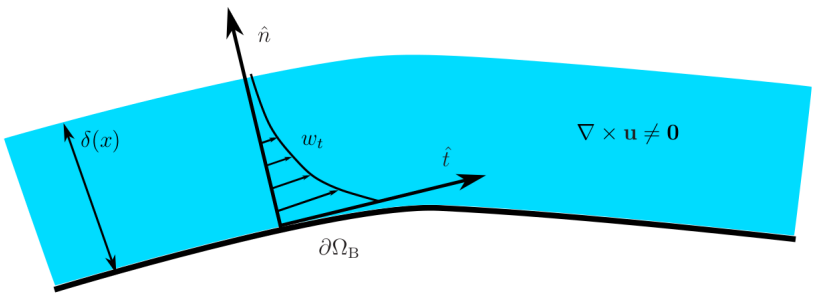

Figure 1.4. A local coordinate system and the boundary layer with thickness δ. In the figure, different notations are used. $\mathbf{n} = \hat{n}$ and $\mathbf{t} = \hat{t}$, $w_t = v^t$, $\delta\Omega_B$ represents the body surface (Rosemurgy, 2014).

the vortical velocity and gradient operator can be decomposed into the normal and tangential components

$$\mathbf{v} = v^n\mathbf{n} + v^t\mathbf{t}, \quad \text{and} \quad \nabla = \frac{\partial}{\partial n}\mathbf{n} + \frac{\partial}{\partial t}\mathbf{t}, \tag{1.7}$$

where $\mathbf{t}$ is an unit tangential vector in local coordinate. Using the continuity equation given in (1.3)

$$\frac{\partial v^n}{\partial n} + \frac{\partial v^t}{\partial t} = 0. \tag{1.8}$$

Integrating the equation along the local normal direction from body surface to the boundary thickness δ

$$\begin{aligned} \int_0^\delta \frac{\partial v^n}{\partial n} dn &= -\int_0^\delta \frac{\partial v^t}{\partial t} dn \\ v^n(\delta) - v^n(0) &= -\int_0^\delta \frac{\partial v^t}{\partial t} dn \\ v^n(0) &= \int_0^\delta \frac{\partial v^t}{\partial t} dn + v^n(\delta). \end{aligned} \tag{1.9}$$

By definition of boundary layer, $v^n(\delta) \approx 0$. Therefore, the body boundary condition given in (1.6) is written as

$$\begin{aligned} \nabla\Phi \cdot \mathbf{n} &= -\mathbf{v} \cdot \mathbf{n} = -v^n(0) \\ &= -\int_0^\delta \frac{\partial v^t}{\partial t} dn. \end{aligned} \tag{1.10}$$

An user-defined threshold is used to calculate boundary layer thickness. Potential and viscous flow satisfying the body boundary condition given in (1.10) are solved iteratively. The details are explained in Edmund (2012); Rosemurgy (2014). Recently, Chen and Maki (2017) extended it up to 3D seakeeping problem.

Ferrant et al. (2003) introduced a functional decomposition method which is named as Spectral Wave Explicit Navier-Stokes Equations (SWENSE). It assumes that the total flow has two components:(1) incident wave flow and (2) complementary wave flow as

$$\chi = \chi_I + \chi_C, \tag{1.11}$$

where χ, χ_I and χ_C are the flow quanties of total, incident wave and complementary waves, respectively. The incident flow terms are subtracted from the Navier-Stokes equation and equations are reconstructed with respect to complementary flow terms. The nonlinear incident wave model being thought to satisfy Euler equations can be canceled. Figure 1.5 shows the SWENSE method to decompose the functional quantities of total flow into incident and complementary parts.

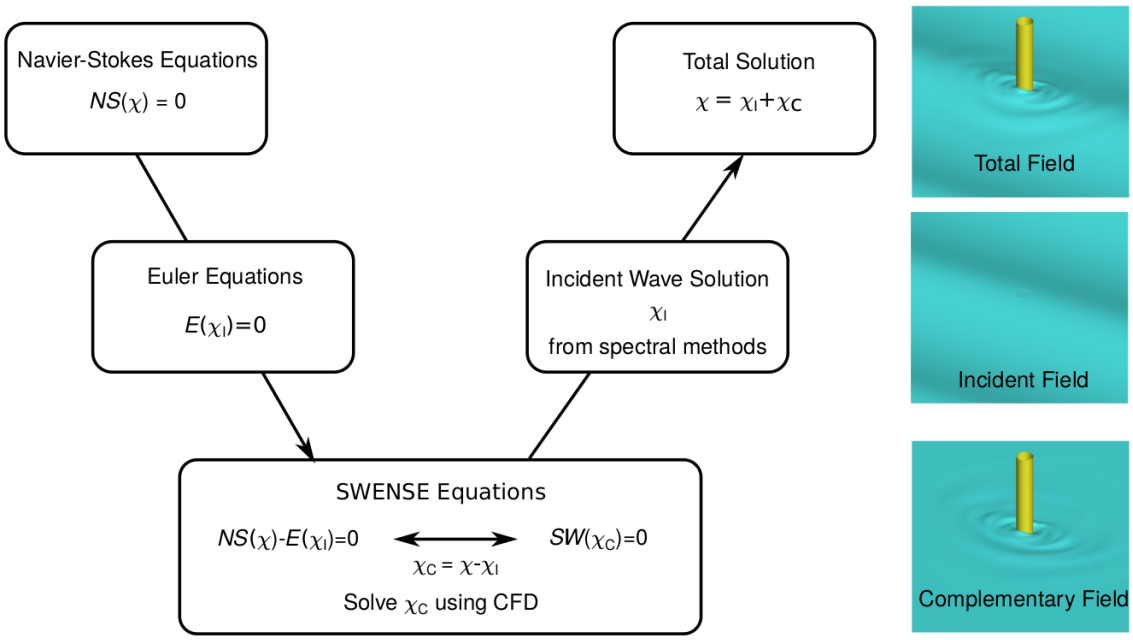

Figure 1.5. The SWENSE method to decomose the functional quantities of total flow into incident and complementary parts (Li, 2018).

It makes the computational grid to be modeled dense near to the body only and is thought as efficient. This methodology has been applied for single-phase fluids by Luquet et al. (2003); Gentaz et al. (2004); Monroy (2010); Reliquet (2013) with marine hydrodynamic purpose. Recently, Vukčević (2016) has reformulated SWENSE in multi-phase flow by decomposing a level-set and fluid velocity, later Li (2018) applied a similar approach with extended incident pressure for VOF field. As boundary conditions, the relaxation schemes are applied in both researches, relaxing the scattering waves with zero.

Summary

The coupling methodology is based on the decomposition of flows that allows to split the computational domain and/or the functional value. The transition of different physics across the components/domains remains a question. The associated previous research is summarized in Table 1.1.

The coupling methodology is categorized by coupling way: (1) Two-way coupling and (2) One-way coupling. The quantities used for coupling are different for research. p and $\mathbf{u}$ are pressure and fluid velocity. Φ is the velocity potential. The subscript $_I$ denotes the incident components and $_n$ and $_t$ are the normal and tangential vector components, respectively. The coupling place where the information is delivered denoted with S and Z when the information is delivered at the surface or volumic zone. SWENSE and FD are when the SWENSE method and functional decomposition is used. S_o, S_s are the case when the overlapped surfaces or one surface is used for coupling. S_{body} and S_∞ are the body surface and the surface at infinity, respectively.

Table 1.1. Summary of previous research on the coupling of potential/viscous flows

Previous research	Coupling way	Coupling values		Coupling region	Numerical model	
		$\Phi \rightarrow NS$	$NS \rightarrow \Phi$		Φ	NS
Tahara et al. (1992)	Two	p, $\mathbf{u}$	Φ_n, Φ_t	S_o	BEM	FVM
Campana et al. (1992)	Two	p, $\mathbf{u} \cdot \mathbf{t}$	Φ_n	S_s	BEM	FVM
Campana et al. (1995)	Two	$\mathbf{u}$	Φ_n	S_s	BEM	FVM
Guillerm (2001)	Two	$\mathbf{u}$	Φ_n, $\nabla \times \Phi$	S_o	Poincaré	FDM
Iafrati and Campana (2003)	Two	p or $\mathbf{u}$	Φ_n or Φ	S_o or S_d	BEM	FVM
Colicchio et al. (2006)	Two	$\mathbf{u}$ or p	Φ_t or Φ_n	S_d	BEM	FVM
Hamilton and Yeung (2011)	Two	u or p	Φ or Φ_n	S_d	Shell func.	FVM
Edmund (2012)	Two	$\mathbf{u}$	Φ_n, $\mathbf{w} \cdot \mathbf{n}$	S_{body}/S_∞	BEM	FVM
Rosemurgy (2014)	Two	$\mathbf{u}$	Φ_n, $\mathbf{w} \cdot \mathbf{n}$	S_{body}/S_∞	BEM	FVM
Fredriksen (2015)	Two	$\mathbf{u}$	Φ	S_o	HPC	FVM
Ferrant et al. (2003)	One	$\mathbf{u}_I$, p_I	-	SWENSE	HOS	FDM
Kim et al. (2005)	One	$\mathbf{u}_I$, p_I	-	FD	BEM	FVM
Kim et al. (2011)	One	$\mathbf{u}_I$, α_I	-	$\mathcal{Z}_R$	Φ_I	FVM
Jacobsen et al. (2012)	One	$\mathbf{u}_I$, α_I	-	$\mathcal{Z}_R$	Φ_I	FVM
Paulsen et al. (2014)	One	$\mathbf{u}_I$, α_I	-	$\mathcal{Z}_R$	FDM	FVM
Vukčević (2016)	One	$\mathbf{u}_I$, ψ_I	-	SWENSE	Φ_I	FVM
Li (2018)	One	$\mathbf{u}_I$, p_I, α_I	-	SWENSE	HOS	FVM

1.3 Governing equations and boundary conditions for viscous and potential flows

1.3.1 Viscous flow

The viscous flow model considers the unsteady, incompressible, and viscous flow. Navier-Stokes equations for viscous flow are given by

$$\nabla \cdot \mathbf{u} = 0, \tag{1.12}$$

$$\frac{\partial(\rho \mathbf{u})}{\partial t} + \nabla \cdot (\rho \mathbf{u}\mathbf{u}) = -\nabla p + \nabla \cdot \boldsymbol{\tau} + \rho \mathbf{g}, \tag{1.13}$$

where $\mathbf{u}$ is fluid velocity, ρ is fluid density, p is pressure, $\boldsymbol{\tau}$ is stress tensor and $\mathbf{g}$ gravitational acceleration. The color function(indicator function) that indicates the fluid region by color function(ϕ^{color}) is used for interface modeling. The transport equation of color function (ϕ^{color}) is given as

$$\frac{\partial \phi^{color}}{\partial t} + \nabla \cdot (\mathbf{u}\phi^{color}) = 0. \tag{1.14}$$

The mathematical and numerical modeling of the interface in the viscous flow model is relatively more flexible than the potential flow model because no assumption of the single-valued function and the series expansion are required. In the present study, the methodology of SWENSE is used to reconstruct the governing equations for complementary components by

$$\mathbf{u} = \mathbf{u}_I + \mathbf{u}_C, \tag{1.15}$$

$$p = p_I + p_C, \tag{1.16}$$

$$\phi^{color} = \phi_I^{color} + \phi_C^{color}, \tag{1.17}$$

where subscript $_{I,C}$ represent the incident wave and complementary components, respectively. The incident waves satisfy the nonlinear free surface boundary condition discussed in the previous section, consequently, the incident wave terms that corresponds to Euler equations can be cancelled. The governing equations for complementary components are written as

$$\nabla \cdot \mathbf{u}_C = 0, \tag{1.18}$$

$$\frac{\partial(\rho \mathbf{u}_C)}{\partial t} + \nabla \cdot (\rho \mathbf{u}\mathbf{u}_C) = -\nabla \cdot (\rho \mathbf{u}_C \mathbf{u}_I) - \nabla p_C + \nabla \cdot \boldsymbol{\tau}, \tag{1.19}$$

$$\frac{\partial \phi_C^{color}}{\partial t} + \nabla \cdot (\mathbf{u}\phi_C^{color}) = -\frac{\partial \phi_I^{color}}{\partial t} - \nabla \cdot (\mathbf{u}\phi_I^{color}). \tag{1.20}$$

In a physical sense, the complementary components are significant in the vicinity of body, and they decay as the distance increases due to energy conservation. Therefore, coarse mesh can be used in the far-field where the complementary potential flow is considered to represent the physical quantities through the two-way coupling.

Interface boundary coditions for viscous flow model will be discussed in Chapter 6.

1.3.2 Potential flow

The potential flow formulation is based on the assumption that the fluid is incompressible and inviscid and the flow is irrotational. A velocity potential can be introduced from the assumption. It satisfies the Laplace equation in the whole fluid domain

$$\nabla^2 \Phi = 0, \qquad \text{in} \qquad \mathbf{x} \in \Omega_w, \tag{1.21}$$

where Φ is the velocity potential and Ω_w is the fluid domain. The free surface (Ξ) is assumed to be a single-valued function

$$\Xi = \Xi(x, y; t) \tag{1.22}$$

and the kinematic free surface condition for potential flow is given as

$$\frac{D\Xi(x,y,t)}{Dt} = 0 \qquad \Leftrightarrow \qquad \frac{\partial \Xi}{\partial t} + \frac{\partial \Phi}{\partial x}\frac{\partial \Xi}{\partial x} + \frac{\partial \Phi}{\partial y}\frac{\partial \Xi}{\partial y} + \frac{\partial \Phi}{\partial z} = 0, \qquad \text{on} \quad \mathbf{x} = \Xi. \tag{1.23}$$

Remark that the total derivatives are given as $\frac{D}{Dt} = \frac{\partial}{\partial t} + (\nabla\Phi - \mathbf{U}) \cdot \nabla$ when a forward speed ($\mathbf{U}$) is considered. The dynamic free surface boundary condition for potential flow is derived from Bernoulli's equation as

$$p_a = p_w \qquad \Leftrightarrow \qquad \frac{\partial \Phi}{\partial t} + \frac{1}{2}\nabla\Phi \cdot \nabla\Phi + g\Xi = 0, \qquad \text{on} \quad \mathbf{x} = \Xi, \tag{1.24}$$

where p_a and p_w are the water and air pressure infinitesimally closed to the free surface. The kinematic and dynamic conditions involve both wave elevation and velocity potential. It is useful to combine the free surface boundary condition expressed in velocity potential as

$$\frac{\partial^2 \Phi}{\partial t^2} + g\frac{\partial \Phi}{\partial z} + 2\nabla\Phi \cdot \nabla \frac{\partial \Phi}{\partial t} + \frac{1}{2}\nabla\Phi \cdot \nabla\left(\nabla\Phi \cdot \nabla\Phi\right) = 0, \quad \text{on} \quad \mathbf{x} = \Xi. \tag{1.25}$$

Note that the free surface boundary condition is highly nonlinear and is imposed on the unknown free surface. Two nonlinearties arise from nonlinear terms and unknown free surface make the free surface problem difficult to solve. Laplacian in the equation (1.21) is linear operator, therefore the perturbation series can be introduced as

$$\Phi = \Phi^{(1)} + \Phi^{(2)} + \Phi^{(3)} + \cdots, \tag{1.26}$$

$$\Xi = \Xi^{(1)} + \Xi^{(2)} + \Xi^{(3)} + \cdots, \tag{1.27}$$

Substituiting the perturbation series into equation (1.25) and applying a Taylor series expansion with respect to wave elevation, the linear free surface boundary condition is obtained as

$$\frac{\partial^2 \Phi^{(1)}}{\partial t^2} + g\frac{\partial \Phi^{(1)}}{\partial z} = 0, \qquad \text{on} \quad z = 0. \tag{1.28}$$

For higher-order potential problem, the nonlinear terms appear in right-hand-sides so that the boundary conditions are non-homogeneous

$$\frac{\partial^2 \Phi^{(m)}}{\partial t^2} + g\frac{\partial \Phi^{(m)}}{\partial z} = Q^{(m)}, \qquad \text{on} \quad z = 0. \tag{1.29}$$

where $Q^{(m)}$ is the source term given by the combination of lower-order free surface quantities. This expansion method is called *Stokes's expansion* and the boundary value problems for each order of velocity potential can be set up. As the order of problem increases, the boundary condition becomes more complex and nonlinear.

The velocity potential can be decomposed again as

$$\Phi = \Phi_I + \Phi_C, \tag{1.30}$$

where Φ_I is an incident wave potential, and Φ_C is a complementary (scattering; diffraction-radiation) potential. In the present study, the fully nonlinear free surface boundary conditions are applied for the incident wave potential

$$\begin{aligned} &\frac{\partial \Xi_I}{\partial t} + \frac{\partial \Phi_I}{\partial x}\frac{\partial \Xi_I}{\partial x} + \frac{\partial \Phi_I}{\partial y}\frac{\partial \Xi_I}{\partial y} + \frac{\partial \Phi_I}{\partial z} = 0 \\ &\frac{\partial \Phi_I}{\partial t} + \frac{1}{2}\nabla\Phi_I \cdot \nabla\Phi_I + g\Xi_I = 0 \end{aligned}, \qquad \text{on} \quad \mathbf{x} = \Xi_I, \tag{1.31}$$

and the linearized free surface boundary condition is used for the complementary potential

$$\begin{aligned} &\frac{\partial \Xi_C}{\partial t} + \frac{\partial \Phi_C}{\partial z} = 0 \\ &\frac{\partial \Phi_C}{\partial t} + g\Xi_C = 0 \end{aligned}, \qquad \text{on} \quad z = 0. \tag{1.32}$$

The incident waves evolve in space and time. And the interaction between waves to waves generates the nonlinearity which is unpredictable and occurs at arbitrary space and time. It is necessary to consider the nonlinear boundary condition for incident waves. Meanwhile, the complementary potential generated by the existence of the body decreases as the distance from body surface increases in the 3D problem. The nonlinearity of potential flow without forward speed is governed by the wave steepness. Therefore a linear free surface boundary condition can be applicable for the complementary potential in the far-field. The nonlinearity from body surface perturbation is not considered here because the complementary potential flow is defined in outer sub-domain only.

1.3.3 Summary and coupling of two flows

The configurations of computational domain and functional quantities considered in previous study are shown in figure 1.6.

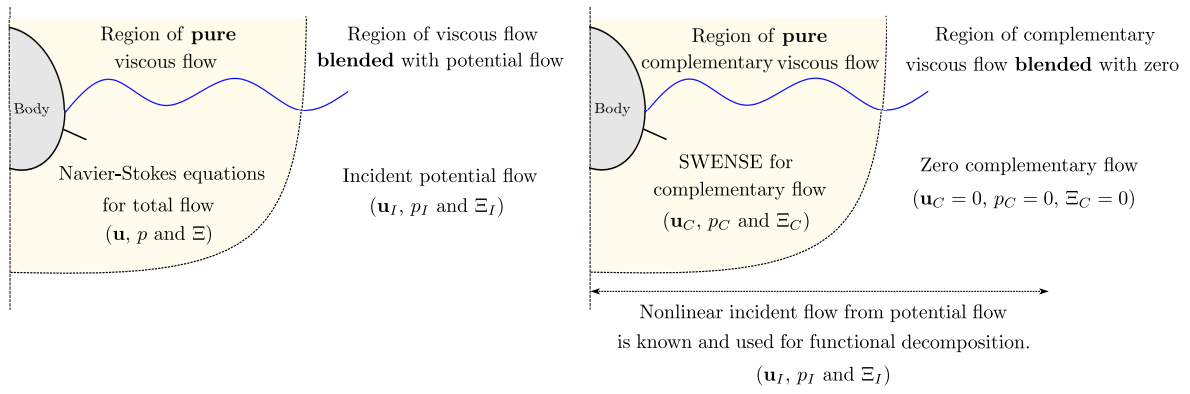

(a) NS equations **(b)** SWENSE method

Figure 1.6. Configurations of computation domain and functional quantities used in previous studies.

Figure 1.6a explains the configuration of computation when the Navier-Stokes equations is solved for wave-structure interaction problem. The total functional quanties considered for computation are blended to the quantities of incident potentital flow in the far-field. This configuration has been commonly applied for wave-structure interaction problem (Seng, 2012; Paulsen et al., 2014; Monroy et al., 2016).

Figure 1.6b states when the SWENSE method is used for computation. The functional quantities of incident flow are already defined in the whole computational domain. Therefore, the complementary functional quanties considered in the viscous flow model is blended to zero in the far-field (Ferrant et al., 2003; Gentaz et al., 2004; Vukčević, 2016; Li, 2018).

The configurations of computational domain and functional quantities considered in the present study is depicted in figure 1.7.

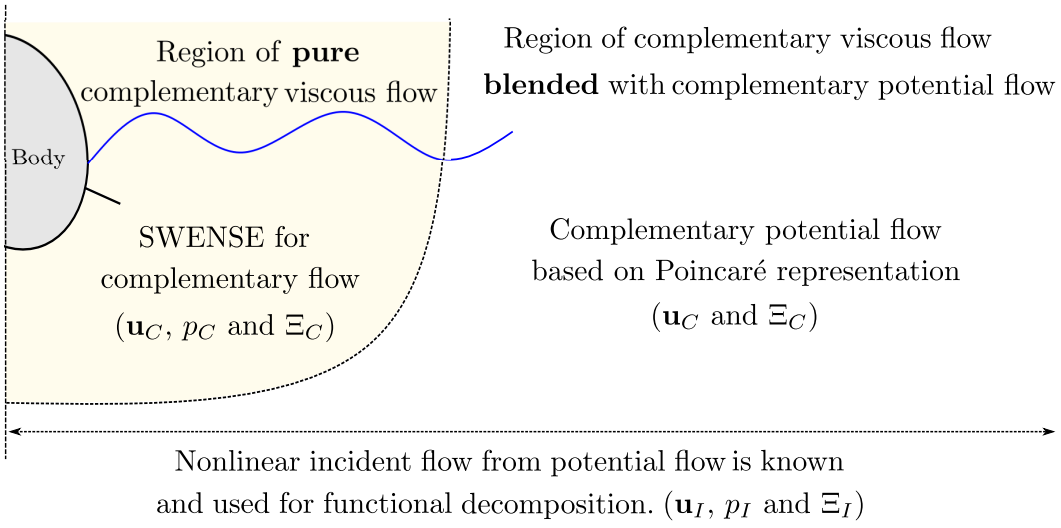

Figure 1.7. Configuration considered in the present study.

A hypothesis that total flow can be decomposed into the incident and complementary is assumed. The functional quantities of potential and viscous flow are decomposed into the incident and complementary flow parts. The functional quantities of nonlinear incident flow is known in a whole fluid domain. The computational domain of potential and viscous flow models are divided for complementary flow. In the vicinity of structure, the viscous flow model based on Spectral Wave Explicit Navier-Stokes Equation (SWENSE) method is used. Turbulence model is not considered. A linear potential flow model based on Poincaré's velocity representation applied in the far-field. No wave breaking is allowed for complementary waves and the interaction between incident waves is not considered.

Figure 1.8 shows the place of coupling between viscous and potential flows.

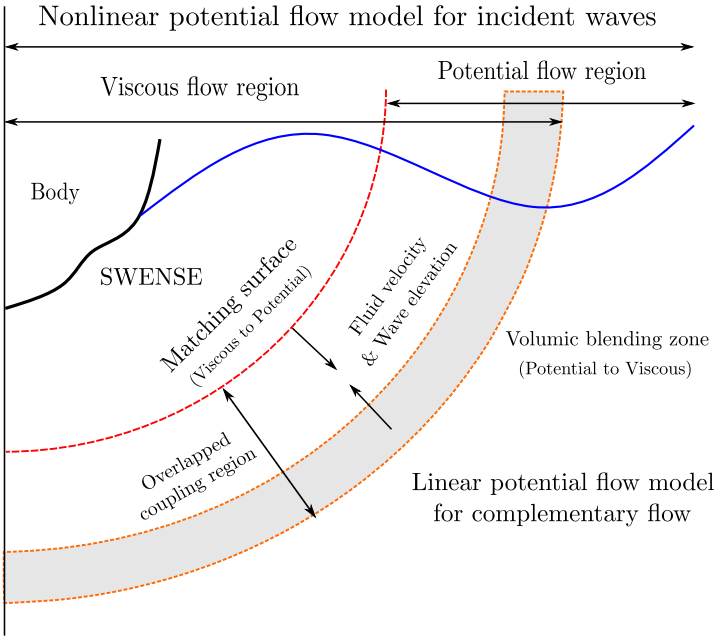

Figure 1.8. Coupling strategy used in the present study.

Overlapped coupling region with the matching surface for potential flow and the volumic blending zone (relaxation zone) for viscous flow are considered in the domain decomposition. The matching surface is located inside of the computational domain of the viscous flow model. The rotational velocity components are assumed to be zero from the matching surface to infinity, e.g. no viscous effects from the matching surface. On the matching surface, the complementary flow velocity and wave elevation obtained from the viscous flow model are used as the boundary condition for potential flow model. By using the linear potential flow model, the complementary flow velocity and wave elevation are reconstructed in the region of far-field. At the volumic blending zone, being located in the region of far-field, the complementary flow velocity and wave elevation from linear potential flow model are imposed as the boundary conditions for viscous flow.

1.4 Contribution of work

The purpose of present study is the two-way coupling between potential and viscous flows in a marine application, especially for unsteady time-domain wave-structure interaction problems.

A hypothesis that total flow can be decomposed into the incident and complementary is assumed. The functional quantities of potential and viscous flow are decomposed into the incident and complementary flow parts. The governing equations and boundary conditions for each flow part are reformulated. It is assumed that the nonlinear potential flow model for incident waves is available in a whole fluid domain and satisfies Euler equations. It makes us divide the computational domain of potential and viscous flow models only for complementary waves. In the vicinity of structure, the viscous flow model based on Spectral Wave Explicit Navier-Stokes Equation(SWENSE) method is used to solve complementary waves generated by the structure. In the far-field, the potential flow model based on Poincaré's velocity representation is applied to simulate complementary waves.

The following specific contributions are made in the present study.

- A preliminary study on the coupling of potential and viscous flows is conducted. The results show that the obtained solution of blending to potential flows gives good results and the solution converges faster. The two-way coupling allows us to use a small computation domain for the same accuracy of the solution, but the total computation time increases due to the extra expenses of calculating the potential flows. Therefore, a fast potential flow model with effective blending schemes is necessary for coupling.
- The generation of nonlinear irregular waves in the three-dimensional viscous domain is proposed with nonlinear potential flow solver which is called Higher Order Spectral (HOS) method Ducrozet et al. (2007, 2012). The algorithm uses a Fast Fourier Transform (FFT) and multi-dimensional cubic spline interpolation, the generation of three-dimensional irregular waves in viscous flow model is achieved fastly. The results are validated againist HOS simulations and experiments.
- A new potential flow in the time domain is introduced based on Poincaré's velocity representation. It is formulated alternatively with arbitary and cylindrical matching surfaces.

The numerical algorithms on the new type of Green function and the elementary functions are proposed. The proposed model is validated by comparing with analytic potential solution based on linear theory.

- A viscous flow model based on SWENSE with Level-set is proposed in the present study. The functional quantities are decomposed into the incident and complementary components. The governing equations are reconstructed with respect to viscous complementary parts. The results are validated with multi-phase solver in a framework of OpenFOAM.
- The numerical algorithm for the coupling of potential and viscous flows is introduced. It is assumed that the nonlinear potential flow model for incident waves is available in a whole fluid domain. The computational domain of potential and viscous flow models only for complementary waves is decomposed. In the vicinity of structure, the viscous flow model based on SWENSE method is used. In the far-field, the potential flow model based on Poincaré's velocity representation is applied. It is assumed that the computed fluid velocity and wave elevations are continuous across the flow models. A benchmark test on the coupling methodology is considered.

1.5 Thesis outline

Chapter 2 presents the preliminary study on the coupling of potential and viscous flows. A parameteric study on the viscous flow solver is investigated before the preliminary study. The wave propagation with inlet/outlet and the two-dimensional radiation problem with different outlet conditions are considered. The necessity of new efficient potential flow representation is drawn from the results of this preliminary study.

Chapter 3 summarizes the nonlinear potential theory on incident waves including regular and irregular cases. A stream function wave theory for regular wave and a pseudo-spectral method for irregular waves are briefly reproduced. For the efficient generation of three-dimensional irregular waves in viscous flow solver, the interpolation methodology with respect to space and time is proposed with the B-spline curve. The generation of nonlinear irregular waves in viscous flow model is validated with nonlinear potential theory and experiment.

Chapter 4 introduces a new potential representation for linear complementary waves which is based on Poincaré's velocity representation. It is newly formulated for an unsteady time domain free surface problem. The complementary fluid velocity at field point is explicitly represented by the distribution of complementary fluid velocity and wave elevation on the matching surface with the help of the time domain Green function. It is proved that a new form of time domain Green function satisfies an ordinary differential equation and the solving technique is presented for efficient evaluation. The analytical solution for a heaving hemisphere based on linear potential theory is selected as a benchmark test case. The results show good agreements when the field point is located underwater. However, a singular behavior is obtained when the field point is located on the mean free surface due to the diverging behavior of the time domain Green function.

Chapter 5 introduces a vertical circular cylindrical matching surface to remove the singular

behavior of the proposed Poincaré's velocity representation. A pseudo-spectral method with Fourier-Laguerre and Fourier approximations of the complementary velocity and wave elevation are applied, respectively. The analytic surface integral with Poincaré's velocity representation requires the evaluation of elementary functions which are the surface integral of a Green function with Fourier-Laguerre modes. Two numerical algorithms based on the *summation and extrapolation* and *steepest descent method* are presented to calculate the elementary functions. After the vertical velocity on the free surface is calculated from Poincaré's velocity representation, the wave elevation is reconstructed by a linear kinematic free surface boundary condition. To couple with the multiphase flow solver, the Wheeler stretching is applied to extend the velocity above the mean free surface. As the benchmark test, the heaving hemisphere and diffraction by vertical circular cylinder are considered. The results show good agreements with the analytical solution.

Chapter 6 presents the viscous flow model based on SWENSE methodology. The momentum and pressure equations are reformulated by introducing the viscous complementary flow. The fluid velocity, pressure and Level-set function are decomposed into the incident and complementary parts. An extrapolation of air velocity with cubic polynomials is introduced to give smooth incident wave velocity profile. Moreover, the re-distancing the Level-set function is adopted to keep the interface sharp. The parametric study on the discretization of time and mesh, wave propagation, and cylinder diffraction problem is conducted for validation.

Chapter7 presents the coupling algorithm of potential and viscous flows. The benchmark tests with the vertical circular cylinder in regular waves and calm buoy in regular and irregular waves are considered. The discussion on the effect of coupling is made from the simulation results of with/without coupling methodology.

Chapter 8 summarizes the contribution of the present study. Conclusions and perspectives are given.

2 Preliminary study on the coupling of potential and viscous flows

2.1 Description on the preliminary study

The objective of the preliminary study is to investigate the feasibility of a coupling methodology between potential and viscous flows when the solution of potential flow is available at the boundaries of the viscous flow model. Therefore, different outlet conditions including the potential flow and other outlets are considered for comparison. In the preliminary study, `foamStar` which is based on the multiphase flow model in the framework of OpenFOAM is used (Seng, 2012; Monroy et al., 2016). The computation algorithm of `foamStar` is described in figure 2.1. When the simulation time is advanced, weight functions in the relaxation zones (boundaries) are updated. In the outer iteration (PIMPLE; Combination of PISO and SIMPLE algorithms), the floating body dynamics is solved by the mechanical solver, the computational mesh is updated from the displacement of the floating body, and the α transport equation is solved and relaxed to target α^{Target} at the boundaries. After solving PISO loop, $\mathbf{u}$ is also relaxed to target velocity $\mathbf{u}^{Target}$ at boundaries. A parametric study on `foamStar` is conducted before the preliminary study. The propagating incident waves in a numerical wave tank and the swaying Lewis form are considered as the benchmark test cases for different outlets.

2.2 Parametric study on the viscous solver

The parametric study is conducted on `foamStar` to find proper parameters for wave propagation. Fully nonlinear regular wave are considered and the condition is given in Table 2.1. The case considered here is a two-dimensional domain with a cyclic lateral boundary condition, where waves are initialized at the initial time from a fully nonlinear stream function waves (Rienecker and Fenton, 1981; Ducrozet et al., 2019). The schematic view of the problem, the initialized Volume Of Fluid (VOF; α) and the computational mesh are shown in figure 2.2. The computational domain has the length of one wavelength (1λ) and the height is taken to be $2h$ ($h = 0.6m$; water depth). Except if indicated otherwise in the parametric study, the computational meshes are uniformly spaced in a longitudinal direction with length $\Delta x = \lambda/100$. For vertical direction, the cell height is taken to be $\Delta z = H/40$ in $z \in [-H, H]$ and the cell height is gradually stretched as it goes far from the mean free surface.

Table 2.1. Wave condition for parametric study of foamStar.

Item	Unit	Value
Water depth (h)	[m]	0.6
Wave period (T)	[s]	0.7018
Wave height (H)	[m]	0.0575
Wavelength (λ)	[m]	0.8082
H/λ	[-]	0.0712

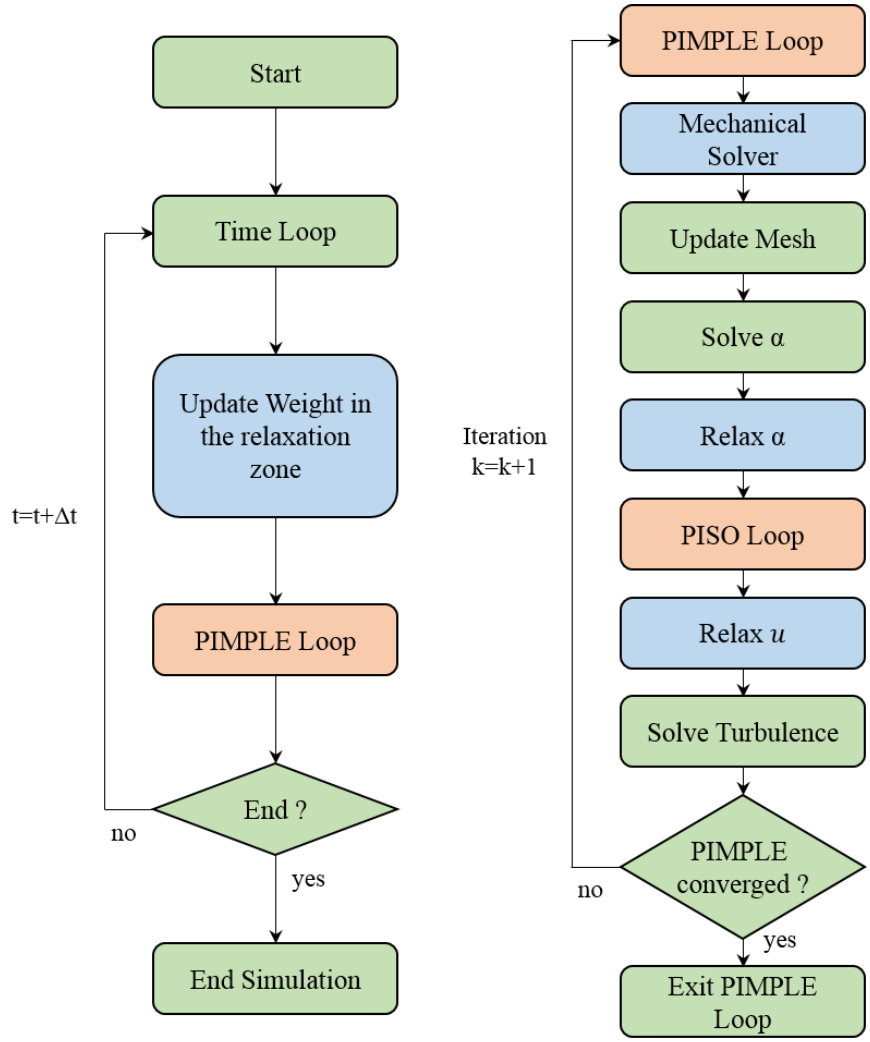

Figure 2.1. The computational algorithm in foamStar (from Monroy et al. (2016))

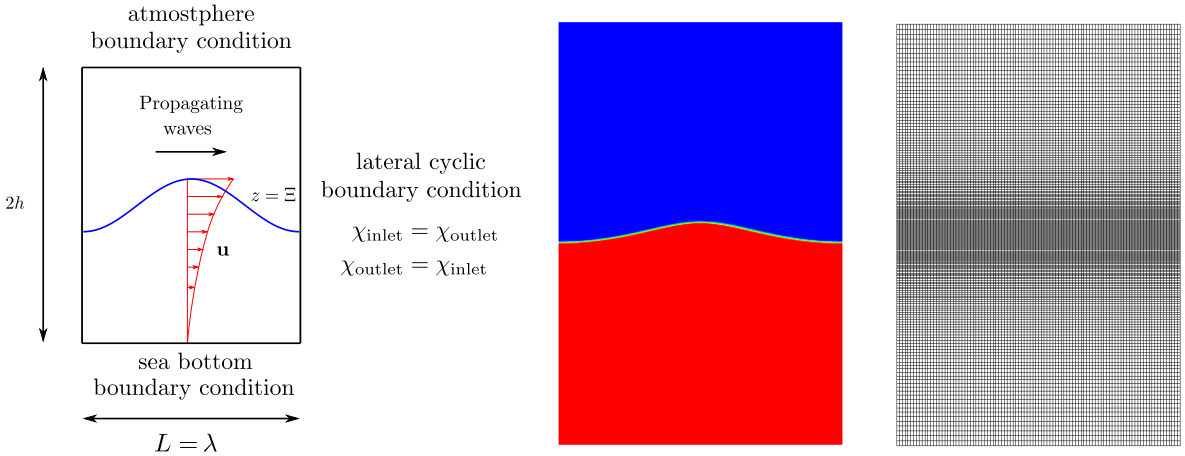

(a) Computational domain **(b)** Initialized α-field **(c)** Computational mesh

Figure 2.2. Schematic view on the parametric study of propagating waves with the cyclic lateral boundary condition.

2.2.1 Time integration scheme

Time integration schemes for an unsteady problem in OpenFOAM can be selected among Implicit Euler, Crank-Nicolson, and second-order backward schemes. The standard multi-phase solver of OpenFOAM, `interDymFoam`, uses a special module which is called MULES to solve the α-transport equation, where α is the Volume Of Fluid (VOF). MULES employs the Flux-Corrected Transport (FCT) scheme by Boris and Book (1973); Zalesak (1979), therefore the computation procedure is decomposed into the predictor and corrector steps, for controlling the α boundedness. As an example, α is computed with the implicit Euler scheme in the predictor step

$$\frac{(V)_P^{n+1}(\alpha)_P^* - (V)_P^n(\alpha)_P^n}{\Delta t} + \sum_f F_{\alpha,f}^b = 0, \tag{2.1}$$

where the superscript ^{*,n} denotes the predictor and time iteration respectively, V is a cell volume, and subscript $_P$ denotes an owner cell. Δt is the time step between two successive time iterations, f represents the face index surrounding the owner cell. $F_{\alpha,f}^b$ is the bounded flux computed by using a low-order convection scheme. After the predictor step, the flux limiter λ_f^{limit} is evaluated by the predicted α^* and the unbounded flux ($F_{\alpha,f}^u$) which is computed with a high-order scheme. In the corrector step, α is corrected with flux limiter and unbounded flux

$$\frac{(V)_P^{n+1}(\alpha)_P^{n+1} - (V)_P^{n+1}(\alpha)_P^*}{\Delta t} + \sum_f \lambda_f^{limit}(F_{\alpha,f}^u - F_{\alpha,f}^b) = 0. \tag{2.2}$$

By summing equations (2.1) and (2.2), the original discretized α transport equation is obtained. The detailed algorithm of MULES can be found in Damián (2013). Because MULES needs the α flux to be bounded in the predictor step, the time integration schemes are limited to Euler implicit and Crank-Nicolson schemes in OpenFOAM. Euler and Crank-Nicolson time integrations are obtained by applying different weights on the present and next time steps. When an ordinary differential equation, $\dot{y} = f(t, y)$, is given, a weight factor is applied on the right-hand-side to solve the equation

$$\frac{y^{n+1} - y^n}{\Delta t} = \gamma f^{n+1} + (1-\gamma) f^n. \tag{2.3}$$

where $\gamma \in [0, 1]$. $\gamma = 0$ and $\gamma = 1$ represent the explicit and implicit Euler time integration schemes respectively, and $\gamma = \frac{1}{2}$ is classified as an original Crank-Nicolson scheme. In OpenFOAM, γ is selectable between in range of $\gamma \in \left[\frac{1}{2}, 1\right]$ for numerical stability and Crank-Nicolson number (c_{CN}) is introduced instead of γ

$$c_{CN} = \frac{1-\gamma}{\gamma}, \qquad c_{CN} \in [0, 1]. \tag{2.4}$$

where $c_{CN} = 0$ represents fully implicit Euler integration, and $c_{CN} = 1$ is the original Crank-Nicolson scheme. It is commonly recommended to use $c_{CN} \approx 0.9$ as a compromise between stability and accuracy. It is known that the Crank-Nicolson scheme is unconditionally stable and has a second-order accuracy, but the obtained solution is characterized by an oscillatory behavior which results in numerical instability. Implicit Euler schemes are unconditionally stable and are immune to the oscillatory behavior. Nevertheless, it induces significant numerical damping leading to poor results, especially for wave propagation problems.

Simulations were performed with different Crank-Nicolson numbers, $c_{CN} = 0$ (Euler implicit), 0.5 and 0.95 to observe the effect of the time integration scheme. Figure 2.3 compares the measured wave elevation at the center of domain with the wave crest and trough values given by stream function wave theory. The moving window Fast Fourier Transform (mwFFT) is applied to wave elevation time series and the first harmonic amplitudes and phases are plotted in figure 2.4. The measured wave amplitudes, evaluated with the implicit Euler scheme and the Crank-Nicolson scheme, decrease gradually over simulation time. Moreover, the phase difference between the CFD result and the analytical solution becomes larger when the low-order time integration scheme is adopted. Results show that propagating waves need at least second order time integration scheme not to damp it out. In the present study, the Crank-Nicolson scheme with $c_{CN} = 0.95$ is selected for time integration.

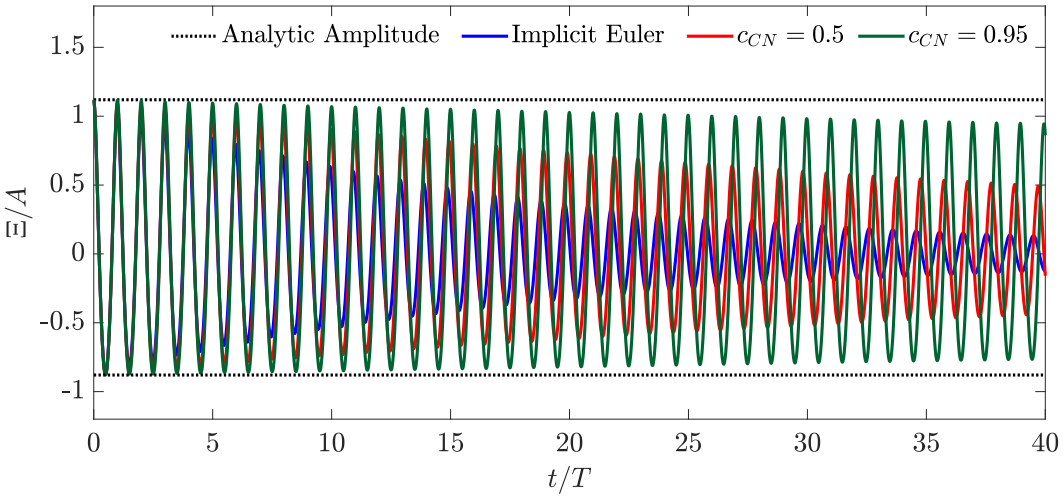

Figure 2.3. The measured wave elevation time series with respect to different Crank-Nicolson numbers (c_{CN}).

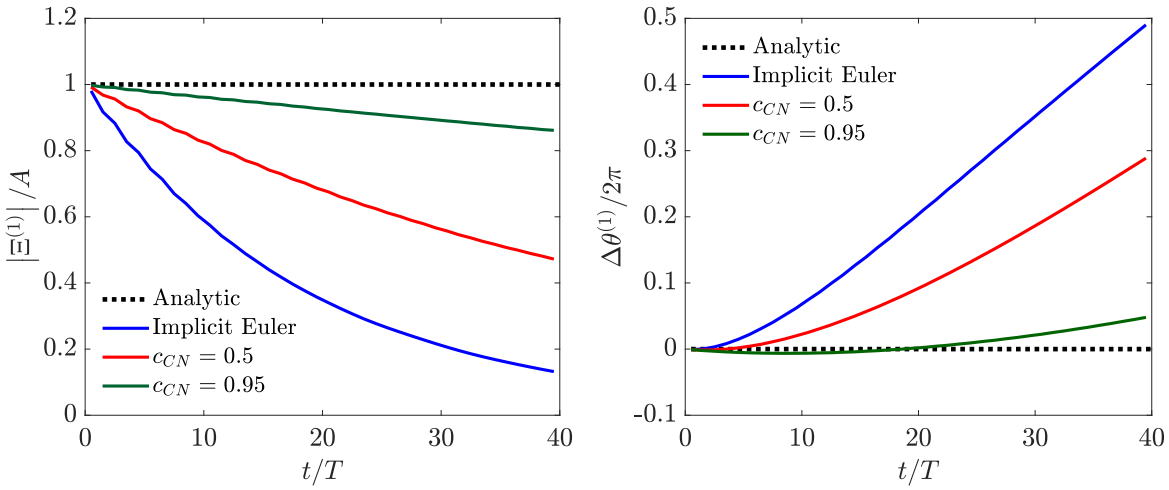

(a) Hamonic amplitudes **(b)** Phase differences

Figure 2.4. Comparison of first-harmonic wave amplitudes and its phase differences with respect to Crank-Nicolson number (c_{CN}).

2.2.2 Mesh and time convergence

The computational grid and time steps are tested with different discretizations to check the order of convergence of the solver. The considered cell length Δx, height Δz, and time step Δt are given in Table 2.2. The representative Courant (Co) and cell-Reynolds (Re_Δ) numbers are defined by using analytic wave fluid velocities as

$$\mathrm{Co} = \sqrt{\mathrm{Co}_x^2 + \mathrm{Co}_z^2}, \qquad \mathrm{Re}_\Delta = \sqrt{\mathrm{Re}_{\Delta x}^2 + \mathrm{Re}_{\Delta z}^2} \tag{2.5}$$

with,

$$\mathrm{Co}_x = \frac{u_{\mathrm{wave}}\Delta t}{\Delta x}, \quad \mathrm{Co}_z = \frac{w_{\mathrm{wave}}\Delta t}{\Delta z}, \quad \mathrm{Re}_{\Delta x} = \frac{u_{\mathrm{wave}}\Delta x}{\nu}, \quad \mathrm{Re}_{\Delta z} = \frac{w_{\mathrm{wave}}\Delta z}{\nu}$$

where u_{wave} and v_{wave} are the horizontal and vertical fluid velocities given by stream function waves, ν is the kinematic viscosity of water. Two series of tests are conducted, one where grid and time steps are set to change the cell Reynolds number keeping the Courant number fixed and the second where the grid is fixed and the time step is only varied to have different Courant numbers. The first-harmonic amplitudes of the wave elevation obtained over time for different Courant and cell Reynolds numbers are compared in figure 2.5. The results are compared with different convection schemes used for momentum equation $\rho\mathtt{U}$. The V-scheme means that the flow limiters are calculated separately for each vector components. It results in a more stable but less accurate simulation than the simulation case without V-scheme. The results with V-scheme are more accurate than without V-scheme, but the simulation becomes unstable with increasing time. The parameter used for the convergence analysis is the wave elevation first harmonic amplitude computed for the first ten wave periods. The order of convergence is computed by the procedure of Eça and Hoekstra (2014), which applies the least square method to get the order of convergence (p) and uncertainty. The order of convergence for the discretization of Courant and cell-Reynolds numbers with different convection schemes are plotted in figure 2.6.

Table 2.2. Mesh and time discretization for the convergence tests.

Case	$\lambda/\Delta x$	$H/\Delta z$	$T/\Delta t$	Co	Re_Δ
Mesh025-dt100	25	5	100	0.171	8,836
Mesh050-dt200	50	10	200	0.171	4,418
Mesh100-dt400	100	20	400	0.171	2,209
Mesh200-dt800	200	40	800	0.171	1,105
Mesh100-dt100	100	20	100	0.684	2,209
Mesh100-dt200	100	20	200	0.342	2,209
Mesh100-dt800	100	20	800	0.086	2,209
Mesh100-dt1600	100	20	1600	0.043	2,209

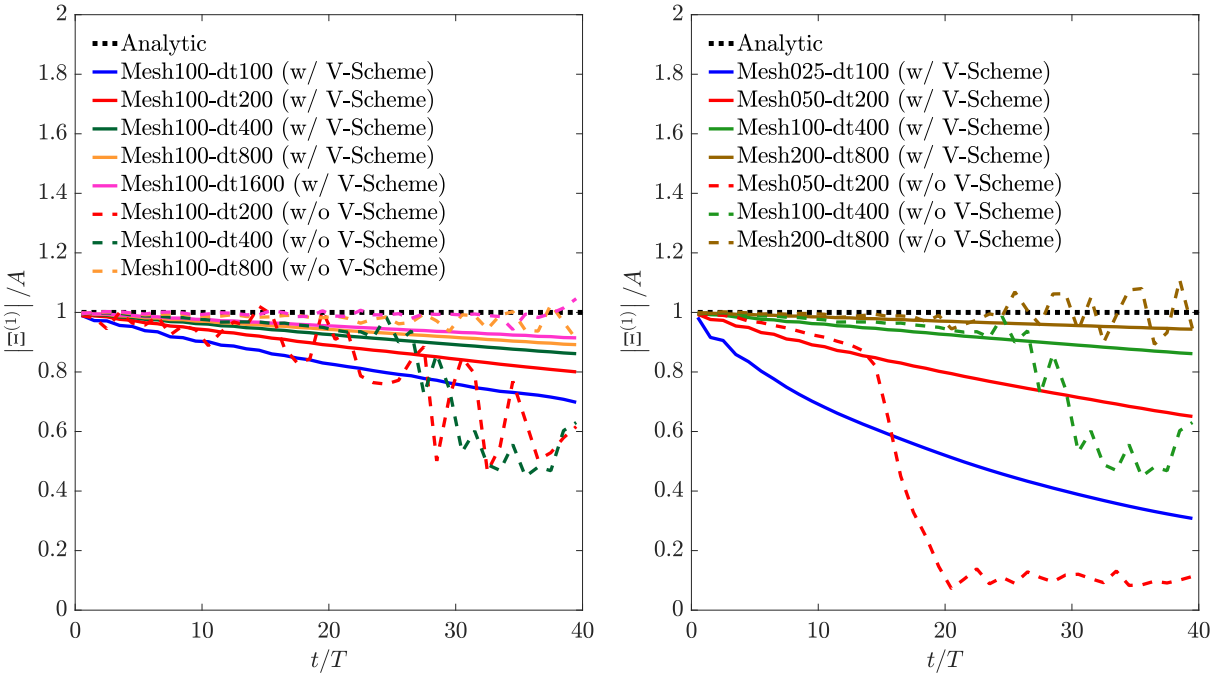

(a) Different Co **(b)** Different Re

Figure 2.5. Comparison of first-harmonic wave amplitudes with mesh and time difference discretization.

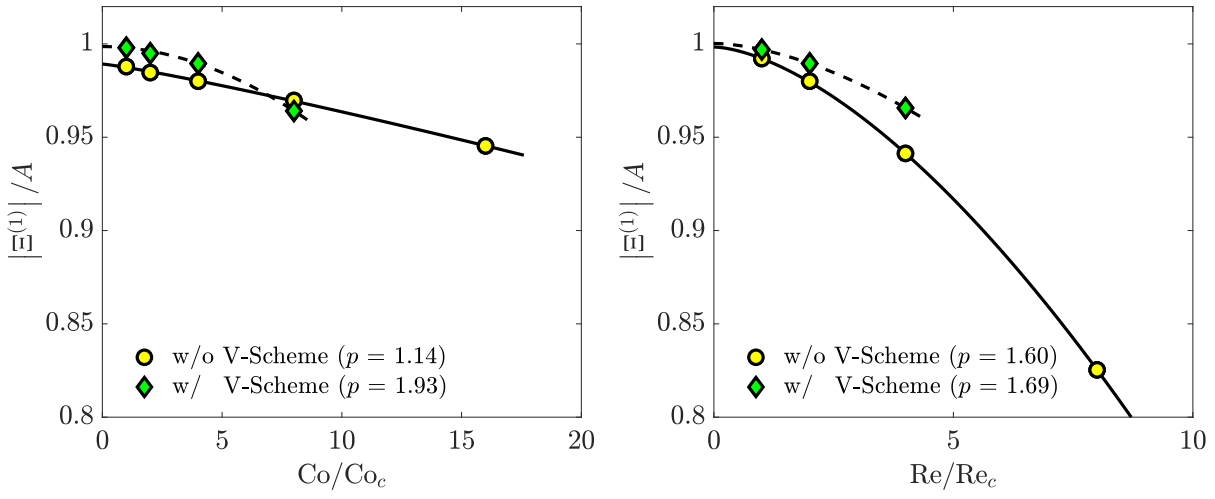

(a) Co discretization, $\mathrm{Co}_c = 0.043$ **(b)** Re discretization, $\mathrm{Re}_c = 1105$

Figure 2.6. The order of convergence with respect to discretization of Co and Re_Δ.

The order of convergence (p) for Courant and Reynolds number discretizations with V-scheme are estimated as 1.14 and 1.60, respectively. The order of convergence increases to 1.93 and 1.69 without V-scheme. From the parametric study on propagating waves with cyclic lateral boundary conditions, the simulation time and meshes should be discretized over than $T/\Delta T \geq 400$, $\lambda/\Delta x \geq 100$ and $H/\Delta z \geq 40$ to have 3.5% of amplitude reduction at $t = 10T$.

2.2.3 Mesh spacing in the vertical direction

The velocity profile of propagating waves underwater has an exponential behavior in the vertical direction. In wave theory, the maximum velocity occurs at the free surface and it decays going far from the free surface. Therefore, the meshes are modeled to be dense near the free surface to save computational cost. The vertical mesh spacing is varied to observe the effects on the simulation of given wave conditions. The meshes are divided into 3 zones: (1) underwater zone ($z \in [-h, -H]$), (2) free surface zone ($z \in [-H, H]$) and (3) air zone ($z \in [H, h]$). To distinguish different meshes, they are denoted as Mesh-ijk where i, j, and k represents the ratio of maximum to minimum height of a cell in the underwater, the free surface, and the air zones, respectively. Mesh-212, Mesh-515 (original) and Mesh-818 are considered in the present study, and they are shown in figure 2.7. The first-harmonic amplitudes and the phase differences for different vertical mesh spacing are compared in figure 2.8. The first-harmonic amplitudes and phase differences for different vertical mesh spacings are almost identical, and the vertical mesh spacings used here do not affect the simulation of the given wave conditions.

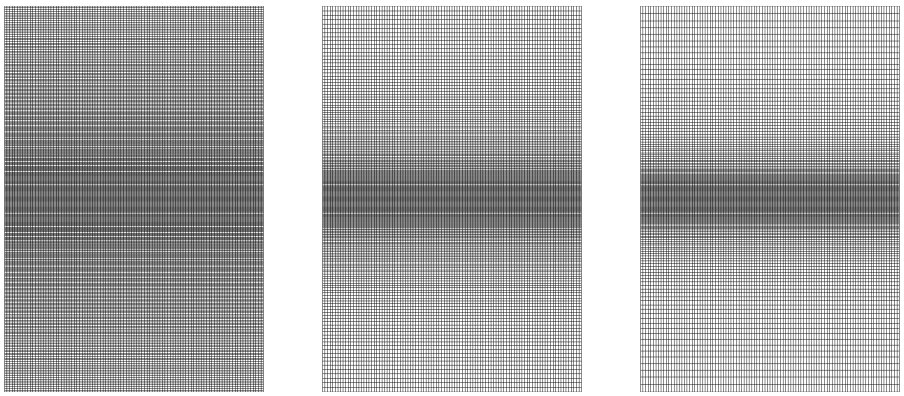

(a) Mesh-212 **(b)** Mesh-515(original) **(c)** Mesh-818

Figure 2.7. Different vertical mesh spacings of three divided zones with the geometric ratio.

2.3 Description on the inlet/outlet condition

2.3.1 Relaxation scheme

The method for generation and absorption of waves in `foamStar` is based on explicit relaxation schemes which blend the computed solution with target solution in relaxation zones (Jacobsen et al., 2012; Mayer et al., 1998; Fuhrman, 2004; Engsig-Karup, 2006; Seng, 2012). The explicit relaxation scheme uses a weight function which varies between 0 and 1 in the relaxation zone. After solving the governing equations, the computed solution is relaxed with target solution as

$$\chi = (1 - w)\chi + w\chi^{Target}, \tag{2.6}$$

where χ is the computed solution, w is a weight function and χ^{Target} is a target solution. The computed values shall be blended smoothly if a smooth weight function is used. Implicit blending schemes, which blend the governing equations with target governing equations, have been applied

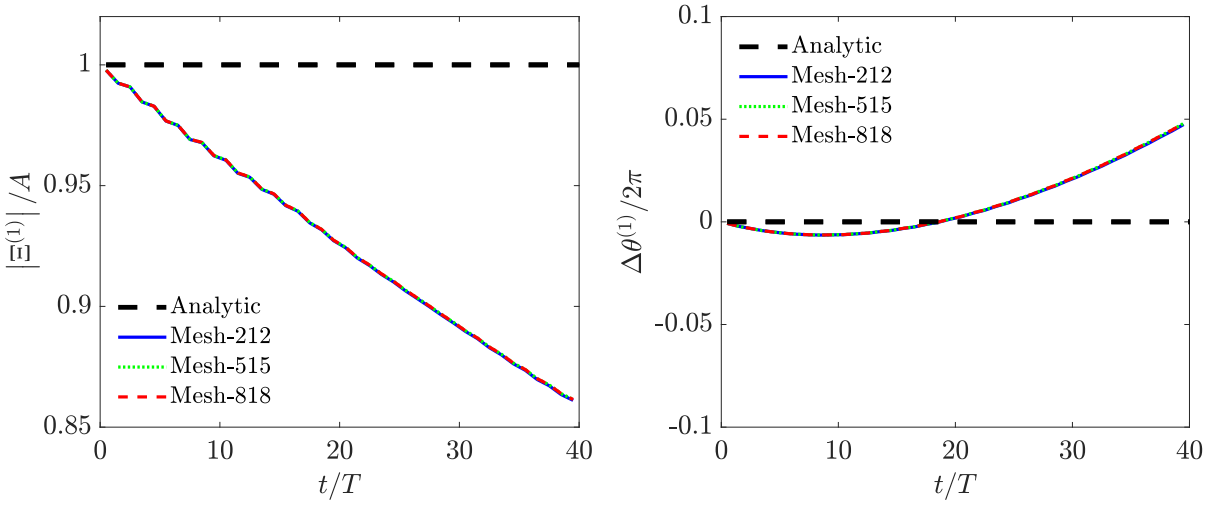

(a) Amplitude **(b)** Phase differences

Figure 2.8. The first-harmonic amplitudes and phase differences with respect to vertical mesh spacing.

by many researchers (Kim et al., 2012; Vukčević, 2016). Only the explicit relaxation scheme is considered in the present study. The choice of weight function is an important key to minimize wave reflection. Engsig-Karup (2006) analyzed the condition of w, which satisfies the original governing equations, and he showed that it is the case for the Heaviside step function. However, the Heaviside step function has a jump in the middle of the relaxation zone, which causes undesirable reflection and instability, so the choice of the weight function has to be different. As a weight function, Mayer et al. (1998) and Engsig-Karup (2006) applied polynomials, and Jacobsen et al. (2012) used an exponential scaled function. Seng (2012), for its own part, introduced a dynamic weight as

$$w^d = 1 - (1 - w)^{|\mathbf{u}-\mathbf{u}^{Target}|\Delta t/\Delta x}, \tag{2.7}$$

where $\mathbf{u}$ is a computed fluid velocity, $\mathbf{u}^{Target}$ is the target fluid velocity, w^d is a dynamic weight and Δx is a size of the cell. The dynamic weight is applied adaptively based on the difference between target and computed velocity after PISO loop, $|\mathbf{u} - \mathbf{u}^{Target}|$. w is the base weight functions which are categorized into polynomial and exponential functions

$$w(\xi) = \begin{cases} \dfrac{e^{\xi_{relax}^{3.5}} - 1}{e - 1}, & \text{exponential weight,} \\ -2\xi_{relax}^3 + 3\xi_{relax}^2, & \text{polynomial weight ,} \end{cases} \tag{2.8}$$

where $\xi \in [0, 1]$ is a normalized coordinate in relaxation zones.

In summary, the weight functions in `foamStar` are categorized into exponential/polynomial and static/dynamic weights. The size of the relaxation zone is also important for determining an optimal size of inlet/outlet zones in terms of numerical cost against accuracy.

2.3.2 Damping layer method

The damping layer method, which is also called 'sponge layer method', is considered here (Israeli and Orszag, 1981). Linear and quadratic damping source terms are commonly used to damp waves (Park et al., 1999; Perić and Abdel-Maksoud, 2016). The momentum equations of multiphase flow with the damping source terms

$$\frac{\partial(\rho\mathbf{u})}{\partial t} + \nabla\cdot(\rho\mathbf{u}\mathbf{u}^T) - \nabla\cdot\left[\mu\left(\nabla\mathbf{u} + \nabla\mathbf{u}^T\right)\right] = -\nabla p_d - (\mathbf{g}\cdot\mathbf{x})\nabla\rho + \mathbf{S}, \tag{2.9}$$

where μ is a dynamic viscosity, $p_d = p - \rho\mathbf{g}\cdot\mathbf{x}$ is a dynamic pressure which is equivalent to the value of subtracted hydrostatic pressure ($\rho\mathbf{g}\cdot\mathbf{x}$) from total pressure ($p$). $\mathbf{S}$ is the linear and quadratic damping source. The damping sources are only applied in vertical velocity components

$$\mathbf{S} = [0, 0, \rho(C_1 + C_2 u_z) w u_z]^T \tag{2.10}$$

where C_1 and C_2 are the linear and quadratic damping coefficients and w is weight function. The parametric study on the damping coefficients conducted by Perić and Abdel-Maksoud (2016) showed that an optimal choice of coefficients can minimize wave reflections. Recently, Perić et al. (2018b) proposed a method for evaluating the wave reflection coefficients with numerical parameters such as linear damping coefficient and the outlet length. Furthermore, they proposed a method for calculating the linear damping coefficient, which minimizes the reflection coefficient. Based on their method, the optimal linear damping coefficient (C_1) is around 7.5 when the outlet length is equal to 1.5λ and target waves are set to zero. In the present study, the linear damping coefficients are considered for the damping layer method due to the complexity of the combination of quadratic damping coefficient.

2.3.3 Increased viscosity in the outlet / Stretched mesh outlet

The viscosity can be increased artificially in the outlet zone to damp the waves. The momentum equation with increased viscosity in the outlet is given as

$$\frac{\partial(\rho\mathbf{u})}{\partial t} + \nabla\cdot(\rho\mathbf{u}\mathbf{u}^T) - \nabla\cdot\left[(\mu + \mu_{add})\left(\nabla\mathbf{u} + \nabla\mathbf{u}^T\right)\right] = -\nabla p_d - (\mathbf{g}\cdot\mathbf{x})\nabla\rho, \tag{2.11}$$

where μ_{add} is the increased viscosity in the outlet zone. The stretched mesh outlet, which triggers numerical damping by stretching meshes, is also considered in the present study.

2.3.4 Modified waves: Adaptive wave absorption

When relaxation schemes are used, the target flow can be selected by the user. For the wave-structure interaction problem, the target flow can correspond to incident waves only. Diffracted waves generated by structure are then relaxed to zero. For 2D propagating waves, the adaptive absoption scheme, which adapts its wave amplitude and phase by measuring the wave elevation in front of the outlet, can be applied. It is assumed that the propagating wave do not change wave frequency and wave number. Then, the first harmonic wave amplitude and phase difference

are calculated by applying a Fourier transform on the measured wave elevation in front of the outlet zone as

$$A' = \frac{2}{T\cos\Delta\phi}\int_{t-T}^{t}\Xi(x_0,\tau)\cos(k(x-x_0)-\omega\tau)d\tau \tag{2.12}$$

and

$$\tan(\Delta\phi) = -\frac{\int_{t-T}^{t}\Xi(x_0,\tau)\sin(k(x-x_0)-\omega\tau)d\tau}{\int_{t-T}^{t}\Xi(x_0,\tau)\cos(k(x-x_0)-\omega\tau)d\tau} \tag{2.13}$$

where A' is the first harmonic amplitude of modified waves, $\Delta\phi$ is the phase difference between incident and modified waves. $\Xi(x_0,\tau)$ is measured wave elevation in front of outlet zone at x_0. The wave elevation and fluid velocity of modified waves are then given by

$$\Xi_I = \frac{2A'}{H}\Xi_I^{streamWave}, \qquad \mathbf{u}_I = \frac{2A'}{H}\mathbf{u}_I^{streamWave}, \tag{2.14}$$

where $\Xi_I^{streamWave}$ and $\mathbf{u}_I^{streamWave}$ are the wave elevation and fluid velocity by stream function wave theory (Rienecker and Fenton, 1981).

2.4 Preliminary study 1: Numerical wave tank

2.4.1 Description

The wave described in table 2.1 is used here, but the length of the domain increases and relaxation zones are introduced. Based on the vertical mesh spacing of Mesh-515, the computational domain with relaxation zones is described in figure 2.9. The inlet length, L^{inlet}, is taken to be 1.5λ for

$$\chi = (1-w)\chi + w\chi^{Target}$$

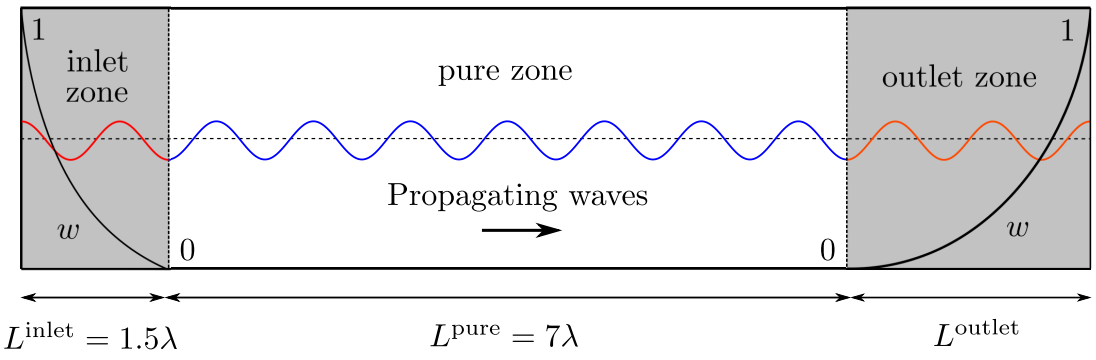

Figure 2.9. Schematic view of the NWT for a parametric study on the relaxation schemes.

wave generation. The stream function wave is used as the target flow field at the inlet zone. The pure CFD zone where no relaxation schemes are applied has a length of 7λ. 250 wave gauges are uniformly distributed from $x = 2.5\lambda$ to $x = 7.5\lambda$. The first and last wave gauges are located 1λ apart from inlet and outlet. The wave reflection coefficient is evaluated from the extracted first harmonic amplitudes of distributed wave gauges. When the generated waves propagate through the pure CFD zone, their amplitude, and phase change due to numerical dissipation and dispersion.

2.4.2 Reflection coefficients

The quality of the wave propagation will be assessed through the estimation of linear reflection coefficients. Linear incident and reflected waves in the system are written as

$$\begin{aligned} \Xi_I &= A_I \cos(kx - \omega t) \\ \Xi_R &= A_R \cos(kx + \omega t + \Delta\phi) \end{aligned} \tag{2.15}$$

where subrscript $_{I,R}$ represent the incident and reflected waves. $\Delta\phi$ is phase difference. The wave reflection coefficient is evaluated as in (Dean and Dalrymple, 1991)

$$\kappa_R = \frac{A_R}{A_I} = \frac{a_{\max} - a_{\min}}{a_{\max} + a_{\min}}, \tag{2.16}$$

where κ_R is reflection coefficient, $a_{\max}$ and $a_{\min}$ is the measured maximum and minimum wave amplitudes in the region of interest, respectively. The propagating waves in the present study are nonlinear. Consequently, the equation 2.16 is not directly applicable. Likewise Carmigniani and Violeau (2018), the first harmonic amplitudes are used to evaluate the wave reflection coefficients. The first harmonic amplitude by Fourier transform is given as

$$a_i(t) = \frac{2}{T} \int_{t-T}^{t} \Xi(x_i, t) \cos(kx_i - \omega\tau) d\tau, \tag{2.17}$$

where subscript i denotes i-th wave gauge. In the middle of the computation zone, 250 wave gauges are distributed along 5λ to detect the amplitudes of wave envelope. The wave reflection coefficient for each simulation time step is evaluated as

$$\kappa^R(t) = \frac{\max(a_i(t)) - \min(a_i(t))}{\max(a_i(t)) + \min(a_i(t))}. \tag{2.18}$$

2.4.3 Parametric study on the relaxation schemes

Different weight functions categorized as static-exponential, static-polynomial, dynamic-exponential and dynamic-polynomial are applied with various outlet lengths ($L^{\text{outlet}} = 1.5\lambda, 3\lambda$ and 6λ). The weight functions are changed both inside the inlet zone and the outlet zone. The stream function waves are used as target flow. Maximum Courant numbers ($\text{Co}_{\max}$) with respect to different relaxation schemes and outlet lengths is given in figure 2.10. The relaxation scheme with dynamic polynomial weight gives a stable simulation in comparison with others. It is less sensitive to the length of relaxation zones though it becomes unstable when the outlet length is equal to the half wavelength. The static and dynamic exponential weight functions show a more stable simulation until $t = 20T$, but the results show that more extended outlets do not guarantee the reduction of numerical instability. Meanwhile, the maximum Courant number with static polynomial weight is higher than other relaxation schemes for all simulations. The wave reflection coefficients for different relaxation schemes and outlet lengths are compared in figure 2.11. It appears that wave reflection increases until $t = 20T$ for any length of the outlet zone. This increase is maximal when the length of the outlet zone is smaller than 1.5 wavelengths. After $t = 20T$, the wave reflection depends mainly on relaxation schemes. Wave reflection coefficients are less sensitive

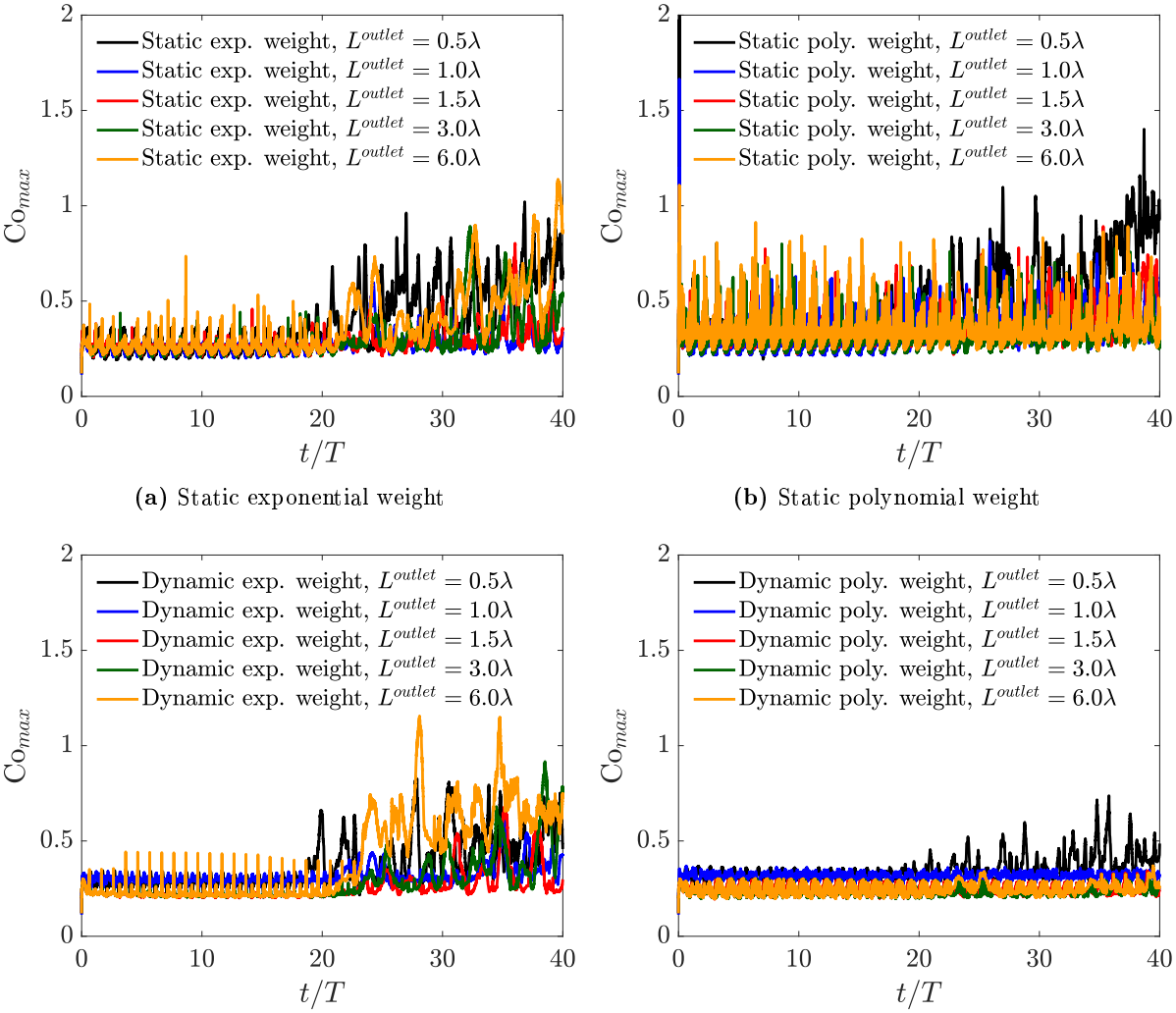

(a) Static exponential weight

(b) Static polynomial weight

(c) Dynamic exponential weight

(d) Dynamic polynomial weight

Figure 2.10. The maximum Courant number during wave propagation simulation with relaxation to incident waves.

for the dynamic polynomial weight with outlet length over than 1.5 wavelengths. Moreover, wave reflection increases faster for the relaxation zone less than 1.5 wavelengths. The measured first harmonic amplitudes and reflection coefficients with respect to weight functions are compared in figure 2.12. The first harmonic amplitudes with static weight give a lower dissipation than with dynamic weight. The difference of wave amplitude between static and dynamic weights with outlet lengths over than 1.5 wavelengths is 1.33 %. Moreover, the wave reflection increases when the outlet length is less than one wavelength. Simulation results should not be sensitive to the selection of outlet length. We hope to get predictable results, the dynamic-polynomial weight is selected as a representative relaxation scheme because it shows a stable velocity field even if it has a slightly smaller wave amplitude compared the simulation cases with static weight. Finally, it is identified that the outlet length should be longer than 1.5 wavelengths to decrease the reflection more efficiently.

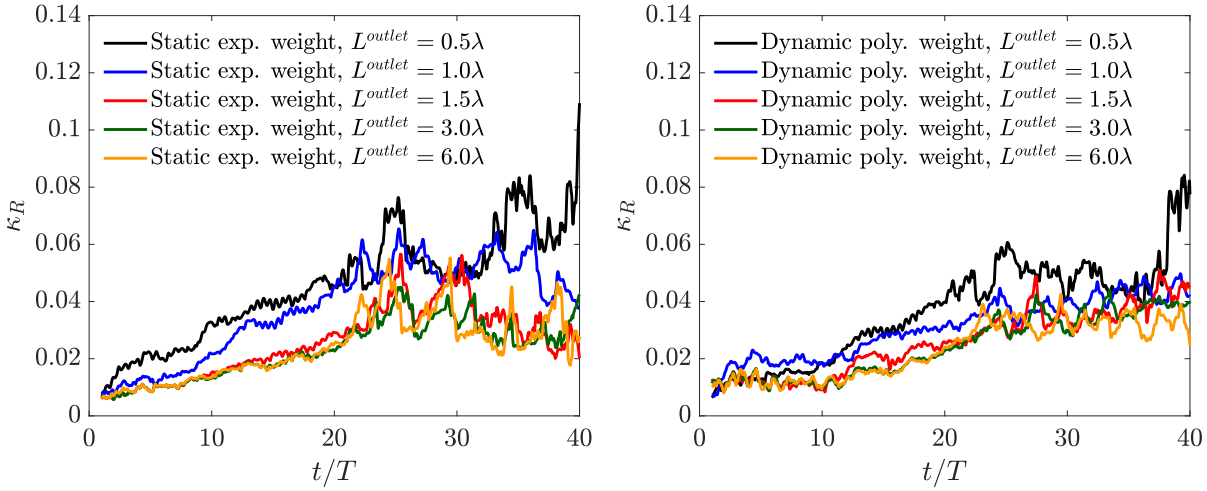

(a) Static exponential weight **(b)** Dynamic polynomial weight

Figure 2.11. Comparison of reflection coefficient time series with respect to different relaxation schemes and outlet lengths.

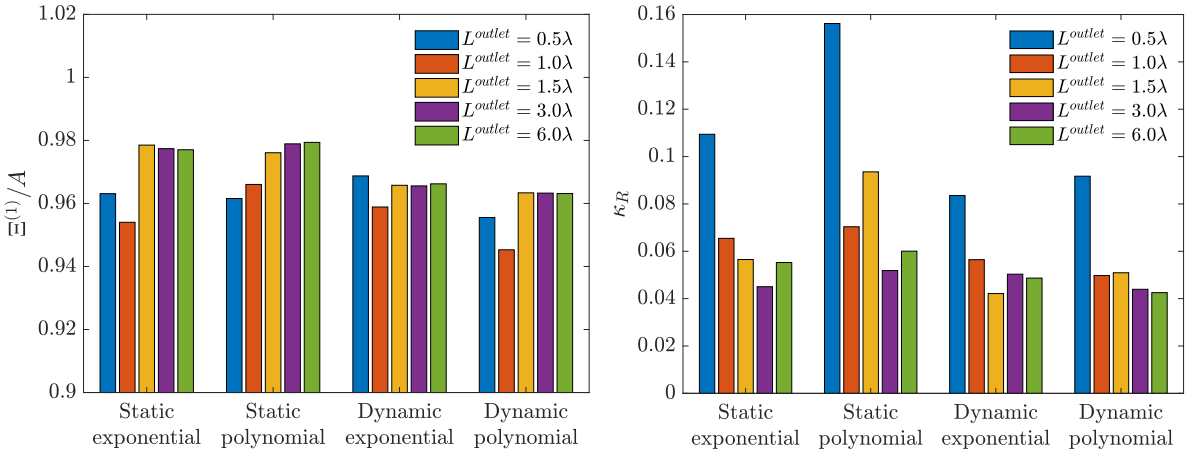

(a) First-harmonic amplitudes **(b)** Wave reflection coefficients

Figure 2.12. Comparison of wave amplitudes and reflection coefficients with respect to relaxation zones and relaxation schemes.

2.4.4 Parametric study on the stretched mesh outlet

As the stretched mesh schemes depend on cases and on authors (Monroy et al., 2011; Perić and Abdel-Maksoud, 2015), it is difficult to find a standard for wave propagation. Therefore, the cell length is stretched with a ratio (r_x) of an adjusted cell which is located at upstream as

$$\Delta x_n = r_x \Delta x_{n-1} \tag{2.19}$$

where Δx_n and r_x represents a longitudinal length of the n-th cell and the stretching ratio, respectively. To find a representative result of stretched mesh outlet, the different stretching

ratios are considered as

$$r_x = \begin{cases} c, & \text{constant stretching; } c = 1.02,\ 1.05 \text{ and } 1.08 \\ \cosh(\gamma n), & \text{exponential stretching; } \gamma = 1.001 \end{cases} \tag{2.20}$$

The outlet meshes are stretched until the length of the last three cells is larger than one wavelength ($\Delta x \geq 1\lambda$). The properties of stretched mesh outlets are summarized in Table 2.3. The computational meshes near the entrance of the outlet zone are shown in figure 2.13. Compared to the constant stretching ratio, the exponential stretching gives a dense distribution near the entrance of the outlet zone. The wave reflection coefficients with respect to different stretched mesh outlets are given in Table 2.4. The constant geometric ratio of $r_x = 1.02$ gives the smallest wave reflection coefficient among stretched mesh outlet conditions. Thus, it is selected for comparison with other numerical outlets.

Table 2.3. Information of stretched mesh outlets for propagating waves.

Choice of r_x	Number of cells	L/λ	$L^{\text{outlet}}/\lambda$	$\Delta x^{max}/\lambda$
$\gamma = 1.001$	225,420	39.6	31.1	1.11
$r_x = 1.02$	206,340	59.5	58.0	1.05
$r_x = 1.05$	180,120	29.9	21.4	1.14
$r_x = 1.08$	173,470	22.0	13.5	1.18

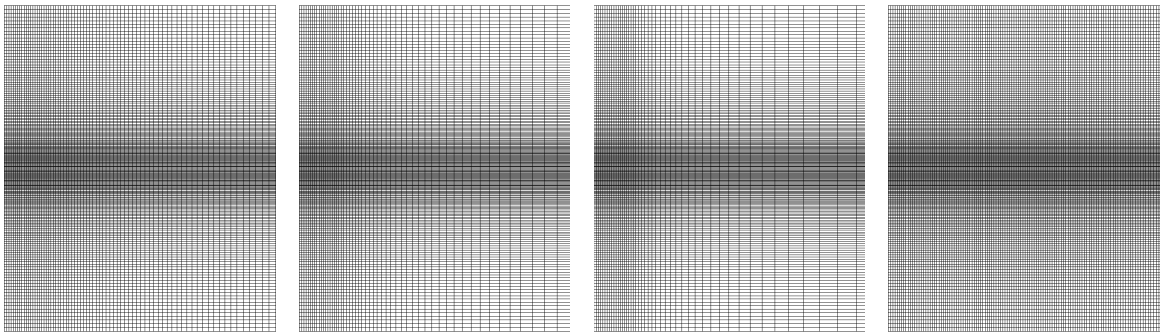

(a) $r_x = 1.02$ **(b)** $r_x = 1.05$ **(c)** $r_x = 1.08$ **(d)** $\gamma = 1.001$

Figure 2.13. Meshes near to the outlet with different stretching.

Table 2.4. Reflection coefficients with respect to stretched mesh outlets.

Choice of r_x	$\gamma = 1.001$	$r_x = 1.02$	$r_x = 1.05$	$r_x = 1.08$
κ_R	0.0499	0.0474	0.0569	0.1046

2.4.5 Linear damping source outlet

Perić and Abdel-Maksoud (2016) showed that an unappropriate use of damping coefficient leads to unwanted wave reflections. The authors used a Froude scaling law to find a dependency of

damping coefficients. They showed that the linear and quadratic damping coefficients could be scaled by wave frequency and wavelength, respectively. Perić et al. (2018b) proposed the method on wave reflection by analyzing the wave equation in the case of a linear damping source. The minimal wave reflection coefficients with linear damping coefficients are available by the code published in (Perić et al., 2018a). The algorithm predicted that the wave reflection coefficient would be 1.5% with the linear damping coefficient $C_1 \approx 7.5$ for outlet length 1.5λ. Note that the target flow is no waves, and the static exponential function is used in their approach. Shen and Wan (2016) used the linear damping coefficient of $C_1 = 20$ with second order polynomial weight function for irregular wave simulation. It is thought that the damping coefficients should be tuned with the different outlets and weight functions to minimize the wave reflection. In the present study, the linear damping coefficient with cubic polynomials weight given in equation (2.8) is studied with different outlet lengths. Considered linear damping coefficients with reflection coefficients are tabulated in Table 2.5. The linear damping coefficient of $C_1 = 20$ is selected as a

Table 2.5. Reflection coefficient with respect to linear damping source outlet.

L^{outlet}	C_1				
	30	20	10	5	1
1.5λ	0.0579	0.0513	0.0521	0.0817	-
3.0λ	-	0.0460	0.0468	0.0474	-
6.0λ	-	-	0.0400	0.0406	0.0406

representative case of damping source outlet because it gives the lowest wave reflection coefficient with the limited outlet length $L^{outlet} = 1.5\lambda$.

2.4.6 Increased viscosity in the outlet

The increased viscosity in the outlet, imposing a high viscosity in the outlet zone compared to original fluid media, is easy to implement. For a smooth change of viscosity, the added viscosity μ_{add} is multiplied by the cubic polynomial weight function given in equation (2.8). As the user artificially introduces the added viscosity, the added viscosity and outlet length need to be tuned. Three different added viscosities are considered that have the values of $\mu_{add} = 0.5, 0.2$ and $0.1 kg \cdot m^{-1} \cdot s^{-2}$, respectively. The wave reflection coefficients for added viscosity and different outlet lengths are given in Table 2.6.

Table 2.6. Reflection coefficient with respect to the increased viscosity in the outlet.

L^{outlet}	$\mu_{add}[N \cdot s/m^2]$		
	0.5 ($500\mu_{water}$)	0.2 ($200\mu_{water}$)	0.1 ($100\mu_{water}$)
1.5λ	0.1446	0.0996	0.0769
3.0λ	0.0764	0.0785	0.0651
6.0λ	0.0739	0.0931	0.0563

2.4.7 Comparison and discussion

The stretched mesh, linear damping source, increased viscosity, relaxation to no waves, incident waves, and modified waves are compared for different wave outlets. Only the limited outlet length of $L^{outlet} = 1.5\lambda$, except for mesh stretching, is considered. The representative results from the parametric study on each wave outlet are taken for comparison. The first harmonic amplitudes and phase differences with respect to the different outlets are compared in figure 2.14.

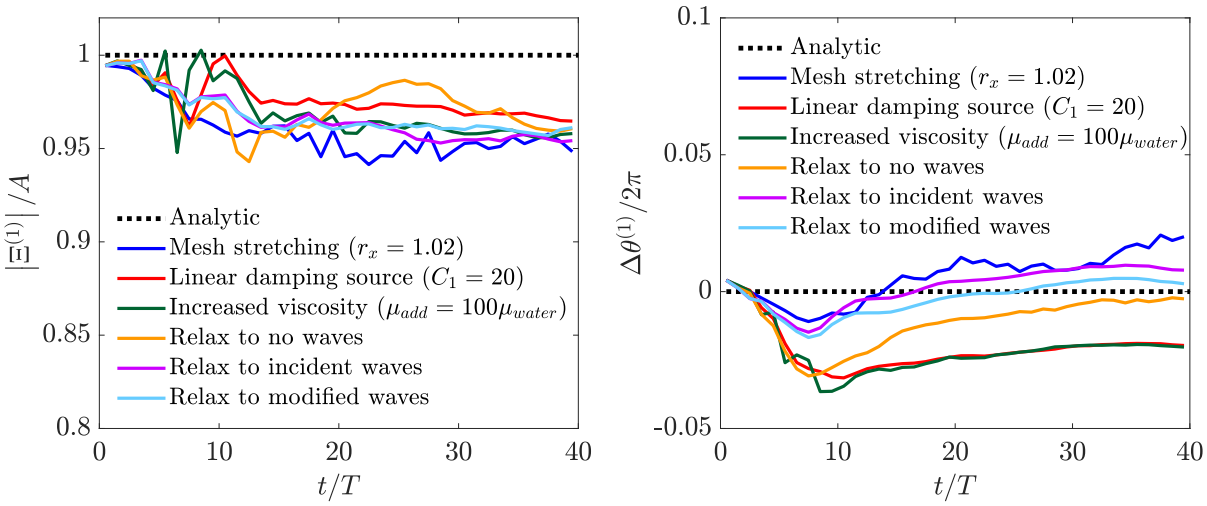

(a) Amplitude **(b)** Phase differences

Figure 2.14. The first harmonic amplitudes and phase differences with respect to different outlet.

The measured first harmonic amplitudes during 40 wave periods have an error range of 7%. Amplitude modulations over simulation time are observed for all cases, and stable results are obtained for relaxation to incident waves and modified waves. Waves are propagating with a constant phase difference after a certain time of simulation for linear damping source and increased viscosity outlets. The phase differences of relaxation to the incident and modified waves are smaller than other boundary conditions. Relax to no waves slowly converges to the analytic solution. The reflection coefficients for the different outlets during simulation are plotted in figure 2.15.

At the initial simulation stage, the high reflection coefficients are measured for linear damping outlet, increased viscosity, and relax to no waves. It is thought that the different outlet configurations such as different viscosity quantities, artificial sources, and no flow, affect the flow fields immediately due to the limited length of the outlet. After an initial disturbance, the wave reflection with linear damping source and increased viscosity decreases, and has a similar reflection with relaxation to waves from $t = 22T$. Meanwhile, the relax to no waves shows a higher wave reflection over simulation time after initial disturbance. It shows that blending to wrong target function in the relaxation zone do not promise a good result. The mesh stretching outlet and relaxation to the incident and the modified waves have gradually increasing wave reflection over

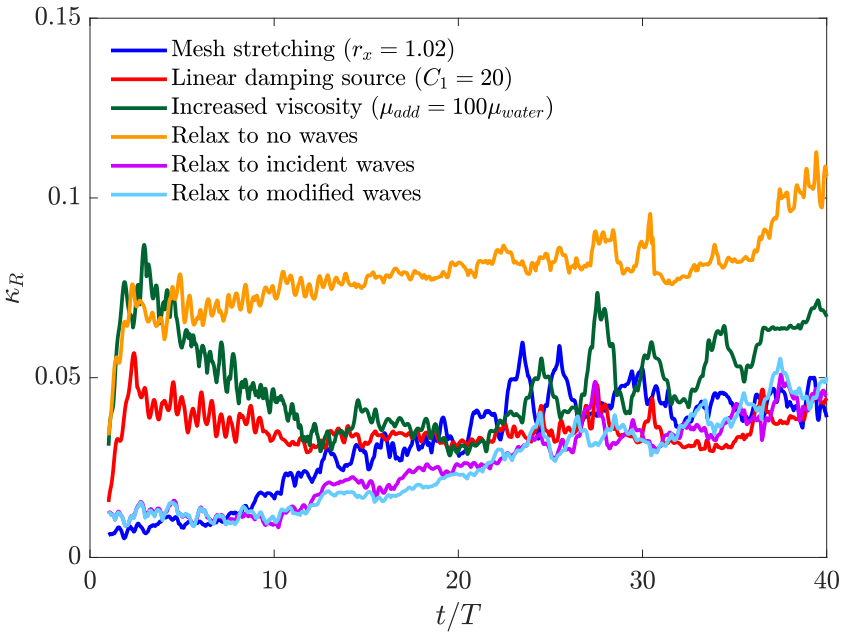

Figure 2.15. Evolution of reflection coefficients for different outlet.

simulation time.

The maximum wave reflection coefficients during the simulation for different outlets are tabulated in Table 2.7.

Table 2.7. Reflection coefficient with respect to different outlet.

Outlet	κ_R
Mesh stretching ($r_x = 1.02$)	0.047
Linear damping source ($C_1 = 20$)	0.051
Increased viscosity ($\mu_{add} = 100\mu_{water}$)	0.077
Relax to no waves	0.077
Relax to incident waves	0.042
Relax to modified waves	0.039

The smallest wave reflections are obtained for relaxation to modified waves, and the other outlet conditions also give good results. Proper tuning of linear damping source and increased viscosity would give probably better results. Nevertheless, the parametric study of these outlets needs more work than relaxation schemes, and it is difficult to understand the physics with tuned parameter.

To conclude, comparison of different outlets shows that the relaxation schemes with out-going waves at the boundaries give good results compared to other outlets.

2.5 Preliminary study 2: Swaying Lewis form

2.5.1 Description

A swaying Lewis form in a two-dimensional domain is introduced to study the effect of relaxation schemes and to compare different outlets. The schematic view of swaying Lewis form with different outlets is depicted in figure 2.16.

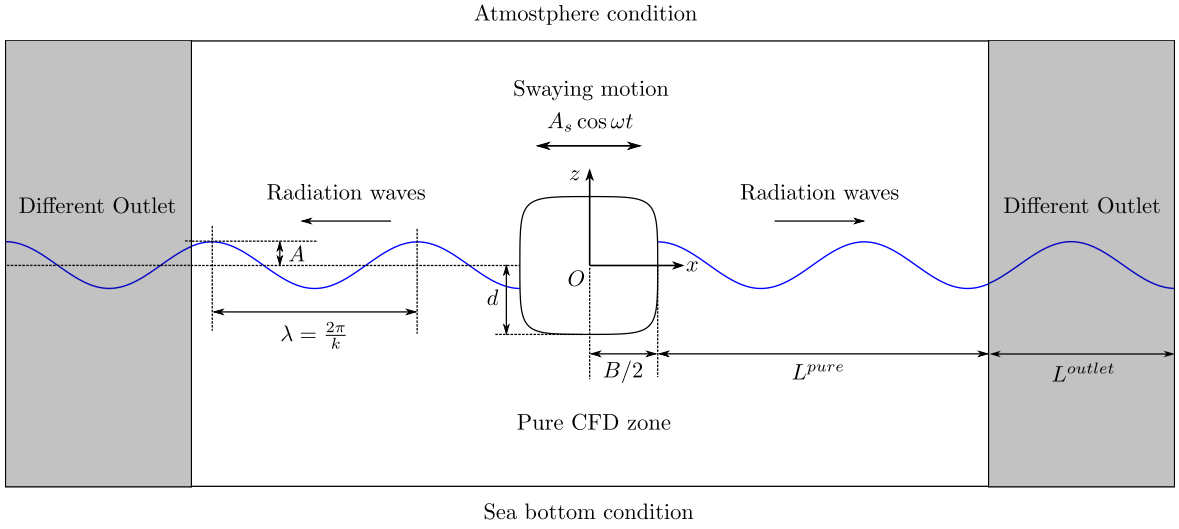

Figure 2.16. Schematic view of swaying Lewis form with different outlet.

In the middle of the domain, the Lewis form moves with its motion amplitude (A_s) and frequency (ω). The pure CFD zone length is defined from the wall of Lewis form to entrance of outlet. The meshes are moving with Lewis form without deformation to keep the mesh quality. The underwater offset of Lewis form is given as (Kashiwagi, 2003)

$$x = M\left\{(1 + a_1)\sin\theta - a_3 \sin 3\theta\right\} \tag{2.21a}$$

$$z = -M\left\{(1 - a_1)\cos\theta + a_3 \cos 3\theta\right\} \tag{2.21b}$$

with

$$a_1 = \frac{H_0 - 1}{2(M/d)}, \qquad a_3 = \frac{H_0 + 1}{2(M/d)} - 1$$

$$\frac{M}{d} = \frac{3(H_0 + 1) - \sqrt{(H_0 + 1)^2 + 8H_0(1 - 4\sigma/\pi)}}{4}$$

where x, z and $\theta \in= [-\pi/2, \pi/2]$ are the underwater offsets of Lewis form and corresponding angle, respectively. M is a magnification factor. B and d are breadth and draft, respectively. $H_0 = \frac{B/2}{d}$ is a ratio of half breadth to draft. $\sigma = \frac{S}{Bd}$ is an area coefficient corresponding to the block coefficient of a ship. The geometric coefficients of Lewis form used in this study are $B/2 = 1.0m$, $d = 1.0m$ and $\sigma = 0.95$. The offset above the free surface is generated by mirroring with respect to $z = 0$.

Different moving frequencies and swaying amplitudes have been considered and are given in Table 2.8.

Table 2.8. Motion frequency and amplitudes of Lewis form.

Item	Frequency (ω)		
	2.4 rad/s	4.2 rad/s	7.0 rad/s
Swaying amplitude (A_s)	0.118 m	0.055 m	0.025 m
Wavelength (λ)	10.70 m	3.494 m	1.258 m
Wave amplitude (A)	0.102 m	0.089 m	0.050 m
Wave steepness (kA)	0.06	0.16	0.25

The motion amplitudes are selected to have enough computational cells in a wavelength and a wave height using far-field wave amplitudes and wavelength. The `snappyHex` mesh discretization is used to describe the body surface. The mesh refinements in x- and z-directions are conducted to match $\lambda/\Delta x \geq 100$ and $A/\Delta z \geq 10$. Then, the local refinement near the body surface is applied. The computational meshes of $\omega = 4.2 rad/s$ with $L^{pure} = 1\lambda$ and $L^{outlet} = 2.5\lambda$ are shown in figure 2.17.

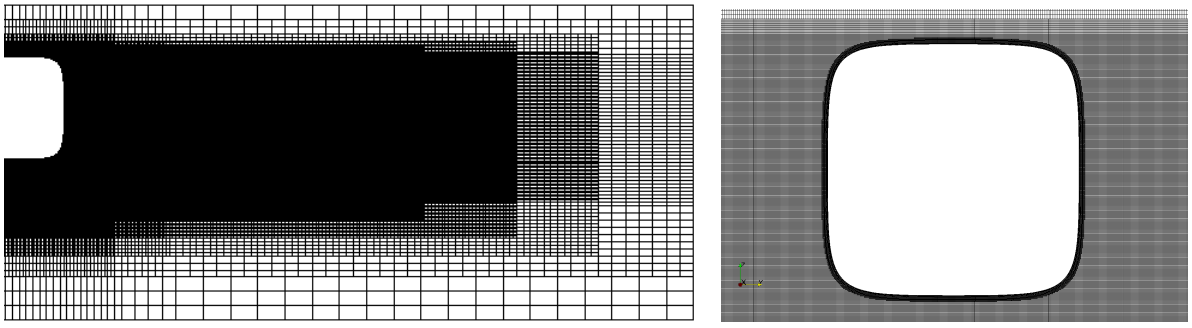

(a) Half domain **(b)** Mesh near to the body

Figure 2.17. The computational meshes of swaying 2D Lewis form; $\omega = 4.2 rad/s$, $L^{pure} = 1\lambda$ and $L^{outlet} = 2.5\lambda$.

2.5.2 Comparison of different outlets

From the results of the previous parametric study, the parameters $r_x = 1.02$, $C_1 = 20$ and $\mu_{add} = 100\mu_{water}$ are selected for the different outlets of mesh stretching, linear damping source and increased viscosity, respectively. The target functions of relaxation schemes are set to no waves and linear potential flow. To determine the size of pure and outlet zones, the relaxation schemes are firstly tested with different zone sizes. The linear potential flow of 2D Lewis form is available by Ursell-Tasai's multipole expansion (Ursell, 1949; Tasai, 1960, 1961). Wheeler stretching is applied to describe the velocity profile with changing wave elevation. This comparison attempts to compare the reduction limit of outlet zones for different outlets. The domains are constructed between $z \in [-d-0.75\lambda, 2m]$ and zone length changes with respect to wavelength. The considered

domain sizes are given in Table 2.9. The mesh size near the body surface is kept in similar size for each frequency. When the length of pure and outlet zones is reduced, the mesh resolution of each domain is maintained by shortening length and excluding the computational meshes in the far-field.

Table 2.9. The meshes used for the parametric study

Mesh name	L^{pure}	L^{outlet}	$N_{cell}(\omega = 2.4rad/s)$	$N_{cell}(\omega = 4.2rad/s)$	$N_{cell}(\omega = 7.0rad/s)$
P150R35	1.5λ	3.5λ	317,094	350,024	202,022
P100R35	1.0λ	3.5λ	273,996	313,784	172,666
P050R35	0.5λ	3.5λ	239,802	277,738	136,892
P025R35	0.25λ	3.5λ	219,020	254,010	131,968
P100R25	1λ	2.5λ	291,678	320,090	173,736
P100R20	1λ	2.0λ	283,824	323,276	174,260
P100R15	1λ	1.5λ	270,782	308,766	160,890

From the measured force time series acting on the body surface, the added mass and radiation damping are extracted by Fourier transform. Normalized added mass and radiation damping coefficients are defined as

$$a'_{22} = \frac{a_{22}}{\rho(B/2)^2}, \qquad b'_{22} = \frac{b_{22}}{\rho\omega(B/2)^2}, \tag{2.22}$$

where a_{22} and b_{22} are the added mass and radiation damping defined by

$$\frac{1}{T}\int_{t-T}^{t} F_2(\tau)e^{i\omega\tau}d\tau = A_s(\omega^2 a_{22} + i\omega b_{22}), \tag{2.23}$$

where $F_2(\tau)$ is the horizontal force, T is the period.

The radiation forces for moving frequency $\omega = 4.2rad/s$ with domain of $L^{pure} = 1\lambda$ and $L_{outlet} = 3.5\lambda$ are plotted in figure 2.18.

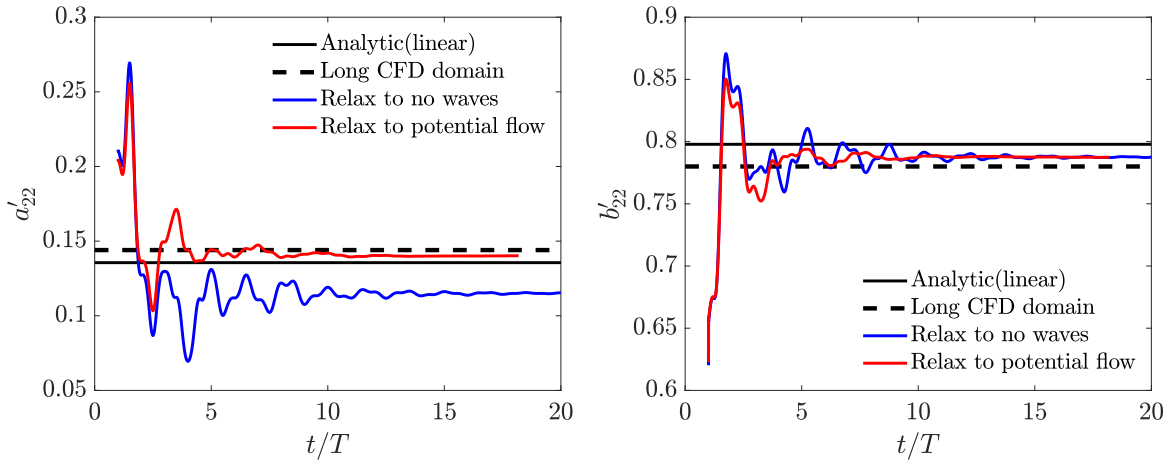

(a) Added mass **(b)** Radiation damping

Figure 2.18. Radiation force time series with respect to target flows, $L^{pure} = 1\lambda$ and $L_{outlet} = 2.5\lambda$ for $\omega = 4.2rad/s$.

It is noticeable that the radiation forces converge faster when the target function is set to potential flow, which is more like outgoing waves. They converge 1.4-2 times(average 1.6 times) faster for given convergence tolerance (1%) in simulation time. The large domain which has a pure zone $L^{pure} = 12.5\lambda$ ($\approx 20c_gT$; $c_g = \frac{d\omega}{dk}$ is a group velocity) and an outlet zone $L^{outlet} = 5.0\lambda$ with same mesh quality is used as another reference because the wave steepness (kA) varies between 0.06 and 0.25, which are in range of nonlinear waves. This implies that the computed radiation forces may not match with values using linear potential flow due to nonlinearity.

The radiation forces computed by linear potential theory, long domain and target flows of no waves with different domain sizes are summarized in Table 2.10.

Table 2.10. Radiation coefficient of pure zone size (Relaxation to no waves).

Coef.	a'_{22}			b'_{22}		
ω $[rad/s]$	2.4	4.2	7.0	2.4	4.2	7.0
Analytic	1.304	0.136	0.365	2.169	0.798	0.156
Long Domain	1.297	0.144	0.388	2.162	0.780	0.148
P150R35	1.279	0.129	0.386	2.190	0.779	0.146
P100R35	1.283	0.129	0.380	2.194	0.781	0.146
P050R35	1.278	0.129	0.391	2.192	0.781	0.146
P025R35	1.312	0.146	0.382	2.136	0.743	0.140
P100R25	1.281	0.115	0.375	2.194	0.788	0.149
P100R20	1.276	0.103	0.372	2.209	0.802	0.154
P100R15	1.276	0.096	0.368	2.248	0.832	0.162

The difference of radiation forces between linear potential flow and long domain becomes larger as the wave steepness increases. Also, the computed forces with no waves converge to values of the long domain as the domain increases.

The relative errors with pure zone sizes for relaxation schemes are shown in figure 2.19a.

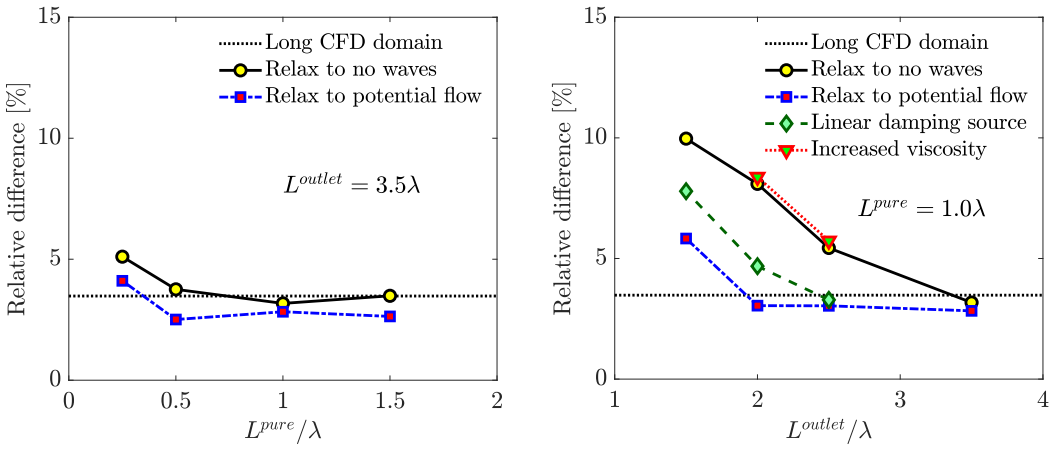

(a) Pure zone size **(b)** Outlet zone size

Figure 2.19. Relative errors with respect to the size of domain.

The results show that the solutions are not much sensitive to the pure zone size and the relative errors of both relaxation schemes (to no waves and to potential flow) are in the range of long domain. The relative errors between linear wave theory with different outlets are plotted in figure 2.19b. The relative errors of all outlets decrease as the outlet zone becomes larger and get close to the relative error of long domain. And the results show that the solution is more sensitive to the reduction of outlet zone rather than that of the pure zone. When the target function is similar to outgoing waves, the pure and outlet zone can be reduced.

The radiation forces of the different outlets with fixed lengths of domain which are $L^{pure} = 1.0\lambda$ and $L^{outlet} = 2.0\lambda$ are tabulated in Table 2.11.

Table 2.11. Radiation coefficient of different outlets ($L^{pure} = 1.0\lambda$ and $L^{outlet} = 2.0\lambda$).

Coef.	a'_{22}			b'_{22}		
ω $[rad/s]$	2.4	4.2	7.0	2.4	4.2	7.0
Analytic	1.304	0.136	0.365	2.169	0.798	0.156
Long Domain	1.297	0.144	0.388	2.162	0.780	0.148
Relax to no waves	1.276	0.103	0.372	2.209	0.802	0.154
Relax to potential flow	1.316	0.141	0.392	2.185	0.798	0.151
Linear damping source	1.270	0.121	0.384	2.263	0.782	0.148
Increased viscosity	-	0.154	0.388	-	0.842	0.147

The increased viscosity outlet ($\mu_{add} = 100\mu_{water}$) does not damp the radiation waves properly, the force time series has modulation and increases dramatically due to reflection. Therefore, the computed radiation forces are taken from meaningful simulation results. It is thought that the increased viscosity should be determined based on wave frequency.

In summary, when the target function is similar to outgoing waves, the domain and simulation time both can be reduced. The other outlets are also good choices when relatively large domain ($L^{pure} \geq 0.5\lambda$ and $L^{outlet} \geq 3\lambda$) are used.

2.6 Conclusion

In the preliminary study, a parametric study of propagating waves with viscous flow model solving RANSE based on FVM is conducted. This parametric study shows that the time integration scheme for wave-propagation problem should have at least second-order accuracy to keep the wave amplitude and its phase. The convection schemes affect the order of convergence and the stability of simulation. High-order convection schemes give good results but the simulation becomes unstable as time goes.

As the outlets need different parameters to absorb waves well at the boundary, parametric studies on different outlets are conducted and the representative cases are compared with each other. The considered outlets are listed as the stretched mesh, increased viscosity, momentum sources and relaxation schemes. It is thought that the different outlets which are properly tuned would

give good results but it is difficult to tune outlet parameters of mesh stretching, linear damping source and increased viscosity even if there are some suggestions by other researchers.

The relaxation scheme with properly given target flows that are similar to the outgoing waves, gives stable and good results compared to the others. In the benchmark test of swaying Lewis form, the computational domain and outlet zones can be reduced when the relaxation zone with target flow of outgoing wave is used. Furthermore, the simulation time to obtain the converged solution decreases. Though, relaxation zone larger than 2 wavelengths is necessary to obtain similar results of relatively large computational domain. The preliminary study confirms that two-way coupling can reduce both computational domain and simulation time. To succeed in coupling two flow models, two things are required

- Efficient evaluation of outgoing waves in the relaxation zones from potential flow model.
- Enhanced relaxation scheme to minimize the effect of weight function.

3 Potential flow: Incident waves

The boundary value problem for an incident wave is recalled. Perfect fluid with irrotational flow is assumed to introduce the incident wave potential. The incident wave potential satisfies Laplace's equation

$$\nabla^2 \Phi_I = 0, \qquad \mathbf{x} \in \Omega.$$

where Φ_I is the velocity potential, and Ω is the fluid domain. The flat sea bottom condition is given as

$$\frac{\partial \Phi_I}{\partial z} = 0, \qquad \text{on} \quad z = -h, \tag{3.1}$$

where h is water depth. Overturning of waves is not considered, therefore the incident wave elevation (Ξ_I) is a single-valued function

$$\Xi_I = \Xi_I(x, y; t), \tag{3.2}$$

where x and y are horizontal coordinate, t is time. The nonlinear kinematic and dynamic free surface boundary conditions for incident waves are given as

$$\begin{aligned} \frac{\partial \Xi_I}{\partial t} + \frac{\partial \Phi_I}{\partial x}\frac{\partial \Xi_I}{\partial x} + \frac{\partial \Phi_I}{\partial y}\frac{\partial \Xi_I}{\partial y} + \frac{\partial \Phi_I}{\partial z} = 0 \\ \frac{\partial \Phi_I}{\partial t} + \frac{1}{2}\nabla\Phi_I \cdot \nabla\Phi_I + g\Xi_I = 0 \end{aligned}, \qquad \text{on} \quad z = \Xi_I.$$

The lateral (or infinity) boundary condition for incident waves are different for wave model and will be discussed in the following section.

3.1 Regular waves

The simplest potential theory on 2D regular waves, which is called Airy waves, assumes that the wave height is small compared to its wavelength, and therefore the linearized free surface boundary condition is imposed on the mean free surface (Airy, 1845). Later, the potential theory is expanded with a perturbation series approach, which is known as *Stokes expansion*, with respect to wave steepness (kA) to apply nonlinear free surface boundary conditions (Stokes, 1847). After his works, the perturbation theory based on *Stokes expansion* have been extended for deep and finite water depth (Wilton, 1914; De, 1955). As the order of perturbation increases, free surface boundary conditions become complex and can be solved by the help of computer up to 117-th order (Schwartz, 1974).

Instead of using the velocity potential, Rienecker and Fenton (1981) introduced a stream function theory by Fourier series expansion to solve the nonlinear 2D regular wave. The wave elevation and stream function in Fourier series are given as

$$\Xi_I(x; t) = \eta_I(x) e^{-\mathrm{i}\omega t} = \left[A_0 + \sum_{j=1}^{N_A} A_j \cos k_j x \right] e^{-\mathrm{i}\omega t}, \tag{3.3}$$

$$\Psi_I(x, z; t) = \psi_I(x, z) e^{-\mathrm{i}\omega t} = \left[B_0 z + \sum_{j=1}^{N_B} B_j \frac{\sinh k_j(z + h)}{\cosh k_j h} \cos k_j x \right] e^{-\mathrm{i}\omega t}, \tag{3.4}$$

where Ψ_I is an incident wave stream function, A_j and B_j are the modal amplitudes of Fourier modes, k_j is a modal wavenumber. N_A and N_B are the number of truncated Fourier series. As the stream function of constant value represents the streamline, variation of stream function between two isolines is equal to flow rate (Q). Consequently, the bottom and free surface boundary conditions are simply given as

$$\psi_I(x, z = -h) = 0, \qquad \psi_I(x, z = \Xi_I) = -Q. \tag{3.5}$$

The fluid velocity is calculated from the stream function as

$$u_I^x(x, z; t) = \frac{\partial \Psi_I}{\partial z} = \left[B_0 z + \sum_{j=1}^{N_B} k_j B_j \frac{\cosh k_j(z+h)}{\cosh k_j h} \cos k_j x \right] e^{-\mathrm{i}\omega t}, \tag{3.6}$$

$$u_I^z(x, z; t) = -\frac{\partial \Psi_I}{\partial x} = \left[B_0 z + \sum_{j=1}^{N_B} k_j B_j \frac{\sinh k_j(z+h)}{\cosh k_j h} \sin k_j x \right] e^{-\mathrm{i}\omega t}, \tag{3.7}$$

where u_I^x and u_I^z are horizontal and vertical fluid velocity by incident wave, respectively. The incident wave pressure (p_I) is given by Bernoulli equation

$$\frac{p_I}{\rho} = R - gz - \frac{1}{2}\left[(u_I^x)^2 + (u_I^z)^2 \right], \tag{3.8}$$

where R is Bernoulli constant. The important dimensionless parameters in regular waves are the wave steepness kH and Ursell number $Ur = \frac{H\lambda^3}{h^3}$ (Ursell, 1953). Ursell number becomes important when the water depth is limited. The limitation of regular wave theory in a sense of application is given by a combination of two dimensionless parameters in Le Méhauté's diagram (Le Méhauté, 1976) in figure 3.1. The stream function theory covers the regular wave up to wave breaking, and consequently is adopted in the present study for the generation of regular waves. Fenton (1988) published a Fortran algorithm calculating the stream function waves. Recently, Ducrozet et al. (2019) published an open-source program based on stream function wave theory with a self-adjusting algorithm to cover all wave steepness and Ursell number combinations with desired error tolerance.

3.2 Irregular waves and waves in wave tank

3.2.1 Linear theory and related research on irregular waves

The simplest method to generate irregular waves is the superposition of linear Airy waves with random phases. 2D irregular waves with each of regular wave amplitudes are given in

$$\Phi_I(\mathbf{x}; t) = \sum_{i=1}^{N_{wave}} \frac{g A_i^I}{\omega_i} \frac{\cosh |\mathbf{k}_i| (z+h)}{\cosh |\mathbf{k}_i| h} e^{-\mathrm{i}(\mathbf{k}_i \cdot \mathbf{x} - \omega_i t + \delta_i)}, \tag{3.9}$$

where $\omega_i = g|\mathbf{k}_i| \tanh(|\mathbf{k}_i h|)$ is i-th wave frequency, $\mathbf{k}_i$ is a directional wave number, N_{wave} is the number of waves and δ_i is a random phase, respectively. A_i^I is i-th wave amplitudes which is given by wave spectrum

$$A_i^I = \sqrt{2S(\omega_i)\Delta\omega_i}, \tag{3.10}$$

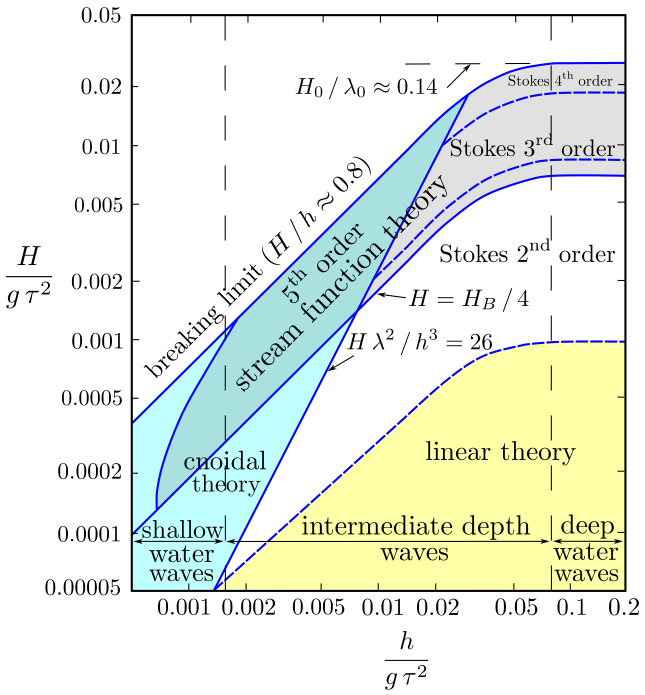

Figure 3.1. Le Méhauté's diagram, (Kraaiennest, 2009)

The wave spectrum ($S(\omega)$) has various forms. The commonly used wave spectra are Pierson-Moskowitz and JONSWAP which were invented for unlimited and limited fetch sea, respectively (Pierson and Moskowitz, 1964; Hasselmann et al., 1973). Ochi-Hubble wave spectrum, which has two peaks by the combination of JONSWAP, is used to describe west Africa sea state (Ochi and Hubble, 1976). For three dimensional irregular waves, the directional spreading function, which is denoted as $D(\omega|\theta)$ is multiplied to wave spectrum as

$$A_i^I = \sqrt{2S(\omega_i)D(\omega_i|\theta_i)\Delta\omega_i\Delta\theta_i}, \tag{3.11}$$

of which, $D(\omega|\theta)$ satisfies

$$\int_{\theta_{\min}}^{\theta_{\max}} D(\omega|\theta)d\theta = 1,$$

of which, the spreading angle θ_i is between $\theta_{\min}$ and $\theta_{\max}$. Half-cosine $2s$ power directional spreading function, which is modified version of cosine $2l$ power, is commonly used in nowadays (Pierson et al., 1955; Longuet-Higgins et al., 1963). Goda (1999) summarized wave spectra and directional spreading functions.

The linear superposition of Airy waves assumes that each wave component is independent, but in reality interferences between waves exists. Goda (1983) analyzed the wave measurement at Caldera port in Costa Rica. He showed the sea spectrum was exhibiting the secondary peak due to the interaction of waves and nonlinearities are noticeable in shallow water. Though the second order wave spectrum model is proposed by Tick (1963); Hamada (1965), the superposition model is not adopted to describe a higher-order interaction between waves. In addition, the superposition of regular waves needs a discretization of sea spectrum that gives a huge computational

burden to reconstruct irregular waves in viscous flow grid.

To overcome the limits of linear superposition theory, the direct simulation with nonlinear free surface boundary conditions has been studied. Engsig-Karup et al. (2009) applied the finite-difference method based fully nonlinear potential flow model to simulate 3D irregular waves. As the computational meshes are discretized in a manner of finite difference, numerical errors due to discretization are involved. Ducrozet et al. (2007, 2016) applied a pseudo-spectral method to simulate the 3D irregular waves with fully nonlinear free surface boundary condition. Moreover, Ducrozet et al. (2012) extended this methodology to the numerical wave tank problem by adding extra velocity potential in the same principle of pseudo-spectral. It is called a Higher-order spectral method (HOS) because its basis functions are expanded in a pseudo-spectral way. The fast Fourier transform (FFT) reduces the computational burden, furthermore, the treatment of spatial gradient is easier than other numerical methods. In the present study, HOS wave model is adopted to simulate irregular waves.

3.2.2 Nonlinear irregular waves: Open-ocean

The higher-order spectral method has been initiated by Dommermuth and Yue (1987); West et al. (1987). Cartesian coordinates are applied with rectangular computation domain with its horizontal lengths, L_x and L_y along x and y directions, respectively. The origin O is located at the corner of domain on the mean free surface $z = 0$. In the open ocean, the domain is horizontally periodic, and has a flat bottom. The free surface boundary condition is constructed by introducing the surface velocity potential $\tilde{\Phi}_I(x, y; t) = \Phi_I(x, y, \Xi_I(x, y); t)$ defined on the free surface as

$$\frac{\partial \tilde{\Phi}_I}{\partial t} + g\Xi_I = \mathcal{Q}(\Xi_I, \tilde{\Phi}_I, w) = -\frac{1}{2}\nabla\tilde{\Phi}_I \cdot \nabla\tilde{\Phi}_I + \frac{1}{2}\left(1 + \nabla\Xi_I \cdot \nabla\Xi_I\right) w^2, \tag{3.12}$$

$$\frac{\partial \Xi_I}{\partial t} = \mathcal{P}(\Xi_I, \tilde{\Phi}, w) = \left(1 + \nabla\Xi_I \cdot \nabla\Xi_I\right) w - \nabla\tilde{\Phi}_I \cdot \nabla\Xi_I, \tag{3.13}$$

where $w = \frac{\partial \Phi}{\partial z}$ is the vertical velocity. The surface velocity potential and wave elevation are calculated by solving the above equations. The periodic lateral and flat sea bottom boundary conditions are given in

$$\begin{aligned} \Phi_I(0, y, z; t) &= \Phi_I(L_x, y, z; t), \qquad \Xi_I(0, y; t) = \Xi_I(L_x, y; t), \\ \Phi_I(x, 0, z; t) &= \Phi_I(x, L_y, z; t), \qquad \Xi_I(x, 0; t) = \Xi_I(x, L_y; t) \end{aligned} \tag{3.14}$$

and

$$\frac{\partial \Phi_I}{\partial z} = 0, \qquad z = -h. \tag{3.15}$$

As the domain is limited in horizontal lengths and water depth, the velocity potential is expanded with the linear set of mode functions $\phi_{I,mn}(x, y, z)$ which satisfy the periodic and sea bottom boundary conditions

$$\Phi_I(x, y, z; t) = \sum_{m=0}^{\infty}\sum_{n=0}^{\infty} A^I_{mn}(t)\phi_{I,mn}(x, y, z) \tag{3.16}$$

with

$$\phi_{I,mn}(x,y,z) = \frac{\cosh k_{mn}(z+h)}{\cosh k_{mn}h} e^{\mathrm{i}k_m^x x} e^{\mathrm{i}k_n^y y} \tag{3.17}$$

where $A_{mn}^I(t)$ are the amplitudes of modes. $k_m^x = m\frac{2\pi}{L_x} = m\Delta k^x$, $k_n^y = n\frac{2\pi}{L_y} = n\Delta k^y$ and $k_{mn}^2 = (k_m^x)^2 + (k_n^y)^2$ are the modal wavenumbers for x, y and z directions, respectively. Though the basis functions satisfy the lateral, sea bottom and linearized free surface boundary conditions, the wavenumbers are not eigenvalues. Therefore, the problem is solved in a pseudo-spectral way. The open ocean conditions are approximated by applying periodicity conditions on the side of a rectangular domain. Fourier series are applied to express the surface velocity potential and incident wave elevation

$$\tilde{\Phi}_I(x,y;t) = \sum_{m=0}^{M_x}\sum_{n=0}^{N_y} B_{mn}^{\phi}(t) e^{\mathrm{i}k_m^x x} e^{\mathrm{i}k_n^y y}, \tag{3.18}$$

$$\Xi_I(x,y;t) = \sum_{m=0}^{M_x}\sum_{n=0}^{N_y} B_{mn}^{\Xi}(t) e^{\mathrm{i}k_m^x x} e^{\mathrm{i}k_n^y y}, \tag{3.19}$$

where M_x and N_y are the number of truncated Fourier modes. Because the free surface boundary conditions, given in equations (3.12) and (3.13), are nonlinear, *Stokes's expansion* is applied on the incident velocity potential and wave elevation. The perturbation series expansion with wave steepness (kH) are given as

$$\Phi_I(x,y,z;t) = \sum_{m=1}^{M_{HOS}} \Phi_I^{(m)}(x,y,z;t), \tag{3.20}$$

where M_{HOS} is a HOS order that represents the nonlinearity order. Unknown wave elevation position needs an iterative Taylor series expansion at $z=0$ with respect to wave elevation

$$\Phi_I^{(1)}(x,y,0,t) = \tilde{\Phi}_I(x,y;t), \tag{3.21}$$

$$\Phi_I^{(m)}(x,y,0,t) = -\sum_{k=1}^{m-1} \frac{(\Xi_I)^k}{k!} \frac{\partial \Phi_I^{(m-k)}}{\partial z^k}(x,0,t), \qquad \text{for} \qquad m \geq 2. \tag{3.22}$$

The free surface boundary condition for Φ_I on $z = \Xi_I$ is transformed into the simple boundary condition for $\Phi_I^{(m)}$ on $z=0$. As the nonlinear boundary conditions are given explicitly, m-th order velocity potentials $\Phi_I^{(m)}$ are solved by applying the modal functions in equation (3.16). Initialization of wave fields for $\Xi(x,y;t=0)$ and $\tilde{\Phi}(x,y;t=0)$ are necessary for propagating waves in HOS-ocean model. Both regular and irregular waves can be used to initialize the wave field. As a regular waves, the nonlinear stream function wave theory is used in HOS model, and the linear superposition of irregular waves is used to initialize the wave fields for irregular waves. At the initial condition, the magnitudes of modes for irregular waves are given in

$$\frac{1}{2}\left|B_{mn}^{\Xi}(t=0)\right|^2 = S(k_x,k_y)\Delta k_x \Delta k_y = \frac{1}{k}\frac{\partial \omega}{\partial k} S(\omega) D(\omega|\theta) \Delta k_x \Delta k_y, \tag{3.23}$$

where Δk_x and Δk_y are modal wave number discretization in x and y directions. By considering random phase (δ_{mn}^{θ}), the wave elevation modal amplitudes are determine by

$$B_{mn}^{\Xi}(t=0) = \Re\left[e^{\mathrm{i}\delta_{mn}^{\theta}} \left|B_{mn}^{\Xi}(t=0)\right|\right]. \tag{3.24}$$

The initial mode amplitudes of velocity potentials are derived from linearized free surface boundary condition

$$B^{\phi}_{mn}(t=0) = -\mathrm{i}\frac{\omega_{mn}}{g} B^{\Xi}_{mn}(t=0). \tag{3.25}$$

It must be noticed that simulating the nonlinear HOS wave model with the initial condition which is given by linear superposition model may lead to instability (Ducrozet et al., 2016).

A ramping function ($f^{ramp}(t)$), allowing a smooth transition from linear to nonlinear sea state, is used as a multiplication fact for the nonlinear terms in free surface boundary condition

$$\frac{\partial \tilde{\Phi}_I}{\partial t} + g\Xi_I = f^{ramp}(t)\mathcal{Q}(\Xi_I, \tilde{\Phi}_I, w), \tag{3.26}$$

$$\frac{\partial \Xi_I}{\partial t} - w^{(1)} = f^{ramp}(t)\left(\mathcal{P}(\Xi_I, \tilde{\Phi}_I, w) - w^{(1)}\right), \tag{3.27}$$

with

$$f^{ramp}(t) = 1 - e^{-(t/T_{ramp})^{n^{ramp}}}. \tag{3.28}$$

where T_{ramp} and n^{ramp} are a transition time and ramp parameter, respectively. $w^{(1)}$ is the linear vertical velocity.

The details on mathematical formulation and procedures are explained in (Ducrozet et al., 2007, 2016; Bonnefoy et al., 2009).

3.2.3 Nonlinear waves: Numerical wave tank(NWT)

The HOS model can be formulated for a 3D rectangular wave tank equipped with wavemaker at rest position $x = 0$, and surrounded by vertical walls. The wave absorbing beach is placed at the end of wave tank. The kinematic boundary condition on the wavemaker is given in

$$\frac{D}{Dt}(\mathbf{x} - X_{wm}(y,z;t)) = 0, \qquad \text{on} \qquad \mathbf{x} = X_{wm}(y,z;t), \tag{3.29}$$

where $X_{wm}(y,z;t)$ is a displacement of wavemaker. The above equation is rewritten as

$$\frac{\partial X_{wm}}{\partial t} = \frac{\partial \Phi_I}{\partial x} - \frac{\partial X_{wm}}{\partial y}\frac{\partial \Phi_I}{\partial y} - \frac{\partial X_{wm}}{\partial z}\frac{\partial \Phi_I}{\partial z}, \qquad \text{on} \qquad \mathbf{x} = X_{wm}(y,z;t). \tag{3.30}$$

The vertical wall condition is given as

$$\begin{aligned} \frac{\partial \Phi_I(L_x, y, z; t)}{\partial x} &= 0, \\ \frac{\partial \Phi_I(x, 0, z; t)}{\partial y} &= \frac{\partial \Phi_I(x, L_y, z; t)}{\partial y} = 0. \end{aligned} \tag{3.31}$$

To solve the boundary value problem, $\Phi_I(x,y,z;t)$ and $\Xi_I(x,y;t)$ are decomposed into

$$\Phi_I(x,y,z;t) = \Phi_H(x,y,z;t) + \Phi_L(x,y,z;t), \tag{3.32}$$

$$\Xi_I(x,y;t) = \Xi_H(x,y;t) + \Xi_L(x,y;t), \tag{3.33}$$

where $\Phi_H(x,y,z;t)$ and $\Phi_L(x,y,z;t)$ are the harmonic and local velocity potentials. The lateral boundary conditions for $\Phi_L(x,y,z;t)$ are given as

$$\begin{aligned} \left.\frac{\partial \Phi_L}{\partial x}\right|_{\mathbf{x}=X} &= \frac{\partial X_{wm}}{\partial t} + \frac{\partial X_{wm}}{\partial y}\frac{\partial \Phi_L}{\partial y} + \frac{\partial X_{wm}}{\partial z}\frac{\partial \Phi_L}{\partial z}, & \left.\frac{\partial \Phi_L}{\partial x}\right|_{x=L_x} &= 0, \\ \left.\frac{\partial \Phi_L}{\partial y}\right|_{y=0} &= 0, & \left.\frac{\partial \Phi_L}{\partial y}\right|_{y=L_y} &= 0, \end{aligned} \tag{3.34}$$

The perturbation series expansion of the wavemaker boundary condition needs a vertically extended domain with artificial height h_{add}, depicted in figure 3.2.

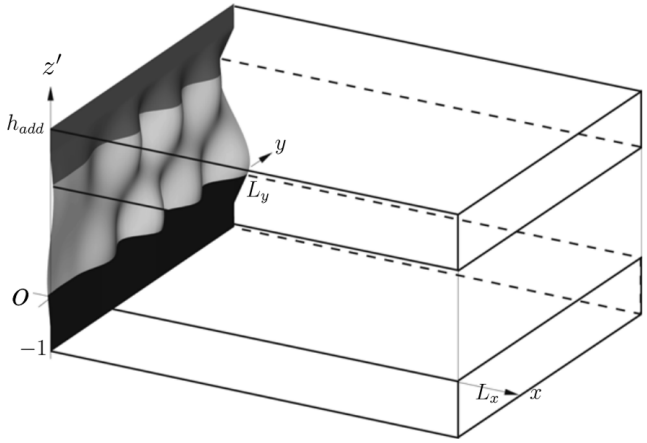

Figure 3.2. The extended HOS-NWT domain (Ducrozet et al., 2012).

The extended domain consists of three zones: (1) original domain is mapped into $z' = -1$ to $z' = 0$. (2) The mirror of original domain with respect to $z' = (h_{add} - 1)/2$. This zone is defined between $z' = h_{add} - 1$ and $z' = h_{add}$. (3) A smoothly varying surface domain between original and mirror domain, from $z' = 0, z' = h_{add} - 1$. The displacement of wavemaker is applied $z' \in [-1, 0]$ and $z' = [h_{add} - 1, h_{add}]$ with symmetry. Between two zones, the wave motions are extrapolated with polynomial functions. The artificial height is taken to be $h_{add} = 3$. For the local velocity potential, the symmetric condition with respect to $z' = (h_{add} - 1)/2$ is applied, instead of free surface boundary condition. The perturbation series is also applied to local velocity components upto third order as

$$\Phi_L(x,y,z';t) = \sum_{m=0}^{3} \Phi_L^{(m)}(x,y,z';t), \tag{3.35}$$

m-th order potential is expanded with the pseudo-spectral method as

$$\Phi_L^{(m)}(x,y,z';t) = \sum_{n=0}^{N_y}\sum_{p=0}^{N_{add}} B_{np}^{add}(t)\phi_{L,mn}(x,y,z') \tag{3.36}$$

with

$$\phi_{L,mn}(x,y,z') = \cos(k_n^y y)\cos\left(k_p^{add}(z'+1)\right)\frac{\cosh k_{np}^{add}(L_x - x)}{\cosh k_{np}^{add} L_x}, \tag{3.37}$$

where $k_n^y = \frac{n\pi}{L_y}$, $k_p^{add} = \frac{p\pi}{h_{add}+1}$ and $k_{np}^{add} = \sqrt{(k_n^y)^2 + (k_p^{add})^2}$. The local velocity potential can be solved with the Taylor series expansion with respect to the nonlinear wavemaker boundary condition at $x = 0$.

The non-homogeneous wavemaker boundary condition at $x = 0$ is satisfied by local velocity potential, the lateral boundary condition for harmonic velocity potential is given by

$$\begin{aligned} \left.\frac{\partial \Phi_H}{\partial x}\right|_{\mathbf{x}=X} &= 0, \qquad \left.\frac{\partial \Phi_H}{\partial x}\right|_{x=L_x} = 0, \\ \left.\frac{\partial \Phi_H}{\partial y}\right|_{y=0} &= 0, \qquad \left.\frac{\partial \Phi_H}{\partial y}\right|_{y=L_y} = 0. \end{aligned} \tag{3.38}$$

The harmonic velocity potential and wave elevation in perturbation series

$$\Phi_H(x, y, z'; t) = \sum_{m=0}^{M_{HOS}} \Phi_H^{(m)}(x, y, z'; t), \tag{3.39}$$

$$\Xi_I(x, y; t) = \sum_{m=0}^{M_{HOS}} \Xi_I^{(m)}(x, y; t), \tag{3.40}$$

and m-th order harmonic velocity potentials and wave elevations are expressed with eigenfunction expansion as

$$\Phi_H^{(m)}(x, y, z'; t) = \sum_{m=0}^{M_x} \sum_{n=0}^{N_y} B_{mn}^{\Phi}(t) \phi_{H,mn}(x, y, z'), \tag{3.41}$$

$$\Xi_I^{(m)}(x, y; t) = \sum_{m=0}^{M_x} \sum_{n=0}^{N_y} B_{mn}^{\Xi}(t) \cos(k_m^x x) \cos(k_n^y y), \tag{3.42}$$

with

$$\phi_{H,mn}(x, y, z') = \cos(k_m^x x) \cos(k_n^y y) \frac{\cosh(k_{mn}(z' + 1))}{\cosh k_{mn}} \tag{3.43}$$

where $k_m^x = \frac{m\pi}{L_x}$ and $k_{mn} = \sqrt{(k_m^x)^2 + (k_n^y)^2}$ are eigenvalues of wave tank. It is solved by applying nonlinear free surface boundary conditions, considering absorbing beach by a modification of pressure $\frac{p}{\rho} = D(\mathbf{x})w = D(\mathbf{x})\frac{\partial \Xi}{\partial t}$

$$\begin{aligned} \frac{\partial \Phi_H}{\partial t} + g\Xi_I = &-\frac{1}{2}\nabla\Phi_H \cdot \nabla\Phi_H + \frac{1}{2}\left(1 + \nabla\Xi_I \cdot \nabla\Xi_I\right)(u_I^z)^2 \\ &- \nabla\Phi_I \cdot \nabla\Phi_L - \frac{1}{2}\nabla\Phi_L \cdot \nabla\Phi_L - \frac{\partial \Phi_L}{\partial t} - D(\mathbf{x})\frac{\partial \Xi}{\partial t} \end{aligned} \tag{3.44}$$

$$\frac{\partial \Xi_I}{\partial t} = \left(1 + \nabla\Xi_I \cdot \nabla\Xi_I\right) w - \nabla\Phi_I \cdot \nabla\Xi_I + u_L^z. \tag{3.45}$$

Note that the nonlinear terms involve the local velocity potentials. The details of formulation and numerical algorithm are explained in (Ducrozet et al., 2012).

3.2.4 Reconstruction of nonlinear irregular waves in viscous model

The nonlinear models based on HOS for irregular waves have been developed and validated for several years (Ducrozet et al., 2007; Bonnefoy et al., 2009; Ducrozet et al., 2012, 2016).

Those HOS wave solvers are released as open-source codes, which anyone can develop, use and distribute under the terms of GNU General Public Licence (GPLv3). As the pseudo-spectral method is used, the free surface grid is discretized with equal spacing to apply FFTs. Therefore, the reconstruction of wave fields is necessary to deliver flow quantities to the viscous flow model. The reconstructed nonlinear flows are able to be used for the initialization of domain and the boundary.

A HOS wrapper program, which is called as `Grid2Grid`, has been developed to reconstruct the wave fields from the results of HOS computation (Choi et al., 2018). `Grid2Grid` applies an inverse FFTs and a quick B-spline module to reconstruct the nonlinear wave fields for arbitrary simulation time and space (Frigo and Johnson, 2005; Williams, 2018). The simulated nonlinear irregular waves by HOS provide the time histories of mode amplitudes. By applying inverse FFTs with vertical functions, $f(z) = \frac{\cosh k_{mn}(z+h)}{\cosh k_{mn}h}$ and $f^{add}(z') = \cos k_p^{add}(z'+1)$, the exact nonlinear wave fields are reconstructed in rectilinear grid at HOS simulation time $t = t^{HOS}$. As the rectilinear grid does not change with respect to time, the continuous HOS wave fields in discrete time are reconstructed via interpolation. B-spline interpolation at arbitrary points, $x_1, x_2, \cdots, x_N$ are evaluated with known interpolation nodes $x_{i_1}, x_{i_2}, \cdots, x_{i_N}$ and their function values $f(x_{i_1}, x_{i_2}, \cdots, x_{i_N})$

$$f(x_1, x_2, \cdots, x_N) = \sum_{i_1, i_2, \cdots, i_N = -N_{mod}}^{N_{mod}+1} f(x_{i_1}, x_{i_2}, \cdots, x_{i_N}) \prod_{j=1}^{N} b_{ij}^{(p)}(x_j) \tag{3.46}$$

where $N_{mod} = N_{interp}/2$, $p = N_{interp} - 1$, and N_{interp} is an interpolation order. $b_{ij}^{(p)}(x_j)$ is B-spline function defined by

$$b_{ij}^{(0)}(x_j) = \begin{cases} 1 & \text{if} \quad x_{j_i} < x_j < x_{j_{i+1}}, \\ 0 & \text{otherwise} \end{cases} \tag{3.47}$$

$$b_{ij}^{(p)}(x_j) = \frac{x_j - x_{j_i}}{x_{j_{i+p}} - x_{j_i}} b_{ij}^{(p-1)}(x_j) + \frac{x_{j_{i+p+1}} - x_j}{x_{j_{i+p+1}} - x_{j_{i+1}}} b_{i+1,j}^{(p-1)}(x_j), \qquad p \geq 1. \tag{3.48}$$

The B-spline function with respect to p is shown in figure 3.3. The reconstructed HOS wave fields have 3 spatial and time variables.

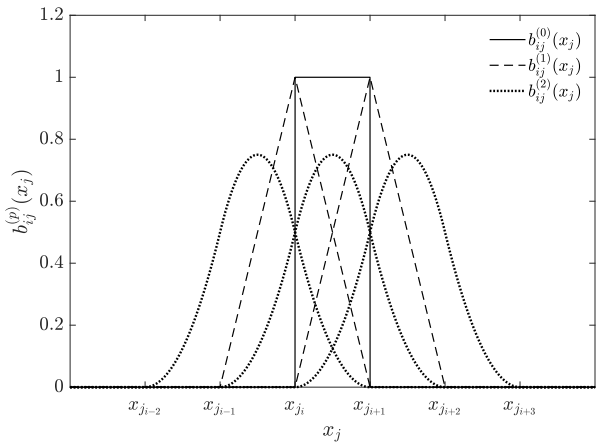

Figure 3.3. The basis functions, $b_{ij}^{(p)}(x_j)$.

The computation algorithm does not calculate the basis functions, $b_{ij}^{(p)}(x_j)$, but evaluates the function value by recursive way. The computational algorithm is called *De Boor's algorithm* (De Boor, 1978). The cubic spline interpolation is used for evaluating fluid velocity, pressure and wave elevation with respect to spatial and temporal variables.

3.3 Validation on the generation of nonlinear waves in the viscous flow solver

The generation of stream function wave theory in viscous flows is tested and validated in Chapter 2.1. The generation of HOS nonlinear waves in viscous flows is important to simulate realistic irregular waves, to investigate its effects on the floating body and to regenerate the experimental waves in the numerical simulation. The HOS waves in viscous flow solver are regenerated by open-source library `Grid2Grid` (Choi et al., 2018). The time series of mode amplitudes are obtained to reconstruct HOS waves by inverse FFTs and interpolation module. The flow quantities of nonlinear incident waves are possibly calculated for a particular position and time where the specific nonlinear phenomenon occurs.

For the validation, `foamStar`, which is based on multiphase solver with the VOF model, is used (Seng, 2012; Monroy et al., 2016). The relaxation schemes, described in section 2.3.1 is used. The reconstructed nonlinear incient waves are used to initialize the computational domain and to give the target values in the viscous flow solver.

3.3.1 Validation with HOS simulations

The generation of HOS wave models in the viscous flow model is validated with HOS simulations. Gatin et al. (2017) simulated the nonlinear 3D irregular waves based on HOS-ocean (open sea waves) in a multiphase flow solver, however the scheme was not tested with waves generated in a wave tank (HOS-NWT). In the present study, the generation of both HOS wave theories in viscous flow solver is validated.

The considered wave conditions for validation are given in Table 3.1. For HOS-NWT 3D regular waves, the oblique wave of propagation angle, $\theta = 60°$ is considered.

Table 3.1. HOS wave condition for validation

Wave Type	Value	HOS-Ocean		HOS-NWT	
		2D	3D	2D	3D
Regular Wave	T [s]	-	-	0.702	0.702
	H [m]	-	-	0.0431	0.0288
Irregular Waves	T_p [s]	0.702	1.0	1.0	0.702
	H_s[m]	0.0288	0.10	0.05	0.0384
	γ [-]	3.3	3.3	3.3	3.3

The computational domain of viscous solver is depicted in figure 3.4.

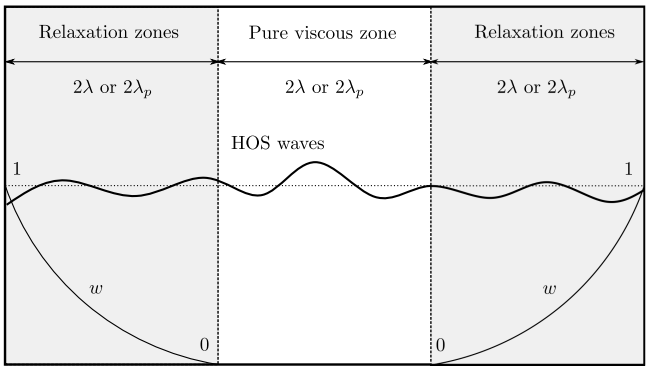

Figure 3.4. The computational domain of viscous flow solver for generation of HOS waves.

The length of relaxation zones is two times of wavelength (λ or λ_p) and the same length is used for pure viscous flow zone where no weight function is applied. The same principle is adopted for the 3D waves. The snapshots of 3D regular/irregular wave simulation with viscous solver are shown in figures 3.5. The relaxation zones are colored with transparent grey.

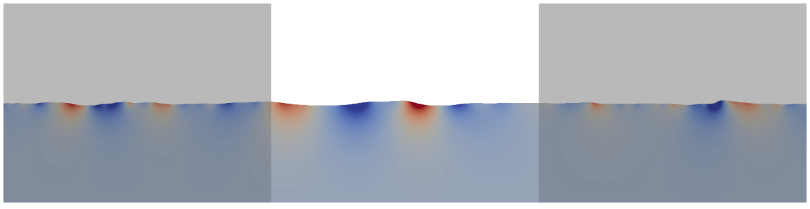

(a) HOS-Ocean 2D Irregular waves

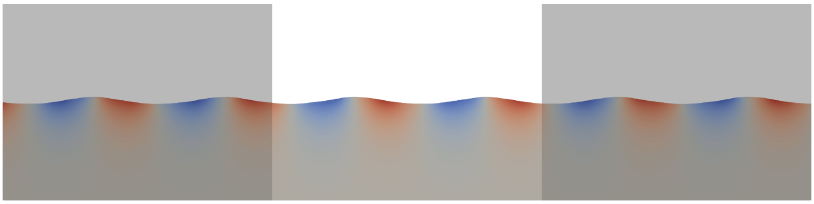

(b) HOS-NWT 2D Regular waves

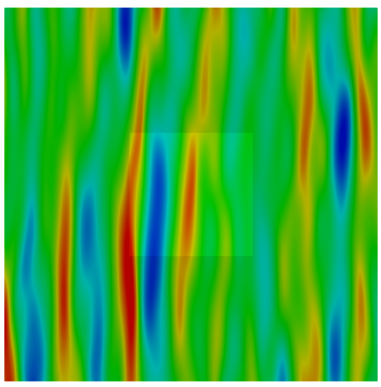

(c) HOS-Ocean 2D Irregular waves

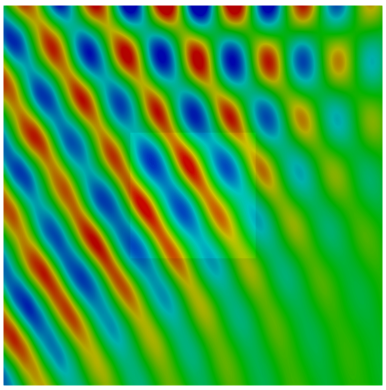

(d) HOS-NWT 3D Regular waves

Figure 3.5. Simulation of nonlinear HOS waves in viscous flow model.

The waves generated at inlet relaxation zones are propagating to the pure viscous flow domain. After traveling across the pure viscous flow domain, waves enter the outlet relaxation zones. For the HOS-NWT 3D regular waves, the reflection waves due to the lateral wall are well shown in simulation.

The measured wave time series in viscous flow are compared with the results of HOS simulation in figure 3.6.

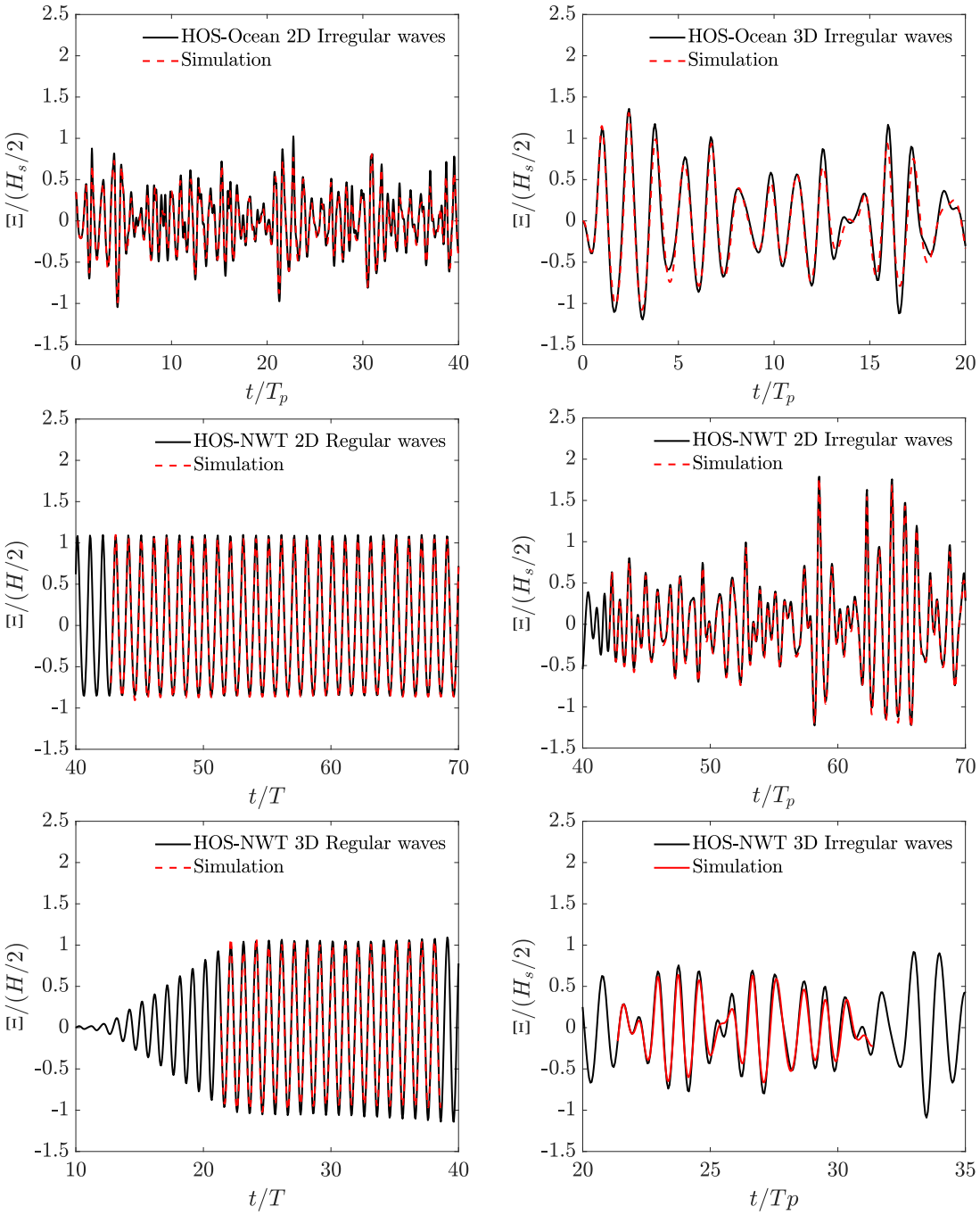

Figure 3.6. Generation of nonlinear HOS waves in viscous flow solver and comparison with HOS wave model (top : HOS-Ocean 2D, 3D irregular waves, middle : HOS-NWT 2D regular/irregular waves, bottom:HOS-NWT 3D regular/irregular waves)

The measured wave elevation at the center of viscous flow domain shows a good agreement with the results of HOS wave theory. The discrepancies between viscous flow and HOS simulation come from

- The computational meshes need to be fine sufficiently to describe the waves, especially for irregular waves which have short/long waves with various wave heights.
- Interpolation errors in the wrapper program could provide an error source in viscous flow. The cubic-spline interpolated velocity in HOS grid may not satisfy the mass conservation (Li, 2018). Therefore, the extra sources may appear in momentum/pressure equation.
- HOS is based on a psuedo-spectral method that may lead to high-frequency components. The zero-padding on spectral quantities is used to remove this phenomenon. It may lose the wave energy.
- Relaxation scheme with weight function generates undesired waves in the relaxation zones. Introduced weight function appears as source terms in VOF transport and momentum equations, and is able to give an extra error for wave propagation problem. Perić et al. (2018b) investigated the effect of weight function and showed that the wave reflection is inevitable with the relaxation scheme.
- Other factors like numerical damping, fluid viscosity, numerical errors, ...

3.3.2 Validation with HOS simulations and Experiments

Extreme waves corresponding to the 1000 year return period of irregular waves in the Gulf of Mexico (GOM) is regenerated by the proposed reconstruction procedure in the viscous flow model. The results is validated with HOS simulation and experiments.

The wave condition is given in Table 3.2. HOS-NWT 2D model is used to simulate extreme waves. The same configuration of computational doamin described in figure 3.4 is used for numerical setup. The convergence of HOS-NWT model is conducted with respect to the number of modes and the order of HOS.

Table 3.2. Extreme wave condition

Item	Value
Peak period (T_p)	15.5 s
Significant wave height (H_s)	17.5 m
Peak enhancement factor (γ)	3.3
Wave spectrum	JONSWAP

The wave breaking events are identified during HOS simulation with a criterion defined by a ratio of local energy flux velocity to local crest velocity (Barthelemy et al., 2018)

$$\frac{F_{wave}/E}{c_p} = \frac{u_{wave}}{c_p} = \frac{1}{c_p}\left.\frac{\partial \Phi_I}{\partial x}\right|_{z=\Xi_I} \geq 0.75. \tag{3.49}$$

where F_{wave} is a local energy flux in wave propagation direction and E is local energy density. The ratio is approximated to the water particle velocity under the crest, u_{wave}. c_p is a local phase velocity. The breaking criterion is taken from Tian et al. (2012). The complexity of evaluating the local phase velocity for all computational domain and time are explained in (Seiffert et al., 2017). The breaking model considers the local energy dissipations appearing as Laplacian term in nonlinear free surface boundary conditions as

$$\frac{\partial \tilde{\Phi}_I}{\partial t} + g\Xi_I = -\frac{1}{2}\nabla\tilde{\Phi}_I \cdot \nabla\tilde{\Phi}_I + \frac{1}{2}\left(1 + \nabla\Xi_I \cdot \nabla\Xi_I\right)\left(u_I^z\right)^2 + 2\nu_{eddy}\nabla \cdot \nabla\tilde{\Phi}_I, \tag{3.50}$$

$$\frac{\partial \Xi_I}{\partial t} = \left(1 + \nabla\Xi_I \cdot \nabla\Xi_I\right) u_I^z - \nabla\tilde{\Phi}_I \cdot \nabla\Xi_I + 2\nu_{eddy}\nabla \cdot \nabla\Xi_I, \tag{3.51}$$

with eddy viscosity

$$\nu_{eddy} = \alpha_{br}\frac{H_{br}L_{br}}{T_{br}}, \tag{3.52}$$

where T_{br} is a breaking duration time from when the wave crest begins to fall until the surface disturbance front is no longer obvious, L_{br} is a distance from wave breaking to the obvious surface disturbance ends, H_{br} is a falling crest height, α_{br} is a parameter and the value $\alpha_{br} = 0.02$ is used by Tian et al. (2010). The wave breaking model indroduced in HOS is validated with experimental measurement in (Seiffert and Ducrozet, 2018). Wave breaking events are recorded during the HOS simulation of extreme waves and shown in figure 3.7 as markers. At the moments of wave breaking, the wave heights are measured and colored differently in the figure 3.7. The wave breaking event, occurs at $x/L_w \approx 5$ and $t/T_p \approx 85$, is selected for benchmark case.

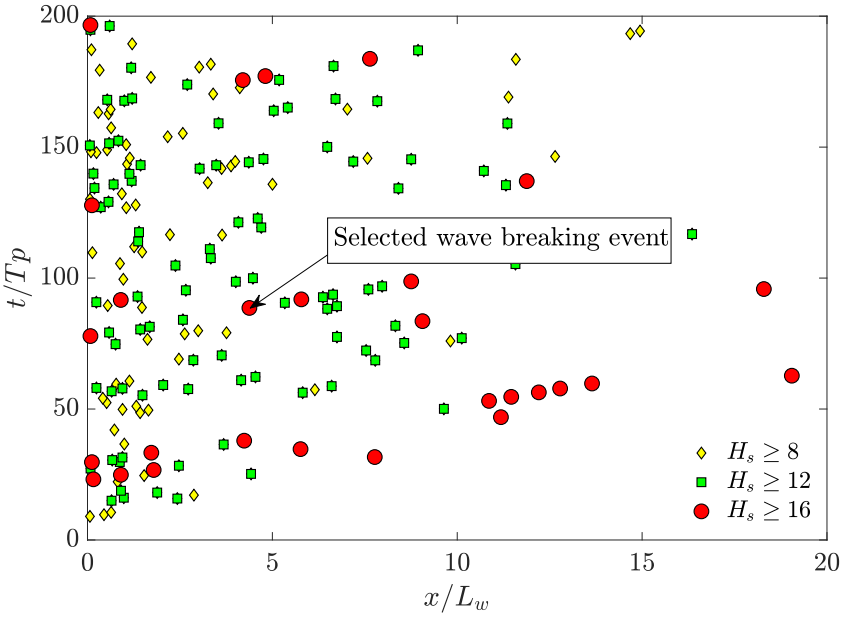

Figure 3.7. The wave breaking event in HOS simulation

The experiments were conducted in the 3D ocean wave tank in Ecole Centrale de Nantes(ECN), and its dimensions are $L \times B \times h = 46.4 \times 29.7 \times 5.0m$ with absorbing beach of length $9.7m$ at ends. The flap-type wavemakers, which have $3m$ depth and can move independently, allow us to

generate various type of waves. The specification of wave tank is shown in figure 3.8. The waves are scaled with ratio 1/100 in experiments and the re-generation of waves are restricted near to the time of selected wave breaking event to minimize the wave reflection. Three probes are aligned at the distance $20.81m$ of the wavemaker with horizontal interval $2.3m$ (and consequently at the different transverse direction in the tank).

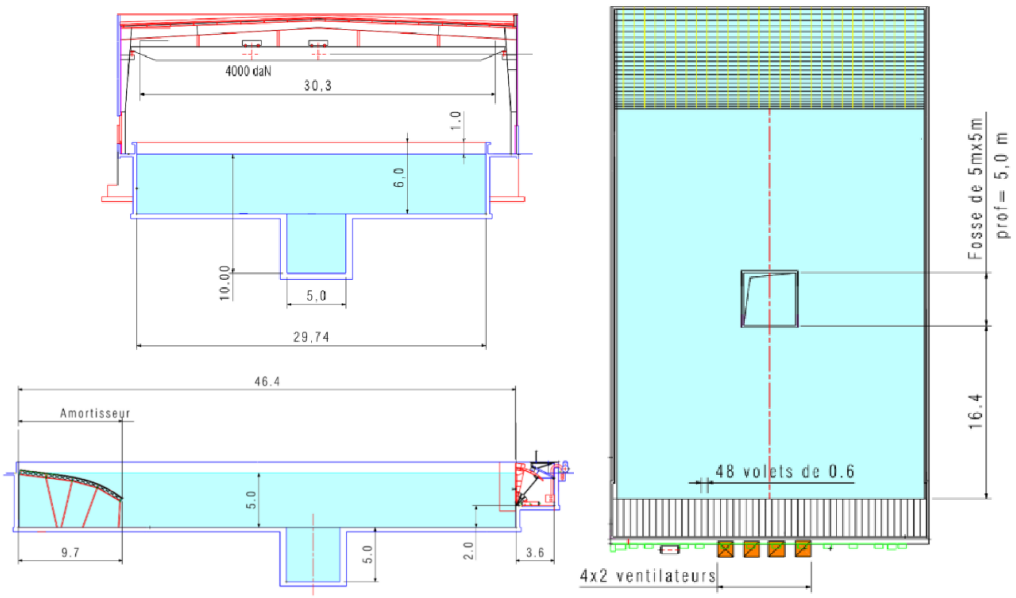

Figure 3.8. Specification of wave tank in Ecole Centrale de Nantes(ECN)

The time and mesh discretization considered in viscous flow are given in Table 3.3. Note that the computational mesh denoted as *normal* is set from the result of preliminary test on the incident waves in Chapter 2.1. The measured wave elevation at the breaking point are compared in figure 3.9 with respect to discretization. The results show that a small difference is shown for a coarse mesh with others. Results are slightly different after wave breaking event, but they give good results for overall simulation time. Possible numerical errors has discussed in previous section 3.3.1. The extreme event in simulation and experiment are shown in figure 3.10. A small spilling breaker is observed in the front crest of waves in simulation and experiments. In the experiment, 3D effects along horizontal directions are observed.

Table 3.3. Time and mesh discretizations used for the simulation of extreme waves

Mesh type	$\lambda_p/\Delta x$	$H_s/\Delta z$	$\Delta x/\Delta z$	$T_p/\Delta t$
coarse	62.5	18.4	6.5	300
normal	125	36.8	6.5	600
fine	250	73.5	6.5	1,200
very fine	500	73.5	3.25	2,400

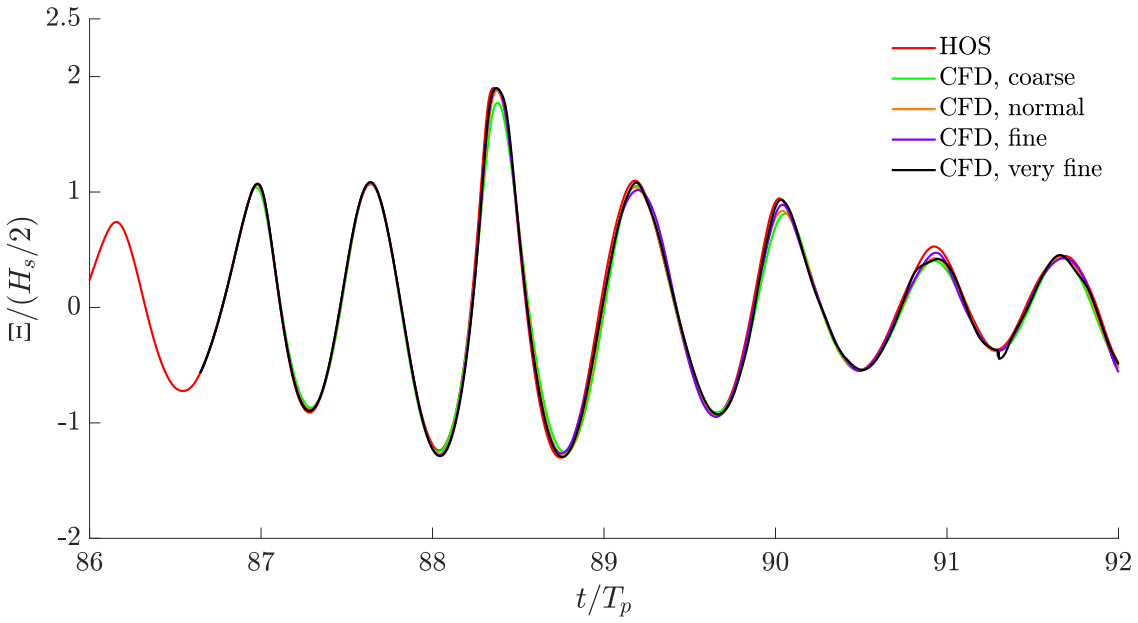

Figure 3.9. Convergence test on the simulation of extreme waves

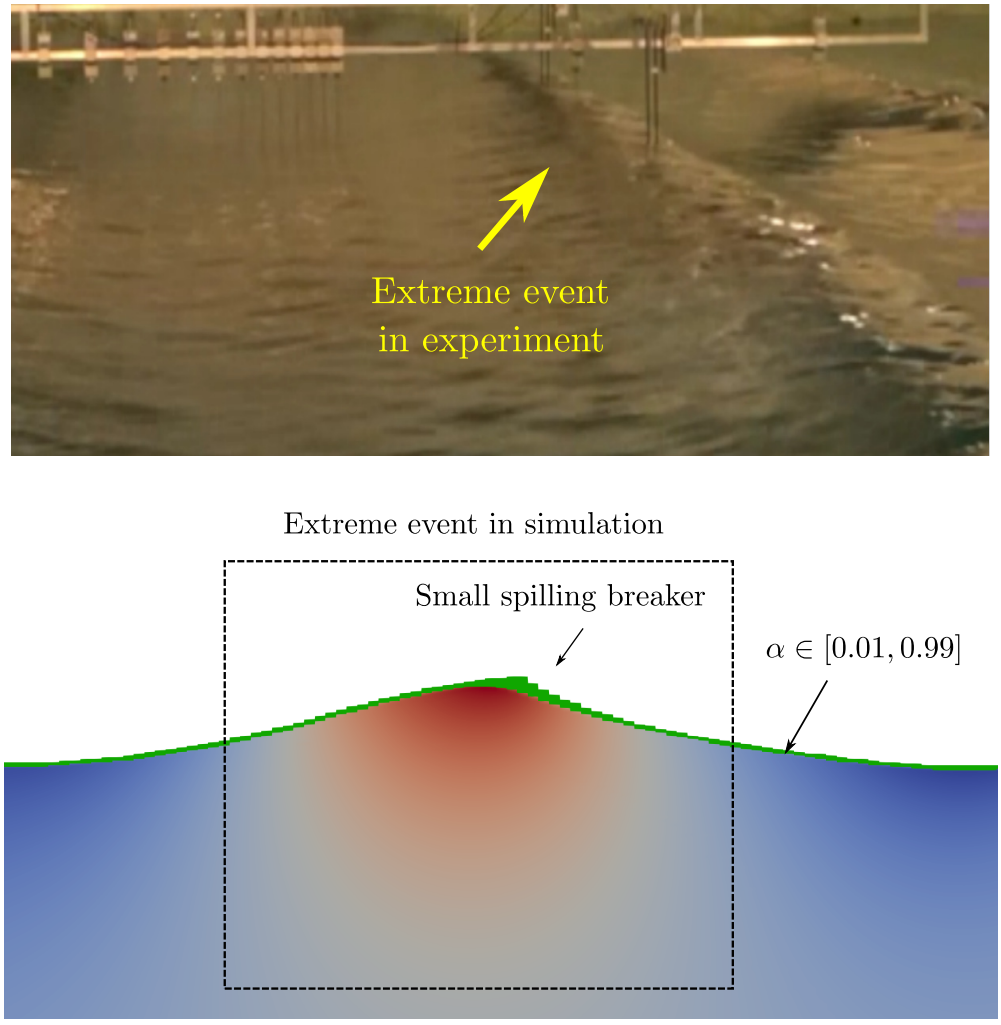

Figure 3.10. Observed extreme wave events in experiment and simulation

The measured wave elevation in experiments is compared with the results of HOS and CFD (viscous flow model with relaxation with HOS) in figure 3.11. To minimize the 3D effects due to wave absorption in the experiment, the waves in experiments were generated near to the time of extreme event.

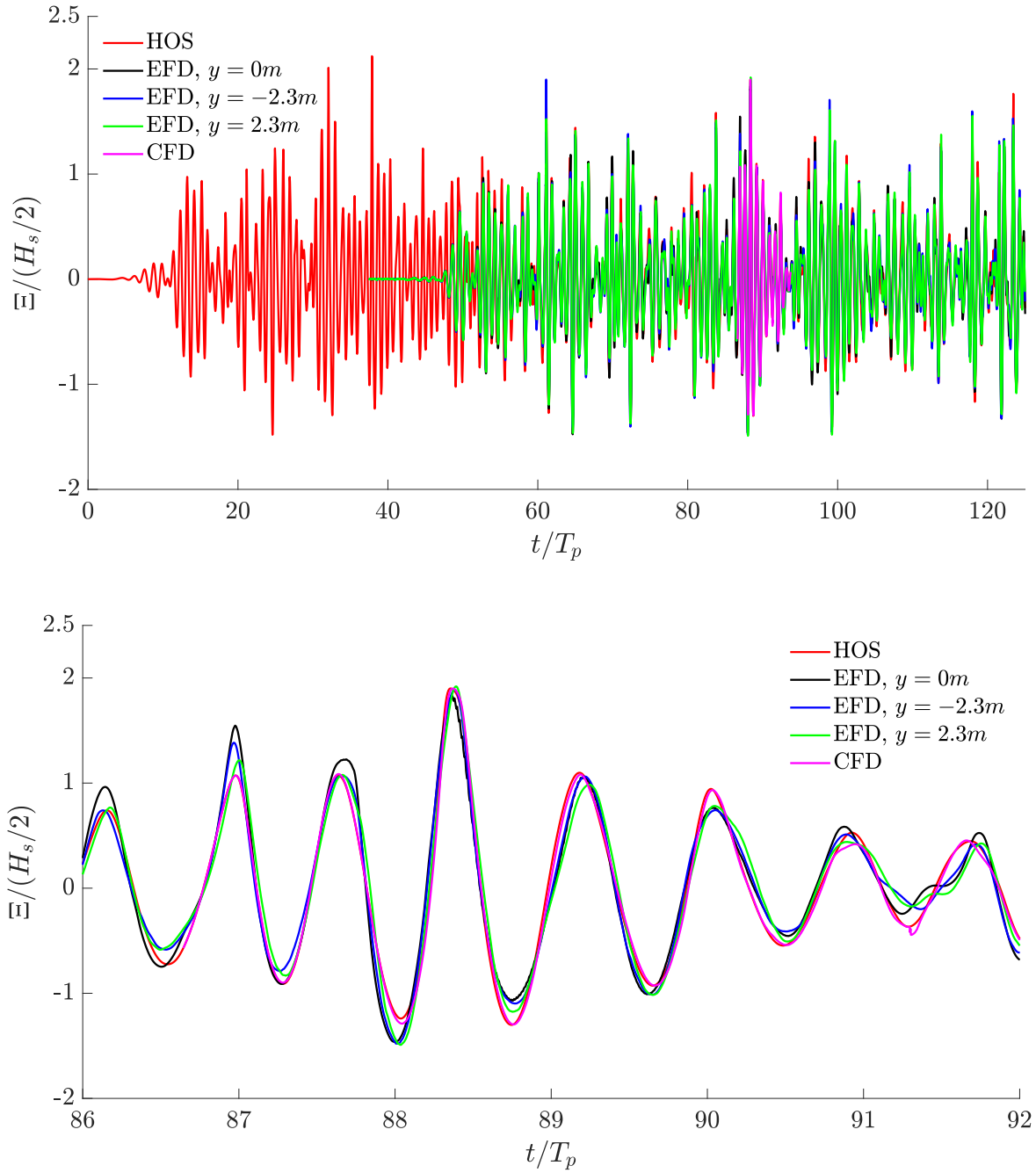

Figure 3.11. Comparision of wave elevation time series for extreme wave condition.

Both CFD and HOS show good agreements with each other, however the differences between experiment and simulations exist though the experimental result has 3D effects in horizontal direction. The possible errors are:

- Perturbation series of HOS-NWT wave theory.
- Simple wave breaking model in HOS (events appearing before the one simulated).
- Wave maker transfer function to regenerate the HOS waves in experiments. HOS-NWT model uses a linear transfer function.
- The reflection by wave absorber, 3D effects and different water depths in experiments.

3.4 Conclusion

Potential flow theories on nonlinear incident waves are summarized. Stream function wave theory for regular waves is reviewed in view of boundary value problem and the eigenfunction expansion. HOS wave theories based on the pseudo-spectral way is summarized for irregular waves and waves in NWT. The reconstruction of HOS wave fields in viscous flow is introduced in the present study based on inverse FFT and B-spline interpolation.

The proposed reconstruction procedure is validated with HOS simulation for different HOS models. Furthermore, a nonlinear wave breaking event predicted by the simple wave breaking model in HOS simulation is simulated in the viscous flow model. Time and space limited simulation has been conducted on breaking event. The experiment has been conducted to validate the procedure at the wave tank of Ecole Centrale de Nantes. The result shows a good agreement with the results of HOS simulation and experimental measurement.

4 Potential flow: Complementary waves with an arbitrary matching surface

The linear potential flow model for complementary waves generated by the existence of the body is considered in this chapter.

4.1 Boundary value problem

The complementary waves are generated by wave-structure interaction and they propagate in perfect fluid medium in the presence of a free surface. The fluid domain and boundaries are depicted in figure 4.1. The grey color defines the fluid domain of interest. At $t = 0$ no complementary waves exist in the fluid domain of interest. The fluid is surrounded by boundary surfaces, such as the matching surface (S_M), the free surface (S_F) and the surface at infinity (S_∞). The body is located inside the matching surface.

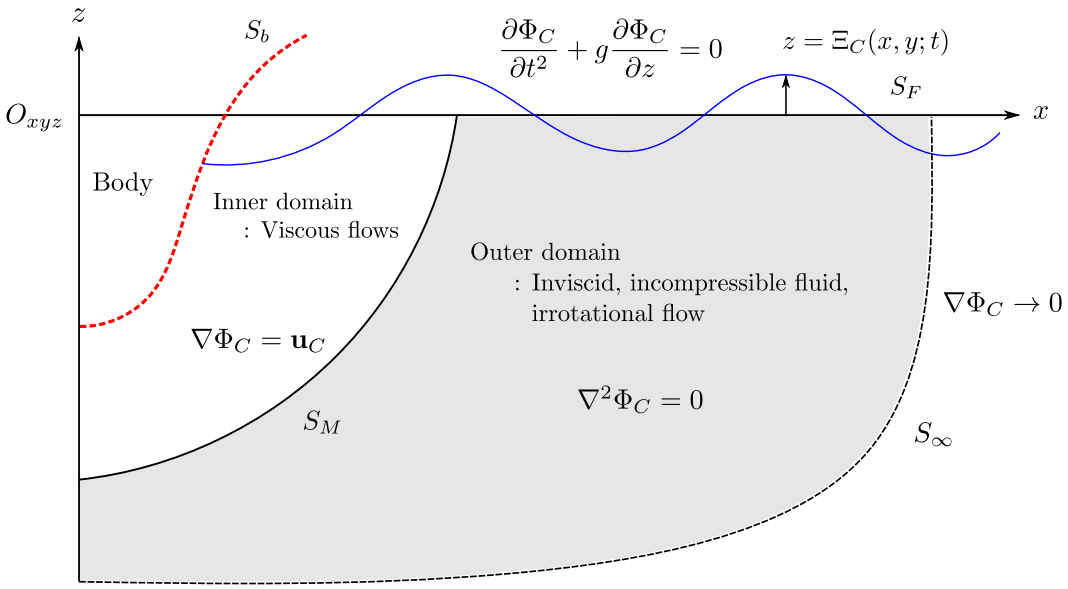

Figure 4.1. Domain definition for complementary potential flow with matching surface.

The perfect fluid and irrotational flow hypothesis are assumed, in order to introduce the velocity potential. The complementary potential (Φ_C) satisfies the Laplace's equation

$$\nabla^2 \Phi_C = 0, \qquad \text{for} \qquad \mathbf{x} \in \Omega. \tag{4.1}$$

where Ω represents the fluid domain. On the matching surface, complementary fluid velocity can be decomposed into the irrotational and vortical velocity by Helmholtz decomposition theorem (Arfken et al., 1995)

$$\mathbf{u}_C = \nabla \Phi_C + \mathbf{v}_C, \qquad \text{on} \qquad \mathbf{x} \in S_M. \tag{4.2}$$

where $\mathbf{u}_C$ is the complementary fluid velocity obtained by the viscous flow model. $\nabla\Phi_C$ and $\mathbf{v}_C$ are complementary irrotational and vortical velocities, respectively. In the present study, the vortical velocity $\mathbf{v}_C$ is assumed to be sufficiently small on the matching surface as

$$\mathbf{v}_C \approx 0, \qquad \text{on} \qquad \mathbf{x} \in S_M. \tag{4.3}$$

Therefore, the following boundary condition is imposed on the matching surface as

$$\nabla\Phi_C = \mathbf{u}_C, \qquad \text{on} \qquad \mathbf{x} \in S_M. \tag{4.4}$$

The linearized free surface conditions on the mean free surface are given as

$$\begin{aligned} \frac{\partial^2\Phi_C}{\partial t^2} + g\frac{\partial\Phi_C}{\partial z} &= 0, \\ \frac{\partial\Xi_C}{\partial t} - \frac{\partial\Phi_C}{\partial z} &= 0, \end{aligned} \qquad \text{on} \qquad z = 0, \tag{4.5}$$

The radiation condition on the surface at infinity is given as

$$\nabla\Phi_C = 0, \qquad \text{for} \qquad \mathbf{x} \in S_\infty. \tag{4.6}$$

4.2 Poincaré's velocity representation

4.2.1 Poincaré's velocity representation for source

The boundary integral equation for the complementary velocity potential is given as

$$-4\pi\Phi_C(\mathbf{x}) = \oiint_S \left[G(\mathbf{x},\boldsymbol{\xi})\left\{\mathbf{n}\cdot\nabla_\xi\Phi_C(\boldsymbol{\xi})\right\} - \Phi_C(\boldsymbol{\xi})\left\{\mathbf{n}\cdot\nabla_\xi G(\mathbf{x},\boldsymbol{\xi})\right\}\right] dS(\boldsymbol{\xi}), \tag{4.7}$$

where $G(\mathbf{x},\boldsymbol{\xi})$ is the Green function. $\mathbf{x}$ and $\boldsymbol{\xi}$ are the field and source points defined as

$$\mathbf{x} = (x, y, z), \qquad \text{and} \qquad \boldsymbol{\xi} = (\xi, \eta, \zeta). \tag{4.8}$$

$\mathbf{n}$ is a unit normal vector to the closed boundary surfaces S and it points inside of the fluid domain. ∇_ξ is the spatial derivative with respect to source point coordinate

$$\nabla_\xi = \left(\frac{\partial}{\partial\xi}, \frac{\partial}{\partial\eta}, \frac{\partial}{\partial\zeta}\right). \tag{4.9}$$

The fluid velocity at field point is obtained by applying the gradient with respect to field point coordinate (∇_x) defined as

$$\nabla_x = \left(\frac{\partial}{\partial x}, \frac{\partial}{\partial y}, \frac{\partial}{\partial z}\right), \tag{4.10}$$

to the equation (4.7) as

$$-4\pi\nabla_x\Phi_C(\mathbf{x}) = \oiint_S \left\{\mathbf{n}\cdot\nabla_\xi\Phi_C(\boldsymbol{\xi})\right\}\nabla_x G(\mathbf{x},\boldsymbol{\xi}) - \Phi_C(\boldsymbol{\xi})\,\nabla_x\left\{\mathbf{n}\cdot\nabla_\xi G(\mathbf{x},\boldsymbol{\xi})\right\} dS(\boldsymbol{\xi}). \tag{4.11}$$

The above expressions denote that the fluid velocity at the field point can be calculated by the distribution of sources and dipoles on the boundary surfaces. The fluid velocity at the field point can be decomposed as

$$-4\pi\nabla_x\Phi_C(\mathbf{x}) = \nabla_x\psi - \nabla_x\chi, \tag{4.12}$$

where $\nabla_x\psi$ and $\nabla_x\chi$ are the contributions of sources and dipoles given by

$$\nabla_x\psi = \iint_S \{\mathbf{n}\cdot\nabla_\xi\Phi_C(\boldsymbol{\xi})\}\,\nabla_x G(\mathbf{x},\boldsymbol{\xi})dS, \tag{4.13}$$

and

$$\nabla_x\chi = -\left[u^{xd},u^{yd},u^{zd}\right]^T = \iint_S \Phi_C(\boldsymbol{\xi})\,\nabla_x\{\mathbf{n}\cdot\nabla_\xi G(\mathbf{x},\boldsymbol{\xi})\}\,dS. \tag{4.14}$$

The contribution of dipoles can be given alternatively (see Appendix 2 in Noblesse et al. (1997))

$$\left[u^{xd},u^{yd},u^{zd}\right]^T = -\iint_S \{\nabla_\xi\Phi_C(\boldsymbol{\xi})\times\mathbf{n}\}\times\nabla_x G(\mathbf{x},\boldsymbol{\xi})\,dS(\boldsymbol{\xi}). \tag{4.15}$$

for a Green function satisfying the relationships

$$(G_x,G_y,G_z) = (-G_\xi,-G_\eta,-G_\zeta), \tag{4.16}$$

where the subscripts denote the derivative with respect to coordinate. Therefore, the fluid velocity can be expressed in compact form

$$\nabla_x\Phi_C(\mathbf{x}) = \frac{1}{4\pi}\iint_S [\{\mathbf{n}\cdot\nabla_\xi\Phi_C(\boldsymbol{\xi})\}\,\nabla_\xi G(\mathbf{x},\boldsymbol{\xi}) + \nabla_\xi G(\mathbf{x},\boldsymbol{\xi})\times\{\nabla_\xi\Phi_C(\boldsymbol{\xi})\times\mathbf{n}\}]\,dS(\boldsymbol{\xi}) \tag{4.17}$$

The above velocity representation is called *Poincaré's velocity representation* in (Hunt, 1980; Noblesse, 2001). Note that the factor 4π in equation (4.17) is divided in Noblesse (2001) due to definition of Green function. Comparing (4.17) to the original velocity representation in (4.12), the spatial derivatives on Green function are moved to the velocity potential.

Therefore, the expression is less singular than the case of original integral equation. The fluid velocity at the field point is explicitly expressed by definition of the velocity potential, e.g., $\nabla_\xi\Phi_C = \mathbf{u}_C(\mathbf{x}_\xi)$. It means that the dipole contribution multiplied by unknown potential value (Φ_C) is replaced by equivalent source contributions multiplied by a known value (e.g., tangential velocity, $\nabla_\xi\Phi_C\times\mathbf{n}$) at the boundary surface. Therefore, the system matrix obtained by discretizing the equation (4.7) does not need to be solved to get the velocity potential on the boundary surface.

However the velocity potential, which is necessary for evaluating the pressure, is not obtained from this velocity representation. To overcome this, Noblesse and Yang (2004) integrated the *Poincaré's velocity representation* to get the velocity potential at the field point.

4.2.2 Poincaré's velocity representation for image source and free surface term

The Green function for deep water and free surface flow has a generic form of

$$G(\mathbf{x},\boldsymbol{\xi}) = \frac{1}{r_1} + G^F = G^S + G^h + G^W, \tag{4.18}$$

where, G^S is the source given by

$$G^S = \frac{1}{r_1}, \qquad r_1 = \sqrt{R^2+(z-\zeta)^2}, \qquad R^2 = (x-\xi)^2+(y-\eta)^2, \tag{4.19}$$

and G^F is a function satisfying the Laplace equation and the boundary condtions on the sea bottom, free surface and surface at infinity. It is usually composed with two terms as

$$G^F = G^h + G^W, \tag{4.20}$$

where G^h is function satisfying the homogeneous Neumann or Dirichlet condition at the mean free surface. It is taken as the image source or sink located at $z = -\zeta$ above the plane of mean free surface for deep water. G^W is a wave function introduced to satisfy free surface and far-field boundary conditions.

The contribution of dipoles in equation (4.14) can be given as (see Appendix A in Noblesse (2001))

$$\left[u^{xd}, u^{yd}, -u^{zd}\right]^T = -\oiint_S \left\{\nabla_\xi \Phi_C\left(\boldsymbol{\xi}\right) \times \mathbf{n}\right\} \times \nabla_x G^F\left(\mathbf{x}, \boldsymbol{\xi}\right) dS(\boldsymbol{\xi}). \tag{4.21}$$

for the Green function (G^F) satisfying the relationships

$$\left(G^F_x, G^F_y, G^F_z\right) = \left(-G^F_\xi, -G^F_\eta, G^F_\zeta\right) \tag{4.22}$$

Therefore, two alternative expressions given in equations (4.15) and (4.21) lead to the velocity representation given as

$$\mathbf{u}_C(\mathbf{x}) = \mathbf{u}^S_C(\mathbf{x}) + \mathbf{u}^F_C(\mathbf{x}) \tag{4.23}$$

The velocity components $\mathbf{u}^S_C$ and $\mathbf{u}^F_C$ are expressed in the form of

$$4\pi \mathbf{u}^S_C(\mathbf{x}) = \oiint_S \left[\left\{\mathbf{n} \cdot \nabla_\xi \Phi_C\left(\boldsymbol{\xi}\right)\right\} \nabla_\xi G^S(\mathbf{x}, \boldsymbol{\xi}) - \left\{\nabla_\xi \Phi_C\left(\boldsymbol{\xi}\right) \times \mathbf{n}\right\} \times \nabla_\xi G^S\left(\mathbf{x}, \boldsymbol{\xi}\right)\right] dS(\boldsymbol{\xi}), \tag{4.24}$$

$$4\pi \hat{\mathbf{u}}^F_C(\mathbf{x}) = \oiint_S \left[\left\{\mathbf{n} \cdot \nabla_\xi \Phi_C\left(\boldsymbol{\xi}\right)\right\} \nabla_\xi G^F(\mathbf{x}, \boldsymbol{\xi}) - \left\{\nabla_\xi \Phi_C\left(\boldsymbol{\xi}\right) \times \mathbf{n}\right\} \times \nabla_\xi G^F\left(\mathbf{x}, \boldsymbol{\xi}\right)\right] dS(\boldsymbol{\xi}), \tag{4.25}$$

where $\hat{\mathbf{u}}$ is an operator defined as

$$\hat{\mathbf{u}} = (u, v, -w). \tag{4.26}$$

A generic velocity representation for free surface flows can be introduced (Noblesse, 2001)

$$4\pi \begin{bmatrix} u_C \\ v_C \\ w_C \end{bmatrix} = \oiint_S \begin{bmatrix} (\nabla_\xi \Phi_C \cdot \mathbf{n}) G^+_\xi + (\nabla_\xi \Phi_C \times \mathbf{n})^\zeta G^+_\eta - (\nabla_\xi \Phi_C \times \mathbf{n})^\eta G^+_\zeta \\ (\nabla_\xi \Phi_C \cdot \mathbf{n}) G^+_\eta + (\nabla_\xi \Phi_C \times \mathbf{n})^\xi G^+_\zeta - (\nabla_\xi \Phi_C \times \mathbf{n})^\zeta G^+_\xi \\ (\nabla_\xi \Phi_C \cdot \mathbf{n}) G^-_\zeta + (\nabla_\xi \Phi_C \times \mathbf{n})^\eta G^-_\xi - (\nabla_\xi \Phi_C \times \mathbf{n})^\xi G^-_\eta \end{bmatrix} dS, \tag{4.27}$$

by defining $G^\pm$ as

$$G^\pm = G^S \pm G^F. \tag{4.28}$$

The surface integral given in equation 4.27 can be decomposed into three surface integrals for problem described in figure 4.1 as

$$\oiint_S \{\cdot\}\, dS = \iint_{S_M} \{\cdot\}\, dS + \iint_{S_F} \{\cdot\}\, dS + \iint_{S_\infty} \{\cdot\}\, dS. \tag{4.29}$$

Surface integral on the matching surface (S_M) is necessary to impose boundary condition. The integral along S_∞ is zero thanks to time domain radiation condition that complementary terms are zero in the far-field ($\nabla \Phi_C \to 0$). However, the free surface integral $\iint_{S_F} \{\cdot\}\, dS$ needs to be transformed into a proper line integral because it is defined from matching surface to infinity.

4.2.3 Generic representation for free surface integral

The wave Green function for deep water is given by

$$G = G^S + G^F, \tag{4.30}$$

where $G^S = \frac{1}{r_1}$ is source and G^F can be selected by sign of image source as

$$G^F = \begin{cases} -\dfrac{1}{r_2} + H \\ \dfrac{1}{r_2} + F \end{cases}, \qquad \frac{1}{r_2} = \frac{1}{\sqrt{R^2 + Z^2}}, \qquad \text{with} \qquad Z = z + \zeta, \tag{4.31}$$

where $\frac{1}{r_2}$ is the image source. H and F are the corresponding wave terms. The generic Green function for deep water can be given by substituting above equation into equation (4.28) as

$$G^{\pm} = \begin{cases} \dfrac{1}{r_1} \mp \dfrac{1}{r_2} \pm H \\ \dfrac{1}{r_1} \pm \dfrac{1}{r_2} \pm F \end{cases}. \tag{4.32}$$

On the mean free surface, $z = 0$, the generic Green function satisfies the relationships

$$\begin{matrix} (G^+, G^+_\xi, G^+_\eta, G^+_\zeta) = (H, H_\xi, H_\eta, F_\zeta) \\ (G^-, G^-_\xi, G^-_\eta, G^-_\zeta) = -(F, F_\xi, F_\eta, H_\zeta) \end{matrix}, \qquad z = 0, \tag{4.33}$$

by using the relationships of source and image source on $z = 0$

$$\left[\frac{1}{r_1} - \frac{1}{r_2}\right]_{\zeta=0} = 0, \qquad \text{and} \qquad \frac{\partial}{\partial\zeta}\left[\frac{1}{r_1} + \frac{1}{r_2}\right]_{\zeta=0} = 0. \tag{4.34}$$

Therefore, the integral over the free surface in the generic velocity representation is given in

$$\iint_{S_F} \begin{bmatrix} \Phi_n G^+_\xi + (\nabla_\xi \Phi \times \mathbf{n})^\zeta \, G^+_\eta - (\nabla_\xi \Phi \times \mathbf{n})^\eta \, G^+_\zeta \\ \Phi_n G^+_\eta + (\nabla_\xi \Phi \times \mathbf{n})^\xi \, G^+_\zeta - (\nabla_\xi \Phi \times \mathbf{n})^\zeta \, G^+_\xi \\ \Phi_n G^-_\zeta + (\nabla_\xi \Phi \times \mathbf{n})^\eta \, G^-_\xi - (\nabla_\xi \Phi \times \mathbf{n})^\xi \, G^-_\eta \end{bmatrix} dS = - \iint_{S_F} \begin{bmatrix} \Phi_\zeta H_\xi + F_\zeta \Phi_\xi \\ \Phi_\zeta H_\eta + F_\zeta \Phi_\eta \\ \Phi_\xi F_\xi + \Phi_\eta F_\eta - \Phi_\zeta H_\zeta \end{bmatrix} dS. \tag{4.35}$$

where $\Phi_n = \nabla_\xi \Phi \cdot \mathbf{n}$. The above equation is introduced by Noblesse (2001) as generic free surface integral representation.

He suggested the velocity representation for the cases of free surface problems listed as:

- Case of rigid free surface boundary condition: $\frac{\partial \Phi}{\partial z} = 0$ on $z = 0$.
- Case of soft free surface boundary condition: $\Phi = 0$ on $z = 0$.
- Steady ship waves.
- Time-harmonic wave radiation-diffraction without forward speed.
- Time-harmonic ship waves.

However, the velocity representation for unsteady time domain free surface flows has never been suggested nor studied.

4.3 Poincaré's velocity representation in time domain free surface flow

For the convenience, the complementary velocity potential Φ_C is replaced by Φ and the complementary fluid velocity $\mathbf{u}_C$ is replaced by $\mathbf{u}$ in this section.

The Green's identity with time derivatives of velocity potential gives a boundary integral equation with respect to Φ_τ (see Appendix A.1 in Bingham (1994))

$$-4\pi\Phi_\tau(\mathbf{x},\tau) = \iint\!\!\!\!\!\!\bigcirc_S \Big[\Phi_{n\tau}(\boldsymbol{\xi},\tau)G(\mathbf{x},\boldsymbol{\xi},t-\tau) - \Phi_\tau(\boldsymbol{\xi},\tau)G_n(\mathbf{x},\boldsymbol{\xi},t-\tau)\Big]dS(\boldsymbol{\xi}), \tag{4.36}$$

with time domain Green function for deep water

$$G(\mathbf{x},\boldsymbol{\xi},t-\tau) = \frac{1}{r_1} - \frac{1}{r_2} + H(\mathbf{x},\boldsymbol{\xi},t-\tau), \tag{4.37}$$

with

$$H(\mathbf{x},\boldsymbol{\xi},t-\tau) = 2\int_0^\infty e^{kZ}\left[1-\cos\left(\sqrt{gk}(t-\tau)\right)\right]J_0(kR)dk. \tag{4.38}$$

Note that the factor 4π is taken in the present study because the field point is not located on the boundary surface. Poincaré's velocity representation given in equation (4.27) is derived by manipulating the spatial derivatives on the boundary integral equation, the time derivative of fluid velocity can also be established as

$$4\pi\begin{bmatrix} u^x_\tau(\mathbf{x},\tau)\\ u^y_\tau(\mathbf{x},\tau)\\ u^z_\tau(\mathbf{x},\tau)\end{bmatrix} = \iint_{S_M\cup S_F\cup S_\infty}\begin{bmatrix}\Phi_{n\tau}(\boldsymbol{\xi},\tau)G^+_\xi(\mathbf{x},\boldsymbol{\xi},t-\tau) + (\nabla_\xi\Phi_\tau(\boldsymbol{\xi},\tau)\times\mathbf{n})^\zeta\, G^+_\eta(\mathbf{x},\boldsymbol{\xi},t-\tau)\\ \Phi_{n\tau}(\boldsymbol{\xi},\tau)G^+_\eta(\mathbf{x},\boldsymbol{\xi},t-\tau) + (\nabla_\xi\Phi_\tau(\boldsymbol{\xi},\tau)\times\mathbf{n})^\xi\, G^+_\zeta(\mathbf{x},\boldsymbol{\xi},t-\tau)\\ \Phi_{n\tau}(\boldsymbol{\xi},\tau)G^-_\zeta(\mathbf{x},\boldsymbol{\xi},t-\tau) + (\nabla_\xi\Phi_\tau(\boldsymbol{\xi},\tau)\times\mathbf{n})^\eta\, G^-_\xi(\mathbf{x},\boldsymbol{\xi},t-\tau)\\ \quad -(\nabla_\xi\Phi_\tau(\boldsymbol{\xi},\tau)\times\mathbf{n})^\eta\, G^+_\zeta(\mathbf{x},\boldsymbol{\xi},t-\tau)\\ \quad -(\nabla_\xi\Phi_\tau(\boldsymbol{\xi},\tau)\times\mathbf{n})^\zeta\, G^+_\xi(\mathbf{x},\boldsymbol{\xi},t-\tau)\\ \quad -(\nabla_\xi\Phi_\tau(\boldsymbol{\xi},\tau)\times\mathbf{n})^\xi\, G^-_\eta(\mathbf{x},\boldsymbol{\xi},t-\tau)\end{bmatrix} dS(\boldsymbol{\xi}), \tag{4.39}$$

the fluid domain is surrounded by the matching surface(S_M), free surface(S_F) and surface at infinity(S_∞). The contribution of infinity surface integral for fluid velocity at field point is zero by radiation condition

$$\nabla_\xi\Phi(\boldsymbol{\xi}) \to 0, \qquad \text{on} \qquad \boldsymbol{\xi}\in S_\infty. \tag{4.40}$$

The notation of Green function is replaced for the sake of convenience by

$$\mathcal{G} = \begin{cases} G^+, & \text{if the velocity component is horizontal, e.g. } (u^x,u^y)\\ G^-, & \text{if the velocity component is vertical, e.g. } (u^z)\end{cases} \tag{4.41}$$

Then, the acceleration of the fluid is given in vectorial form

$$4\pi\mathbf{u}_\tau(\mathbf{x},\tau) = \iint_{S_M\cup S_F}\left[\Phi_{n\tau}(\boldsymbol{\xi},\tau)\nabla_\xi\mathcal{G}(\mathbf{x},\boldsymbol{\xi},t-\tau) + \nabla_\xi\mathcal{G}(\mathbf{x},\boldsymbol{\xi},t-\tau)\times\{\nabla_\xi\Phi_\tau(\boldsymbol{\xi},\tau)\times\mathbf{n}\}\right]dS(\boldsymbol{\xi}), \tag{4.42}$$

The matching surface is not moving with respect to time. Applying the integral by parts in time to the right-hand-side in equation (4.42)

$$\begin{aligned}&\iint_S\left\{\Phi_{n\tau}\nabla_\xi\mathcal{G} + \nabla_\xi\mathcal{G}\times(\nabla_\xi\Phi_\tau\times\mathbf{n})\right\}dS(\boldsymbol{\xi})\\ &= \frac{d}{d\tau}\iint_S\left\{\Phi_n\nabla_\xi\mathcal{G} + \nabla_\xi\mathcal{G}\times(\nabla_\xi\Phi\times\mathbf{n})\right\}dS(\boldsymbol{\xi}) - \iint_S\left\{\Phi_n\nabla_\xi\mathcal{G}_\tau + \nabla_\xi\mathcal{G}_\tau\times(\nabla_\xi\Phi\times\mathbf{n})\right\}dS(\boldsymbol{\xi})\end{aligned} \tag{4.43}$$

Then, the acceleration of the fluid is given as

$$4\pi\mathbf{u}_\tau(\mathbf{x},\tau) = \frac{d}{d\tau}\iint_{S_M\cup S_F}\{\Phi_n\nabla_\xi\mathcal{G} + \nabla_\xi\mathcal{G}\times(\nabla_\xi\Phi\times\mathbf{n})\}\,dS(\boldsymbol{\xi}) - \iint_{S_M\cup S_F}\{\Phi_n\nabla_\xi\mathcal{G}_\tau + \nabla_\xi\mathcal{G}_\tau\times(\nabla_\xi\Phi\times\mathbf{n})\}\,dS(\boldsymbol{\xi}). \tag{4.44}$$

After integrating in time, the fluid's velocity at field point is given with initial condition and time convolution integral

$$\begin{aligned}4\pi\{\mathbf{u}(\mathbf{x},t)-\mathbf{u}(\mathbf{x},t_0)\} &= \iint_{S_M\cup S_F}\{\Phi_n(\boldsymbol{\xi},t)\nabla_\xi\mathcal{G}(\mathbf{x},\boldsymbol{\xi},0)+\nabla_\xi\mathcal{G}(\mathbf{x},\boldsymbol{\xi},0)\times(\nabla_\xi\Phi(\boldsymbol{\xi},t)\times\mathbf{n})\}\,dS(\boldsymbol{\xi})\\ &-\iint_{S_M\cup S_F}\{\Phi_n(\boldsymbol{\xi},t_0)\nabla_\xi\mathcal{G}(\mathbf{x},\boldsymbol{\xi},t-t_0)+\nabla_\xi\mathcal{G}(\mathbf{x},\boldsymbol{\xi},t-t_0)\times(\nabla_\xi\Phi(\boldsymbol{\xi},t_0)\times\mathbf{n})\}\,dS(\boldsymbol{\xi})\\ &-\int_{t_0}^{t}d\tau\iint_{S_M\cup S_F}\{\Phi_n(\boldsymbol{\xi},\tau)\nabla_\xi\mathcal{G}_\tau(\mathbf{x},\boldsymbol{\xi},t-\tau)+\nabla_\xi\mathcal{G}_\tau(\mathbf{x},\boldsymbol{\xi},t-\tau)\times(\nabla_\xi\Phi(\boldsymbol{\xi},\tau)\times\mathbf{n})\}\,dS(\boldsymbol{\xi}).\end{aligned} \tag{4.45}$$

Terms involving $\nabla_\xi\Phi(\boldsymbol{\xi},t_0)$ in the integrals and $\mathbf{u}(\mathbf{x},t_0)$ vanish due to the initial condition that the complementary fluid velocity is zero over boundary surfaces and fluid domain at initial time, $t=t_0$. Therefore, the velocity representation with two surface contributions is given to be

$$\begin{aligned}4\pi\mathbf{u}(\mathbf{x},t) &= \iint_{S_M\cup S_F}\{\Phi_n(\boldsymbol{\xi},t)\nabla_\xi\mathcal{G}(\mathbf{x},\boldsymbol{\xi},0)+\nabla_\xi\mathcal{G}(\mathbf{x},\boldsymbol{\xi},0)\times(\nabla_\xi\Phi(\boldsymbol{\xi},t)\times\mathbf{n})\}\,dS(\boldsymbol{\xi})\\ &-\int_{t_0}^{t}\left\{\iint_{S_M\cup S_F}\{\Phi_n(\boldsymbol{\xi},\tau)\nabla_\xi\mathcal{G}_\tau(\mathbf{x},\boldsymbol{\xi},t-\tau)+\nabla_\xi\mathcal{G}_\tau(\mathbf{x},\boldsymbol{\xi},t-\tau)\times(\nabla_\xi\Phi(\boldsymbol{\xi},\tau)\times\mathbf{n})\}\,dS(\boldsymbol{\xi})\right\}d\tau.\end{aligned} \tag{4.46}$$

4.3.1 Contribution of the matching surface integral

The contribution of the matching surface integral in time domain Poincaré's velocity representation is defined as

$$\begin{aligned}\mathbf{u}_M(\mathbf{x},t) &= \iint_{S_M}\{\Phi_n(\boldsymbol{\xi},t)\nabla_\xi\mathcal{G}(\mathbf{x},\boldsymbol{\xi},0)+\nabla_\xi\mathcal{G}(\mathbf{x},\boldsymbol{\xi},0)\times(\nabla_\xi\Phi(\boldsymbol{\xi},t)\times\mathbf{n})\}\,dS(\boldsymbol{\xi})\\ &-\int_{t_0}^{t}\left\{\iint_{S_M}\{\Phi_n(\boldsymbol{\xi},\tau)\nabla_\xi\mathcal{G}_\tau(\mathbf{x},\boldsymbol{\xi},t-\tau)+\nabla_\xi\mathcal{G}_\tau(\mathbf{x},\boldsymbol{\xi},t-\tau)\times(\nabla_\xi\Phi(\boldsymbol{\xi},\tau)\times\mathbf{n})\}\,dS(\boldsymbol{\xi})\right\}d\tau.\end{aligned} \tag{4.47}$$

The time domain Green function for deep water given in equation (4.37) satisfies the relationships

$$\nabla_\xi G^{\pm}(\mathbf{x},\boldsymbol{\xi},0) = \nabla_\xi\{\mathcal{R}(\mathbf{x},\boldsymbol{\xi})\pm\mathcal{R}^*(\mathbf{x},\boldsymbol{\xi})\} \tag{4.48}$$

and

$$\nabla_\xi G_\tau^{\pm}(\mathbf{x},\boldsymbol{\xi},t-\tau) = \pm\nabla_\xi H_\tau(\mathbf{x},\boldsymbol{\xi},t-\tau) \tag{4.49}$$

where the source and image source are denoted as $\mathcal{R}(\mathbf{x},\boldsymbol{\xi}) = 1/r_1$ and $\mathcal{R}^*(\mathbf{x},\boldsymbol{\xi}) = -1/r_2$.

The matching surface integral can be decomposed into three velocity contributions

$$\mathbf{u}_M(\mathbf{x},t) = \mathbf{u}_R(\mathbf{x},t)+\mathbf{u}_{R*}(\mathbf{x},t)+\mathbf{u}_H(\mathbf{x},t) \tag{4.50}$$

where

$$\mathbf{u}_R(\mathbf{x},t) = \begin{bmatrix} u_R^x \\ u_R^y \\ u_R^z \end{bmatrix} = \iint_{S_M} \{\Phi_n(\boldsymbol{\xi},t)\nabla_\xi \mathcal{R}(\mathbf{x},\boldsymbol{\xi}) + \nabla_\xi \mathcal{R}(\mathbf{x},\boldsymbol{\xi}) \times (\nabla_\xi \Phi(\boldsymbol{\xi},t) \times \mathbf{n})\}\, dS(\boldsymbol{\xi}) \tag{4.51}$$

$$\hat{\mathbf{u}}_{R*}(\mathbf{x},t) = \begin{bmatrix} u_{R*}^x \\ u_{R*}^y \\ -u_{R*}^z \end{bmatrix} = \iint_{S_M} \{\Phi_n(\boldsymbol{\xi},t)\nabla_\xi \mathcal{R}^*(\mathbf{x},\boldsymbol{\xi}) + \nabla_\xi \mathcal{R}^*(\mathbf{x},\boldsymbol{\xi}) \times (\nabla_\xi \Phi(\boldsymbol{\xi},t) \times \mathbf{n})\}\, dS(\boldsymbol{\xi}) \tag{4.52}$$

$$\hat{\mathbf{u}}_H(\mathbf{x},t) = \begin{bmatrix} u_H^x \\ u_H^y \\ -u_H^z \end{bmatrix} = -\int_{t_0}^{t} \iint_{S_M} \{\Phi_n(\boldsymbol{\xi},\tau)\nabla_\xi H_\tau(\mathbf{x},\boldsymbol{\xi},t-\tau) + \nabla_\xi H_\tau(\mathbf{x},\boldsymbol{\xi},t-\tau) \times (\nabla_\xi \Phi(\boldsymbol{\xi},\tau) \times \mathbf{n})\}\, dS(\boldsymbol{\xi}) d\tau \tag{4.53}$$

Each of the velocity components represents the surface integral contribution of source, image source, and wave terms.

4.3.2 Contribution of the free surface integral

The contribution of the free surface integral is given by

$$\mathbf{u}_F(\mathbf{x},t) = \iint_{S_F} \{\Phi_n(\boldsymbol{\xi},t)\nabla_\xi \mathcal{G}(\mathbf{x},\boldsymbol{\xi},0) + \nabla_\xi \mathcal{G}(\mathbf{x},\boldsymbol{\xi},0) \times (\nabla_\xi \Phi(\boldsymbol{\xi},t) \times \mathbf{n})\}\, dS(\boldsymbol{\xi}) - \int_{t_0}^{t} d\tau \iint_{S_F} \{\Phi_n(\boldsymbol{\xi},\tau)\nabla_\xi \mathcal{G}_\tau(\mathbf{x},\boldsymbol{\xi},t-\tau) + \nabla_\xi \mathcal{G}_\tau(\mathbf{x},\boldsymbol{\xi},t-\tau) \times (\nabla_\xi \Phi(\boldsymbol{\xi},\tau) \times \mathbf{n})\}\, dS(\boldsymbol{\xi}). \tag{4.54}$$

The free surface is the region from the waterline of matching surface to infinity. The transformation to waterline integral is necessary for its evaluation. Using the general representation for free surface integral discussed in section 4.2.3, the velocity contribution of the free surface integral is given by

$$\mathbf{u}_F(\mathbf{x},t) = \mathbf{u}_F^{(0)}(\mathbf{x},t) + \mathbf{u}_F^{(t)}(\mathbf{x},t) \tag{4.55}$$

with the current time free surface integral contribution

$$\mathbf{u}_F^{(0)}(\mathbf{x},t) = -\iint_{S_F} \begin{bmatrix} F_\zeta(\mathbf{x},\boldsymbol{\xi},0)\Phi_\xi(\boldsymbol{\xi},t) \\ F_\zeta(\mathbf{x},\boldsymbol{\xi},0)\Phi_\eta(\boldsymbol{\xi},t) \\ F_\xi(\mathbf{x},\boldsymbol{\xi},0)\Phi_\xi(\boldsymbol{\xi},t) + F_\eta(\mathbf{x},\boldsymbol{\xi},0)\Phi_\eta(\boldsymbol{\xi},t) \end{bmatrix} dS(\boldsymbol{\xi}). \tag{4.56}$$

The convolution integral is given by

$$\mathbf{u}_F^{(t)}(\mathbf{x},t) = \int_{t_0}^{t} \iint_{S_F} \begin{bmatrix} H_{\xi\tau}(\mathbf{x},\boldsymbol{\xi},t-\tau)\Phi_\zeta(\boldsymbol{\xi},\tau) + F_{\zeta\tau}(\mathbf{x},\boldsymbol{\xi},t-\tau)\Phi_\xi(\boldsymbol{\xi},\tau) \\ H_{\eta\tau}(\mathbf{x},\boldsymbol{\xi},t-\tau)\Phi_\zeta(\boldsymbol{\xi},\tau) + F_{\zeta\tau}(\mathbf{x},\boldsymbol{\xi},t-\tau)\Phi_\eta(\boldsymbol{\xi},\tau) \\ F_{\xi\tau}(\mathbf{x},\boldsymbol{\xi},t-\tau)\Phi_\xi(\boldsymbol{\xi},\tau) + F_{\eta\tau}(\mathbf{x},\boldsymbol{\xi},t-\tau)\Phi_\eta(\boldsymbol{\xi},\tau) - H_{\zeta\tau}(\mathbf{x},\boldsymbol{\xi},t-\tau)\Phi_\zeta(\boldsymbol{\xi},\tau) \end{bmatrix} dS(\boldsymbol{\xi}) d\tau. \tag{4.57}$$

The linearized free surface boundary conditions for velocity potential and Green function for time domain free surface flow are given in

$$\Phi_{\tau\tau} + g\Phi_{\zeta} = 0, \qquad H_{\tau\tau} + gF_{\zeta} = 0, \qquad \text{on} \qquad \zeta = 0. \tag{4.58}$$

Using the free surface boundary conditions, the x-component in the convolution integral given in (4.57) is modified as belows

$$\begin{aligned} H_{\xi\tau}\Phi_{\zeta} + F_{\zeta\tau}\Phi_{\xi} &= (F_{\zeta}\Phi_{\xi})_{\tau} + H_{\xi\tau}\Phi_{\zeta} - F_{\zeta}\Phi_{\xi\tau} \\ &= (F_{\zeta}\Phi_{\xi})_{\tau} - (F_{\zeta}\Phi_{\tau})_{\xi} - \frac{1}{g}(H_{\xi\tau}\Phi_{\tau})_{\tau}. \end{aligned} \tag{4.59}$$

Likewise, the y-component is expressed as the following

$$H_{\eta\tau}\Phi_{\zeta} + F_{\zeta\tau}\Phi_{\eta} = (F_{\zeta}\Phi_{\eta})_{\tau} - (F_{\zeta}\Phi_{\tau})_{\eta} - \frac{1}{g}(H_{\eta\tau}\Phi_{\tau})_{\tau}. \tag{4.60}$$

The z-component is transformed by using $\nabla^2 F = 0$

$$\begin{aligned} F_{\xi\tau}\Phi_{\xi} + F_{\eta\tau}\Phi_{\eta} - H_{\zeta\tau}\Phi_{\zeta} &= (F_{\xi}\Phi_{\xi} + F_{\eta}\Phi_{\eta})_{\tau} - F_{\xi}\Phi_{\xi\tau} - F_{\eta}\Phi_{\eta\tau} - H_{\zeta\tau}\Phi_{\zeta} \\ &= (F_{\xi}\Phi_{\xi} + F_{\eta}\Phi_{\eta})_{\tau} - (F_{\xi}\Phi_{\tau})_{\xi} - (F_{\eta}\Phi_{\tau})_{\eta} + \frac{1}{g}(H_{\zeta\tau}\Phi_{\tau})_{\tau}. \end{aligned} \tag{4.61}$$

Substituiting equations (4.59), (4.60) and (4.61) into (4.57)

$$\begin{aligned} \mathbf{u}_F^{(t)}(\mathbf{x},t) = &\int_{t_0}^{t} d\tau \iint_{S_F} \begin{bmatrix} (F_{\zeta}\Phi_{\xi})_{\tau} \\ (F_{\zeta}\Phi_{\eta})_{\tau} \\ (F_{\xi}\Phi_{\xi} + F_{\eta}\Phi_{\eta})_{\tau} \end{bmatrix} dS - \int_{t_0}^{t} d\tau \iint_{S_F} \begin{bmatrix} (F_{\zeta}\Phi_{\tau})_{\xi} \\ (F_{\zeta}\Phi_{\tau})_{\eta} \\ (F_{\xi}\Phi_{\tau})_{\xi} + (F_{\eta}\Phi_{\tau})_{\eta} \end{bmatrix} dS \\ &- \frac{1}{g}\int_{t_0}^{t} d\tau \iint_{S_F} \begin{bmatrix} (H_{\xi\tau}\Phi_{\tau})_{\tau} \\ (H_{\eta\tau}\Phi_{\tau})_{\tau} \\ -(H_{\zeta\tau}\Phi_{\tau})_{\tau} \end{bmatrix} dS, \end{aligned} \tag{4.62}$$

The Reynolds transport and Stokes theorems on the free surface are given as

$$\iint_{S_F(t)} \frac{\partial f}{\partial t} dS = \frac{d}{dt} \iint_{S_F(t)} f dS - \oint_{C(t)} f U_n^{2D} dl, \tag{4.63}$$

and

$$\iint_{S_F(t)} f_x dS = \oint_{C(t)} t^y f dl, \qquad \iint_{S_F(t)} f_y dS = -\oint_{C(t)} t^x f dl \tag{4.64}$$

where $C(t) = C_M \cup C_\infty$ is the closed line of free surface. C_M is waterline of matching surface and C_∞ is the closed curve at infinity. $U_n^{2D} = \mathbf{u} \cdot \mathbf{n}_{2D}$ is the transport velocity at line. $\mathbf{t} = (t^x, t^y, 0)$ is the unit vector tangent to the boundary curve of the free surface. It is oriented clockwise along the curve of matching waterline and anticlockwise along the curve at infinite distance. Applying Reynolds transport and Stokes theorems on the convolution integral in equation (4.62) allows us

to obtain

$$\begin{aligned}\mathbf{u}_F^{(t)}(\mathbf{x},t) = &\iint_{S_F}\begin{bmatrix} F_\zeta(\mathbf{x},\boldsymbol{\xi},0)\Phi_\xi(\boldsymbol{\xi},t) \\ F_\zeta(\mathbf{x},\boldsymbol{\xi},0)\Phi_\eta(\boldsymbol{\xi},t) \\ F_\xi(\mathbf{x},\boldsymbol{\xi},0)\Phi_\xi(\boldsymbol{\xi},t)+F_\eta(\mathbf{x},\boldsymbol{\xi},0)\Phi_\eta(\boldsymbol{\xi},t)\end{bmatrix} dS \\ &-\int_{t_0}^{t} d\tau \oint_{C(t)}\begin{bmatrix} F_\zeta(\mathbf{x},\boldsymbol{\xi},t-\tau)\Phi_\xi(\boldsymbol{\xi},\tau) \\ F_\zeta(\mathbf{x},\boldsymbol{\xi},t-\tau)\Phi_\eta(\boldsymbol{\xi},\tau) \\ F_\xi(\mathbf{x},\boldsymbol{\xi},t-\tau)\Phi_\xi(\boldsymbol{\xi},\tau)+F_\eta(\mathbf{x},\boldsymbol{\xi},t-\tau)\Phi_\eta(\boldsymbol{\xi},\tau)\end{bmatrix} U_n^{2D} dl \\ &-\int_{t_0}^{t} d\tau \oint_{C(t)}\begin{bmatrix} t^y F_\zeta(\mathbf{x},\boldsymbol{\xi},t-\tau) \\ -t^x F_\zeta(\mathbf{x},\boldsymbol{\xi},t-\tau) \\ t^y F_\xi(\mathbf{x},\boldsymbol{\xi},t-\tau)-t^x F_\eta(\mathbf{x},\boldsymbol{\xi},t-\tau)\end{bmatrix} \Phi_\tau(\boldsymbol{\xi},\tau) dl \\ &-\frac{1}{g}\oint_{C(t)}\begin{bmatrix} H_{\xi\tau}(\mathbf{x},\boldsymbol{\xi},0) \\ H_{\eta\tau}(\mathbf{x},\boldsymbol{\xi},0) \\ -H_{\zeta\tau}(\mathbf{x},\boldsymbol{\xi},0)\end{bmatrix}\Phi_\tau(\boldsymbol{\xi},t)dl + \frac{1}{g}\int_{t_0}^{t} d\tau \oint_{C(t)}\begin{bmatrix} H_{\xi\tau}(\mathbf{x},\boldsymbol{\xi},t-\tau) \\ H_{\eta\tau}(\mathbf{x},\boldsymbol{\xi},t-\tau) \\ -H_{\zeta\tau}(\mathbf{x},\boldsymbol{\xi},t-\tau)\end{bmatrix}\Phi_\tau(\boldsymbol{\xi},\tau)U_n^{2D} dl.\end{aligned} \tag{4.65}$$

Substituting equations in (4.56) and (4.65) into (4.55), the velocity contribution of free surface integral is given in compact form

$$\begin{aligned}\mathbf{u}_F(\mathbf{x},t) = &-\int_{t_0}^{t} d\tau \oint_{C(t)}\begin{bmatrix} F_\zeta\Phi_\xi \\ F_\zeta\Phi_\eta \\ F_\xi\Phi_\xi+F_\eta\Phi_\eta\end{bmatrix} U_n^{2D} dl - \int_{t_0}^{t} d\tau \oint_{C(t)}\begin{bmatrix} t^y F_\zeta \\ -t^x F_\zeta \\ t^y F_\xi - t^x F_\eta\end{bmatrix}\Phi_\tau dl \\ &+\frac{1}{g}\int_{t_0}^{t} d\tau \oint_{C(t)}\begin{bmatrix} H_{\xi\tau} \\ H_{\eta\tau} \\ -H_{\zeta\tau}\end{bmatrix}\Phi_\tau U_n^{2D} dl.\end{aligned} \tag{4.66}$$

The radiation and kinematic free surface boundary condition gives an explicit velocity expression

$$\begin{aligned}\mathbf{u}_F(\mathbf{x},t) = &-\int_{t_0}^{t} d\tau \int_{C_M}\begin{bmatrix} F_\zeta\Phi_\xi \\ F_\zeta\Phi_\eta \\ F_\xi\Phi_\xi+F_\eta\Phi_\eta\end{bmatrix} U_n^{2D} dl + g\int_{t_0}^{t} d\tau \int_{C_M}\begin{bmatrix} t^y F_\zeta \\ -t^x F_\zeta \\ t^y F_\xi - t^x F_\eta\end{bmatrix}\Xi_C(\boldsymbol{\xi},\tau) dl \\ &-\int_{t_0}^{t} d\tau \int_{C_M}\begin{bmatrix} H_{\xi\tau} \\ H_{\eta\tau} \\ -H_{\zeta\tau}\end{bmatrix}\Xi_C(\boldsymbol{\xi},\tau)U_n^{2D} dl,\end{aligned} \tag{4.67}$$

where $\Xi_C(\boldsymbol{\xi},t)$ is the complementary wave elevation on waterline of matching surface. Note that the free surface integral representation needs both the complementary fluid velocity and wave elevation on the waterline.

4.3.3 Summary: Poincaré's velocity represenation in time domain free surface flow

The complementary velocity potential and fluid velocity are denoted here with subscript $_C$. The gradient of velocity potential is replaced by fluid velocity as

$$\nabla_\xi \Phi_C = \mathbf{u}_C, \tag{4.68}$$

The normal and tangential fluid velocities are written in the following form

$$u_C^{\mathbf{n}} = \mathbf{u}_C \cdot \mathbf{n}, \qquad \mathbf{w}_C = \mathbf{u}_C \times \mathbf{n}, \tag{4.69}$$

The complementary fluid velocity at field point by Poincaré's velocity representation is given by four velocity contributions

$$4\pi \mathbf{u}_C(\mathbf{x},t) = \mathbf{u}_R(\mathbf{x},t) + \mathbf{u}_{R^*}(\mathbf{x},t) + \mathbf{u}_H(\mathbf{x},t) + \mathbf{u}_F(\mathbf{x},t) \tag{4.70}$$

and each of the velocity representations is given explicitly with flow values at the boundary surface as follows

$$\mathbf{u}_R(\mathbf{x},t) = \iint_{S_M} \left\{ u_C^{\mathbf{n}}(\boldsymbol{\xi},t) \nabla_\xi \mathcal{R}(\mathbf{x},\boldsymbol{\xi}) + \nabla_\xi \mathcal{R}(\mathbf{x},\boldsymbol{\xi}) \times \mathbf{w}_C(\boldsymbol{\xi},t) \right\} dS, \tag{4.71}$$

$$\hat{\mathbf{u}}_{R^*}(\mathbf{x},t) = \iint_{S_M} \left\{ u_C^{\mathbf{n}}(\boldsymbol{\xi},t) \nabla_\xi \mathcal{R}^*(\mathbf{x},\boldsymbol{\xi}) + \nabla_\xi \mathcal{R}^*(\mathbf{x},\boldsymbol{\xi}) \times \mathbf{w}_C(\boldsymbol{\xi},t) \right\} dS, \tag{4.72}$$

$$\hat{\mathbf{u}}_H(\mathbf{x},t) = -\int_{t_0}^{t} d\tau \iint_{S_M} \left\{ u_C^{\mathbf{n}}(\boldsymbol{\xi},\tau) \nabla_\xi H_\tau(\mathbf{x},\boldsymbol{\xi},t-\tau) + \nabla_\xi H_\tau(\mathbf{x},\boldsymbol{\xi},t-\tau) \times \mathbf{w}_C(\boldsymbol{\xi},\tau) \right\} dS, \tag{4.73}$$

$$\begin{aligned} \hat{\mathbf{u}}_F(\mathbf{x},t) = &-\int_{t_0}^{t} d\tau \int_{C_M} \nabla_\xi F(\mathbf{x},\boldsymbol{\xi},t-\tau) \times \left\{ \mathbf{u}_C(\boldsymbol{\xi},\tau) \times \mathbf{e}_z \right\} U_n^{2D} dl \\ &+ g \int_{t_0}^{t} d\tau \int_{C_M} \left\{ \nabla_\xi F(\mathbf{x},\boldsymbol{\xi},t-\tau) \times \mathbf{t} \right\} \Xi_C(\boldsymbol{\xi},\tau) dls \\ &- \int_{t_0}^{t} d\tau \int_{C_M} \nabla_\xi H_\tau(\mathbf{x},\boldsymbol{\xi},t-\tau) \Xi_C(\boldsymbol{\xi},\tau) U_n^{2D} dl. \end{aligned} \tag{4.74}$$

The operator $\hat{\mathbf{u}}$ is defined in (4.26) as

$$\hat{\mathbf{u}} = \left[u^x, u^y, -u^z \right].$$

The transport velocity on the waterline is equal to zero, the contribution of the free surface is simply given as

$$\hat{\mathbf{u}}_F(\mathbf{x},t) = g \int_{t_0}^{t} d\tau \int_{C_M} \left\{ \nabla_\xi F(\mathbf{x},\boldsymbol{\xi},t-\tau) \times \mathbf{t} \right\} \Xi_C(\boldsymbol{\xi},\tau) dl. \tag{4.75}$$

4.4 Time domain Green function for deep water

4.4.1 Time domain Green function for Poincaré's velocity representation

The time domain Green function of the free surface flow for unsteady problem satisfies the Laplace equation

$$\nabla^2 G(\mathbf{x},\boldsymbol{\xi},t) = \delta(\mathbf{x}-\boldsymbol{\xi})\delta(t-\tau), \qquad \text{for} \qquad \mathbf{x}\in\Omega; \quad t\geq 0 \tag{4.76}$$

and the linearized free surface boundary condition

$$\frac{\partial^2 G}{\partial t^2} + g\frac{\partial G}{\partial z} = 0, \qquad \text{on} \qquad z=0, \tag{4.77}$$

the radiation and sea bottom condition

$$|\nabla_x G| \to 0, \qquad \text{as} \qquad r\to\infty; \quad \forall t\geq 0, \tag{4.78}$$

with the initial conditions

$$G(\mathbf{x},\boldsymbol{\xi},0) = 0, \quad \frac{\partial G(\mathbf{x},\boldsymbol{\xi},0)}{\partial t} = 0, \qquad \text{for} \qquad \mathbf{x}\in\Omega. \tag{4.79}$$

The solution of above initial-boundary value problem is given by Brard (1948)

$$G(\mathbf{x},\boldsymbol{\xi},t) = \frac{1}{r_1} - \frac{1}{r_2} + 2\int_0^\infty \left\{1-\cos\left(\sqrt{gk}t\right)\right\} e^{kZ} J_0\left(kR\right) dk \tag{4.80}$$

The Bessel function integral relation is given as [using the equation 6.621 in (Gradshteyn and Ryzhik, 2007)]

$$\int_0^\infty e^{-\alpha x} J_0(x) dx = \frac{1}{\sqrt{1+\alpha^2}}, \qquad \alpha > 0. \tag{4.81}$$

The image source is replaced by integral of Bessel and exponential functions

$$\frac{1}{r_2} = \int_0^\infty e^{kZ} J_0\left(kR\right) dk. \tag{4.82}$$

where $Z = z+\zeta$. Substituting the integral relation into equation (4.80), the time domain Green function can be expressed with image source having a positive sign as

$$G(\mathbf{x},\boldsymbol{\xi},t) = \frac{1}{r_1} + \frac{1}{r_2} - 2\int_0^\infty \cos\left(\sqrt{gk}t\right) e^{kZ} J_0\left(kR\right) dk. \tag{4.83}$$

Following the generic Green function defined in equation (4.32), the wave terms in time domain free surface Green functions are given as

$$H(\mathbf{x},\boldsymbol{\xi},t) = 2\int_0^\infty \left\{1-\cos\left(\sqrt{gk}t\right)\right\} e^{kZ} J_0\left(kR\right) dk, \tag{4.84}$$

$$F(\mathbf{x},\boldsymbol{\xi},t) = -2\int_0^\infty \cos\left(\sqrt{gk}t\right) e^{kZ} J_0\left(kR\right) dk. \tag{4.85}$$

4.4.2 Evaluation of time domain Green functions

The evaluation of two wave terms given in equations (4.84) and (4.85) are necessary for Poincaré's velocity representation with arbitrary matching surfaces. Many pieces of research have been dedicated to the time derivatives of first wave term denoted as H_τ for efficient and accurate computation. Beck and Liapis (1987) decomposed the computational domain of variables and applied a series expansion and numerical quadrature for different domain. Newman (1992) presented an algorithm based on Beck and Liapis (1987). Later, Clément (1998) announced a new theorem showing that the time domain Green function is the solution of 4-th order ordinary differential equation. Instead of computing the Green function itself, he solved the ordinary differential equation for the evaluation of Green function and its derivatives with Runge-Kutta 4-th order scheme. Chuang et al. (2007) proposed a time-marching Frobenius method to evaluate the Green function analytically. Li et al. (2015) suggested a precise integration (PI) method to solve the ordinary differential equation. Recently, Bingham (2016) compared the accuracy and efficiency of computation algorithms based on the interpolation of tabulated data, solving the ordinary differential equations by Runge-Kutta 4-th order scheme, time-marching Frobenius method, and PI method. He reported that the interpolation with tabulated data is faster than solving the ordinary differential equations with 5-6 digits of accuracy. Also, the time-marching Frobenius method is about two times faster than the Runge-Kutta scheme.

Nevertheless, the velocity representation needs two expressions of wave term and their derivatives which are

$$H(\mathbf{x},\boldsymbol{\xi},t) = 2\int_0^\infty \left\{1-\cos\left(\sqrt{gk}t\right)\right\} e^{kZ} J_0\left(kR\right) dk,$$
$$F(\mathbf{x},\boldsymbol{\xi},t) = 2\int_0^\infty e^{kZ}\cos\left(\sqrt{gk}t\right) J_0(kR) dk.$$

Previous researchers have focused on the first term $H_\tau(\mathbf{x},\boldsymbol{\xi},t-\tau)$, but no study has been conducted for the second expression $F(\mathbf{x},\boldsymbol{\xi},t-\tau)$ because F has never been applied in time domain BEM to the author's knowledge. It is convenient to express wave terms with two real variables.

The wave terms with nondimensional spherical coordinates, $\mu = -(z+\zeta)/r_2$ and $\tau = t/\sqrt{g/r_2}$ are given by

$$H_\tau(\mathbf{x},\boldsymbol{\xi},t) = -2\sqrt{\frac{g}{r_2^3}}\tilde{H}_\tau(\mu,\tau), \qquad F(\mathbf{x},\boldsymbol{\xi},t) = \frac{2}{r_2}\tilde{F}(\mu,\tau) \tag{4.86}$$

where

$$\tilde{H}_\tau(\mu,\tau) = \int_0^\infty \sqrt{\lambda} e^{-\mu\lambda} J_0\left(\lambda\sqrt{1-\mu^2}\right)\sin\left(\tau\sqrt{\lambda}\right) d\lambda, \tag{4.87}$$
$$\tilde{F}(\mu,\tau) = \int_0^\infty e^{-\mu\lambda} J_0\left(\lambda\sqrt{1-\mu^2}\right)\cos\left(\tau\sqrt{\lambda}\right) d\lambda. \tag{4.88}$$

Clément (1998) showed that the first integral($\tilde{H}_\tau(\mu,\tau)$) and its derivatives fall into the same kind of integral and they all satisfy the 4-th order ordinary differential equation.

In present study, Clément's ordinary differential equation is extended to include the other wave term.

Proposition 1 *Let ν and l be two real parameters, τ and μ are two real variables with $0 \leq \mu \leq 1$. The functions $A_{\nu,l}$ and $B_{\nu,l}$ defined by*

$$A_{\nu,l}(\mu,\tau) = \int_0^\infty \lambda^l e^{-\mu\lambda} J_\nu\left(\lambda\sqrt{1-\mu^2}\right)\sin\left(\tau\sqrt{\lambda}\right)d\lambda, \tag{4.89}$$

$$B_{\nu,l}(\mu,\tau) = \int_0^\infty \lambda^l e^{-\mu\lambda} J_\nu\left(\lambda\sqrt{1-\mu^2}\right)\cos\left(\tau\sqrt{\lambda}\right)d\lambda \tag{4.90}$$

are the solutions of the differential equation

$$\frac{\partial^4 W_{\nu,l}}{\partial\tau^4} + \mu\tau\frac{\partial^3 W_{\nu,l}}{\partial\tau^3} + \left\{\frac{\tau^2}{4} + \mu\left(3+2l\right)\right\}\frac{\partial^2 W_{\nu,l}}{\partial\tau^2} + \tau\left(l+\frac{5}{4}\right)\frac{\partial W_{\nu,l}}{\partial\tau} + \left\{(l+1)^2-\nu^2\right\}W_{\nu,l} = 0, \tag{4.91}$$

where

$$W_{\nu,l}(\mu,\tau) = A_{\nu,l}(\mu,\tau) \quad or \quad B_{\nu,l}(\mu,\tau).$$

Proof) Clément (1998) proved that the function $A_{\nu,l}(\mu,\tau)$ is a solution of ordinary differential equation

$$A^{(4)}_{\nu,l} + \mu\tau A^{(3)}_{\nu,l} + \left\{\frac{\tau^2}{4} + \mu\left(3+2l\right)\right\}A^{(2)}_{\nu,l} + \tau\left(l+\frac{5}{4}\right)A^{(1)}_{\nu,l} + \left\{(l+1)^2-\nu^2\right\}A_{\nu,l} = 0$$

where superscript $^{(\cdot)}$ represents the derivatives with respect to τ.

Applying the derivative with respect to τ again on the ordinary differential equation leads to

$$A^{(5)}_{\nu,l} + \mu\tau A^{(4)}_{\nu,l} + \left[\frac{\tau^2}{4} + \mu\left\{3+2\left(l+\frac{1}{2}\right)\right\}\right]A^{(3)}_{\nu,l} + \tau\left\{\left(l+\frac{1}{2}\right)+\frac{5}{4}\right\}A^{(2)}_{\nu,l} + \left\{\left(l+\frac{3}{2}\right)^2-\nu^2\right\}A^{(1)}_{\nu,l} = 0.$$

Substituting the following relation between $A_{\nu,l}$ and $B_{\nu,l}$

$$\frac{\partial A_{\nu,l}(\mu,\tau)}{\partial\tau} = B_{\nu,l+\frac{1}{2}}(\mu,\tau,)$$

into the ordinary differential equation given above, the ordinary differential equation with respect to $B_{\nu,l+\frac{1}{2}}$ is derived as

$$B^{(4)}_{\nu,l+\frac{1}{2}} + \mu\tau B^{(3)}_{\nu,l+\frac{1}{2}} + \left[\frac{\tau^2}{4} + \mu\left\{3+2\left(l+\frac{1}{2}\right)\right\}\right]B^{(2)}_{\nu,l+\frac{1}{2}} + \tau\left\{\left(l+\frac{1}{2}\right)+\frac{5}{4}\right\}B^{(1)}_{\nu,l} + \left\{\left(l+\frac{3}{2}\right)^2-\nu^2\right\}B_{\nu,l+\frac{1}{2}} = 0.$$

Because l is arbitrary real, $B_{v,l}$ is the solution of this ordinary differential equation.

Furthermore, the spatial derivatives of two integrals fall into the same integral kind given before.

The interpolation based on tabulated data is efficient compared to solving the ordinary differential equation (Bingham, 2016). However, the development of algorithms based on tabulation method for two wave terms and their derivatives need huge efforts to get accuracy and efficiency in same time.

In the present study, the wave terms and their gradients are evaluted by solving the ordinary differential equation. The initial condition of $A_{\nu,l}$ is given by Clément (1998) by

$$A_{\nu,l}^{(2k)}(\mu,0)=0,\quad A_{\nu,l}^{(2k+1)}(\mu,0)=(-1)^{k+\nu}\Gamma\left(l+\frac{2k+3}{2}-\nu\right)P_{l+k+1/2}^{\nu}(\mu),\quad k=0,1,2,\cdots \tag{4.92}$$

where $\Gamma(x)$ is Gamma function, $P_l^{\nu}(x)$ is Legendre function of the first kind (Abramowitz and Stegun, 1965). The initial conditions for $B_{\nu,l}$ and its derivatives with respect to τ are given by

$$B_{\nu,l}^{(2k)}(\mu,0)=(-1)^k\int_0^{\infty}\lambda^{l+k}e^{-\lambda\mu}J_{\nu}\left(\lambda\sqrt{1-\mu^2}\right)d\lambda,\quad B_{\nu,l}^{(2k+1)}(\mu,0)=0,\quad k=0,1,2,\cdots \tag{4.93}$$

Using the integral relation of Bessel function with the exponential and polynomial (equation 6.625.6 in (Gradshteyn and Ryzhik, 2007))

$$\int_0^{\infty}e^{-t\cos\theta}J_{\mu}(t\cos\theta)t^{\nu}dt=\Gamma(\nu+\mu+1)P_{\nu}^{-\mu}(\cos\theta),\qquad \text{for}\quad \Re\left[\nu+\mu\right]>1,\quad 0\leq\theta\leq\frac{\pi}{2}.$$

The initial condition for even order derivatives of $B_{\nu,l}$ are given by

$$\begin{aligned}B_{\nu,l}^{(2k)}(\mu,0)&=(-1)^{k+\nu}\Gamma(l+k-\nu+1)P_{l+k}^{\nu}(\mu)\\&=(-1)^{k+\nu}(l+k-\nu)!(1-\mu)^{\frac{\nu}{2}}\frac{d^{\nu}}{d\mu^{\nu}}P_{l+k}(\mu).\end{aligned}$$

The initial conditions for H_{τ} are given in Clément (1998) by using above relationships. The initial conditions for H_{τ} and F are therefore given by

$$\tilde{H}_{\tau}(\mu,0)=0,\qquad \tilde{H}_{R\tau}^{(1)}(\mu,0)=1,\qquad \tilde{H}_{\tau}^{(2)}(\mu,0)=0,\qquad \tilde{H}_{R\tau}^{(3)}(\mu,0)=-2\mu.$$

and

$$\tilde{F}(\mu,0)=1,\qquad \tilde{F}^{(1)}(\mu,0)=0,\qquad \tilde{F}^{(2)}(\mu,0)=-\mu,\qquad \tilde{F}^{(3)}(\mu,0)=0.$$

In a similar way, the initial condition of horizontal and vertical gradients of H_{τ} and F are given by

$$\begin{aligned}&\tilde{H}_{R\tau}(\mu,0)=0, && \tilde{H}_{Z\tau}(\mu,0)=0,\\&\tilde{H}_{R\tau}^{(1)}(\mu,0)=3\mu\sqrt{1-\mu^2}, && \tilde{H}_{Z\tau}^{(1)}(\mu,0)=3\mu^2-1,\\&\tilde{H}_{R\tau}^{(2)}(\mu,0)=0, && \tilde{H}_{Z\tau}^{(2)}(\mu,0)=0,\\&\tilde{H}_{R\tau}^{(3)}(\mu,0)=-(15\mu^2-3)\sqrt{1-\mu^2}, && \tilde{H}_{Z\tau}^{(3)}(\mu,0)=-15\mu^3+9\mu,\end{aligned}$$

and

$$\begin{aligned}&\tilde{F}_R(\mu,0)=\sqrt{1-\mu^2}, && \tilde{F}_Z(\mu,0)=\mu,\\&\tilde{F}_R^{(1)}(\mu,0)=0, && \tilde{F}_Z^{(1)}(\mu,0)=0,\\&\tilde{F}_R^{(2)}(\mu,0)=-3\mu\sqrt{1-\mu^2}, && \tilde{F}_Z^{(2)}(\mu,0)=-3\mu^2+1,\\&\tilde{F}_R^{(3)}(\mu,0)=0, && \tilde{F}_Z^{(3)}(\mu,0)=0.\end{aligned}$$

To solve the ordinary differential equation, the time marching Frobenius method proposed by Chuang et al. (2007) is adopted in the present study. The 4-th order ordinary differential equation is given in (4.91) as

$$W_{\nu,l}^{(4)} + \mu\tau W_{\nu,l}^{(3)} + \left(\frac{\tau^2}{4} + \alpha\mu\right) W_{\nu,l}^{(2)} + \beta\tau W_{\nu,l}^{(1)} + \gamma W_{\nu,l} = 0$$

where

$$\alpha = 3 + 2l, \qquad \beta = l + \frac{5}{4}, \qquad \gamma = (l+1)^2 - \nu^2.$$

The solution of the ordinary differential equation of next time step τ is expanded with the power series of the previous time step τ_0 as

$$W_{v,l}(\tau) = \sum_{n=0}^{\infty} a_n \left(\tau - \tau_0\right)^n . \tag{4.94}$$

Substituting the power series expanded solution into the ordinary differential equation, the first four coefficients are given as

$$a_0 = W_{\nu,l}(\mu, \tau_0), \qquad a_1 = W_{\nu,l}^{(1)}(\mu, \tau_0), \tag{4.95}$$

$$a_2 = \frac{1}{2} W_{\nu,l}^{(2)}(\mu, \tau_0), \qquad a_3 = \frac{1}{6} W_{\nu,l}^{(3)}(\mu, \tau_0). \tag{4.96}$$

By defining the variable coefficients of the ordinary differential equation as

$$\kappa_1 = 1, \quad \kappa_2 = \mu, \quad \kappa_3 = \mu\tau_0, \quad \kappa_4 = \frac{1}{4}, \quad \kappa_5 = \frac{1}{2}\tau_0, \tag{4.97}$$

$$\kappa_6 = \frac{1}{4}\tau_0^2 + \alpha\mu, \quad \kappa_7 = \beta \quad \kappa_8 = \beta\tau_0, \quad \kappa_9 = \gamma. \tag{4.98}$$

The recursion relations of a_n for $n \geq 4$ is given as

$$a_{n+4} = -\frac{1}{\lambda_{n+4}} \left(\lambda_{n+3} a_{n+3} + \lambda_{n+2} a_{n+2} + \lambda_{n+1} a_{n+1} + \lambda_n a_n\right), \qquad \text{for} \qquad n \geq 0,$$

with

$$\begin{aligned}
\lambda_{n+4} &= \kappa_1 (n+4)(n+3)(n+2)(n+1), \\
\lambda_{n+3} &= \kappa_3 (n+3)(n+2)(n+1), \\
\lambda_{n+2} &= \kappa_2 (n+2)(n+1)n + \kappa_6 (n+2)(n+1), \\
\lambda_{n+1} &= \kappa_5 n(n+1) + \kappa_8 (n+1), \\
\lambda_n &= \kappa_4 n(n-1) + \kappa_7 n + \kappa_9 .
\end{aligned}$$

Therefore, the next time step solution $W_{\nu,l}(\tau)$ is given by the summation of coefficients with the desired accuracy. The evaluated wave terms and their derivatives are plotted in figure 4.2.

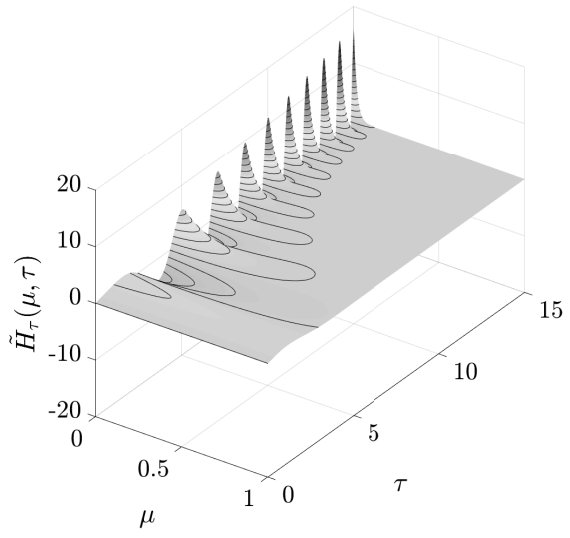

(a) $\tilde{H}_\tau(\mu,\tau)$

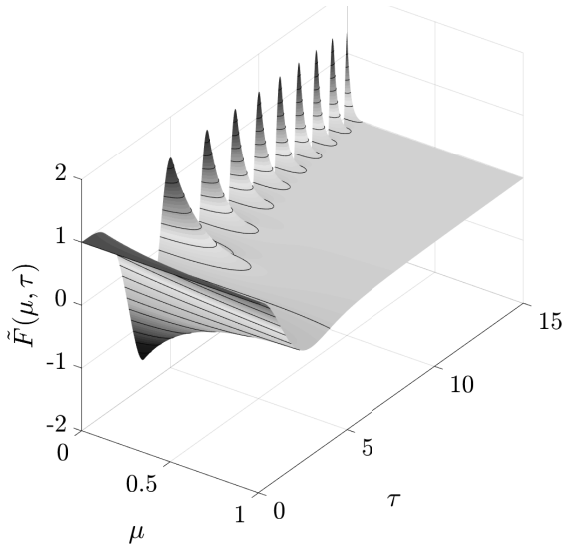

(b) $\tilde{F}(\mu,\tau)$

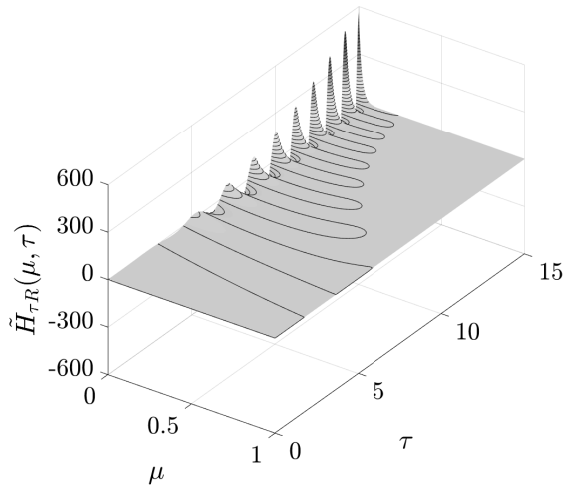

(c) Horizontal gradient, $\tilde{H}_{\tau R}$

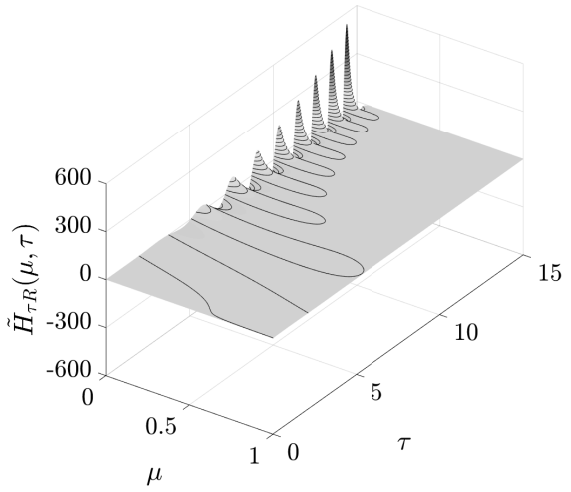

(d) Vertical gradient , $\tilde{H}_{\tau Z}$

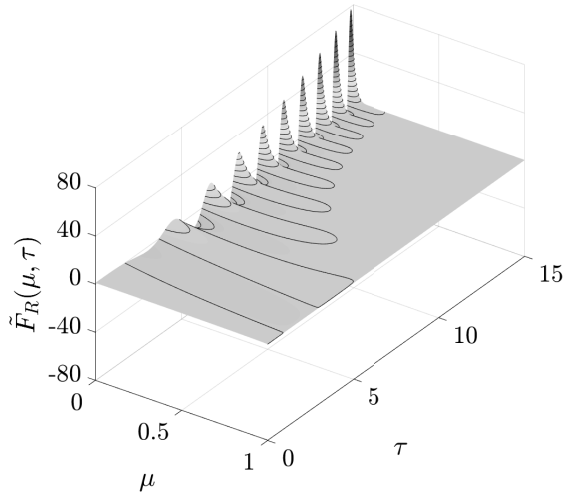

(e) Horizontal gradient, $\tilde{F}_R$

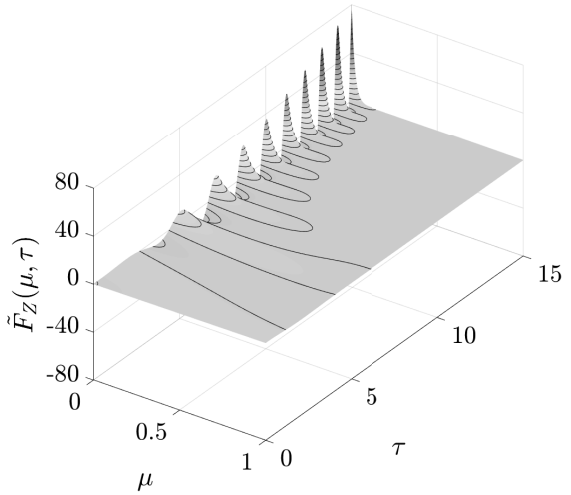

(f) Vertical gradient, $\tilde{F}_Z$

Figure 4.2. Time domain Green function and their derivatives, $\tilde{H}_\tau(\mu,\tau)$ and $\tilde{F}(\mu,\tau)$.

4.5 Validation and discussion

4.5.1 A heaving hemisphere on the mean free surface

The Humle's heaving hemisphere is considered to validate the proposed Poincaré's velocity representation with matching surface (Hulme, 1982). The analytical solution of surface-piercing hemisphere is given by Hulme (1982) for surging and heaving motion. A heaving hemisphere on the mean free surface is shown in figure 4.3.

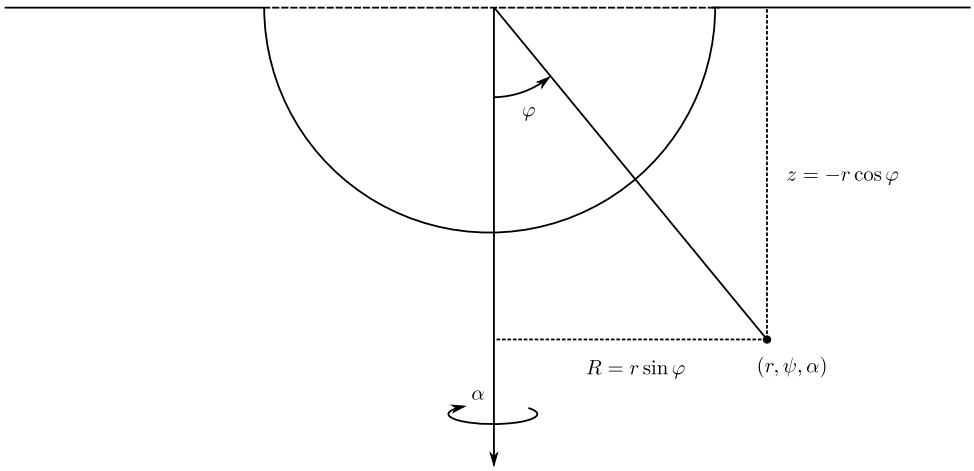

Figure 4.3. A heaving hemisphere on the mean free surface.

Spherical polar coordinates(r, φ, α) and cylindrical polar coordinates(R, θ, z) defined by

$$x = R\cos\theta, \quad y = R\sin\theta, \quad z = -r\cos\varphi, \quad R = r\sin\varphi, \tag{4.99}$$

are used.

When the hemisphere motion is given in $A_{heave}\sin\omega t$ where A_{heave} and ω are motion amplitude and frequency, respectively, velocity potential is given in series of multipoles as

$$\Phi_R = \omega A_{heave}\Re\left[\phi_R e^{-\mathrm{i}\omega t}\right], \tag{4.100}$$

with radiation potential (ϕ_R) in frequency domain

$$\phi_R = c_0 a^2\left(\psi_0^s + \sum_{n=1}^{\infty} c_n a^{2n}\psi_{2n}^s\right) \tag{4.101}$$

where c_n denotes the multipole strengths and ψ_{2n} are the wave-free potentials by multipoles which are given in

$$\psi_0 = \frac{1}{r_1} + \pi\mathrm{i}k\sum_{n=0}^{\infty}\frac{(-kr)^n}{n!}P_n(\mu) - k\sum_{n=0}^{\infty}(-1)^n\frac{\partial}{\partial\nu}\left\{\frac{(kr)^\nu}{nu!}P_\nu(\mu)\right\}_{\nu=n}, \tag{4.102}$$

$$\psi_{2n} = \frac{P_{2n}(\mu)}{r^{2n+1}} + \frac{k}{2n}\frac{P_{2n-1}(\mu)}{r^{2n}}, \tag{4.103}$$

where $\mu = \cos\varphi$, $k = \omega^2/g$, $P_\nu(\mu)$ are Legendre polynomials given by

$$\begin{aligned} P_0(\mu) &= 1, \\ P_1(\mu) &= \mu, \\ (n+1)P_{n+1}(\mu) &= (2n+1)\mu P_n(\mu) - nP_{n-1}(\mu), \qquad \text{for} \qquad n \geq 1. \end{aligned} \tag{4.104}$$

The body boundary condition is given by

$$\frac{\partial \phi_R}{\partial r} = \cos\varphi, \qquad \text{on} \quad r = a, \quad \text{for} \quad \varphi \in [0, \pi/2]. \tag{4.105}$$

Subtituting the velocity potential into body boundary condition

$$\mathscr{F}(\mu, ka) - \sum_{n=1}^{\infty} c_n \left\{ kaP_{2n-1}(\mu) + (2n+1)P_{2n}(\mu) \right\} = \frac{P_1(\mu)}{c_0}, \tag{4.106}$$

with $\mathscr{F}(\mu, ka) = a^2 \frac{\partial \psi_0}{\partial r}$. After integrating above expression with respect to φ over $[0, 1]$ gives

$$\int_0^1 \mathscr{F}(\mu, ka) d\mu - ka \sum_{n=1}^{\infty} c_n I_{0,2n-1} = \frac{1}{2c_0}, \tag{4.107}$$

where the integrals of Legendre functions are defined by

$$I_{m,n} = \int_0^1 P_m(\mu) P_n(\mu) d\mu. \tag{4.108}$$

Recalling the body boundary condition given in equation (4.106) leads to:

$$\begin{aligned} \mathscr{F}(\mu, ka) - \sum_{n=1}^{\infty} c_n \left\{ kaP_{2n-1}(\mu) + (2n+1)P_{2n}(\mu) \right\} \\ = 2P_1(\mu) \left(\int_0^1 \mathscr{F}(\mu, ka) d\mu - ka \sum_{n=1}^{\infty} c_n I_{0,2n-1} \right) \end{aligned} \tag{4.109}$$

After manipulating previous equation, multiplying $P_{2m}(\mu)$ and integrating with respect to μ over $(0, 1)$, we can obtain the equations for multipole strengths

$$\frac{2m+1}{4m+1} c_m + ka \sum_{n=1}^{\infty} \left\{ I_{2m,2n-1} - 2I_{2m,1} I_{0,2n-1} \right\} c_n = \mathscr{J}_{2m} - 2\mathscr{J}_0 I_{2m,1} \tag{4.110}$$

with

$$\begin{aligned} \mathscr{J}_m &= \int_0^1 \mathscr{F}(\mu, ka) P_m(\mu) d\mu \\ &= -I_{m,0} - ka \sum_{n=1}^{\infty} \frac{(-ka)^n}{(n-1)!} \left. \frac{\partial I_{m,\nu}}{\partial \nu} \right|_{\nu=n} + ka \sum_{n=0}^{\infty} \frac{(-ka)^n}{n!} \left[n \left\{ \psi(n+1) + \pi \mathrm{i} - \ln ka \right\} - 1 \right] I_{m,n} \end{aligned} \tag{4.111}$$

where $\psi(x) = \frac{d}{dx} \ln(\Gamma(x)) = \frac{\Gamma'(x)}{\Gamma(x)}$ is digamma function. Note that digamma function in Hulme (1982) is mistyped, e.g. written as $\phi(n)$. After solving the algebraic equations (4.109), c_0 is determined by equation (4.107). The computed radiation forces are compared in figure 4.4 with the results of Hulme (1982).

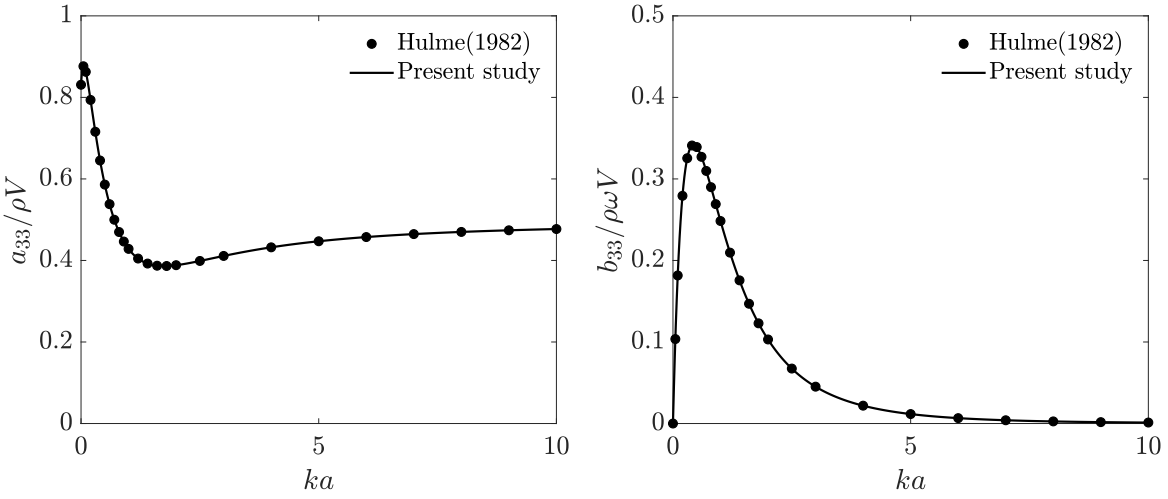

(a) Added mass **(b)** Radiation damping

Figure 4.4. Nondimensionalized radiation forces acting on heaving hemisphere.

4.5.2 Configuration of benchmark test

The schematic view of benchmark test is depicted in figure 4.5. The fluid velocity and wave elevation on the matching surface and waterline are calculated from analytic solution. They are used to calculate the fluid velocity at field point from Poincaré's velocity representation. The fluid velocity at field point calculated by velocity representation is compared with the analytical solution.

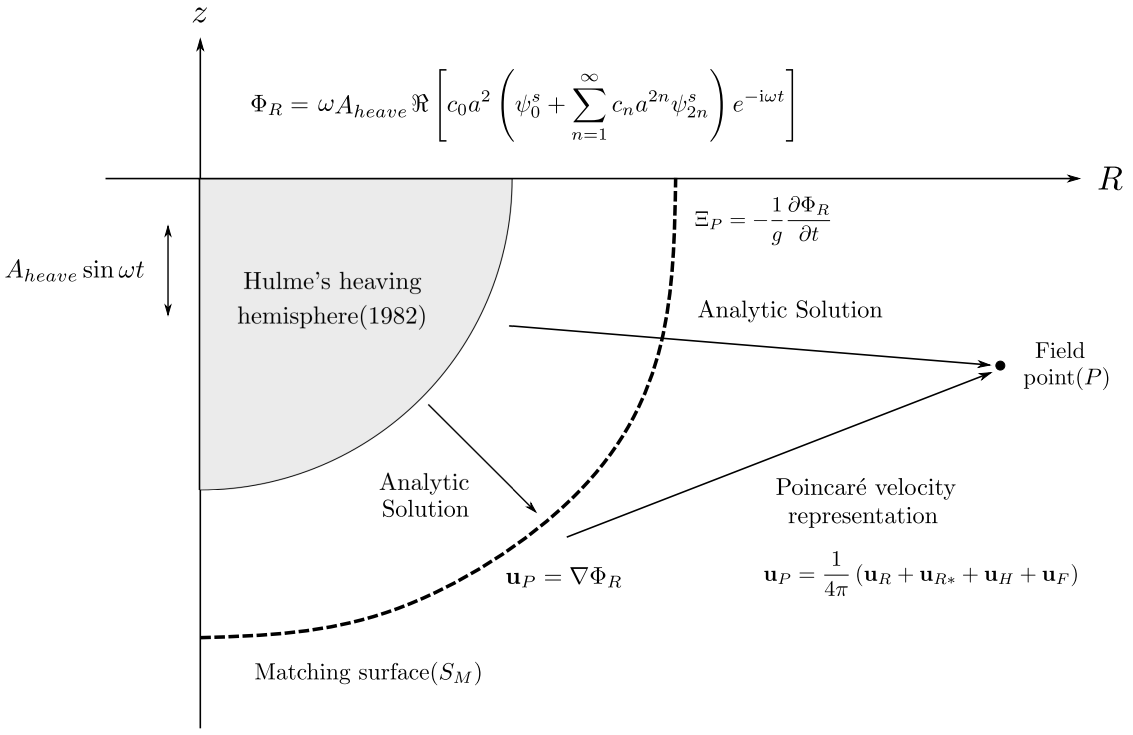

Figure 4.5. Benchmark test.

Poincaré's velocity representation with arbitrary matching surface is validated with following cases:

- **Discretization of matching surface**: The field point is located underwater, the hemisphere shaped matching surface is refined to see the convergence.
- **Discretization of convolution time difference**: The field point is located underwater, the convolution time difference is refined with hemisphere shaped matching surface.
- **Different heaving frequencies**: The field point is located underwater at fixed position, the heaving frequency of hemisphere is changed.
- **Different matching surfaces**: The field point is located underwater at fixed position, various shaped matching surfaces are applied.
- **Field point is located on $\mathbf{z = 0}$**: When the field point is located on $z = 0$, the fluid velocity reconstructed by Poincaré's velocity representation will be discussed.

4.5.3 Discretization of matching surface

Hemisphere shaped matching surfaces with a radius of $2a$ are shown in figure 4.6. The heaving hemisphere is located inside of this matching surface. The fluid velocities at two field points, $kR = 3.19, kz = -0.637$ and $kR = 23.54, kz = -0.637$ are reconstructed by Poincaré's velocity representation, respectively. The reconstructed fluid velocity are compared with the analytical solution in figures 4.7 and 4.8. In the figures, $A(f)$ is the amplitude of f.

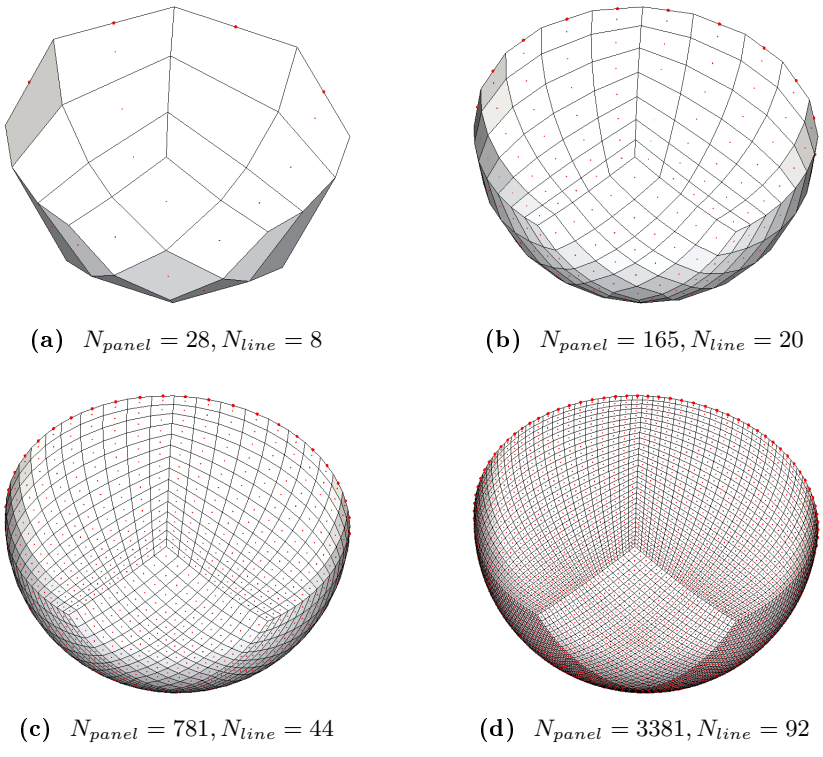

(a) $N_{panel} = 28, N_{line} = 8$ **(b)** $N_{panel} = 165, N_{line} = 20$

(c) $N_{panel} = 781, N_{line} = 44$ **(d)** $N_{panel} = 3381, N_{line} = 92$

Figure 4.6. Discretized matching surfaces of hemisphere shape.

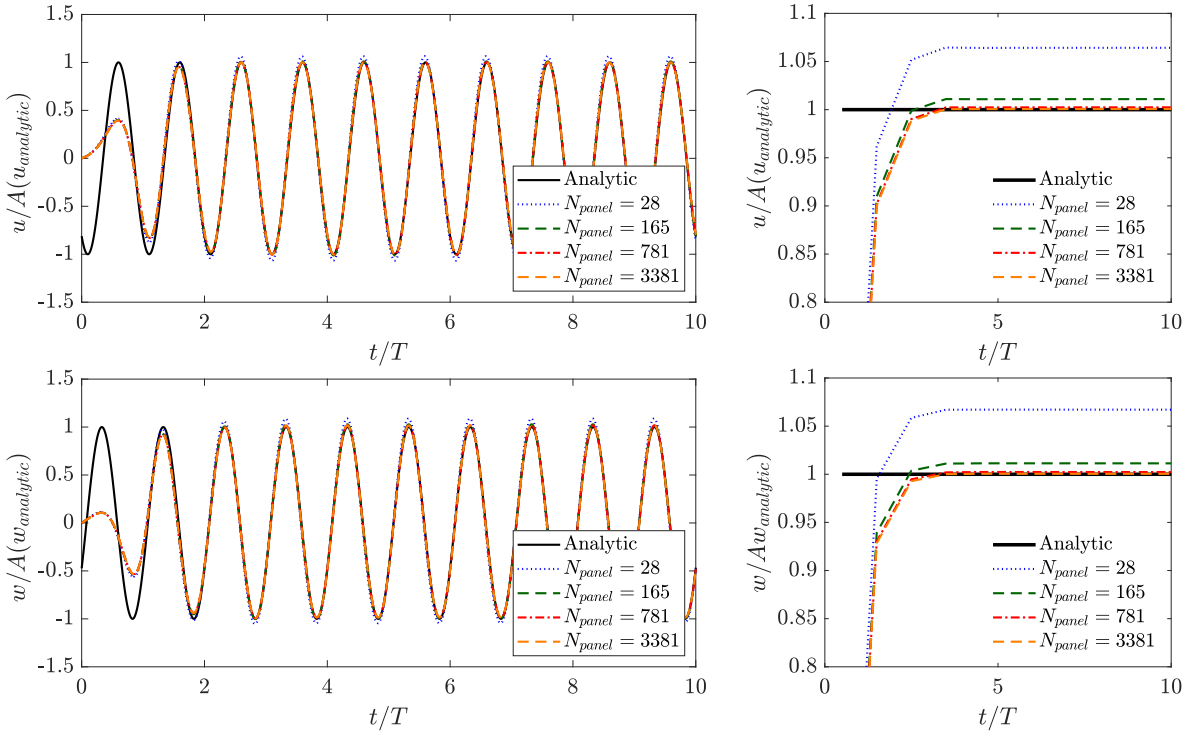

Figure 4.7. The reconstructed velocity with respect to matching surface discretization at $kR = 3.19$ and $kz = -0.637$ (left : time series, right : mwFFT, top : horizonal velocity, bottom : vertical velocity)

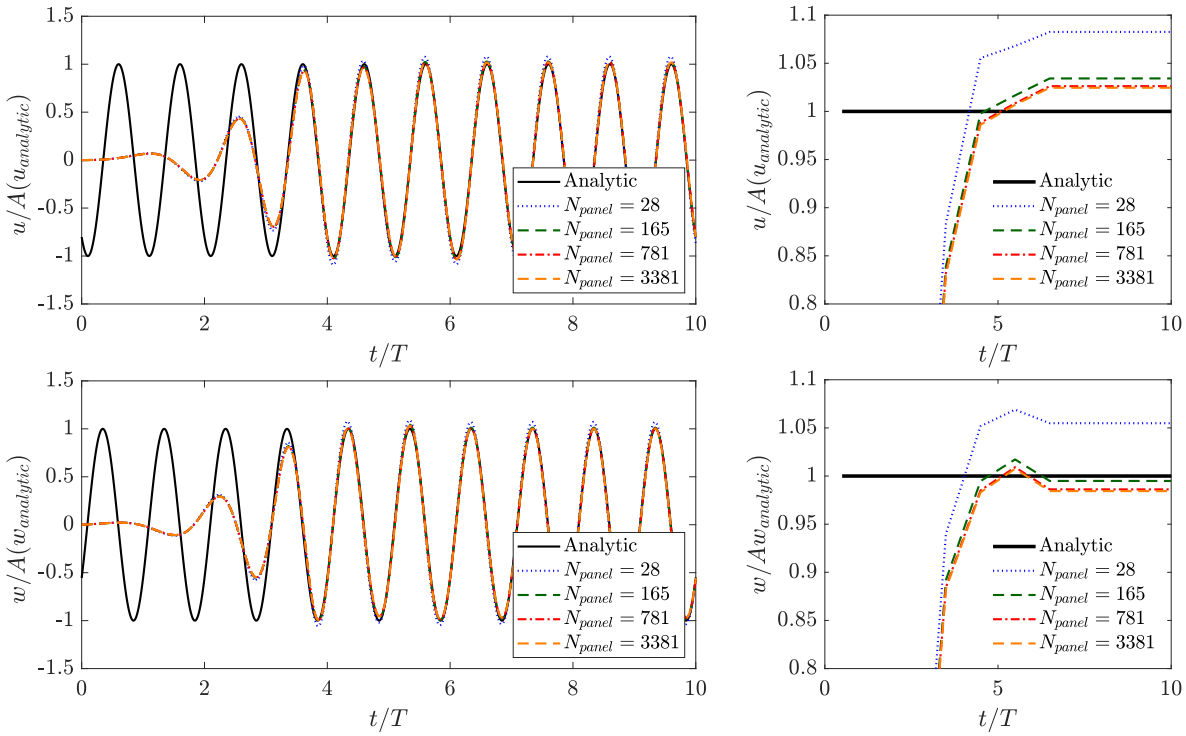

Figure 4.8. The reconstructed velocity with respect to matching surface discretization at $kR = 23.54$ and $kz = -0.637$ (left : time series, right : mwFFT, top : horizonal velocity, bottom : vertical velocity)

The reconstructed velocity converges to the analytic solution as the mesh is refined for field point $kR = 3.19$. For the discretized matching surfaces of $N_{panel} = 165, 781$ and 3381, the relative errors are 1.1% 0.2% and 0.05%, respectively. The relative errors of the fluid velocity field point $kR = 23.54$ with $N_{panel} = 3381$ increases up to 2.5%.

The obtained results show good agreement with analytical solution. Poincaré's velocity representation gives good convengence with respect to mesh discretization. When the field point locates far from the matching surface, matching surface and its waterline need to be discretized sufficiently.

4.5.4 Discretization of convolution time step

The convolution time step sizes are varied for $T/\Delta\tau = 16, 32, 64, 128$ with the spherical matching surface of $N_{panel} = 781$. The moving window for convolution integral is set to $4.1T$. The fluid velocity at $kR = 3.19$, $kz = -0.637$ calculated by Poincaré's velocity representation is compared with the analytical solution in figure 4.9.

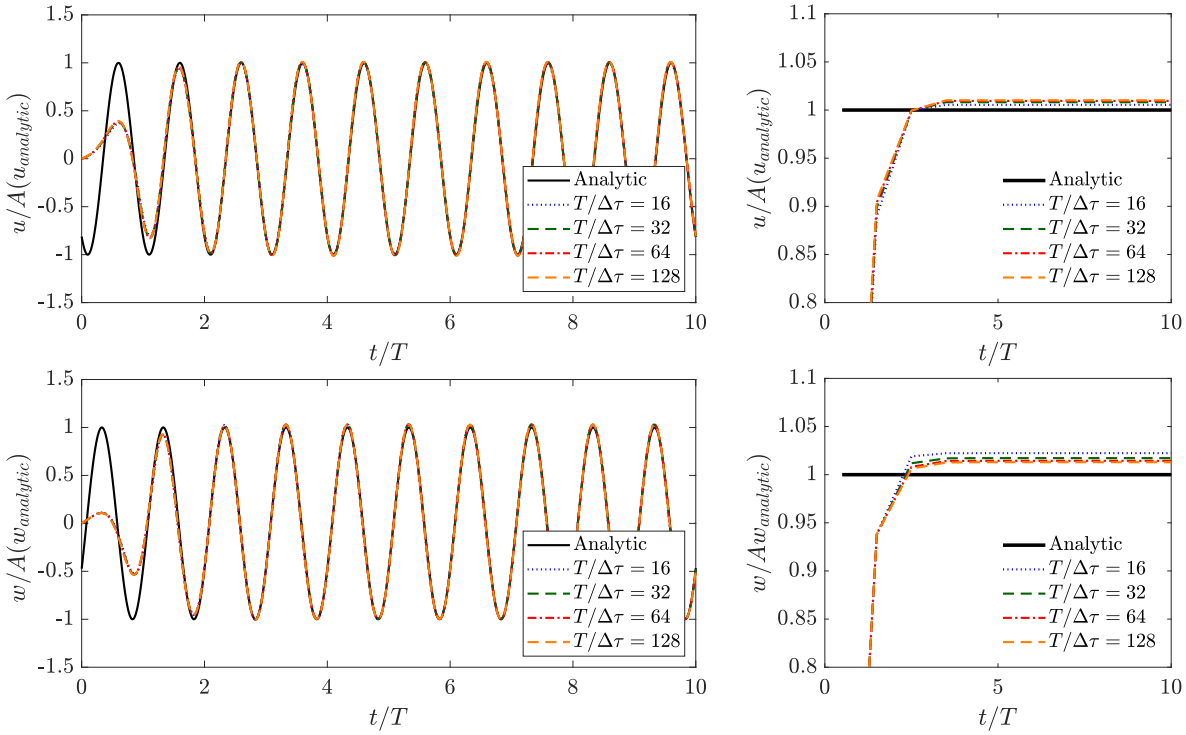

Figure 4.9. The reconstructed velocity with respect to convolution time difference $\Delta\tau$ at $kR = 3.19$ and $kz = -0.637$ (left : time series, right : mwFFT, top : horizonal velocity, bottom : vertical velocity)

In the result of mwFFT, 1.3% of error is shown for vertical velocity component with refined convolution time difference $T/\Delta\tau = 128$. It is thought that sufficient discretizations with respect to mesh and convolution time steps are necessary to obtain accurate results.

4.5.5 Different heaving frequencies

Three differerent heaving frequencies, $\omega = 1.0, 2.5$ and 4.0 rad/s, have been considered for validation. Fluid velocities are reconstructed at fixed field point $R = 5.0m$ and $z = -1.0m$. The spherical matching surface with the number of panels, $N_{panel} = 781$ is used. The convolution time step is $\Delta\tau = 0.01s$ and the convolution integral is calculated over $15s$.

Time series of reconstructed velocities are compared with the analytical solution in figure 4.10.

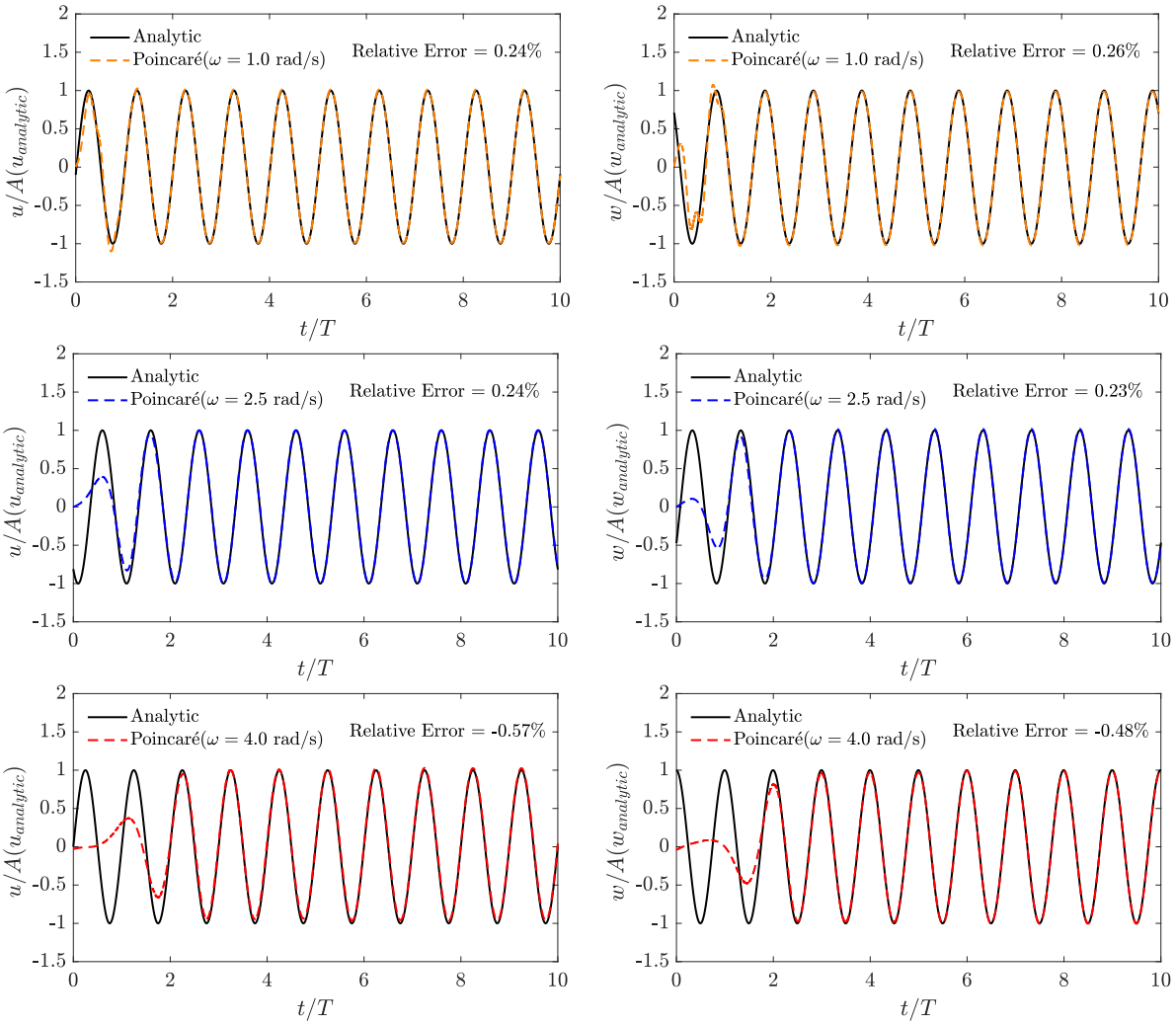

Figure 4.10. The reconstructed velocity with respect to different heaving frequency ω at $R = 5.0m$ and $z = -1m$ (left : horizontal velocity, right : vertical velocity)

After the initial evolution of memory effects, the reconstructed velocities show good agreement with analytical solution. The amplitudes of reconstructed velocities for different frequencies have relative errors less than the value of 0.6%.

In the results, we can verify that the reconstructed waves by Poincaré's velocity representation are propagating with different speed. This is the effects of dispersion on the speed of the waves.

4.5.6 Different matching surfaces

A set of different matching surfaces such as hemisphere, bottom-opened circular cylinder, ellipsoid and parallel-pipe shown in figure 4.11, are considered to check the sensitivity of the proposed velocity representation to the geometry of the matching surface. The convolution time step of $\Delta\tau = 0.01s$ is used and the convolution integral is calculated over $15s$.

Time series and mwFFT of reconstructed fluid velocity at field point $(kR = 3.19, kz = -0.6370)$ are compared with the analytical solution in figure 4.12. The reconstructed velocity with closed matching surfaces have relative errors of less than 0.4% and the velocity with bottom-opened circular cylinder has a relative error of 1%.

The results are summarized as follows:

- The proposed velocity representation is validated for arbitrary matching surfaces. For submerged field point, the reconstructed velocity shows good agreements with analytical solution.
- For a matching surface deep sufficiently, the proposed velocity representation works even when the bottom surface is opened. When the source point is deeply submerged and the distance between field and source points is large enough, the time domain Green function has very small value and the fluid velocity at the source point is negligible.

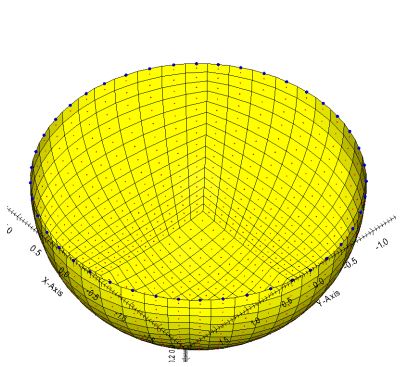

(a) Hemisphere ($N_{panel} = 781, N_{line} = 44$)

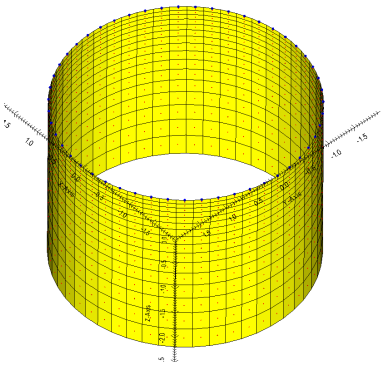

(b) Circular cylinder ($N_{panel} = 816, N_{line} = 51$)

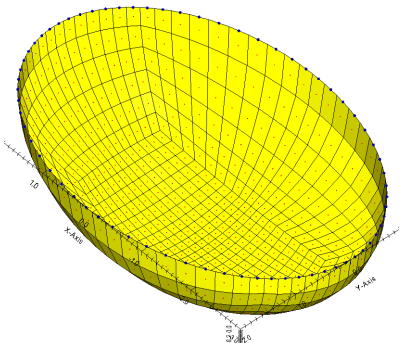

(c) Ellipsoid ($N_{panel} = 688, N_{line} = 68$)

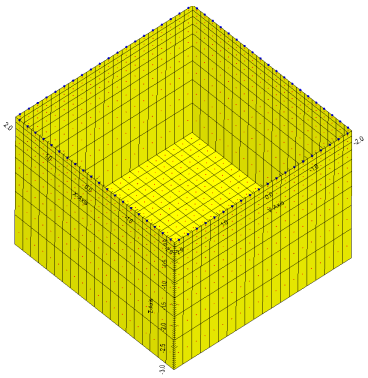

(d) Parallel-pipe ($N_{panel} = 1120, N_{line} = 80$)

Figure 4.11. Different matching surfaces.

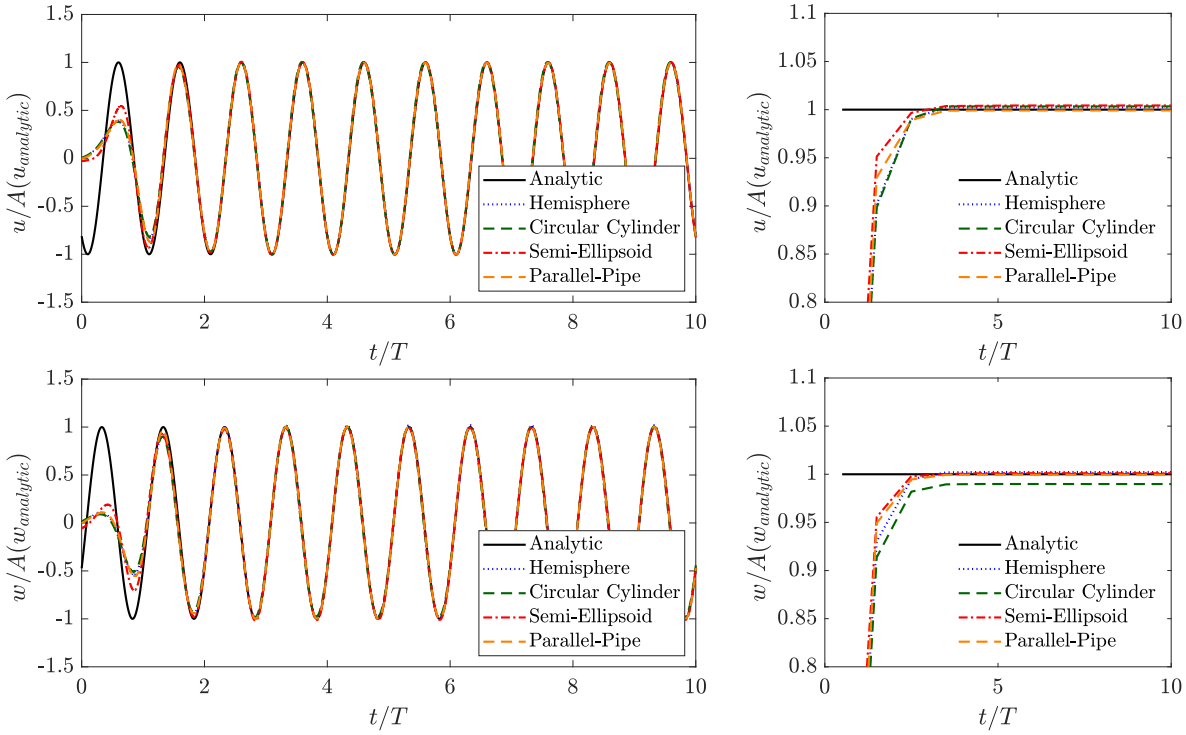

Figure 4.12. Reconstructed velocity with respect to different matching surfaces at $kR = 3.19$ and $kz = -0.637$ (left : time series, right : mwFFT, top : horizontal velocity, bottom : vertical velocity)

4.5.7 Singular behavior and discussion

When the field point is located on the mean free surface($z = 0$), the reconstructed velocity shown in figure 4.13 has a singular behavior.

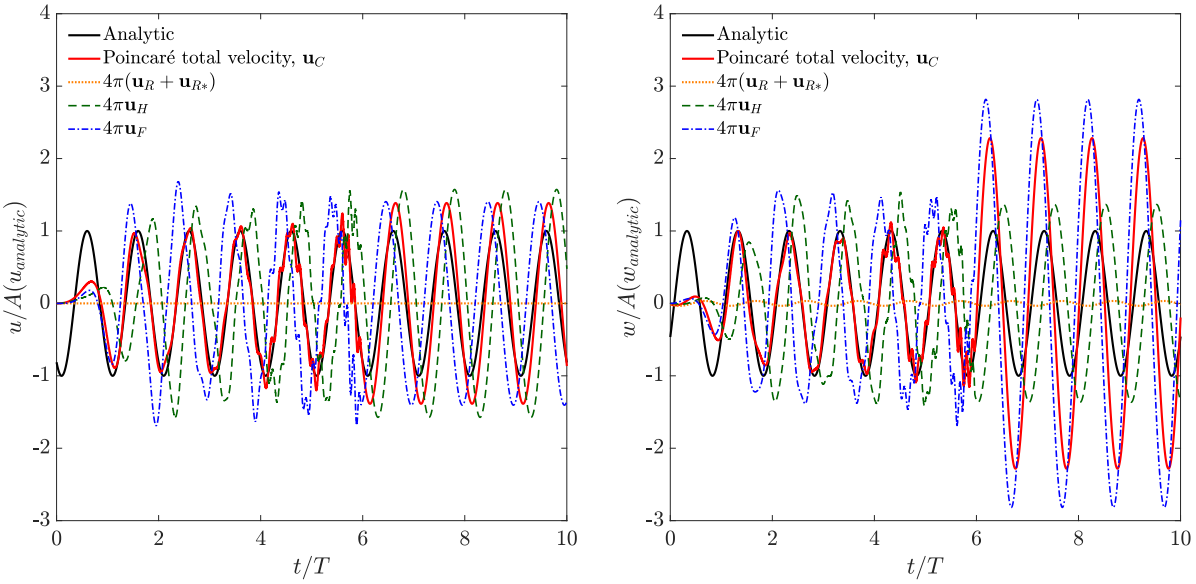

Figure 4.13. A singular behavior of reconstructed fluid velocity and its components with respect to integral contributions.

Two velocity contributions may cause this singular behavior:

- Contribution of harmonic component ($\mathbf{u}_H$) has a highly oscillatory unstable velocity profile when convolution integral is partially evaluated with a moving window interval. It becomes smooth after the moving window convolution time interval(T_0) passes the simulation time $t > T_0$.
- Contribution of free surface component ($\mathbf{u}_F$) has a highly oscillatory unstable velocity profile when the convolution integral is partially evaluated with moving integral interval as:

$$\int_{t-T_0}^{t} \{\cdot\}\, d\tau \tag{4.112}$$

  where T_0 is moving window convolution time interval. The contribution of free surface integral is unstable after simulation time $t > T_0$, e.g., $t - T_0 > 0$.

This singular behavior is thought to be similar to the *singular behavior of waterline integral* in the time domain problem (Bingham, 1994). When source and field points move towards mean free surface, the nondimensionalized spatial variable of the time domain Green function is given by

$$\mu = \frac{z+\zeta}{r_2} \to 0. \tag{4.113}$$

The time domain Green functions and their spatial derivatives, shown in figure 4.2, have the diverging behaviors when $\mu = 0$. At the limit $\mu = 0$, the time domain Green function $\tilde{H}_\tau(\mu, \tau)$ is expressed in the combination of Bessel functions (Wehausen and Laitone, 1960):

$$\tilde{H}_\tau(0,\tau) = \frac{\pi\tau}{2\sqrt{2}} \left\{ J_{1/4}\left(\frac{\tau^2}{8}\right) J_{-1/4}\left(\frac{\tau^2}{8}\right) + J_{3/4}\left(\frac{\tau^2}{8}\right) J_{-3/4}\left(\frac{\tau^2}{8}\right) \right\} \frac{\tau^2}{8}, \tag{4.114}$$

and it is bounded but has diverging behavior for $\tau \to \infty$:

$$-\frac{\tau}{\sqrt{2}} \le \tilde{H}_\tau(0,\tau) \le \frac{\tau}{\sqrt{2}}. \tag{4.115}$$

The diverging behavior of time domain Green function with the limited number of discretized constant panels make the reconstructed velocity unstable. Numerical singularity due to the discretization of panels and diverging behavior of time domain Green function for $\mu = 0$ is depicted in figure 4.14.

To verify that the mesh and waterline discretizations causes the singular behavior, the waterline segements are discretized into subline segments. $N_{subline} = 21$ means that one original line segment is discretized into 21 sub-line segments. Reconstructed horizontal and vertical velocities with respect to waterline discretization are shown in figure 4.15.

Results show that the waterline discretization helps to remedy the singular behavior of reconstructed fluid velocity on the mean free surface. However, highly oscillatory behavior of fluid velocity does not be cured by discretizing waterline segment.

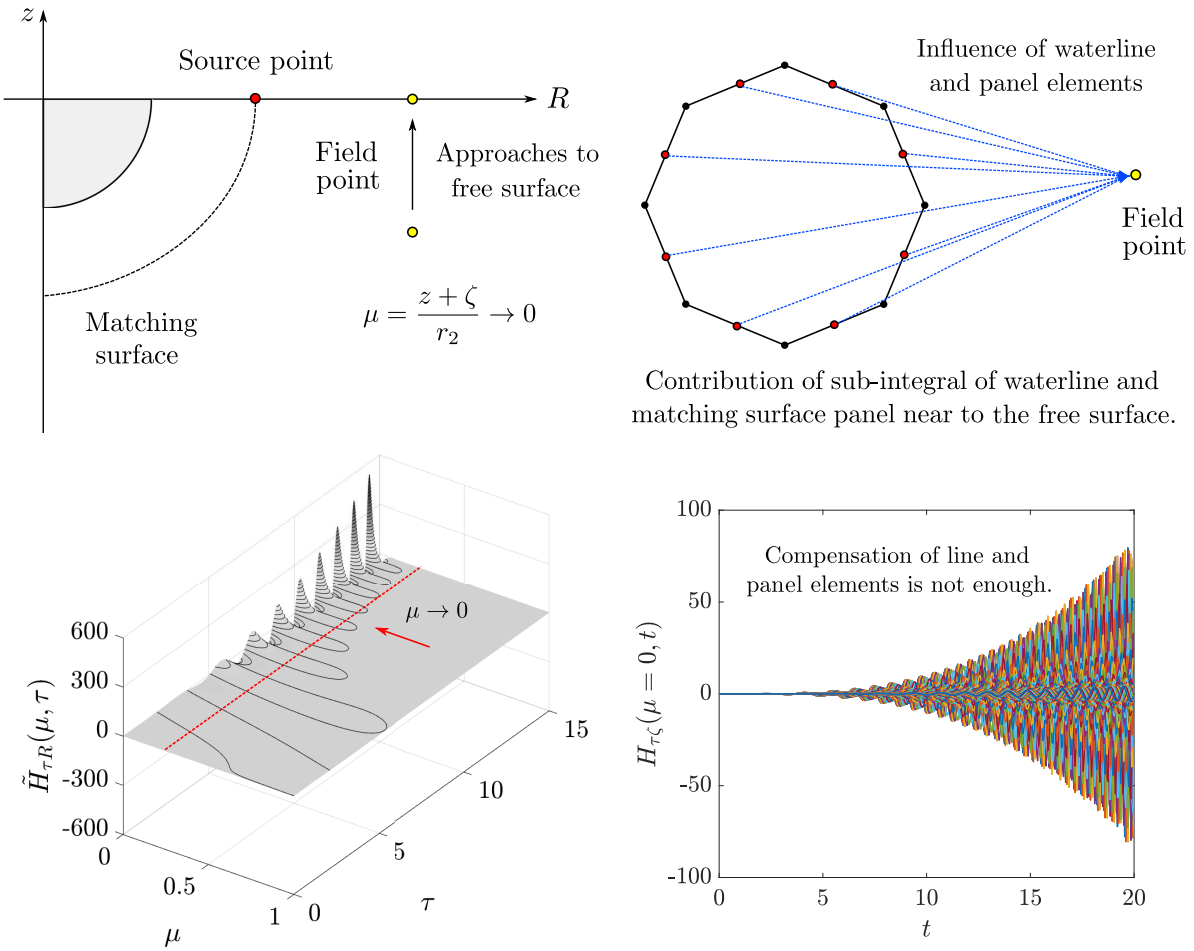

Figure 4.14. Understanding of numerical singularity due to the discretization of matching surface and waterline with time domain Green function.

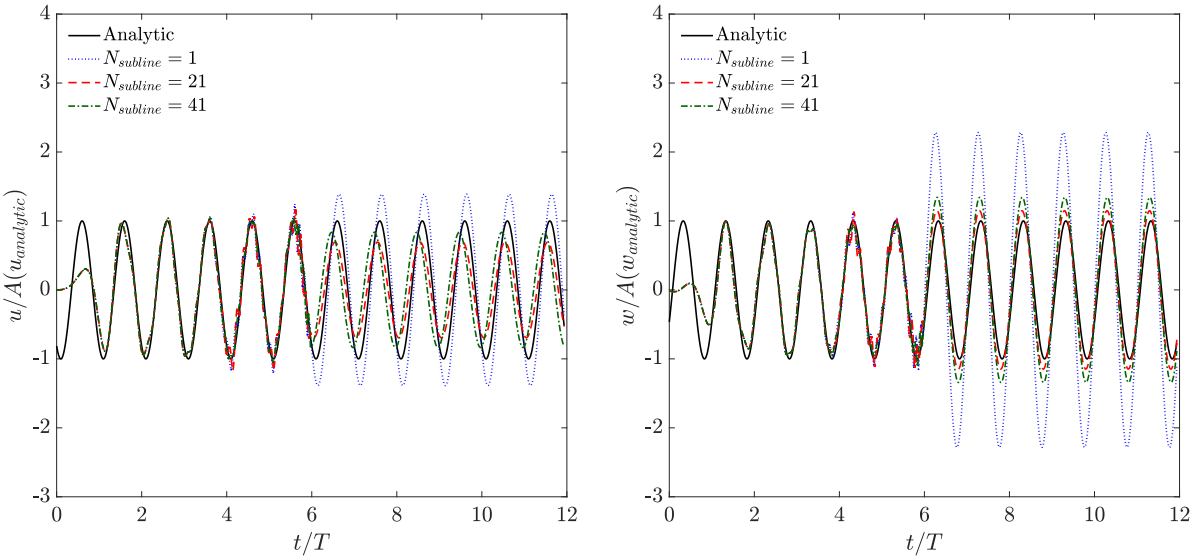

Figure 4.15. Understanding of numerical singularity due to the discretization of matching surface and waterline with time domain Green function.

Remarks on singular behavior

When both field and source points are located on the mean free surface, the time domain Green function and its derivatives fall into the integral type

$$\int_0^\infty k^p J_0(kR) \begin{Bmatrix} \cos t\sqrt{gk} \\ \sin t\sqrt{gk} \end{Bmatrix} dk, \tag{4.116}$$

where p is polynomial order. The time domain Green function has a diverging behavior when p is large and the oscillating band of Green function increases with p. Therefore, it is necessary to reduce the order of polynomial p on a mathematical point of view.

Derivating above integral with respect to time and space, the polynomial order (p) increases by 0.5 and 1, respectively, as shown below:

$$\frac{\partial}{\partial t}\int_0^\infty k^p J_0(kR) \begin{Bmatrix} \cos t\sqrt{gk} \\ \sin t\sqrt{gk} \end{Bmatrix} dk = \sqrt{g}\int_0^\infty k^{p+0.5} J_0(kR) \begin{Bmatrix} -\sin t\sqrt{gk} \\ \cos t\sqrt{gk} \end{Bmatrix} dk, \tag{4.117}$$

$$\frac{\partial}{\partial R}\int_0^\infty k^p J_0(kR) \begin{Bmatrix} \cos t\sqrt{gk} \\ \sin t\sqrt{gk} \end{Bmatrix} dk = \int_0^\infty k^{p+1} J_0'(kR) \begin{Bmatrix} \cos t\sqrt{gk} \\ \sin t\sqrt{gk} \end{Bmatrix} dk. \tag{4.118}$$

It means that derivating the time domain Green function gives poor results in numerical simulation.

When the surface and time integrals are applied to Poincaré's velocity representation, the order of polynomial (p) in time domain Green function is reversely reduced by 1 and 0.5, respectively. Therefore, a circular cylindrical shaped matching surface is introduced in the next Chapter 5. Integrating Poincaré's velocity representation along cylindrical matching surface makes the velocity representation less singular.

4.6 Conclusion

Poincaré's velocity representation, based on a modification of the boundary integral equation, is introduced. Consequently, the velocity representation becomes weakly singular and the fluid velocity at the field point is given explicitly from the normal and tangential velocity at boundary surfaces.

The velocity representation is applied to the unsteady time-domain problem with the linearized free surface boundary condition without forward speed. The free surface integral is transformed into a waterline integral by Reynolds transport and Stokes theorems. As a result, the fluid velocity at field point is given by the distribution of fluid velocities and wave elevations on the matching surface and waterline explicitly. It is shown that the various forms of wave term in the time domain Green functions satisfy the same 4-th order differential equations proposed by Clément (1998). Initial conditions of wave terms are suggested to solve the ordinary differential equation with respect to τ. A time-marching Frobenius method proposed by Chuang et al. (2007) is applied to calculate the wave terms.

The heaving hemisphere is considered as a benchmark test to validate the proposed velocity representation Hulme (1982).

When the field point is located underwater, the proposed Poincaré's velocity representation is show good agreements with analytical solution. It is validated for the cases of the discretization of matching surface, discretization of convolution time step size, different heaving frequency and various shaped matching surface.

However, a singular behavior of reconstructed velocity appears when the field point is located on mean free surface ($z = 0$). Discretization of matching surface and its waterline with diverging behavior of time domain Green function causes this singular problem.

It has been shown that integrating the time domain Green function along matching surface or its waterline makes the problem weakly singular. In the following Chapter 5, a circular cylindrical matching surface with pseudo-spectral method based on Fourier-Laguerre appoximation is introduced.

5 Potential flow: Complementary waves with a vertical circular cylindrical matching surface

The velocity representation given in the previous section is formulated for an arbitrary matching surface and its waterline. The discretization of matching surface and waterline into panels and line segments causes numerical difficulties when the field point is located on the mean free surface, due to the singular behavior of the time domain Green function. Futhermore, discretization requires multiple summations with respect to panels, line segments and convolution integral. It needs also huge computation time and resources.

The matching surface does not necessarily need to be arbitrarily shaped. Even if the fluid velocity is possibly computed by discretized panels and line segments, it is numerically favorable to use an analytical shape as the matching surface. Applying the surface integral to the velocity representation over an analytic matching surface can reduce the computational cost and minimize the singular behavior.

The complementary waves which are generated by the body without forward speed propagate in all directions. In the far-field, the complementary waves can be approximated by Fourier series. Therefore, a vertical circular cylindrical matching surface, which has a radius larger than body dimension, is introduced in the present study. The body is located inside the matching surface. On the matching surface and its waterline, the fluid velocities and wave elvations are approximated into Fourier-Laguerre series.

5.1 A vertical circular cylindrical matching surface

The coordinates with cylindrical matching surface are depicted in figure 5.1. The field point $P = (r, \theta, z)$ is located at the outside of matching surface, $r > a, z < 0$. The source point $Q = (a, \theta', \zeta)$ is on the vertical circular cylindrical matching surface with radius of a. By the law of cosines, the distance between the source and field points (R) is given by

$$\begin{aligned} R^2 &= a^2 + r^2 - 2ar\cos(\theta - \theta'), \\ R &= 2a\sin\frac{|\theta - \theta'|}{2}, \qquad \text{if} \qquad r = a. \end{aligned} \tag{5.1}$$

A vector in cartesian coordinates is transformed into cylindrical coordinates using

$$\mathbf{f} = \begin{bmatrix} f^x \\ f^y \\ f^z \end{bmatrix} = \begin{bmatrix} \cos\theta & -a\sin\theta & 0 \\ \sin\theta & a\cos\theta & 0 \\ 0 & 0 & 1 \end{bmatrix} \begin{bmatrix} f^r \\ f^\theta \\ f^z \end{bmatrix} \tag{5.2}$$

where the superscript is a corresponding directional vector component.

The normal unit vector on the cylindrical matching surface is given by

$$\mathbf{n} = \cos\theta'\mathbf{e}_x + \sin\theta'\mathbf{e}_y + 0 \cdot \mathbf{e}_z = 1 \cdot \hat{\mathbf{e}}_r + 0 \cdot \hat{\mathbf{e}}_\theta + 0 \cdot \mathbf{e}_z \tag{5.3}$$

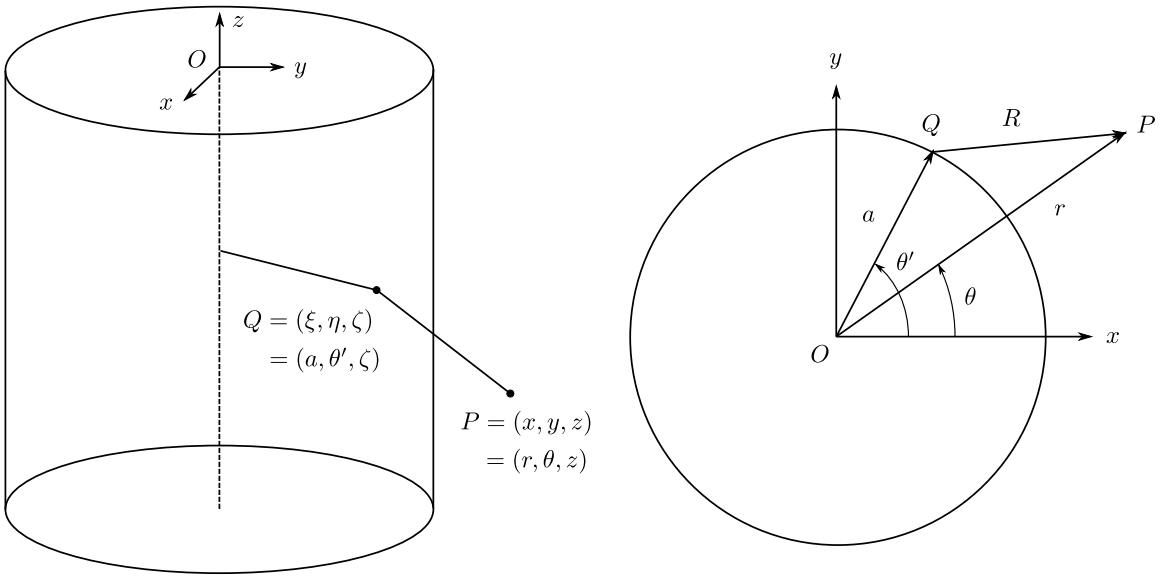

(a) 3D view **(b)** Bird's eye view

Figure 5.1. The coordinates with a vertical circular cylindrical matching surface

where $\hat{\mathbf{e}}_x$, $\hat{\mathbf{e}}_y$ and $\hat{\mathbf{e}}_z$ are unit basis vectors with respect to cartesian coordinates. $\hat{\mathbf{e}}_r$ and $\hat{\mathbf{e}}_\theta$ are unit basis vector with respect to cylindrical coordinates. The normal fluid velocity is given by

$$u_C^{\mathbf{n}} = \mathbf{u}_C \cdot \mathbf{n} = \cos\theta' u_C^\xi + \sin\theta' u_C^\eta, \tag{5.4}$$

and the tangential velocity is given by

$$\mathbf{w}_C = \mathbf{u}_C \times \mathbf{n} = w_C^\xi \mathbf{e}_x + w_C^\eta \mathbf{e}_y + w_C^\zeta \mathbf{e}_z, \tag{5.5}$$

with

$$w_C^\xi = -u_C^\zeta \sin\theta', \qquad w_C^\eta = u_C^\zeta \cos\theta', \qquad w_C^\zeta = u_C^\xi \sin\theta' - u_C^\eta \cos\theta'. \tag{5.6}$$

The gradients in cylindrical coordinates are defined by

$$\nabla_x f = f_r \hat{\mathbf{e}}_r + f_\theta \hat{\mathbf{e}}_\theta + f_z \mathbf{e}_z, \qquad \nabla_\xi f = f_a \hat{\mathbf{e}}_r + f_{\theta'} \hat{\mathbf{e}}_\theta + f_\zeta \mathbf{e}_z \tag{5.7}$$

with

$$(f_r, f_\theta, f_z) = \left(\frac{\partial f}{\partial r}, \frac{1}{r}\frac{\partial f}{\partial \theta}, \frac{\partial f}{\partial z}\right), \qquad (f_a, f_{\theta'}, f_\zeta) = \left(\frac{\partial f}{\partial a}, \frac{1}{a}\frac{\partial f}{\partial \theta'}, \frac{\partial f}{\partial \zeta}\right). \tag{5.8}$$

Applying coordinates transformation in equation (5.2), the derivatives of Green functions are given by

$$\mathcal{R}_\xi = \cos\theta' \mathcal{R}_a - \sin\theta' \mathcal{R}_{\theta'}, \qquad \mathcal{R}_\eta = \sin\theta' \mathcal{R}_a + \cos\theta' \mathcal{R}_{\theta'}, \tag{5.9}$$

$$\mathcal{R}^*_\xi = \cos\theta' \mathcal{R}^*_a - \sin\theta' \mathcal{R}^*_{\theta'}, \qquad \mathcal{R}^*_\eta = \sin\theta' \mathcal{R}^*_a + \cos\theta' \mathcal{R}^*_{\theta'}, \tag{5.10}$$

$$H_\xi = \cos\theta' H_a - \sin\theta' H_{\theta'}, \qquad H_\eta = \sin\theta' H_a + \cos\theta' H_{\theta'}, \tag{5.11}$$

$$F_\xi = \cos\theta' F_a - \sin\theta' F_{\theta'}, \qquad F_\eta = \sin\theta' F_a + \cos\theta' F_{\theta'}. \tag{5.12}$$

Substituting above relationships into velocity representation in equations (4.71), (4.72), (4.73) and (4.74) and applying surface integral along vertical circular cylindrical matching surface gives

$$\begin{bmatrix} u_C^x \\ u_C^y \\ u_C^z \end{bmatrix} = \begin{bmatrix} u_R^x + u_{R*}^x + u_H^x + u_F^x \\ u_R^y + u_{R*}^y + u_H^y + u_F^y \\ u_R^z + u_{R*}^z + u_H^z + u_F^z \end{bmatrix}, \tag{5.13}$$

where each of velocity components with vertical circular cylindrical matching surface is given by

- Rankine source contribution

$$\begin{bmatrix} u_R^x \\ u_R^y \\ u_R^z \end{bmatrix} = \int_{-\infty}^{0}\int_{0}^{2\pi} \begin{bmatrix} \mathcal{R}_a \cos\theta' u_C^{\mathbf{n}} - \mathcal{R}_{\theta'} \sin\theta' u_C^{\mathbf{n}} + \mathcal{R}_a \sin\theta' w_C^{\zeta} + \mathcal{R}_{\theta'} \cos\theta' w_C^{\zeta} - \mathcal{R}_\zeta w_C^{\eta} \\ \mathcal{R}_a \sin\theta' u_C^{\mathbf{n}} + \mathcal{R}_{\theta'} \cos\theta' u_C^{\mathbf{n}} - \mathcal{R}_a \cos\theta' w_C^{\zeta} + \mathcal{R}_{\theta'} \sin\theta' w_C^{\zeta} + \mathcal{R}_\zeta w_C^{\xi} \\ \mathcal{R}_\zeta u_C^{\mathbf{n}} + \mathcal{R}_a w_C^{\theta'} - \mathcal{R}_{\theta'} w_C^{a} \end{bmatrix} a d\theta' d\zeta \tag{5.14}$$

- Image source contribution

$$\begin{bmatrix} u_{R*}^x \\ u_{R*}^y \\ -u_{R*}^z \end{bmatrix} = \int_{-\infty}^{0}\int_{0}^{2\pi} \begin{bmatrix} \mathcal{R}_a^* \cos\theta' u_C^{\mathbf{n}} - \mathcal{R}_{\theta'}^* \sin\theta' u_C^{\mathbf{n}} + \mathcal{R}_a^* \sin\theta' w_C^{\zeta} + \mathcal{R}_{\theta'}^* \cos\theta' w_C^{\zeta} - \mathcal{R}_\zeta^* w_C^{\eta} \\ \mathcal{R}_a^* \sin\theta' u_C^{\mathbf{n}} + \mathcal{R}_{\theta'}^* \cos\theta' u_C^{\mathbf{n}} - \mathcal{R}_a^* \cos\theta' w_C^{\zeta} + \mathcal{R}_{\theta'}^* \sin\theta' w_C^{\zeta} + \mathcal{R}_\zeta^* w_C^{\xi} \\ \mathcal{R}_\zeta^* u_C^{\mathbf{n}} + \mathcal{R}_a^* w_C^{\theta'} - \mathcal{R}_{\theta'}^* w_C^{a} \end{bmatrix} a d\theta' d\zeta \tag{5.15}$$

- Harmonic contribution

$$\begin{bmatrix} u_H^x \\ u_H^y \\ -u_H^z \end{bmatrix} = -\int_{t_0}^{t}\int_{-\infty}^{0}\int_{0}^{2\pi} \begin{bmatrix} H_{\tau a} \cos\theta' u_C^{\mathbf{n}} - H_{\tau\theta'} \sin\theta' u_C^{\mathbf{n}} + H_{\tau a} \sin\theta' w_C^{\zeta} + H_{\tau\theta'} \cos\theta' w_C^{\zeta} - H_{\tau\zeta} w_C^{\eta} \\ H_{\tau a} \sin\theta' u_C^{\mathbf{n}} + H_{\tau\theta'} \cos\theta' u_C^{\mathbf{n}} - H_{\tau a} \cos\theta' w_C^{\zeta} + H_{\tau\theta'} \sin\theta' w_C^{\zeta} + H_{\tau\zeta} w_C^{\xi} \\ H_{\tau\zeta} u_C^{\mathbf{n}} + H_{\tau a} w_C^{\theta'} - H_{\tau\theta'} w_C^{a} \end{bmatrix} a d\theta' d\zeta d\tau \tag{5.16}$$

- Free surface contribution

$$\begin{bmatrix} u_F^x \\ u_F^y \\ u_F^z \end{bmatrix} = -\int_{t_0}^{t}\int_{0}^{2\pi} \begin{bmatrix} F_\zeta \cos\theta' (g\Xi_C) \\ F_\zeta \sin\theta' (g\Xi_C) \\ F_a (g\Xi_C) \end{bmatrix} a d\theta' d\tau \tag{5.17}$$

with

$$w_C^a = w_C^{\xi} \cos\theta' - w_C^{\eta} \sin\theta', \tag{5.18}$$

$$w_C^{\theta'} = \frac{1}{a}\left(w_C^{\xi} \sin\theta' + w_C^{\eta} \cos\theta' \right). \tag{5.19}$$

5.2 Fourier-Laguerre and Fourier approximations

5.2.1 Fourier-Laguerre approximation of fluid velocity

Fluid velocities at field point and matching surface are expanded with Fourier-Laguerre series by

$$\begin{bmatrix} u_C^x \\ u_C^y \\ u_C^z \end{bmatrix} \approx \sum_{q=-N}^{N}\sum_{q=0}^{M} \begin{bmatrix} \mathcal{U}_{pq}^x \\ \mathcal{U}_{pq}^y \\ \mathcal{U}_{pq}^z \end{bmatrix} e^{\mathrm{i}q\theta} \mathcal{L}_p(-sz), \tag{5.20}$$

and

$$\begin{bmatrix} u_C^{\mathbf{n}} \\ w_C^{\xi} \\ w_C^{\eta} \\ w_C^{\zeta} \end{bmatrix}_{r=a} \approx \sum_{n=-N}^{N} \sum_{m=0}^{M} \begin{bmatrix} \mathcal{C}_{mn}^{\mathbf{n}} \\ \mathcal{W}_{mn}^{\xi} \\ \mathcal{W}_{mn}^{\eta} \\ \mathcal{W}_{mn}^{\zeta} \end{bmatrix} \mathcal{L}_m\left(-s\zeta\right) e^{in\theta'}. \tag{5.21}$$

where $\mathcal{U}$,$\mathcal{C}$ and $\mathcal{W}$ are Fourier-Laguerre coefficients for fluid velocity at field point, normal and tangential velocities at matching surface, respectively. The series expansion are truncated with the number of Fourier modes, N, and Laguerre modes, M. $\mathcal{L}_m(-s\zeta)$ is Laguerre function defined by

$$\mathcal{L}_m(-s\zeta) = e^{\frac{s}{2}\zeta} L_m(-s\zeta), \tag{5.22}$$

where $L_m(-s\zeta)$ is Laguerre polynomial

$$L_m(x) = \frac{e^x}{m!}\frac{d^m}{dx^m}\left(e^{-x}x^m\right) = \frac{1}{m!}\left(\frac{d}{dx} - 1\right)^m x^m, \tag{5.23}$$

where s is an user-defined parameter. The Laguerre functions for different m are depicted in figure 5.2.

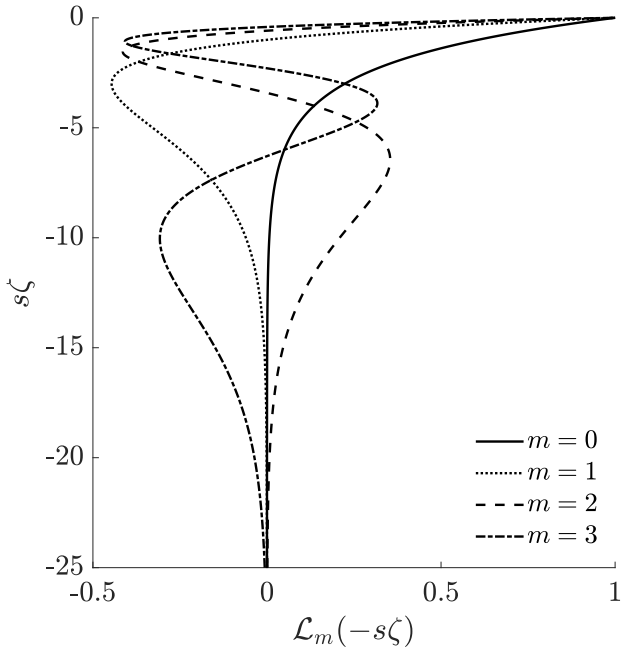

Figure 5.2. Laguerre functions $\mathcal{L}_m(-s\zeta)$.

The Laguerre function for $m = 0$ reduces to an exponential function

$$\mathcal{L}_0(-s\zeta) = e^{\frac{s}{2}\zeta}. \tag{5.24}$$

The user-defined parameter s is selected to be two times the representative wave number ($s = 2k_0$) for a good approximation. For regular waves, the representative wave number is easily selected with $k_0 = \omega^2/g$. In the case of irregular waves, the representative wave number is taken from the wave number of peak wave periods ($k_0 = k_p$).

The orthogonalities of Laguerre functions and Fourier series are given as

$$\int_{-\infty}^{0} \mathcal{L}_m(-s\zeta)\mathcal{L}_p(-s\zeta)d\zeta = \frac{1}{s}\delta_{mp}, \tag{5.25}$$

and

$$\int_{0}^{2\pi} e^{\mathrm{i}(n-l)\theta} d\theta d\theta = 2\pi\delta_{nl}, \tag{5.26}$$

where δ_{mn} is a Kronecker delta given by

$$\delta_{mn} = \begin{cases} 1 & m = n \\ 0 & m \neq n \end{cases}. \tag{5.27}$$

In a previous research, Hamilton and Yeung (2011) applied Fourier-Chebyshev series on the velocity potential for finite water depth problems, while Liang and Chen (2017); Liang et al. (2018) applied Fourier-Laguerre series for deep water cases.

To evaluate the Fourier-Laguerre coefficients, the surface integral with Fourier-Laguerre function is applied to equation (5.21) as

$$\begin{aligned} &\int_{-\infty}^{0}\int_{0}^{2\pi} \begin{bmatrix} u_C^{\mathbf{n}} \\ w_C^{\xi} \\ w_C^{\eta} \\ w_C^{\zeta} \end{bmatrix}_{r=a} L_p(-s\zeta)e^{-il\theta'} a d\zeta d\theta' \\ &\qquad = \int_{-\infty}^{0}\int_{0}^{2\pi} \sum_{n=-N}^{N}\sum_{m=0}^{M} \begin{bmatrix} \mathcal{C}_{mn}^{\mathbf{n}} \\ \mathcal{W}_{mn}^{\xi} \\ \mathcal{W}_{mn}^{\eta} \\ \mathcal{W}_{mn}^{\zeta} \end{bmatrix} \mathcal{L}_m(-s\zeta)\, L_p(-s\zeta)e^{i(n-l)\theta'} a d\zeta d\theta' \end{aligned} \tag{5.28}$$

The orthogonalities given in equations (5.25) and (5.26) are applied to evaluate the coefficients used for approximation as

$$\begin{bmatrix} \mathcal{C}_{mn}^{\mathbf{n}} \\ \mathcal{W}_{mn}^{\xi} \\ \mathcal{W}_{mn}^{\eta} \\ \mathcal{W}_{mn}^{\zeta} \end{bmatrix} = \frac{s}{2\pi}\int_{0}^{2\pi}\int_{-\infty}^{0} \begin{bmatrix} u_C^{\mathbf{n}} \\ w_C^{\xi} \\ w_C^{\eta} \\ w_C^{\zeta} \end{bmatrix}_{r=a} \mathcal{L}_m(-s\zeta)\, e^{-in\theta'} d\zeta d\theta'. \tag{5.29}$$

5.2.2 Fourier approximation of wave elevation

The wave elevation on the waterline is approximated by Fourier series with Fourier coefficient $\mathcal{E}_n$

$$[g\Xi_C]_{r=a} \approx \sum_{n=-N}^{N} \mathcal{E}_n e^{in\theta'}. \tag{5.30}$$

Fourier coefficients for wave elevation are calculated by applying an integral over waterline to (5.30) by

$$\int_{0}^{2\pi} [g\Xi_C]_{r=a}\, e^{-il\theta'} a d\theta' \approx \int_{0}^{2\pi} \sum_{n=-N}^{N} \mathcal{E}_n e^{i(n-l)\theta'} a d\theta'. \tag{5.31}$$

Using the orthogonality given in equation (5.26)

$$\mathcal{E}_n = \frac{1}{2\pi}\int_0^{2\pi} [g\Xi_C]_{r=a}\, e^{-in\theta'} d\theta'. \tag{5.32}$$

5.3 Elementary functions

5.3.1 The elementary functions for the circular cylindrical matching surface integral

Right-hand-sides of velocity representation given in equations (5.14), (5.15) and (5.16) are given by surface integral on the flow quantities with Green function. The harmonic velocity contribution are expressed with multiple integrals including the convolution and surface integrals on the flow component over the matching surface with Green function as

$$f(r,\theta,z,t) = \int_{t_0}^{t}\int_0^{2\pi}\int_{-\infty}^{0} f(a,\theta',\zeta,\tau) G(\mathbf{x},\boldsymbol{\xi},t-\tau) a d\zeta d\theta' d\tau, \tag{5.33}$$

where $f(r,\theta,z)$ is the flow component at field point, $f(a,\theta',\zeta)$ is the flow component at the matching surface. Fourier-Laguerre expansions on flow components are given by

$$f(r,\theta,z,t) = \sum_{q=-\infty}^{\infty}\sum_{p=0}^{\infty} C_{pq}(r,t) e^{\mathrm{i}q\theta} \mathcal{L}_p(-sz), \tag{5.34}$$

$$f(a,\theta',\zeta,\tau) = \sum_{n=-\infty}^{\infty}\sum_{m=0}^{\infty} C_{mn}(a,\tau) e^{\mathrm{i}n\theta'} \mathcal{L}_m(-s\zeta). \tag{5.35}$$

Substituting equations (5.34) and (5.35) into equation (5.33)

$$\begin{aligned}\sum_{q=-\infty}^{\infty}\sum_{p=0}^{\infty} C_{pq}(r,t) e^{\mathrm{i}q\theta} \mathcal{L}_p(-sz) = \sum_{n=-\infty}^{\infty}\sum_{m=0}^{\infty}\int_{t_0}^{t} C_{mn}(a,\tau) \\ \times \int_0^{2\pi}\int_{-\infty}^{0} e^{\mathrm{i}n\theta'} \mathcal{L}_m(-s\zeta) G(\mathbf{x},\boldsymbol{\xi},t-\tau) a d\zeta d\theta' d\tau,\end{aligned} \tag{5.36}$$

Multiplying by $e^{-iq'\theta} L_{p'}(-sz)$ and integrating with respect to θ' from 0 to 2π and z from $-\infty$ to 0

$$\begin{aligned}\int_0^{2\pi}\int_{-\infty}^{0}\sum_{q=-\infty}^{\infty}\sum_{p=0}^{\infty} C_{pq}(r,t) e^{\mathrm{i}(q-q')\theta} \mathcal{L}_p(-sz) L_{p'}(-sz) dz d\theta = \sum_{n=-\infty}^{\infty}\sum_{m=0}^{\infty}\int_{t_0}^{t} C_{mn}(a,\tau) \\ \times \int_0^{2\pi}\int_{-\infty}^{0}\int_0^{2\pi}\int_{-\infty}^{0} e^{\mathrm{i}(n\theta'-q'\theta)} \mathcal{L}_m(-s\zeta) L_{p'}(-sz) G(\mathbf{x},\boldsymbol{\xi},t-\tau) a d\zeta d\theta' dz d\theta d\tau.\end{aligned} \tag{5.37}$$

Using the orthogonalities in equations (5.25) and (5.26), the Fourier-Laguerre coefficient at the field point is explicitly given by

$$\begin{aligned}C_{pq}(r,t) = \frac{as}{2\pi}\sum_{n=-\infty}^{\infty}\int_{t_0}^{t} C_{mn}(a,\tau) \\ \times \int_0^{2\pi}\int_0^{2\pi}\int_{-\infty}^{0}\int_{-\infty}^{0} e^{\mathrm{i}n\theta'} e^{-\mathrm{i}q\theta} \mathcal{L}_m(-s\zeta) \mathcal{L}_p(-sz) G(\mathbf{x},\boldsymbol{\xi},t-\tau) d\zeta dz d\theta' d\theta d\tau.\end{aligned} \tag{5.38}$$

In the previous section, it is shown that the time domain Green function can be expressed with Fourier series. The Green function in Fourier series is given by

$$G(r,\theta,z,a,\theta',\zeta,t-\tau)=\sum_{l=-\infty}^{\infty}e^{\mathrm{i}l(\theta-\theta')}G_l(r,z,a,\zeta,t-\tau), \tag{5.39}$$

where $G_l(r,z,a,\zeta,t-\tau)$ are the Fourier components of Green function. Substituting above expression into (5.38) and applying orthogonalitygiven in equation (5.26), we obtain

$$C_{pn}(r,t)=\sum_{n=-\infty}^{\infty}\int_{t_0}^{t}C^a_{mn}(a,\tau)\mathcal{S}_{n,mp}(r,a,t-\tau)d\tau, \tag{5.40}$$

where $\mathcal{S}_{n,mp}(r,a,t-\tau)$ are the surface elementary functions

$$\mathcal{S}_{n,mp}(r,a,t-\tau)=2\pi as\int_{-\infty}^{0}\int_{-\infty}^{0}\mathcal{L}_m(-s\zeta)\mathcal{L}_p(-sz)G_n(r,z,a,\zeta,t-\tau)d\zeta dz. \tag{5.41}$$

5.3.2 The elementary functions for the circular waterline integral

The right-hand-sides of equation (5.17) are given by a waterline integral on a flow quantities associated with the Green function. The flow component at the field point is expressed as

$$g(a,\theta,z,t)=\int_{t_0}^{t}\int_{0}^{2\pi}g(a,\theta',\zeta=0,\tau)G(\mathbf{x},\boldsymbol{\xi};t-\tau)ad\theta'd\tau, \tag{5.42}$$

where $g(a,\theta,z;t)$ is the flow component at the field point, $g(a,\theta',0;\tau)$ is the flow component on the waterline of matching surface. Fourier-Laguerre and Fourier expansions on $g(a,\theta,z;t)$ and $g(a,\theta',0;\tau)$ are given by

$$g(a,\theta,z,t)=\sum_{q=-\infty}^{\infty}\sum_{p=0}^{\infty}D_{pq}(r,t)e^{\mathrm{i}q\theta}\mathcal{L}_p(-sz), \tag{5.43}$$

$$g(a,\theta',\zeta=0,\tau)=\sum_{n=-\infty}^{\infty}D_n(a,\tau)e^{\mathrm{i}n\theta'}, \tag{5.44}$$

Substituting these two expansions into equation (5.42)

$$\sum_{q=-\infty}^{\infty}\sum_{p=0}^{\infty}D^r_{pq}e^{\mathrm{i}q\theta}\mathcal{L}_p(-sz)=\sum_{n=-\infty}^{\infty}\int_{t_0}^{t}D_n(\tau)\int_{0}^{2\pi}e^{\mathrm{i}n\theta'}G(\mathbf{x},\boldsymbol{\xi};t-\tau)ad\theta'd\tau, \tag{5.45}$$

Multiplying $e^{-iq'\theta}L_{p'}(-sz)$ and integrating with respect to θ from 0 to 2π and z from $-\infty$ to 0

$$\begin{aligned}\int_0^{2\pi}\int_{-\infty}^{0}\sum_{q=-\infty}^{\infty}\sum_{p=0}^{\infty}D_{pq}(r,t)e^{\mathrm{i}(q-q')\theta}\mathcal{L}_p(-sz)L_{p'}(-sz)d\theta dz=\sum_{n=-\infty}^{\infty}\int_{t_0}^{t}D_n(a,\tau)\\ \times\int_0^{2\pi}\int_{-\infty}^{0}\int_0^{2\pi}e^{\mathrm{i}(n\theta'-q'\theta)}L_{p'}(-sz)G(\mathbf{x},\boldsymbol{\xi};t-\tau)ad\theta' dzd\theta d\tau,\end{aligned} \tag{5.46}$$

Using the orthogonal relationships given in equations (5.25) and (5.26), the Fourier-Laguerre coefficient at field point is given by

$$D_{pq}(r,t)=\frac{as}{2\pi}\sum_{n=-\infty}^{\infty}\int_{t_0}^{t}D_n(a,\tau)\int_0^{2\pi}\int_0^{2\pi}\int_{-\infty}^{0}e^{\mathrm{i}n\theta'}e^{-\mathrm{i}q\theta}\mathcal{L}_p(-sz)G(\mathbf{x},\boldsymbol{\xi};t-\tau)dzd\theta' d\theta d\tau. \tag{5.47}$$

Substituting the Green function given by Fourier-series in equation (5.39) into the above equation, we obtain

$$D_{pn}(r,t) = \sum_{n=-\infty}^{\infty} \int_{t_0}^{t} D_n(a,\tau)\mathcal{F}_{n,p}(r,a,t-\tau)d\tau, \tag{5.48}$$

where $\mathcal{F}_{n,p}(r,a,t-\tau)$ are the waterline elementary functions

$$\mathcal{F}_{n,p}(r,a,t-\tau) = 2\pi as \int_{-\infty}^{0} \mathcal{L}_p(-sz)G_n(r,z,a,\zeta=0,t-\tau)dz. \tag{5.49}$$

5.4 Elementary functions for the time domain Green function

5.4.1 Green function in circular cylindrical coordinates

The source and image source are expressed with Bessel function integrals as

$$\begin{aligned}
\mathcal{R}(\mathbf{x},\boldsymbol{\xi}) &= \frac{1}{r_1} = \frac{1}{\sqrt{R^2+(z-\zeta)^2}} = \int_0^\infty e^{-k|z-\zeta|}J_0(kR)dk, \\
\mathcal{R}^*(\mathbf{x},\boldsymbol{\xi}) &= -\frac{1}{r_2} = -\frac{1}{\sqrt{R^2+(z+\zeta)^2}} = -\int_0^\infty e^{k(z+\zeta)}J_0(kR)dk.
\end{aligned} \tag{5.50}$$

Applying Graf's addition theorem on Bessel function

$$J_0(kR) = \sum_{l=-\infty}^{\infty} J_l(kr)J_l(ka)e^{\mathrm{i}l(\theta-\theta')}, \tag{5.51}$$

Therefore, source and image source can be expressed by Fourier series

$$\mathcal{R}(\mathbf{x},\boldsymbol{\xi}) = \sum_{l=-\infty}^{\infty} e^{\mathrm{i}l(\theta-\theta')}\mathcal{R}_l(r,z,a,\zeta), \tag{5.52}$$

$$\mathcal{R}^*(\mathbf{x},\boldsymbol{\xi}) = \sum_{l=-\infty}^{\infty} e^{\mathrm{i}l(\theta-\theta')}\mathcal{R}_l^*(r,z,a,\zeta). \tag{5.53}$$

with their Fourier components

$$\mathcal{R}_l(r,z,a,\zeta) = \int_0^\infty e^{-k|z-\zeta|}J_l(kr)J_l(ka)dk, \tag{5.54}$$

$$\mathcal{R}_l^*(r,z,a,\zeta) = -\int_0^\infty e^{k(z+\zeta)}J_l(kr)J_l(ka)dk. \tag{5.55}$$

The wave terms in Fourier series are given by

$$\begin{aligned}
H(\mathbf{x},\boldsymbol{\xi},t-\tau) &= 2\int_0^\infty e^{k(z+\zeta)}J_0(kR)\left\{1-\cos\left(\sqrt{gk}(t-\tau)\right)\right\}dk \\
&= \sum_{l=-\infty}^{\infty} e^{\mathrm{i}l(\theta-\theta')}H_l(r,z,a,\zeta,t-\tau),
\end{aligned} \tag{5.56}$$

$$\begin{aligned}
F(\mathbf{x},\boldsymbol{\xi},t-\tau) &= -2\int_0^\infty e^{k(z+\zeta)}J_0(kR)\left\{\cos\left(\sqrt{gk}(t-\tau)\right)\right\}dk \\
&= \sum_{l=-\infty}^{\infty} e^{\mathrm{i}l(\theta-\theta')}F_l(r,z,a,\zeta,t-\tau),
\end{aligned} \tag{5.57}$$

where

$$H_l(r,z,a,\zeta,t-\tau) = 2\int_0^\infty e^{k(z+\zeta)}J_l(kr)J_l(ka)\left\{1-\cos\left(\sqrt{gk}(t-\tau)\right)\right\}dk, \tag{5.58}$$

$$F_l(r,z,a,\zeta,t-\tau) = -2\int_0^\infty e^{k(z+\zeta)}J_l(kr)J_l(ka)\left\{\cos\left(\sqrt{gk}(t-\tau)\right)\right\}dk. \tag{5.59}$$

5.4.2 Surface elementary functions for the source

Fourier-series expansion of the source is given in equation (5.52) as:

$$\mathcal{R}(r,a,\theta,\theta',z,\zeta) = \sum_{l=-\infty}^{\infty} e^{\mathrm{i}l(\theta-\theta')}\mathcal{R}_l(r,a,z,\zeta),$$

with its Fourier components

$$\mathcal{R}_l(r,a,z,\zeta) = \int_0^\infty e^{-k|z-\zeta|}J_l(kr)J_l(ka)dk.$$

Spatial derivatives of the source can be expressed with Fourier-series as

$$\nabla_\xi\mathcal{R}(r,a,\theta,\theta',z,\zeta) = \sum_{l=-\infty}^{\infty} e^{\mathrm{i}l(\theta-\theta')}\left(\mathcal{R}_{a,l}\hat{\mathbf{e}}_r + \mathcal{R}_{\theta',l}\hat{\mathbf{e}}_\theta + \mathcal{R}_{\zeta,l}\mathbf{e}_z\right), \tag{5.60}$$

where vector components are given by

$$\mathcal{R}_{a,l} = \int_0^\infty ke^{-k|z-\zeta|}J_l(kr)J_l'(ka)dk, \tag{5.61}$$

$$\mathcal{R}_{\theta',l} = -\frac{\mathrm{i}l}{a}\int_0^\infty e^{-k|z-\zeta|}J_l(kr)J_l(ka)dk, \tag{5.62}$$

$$\mathcal{R}_{\zeta,l} = \int_0^\infty \frac{\partial}{\partial\zeta}\left(e^{-k|z-\zeta|}\right)J_l(kr)J_l(ka)dk = \int_0^\infty \frac{z-\zeta}{|\zeta-z|}ke^{-k|z-\zeta|}J_l(kr)J_l(ka)dk. \tag{5.63}$$

Substituting the Fourier components into equation (5.41), the surface elementary functions for derivatives of source are given by

$$\begin{aligned}\mathcal{S}^R_{a,n,mp}(s;r,a) &= 2\pi as\int_{-\infty}^0\int_{-\infty}^0 \mathcal{L}_m(-s\zeta)\mathcal{L}_p(-sz)\mathcal{R}_{a,n}(r,z,a,\zeta)d\zeta dz\\ &= 2\pi a\int_0^\infty k\mathcal{Z}^{(1)}_{mp}(s;k)J_n(kr)J_n'(ka)dk,\end{aligned} \tag{5.64}$$

$$\begin{aligned}\mathcal{S}^R_{\theta',n,mp}(s;r,a) &= 2\pi as\int_{-\infty}^0\int_{-\infty}^0 \mathcal{L}_m(-s\zeta)\mathcal{L}_p(-sz)\mathcal{R}_{\theta',n}(r,z,a,\zeta)d\zeta dz\\ &= -2\pi n\mathrm{i}\int_0^\infty \mathcal{Z}^{(1)}_{mp}(s;k)J_n(kr)J_n(ka)dk,\end{aligned} \tag{5.65}$$

$$\begin{aligned}\mathcal{S}^R_{\zeta,n,mp}(s;r,a) &= 2\pi as\int_{-\infty}^0\int_{-\infty}^0 \mathcal{L}_m(-s\zeta)\mathcal{L}_p(-sz)\mathcal{R}_{\zeta,n}(r,z,a,\zeta)d\zeta dz\\ &= 2\pi a\int_0^\infty k\mathcal{Z}^{(2)}_{mp}(s;k)J_n(kr)J_n(ka)dk,\end{aligned} \tag{5.66}$$

where $\mathcal{Z}^{(1)}_{mp}(s;k)$ and $\mathcal{Z}^{(2)}_{mp}(s;k)$ are defined here by the vertical integral functions of first and second kind

$$\mathcal{Z}^{(1)}_{mp}(s;k) = s\int_{-\infty}^{0}\int_{-\infty}^{0} e^{-k|z-\zeta|}\mathcal{L}_m(-s\zeta)\mathcal{L}_p(-sz)d\zeta dz, \tag{5.67}$$

$$\mathcal{Z}^{(2)}_{mp}(s;k) = s\int_{-\infty}^{0}\int_{-\infty}^{0} \frac{z-\zeta}{|\zeta-z|}e^{-k|z-\zeta|}\mathcal{L}_m(-s\zeta)\mathcal{L}_p(-sz)d\zeta dz, \tag{5.68}$$

respectively.

5.4.3 Surface elementary functions for the image source

Fourier-series expansion of the image sources is given in equation (5.53) as

$$\mathcal{R}^*(r,a,\theta,\theta',z,\zeta) = \sum_{l=-\infty}^{\infty} e^{\mathrm{i}l(\theta-\theta')}\mathcal{R}^*_l(r,a,z,\zeta)$$

with its Fourier components

$$\mathcal{R}^*_l(r,a,z,\zeta) = -\int_0^{\infty} e^{k(z+\zeta)}J_l(kr)J_l(ka)dk.$$

Fourier series expansion of the spatial derivatives of the image sources is given by

$$\nabla_\xi\mathcal{R}^*(r,a,\theta,\theta',z,\zeta) = \sum_{l=-\infty}^{\infty} e^{\mathrm{i}l(\theta-\theta')}\left(\mathcal{R}^*_{a,l}\hat{\mathbf{e}}_r + \mathcal{R}^*_{\theta',l}\hat{\mathbf{e}}_\theta + \mathcal{R}^*_{\zeta,l}\mathbf{e}_z\right), \tag{5.69}$$

where vector components are given by

$$\mathcal{R}^*_{a,l} = -\int_0^{\infty} ke^{k(z+\zeta)}J_l(kr)J'_l(ka)dk, \tag{5.70}$$

$$\mathcal{R}^*_{\theta',l} = \frac{\mathrm{i}l}{a}\int_0^{\infty} e^{k(z+\zeta)}J_l(kr)J_l(ka)dk, \tag{5.71}$$

$$\mathcal{R}^*_{\zeta,l} = -\int_0^{\infty} ke^{k(z+\zeta)}J_l(kr)J_l(ka)dk. \tag{5.72}$$

Substituting the Fourier components into equation (5.41), the surface elementary functions for spatial derivatives of the image source are given by

$$\begin{aligned}\mathcal{S}^{R*}_{a,n,mp}(s;r,a) &= 2\pi as\int_{-\infty}^{0}\int_{-\infty}^{0}\mathcal{L}_m(-s\zeta)\mathcal{L}_p(-sz)\mathcal{R}^*_{a,n}(r,z,a,\zeta)d\zeta dz\\ &= -2\pi a\int_0^{\infty} k\mathcal{Z}^{(3)}_{mp}(s;k)J_n(kr)J'_n(ka)dk,\end{aligned} \tag{5.73}$$

$$\begin{aligned}\mathcal{S}^{R*}_{\theta',n,mp}(s;r,a) &= 2\pi as\int_{-\infty}^{0}\int_{-\infty}^{0}\mathcal{L}_m(-s\zeta)\mathcal{L}_p(-sz)\mathcal{R}^*_{\theta',n}(r,z,a,\zeta)d\zeta dz\\ &= 2\pi n\mathrm{i}\int_0^{\infty}\mathcal{Z}^{(3)}_{mp}(s;k)J_n(kr)J_n(ka)dk,\end{aligned} \tag{5.74}$$

$$\begin{aligned}\mathcal{S}^{R*}_{\zeta,n,mp}(s;r,a) &= 2\pi as\int_{-\infty}^{0}\int_{-\infty}^{0}\mathcal{L}_m(-s\zeta)\mathcal{L}_p(-sz)\mathcal{R}^*_{\zeta,n}(r,z,a,\zeta)d\zeta dz\\ &= -2\pi a\int_0^{\infty} k\mathcal{Z}^{(3)}_{mp}(s;k)J_n(kr)J_n(ka)dk,\end{aligned} \tag{5.75}$$

where $\mathcal{Z}^{(3)}_{mp}(s;k)$ are defined as the vertical integral functions of third kind

$$\mathcal{Z}^{(3)}_{mp}(s;k) = s\int_{-\infty}^{0}\int_{-\infty}^{0} e^{k(z+\zeta)}\mathcal{L}_m(-s\zeta)\mathcal{L}_p(-sz)d\zeta dz. \tag{5.76}$$

5.4.4 Surface elementary functions for the harmonic component

The time derivative of wave term in the Green function expanded with Fourier series is given in equation (5.56) as

$$H_\tau(r,a,\theta,\theta',z,\zeta,t) = \sum_{l=-\infty}^{\infty} e^{\mathrm{i}l(\theta-\theta')}H_{\tau l}(r,a,z,\zeta,t), \tag{5.77}$$

and its Fourier components

$$H_{\tau l}(r,a,z,\zeta,t) = 2\sqrt{g}\int_0^\infty k^{\frac{1}{2}}e^{k(z+\zeta)}J_l(kr)J_l(ka)\sin(\sqrt{gk}t)dk. \tag{5.78}$$

Spatial derivatives of wave term in Green function can be expressed with Fourier series

$$\nabla_\xi H_\tau = \sum_{l=-\infty}^{\infty} e^{\mathrm{i}l(\theta-\theta')}\left(H_{\tau a,l}\hat{\mathbf{e}}_r + H_{\tau\theta',l}\hat{\mathbf{e}}_\theta + H_{\tau\zeta,l}\mathbf{e}_z\right), \tag{5.79}$$

with

$$H_{\tau a,l} = 2\sqrt{g}\int_0^\infty k^{\frac{3}{2}}e^{k(z+\zeta)}J_l(kr)J_l'(ka)\sin(\sqrt{gk}t)dk, \tag{5.80}$$

$$H_{\tau\theta',l} = -2\sqrt{g}\frac{\mathrm{i}l}{a}\int_0^\infty k^{\frac{1}{2}}e^{k(z+\zeta)}J_l(kr)J_l(ka)\sin(\sqrt{gk}t)dk, \tag{5.81}$$

$$H_{\tau\zeta,l} = 2\sqrt{g}\int_0^\infty k^{\frac{3}{2}}e^{k(z+\zeta)}J_l(kr)J_l(ka)\sin(\sqrt{gk}t)dk. \tag{5.82}$$

Substituting the Fourier components into equation (5.41), the surface elementary functions for derivatives of the harmonic term are given by

$$\begin{aligned}\mathcal{S}^H_{a,n,mp}(s;r,a,t) &= 2\pi as\int_{-\infty}^{0}\int_{-\infty}^{0}\mathcal{L}_m(-s\zeta)\mathcal{L}_p(-sz)H_{\tau a,n}(r,z,a,\zeta)d\zeta dz\\ &= 4\pi a\sqrt{g}\int_0^\infty k^{\frac{3}{2}}\mathcal{Z}^{(3)}_{mp}(s;k)J_n(kr)J_n'(ka)\sin(\sqrt{gk}t)dk,\end{aligned} \tag{5.83}$$

$$\begin{aligned}\mathcal{S}^H_{\theta',n,mp}(s;r,a,t) &= 2\pi as\int_{-\infty}^{0}\int_{-\infty}^{0}\mathcal{L}_m(-s\zeta)\mathcal{L}_p(-sz)H_{\tau\theta',n}(r,z,a,\zeta)d\zeta dz\\ &= -4\pi n\mathrm{i}\sqrt{g}\int_0^\infty k^{\frac{1}{2}}\mathcal{Z}^{(3)}_{mp}(s;k)J_n(kr)J_n(ka)\sin(\sqrt{gk}t)dk,\end{aligned} \tag{5.84}$$

$$\begin{aligned}\mathcal{S}^H_{\zeta,n,mp}(s;r,a,t) &= 2\pi as\int_{-\infty}^{0}\int_{-\infty}^{0}\mathcal{L}_m(-s\zeta)\mathcal{L}_p(-sz)H_{\tau\zeta,n}(r,z,a,\zeta)d\zeta dz\\ &= 4\pi a\sqrt{g}\int_0^\infty k^{\frac{3}{2}}\mathcal{Z}^{(3)}_{mp}(s;k)J_n(kr)J_n(ka)\sin(\sqrt{gk}t)dk.\end{aligned} \tag{5.85}$$

5.4.5 Waterline elementary functions

The wave term F in Fourier series is given in equation (5.57) as

$$F(r,a,\theta,\theta',z,\zeta,t)=\sum_{l=-\infty}^{\infty}e^{\mathrm{i}l(\theta-\theta')}F_l(r,a,z,\zeta,t)$$

with its Fourier components

$$F_l(r,a,z,\zeta,t)=-2\int_0^{\infty}e^{k(z+\zeta)}J_l(kr)J_l(ka)\cos(\sqrt{gk}t)dk.$$

Spatial derivatives of the wave term can be expressed with Fourier series

$$\nabla_\xi F=\sum_{l=-\infty}^{\infty}e^{\mathrm{i}l(\theta-\theta')}\left(F_{a,l}\hat{\mathbf{e}}_r+F_{\theta',l}\hat{\mathbf{e}}_\theta+F_{\zeta,l}\mathbf{e}_z\right), \tag{5.86}$$

where its Fourier components are given by

$$F_{a,l}=-2\int_0^{\infty}ke^{k(z+\zeta)}J_l(kr)J_l'(ka)\cos(\sqrt{gk}t)dk, \tag{5.87}$$

$$F_{\theta',l}=\frac{2\mathrm{i}l}{a}\int_0^{\infty}e^{k(z+\zeta)}J_l(kr)J_l(ka)\cos(\sqrt{gk}t)dk, \tag{5.88}$$

$$F_{\zeta,l}=-2\int_0^{\infty}ke^{k(z+\zeta)}J_l(kr)J_l(ka)\cos(\sqrt{gk}t)dk. \tag{5.89}$$

Substituting above Fourier components into equation (5.49), the waterline elementary functions for derivatives of the wave term are given by

$$\begin{aligned}\mathcal{F}^F_{a,n,p}(s;r,a,t)&=2\pi as\int_{-\infty}^{0}\mathcal{L}_p(-sz)F_{a,n}(r,z,a,\zeta=0,t-\tau)dz\\&=-4\pi a\int_0^{\infty}k\mathcal{Z}_p^{(4)}(s;k)J_n(kr)J_n'(ka)\cos(\sqrt{gk}t)dk,\end{aligned} \tag{5.90}$$

$$\begin{aligned}\mathcal{F}^F_{\theta',n,p}(s;r,a,t)&=2\pi as\int_{-\infty}^{0}\mathcal{L}_p(-sz)F_{\theta',n}(r,z,a,\zeta=0,t-\tau)dz\\&=4\pi n\mathrm{i}\int_0^{\infty}\mathcal{Z}_p^{(4)}(s;k)J_n(kr)J_n(ka)\cos(\sqrt{gk}t)dk,\end{aligned} \tag{5.91}$$

$$\begin{aligned}\mathcal{F}^F_{\zeta,n,p}(s;r,a,t)&=2\pi as\int_{-\infty}^{0}\mathcal{L}_p(-sz)F_{\zeta,n}(r,z,a,\zeta=0,t-\tau)dz\\&=-4\pi a\int_0^{\infty}k\mathcal{Z}_p^{(4)}(s;k)J_n(kr)J_n(ka)\cos(\sqrt{gk}t)dk,\end{aligned} \tag{5.92}$$

where $\mathcal{Z}_p^{(4)}(s;k)$ are the vertical integral function of the fourth kind defined by

$$\mathcal{Z}_p^{(4)}(s;k)=s\int_{-\infty}^{0}e^{kz}\mathcal{L}_p(-sz)dz. \tag{5.93}$$

5.4.6 The vertical integral functions

The vertical integral functions are defined in equations (5.67), (5.68), (5.76) and (5.93) as

$$\mathcal{Z}^{(1)}_{mp}(s;k) = s\int_{-\infty}^{0}\int_{-\infty}^{0} e^{-k|z-\zeta|}\mathcal{L}_m(-s\zeta)\mathcal{L}_p(-sz)d\zeta dz,$$
$$\mathcal{Z}^{(2)}_{mp}(s;k) = s\int_{-\infty}^{0}\int_{-\infty}^{0} \frac{z-\zeta}{|\zeta-z|}e^{-k|z-\zeta|}\mathcal{L}_m(-s\zeta)\mathcal{L}_p(-sz)d\zeta dz,$$
$$\mathcal{Z}^{(3)}_{mp}(s;k) = s\int_{-\infty}^{0}\int_{-\infty}^{0} e^{k(z+\zeta)}\mathcal{L}_m(-s\zeta)\mathcal{L}_p(-sz)d\zeta dz,$$
$$\mathcal{Z}^{(4)}_{p}(s;k) = s\int_{-\infty}^{0} e^{kz}\mathcal{L}_p(-sz)dz.$$

The vertical integral functions of the first and second kind can be decomposed into two sub-integrals as

$$\mathcal{Z}^{(1)}_{mp}(s;k) = s\int_{-\infty}^{0}\int_{z}^{0} e^{k(z-\zeta)}\mathcal{L}_m(-s\zeta)\mathcal{L}_p(-sz)d\zeta dz + s\int_{-\infty}^{0}\int_{-\infty}^{z} e^{-k(z-\zeta)}\mathcal{L}_m(-s\zeta)\mathcal{L}_p(-sz)d\zeta dz \tag{5.94}$$

$$\mathcal{Z}^{(2)}_{mp}(s;k) = s\int_{-\infty}^{0}\int_{z}^{0} e^{k(z-\zeta)}\mathcal{L}_m(-s\zeta)\mathcal{L}_p(-sz)d\zeta dz - s\int_{-\infty}^{0}\int_{-\infty}^{z} e^{-k(z-\zeta)}\mathcal{L}_m(-s\zeta)\mathcal{L}_p(-sz)d\zeta dz \tag{5.95}$$

Using a recursion relationship of Laguerre functions

$$\frac{\partial}{\partial\zeta}L_m(-s\zeta) = \frac{\partial}{\partial\zeta}L_{m-1}(-s\zeta) + sL_{m-1}(-s\zeta). \tag{5.96}$$

the recursion relationship of integral is given as follows

$$\int_{-\infty}^{z} e^{-k(z-\zeta)}\mathcal{L}_m(-s\zeta)d\zeta = \frac{\mathcal{L}_m(-sz)-\mathcal{L}_{m-1}(-sz)}{\left(k+\frac{s}{2}\right)} + \frac{\left(k-\frac{s}{2}\right)}{\left(k+\frac{s}{2}\right)}\int_{-\infty}^{z} e^{-k(z-\zeta)}\mathcal{L}_{m-1}(-s\zeta)d\zeta \tag{5.97}$$

$$\int_{z}^{0} e^{k(z-\zeta)}\mathcal{L}_m(-s\zeta)d\zeta = \frac{\mathcal{L}_m(-sz)-\mathcal{L}_{m-1}(-sz)}{\left(k-\frac{s}{2}\right)} + \frac{\left(k+\frac{s}{2}\right)}{\left(k-\frac{s}{2}\right)}\int_{z}^{0} e^{k(z-\zeta)}\mathcal{L}_{m-1}(-s\zeta)d\zeta \tag{5.98}$$

with the integral values when $m = 0$

$$\int_{-\infty}^{z} e^{-k(z-\zeta)}\mathcal{L}_0(-s\zeta)d\zeta = \frac{e^{\frac{sz}{2}}}{k+\frac{s}{2}}, \qquad \int_{z}^{0} e^{k(z-\zeta)}\mathcal{L}_0(-s\zeta)d\zeta = \frac{e^{\frac{sz}{2}}-e^{kz}}{k-\frac{s}{2}}, \tag{5.99}$$

Two sub-integrals are given by

$$\int_{-\infty}^{0}\int_{-\infty}^{z} e^{-k(z-\zeta)}\mathcal{L}_m(-s\zeta)\mathcal{L}_q(-sz)d\zeta dz = \begin{cases} -\frac{\left(k-\frac{s}{2}\right)^{|p-m|-1}}{\left(k+\frac{s}{2}\right)^{|p-m|+1}} & m > p \\ \frac{1}{s}\frac{1}{k+\frac{s}{2}} & m = p \\ 0 & m < p \end{cases},$$

$$\int_{-\infty}^{0}\int_{z}^{0} e^{k(z-\zeta)}\mathcal{L}_m(-s\zeta)\mathcal{L}_q(-sz)d\zeta dz = \begin{cases} 0 & m > p \\ \frac{1}{s}\frac{1}{k+\frac{s}{2}} & m = p \\ -\frac{\left(k-\frac{s}{2}\right)^{|p-m|-1}}{\left(k+\frac{s}{2}\right)^{|p-m|+1}} & m < p \end{cases}.$$

Consequently, the vertical integral functions of first and second kinds are expressed as

$$\mathcal{Z}_{mp}^{(1)}(s;k) = \begin{cases} \dfrac{2}{(k+\frac{s}{2})} & m = p \\ -s\dfrac{(k-\frac{s}{2})^{|m-p|-1}}{(k+\frac{s}{2})^{|m-p|+1}} & m \neq p \end{cases}, \tag{5.100}$$

$$\mathcal{Z}_{mp}^{(2)}(s;k) = \begin{cases} 0 & m = p \\ (-s)\mathrm{sgn}(m-p)\dfrac{(k-\frac{s}{2})^{|m-p|-1}}{(k+\frac{s}{2})^{|m-p|+1}} & m \neq p \end{cases}. \tag{5.101}$$

Using the integral relationship of Laguerre function multiplied by exponential function

$$\int_{-\infty}^{0} e^{k\zeta}\mathcal{L}_m(-s\zeta)d\zeta = \frac{(k-\frac{s}{2})^m}{(k+\frac{s}{2})^{m+1}}, \tag{5.102}$$

The vertical integral functions of third and fourth kinds are given by

$$\mathcal{Z}_{mp}^{(3)}(s;k) = s\frac{(k-\frac{s}{2})^{m+p}}{(k+\frac{s}{2})^{m+p+2}}, \tag{5.103}$$

$$\mathcal{Z}_{p}^{(4)}(s;k) = s\frac{(k-\frac{s}{2})^{p}}{(k+\frac{s}{2})^{p+1}}. \tag{5.104}$$

Note that the vertical integral functions have the following symmetry and antisymmetry properties

$$Z_{mp}^{(i)}(s;k) = Z_{pm}^{(i)}(s;k), \qquad i = 1,3 \tag{5.105}$$

and

$$Z_{mp}^{(2)}(s;k) = -Z_{pm}^{(2)}(s;k) \tag{5.106}$$

Consequently, the elementary functions also have the following symmetry or antisymmetry relationship with respect to Laguerre mode m and p:

$$\mathcal{S}_{n,mp}(s;r,a,t) = \mathcal{S}_{n,pm}(s;r,a,t), \qquad \text{when the integral involves} \qquad Z_{mp}^{(1,3)}(s;k), \tag{5.107}$$

$$\mathcal{S}_{n,mp}(s;r,a,t) = -\mathcal{S}_{n,pm}(s;r,a,t), \qquad \text{when the integral involves} \qquad Z_{mp}^{(2)}(s;k). \tag{5.108}$$

Therefore, the vertical derivative of source elementary function has an antisymmetry relationship, and the other elementary functions satisfy the symmetry relationship with respect to m and p. Using the symmetry and antisymmetry properties, the computational efforts for calculating the elementary functions can be reduced.

5.5 Poincaré's velocity representation with a vertical circular cylindrical matching surface

5.5.1 Integrals involving cosine, sine functions or normal and azimuth directional components

The velocity contributions given in equations (5.14), (5.15), (5.16) and (5.17) include $\cos\theta'$ and $\sin\theta'$. Therefore, the integrals involving $\cos\theta'$ and $\sin\theta'$ are necessarily as given by

$$\frac{s}{2\pi}\int_0^{2\pi}\int_{-\infty}^{0} f(a,\theta',\zeta)\begin{Bmatrix}\cos\theta'\\ \sin\theta'\end{Bmatrix}\mathcal{L}_m\left(-s\zeta\right)e^{-\mathrm{i}n\theta'}d\zeta d\theta', \tag{5.109}$$

and

$$\frac{1}{2\pi}\int_0^{2\pi} f(a,\theta',0)\begin{Bmatrix}\cos\theta'\\ \sin\theta'\end{Bmatrix}e^{-\mathrm{i}n\theta'}d\theta'. \tag{5.110}$$

The coefficients of Fourier-Laguerre and Fourier series on the matching surface are given by

$$C_{mn} = \frac{s}{2\pi}\int_0^{2\pi}\int_{-\infty}^{0} f(a,\theta',\zeta)\mathcal{L}_m\left(-s\zeta\right)e^{-\mathrm{i}n\theta'}d\zeta d\theta', \tag{5.111}$$

$$D_n = \frac{1}{2\pi}\int_0^{2\pi} g(a,\theta',0)e^{-\mathrm{i}n\theta'}d\theta'. \tag{5.112}$$

Using the relationships of trigonometric functions

$$\cos\theta' = \frac{e^{\mathrm{i}\theta'}+e^{-\mathrm{i}\theta'}}{2}, \qquad \sin\theta' = \frac{e^{\mathrm{i}\theta'}-e^{-\mathrm{i}\theta'}}{2\mathrm{i}}, \tag{5.113}$$

the integrals can be given by the Fourier coefficients of $n-1$ and $n+1$ modes as

$$\frac{s}{2\pi}\int_0^{2\pi}\int_{-\infty}^{0} f(a,\theta',\zeta)\begin{Bmatrix}\cos\theta'\\ \sin\theta'\end{Bmatrix}\mathcal{L}_m\left(-s\zeta\right)e^{-\mathrm{i}n\theta'}d\zeta d\theta' = \frac{1}{2}\begin{Bmatrix}C_{mn+1}+C_{mn-1}\\ \mathrm{i}(C_{mn+1}-C_{mn-1})\end{Bmatrix}, \tag{5.114}$$

and

$$\frac{1}{2\pi}\int_0^{2\pi} f(a,\theta',0)\begin{Bmatrix}\cos\theta'\\ \sin\theta'\end{Bmatrix}e^{-\mathrm{i}n\theta'}d\theta' = \frac{1}{2}\begin{Bmatrix}D_{n+1}+D_{n-1}\\ \mathrm{i}(D_{n+1}-D_{n-1})\end{Bmatrix}. \tag{5.115}$$

The normal and azimuth directional vector components are given by coordinates transformations given in equation (5.2)

$$f^a = \cos\theta' f^\xi - \sin\theta' f^\eta, \qquad f^{\theta'} = \frac{1}{a}\left(\sin\theta f^\xi + \cos\theta f^\eta\right).$$

Using the relationships given in (5.113), the integrals involving normal and azimuth directional

vector component can be given by

$$C^a_{mn} = \frac{s}{2\pi}\int_0^{2\pi}\int_{-\infty}^{0} f^a(a,\theta',\zeta)\mathcal{L}_m(-s\zeta)e^{-\mathrm{i}n\theta'}d\zeta d\theta' = \frac{1}{2}\left(C^\xi_{mn+1} + C^\xi_{mn-1} - \mathrm{i}C^\eta_{mn+1} + \mathrm{i}C^\eta_{mn-1}\right) \tag{5.116}$$

$$C^{\theta'}_{mn} = \frac{s}{2\pi a}\int_0^{2\pi}\int_{-\infty}^{0} f^{\theta'}(a,\theta',\zeta)\mathcal{L}_m(-s\zeta)e^{-\mathrm{i}n\theta'}d\zeta d\theta' = \frac{1}{2}\left(\mathrm{i}C^\xi_{mn+1} - \mathrm{i}C^\xi_{mn-1} + C^\eta_{mn+1} + C^\eta_{mn-1}\right) \tag{5.117}$$

$$D^a_n = \frac{1}{2\pi}\int_0^{2\pi} f^a(a,\theta',0)e^{-\mathrm{i}n\theta'}d\theta' = \frac{1}{2}\left(D^\xi_{n+1} + D^\xi_{n-1} - \mathrm{i}D^\eta_{n+1} + \mathrm{i}D^\eta_{n-1}\right) \tag{5.118}$$

$$D^{\theta'}_n = \frac{1}{2\pi a}\int_0^{2\pi} f^{\theta'}(a,\theta',0)e^{-\mathrm{i}n\theta'}d\theta' = \frac{1}{2}\left(\mathrm{i}D^\xi_{n+1} - \mathrm{i}D^\xi_{n-1} + D^\eta_{n+1} + D^\eta_{n-1}\right) \tag{5.119}$$

where C^ξ_{mn}, C^η_{mn}, D^ξ_n, D^η_n are Fourier-Laguerre and Fourier coefficients involving f^ξ and f^η defined by

$$C^\xi_{mn} = \frac{s}{2\pi}\int_0^{2\pi}\int_{-\infty}^{0} f^\xi(a,\theta',\zeta)\mathcal{L}_m(-s\zeta)e^{-\mathrm{i}n\theta'}d\zeta d\theta',$$
$$C^\eta_{mn} = \frac{s}{2\pi}\int_0^{2\pi}\int_{-\infty}^{0} f^\eta(a,\theta',\zeta)\mathcal{L}_m(-s\zeta)e^{-\mathrm{i}n\theta'}d\zeta d\theta',$$
$$D^\xi_n = \frac{1}{2\pi}\int_0^{2\pi} f^\xi(a,\theta',0)e^{-\mathrm{i}n\theta'}d\theta',$$
$$D^\eta_n = \frac{1}{2\pi}\int_0^{2\pi} f^\eta(a,\theta',0)e^{-\mathrm{i}n\theta'}d\theta'.$$

5.5.2 Poincaré's velocity representation with elementary functions

The fluid velocity at field point in Fourier-Laguerre series obtained by using elementary functions and flows in Fourier-Laguerre series are given by

$$\begin{bmatrix} u^x_C \\ u^y_C \\ u^z_C \end{bmatrix} = \frac{1}{4\pi}\sum_{n=-N}^{N}\sum_{p=0}^{M}\begin{bmatrix} \mathcal{U}^x_{pn} \\ \mathcal{U}^y_{pn} \\ \mathcal{U}^z_{pn} \end{bmatrix} e^{\mathrm{i}n\theta}\mathcal{L}_p(-sz), \tag{5.120}$$

where $\mathcal{U}^x_{pn}$, $\mathcal{U}^y_{pn}$ and $\mathcal{U}^z_{pn}$ are Fourier-Laguerre coefficients of the fluid velocity at field point and superscripts are corresponding direction respectively. Fourier-Laguerre coefficients of the fluid velocity have four contributions given by

$$\mathcal{U}^x_{pn} = \mathcal{U}^{Rx}_{pn} + \mathcal{U}^{Rx*}_{pn} + \mathcal{U}^{Hx}_{pn} + \mathcal{U}^{Fx}_{pn}, \tag{5.121}$$
$$\mathcal{U}^y_{pn} = \mathcal{U}^{Ry}_{pn} + \mathcal{U}^{Ry*}_{pn} + \mathcal{U}^{Hy}_{pn} + \mathcal{U}^{Fy}_{pn}, \tag{5.122}$$
$$\mathcal{U}^z_{pn} = \mathcal{U}^{Rz}_{pn} + \mathcal{U}^{Rz*}_{pn} + \mathcal{U}^{Hz}_{pn} + \mathcal{U}^{Fz}_{pn}. \tag{5.123}$$

The terms in right-hand-side of above equations correspond to contributions of source, image source, harmonic and waterline integrals, respectively. These contributions are summarized as follows:

- Source and image source contributions

$$\begin{aligned}\mathcal{U}^{Rx}_{pn}+\mathcal{U}^{Rx*}_{pn}=\frac{1}{2}\sum_{n=-N}^{N}\sum_{m=0}^{M}[&\left(\mathcal{C}^{n}_{mn+1}+\mathcal{C}^{n}_{mn-1}+\mathrm{i}\mathcal{W}^{z}_{mn+1}-\mathrm{i}\mathcal{W}^{z}_{mn-1}\right)\left(\mathcal{S}^{R}_{a,n,mp}+\mathcal{S}^{R*}_{a,n,mp}\right)\\&+\left(\mathcal{W}^{z}_{mn+1}+\mathcal{W}^{z}_{mn-1}-\mathrm{i}\mathcal{C}^{n}_{mn+1}+\mathrm{i}\mathcal{C}^{n}_{mn-1}\right)\left(\mathcal{S}^{R}_{\theta',n,mp}+\mathcal{S}^{R*}_{\theta',n,mp}\right)\\&-2\mathcal{W}^{y}_{mn}(\mathcal{S}^{R}_{\zeta,n,mp}+\mathcal{S}^{R*}_{\zeta,n,mp})],\end{aligned}\tag{5.124}$$

$$\begin{aligned}\mathcal{U}^{Ry}_{pn}+\mathcal{U}^{Ry*}_{pn}=\frac{1}{2}\sum_{n=-N}^{N}\sum_{m=0}^{M}[&\left(\mathrm{i}\mathcal{C}^{n}_{mn+1}-\mathrm{i}\mathcal{C}^{n}_{mn-1}-\mathcal{W}^{z}_{mn+1}-\mathcal{W}^{z}_{mn-1}\right)\left(\mathcal{S}^{R}_{a,n,mp}+\mathcal{S}^{R*}_{a,n,mp}\right)\\&+\left(\mathcal{C}^{n}_{mn+1}+\mathcal{C}^{n}_{mn-1}+\mathrm{i}\mathcal{W}^{z}_{mn+1}-\mathrm{i}\mathcal{W}^{z}_{mn-1}\right)\left(\mathcal{S}^{R}_{\theta',n,mp}+\mathcal{S}^{R*}_{\theta',n,mp}\right)\\&+2\mathcal{W}^{x}_{mn}(\mathcal{S}^{R}_{\zeta,n,mp}+\mathcal{S}^{R*}_{\zeta,n,mp})],\end{aligned}\tag{5.125}$$

$$\begin{aligned}\mathcal{U}^{Rz}_{pn}+\mathcal{U}^{Rz*}_{pn}=\sum_{n=-N}^{N}\sum_{m=0}^{M}[&\mathcal{C}^{n}_{mn}(\mathcal{S}^{R}_{\zeta,n,mp}-\mathcal{S}^{R*}_{\zeta,n,mp})+\mathcal{W}^{\theta'}_{mn}(\mathcal{S}^{R}_{a,n,mp}-\mathcal{S}^{R*}_{a,n,mp})\\&-\mathcal{W}^{a}_{mn}(\mathcal{S}^{R}_{\theta',n,mp}-\mathcal{S}^{R*}_{\theta',n,mp})],\end{aligned}\tag{5.126}$$

where $\mathcal{W}^{a}_{mn}$ and $\mathcal{W}^{\theta'}_{mn}$ are Fourier-Laguerre coefficients of normal and azimuth directional components of tangential velocity. Using the equations (5.116) and (5.117), they are given by

$$\begin{aligned}\mathcal{W}^{a}_{mn}&=\frac{s}{2\pi}\int_{0}^{2\pi}\int_{-\infty}^{0}w^{a}\mathcal{L}_{m}(-s\zeta)e^{-\mathrm{i}n\theta'}d\zeta d\theta'\\&=\frac{1}{2}\left(\mathcal{W}^{x}_{mn+1}+\mathcal{W}^{x}_{mn-1}-\mathrm{i}\mathcal{W}^{y}_{mn+1}+\mathrm{i}\mathcal{W}^{y}_{mn-1}\right)\end{aligned}\tag{5.127}$$

$$\begin{aligned}\mathcal{W}^{\theta'}_{mn}&=\frac{s}{2\pi}\int_{0}^{2\pi}\int_{-\infty}^{0}w^{\theta'}\mathcal{L}_{m}(-s\zeta)e^{-\mathrm{i}n\theta'}d\zeta d\theta'\\&=\frac{1}{2}\left(\mathrm{i}\mathcal{W}^{x}_{mn+1}-\mathrm{i}\mathcal{W}^{x}_{mn-1}+\mathcal{W}^{y}_{mn+1}+\mathcal{W}^{y}_{mn-1}\right)\end{aligned}\tag{5.128}$$

- Harmonic contributions

$$\begin{aligned}\mathcal{U}^{Hx}_{pn}=-\frac{1}{2}\sum_{n=-N}^{N}\sum_{m=0}^{M}\int_{t_0}^{t}[&\left(\mathcal{C}^{n}_{mn+1}+\mathcal{C}^{n}_{mn-1}+\mathrm{i}\mathcal{W}^{z}_{mn+1}-\mathrm{i}\mathcal{W}^{z}_{mn-1}\right)\mathcal{S}^{H}_{a,n,mp}-2\mathcal{W}^{y}_{mn}\mathcal{S}^{H}_{\zeta,n,mp}\\&+\left(\mathcal{W}^{z}_{mn+1}+\mathcal{W}^{z}_{mn-1}-\mathrm{i}\mathcal{C}^{n}_{mn+1}+\mathrm{i}\mathcal{C}^{n}_{mn-1}\right)\mathcal{S}^{H}_{\theta',n,mp}]d\tau,\end{aligned}\tag{5.129}$$

$$\begin{aligned}\mathcal{U}^{Hy}_{pn}=-\frac{1}{2}\sum_{n=-N}^{N}\sum_{m=0}^{M}\int_{t_0}^{t}[&\left(\mathrm{i}\mathcal{C}^{n}_{mn+1}-\mathrm{i}\mathcal{C}^{n}_{mn-1}-\mathcal{W}^{z}_{mn+1}-\mathcal{W}^{z}_{mn-1}\right)\mathcal{S}^{H}_{a,n,mp}+2\mathcal{W}^{x}_{mn}\mathcal{S}^{H}_{\zeta,n,mp}\\&+\left(\mathcal{C}^{n}_{mn+1}+\mathcal{C}^{n}_{mn-1}+\mathrm{i}\mathcal{W}^{z}_{mn+1}-\mathrm{i}\mathcal{W}^{z}_{mn-1}\right)\mathcal{S}^{H}_{\theta',n,mp}]d\tau,\end{aligned}\tag{5.130}$$

$$\mathcal{U}^{Hz}_{pn}=\sum_{n=-N}^{N}\sum_{m=0}^{M}\int_{t_0}^{t}[\mathcal{C}^{n}_{mn}\mathcal{S}^{H}_{\zeta,n,mp}+\mathcal{W}^{\theta'}_{mn}\mathcal{S}^{H}_{a,n,mp}-\mathcal{W}^{a}_{mn}\mathcal{S}^{H}_{\theta',n,mp}]d\tau.\tag{5.131}$$

- Waterline contributions

$$\mathcal{U}_{pn}^{Fx} = -\frac{1}{2}\sum_{n=-N}^{N}\int_{t_0}^{t}(\mathcal{E}_{n+1}+\mathcal{E}_{n-1})\mathcal{F}_{\zeta,n,p}^{F}d\tau, \tag{5.132}$$

$$\mathcal{U}_{pn}^{Fy} = -\frac{\mathrm{i}}{2}\sum_{n=-N}^{N}\int_{t_0}^{t}(\mathcal{E}_{n+1}-\mathcal{E}_{n-1})\,\mathcal{F}_{\zeta,n,p}^{F}d\tau, \tag{5.133}$$

$$\mathcal{U}_{pn}^{Fz} = -\sum_{n=-N}^{N}\int_{t_0}^{t}\mathcal{E}_{n}\mathcal{F}_{a,n,p}^{F}d\tau. \tag{5.134}$$

5.6 Evaluation of elementary functions

5.6.1 Elementary functions involving semi-infinite integrals

The surface and waterline elementary functions involve the integrals

$$\int_0^\infty k^\nu \begin{Bmatrix}\mathcal{Z}_{mp}^{(i)}(s;k)\\ \mathcal{Z}_{p}^{(4)}(s;k)\end{Bmatrix}\times J_n(kr)\begin{Bmatrix}J_n'(ka)\\ J_n(ka)\end{Bmatrix}\times\begin{Bmatrix}\cos t\sqrt{gk}\\ \sin t\sqrt{gk}\end{Bmatrix}dk, \qquad i=1,2,3. \tag{5.135}$$

where $\mathcal{Z}_{mp}^{(i)}(s;k)$ and $\mathcal{Z}_{mp}^{(4)}(s;k)$ are the vertical integral functions discussed in section 5.4.6. They are written again

$$\mathcal{Z}_{mp}^{(1)}(s;k) = \begin{cases}\dfrac{2}{(k+\frac{s}{2})} & m=p\\ -s\dfrac{(k-\frac{s}{2})^{|m-p|-1}}{(k+\frac{s}{2})^{|m-p|+1}} & m\neq p\end{cases},$$

$$\mathcal{Z}_{mp}^{(2)}(s;k) = \begin{cases}0 & m=p\\ (-s)\mathrm{sgn}(m-p)\dfrac{(k-\frac{s}{2})^{|m-p|-1}}{(k+\frac{s}{2})^{|m-p|+1}} & m\neq p\end{cases}.$$

and

$$\mathcal{Z}_{mp}^{(3)}(s;k) = s\frac{(k-\frac{s}{2})^{m+p}}{(k+\frac{s}{2})^{m+p+2}}, \qquad \mathcal{Z}_{p}^{(4)}(s;k) = s\frac{(k-\frac{s}{2})^{p}}{(k+\frac{s}{2})^{p+1}}.$$

All vertical integral functions can be expressed as functions of k as

$$\frac{(k-\frac{s}{2})^{q}}{(k+\frac{s}{2})^{r}}, \qquad q<r, \tag{5.136}$$

where q and r are integer.

The derivative of the Bessel function of the first kind can be given by a Bessel function of the first kind with different order as (Abramowitz and Stegun, 1965)

$$J_n'(x) = \frac{1}{2}\left\{J_{n-1}(x)-J_{n+1}(x)\right\}, \tag{5.137}$$

$$J_n'(x) = -J_{n+1}(x)+\frac{n}{x}J_n(x). \tag{5.138}$$

Therefore, the surface and waterline elementary functions need the evaluation of semi-infinite integrals with respect to k

$$\mathcal{I}^{pqr}_{mn}(s;r,a,t) = \int_0^\infty k^p \frac{(k-\frac{s}{2})^q}{(k+\frac{s}{2})^r} J_m(kr) J_n(ka) \begin{Bmatrix} \cos t\sqrt{gk} \\ \sin t\sqrt{gk} \end{Bmatrix} dk. \tag{5.139}$$

where p is a real number. q and r are integers. s is a positive real number ($s > 0$). m and n are integers. r and a are real positive numbers satisfying $r > a$. t is a positive real number with $t \geq 0$.

5.6.2 Semi-infinite integrals

The integrals given in equation (5.139) are rewritten by applying the change of variable $x = ka$

$$\mathcal{I}^{pqr}_{mn}(s;r,a,t) = a^{r-p-q-1} \int_0^\infty x^p \frac{(x-\sigma)^q}{(x+\sigma)^r} J_m(\alpha x) J_n(x) \begin{Bmatrix} \cos \tau\sqrt{x} \\ \sin \tau\sqrt{x} \end{Bmatrix} dx \tag{5.140}$$

with the following parameters

$$\sigma = \frac{sa}{2}, \qquad \alpha = \frac{r}{a}, \qquad \tau = t\sqrt{g/a}. \tag{5.141}$$

The field point (r) being located outside of vertical circular cylindrical matching surface of radius (a) and time being always positive, then

$$\alpha \geq 1, \qquad \tau \geq 0. \tag{5.142}$$

The evaluation of two semi-infinite integrals involving two Bessel and trigonometric functions given in following equations are necessary

$$\mathcal{I}_{c,mn}(\alpha;\tau) = \int_0^\infty f(x) J_m(\alpha x) J_n(x) \cos \tau\sqrt{x} dx, \tag{5.143}$$

$$\mathcal{I}_{s,mn}(\alpha;\tau) = \int_0^\infty f(x) J_m(\alpha x) J_n(x) \sin \tau\sqrt{x} dx, \tag{5.144}$$

with the function

$$f(x) = x^p \frac{(x-\sigma)^q}{(x+\sigma)^r}. \tag{5.145}$$

The integral can be split into three integrals defined by

$$\int_0^\infty \{\cdot\}\, dx = \int_0^{\frac{1}{4}} \{\cdot\}\, dx + \int_{\frac{1}{4}}^{x_c} \{\cdot\}\, dx + \int_{x_c}^\infty \{\cdot\}\, dx. \tag{5.146}$$

where x_c is the semi-infinite integral bound and will be discussed later.

5.6.3 Integrals near zero and intermediate interval

The integral near zero is given by

$$\begin{Bmatrix} \mathcal{I}^{(0)}_{c,mn} \\ \mathcal{I}^{(0)}_{s,mn} \end{Bmatrix} = \int_0^{\frac{1}{4}} f(x) J_m(\alpha x) J_n(x) \begin{Bmatrix} \cos \tau\sqrt{x} \\ \sin \tau\sqrt{x} \end{Bmatrix} dx. \tag{5.147}$$

Applying the change of variable, $x = u^2$ leads to

$$\int_0^{\frac{1}{4}} f(x) J_m(\alpha x) J_n(x) \begin{Bmatrix} \cos\tau\sqrt{x} \\ \sin\tau\sqrt{x} \end{Bmatrix} dx = 2\int_0^{\frac{1}{2}} u f(u^2) J_m(\alpha u^2) J_n(u^2) \begin{Bmatrix} \cos\tau u \\ \sin\tau u \end{Bmatrix} du. \tag{5.148}$$

The original and transformed integrands given in the above equation are compared in figure 5.3. In the figure 5.3, the original integrand shows a highly oscillatory behaviour near $x = 0$. It gives

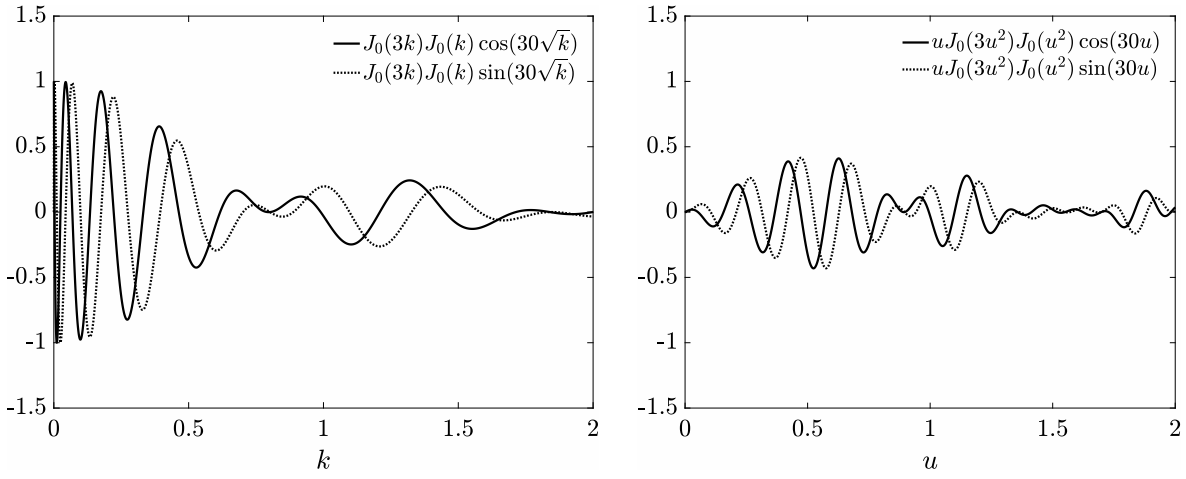

(a) $J_m(ax)J_n(bx)\begin{pmatrix}\cos(c\sqrt{x})\\ \sin(c\sqrt{x})\end{pmatrix}$ **(b)** $uJ_m(au^2)J_n(bu^2)\begin{pmatrix}\cos(cu)\\ \sin(cu)\end{pmatrix}$

Figure 5.3. The behavior of oscillatory integrands near to zero.

poor results when a direct numerical integration is applied. On the contrary, the transformed integrand shows a relatively smooth behavior near $u = 0$. A numerical integration for transformed integrand gives a reliable result for small u. The integral upper bound is set to $x = \frac{1}{4}, u = \frac{1}{2}$ by numerical test. The adaptive 3-point Gaussian quadrature with discretized integral integral

$$\Delta u = \min\left(\frac{0.2\pi}{\max(\alpha+1, \tau+0.001)}, 0.05\right) \tag{5.149}$$

is applied to calculate the integral from $x = 0$ to $x = \frac{1}{4}$.

The integrals having intermediate interval from $x = \frac{1}{4}$ to x_c are defined by

$$\begin{Bmatrix} \mathcal{I}^{(i1)}_{c,mn} \\ \mathcal{I}^{(i1)}_{s,mn} \end{Bmatrix} = \int_{\frac{1}{4}}^{x_c} f(x) J_m(\alpha x) J_n(x) \begin{Bmatrix} \cos\tau\sqrt{x} \\ \sin\tau\sqrt{x} \end{Bmatrix} dx, \tag{5.150}$$

The numerical integration by applying 3-point adaptive Gaussian quadrature with discretized interval $\Delta x = \Delta u$ is used. The choice of integral upper bound x_c will be discussed later.

5.6.4 Evaluation of semi-infinite integral by splitting oscillatory functions

Computing a semi-infinite integral of an oscillatory function with slowly decaying amplitude is more complicated than for a monotonic function. Blackemore et al. (1976) compared numerical methods, evaluating the semi-infinite integral of an oscillatory function. They concluded that

the *integration, then summation* algorithm provided good results over a wide range of functions. The efficiency of the numerical algorithm increases by using an accelerator. The accelerator is numerical algorithm extrapolating an infinite summation from finite summation.

Lucas and Stone (1995) applied the *integration, then summation* algorithm on the integral involving a single Bessel function with various accelerators, e.g, Euler transform, ϵ-algorithm and mW-transform with a different sub-integral interval (Davis and Rabinowitz, 1988; Shanks, 1955; Wynn, 1956; Sidi, 1988; Lyness, 1985). They showed that all accelerators enhanced numerical efficiency and concluded that mW-transform with successive zeros of the Bessel function gives better results than others. Following previous works, Lucas (1995) applied the same idea on the integral involving two Bessel functions. Two Bessel functions are split into two oscillatory functions and zeros are found by asymptotic forms of oscillatory functions.

The present study extended their idea for the case of the integral involving two Bessel function multiplied by sine or cosine functions. The integrals involving two Bessel functions multiplied by sine or cosine functions are defined by

$$\begin{Bmatrix} \mathcal{I}^{\infty}_{c,mn}(\alpha,\tau) \\ \mathcal{I}^{\infty}_{s,mn}(\alpha,\tau) \end{Bmatrix} = \int_{x_c}^{\infty} f(x) J_m(\alpha x) J_n(x) \begin{Bmatrix} \cos\tau\sqrt{x} \\ \sin\tau\sqrt{x} \end{Bmatrix} dx. \tag{5.151}$$

Using the asymptotic forms of Bessel function for large arguments given by (Abramowitz and Stegun, 1965)

$$J_n(x) = \sqrt{\frac{2}{\pi x}} \cos\left(x - \frac{n\pi}{2} - \frac{\pi}{4}\right), \tag{5.152}$$

$$Y_n(x) = \sqrt{\frac{2}{\pi x}} \sin\left(x - \frac{n\pi}{2} - \frac{\pi}{4}\right), \tag{5.153}$$

and the relationships of trigonometric functions given by

$$\cos(A \pm B) = \cos A \cos B \mp \sin A \sin B, \tag{5.154}$$

$$\sin(A \pm B) = \sin A \cos B \pm \sin B \cos A, \tag{5.155}$$

the oscillatory terms in the integrand are split into four functions

$$J_m(\alpha x) J_n(x) \cos\tau\sqrt{x} = \frac{1}{4} \sum_{i=1}^{4} \mathcal{J}^{(i)}_{mn}(\alpha,\tau;x), \tag{5.156}$$

$$J_m(\alpha x) J_n(x) \sin\tau\sqrt{x} = \frac{1}{4} \sum_{i=1}^{4} \mathcal{Y}^{(i)}_{mn}(\alpha,\tau;x) \tag{5.157}$$

where $\mathcal{J}^{(i)}_{mn}$ and $\mathcal{Y}^{(i)}_{mn}$ are the oscillatory functions defined as

$$\mathcal{J}^{(1)}_{mn}(\alpha,\tau;x) = J^{-}_{mn}(\alpha;x)\cos\tau\sqrt{x} + Y^{-}_{mn}(\alpha;x)\sin\tau\sqrt{x}, \tag{5.158}$$

$$\mathcal{J}^{(2)}_{mn}(\alpha,\tau;x) = J^{-}_{mn}(\alpha;x)\cos\tau\sqrt{x} - Y^{-}_{mn}(\alpha;x)\sin\tau\sqrt{x}, \tag{5.159}$$

$$\mathcal{J}^{(3)}_{mn}(\alpha,\tau;x) = J^{+}_{mn}(\alpha;x)\cos\tau\sqrt{x} + Y^{+}_{mn}(\alpha;x)\sin\tau\sqrt{x}, \tag{5.160}$$

$$\mathcal{J}^{(4)}_{mn}(\alpha,\tau;x) = J^{+}_{mn}(\alpha;x)\cos\tau\sqrt{x} - Y^{+}_{mn}(\alpha;x)\sin\tau\sqrt{x}, \tag{5.161}$$

and

$$\mathcal{Y}^{(1)}_{mn}(\alpha,\tau;x) = J^{-}_{mn}(\alpha;x)\sin\tau\sqrt{x} - Y^{-}_{mn}(\alpha;x)\cos\tau\sqrt{x}, \tag{5.162}$$
$$\mathcal{Y}^{(2)}_{mn}(\alpha,\tau;x) = J^{-}_{mn}(\alpha;x)\sin\tau\sqrt{x} + Y^{-}_{mn}(\alpha;x)\cos\tau\sqrt{x}, \tag{5.163}$$
$$\mathcal{Y}^{(3)}_{mn}(\alpha,\tau;x) = J^{+}_{mn}(\alpha;x)\sin\tau\sqrt{x} - Y^{+}_{mn}(\alpha;x)\cos\tau\sqrt{x}, \tag{5.164}$$
$$\mathcal{Y}^{(4)}_{mn}(\alpha,\tau;x) = J^{+}_{mn}(\alpha;x)\sin\tau\sqrt{x} + Y^{+}_{mn}(\alpha;x)\cos\tau\sqrt{x}, \tag{5.165}$$

with

$$J^{\pm}_{mn}(\alpha;x) = J_m(\alpha x)J_n(x) \mp Y_m(\alpha x)Y_n(x), \tag{5.166}$$
$$Y^{\pm}_{mn}(\alpha;x) = J_m(\alpha x)Y_n(x) \pm Y_m(\alpha x)J_n(x). \tag{5.167}$$

Using the asymptotic forms of Bessel functions in equations (5.152) and (5.153), the asymptotic forms of oscillatory functions are given by

$$\mathcal{J}^{(1)}_{mn}(\alpha,\tau;x) \sim \frac{2}{\pi x\sqrt{\alpha}}\cos\left\{(\alpha-1)\,x + \tau\sqrt{x} - \frac{\pi}{2}(m-n)\right\}, \tag{5.168}$$
$$\mathcal{J}^{(2)}_{mn}(\alpha,\tau;x) \sim \frac{2}{\pi x\sqrt{\alpha}}\cos\left\{(\alpha-1)\,x - \tau\sqrt{x} - \frac{\pi}{2}(m-n)\right\}, \tag{5.169}$$
$$\mathcal{J}^{(3)}_{mn}(\alpha,\tau;x) \sim \frac{2}{\pi x\sqrt{\alpha}}\cos\left\{(\alpha+1)\,x - \tau\sqrt{x} - \frac{\pi}{2}(m+n+1)\right\}, \tag{5.170}$$
$$\mathcal{J}^{(4)}_{mn}(\alpha,\tau;x) \sim \frac{2}{\pi x\sqrt{\alpha}}\cos\left\{(\alpha+1)\,x + \tau\sqrt{x} - \frac{\pi}{2}(m+n+1)\right\}, \tag{5.171}$$

and

$$\mathcal{Y}^{(1)}_{mn}(\alpha,\tau;x) \sim \frac{2}{\pi x\sqrt{\alpha}}\sin\left\{(\alpha-1)\,x + \tau\sqrt{x} - \frac{\pi}{2}(m-n)\right\}, \tag{5.172}$$
$$\mathcal{Y}^{(2)}_{mn}(\alpha,\tau;x) \sim -\frac{2}{\pi x\sqrt{\alpha}}\sin\left\{(\alpha-1)\,x - \tau\sqrt{x} - \frac{\pi}{2}(m-n)\right\}, \tag{5.173}$$
$$\mathcal{Y}^{(3)}_{mn}(\alpha,\tau;x) \sim -\frac{2}{\pi x\sqrt{\alpha}}\sin\left\{(\alpha+1)\,x - \tau\sqrt{x} - \frac{\pi}{2}(m+n+1)\right\}, \tag{5.174}$$
$$\mathcal{Y}^{(4)}_{mn}(\alpha,\tau;x) \sim \frac{2}{\pi x\sqrt{\alpha}}\sin\left\{(\alpha+1)\,x + \tau\sqrt{x} - \frac{\pi}{2}(m+n+1)\right\}. \tag{5.175}$$

The behaviour of split oscillatory functions follows a sinusoidal function for large x. The phase function is given by

$$\vartheta = \alpha^{\pm}x \pm \tau\sqrt{x} + \gamma. \tag{5.176}$$

where $\alpha^{\pm} = \alpha \pm 1$ and γ is function of m and n. Therefore, the phase functions corresponding to the oscillatory functions are defined by

$$\vartheta^{(1)} = \alpha^{-}x + \tau\sqrt{x} + \gamma_A, \qquad \text{for} \qquad \mathcal{J}^{(1)}_{mn} \text{ and } \mathcal{Y}^{(1)}_{mn}, \tag{5.177}$$
$$\vartheta^{(2)} = \alpha^{-}x - \tau\sqrt{x} + \gamma_A, \qquad \text{for} \qquad \mathcal{J}^{(2)}_{mn} \text{ and } \mathcal{Y}^{(2)}_{mn}, \tag{5.178}$$
$$\vartheta^{(3)} = \alpha^{+}x - \tau\sqrt{x} + \gamma_B, \qquad \text{for} \qquad \mathcal{J}^{(3)}_{mn} \text{ and } \mathcal{Y}^{(3)}_{mn}, \tag{5.179}$$
$$\vartheta^{(4)} = \alpha^{+}x + \tau\sqrt{x} + \gamma_B, \qquad \text{for} \qquad \mathcal{J}^{(4)}_{mn} \text{ and } \mathcal{Y}^{(4)}_{mn}, \tag{5.180}$$

where

$$\gamma_A = -\frac{\pi}{2}(m-n), \qquad \gamma_B = -\frac{\pi}{2}(m+n+1). \tag{5.181}$$

The behavior of the phase functions is plotted with respect to x in figure 5.4.

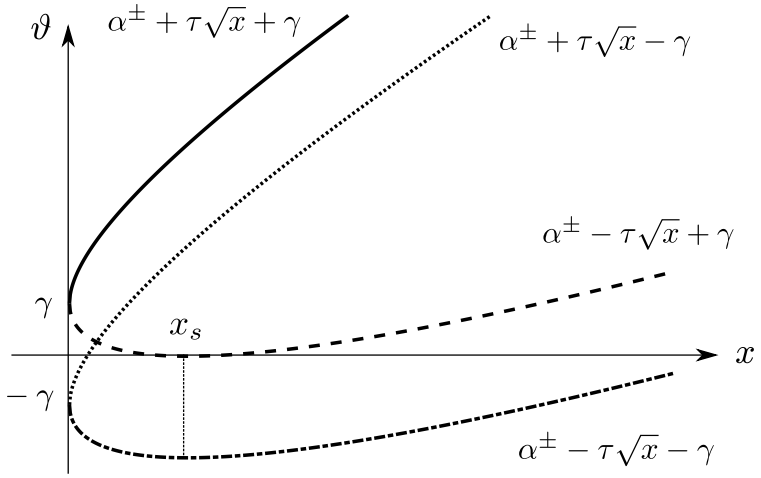

Figure 5.4. The phase function of oscillatory functions along x-axis

The figure shows that $\vartheta^{(i)}$ for $i=1,4$ always increases with respect to x, but $\vartheta^{(i)}$ for $i=2,3$ has a minimal value when

$$\left.\frac{d\vartheta^{(i)}}{dx}\right|_{x=x_s} = \alpha^{\mp} - \frac{\tau}{2\sqrt{x_s}} = 0 \qquad \text{for} \qquad i=2,3. \tag{5.182}$$

The value of x_s minmizing $\vartheta^{(i)}$ for $i=2,3$ is given by

$$x_s = \frac{1}{4}\left(\frac{\tau}{\alpha^{\mp}}\right)^2. \tag{5.183}$$

The phase functions, $\vartheta^{(i)}$ for $i=2,3$, decrease until $x \le x_s$ and increase for $x \ge x_s$. Near x_s where the phase changes slowly, the oscillatory functions, $\mathcal{J}_{mn}^{(i)}$ and $\mathcal{Y}_{mn}^{(i)}$ for $i=2,3$, look stationary. Therefore, x_s is defined here as a stationary point of oscillatory functions in the present study.

Lucas (1995) reported a similar phenomenon as *initial poor behavior* of J_{mn}^{+}. It is understood that *initial poor behavior* happens when the phase function of J_{mn}^{+} is equal to zero.

The semi-infinite integral is separated into the summation of sub-integrals with proper integral intervals. The zeros or maxima/minima of oscillatory functions are used in the *integration, then summation* algorithm but finding maxima/minima of arbitrary oscillatory functions given in equations (5.158)-(5.165) are not easy. Therefore, zeros are used as integral interval for sub-integral in the present study.

Finding the zeros of oscillatory functions, $\mathcal{J}_{mn}^{(i)}, \mathcal{Y}_{mn}^{(1,4)}$ for $i=1,4$, is relatively easy. After finding the first zero by direct searching with marching interval

$$\Delta x = \frac{\pi}{4\alpha^{\mp}}. \tag{5.184}$$

The next zero guess is taken from phase function, $\vartheta^{(i)}$ for $i=1,4$. The next zero guess, x_{j+1}^{*}, is estimated by increasing the phase by π as

$$\alpha^{\mp}x_{j+1}^{*} + \tau\sqrt{x_{j+1}^{*}} = \alpha^{\mp}x_j + \tau\sqrt{x_j} + \pi, \tag{5.185}$$

It gives an explicit expression of next zero guess

$$x_{j+1}^{*}=\left(\frac{-\tau+\sqrt{\tau^{2}+4\alpha^{\mp}\left(\alpha^{\mp}x_{j}+\tau\sqrt{x_{j}}+\pi\right)}}{2\alpha^{\mp}}\right)^{2}. \tag{5.186}$$

From the next zero guess x_{j+1}^{*}, the Newton-Raphson method with the initial guess of $x_{j+1}^{(0)}=x_{j+1}^{*}$ is used to compute the next zero as

$$x_{j+1}^{(n+1)}=x_{j+1}^{(n)}-\frac{d\vartheta^{(i)}(x_{j+1}^{(n)})}{dx},\qquad i=1,4. \tag{5.187}$$

The next zero, x_{j+1}, is taken from the converged value $x_{j+1}^{(n+1)}$. Numerical tests show that the Newton-Raphson method converges within 3-4 steps with accuracy $O(10^{-12})$.

Finding the zeros of oscillatory functions, $\mathcal{J}_{mn}^{(i)},\mathcal{Y}_{mn}^{(i)}$ for $i=2,3$, is complicated due to the existence of a stationary point. The phase of the stationary point is given by

$$\vartheta_{s}=\vartheta^{(i)}(x_{s}),\qquad \text{for}\qquad i=2,3. \tag{5.188}$$

After finding the first zero by direct searching, the next zero guess is given by

$$\alpha^{\pm}x_{i+1}^{*}-\tau\sqrt{x_{i+1}^{*}}=\begin{cases}\alpha^{\pm}x_{i}-\tau\sqrt{x_{i}}, & |\vartheta_{i}-\vartheta_{s}|<1.5\pi,\\ \alpha^{\pm}x_{i}-\tau\sqrt{x_{i}}-\pi, & x_{i}\le x^{0},\quad\text{and}\quad |\vartheta_{i}-\vartheta_{s}|\ge 1.5\pi,\\ \alpha^{\pm}x_{i}-\tau\sqrt{x_{i}}+\pi, & x_{i}\ge x^{0},\quad\text{and}\quad |\vartheta_{i}-\vartheta_{s}|\ge 1.5\pi.\end{cases} \tag{5.189}$$

It also gives an explicit expression of the next zero guess

$$x_{i+1}^{*}=\begin{cases}\left(\frac{\tau+\sqrt{\tau^{2}+4\alpha^{\pm}\left(\alpha^{\pm}x_{i}-\tau\sqrt{x_{i}}\right)}}{2\alpha^{\pm}}\right)^{2}, & \left|x_{i}-x^{0}\right|<1.5\pi,\\ \left(\frac{\tau-\sqrt{\tau^{2}+4\alpha^{\pm}\left(\alpha^{\pm}x_{i}-\tau\sqrt{x_{i}}-\pi\right)}}{2\alpha^{\pm}}\right)^{2}, & x_{i}\le x^{0},\quad\text{and}\quad \left|x_{i}-x^{0}\right|\ge 1.5\pi,\\ \left(\frac{\tau+\sqrt{\tau^{2}+4\alpha^{\pm}\left(\alpha^{\pm}x_{i}-\tau\sqrt{x_{i}}+\pi\right)}}{2\alpha^{\pm}}\right)^{2}, & x_{i}\ge x^{0},\quad\text{and}\quad \left|x_{i}-x^{0}\right|\ge 1.5\pi.\end{cases} \tag{5.190}$$

It is straightforward to apply the Newton-Raphson method to find zeros of oscillatory functions as

$$x_{j+1}^{(n+1)}=x_{j+1}^{(n)}-\frac{d\vartheta^{(i)}(x_{j+1}^{(n)})}{dx},\qquad i=2,3. \tag{5.191}$$

Some of the zeros near the stationary points are not detected by the above procedures. In that case, the zeros are found by applying direct searching with marching interval given in equation (5.184). After finding the first zero after stationary point, the extrapolation procedure is applied to accelerate the evaluation.

The procedures of decomposed oscillatory functions are plotted in figure 5.5. The behaviours of stationary point are observed for the functions, $\mathcal{J}_{mn}^{(i)},\mathcal{Y}_{mn}^{(i)}$ for $i=2,3$, and the singular behaviors are also shown due to Bessel function of the second kind which has a singular behavior at $x=0$

$$\lim_{x\to 0^{+}}Y_{m}(x)=-\infty. \tag{5.192}$$

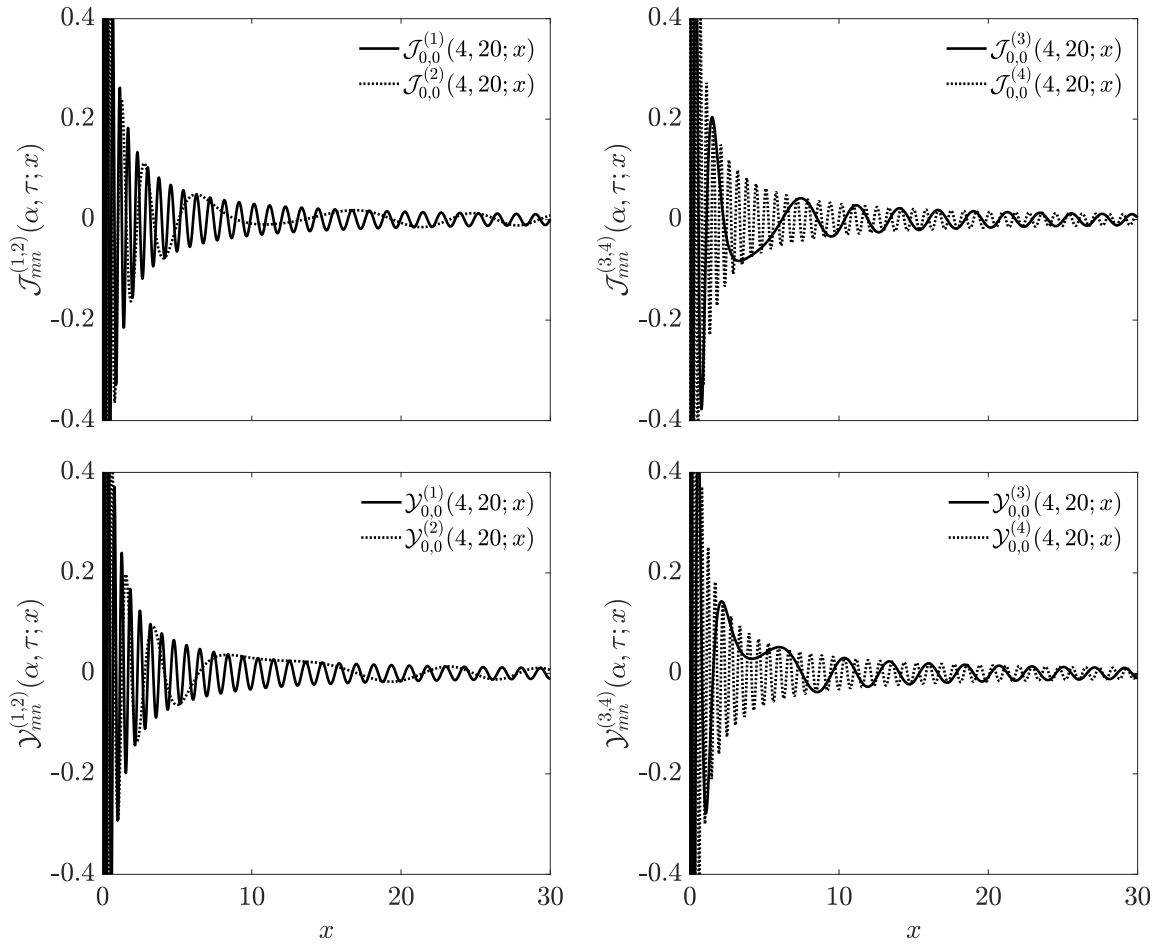

Figure 5.5. The oscillatory functions, $\mathcal{J}_{mn}$ and $\mathcal{Y}_{mn}$, for $m = n = 0$ and $\alpha = 4$, $\tau = 20$.

The singular behaviour of Bessel function near to origin provides a criterion for assessing the integral bound (x_c)

$$x_c = \max\left(\frac{y_{m,1}}{\alpha}, y_{n,1}\right) \tag{5.193}$$

with an approximated first zero of Bessel function of the second kind

$$y_{\nu,1} = \begin{cases} 0.89357697, & \nu = 0, \\ \nu + 0.9315768\nu^{\frac{1}{3}} + 0.260351\nu^{-\frac{1}{3}} + 0.01198\nu^{-1} - 0.006\nu^{-\frac{5}{3}} - 0.001\nu^{-\frac{7}{3}}, & \nu \geq 1. \end{cases} \tag{5.194}$$

Finally, the semi-infinite integral is split into four integrals as

$$\mathcal{I}_{c,mn}^{\infty}(\alpha,\tau) = \frac{1}{4}\sum_{i=1}^{4}\mathcal{I}_{c,mn}^{(i)}(\alpha,\tau), \tag{5.195}$$

$$\mathcal{I}_{s,mn}^{\infty}(\alpha,\tau) = \frac{1}{4}\sum_{i=1}^{4}\mathcal{I}_{s,mn}^{(i)}(\alpha,\tau), \tag{5.196}$$

where eight integrals are defined by

$$\left.\begin{aligned} \mathcal{I}_{c,mn}^{(i)}(\alpha,\tau) &= \int_{x_c}^{\infty} f(x)\mathcal{J}_{mn}^{(i)}(\alpha,\tau;x)dx, \\ \mathcal{I}_{s,mn}^{(i)}(\alpha,\tau) &= \int_{x_c}^{\infty} f(x)\mathcal{Y}_{mn}^{(i)}(\alpha,\tau;x)dx \end{aligned}\right\}, \qquad i = 1,2,3,4. \tag{5.197}$$

The successive zeros of oscillatory functions can be found after the first zero x_0 has been searched from the lower integral bound, x_c. Then, the semi-infinite integral is expressed as

$$\begin{aligned}\mathcal{I}^{(i)}_{c,mn} &= \int_{x_c}^{x_0} f(x)\mathcal{J}^{(i)}_{mn}(\alpha,\tau;x)dx + \int_{x_0}^{x_1} f(x)\mathcal{J}^{(i)}_{mn}(\alpha,\tau;x)dx + \int_{x_1}^{x_2} f(x)\mathcal{J}^{(i)}_{mn}(\alpha,\tau;x)dx + \cdots \\ &= \int_{x_c}^{x_0} f(x)\mathcal{J}^{(i)}_{mn}(\alpha,\tau;x)dx + R^{(i)}_{c,\infty}, \qquad \text{for} \qquad i=1,4, \end{aligned} \tag{5.198}$$

$$\mathcal{I}^{(i)}_{s,mn} = \int_{x_c}^{x_0} f(x)\mathcal{Y}^{(i)}_{mn}(\alpha,\tau;x)dx + R^{(i)}_{s,\infty} \qquad \text{for} \qquad i=1,4, \tag{5.199}$$

with the infinite series summation of sub-integral

$$R^{(i)}_{c,\infty} = \lim_{K\to\infty}\sum_{k=0}^{K} a^{(i)}_{2k}, \qquad R^{(i)}_{s,\infty} = \lim_{K\to\infty}\sum_{k=0}^{K} b^{(i)}_{2k}, \qquad \text{for} \qquad i=1,4, \tag{5.200}$$

where series terms are given by

$$\left.\begin{aligned} a^{(i)}_k &= \int_{x_k}^{x_{k+2}} f(x)\mathcal{J}^{(i)}_{mn}(\alpha,\tau;x)dx, \\ b^{(i)}_k &= \int_{x_k}^{x_{k+2}} f(x)\mathcal{Y}^{(i)}_{mn}(\alpha,\tau;x)dx. \end{aligned}\right\}, \qquad \text{for} \qquad i=1,4. \tag{5.201}$$

Integrals involving $\mathcal{J}^{(i)}_{mn}$ and $\mathcal{Y}^{(i)}_{mn}$ for $i=2,3$ are expressed with sub-integrals considering the stationary point (x_s)

$$\begin{aligned} \mathcal{I}^{(i)}_{c,mn} &= \int_{x_c}^{x_0} f(x)\mathcal{J}^{(i)}_{mn}(\alpha,\tau;x)dx + S^{(i)}_c + R^{(i)}_{c,\infty} \qquad \text{for} \qquad i=2,3, \\ \mathcal{I}^{(i)}_{s,mn} &= \int_{x_c}^{x_0} f(x)\mathcal{Y}^{(i)}_{mn}(\alpha,\tau;x)dx + S^{(i)}_s + R^{(i)}_{s,\infty} \qquad \text{for} \qquad i=2,3, \end{aligned} \tag{5.202}$$

with the finite and infinite series summations

$$S^{(i)}_c = \sum_{k=0}^{l} a^{(i)}_{2k}, \qquad R^{(i)}_{c,\infty} = \lim_{K\to\infty}\sum_{k=0}^{K} a^{(i)}_{2(l+1)+2k} \qquad \text{for} \qquad i=2,3, \tag{5.203}$$

$$S^{(i)}_s = \sum_{k=0}^{l} b^{(i)}_{2k}, \qquad R^{(i)}_{s,\infty} = \lim_{K\to\infty}\sum_{k=0}^{K} b^{(i)}_{2(l+1)+2k} \qquad \text{for} \qquad i=2,3. \tag{5.204}$$

where series terms are given by

$$\left.\begin{aligned} a^{(i)}_k &= \int_{x_k}^{x_{k+2}} f(x)\mathcal{J}^{(i)}_{mn}(\alpha,\tau;x)dx \\ b^{(i)}_k &= \int_{x_k}^{x_{k+2}} f(x)\mathcal{Y}^{(i)}_{mn}(\alpha,\tau;x)dx \end{aligned}\right\}, \qquad \text{for} \qquad i=2,3. \tag{5.205}$$

The summation index l is chosen in order to have $x_l > x_c$. The infinite series summations $R^{(i)}_{c;\infty}$ and $R^{(i)}_{s;\infty}$ are split into

$$R^{(i)}_{c;\infty}(j) = \sum_{k=0}^{j} a^{(i)}_{2k} + \sum_{k=j+1}^{\infty} a^{(i)}_{2k}, \qquad i=1,2,3,4, \tag{5.206}$$

$$R^{(i)}_{s;\infty}(j) = \sum_{k=0}^{j} b^{(i)}_{2k} + \sum_{k=j+1}^{\infty} b^{(i)}_{2k}, \qquad i=1,2,3,4. \tag{5.207}$$

where the right-hand-sided terms $\sum_{k=j+1}^{\infty} a_{2k}^{(i)}$ and $\sum_{k=j+1}^{\infty} b_{2k}^{(i)}$ are able to be extrapolated with successive series terms $a_{2k}^{(i)}$ and $b_{2k}^{(i)}$ by using ϵ-algorithm (Wynn, 1956). The ϵ-algorithm extrapolates the infinite series summation with a polynomial multiplied by a decaying exponential. The following error criterion with a successive increment of j is used to obtain the integral with desired accuracy(ϵ_I)

$$1-\epsilon_I \le \frac{R_{c,s;\infty}^{(i)}(j)}{R_{c,s;\infty}^{(i)}(j-2)} \le 1+\epsilon_I, \quad \text{and} \quad 1-\epsilon_I \le \frac{R_{c,s;\infty}^{(i)}(j)}{R_{c,s;\infty}^{(i)}(j-1)} \le 1+\epsilon_I, \quad j \ge 2. \tag{5.208}$$

The integration procedures of oscillatory functions are depicted in figures 5.6 and 5.7. The series terms $a_{2k}^{(i)}$ and $b_{2k}^{(i)}$ are evalulated by sub-integrals having the integral interval from x_i to x_{i+2}. With the successive move of sub-integration, the extrapolation errors shall be reduced. The starting points of extrapolation depend on the oscillatory functions.

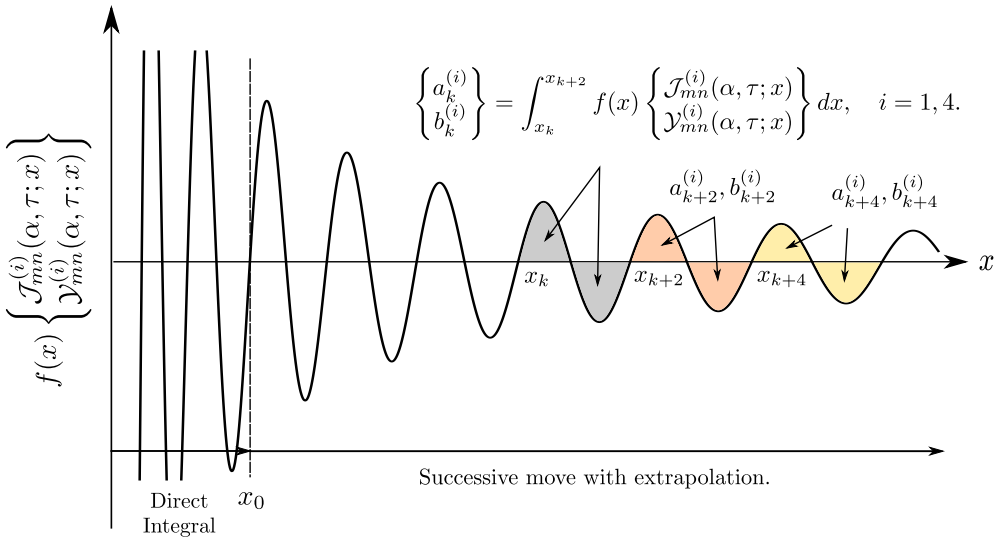

Figure 5.6. The evaluation procedure of semi-infinite integral involving $\mathcal{J}_{mn}^{(i)}$ and $\mathcal{Y}_{mn}^{(i)}$ for $i=1,4$.

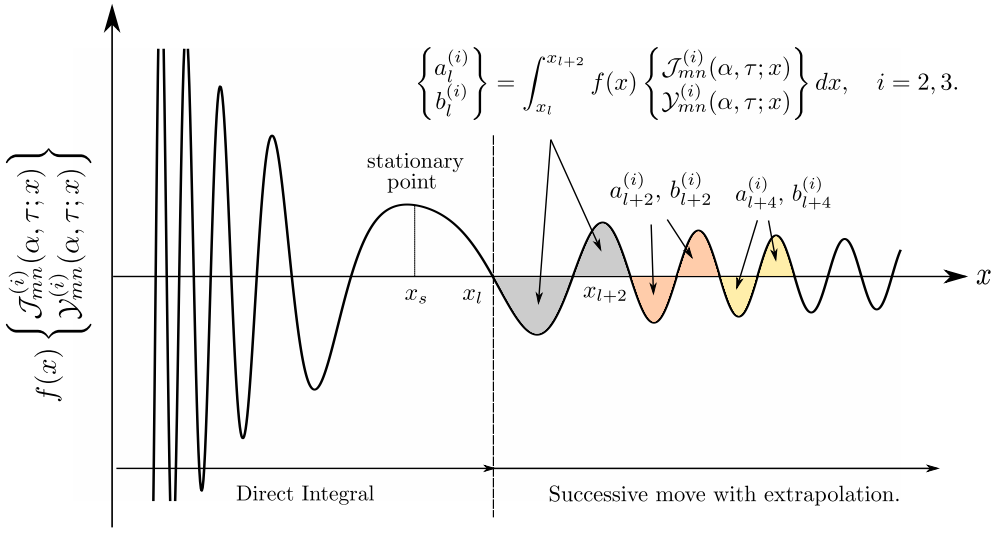

Figure 5.7. The evaluation procedure of semi-infinite integral involving $\mathcal{J}_{mn}^{(i)}$ and $\mathcal{Y}_{mn}^{(i)}$ for $i=2,3$.

Two benchmark functions, which have highly oscillatories but slowly decaying behaviors, are tested with extrapolation. The results are given in Tables 5.1 and 5.2.

Table 5.1. Evaluated integral values of benchmark function 1 with extrapolation algorithm

Integral	Direct integral (with zeros)	Integral with extrapolation	Error(%)
$\int_0^\infty e^{-0.01x} J_0(3x) J_0(x) \cos 10\sqrt{x} dx$	1.249865×10^{-1}	1.249862×10^{-1}	-0.00024
$\int_0^\infty e^{-0.01x} J_0(3x) J_0(x) \sin 10\sqrt{x} dx$	2.209661×10^{-2}	2.209660×10^{-2}	-0.00005
Computation time	0.084 s	0.044 s	-

Table 5.2. Evaluated integral values of benchmark function 2 with extrapolation algorithm

Integral	Direct integral (with zeros)	Integral with extrapolation	Error(%)
$\int_0^\infty x e^{-0.01x} J_0(3x) J_0(x) \cos 10\sqrt{x} dx$	4.828753×10^{-1}	4.828750×10^{-1}	-0.00006
$\int_0^\infty x e^{-0.01x} J_0(3x) J_0(x) \sin 10\sqrt{x} dx$	-2.588788×10^{-2}	-2.588785×10^{-2}	-0.00012
Computation time	0.176 s	0.068 s	-

The relative errors of integral values evaluated by using extrapolation are calculated with the reference integral values. The reference integral values are calculated by numerical quadrature without extrapolation. An absolute integral error criterion of 10^{-9} is used for calculating reference integral values. The relative errors for benchmark test functions are less than $2.4 \times 10^{-4}\%$. Note that the relative errors can be further reduced by adjusting the desired accuracy (ϵ_I) in equation 5.208.

The results show that the evaluated semi-infinite integral with extrapolation gives good results and the computation is accelerated. It is more evident when $f(x)$ has a slowly decaying behavior. It must be noticed that the numerical algorithm with split oscillatory functions can be applicable for an arbitrary but monotonic behavior function. The numerical algorithm is able to be used by selecting the starting point of extrapolation for functions having monotonic behaviours for large x.

5.6.5 Evaluation of semi-infinite integral by steepest descent method

An alternative way of evaluating the semi-infinite integrals based on the steepest descent method has been suggested (Chen and Li, 2019; Li et al., 2019a). The integrands in equation (5.151) have highly oscillatory behaviours when the variable τ is large (Li and Chen, 2018). The computational time of algorithm based on split oscillatory functions for large τ is slightly longer than the case of small τ. The procedure proposed by Chen and Li (2019); Li et al. (2019a) is summarized in this section.

The semi-infinite integral of two Bessel functions multiplied by sinusoidal functions given in equation (5.151) are wirtten again

$$\mathcal{I}^{\infty}_{c,mn}(\alpha,\tau) = \int_{x_c}^{\infty} f(x) J_m(\alpha x) J_n(x) \cos\tau\sqrt{x} dx,$$
$$\mathcal{I}^{\infty}_{s,mn}(\alpha,\tau) = \int_{x_c}^{\infty} f(x) J_m(\alpha x) J_n(x) \sin\tau\sqrt{x} dx.$$

Introducing the complex integral

$$\mathcal{I}^{\infty}_{mn}(\alpha;t) = \mathcal{I}^{\infty}_{c,mn}(\alpha;t) - \mathrm{i}\mathcal{I}^{\infty}_{s,mn}(\alpha;t) = \int_{x_c}^{\infty} f(x) J_m(\alpha x) J_n(x) e^{-\mathrm{i}\tau\sqrt{x}} dx, \tag{5.209}$$

and the relationship between Hankel and Bessel functions

$$J_m(\alpha x) = \frac{1}{2}\left[H^{(1)}_m(\alpha x) + H^{(2)}_m(\alpha x)\right], \qquad J_n(x) = \frac{1}{2}\left[H^{(1)}_n(x) + H^{(2)}_n(x)\right], \tag{5.210}$$

let us obtain for the integrand

$$\begin{aligned}\mathcal{I}^{\infty}_{mn}(\alpha;\tau) = \frac{1}{4}\int_{x_c}^{\infty} f(x) \Big[& H^{(1)}_m(\alpha x) H^{(1)}_n(x) + H^{(2)}_m(\alpha x) H^{(1)}_n(x) \\ & + H^{(1)}_m(\alpha x) H^{(2)}_n(x) + H^{(2)}_m(\alpha x) H^{(2)}_n(x) \Big] e^{-\mathrm{i}\tau\sqrt{x}} dx.\end{aligned} \tag{5.211}$$

The oscillatory parts of Hankel functions can be decomposed from asymptotic forms of Hankel function as (Abramowitz and Stegun, 1965)

$$H^{(1)}_m(\alpha x) = \hat{H}^{(1)}_m e^{\mathrm{i}\alpha x}, \qquad H^{(2)}_m(\alpha x) = \hat{H}^{(2)}_m e^{-\mathrm{i}\alpha x}, \tag{5.212}$$
$$H^{(1)}_m(x) = \hat{H}^{(1)}_m e^{\mathrm{i}x}, \qquad H^{(2)}_m(x) = \hat{H}^{(2)}_m e^{-\mathrm{i}x}. \tag{5.213}$$

where $\hat{H}^{(1)}_m$ and $\hat{H}^{(2)}_m$ are the amplitude functions of Hankel functions. And the exponential terms corrspond to oscillatory parts of Hankel functions. Using the above equations, the semi-infinite integral can be decomposed into four integrals

$$\mathcal{I}^{\infty}_{mn}(\alpha;\tau) = \mathcal{I}^{\infty,A}_{mn}(\alpha;\tau) + \mathcal{I}^{\infty,B}_{mn}(\alpha;\tau) + \mathcal{I}^{\infty,C}_{mn}(\alpha;\tau) + \mathcal{I}^{\infty,D}_{mn}(\alpha;\tau), \tag{5.214}$$

with

$$\mathcal{I}^{\infty,A}_{mn}(\alpha;\tau) = \int_{x_c}^{\infty} f(x) \hat{H}^{(1)}_m(\alpha x) \hat{H}^{(1)}_n(x) e^{\mathrm{i}\left[(\alpha+1)x - \tau\sqrt{x}\right]} dx, \tag{5.215}$$

$$\mathcal{I}^{\infty,B}_{mn}(\alpha;\tau) = \int_{x_c}^{\infty} f(x) \hat{H}^{(1)}_m(\alpha x) \hat{H}^{(2)}_n(x) e^{\mathrm{i}\left[(\alpha-1)x - \tau\sqrt{x}\right]} dx, \tag{5.216}$$

$$\mathcal{I}^{\infty,C}_{mn}(\alpha;\tau) = \int_{x_c}^{\infty} f(x) \hat{H}^{(2)}_m(\alpha x) \hat{H}^{(1)}_n(x) e^{\mathrm{i}\left[-(\alpha-1)x - \tau\sqrt{x}\right]} dx, \tag{5.217}$$

$$\mathcal{I}^{\infty,D}_{mn}(\alpha;\tau) = \int_{x_c}^{\infty} f(x) \hat{H}^{(2)}_m(\alpha x) \hat{H}^{(2)}_n(x) e^{\mathrm{i}\left[-(\alpha+1)x - \tau\sqrt{x}\right]} dx. \tag{5.218}$$

The integrals are further simplified as

$$\mathcal{I}^{\infty,A}(\alpha^+;\tau) = \int_{x_c}^{\infty} f^A(x) e^{\mathrm{i}\left[\alpha^+ x - \tau\sqrt{x}\right]} dx, \qquad \mathcal{I}^{\infty,B}(\alpha^-;\tau) = \int_{x_c}^{\infty} f^B(x) e^{\mathrm{i}\left[\alpha^- x - \tau\sqrt{x}\right]} dx, \tag{5.219}$$

$$\mathcal{I}^{\infty,C}(\alpha^-;\tau) = \int_{x_c}^{\infty} f^C(x) e^{-\mathrm{i}\left[\alpha^- x + \tau\sqrt{x}\right]} dx, \quad \mathcal{I}^{\infty,D}(\alpha^+;\tau) = \int_{x_c}^{\infty} f^D(x) e^{-\mathrm{i}\left[\alpha^+ x + \tau\sqrt{x}\right]} dx, \tag{5.220}$$

with

$$f^A(x) = f(x)\hat{H}_m^{(1)}(\left[\alpha^+ - 1\right]x)\hat{H}_n^{(1)}(x), \qquad f^B(x) = f(x)\hat{H}_m^{(1)}(\left[\alpha^- + 1\right]x)\hat{H}_n^{(2)}(x) \tag{5.221}$$

$$f^C(x) = f(x)\hat{H}_m^{(2)}(\left[\alpha^- + 1\right]x)\hat{H}_n^{(1)}(x), \qquad f^D(x) = f(x)\hat{H}_m^{(2)}(\left[\alpha^+ - 1\right]x)\hat{H}_n^{(2)}(x) \tag{5.222}$$

where parameters $\alpha^\pm = \alpha \pm 1$ are used. The exponential terms in integrands have phase functions similar to ϑ in equation (5.176). Function $f(x)$ is multiplied by amplitude functions of Hankel functions $\hat{H}_m^{(1)}(x)$ and $\hat{H}_m^{(2)}(x)$. Because the amplitude functions $\hat{H}_m^{(1)}(x)$ and $\hat{H}_m^{(2)}(x)$ are smoothly changing with respect to $x > 0$, the functions f^A, f^B, f^C and f^D have smooth behaviors. The oscillatory phase function in exponential term is transformed into

$$\alpha^\pm x \pm \tau\sqrt{x} = \left[x\left(\frac{2\alpha^\pm}{\tau}\right)^2 \pm 2\sqrt{x}\left(\frac{2\alpha^\pm}{\tau}\right) + 1\right]\left(\frac{\tau^2}{4\alpha^\pm}\right) - \left(\frac{\tau^2}{4\alpha^\pm}\right). \tag{5.223}$$

Introducing the integral variable

$$u = \sqrt{x}\left(\frac{2\alpha^\pm}{\tau}\right), \quad \text{or inversely} \quad x = \frac{1}{4}\left(\frac{u\tau}{\alpha^\pm}\right)^2, \tag{5.224}$$

the semi-infinite integrals are given by

$$\mathcal{I}^{\infty,A} = e^{-i\tau^+}\int_{u_c^+}^{\infty} g^A(u) e^{\mathrm{i}\tau^+(u-1)^2} du, \qquad \mathcal{I}^{\infty,B} = e^{-i\tau^-}\int_{u_c^-}^{\infty} g^B(u) e^{\mathrm{i}\tau^-(u-1)^2} du, \tag{5.225}$$

$$\mathcal{I}^{\infty,C} = e^{i\tau^-}\int_{u_c^-}^{\infty} g^C(u) e^{-\mathrm{i}\tau^-(u+1)^2} du, \qquad \mathcal{I}^{\infty,D} = e^{i\tau^+}\int_{u_c^+}^{\infty} g^D(u) e^{-\mathrm{i}\tau^+(u+1)^2} du, \tag{5.226}$$

with smoothly behaving functions

$$g^A(u) = f^A\left(\frac{u^2\tau^+}{\alpha^+}\right)\frac{2u\tau^+}{\alpha^+}, \qquad g^B(u) = f^B\left(\frac{u^2\tau^-}{\alpha^-}\right)\frac{2u\tau^-}{\alpha^-}, \tag{5.227}$$

$$g^C(u) = f^C\left(\frac{u^2\tau^-}{\alpha^-}\right)\frac{2u\tau^-}{\alpha^-}, \qquad g^D(u) = f^D\left(\frac{u^2\tau^+}{\alpha^+}\right)\frac{2u\tau^+}{\alpha^+}. \tag{5.228}$$

The integral parameters are given by

$$u_c^\pm = \sqrt{x_c}\frac{2\alpha^\pm}{\tau} > 0, \qquad \tau^\pm = \frac{\tau^2}{4\alpha^\pm} \geq 0. \tag{5.229}$$

Therefore, the four different integrals fall into two types of integral given by

$$\mathcal{I}^I = \int_{u_c}^{\infty} g(u) e^{-\mathrm{i}\kappa(u+1)^2} du, \tag{5.230}$$

$$\mathcal{I}^{II} = \int_{u_c}^{\infty} g(u) e^{\mathrm{i}\kappa(u-1)^2} du. \tag{5.231}$$

Evaluation of the second integral type is separated into

$$\mathcal{I}^{II} = \begin{cases} \mathcal{I}_0^{II}, & \text{when} \quad u_c \geq 1, \\ \mathcal{I}_0^{II} + \mathcal{I}^{III}, & \text{when} \quad u_c < 1, \end{cases} \tag{5.232}$$

with

$$\mathcal{I}_0^{II} = \int_{u_c}^{\infty} g(u) e^{\mathrm{i}\kappa(u-1)^2} du, \qquad u_c \geq 1, \tag{5.233}$$

$$\mathcal{I}^{III} = \int_{u_c}^{1} g(u) e^{\mathrm{i}\kappa(u-1)^2} du, \qquad u_c < 1. \tag{5.234}$$

Integral type I in the complex plane

The integral type I is given in equation (5.230) as

$$\mathcal{I}^{I} = \int_{u_c}^{\infty} g(u) e^{-\mathrm{i}\kappa(u+1)^2} du$$

Applying the change of integral variable, $w = (u+1)^2$, this integral is transformed into

$$\mathcal{I}^{I} = \int_{w_c^+}^{\infty} \frac{g\left(\sqrt{w}-1\right)}{2\sqrt{w}} e^{-\mathrm{i}\kappa w} dw \tag{5.235}$$

with a lower bound, $w_c^+ = (u_c+1)^2$. The closed contour integral of integral type I is shown in figure 5.8. The integrand does not have singularity inside of closed contour, the integral along closed contour given by using Cauchy theorem as

$$\mathcal{I}^{I} + \mathcal{I}_{\infty}^{I} + \mathcal{I}_{i}^{I} = 0. \tag{5.236}$$

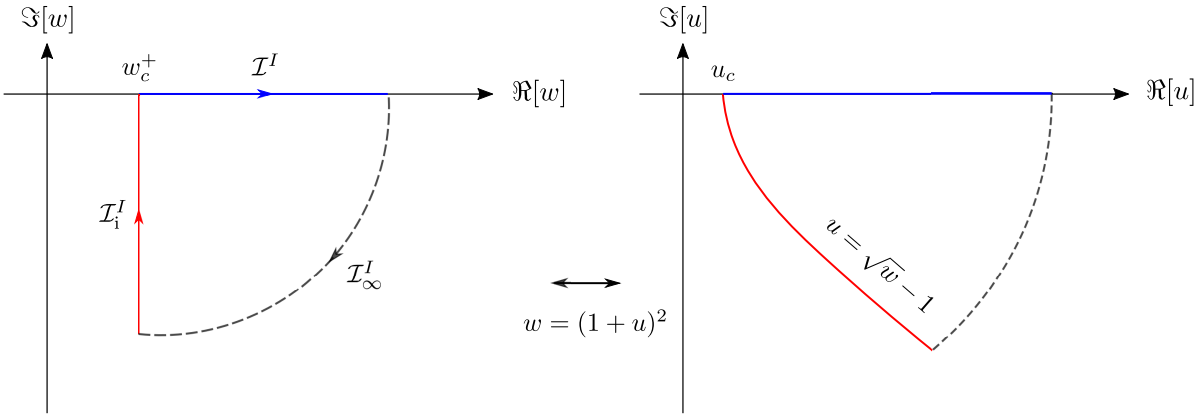

Figure 5.8. Closed contour I integration path in complex w-plane and mapped integration path in complex u-plane.

The infinite integral $\mathcal{I}_{\infty}^{I}$ can be written as

$$\begin{aligned} \mathcal{I}_{\infty}^{I} &= \lim_{\rho\to\infty} \int_0^{\theta_c} \frac{g\left(\sqrt{\rho e^{\mathrm{i}\theta}}-1\right)}{2\sqrt{\rho e^{\mathrm{i}\theta}}} e^{-\mathrm{i}\kappa\rho e^{\mathrm{i}\theta}} \rho d\theta \\ &= \lim_{\rho\to\infty} \int_0^{\theta_c} \frac{g\left(\sqrt{\rho e^{\mathrm{i}\theta}}-1\right)}{2\sqrt{\rho e^{\mathrm{i}\theta}}} e^{-\mathrm{i}\kappa\rho\cos\theta} e^{\kappa\rho\sin\theta} \rho d\theta \end{aligned} \tag{5.237}$$

where the complex variable $w = \rho e^{\mathrm{i}\theta}$ is used. θ_c is integral bound will be discussed soon. The above integral is zero when the real part of exponential function is negative from Jordan's Lemma (Brown and Churchill, 2004). Because κ and ρ are positive, $\sin\theta$ should be negative, in other words, θ should be in range $\theta \in [-\frac{\pi}{2}, 0]$ to make $\mathcal{I}^I_\infty$ be zero. Consequently, the closed contour passes through quadrant 4 of the complex w plane.

The steepest descent path is determined by putting the imaginary part of integrand in equation (5.237) as zero. Therefore, the integral path of $\mathcal{I}^I_i$ is set to be $\theta_c = -\frac{\pi}{2}$.

Using Cauchy's theorem in equation (5.236), the integral along real w axis can be evaluated by steepest descent method as

$$\mathcal{I}^I = -\mathcal{I}^I_i = -e^{-\mathrm{i}\kappa w_c^+}\frac{\mathrm{i}}{2}\int_0^\infty \frac{g\left(\sqrt{w_c^+ - \mathrm{i}w} - 1\right)}{\sqrt{w_c^+ - \mathrm{i}w}} e^{-\kappa w} dw \tag{5.238}$$

The semi-infinite integral involves the exponential factor, $e^{-\kappa w}$, the numerical evaluation of above integral is straightforward and converges fastly for large κ, where κ is proportional to $\frac{\tau^2}{\alpha^2}$.

Integral type II in the complex plane

The second integral type with lower integral bound $u_c \geq 1$ is given in equation (5.230) as

$$\mathcal{I}^{II}_0 = \int_{u_c}^\infty g(u) e^{\mathrm{i}\kappa(u-1)^2} du.$$

Applying the change of variable, $w = (u-1)^2$, this integral is transformed into the following form

$$\mathcal{I}^{II}_0 = \int_{w_c}^\infty \frac{g(\sqrt{w}+1)}{2\sqrt{w}} e^{\mathrm{i}\kappa w} dw \tag{5.239}$$

with lower integral bound $w_c^+ = (u_c - 1)^2$. The contour of integration path for second integral type is depicted in figure 5.9. There is no singularity inside closed contour, the integral along closed path is given by using Cauchy's theorem

$$\mathcal{I}^{II}_0 + \mathcal{I}^{II}_{0\infty} + \mathcal{I}^{II}_{0\mathrm{i}} = 0. \tag{5.240}$$

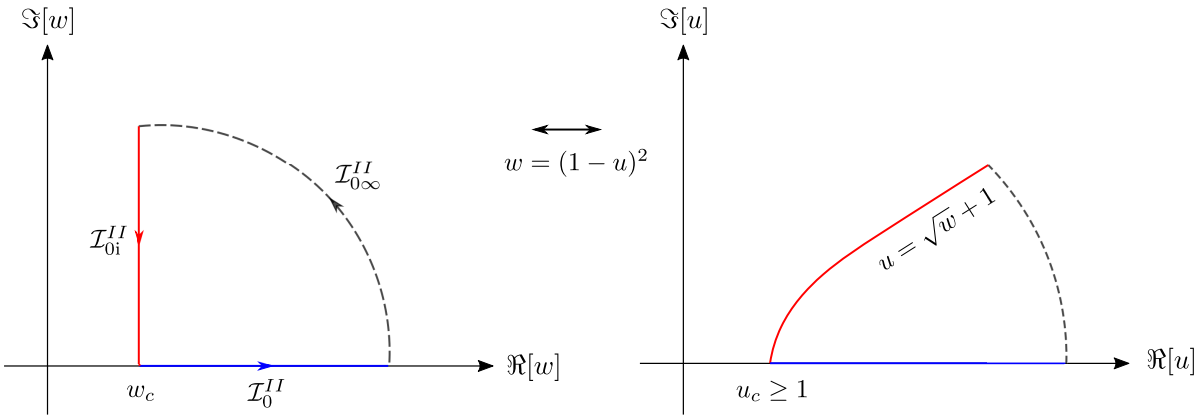

Figure 5.9. Closed contour II integration path in complex w-plane and mapped integration path in complex u-plane.

The integral $\mathcal{I}_{0\infty}^{II}$ can be expressed as

$$\begin{aligned}\mathcal{I}_{0\infty}^{II} &= \lim_{\rho\to\infty}\int_0^{\theta_c}\frac{g(\sqrt{\rho e^{\mathrm{i}\theta}}+1)}{2\sqrt{\rho e^{\mathrm{i}\theta}}}e^{\mathrm{i}\kappa(\rho e^{\mathrm{i}\theta})}\rho d\theta \\ &= \lim_{\rho\to\infty}\int_0^{\theta_c}\frac{g(\sqrt{\rho e^{\mathrm{i}\theta}}+1)}{2\sqrt{\rho e^{\mathrm{i}\theta}}}e^{\mathrm{i}\kappa\rho\cos\theta}e^{-\kappa\rho\sin\theta}\rho d\theta.\end{aligned} \tag{5.241}$$

where the complex variable $w = \rho e^{\mathrm{i}\theta}$ is used. The above integral is zero when the real part of exponential argument is negative. Therefore, θ should be in range $\theta \in [0, \frac{\pi}{2}]$ to make the integral be zero by using Jordan's Lemma. The steepest descent path is determined by making the imaginary part of exponential argument in above integrand to be zero, e.g. $\theta_c = \frac{\pi}{2}$.

The integration along real w-axis can be given by using Cauchy's theorem in equation (5.240) as

$$\mathcal{I}_0^{II} = -\mathcal{I}_{0\mathrm{i}}^{II} = e^{\mathrm{i}\kappa w_c}\frac{\mathrm{i}}{2}\int_0^{\infty}\frac{g(\sqrt{w_c+\mathrm{i}w}+1)}{\sqrt{w_1+\mathrm{i}w}}e^{-\kappa w}dw. \tag{5.242}$$

Integral type III in the complex plane

A supplementary integral is necessary when the lower integration bound u_c is lower than 1 for integral type II. The integral type III is given in equation (5.234) as

$$\mathcal{I}^{III} = \int_{u_c}^{1} g(u)e^{\mathrm{i}\kappa(u-1)^2}du$$

Applying the change of variable, $w = (u-1)^2$, the integral is transformed into

$$\mathcal{I}^{III} = \int_{w_c^-}^{0}\left(-\frac{g(1-\sqrt{w})}{2\sqrt{w}}\right)e^{\mathrm{i}\kappa w}dw \tag{5.243}$$

with lower bound $w_c^- = (u_c-1)^2$.The contour integration path is depicted in figure 5.10. No singularity is located inside the closed integration path, then the integral along closed path can be given as the below:

$$\mathcal{I}^{III} + \mathcal{I}_{\mathrm{i}0}^{III} + \mathcal{I}_{\infty}^{III} + \mathcal{I}_{\mathrm{i}1}^{III} = 0. \tag{5.244}$$

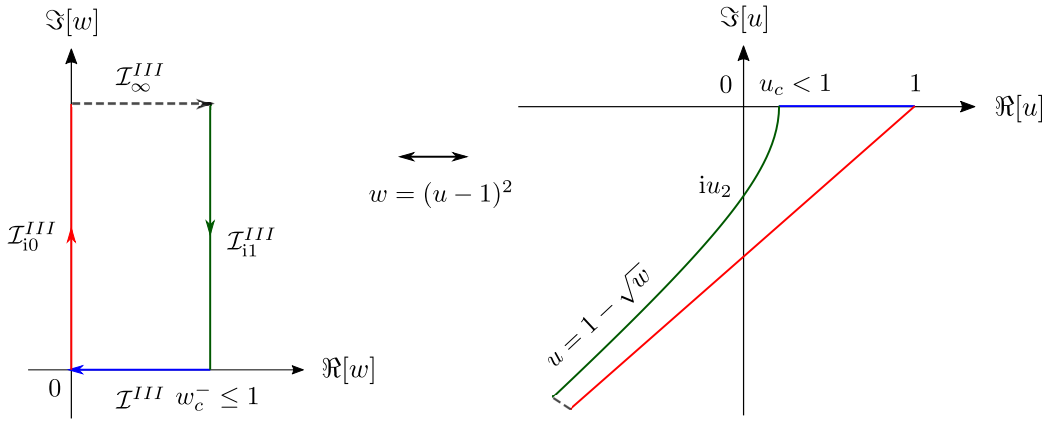

Figure 5.10. Closed contour III integration path in complex w-plane and mapped integration path in complex u-plane.

where the integration $\mathcal{I}_{\infty}^{III}$ can be expressed as

$$\begin{aligned}\mathcal{I}_{\infty}^{III} &= \lim_{w_I\to\infty}\int_0^{w_c^-}\left(-\frac{g(1-\sqrt{w+\mathrm{i}w_I})}{2\sqrt{w+\mathrm{i}w_I}}\right)e^{\mathrm{i}\kappa(w+\mathrm{i}w_I)}dw \\ &= \lim_{w_I\to\infty}\int_0^{w_c^-}\left(-\frac{g(1-\sqrt{w+\mathrm{i}w_I})}{2\sqrt{w+\mathrm{i}w_I}}\right)e^{\mathrm{i}\kappa w}e^{-\kappa w_I}dw.\end{aligned} \tag{5.245}$$

The real part of exponential function in above integral should be negative to make the integral zero. Therefore, w_I should be positive. When w_I is positive infinity, above integral is zero by using Jordan's Lemma. Two integrals along vertical paths are given by

$$\mathcal{I}_{\mathrm{i}0}^{III} = -\frac{\mathrm{i}}{2}\int_0^{\infty}\frac{g\left(1-\sqrt{\mathrm{i}w}\right)}{\sqrt{\mathrm{i}w}}e^{-\kappa w}dw, \tag{5.246}$$

and

$$\mathcal{I}_{\mathrm{i}1}^{III} = e^{\mathrm{i}\kappa w_c^-}\frac{\mathrm{i}}{2}\int_0^{\infty}\frac{g\left(1-\sqrt{w_c^-+\mathrm{i}w}\right)}{\sqrt{w_c^-+\mathrm{i}w}}e^{-\kappa w}dw. \tag{5.247}$$

Therefore, the integration along the real w axis can be calculated by evaluating two integrals along the vertical axis

$$\mathcal{I}^{III} = \frac{\mathrm{i}}{2}\int_0^{\infty}\frac{g\left(1-\sqrt{\mathrm{i}w}\right)}{\sqrt{\mathrm{i}w}}e^{-\kappa w}dw - e^{\mathrm{i}\kappa w_c^-}\frac{\mathrm{i}}{2}\int_0^{\infty}\frac{g\left(1-\sqrt{w_c^-+\mathrm{i}w}\right)}{\sqrt{w_c^-+\mathrm{i}w}}e^{-\kappa w}dw. \tag{5.248}$$

It must be noticed that the contour integrations along the vertical axis are introduced to provide the complete sets of steepest descent method evaluating oscillatory functions. The integration interval for integral type III is defined along the real axis w, and it is finite from w_c^- to 1. There is no numerical difficulty to evaluate the integral type III along real axis w. In the present study, the numerical quadrature is directly applied on equation (5.243) instead of evaluating two semi-infinite integrals though they involve exponential factors in the integrands.

Choice of lower integral bound x_c

Functions $g^A(u)$, $g^B(u)$, $g^C(u)$, $g^D(u)$ defined in equations (5.227) and 5.228 can be expressed by

$$g^T(u) = f^T\left(\frac{u^2\tau^*}{\alpha^*}\right)\frac{2u\tau^*}{\alpha^*}, \qquad T = A, B, C, D. \tag{5.249}$$

with functions $f^T(x)$ can be expressed as

$$f^T(x) = f(x)\,\hat{H}_m^{(i)}\left([\alpha^*\pm 1]x\right)\hat{H}_m^{(j)}(x), \qquad i, j = 1 \text{ or } 2. \tag{5.250}$$

where the change of variable $x = \frac{1}{4}\left(\frac{u\tau}{\alpha^*}\right)^2$ is used. The original function $f(x)$ is given in equation 5.140 as

$$f(x) = x^p\frac{(x-\sigma)^q}{(x+\sigma)^r}. \tag{5.251}$$

Therefore, the functions $g^T(u)$ can be expressed in the forms below with denominator

$$g^T(u) = \frac{h^T(u)}{\left(\frac{1}{4}\frac{u^2\tau^2}{\alpha^2}+\sigma\right)^r} \tag{5.252}$$

where $h^T(u)$ corresponds to the terms related to the nominator of original function $f(x)$, two Hankel funtions and change of variable.

Functions $g^T(u)$ are singular when the denominator is equal to zero. Therefore, the poles are given by:

$$u = \mathrm{i}u_p^{\pm}, \qquad \text{with} \qquad u_p^{\pm} = \pm\frac{2\alpha\sqrt{\sigma}}{\tau}. \tag{5.253}$$

The poles $u = \mathrm{i}u_p^{\pm}$ locate outside of contour integrals I and II, but $u = \mathrm{i}u_p^{-}$ can be located inside the contour integral III depicted in figure 5.10. Value of u_2 is given by mapping function

$$\mathrm{i}u_2 = 1 - \sqrt{w_c^- + \mathrm{i}w}. \tag{5.254}$$

Splitting real and imaginary parts gives the relationship

$$w_c^- = 1 - u_2^2, \qquad \text{and} \qquad w = -2u_2. \tag{5.255}$$

Introducing $w_c^- = (1 - u_c)^2$, the location of pole is obtained as

$$u_2 = -\sqrt{u_c(2 - u_c)}. \tag{5.256}$$

To construct a closed contour integration without pole inside, we use the fact that u_2 satisfies $u_p^- > u_2$. With the relation $u_p^- = -u_c\sqrt{\frac{\sigma}{x_c}}$ the criterion of lower integral bound is given by

$$x_c > \sigma\left(\frac{u_c}{2 - u_c}\right). \tag{5.257}$$

The lower integral bound $x_c = \sigma\left(\frac{u_c}{2-u_c}\right)$ is a motononically increasing function for $0 < u_c \leq 1$ and has a maximum value of 1 when $u_c = 1$. It provides a choice of $x_c > \sigma$. Futhermore, integrals involving Hankel functions $H_m^{(1)}(z) = J_m(z) + \mathrm{i}Y_m(z)$, $H_m^{(2)}(z) = J_m(z) - \mathrm{i}Y_m(z)$ provide the criterion for the lower integral bound due to singular behavior of $Y_m(z)$ near $z = 0$. Therefore, the lower integration bound is selected by

$$x_c = \max\left(\sigma, \max\left(\frac{y_{m,1}}{\alpha}, y_{n,1}\right)\right). \tag{5.258}$$

where $y_{m,1}$ is the approximated first zero of $Y_m(z)$ given in equation (5.194).

5.6.6 Remarks on elementary functions

The numerical evaluation of elementary function proposed in the present study is based on direct numerical quadrature. The computation algorithm could be optimized by constructing sets of approximation functions with decomposed regions, which are commonly used for the evaluation of wave Green function in linear potential codes (Chen, 2004; Lee, 1995; Babarit and Delhommeau, 2015).

It is presumed that the ODEs of time domain Green function may help to evaluate the elementary functions. Furthermore, it probably can accelerate for computation of convolution integrals.

The ODE for wave term of time domain Green function in spatial and time variable is given by (Clément, 1998)

$$\left(R^2+Z^2\right)\frac{\partial^4 H_\tau}{\partial\tau^4}-Z\tau\frac{\partial^3 H_\tau}{\partial\tau^3}+\left(\frac{1}{4}\tau^2-4Z\right)\frac{\partial^2 H_\tau}{\partial\tau^2}+\frac{7}{4}\tau\frac{\partial^3 H_\tau}{\partial\tau^3}+\frac{9}{4}H_\tau=0. \tag{5.259}$$

When the field points are not on the matching surface($R^2+Z^2>0$)

$$\frac{\partial^4 H_\tau}{\partial\tau^4}+\frac{\tau}{2}\frac{\mathcal{U}}{\mathcal{U}_Z}\frac{\partial^3 H_\tau}{\partial\tau^3}+\left(\frac{\tau^2}{4}\mathcal{U}+2\frac{\mathcal{U}}{\mathcal{U}_Z}\right)\frac{\partial^2 H_\tau}{\partial\tau^2}+\frac{7}{4}\tau\mathcal{U}\frac{\partial^3 H_\tau}{\partial\tau^3}+\frac{9}{4}\mathcal{U}H_\tau=0, \tag{5.260}$$

where $\mathcal{U}(R,Z)$ represent the square of source function

$$\mathcal{U}(R,Z)=\frac{1}{R^2+Z^2}. \tag{5.261}$$

If integrals over circular cylindrical surface with weight function on ODEs are evaluated analytically, ODEs for elementary functions can be derived. If ODEs and initial conditions for elementary functions are available, elementary functions can be evaluated by solving the ODEs rather than using the numerical quadrature. Furthermore, Clément (1998) suggested the idea that convolution integrals involving the Green function can be updated by simply integrating ODEs. If ODEs for elementary functions are derived, the convolution integrals involving the elementary functions given by

$$\int_{t_0}^{t} f(\tau)\mathcal{S}_{a,\theta';n,mp}(t-\tau)d\tau, \qquad \int_{t_0}^{t} f(\tau)\mathcal{F}_{a,\theta';n,p}(t-\tau)d\tau, \tag{5.262}$$

where $\mathcal{S}_{a,\theta';n,mp}(\tau)$ and $\mathcal{F}_{a,\theta';n,p}(\tau)$ are the elementary functions. If ODEs are available for elementary functions, the computation of convolution integrals can be accelerated, and a better accuracy is also expected for the convolution integral.

In the present study, the convolution integral is evaluated by direct summation with simulation time step.

5.6.7 Summary on the evaluation of elementary functions

Elementary functions having two Bessel functions and trigonometric function are defined by

$$\mathcal{I}_{c,mn}(\alpha;t)=\int_0^\infty f(x)J_m(\alpha x)J_n(x)\cos\tau\sqrt{x}dx,$$
$$\mathcal{I}_{s,mn}(\alpha;t)=\int_0^\infty f(x)J_m(\alpha x)J_n(x)\sin\tau\sqrt{x}dx.$$

They are evaluated by splitting the integral interval into several sub-integrals

$$\int_0^\infty\{\cdot\}\,dx=\int_0^{\frac{1}{4}}\{\cdot\}\,dx+\int_{\frac{1}{4}}^{x_c}\{\cdot\}\,dx+\int_{x_c}^\infty\{\cdot\}\,dx.$$

The first integral is transformed with the change of variable $u^2=x$ due to the highly oscillatory behavior near to origin, giving

$$\int_0^{\frac{1}{4}} f(x)J_m(\alpha x)J_n(x)\begin{Bmatrix}\cos\tau\sqrt{x}\\ \sin\tau\sqrt{x}\end{Bmatrix}dx=2\int_0^{\frac{1}{2}} uf(u^2)J_m(\alpha u^2)J_n(u^2)\begin{Bmatrix}\cos\tau u\\ \sin\tau u\end{Bmatrix}du.$$

The numerical quadrature is applied to evaluate above integral and the integral along intermediate interval from $\frac{1}{4}$ to x_c with discretization integral $\Delta u = \Delta x = \min\left(\frac{0.2\pi}{\max(\alpha+1,\tau+0.001)}, 0.05\right)$. The numerical quadrature used in present study is the 3-point adaptive Gaussian quadrature. Two numerical algorithms have been suggested for evaluation of semi-infinite integrals from x_c to infinity.

- **Split oscillatory functions**

  Irregularly oscillatory functions are split into interpretable oscillatory functions. Semi-infinite integrals of split functions are transformed into infinite summation of sub-integrals, which corresponds to finite integral between zeros. Infinite summation is extrapolated from finite summation of series with Wynn's ϵ-algorithm (Wynn, 1956).

- **Steepest descent method**

  Oscillatory functions are transformed into the complex plane. Using Jordan's Lemma, steepest descent paths are found for corresponding integrals. Integrals involve exponential factors having negative real arguments. The exponential factors having negative real arguments make the integrand decay to zero fastly. The implementation of numerical quadrature is straightforward due to this decaying behavior. The argument of exponential factor is proportional to τ^2/α^2, implying that numerical efficiency increases for large τ and/or small α.

In computational procedure of steepest descent method, transformed function into complex domain has its phase function:

$$\alpha^{\pm}x \pm \tau\sqrt{x} = \left[x\left(\frac{2\alpha^{\pm}}{\tau}\right)^2 \pm 2\sqrt{x}\left(\frac{2\alpha^{\pm}}{\tau}\right) + 1\right]\left(\frac{\tau^2}{4\alpha^{\pm}}\right) - \left(\frac{\tau^2}{4\alpha^{\pm}}\right),$$

It involves the denominator of τ. It makes the accuracy and efficiency of the steepest descent method being poor for small τ/α compared to the split oscillatory functions algorithm. Therefore, the following criterion is adopted to select algorithm evaluating semi-infinite integral

$$\begin{cases} \dfrac{\tau}{\alpha} < 0.4, & \text{Split oscillatory functions,} \\ \dfrac{\tau}{\alpha} \geq 0.4, & \text{Steepest descent method.} \end{cases} \tag{5.263}$$

Computed harmonic and waterline elementary functions with two numerical algorithms are shown in figures 5.11 and 5.12. The elementary functions are calculated by steepest descent method for $\dfrac{\tau}{\alpha} \geq 0.4$. The results from two numerical algorithms evaluating elementary functions are in good agreement with each other.

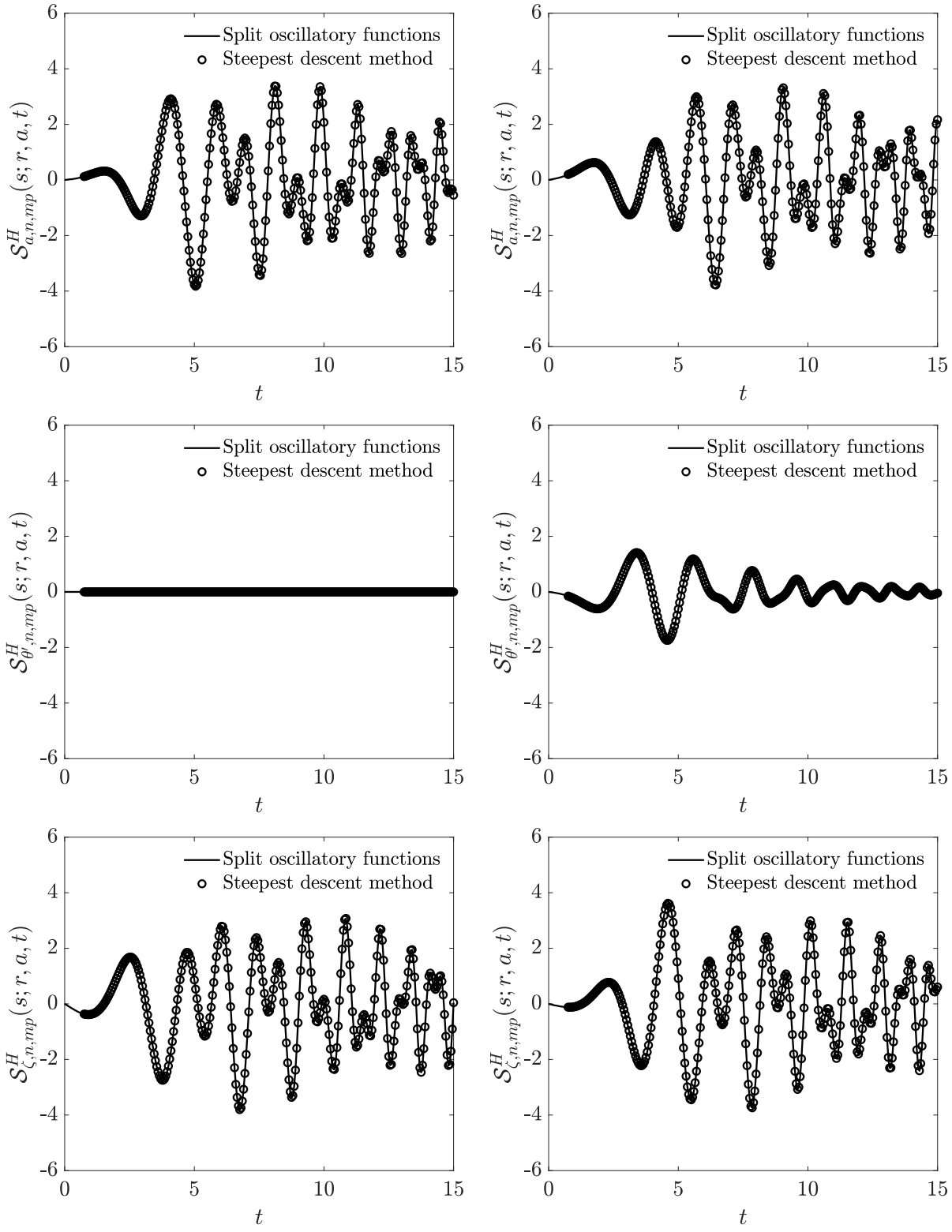

Figure 5.11. Computed harmonic elementary functions with two numerical algorithms, $r = 8.694, a = 2.5, s = 3.26, m + p = 0$, (left: $n = 0$, right: $n = 1$).

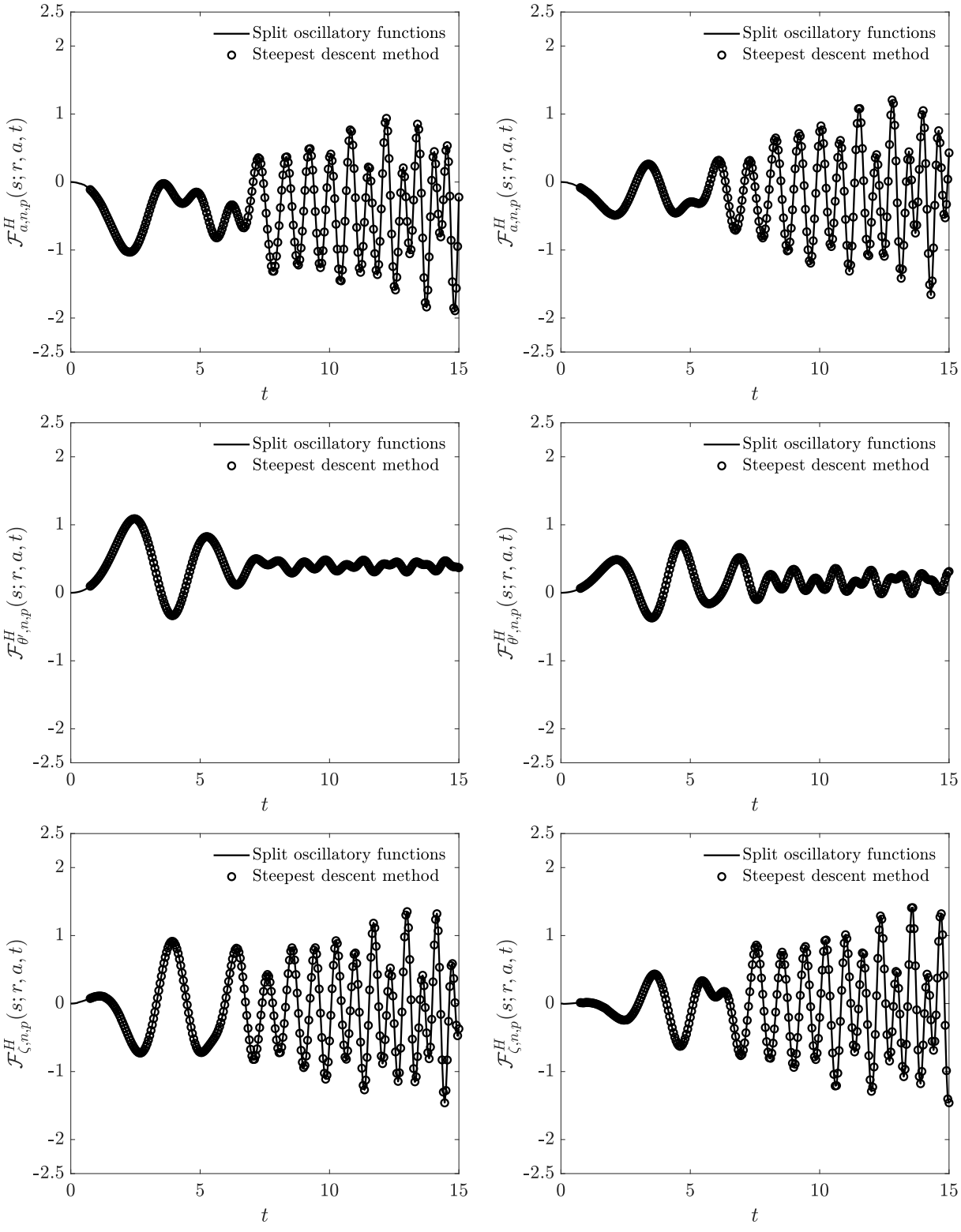

Figure 5.12. Computed waterline elementary functions with two numerical algorithms, $r = 8.694, a = 2.5, s = 3.26, p = 1$, (left: $n = 1$, right: $n = 2$).

5.7 Reconstruction of wave elevation and fluid velocity above the mean free surface

The complementary fluid velocity at the field point is calculated by equation (5.120). The complementary wave elevation can be computed using the kinematic free surface boundary condition by

$$\frac{\partial \Xi_C}{\partial t} = u_C^z(r,\theta,0;t) = \frac{1}{4\pi}\sum_{n=-N}^{N}\sum_{p=0}^{M}\mathcal{U}_{pn}^z e^{\mathrm{i}n\theta}, \tag{5.264}$$

A Crank-Nicolson scheme is applied to calculate the wave elevation for time integration. After the complementary wave elevation has been reconstructed, a pseudo-Wheeler stretching is applied on the Laguerre function for the extrapolation of velocity for $z > 0$ by using Laguerre function (Wheeler, 1970)

$$\begin{bmatrix} u_C^x \\ u_C^y \\ u_C^z \end{bmatrix} = \frac{1}{4\pi}\sum_{n=-N}^{N}\sum_{p=0}^{M}\begin{bmatrix} \mathcal{U}_{pn}^x \\ \mathcal{U}_{pn}^y \\ \mathcal{U}_{pn}^z \end{bmatrix} e^{\mathrm{i}n\theta}\mathcal{L}_p(-sz'), \tag{5.265}$$

with coordinates transformation similar to Wheeler stretching for deep water

$$z' = z - \Xi_C. \tag{5.266}$$

Laguerre functions for $z' > 0$ increase exponentially which give large fluid velocities in the air zone. Therefore the value of Laguerre functions is limited to 2 as follows:

$$\mathcal{L}_p(-sz') = \begin{cases} f_z^{limit} = 2, & \text{if} \quad \mathcal{L}_p(-sz') > 2, \\ \mathcal{L}_p(-sz'), & \text{otherwise.} \end{cases} \tag{5.267}$$

The behavior of Laguerre functions above the mean free surface is shown in figure 5.13.

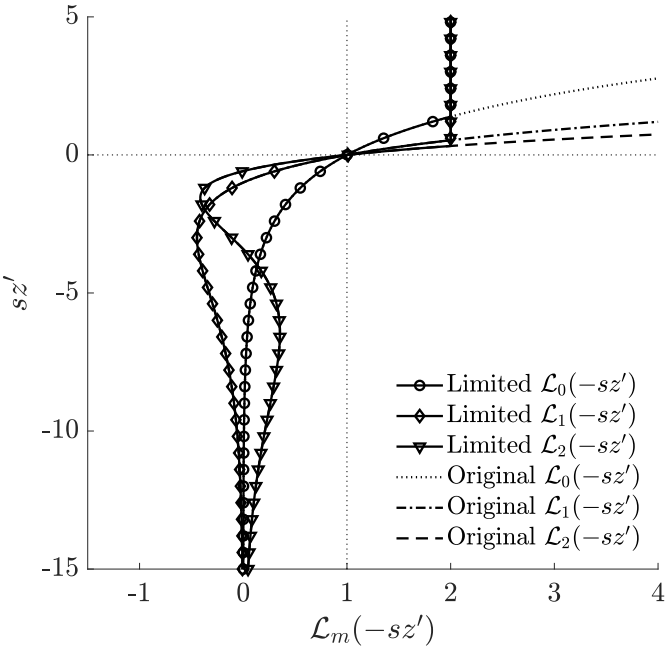

Figure 5.13. Behavior of Laguerre functions for $z' > 0$.

5.8 Reconstruction of complementary wave flow in viscous flow model

The proposed velocity representation with a vertical circular cylindrical matching surface is valid when the field point is located outside the matching surface, e.g., $r > a$. The evaluation of elementary functions and convolution integrals on the computational mesh of the viscous flow model are time-consuming tasks.

Instead of evaluating the flow components at each field point from elementary functions, A B-spline interpolation scheme on the structural grid can be used for calculating the complementary fluid velocity and wave elevation at arbitrary point. A cylindrical interpolation grid is introduced to construct complementary fluid velocity and wave elevation by using Poincaré's velocity representation.

The procedure of calculating complementary fluid velocity and wave elevation is depicted in figure 5.14. The complementary fluid velocities on the matching surface and wave elevations on the waterline of the matching surface are obtained. The complementary fluid velocities at the Gauss points are interpolated from complementary fluid velocities on the matching surface.

The Fourier-Laguerre coefficients of complementary fluid velocities in equation (5.29) are calculated by applying Fast Fourier Transform (FFT) and the integral along vertical axis ζ. Fourier coefficients of wave elevation in equation (5.32) are computed by using FFT. The coefficients are given by

$$\begin{bmatrix} \mathcal{C}^{\mathbf{n}}_{mn} \\ \mathcal{W}^{\xi}_{mn} \\ \mathcal{W}^{\eta}_{mn} \\ \mathcal{W}^{\zeta}_{mn} \end{bmatrix} = \frac{s}{2\pi} \int_0^{2\pi} \int_{-\infty}^{0} \begin{bmatrix} u^{\mathbf{n}}_C \\ w^{\xi}_C \\ w^{\eta}_C \\ w^{\zeta}_C \end{bmatrix}_{r=a} \mathcal{L}_m\left(-s\zeta\right) e^{-in\theta'} d\zeta d\theta'.$$

and

$$\mathcal{E}_n = \frac{1}{2\pi} \int_0^{2\pi} \left[g\Xi_C\right]_{r=a} e^{-in\theta'} d\theta'.$$

Fourier-Laguerre coefficients of complementary fluid velocity at field points are calculated by using Poincaré's velocity representation given in equation (5.121) as

$$\begin{aligned} \mathcal{U}^x_{pn} &= \mathcal{U}^{Rx}_{pn} + \mathcal{U}^{Rx*}_{pn} + \mathcal{U}^{Hx}_{pn} + \mathcal{U}^{Fx}_{pn}, \\ \mathcal{U}^y_{pn} &= \mathcal{U}^{Ry}_{pn} + \mathcal{U}^{Ry*}_{pn} + \mathcal{U}^{Hy}_{pn} + \mathcal{U}^{Fy}_{pn}, \\ \mathcal{U}^z_{pn} &= \mathcal{U}^{Rz}_{pn} + \mathcal{U}^{Rz*}_{pn} + \mathcal{U}^{Hz}_{pn} + \mathcal{U}^{Fz}_{pn}. \end{aligned}$$

The vertical component of complementary fluid velocity on the mean free surface is calculated by applying inverse Fourier-Laguerre series.

$$u^z_C(r,\theta,0;t) = \frac{1}{4\pi} \sum_{n=-N}^{N} \sum_{p=0}^{M} \mathcal{U}^z_{pn} e^{\mathrm{i}n\theta},$$

The complementary wave elevation is reconstructed from kinematic free surface boundary condition as

$$\Xi_C(r,\theta=0;t) = \int_0^t u^z_C(r,\theta,0;\tau) d\tau. \tag{5.268}$$

The complementary wave field is reconstructed by applying inverse FFT. The complementary fluid velocity on the interpolation grid is calculated by applying inverse Fourier-Laguerre series with pseudo Wheeler stretching as

$$\begin{bmatrix} u_C^x \\ u_C^y \\ u_C^z \end{bmatrix} = \frac{1}{4\pi} \sum_{n=-N}^{N} \sum_{p=0}^{M} \begin{bmatrix} \mathcal{U}_{pn}^x \\ \mathcal{U}_{pn}^y \\ \mathcal{U}_{pn}^z \end{bmatrix} e^{in\theta} \mathcal{L}_p(-sz'),$$

with $z' = z - \Xi_C$.

The complementary fluid velocity and wave elevation are now reconstructed in 3D interpolation grid, as shown in figure 5.14b.

The reconstructed complementary fluid velocity and wave elevation on 3D cylindrical interpolation are used to interpolate the velocity and wave elevation at arbitrary position. A cubic spline interpolation, as explained in section 3.2.4, is used to evaluate the complementary fluid velocity and wave elevation at arbitrary point.

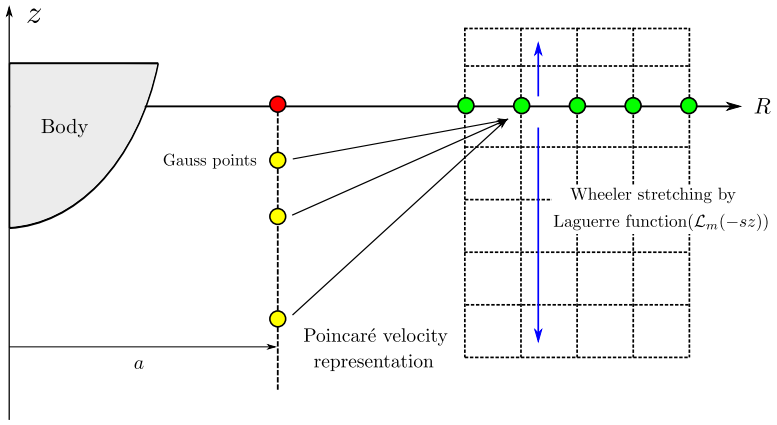

(a) Reconstucted complementary wave field in Fourier space

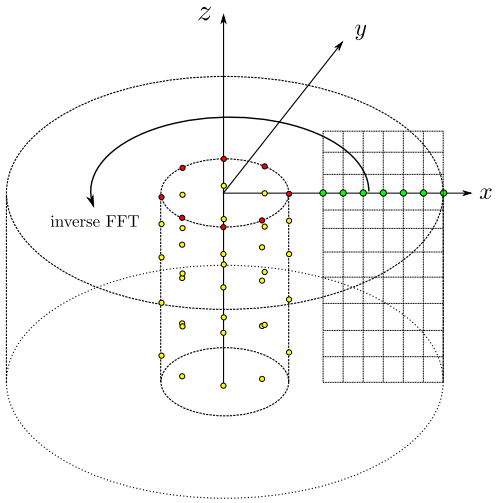

(b) Reconstruction of 3D complementary wave field by inverse Fourier transform

Figure 5.14. Reconstruction of complementary fluid velocity and wave elevation on a cylindrical grid by using a Poincaré's velocity representation.

5.9 Validation and discussion

5.9.1 Benchmark tests

Here we use the same type of benchmark test as the one previously used for the Poincaré's velocity representation with arbitrary matching surface. Two complementary wave problems representing radiation-diffraction problems are considered.

- The radiation problem of a heaving hemisphere introduced in previous section 4.5.1 (Hulme, 1982).
- The diffraction problem of a wave diffraction by a vertical circular cylinder (McCamy and Fuchs, 1954).

In the wave diffraction problem, circular cylindrical coordinates are used. The linear incident wave potential can be expressed in cylindrical coordinates by Graf's addition theorem (Abramowitz and Stegun, 1965)

$$\begin{aligned}\Phi_I &= \Re\left[-\frac{\mathrm{i}gA}{\omega}\frac{\cosh k_0(z+H)}{\cosh k_0 H}e^{\mathrm{i}k_0 x}e^{-\mathrm{i}\omega t}\right] \\ &= \Re\left[-\frac{\mathrm{i}gA}{\omega}\frac{\cosh k_0(z+H)}{\cosh k_0 H}\sum_{m=0}^{\infty}\epsilon_m \mathrm{i}^m J_m(k_0 R)\cos m\theta e^{-\mathrm{i}\omega t}\right],\end{aligned} \tag{5.269}$$

where A is incident wave amplitude. ω is wave frequency. H is water depth. $\epsilon_m = 1$ for $m = 0$ and $\epsilon_m = 2$ for $m > 0$. k_0 is the modal wavenumber satisfying linear dispersion relationship

$$\omega^2 = gk_0 \tanh k_0 H. \tag{5.270}$$

The diffraction potential should satify the body boundary condition given by

$$\frac{\partial \Phi_D}{\partial R} = -\frac{\partial \Phi_I}{\partial R}, \qquad \text{on} \qquad R = a_{cylinder}, \tag{5.271}$$

where Φ_D is the diffraction potential and $a_{cylinder}$ is the radius of cylinder.

The diffraction potential satisfying the above body boundary condition is given by eigenfunction expansion

$$\Phi_D = \Re\left[\frac{\mathrm{i}gA}{\omega}\frac{\cosh k_0(z+H)}{\cosh k_0 H}\sum_{m=0}^{\infty}\epsilon_m \mathrm{i}^m \frac{J'_m(k_0 a_{cylinder})}{H'_m(k_0 a_{cylinder})}H_m(k_0 R)\cos m\theta e^{-\mathrm{i}\omega t}\right]. \tag{5.272}$$

The diffraction problem considered in the present study has various Fourier components. In constrast, the radiation problem has only one Fourier component. Force acting on the cylinder and wave elevation along waterline of cylinder are shown in figures 5.15 and 5.16.

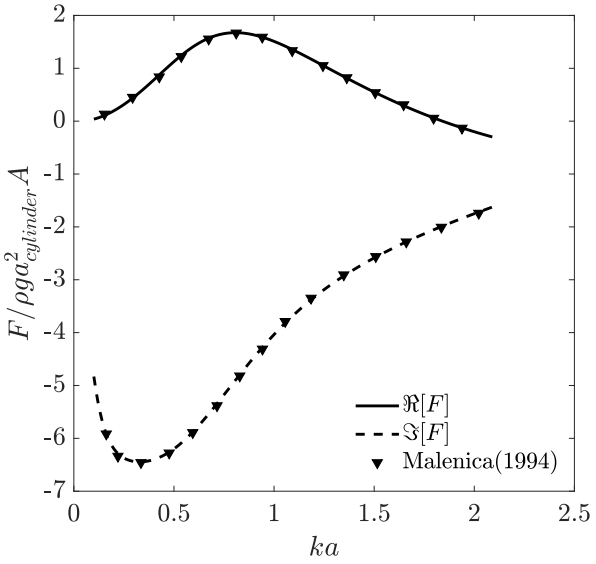

Figure 5.15. Horizontal force acting on vertical circular cylinder, $H = 10a$ (Malenica, 1994).

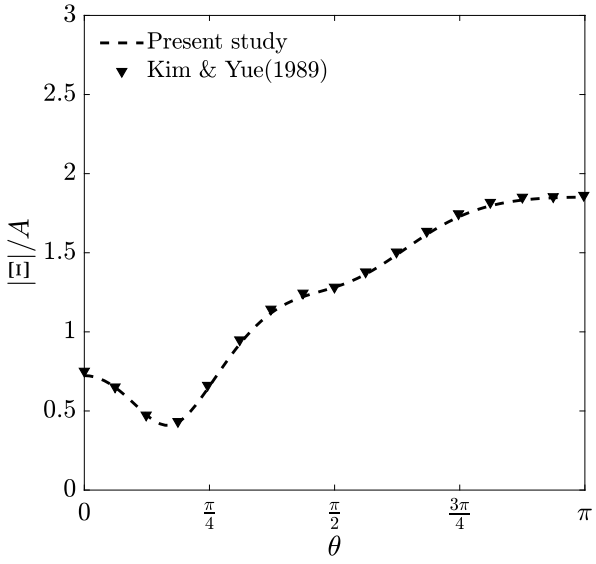

Figure 5.16. Wave elevation along waterline of vertical circular cylinder, $H = a$, $\frac{\omega^2}{g}a = 2$ (Kim and Yue, 1989).

5.9.2 Fourier-Laguerre approximation

The complementary fluid velocity on the vertical circular cylindrical matching surface needs to be approximated by Fourier-Laguerre series with coeffcients in Poincaré's velocity representation. The approximated complementary fluid velocities with Fourier-Laguerre series are given in equation (5.21) as

$$\begin{bmatrix} u_C^{\mathbf{n}} \\ w_C^{\xi} \\ w_C^{\eta} \\ w_C^{\zeta} \end{bmatrix}_{r=a} \approx \sum_{n=-N}^{N} \sum_{m=0}^{M} \begin{bmatrix} \mathcal{C}_{mn}^{\mathbf{n}} \\ \mathcal{W}_{mn}^{\xi} \\ \mathcal{W}_{mn}^{\eta} \\ \mathcal{W}_{mn}^{\zeta} \end{bmatrix} \mathcal{L}_m\left(-s\zeta\right) e^{in\theta'}.$$

where $\mathcal{C}_{mn}^{\mathbf{n}}$, $\mathcal{W}_{mn}^{\xi}$, $\mathcal{W}_{mn}^{\eta}$ and $\mathcal{W}_{mn}^{\zeta}$ are Fourier-Laguerre coefficients.

It is necessary to evaluate the Fourier-Laguerre coefficients for arbitrary function $f(a, \theta', \zeta)$ defined on the matching surface. Let the scalar function defined on the matching surface can be approximated with Fourier-Laguerre series as

$$f(a, \theta', \zeta) \approx \sum_{m=0}^{M} \sum_{n=0}^{N} C_{mn} \mathcal{L}_m(-s\zeta) e^{\mathrm{in}\theta'}, \tag{5.273}$$

where C_{mn} is Fourier-Laguarre coefficients of function $f(a, \theta', \zeta)$.

Using the orthogonal relationships of Laguerre and trigonometric functions given in equations (5.25) and (5.26), the coefficient is given by

$$C_{mn} = \frac{s}{2\pi} \int_{-\infty}^{0} \int_{0}^{2\pi} f(a, \theta', \zeta) \mathcal{L}_m(-s\zeta) e^{-\mathrm{in}\theta'} d\zeta d\theta' \tag{5.274}$$

Integral along θ' can be evaluated easily by using Fast Fourier Transform(FFT). The integral along vertical axis ζ is defined by

$$\begin{aligned}\int_{-\infty}^{0} h(\zeta)\mathcal{L}_m(-s\zeta)d\zeta &= \int_{-\infty}^{0} h(\zeta)e^{\frac{s}{2}\zeta}L_m(-s\zeta)d\zeta = \int_{0}^{\infty} h(-u)L_m(su)e^{-\frac{s}{2}u}du \\ &= \int_0^\infty \hat{h}\,(x)\,e^{-x}dx\end{aligned} \tag{5.275}$$

with

$$h(\zeta) = \frac{s}{2\pi}\int_0^{2\pi} f(a,\theta'\zeta)e^{-\mathrm{i}n\theta'}d\theta', \qquad \text{and} \qquad \hat{h}(x) = \frac{2}{s}h\left(-\frac{2x}{s}\right)L_m(2x). \tag{5.276}$$

The semi-infinite integral along x-axis can be evaluated by using Gauss-Laguerre quadrature. Gauss points and associated weights can be used to evaluate semi-infinite integral as (Abramowitz and Stegun, 1965)

$$\int_0^\infty \hat{h}(x)e^{-x}dx \approx \sum_{i=1}^{N_{Gauss}} w_i\hat{h}(x_i), \tag{5.277}$$

where x_i and w_i are i-th Gauss point(abscissas) and weight. N_{Gauss} is the number of Gauss points. Gauss points is taken from i-th zero of Laguerre polynomial $L_{N_{Gauss}}(x)$ and the weights of Gauss-Laguerre quadrature (w_i) are given by

$$w_i = \frac{(N_{Gauss}!)^2 x_i}{(N_{Gauss}+1)^2[L_{N_{Gauss}+1}(x_i)]^2}. \tag{5.278}$$

Gauss points and weights are obtained by using subroutine `cdgqf` of IQPACK (Elhay and Kautsky, 1987).

Gauss points may be located outside of computational domain because the depth of computational domain is limited. Therefore, extrapolation of scalar function $f(a,\theta',\zeta)$ is necessary to evaluate Gauss-Laguerre quadrature.

Let Gauss points(ζ_i), which is physical axis transformed from mathematical axis x_i, are located in the computational domain with function values f_i. Exponential function is used to extrapolate $f(\zeta)$ as

$$f(\zeta) \approx ae^{bz}, \tag{5.279}$$

where a and b are arbitrary real and b should be equal or greater than zero. If all f_i are positive or negative, a and b can be evaluated by applying the least squre method as

$$\begin{bmatrix}\pm\ln a \\ b\end{bmatrix} = \left(\mathbf{A}_{ls}^T\mathbf{A}_{ls}\right)^{-1}\mathbf{A}_{ls}^T\mathbf{b}_{ls}, \tag{5.280}$$

with

$$\mathbf{A}_{ls} = \begin{bmatrix}1 & \zeta_1 \\ 1 & \zeta_2 \\ \vdots & \vdots \\ 1 & \zeta_{N_{selected}}\end{bmatrix}, \qquad \mathbf{b}_{ls} = \begin{bmatrix}\ln(\pm f_1) \\ \ln(\pm f_2) \\ \vdots \\ \ln(\pm f_{N_{selected}})\end{bmatrix}. \tag{5.281}$$

where $N_{selected}$ is the number of exsiting Gauss points inside of computational domain. Signs of $\ln a$ and $\ln(f_i)$ depend on the sign of function value f_i.

When some of f_i has different sign, e.g., some of f_i are positive and some of f_i are negative, a nonlinear least square method is needed to evaluate a and b. A global nonlinear optimization algorithm based on iterative random search procedure with adaptive movement is applied to minimize the approximation error defined by (Corana et al., 1987)

$$E(a,b) = \sum_{i=1}^{N_{selected}} \left(f_i - ae^{bz_i} \right)^2, \qquad a,b \in \mathbb{R}, \quad b \geq 0. \tag{5.282}$$

where $E(a,b)$ is approximation error. Initial values of a and b for nonlinear optimization algorithm are given by a and b obtained in previous time step. Benchmark tests on nonlinear algorithm for arbitrary function with exponentially decaying behavior are shown in figure 5.17.

The values of arbitrary function f_i are distributed with respect to $z \in [-10, 0]$, as plotted with circle in figure 5.17. f_i have positive and negative sign. Extrapolated function by using nonlinear optimization algorithm is plotted as rigid black line in figure 5.17. They are following the global tendencies of distributed f_i along z axis. The results show that extrapolation for arbitrary functions for $z < 0$ works well.

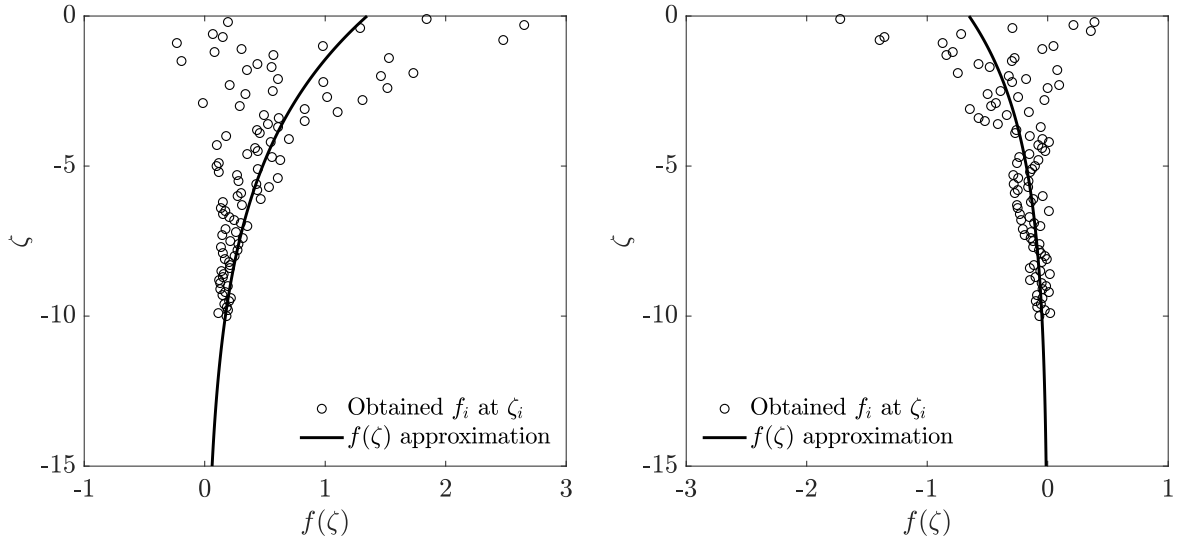

Figure 5.17. Benchmark tests on approximation of exponential function by using nonlinear optimization algorithm.

After applying least square method, Fourier-Laguerre coefficients can be evaluated by

$$C_{mn} = \frac{s}{N_{\theta'}} \sum_{j=0}^{N_{\theta'}-1} \left[\sum_{i=1}^{N_{selected}} w_i f_{i,j+1} + \sum_{i=N_{selected}+1}^{N_{Gauss}} w_i f_{i,j+1} \right] e^{-2\pi i n(j/N_{\theta'})}, \tag{5.283}$$

where $f_{i,j} = f(a, \theta'_j, \zeta_i,)$ are flow quantities obtained at Gauss points $\mathbf{x} = (a, \theta_j, z_i)$. Gauss points are determined from abiscissa of Gauss-Laguerre quadrature and uniformly distributed Fourier points. The complementary fluid velocities on the matching surface for heaving hemisphere is approximated by Fourier-Laguerre series and shown in figure 5.18. The number of Fourier and Laguerre modes used for approximation are $N_{Fourier} = 2$ and $N_{Laguerre} = 1$, respectively. The number of Gauss points used for approximation is 128.

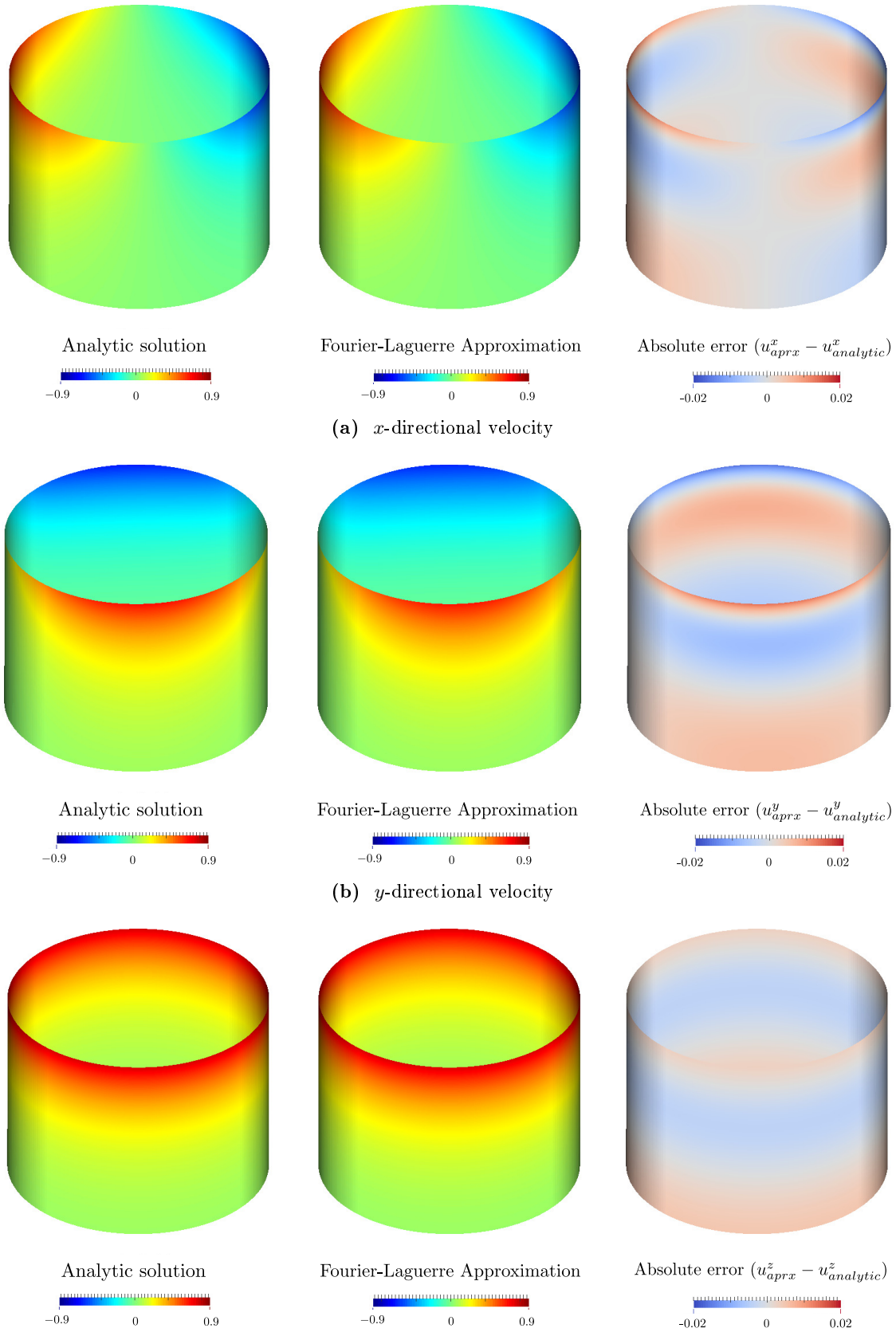

(a) x-directional velocity

(b) y-directional velocity

(c) z-directional velocity

Figure 5.18. Fourier-Laguerre approximation on fluid velocity generated by heaving hemisphere.

These results show that fluid velocities on the matching surface are well approximated by Fourier-Laguerre series.

Fourier-Laguerre approximation of fluid velocity is tested by increasing the number of Fourier-Laguerre modes and Gauss points. Approximation errors of fluid velocity are defined by

$$\begin{bmatrix} \epsilon_u^x \\ \epsilon_u^y \\ \epsilon_u^z \end{bmatrix} = \frac{1}{N_{Gauss}} \sum_{i=1}^{N_{Gauss}} \begin{bmatrix} (u^x_{aprx,i} - u^x_{analytic,i})^2 \\ (u^y_{aprx,i} - u^y_{analytic,i})^2 \\ (u^z_{aprx,i} - u^z_{analytic,i})^2 \end{bmatrix} \tag{5.284}$$

where superscripts denote the directional component. u_{aprx} and $u_{analytic}$ are approximated fluid velocity and analytical fluid velocity at i-th Gauss point, respectively. Approximation errors of fluid velocity with respect to different numbers of Fourier-Laguerre modes and Gauss points are shown in figure 5.19 during one period of heaving motion.

Sudden changes of approximation errors, as shown in 5.19, happen when the calculation switches between linear and nonlinear approximation algorithms. As the number of modes and Gauss points increases, the approximation error decreases. Results confirm that the approximation of fluid velocity by Fourier-Laguerre series show good agreements with analytical solution, and that the approximation errors can be reduced by increasing the number of Gauss points.

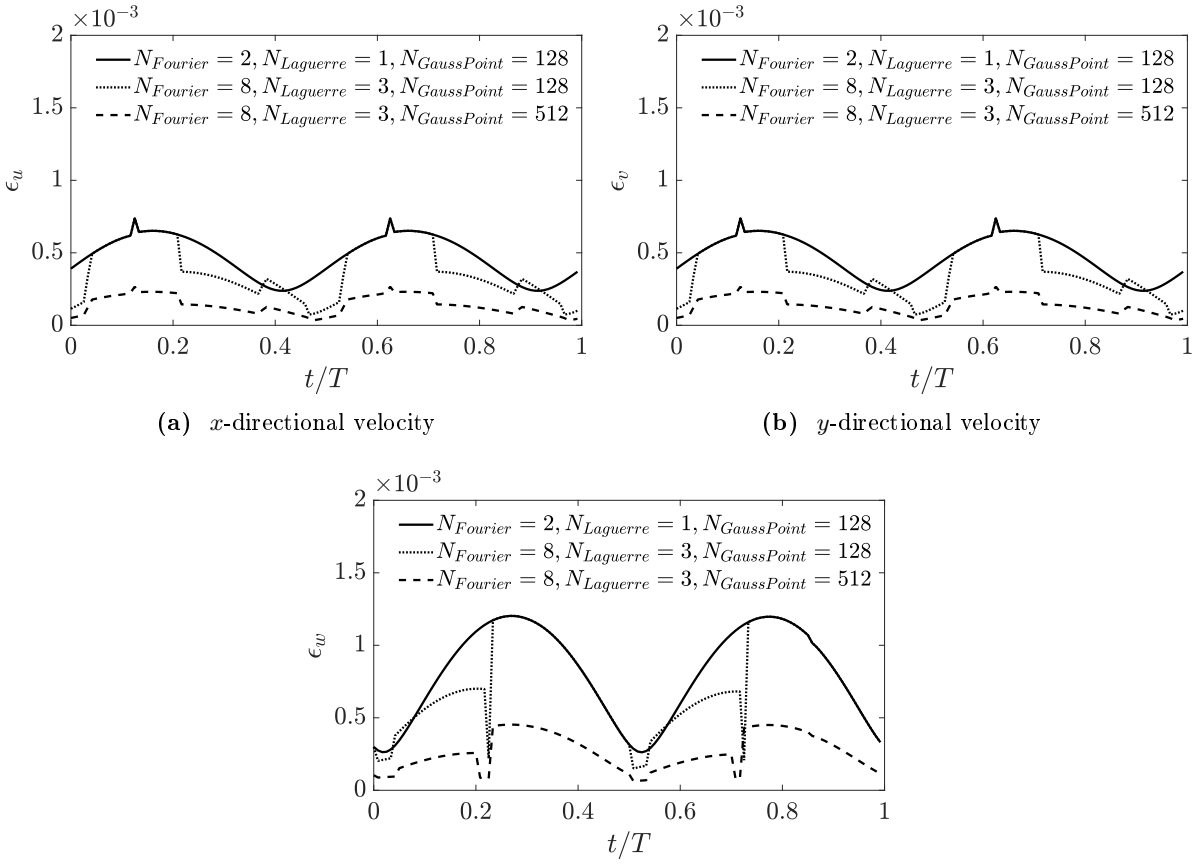

(a) x-directional velocity

(b) y-directional velocity

(c) z-directional velocity

Figure 5.19. Fourier-Laguerre approximation errors of fluid velocity with respect to number of Gauss points and modes.

5.9.3 Poincaré's velocity representation for radiation-diffraction problem

Radiation problem: Heaving hemisphere

Hulme's heaving hemisphere, as explained in section 4.5.1, is considered as a benchmark radiation problem. The complementary fluid velocity and wave elevation at Gauss points are calculated by the analytical solution. The Poincaré's velocity representation with cylindrical matching surface is used to reconstruct the complementary fluid velocity and wave elevation at the field point.

Figure 5.20 shows complementary fluid velocity and wave elevation calculated by the analytical solution and the Poincaré's velocity representation when the field point is located on the mean free surface, $\mathbf{x} = (r, \theta, z) = (8, \frac{\pi}{4}, 0)$. $A(f)$ denotes the first-harmonic amplitude of f. The sphere of radius $1m$ has a heaving frequency $\omega = 2.0$ rad/s and heave motion amplitude of $2.0m$. Time step used for simulation is $\Delta t = 0.01s$. The matching surface has a radius $a = 2m$. The numbers of Fourier and Laguerre modes used for Poincaré's velocity representation are $N_{Fourier} = 6$ and $N_{Laguerre} = 3$, respectively.

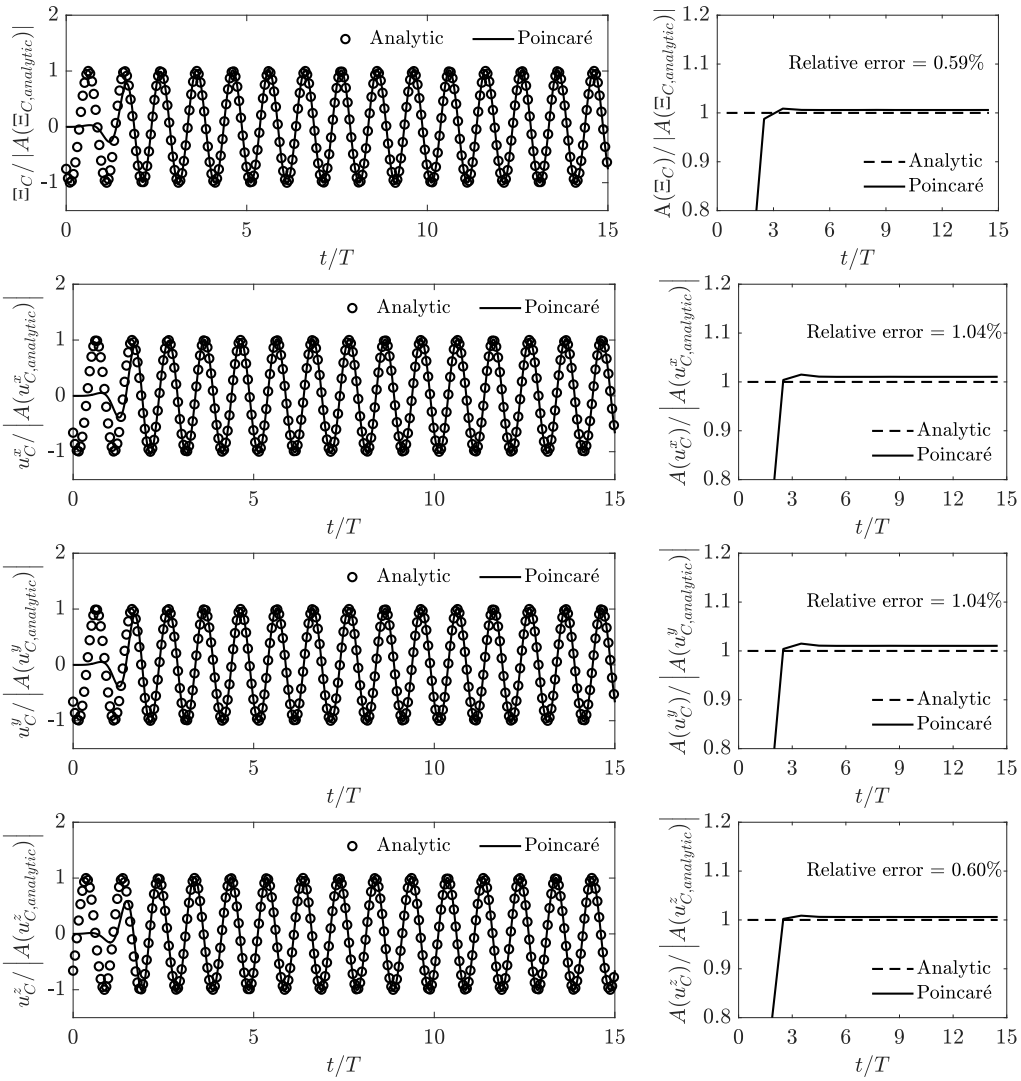

Figure 5.20. Reconstructed complementary wave elevation and velocity on the mean free surface for heaving hemisphere, $(r, \theta, z) = (8.0, \frac{\pi}{4}, 0)$, $\omega = 2.0$ rad/s. From top to bottom : wave elevation, $x-$, $y-$ and z-component velocity, respectively.

After the initial ramp and when the memory effect due to convolution integral has converged, the complementary wave elevation and fluid velocity show good agreements with results of the analytic solution. Results of moving window FFT show that first-harmonic amplitudes of reconstructed fluid velocity and wave elevation have relative errors less than 1.04%.

Figure 5.21 shows complementary fluid velocity and wave elevation fields calculated by the analytical solution and Poincaré's velocity representation. The absolute error is taken by subtracting the analytical solution from the value of Poincaré's velocity representation. The fluid velocity above the mean free surface is not calculated and Wheeler stretching is not applied for comparison. The reconstructed wave fields by using Poincaré's velocity representation show good agreements with the analytical solution.

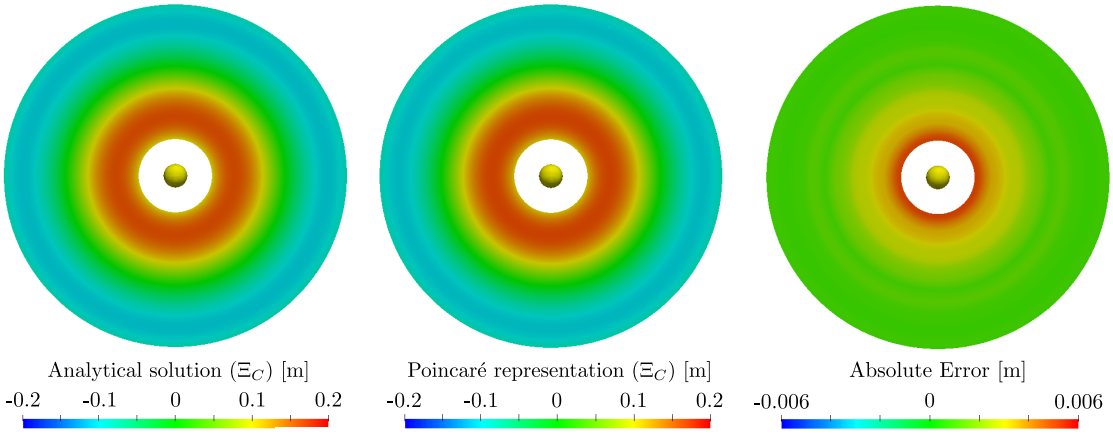

(a) Wave elevation field

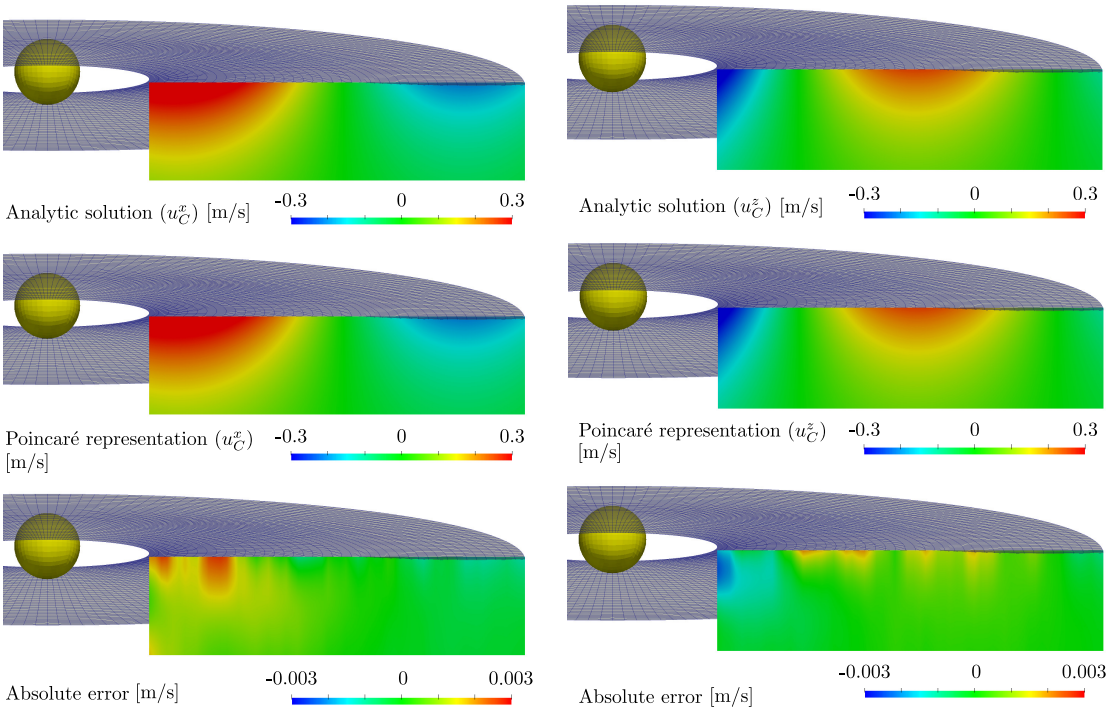

(b) Horizontal velocity field

(c) Vertical velocity field

Figure 5.21. Wave fields calculated by using the analytical solution and Poincaré's velocity representation for heaving hemisphere problem.

Diffraction problem: Diffraction by a vertical circular cylinder

Wave diffraction by a vertical circular cylinder in regular waves is considered here. Similarly to the radiation problem, the complementary fluid velocity and wave elevation at Gauss points are calculated by the analytical soution described in section 5.9.1. The Poincaré's velocity representation with a cylindrical matching surface is used to reconstruct the complementary fluid velocity and wave elevation at the field point.

Figure 5.22 shows the complementary wave elevation and velocities at the field point $\mathbf{x} = (r, \theta, z) = (5, \frac{\pi}{4}, 0)$. The radial frequency and amplitude of regular waves are $\omega = 2.0$ and 0.8m, respectively. The water depth is equal to $8m$ and the radius of vertical circular cylinder is $1m$. The radius of the matching surface for Poincaré's velocity representation is $a = 2m$. The numbers of Fourier and Laguerre modes are $N_{Fourier} = 6$ and $N_{Laguerre} = 3$, respectively. Time step is set to be $\Delta t = 0.01s$.

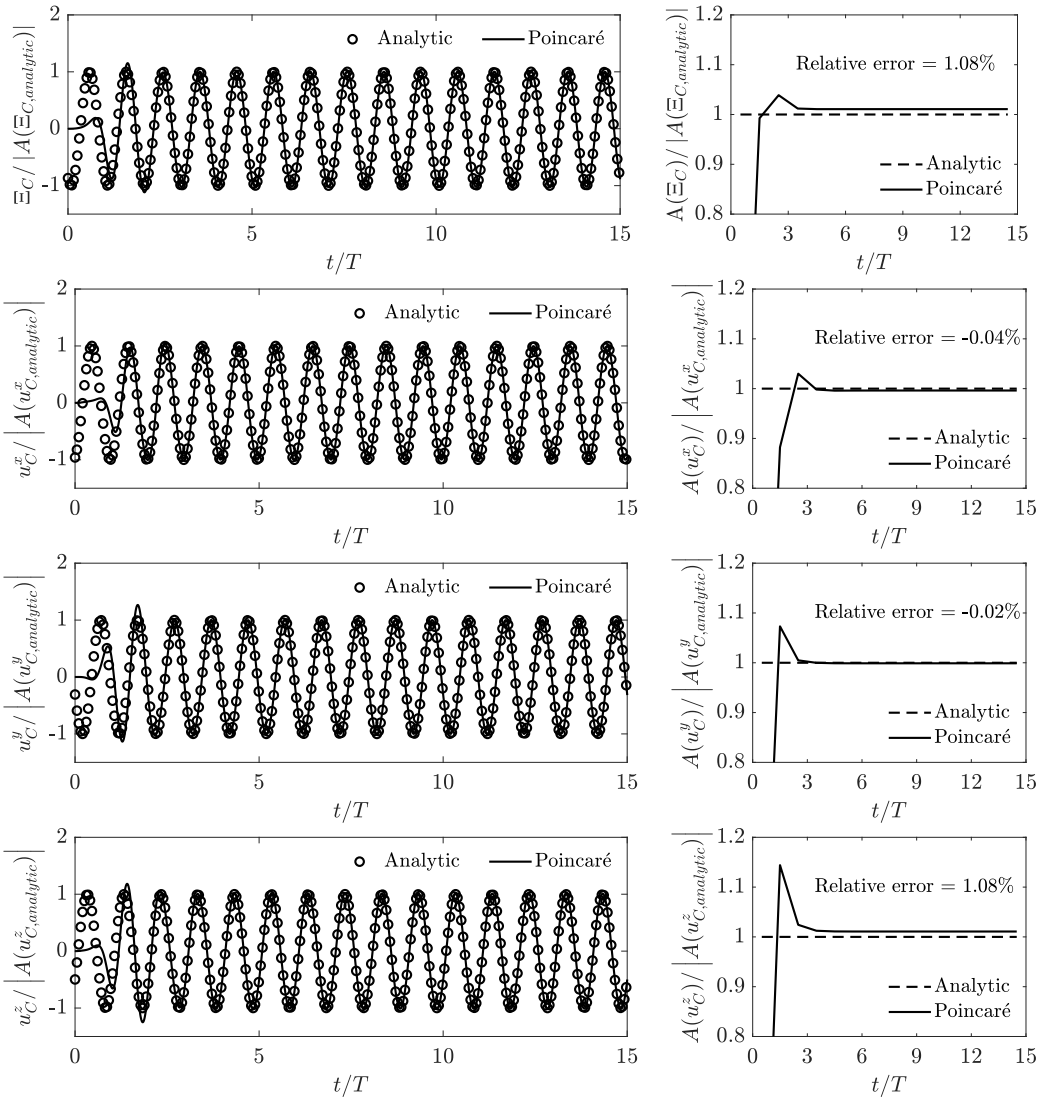

Figure 5.22. Reconstructed complementary wave elevation and velocity on the mean free surface for cylinder diffraction, $(r, \theta, z) = (5.0, \frac{\pi}{4}, 0)$, $\omega = 2.0$ rad/s. From top to bottom : wave elevation, $x-$, $y-$ and z-component velocity, respectively.

Results show good agreements with the analytical solution. The first-harmonic amplitudes obtained by applying moving window FFT and they are compared in the right side of figure 5.22. The relative errors of reconstructed flow are less than 1.08%.

Figure 5.23 shows the complementary fluid velocity and wave elevation fields and their absolute errors. The complementary wave elevation and velocity fields reconstructed from Poincaré's velocity representation show good agreements with the analytical solution. The wave fields for diffraction problem have more than one Fourier mode.

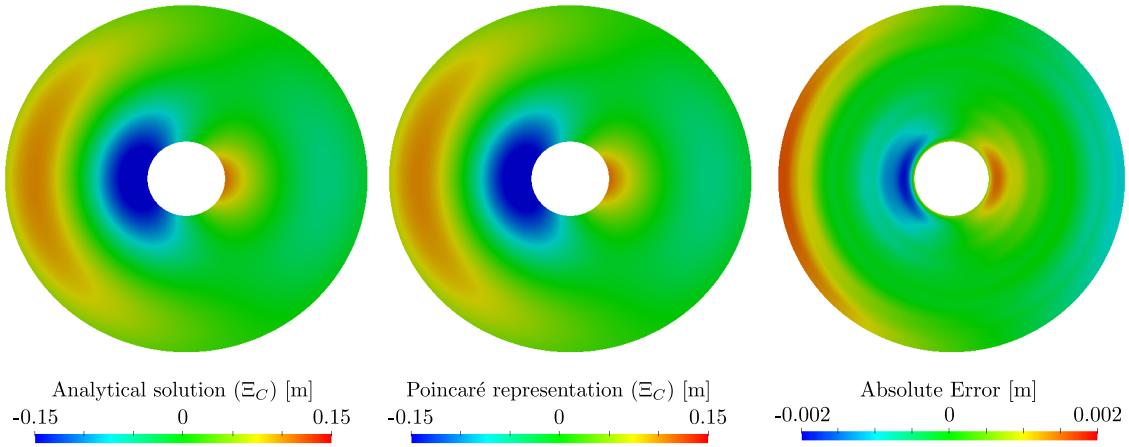

(a) Wave elevation field

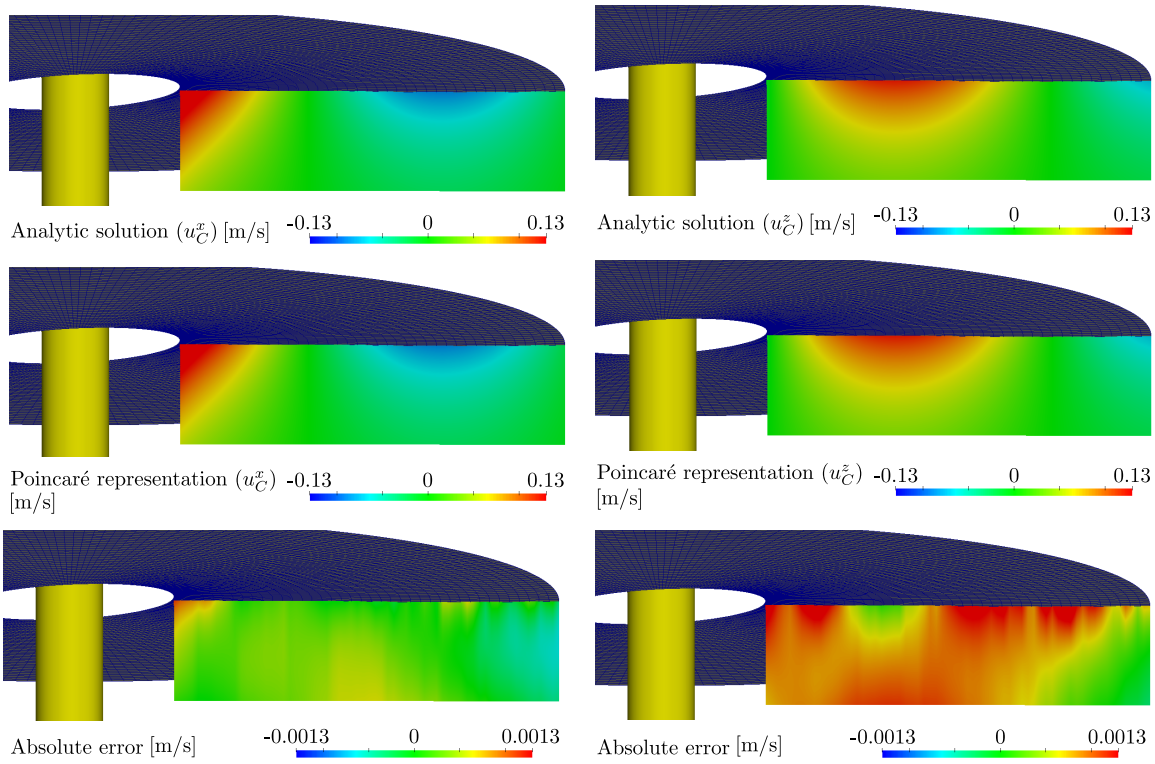

(b) Horizontal velocity field **(c)** Vertical velocity field

Figure 5.23. Wave fields calculated by using the analytical solution and Poincaré's velocity representation for cylinder diffraction problem.

Convergence test on the number of Fourier and Laguerre modes

The complementary wave elevation and velocity on the mean free surface are reconstructed with respect to the different number of Fourier-Laguerre modes. The wave diffraction by the vertical circular cylinder is used because the waves diffracted by cylinder have many Fourier components.

Figure 5.24 shows the complementary wave elevation and velocity reconstructed by Poincaré velocity representation with respect to different number of Fourier modes ($N_{Fourier}$). The number of Laguerre modes is kept to be $N_{Laguerre} = 3$. The results show that the horizontal velocity components are convergent slowly with respect to the number of Fourier modes. Meanwhile, the vertical velocity and wave elevation show good agreements with the analytical solution even if the number of Fourier modes are small.

Figure 5.25 shows the complementary wave elevation and velocity with respect to different number of Laguerre modes ($N_{Laguerre}$). The number of Fourier modes is kept to be $N_{Fourier} = 5$. The results show that the reconstructed flow quantities are not sensitive to the number of Laguerre modes. The optimal choice of s gives good approximations of Laguerre functions to the velocity profile along the matching surface.

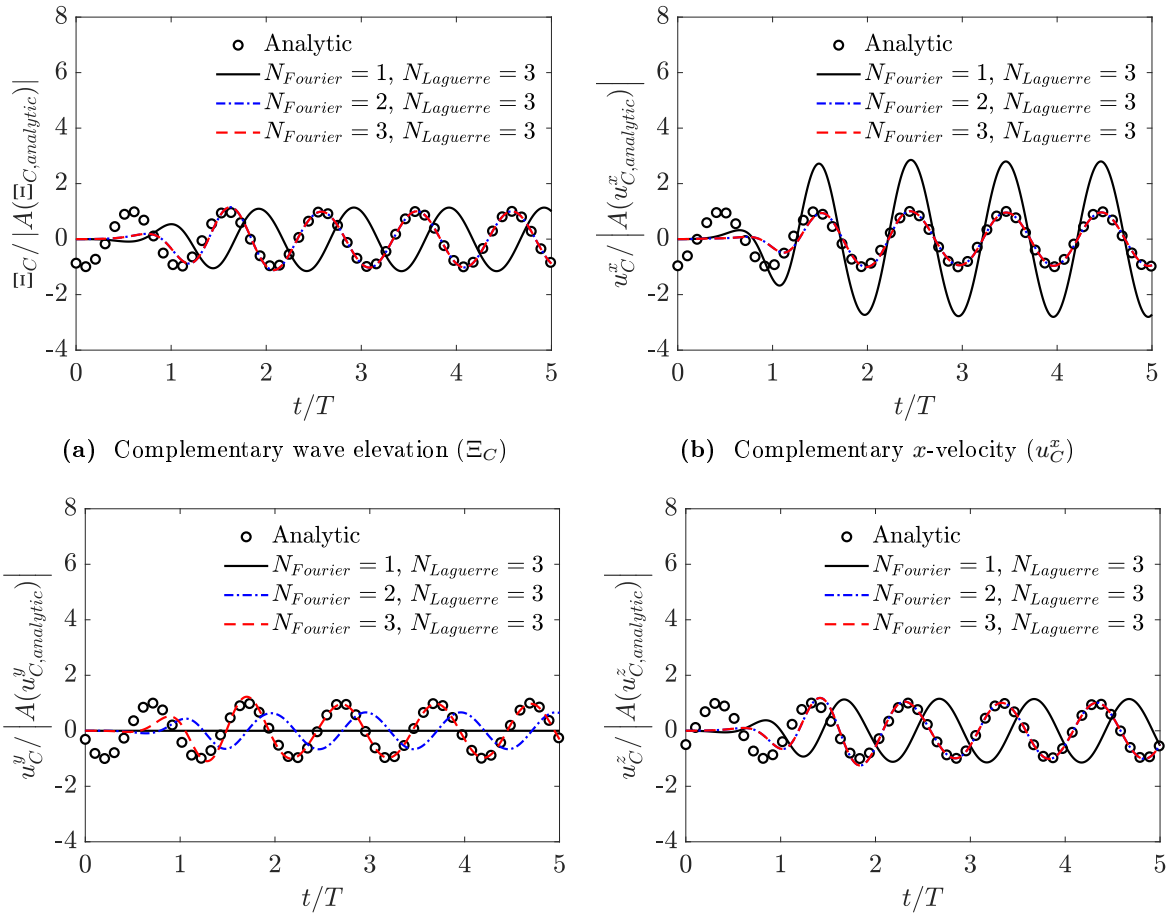

(a) Complementary wave elevation (Ξ_C)

(b) Complementary x-velocity (u_C^x)

(c) Complementary y-velocity (u_C^y)

(d) Complementary z-velocity (u_C^z=

Figure 5.24. Complementary wave elevation and velocity with the different number of Fourier modes. Cylinder diffraction problem $(r, \theta, z) = (5.0, \frac{\pi}{4}, 0)$, $\omega = 2.0$ rad/s.

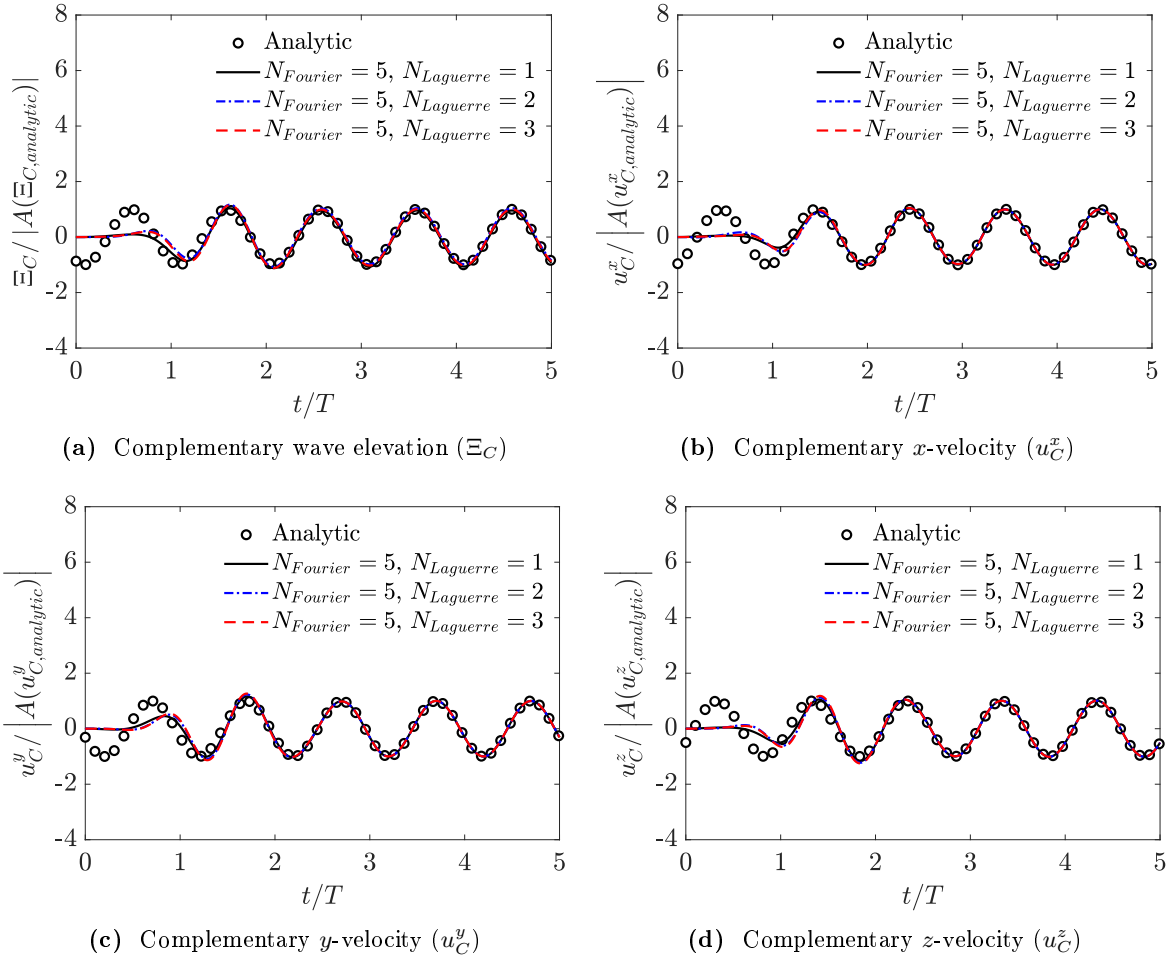

(a) Complementary wave elevation (Ξ_C)

(b) Complementary x-velocity (u_C^x)

(c) Complementary y-velocity (u_C^y)

(d) Complementary z-velocity (u_C^z)

Figure 5.25. Complementary wave elevation and velocity with the different number of Laguerre modes. Cylinder diffraction problem $(r, \theta, z) = (5.0, \frac{\pi}{4}, 0)$, $\omega = 2.0$ rad/s.

Remarks of benchmark tests on radiation and diffraction problems

In numerical computation, following error sources are identified

- s parameter in Laguerre function affects on Fourier-Laguerre approximation of complementary velocity. A bad selection of s needs large number of Laguerre modes for good approximation.
- Truncation of Fourier-Laguerre modes and limited number of Gauss points shall give large approximation errors.
- Convolution integrals with moving window convolution time interval generate numerical errors. The moving window convolution time interval has to be long enough.

5.10 Conclusion

A Poincaré's velocity representation has been formulated with a circular cylindrical matching surface. The surface integral is analytically applied to Poincaré's velocity representation along the matching surface. The complementary fluid velocities and wave elevation are developed in Fourier-Laguerre and Fourier series, respectively. The time domain Green functions are expressed in Fourier series. The analytical integration along the matching surface and the matching waterline enhances the numerical stability. Furthermore, it reduces the computational burden in reconstructing three-dimensional wave fields. However, complex elementary functions, which are surface integral of the time domain Green function and Fourier-Laguerre modes, appear in the formulation. In the final formulation, the complementary fluid velocity at field point is given by convolution integrals of flow at matching surface and elementary functions.

Numerical algorithms to compute the elementary functions have been proposed. The first approach transforms the semi-infinite integral into an infinite series summation of sub-integrals. The infinite series summation is evaluated by the extrapolation using continuous sets of finite summation. The second approach extends an integral variable in the real domain into the complex domain. Semi-infinite integrals along the real axis are evaluated by steepest descent method. Evaluation of elementary functions is validated by comparing two algorithms.

The wave elevation is reconstructed by integrating the vertical velocity on the mean free surface. After the reconstruction of the wave elevation, Wheeler stretching with Laguerre function is used to extrapolate the fluid velocity above mean free surface. 3D cubic spline interpolation is used to calculate the wave elevation and the fluid velocity at arbitrary points.

Finally, the complementary wave problems, which are referred to the radiation and diffraction problems, are considered for validation. A heaving hemisphere is considered for radiation problem (Hulme, 1982). Wave diffraction by a vertical circular cylinder is used for diffraction problem (McCamy and Fuchs, 1954). Numerical results show that the proposed Poincaré's velocity representation shows very good agreements with the analytical solution. Three-dimensional complementary wave fields are reconstructed with the limited number of Fourier-Laguerre modes, and they show good agreements with the wave fields calculated by the analytical solution.

6 Viscous flow: Multi-phase SWENSE with Level-set

6.1 Two-phase flow model

6.1.1 Two-phase mixture model (used in interFoam)

The continuity and Navier-Stokes equations for an incompressible air are written as

$$\nabla \cdot \mathbf{u}_a = 0 \tag{6.1}$$

$$\frac{\partial(\rho_a \mathbf{u}_a)}{\partial t} + \nabla \cdot (\rho_a \mathbf{u}_a \mathbf{u}_a) = -\nabla p_a + \rho_a \mathbf{g} + \nabla \cdot \left(\mu_a \left(\nabla \mathbf{u}_a + \nabla \mathbf{u}_a^T\right)\right), \tag{6.2}$$

and the equations for incompressible water are given by

$$\nabla \cdot \mathbf{u}_w = 0 \tag{6.3}$$

$$\frac{\partial(\rho_w \mathbf{u}_w)}{\partial t} + \nabla \cdot (\rho_w \mathbf{u}_w \mathbf{u}_w) = -\nabla p_w + \rho_w \mathbf{g} + \nabla \cdot \left(\mu_w \left(\nabla \mathbf{u}_w + \nabla \mathbf{u}_w^T\right)\right), \tag{6.4}$$

where subscript $_w$ or $_a$ denotes fluid which is considered as w for water and a for air. ρ and μ are the density and viscosity of the fluid, p is pressure and $\mathbf{g}$ is gravitational acceleration vector. In the Volume Of Fluid method (VOF), α is introduced as the ratio between the water occupied in the cell volume and the total cell volume. For example, $\alpha = 1$ means that the cell is fully submerged and $\alpha = 0$ represents a dry cell. The mixture quantities can be given with α as

$$\begin{aligned} \rho &= \alpha \rho_w + (1-\alpha)\rho_a, \\ \mu &= \alpha \mu_w + (1-\alpha)\mu_a, \end{aligned} \tag{6.5}$$

and

$$\begin{aligned} \mathbf{u} &= \alpha \mathbf{u}_w + (1-\alpha)\mathbf{u}_a, \\ p &= \alpha \mathbf{u}_w + (1-\alpha)p_a \end{aligned} \tag{6.6}$$

where ρ, μ, $\mathbf{u}$ and p represent mixture density ,viscosity, velocity and pressure, respectively. Two-phase Navier-Stokes equations are then rewritten as the equations for single mixture

$$\nabla \cdot \mathbf{u} = 0, \tag{6.7}$$

$$\frac{\partial(\rho \mathbf{u})}{\partial t} + \nabla \cdot (\rho \mathbf{u}\mathbf{u}) - \nabla \cdot (\mu \nabla \mathbf{u}) = -\nabla p + \rho \mathbf{g} + \nabla \mathbf{u} \cdot \nabla \mu + \sigma \kappa \nabla \alpha. \tag{6.8}$$

The surface tension force $\sigma\kappa\nabla\alpha$ is introduced due to the existence of the interface between water and air. The fluid velocity $\mathbf{u}$ and pressure p are the mixture flow quantities. The gravitational force is replaced by introducing the dynamic pressure for numerical modeling of body boundary condition (Rusche, 2002)

$$p_d = p - \rho \mathbf{g} \cdot \mathbf{x}, \tag{6.9}$$

and the momentum equation is rewritten as

$$\frac{\partial(\rho \mathbf{u})}{\partial t} + \nabla \cdot (\rho \mathbf{u}\mathbf{u}) = -\nabla p_d - \mathbf{g} \cdot \mathbf{x} \nabla \rho + \nabla \cdot \left(\mu_{eff} \left(\nabla \mathbf{u} + \nabla \mathbf{u}^T\right)\right) + \sigma \kappa \nabla \alpha. \tag{6.10}$$

The Navier-Stokes equations considering two fluids as one mixture have been commonly used in academic and industrial fields due to easy numerical modeling (Hirt and Nichols, 1981; Damián, 2013; Jacobsen et al., 2012; Paulsen et al., 2014). Recently, Vukčević (2016) stated that the numerical evaluation of the gradient of dynamic pressure with a density gradient

$$\nabla p_d + \mathbf{g} \cdot \mathbf{x} \nabla \rho, \tag{6.11}$$

is not equal to zero for a hydrostatic case where it should be zero. It gives source in the momentum equation, therefore a spurious air velocity appears near the interface during the simulation. The spurious air velocity is factored by density variance of water and air, the flow field near the interface becomes violent and unstable. The density gradient in the momentum equation gives a large numerical value on the interface due to the density jump from one fluid to the other. The jump is smoothed and the interface smears when the color function advects. Solving the two phase flow with single fluid (mixture) makes the numerical modeling easier and the equation looks intuitive.

6.1.2 Two-phase mixture model with interface condition (used in present study)

An alternative two-phase flow model imposes the stress balance across the interface to prevent spurious air velocity near the interface. Navier-Stokes equations for air are rewritten as

$$\frac{\partial \mathbf{u}_a}{\partial t} + \nabla \cdot (\mathbf{u}_a \mathbf{u}_a) = -\frac{1}{\rho_a} \nabla p_a + \mathbf{g} + \nabla \cdot \left(\nu_a \left(\nabla \mathbf{u}_a + \nabla \mathbf{u}_a^T \right) \right), \tag{6.12}$$

and the equations for water are given by

$$\frac{\partial \mathbf{u}_w}{\partial t} + \nabla \cdot (\mathbf{u}_w \mathbf{u}_w) = -\frac{1}{\rho_w} \nabla p_w + \mathbf{g} + \nabla \cdot \left(\nu_w \left(\nabla \mathbf{u}_w + \nabla \mathbf{u}_w^T \right) \right). \tag{6.13}$$

Kinematic condition that fluid particles on the interface move together giving a velocity condition on the interface

$$\mathbf{u}_w = \mathbf{u}_a, \qquad \Leftrightarrow \qquad [\![\mathbf{u}]\!] = \mathbf{u}_a - \mathbf{u}_w = 0, \qquad \text{on} \qquad \mathbf{x} \in S_f \tag{6.14}$$

where the jump operator $[\![f]\!] = f_a - f_w$ is defined at the air/water interface S_f. The jump operator represents the difference of f quantities across the interface. It enables us to express the fluid veloicty for two fluids as the mixture fluid velocity in computational domain.

The dynamic condition condition on the interface represents the stress balance on the fluid particles across the interface (Kang et al., 2000; Carrica et al., 2007; Lervåg, 2008)

$$[\![p\mathbf{I} + 2\mu\mathbf{D}]\!] \cdot \mathbf{n}_f = -(\sigma\kappa\mathbf{n}_f + \nabla_i \sigma), \qquad \text{on} \qquad \mathbf{x} \in S_f \tag{6.15}$$

where $\mathbf{n}_f$ denotes the interface normal vector and ∇_i is a gradient along interface coordinates. $\nabla_i \sigma$ represents Marangoni effect. It becomes important when two fluids have a big temperature difference. Huang et al. (2007) conducted the dimensional analysis on the interface conditions and showed that the contribution of viscosity terms in interface condition is proportional to the

inverse of Reynolds number. Therefore, the contribution of viscosity terms can be considered negligible for naval application. Therefore, above equation can be approximated as

$$[\![p\mathbf{I}]\!] \cdot \mathbf{n}_f = 0, \qquad \text{on} \qquad \mathbf{x} \in S_f. \tag{6.16}$$

The interface normal vector ($\mathbf{n}_f$) is arbitrary and the stress balance condition on the interface simplifies in the pressure boundary condition for naval application as

$$[\![p]\!] = 0, \qquad \text{on} \qquad \mathbf{x} \in S_f. \tag{6.17}$$

Two-phase Navier-Stokes equations with interface boundary conditions are summarized as follows

- Mass conservation
$$\nabla \cdot \mathbf{u} = 0,$$
- Momentum equation
$$\frac{\partial \mathbf{u}}{\partial t} + \nabla \cdot (\mathbf{u}\mathbf{u}) = -\frac{\nabla p}{\rho} + \mathbf{g} + \nabla \cdot \left\{ \nu \left(\nabla \mathbf{u} + \nabla \mathbf{u}^T \right) \right\},$$
- Kinematic interface condition
$$[\![\mathbf{u}]\!] = 0, \qquad \text{on} \qquad \mathbf{x} \in S_f$$
- Pressure balance (Dynamic condition) on the interface
$$[\![p]\!] = 0, \qquad \text{on} \qquad \mathbf{x} \in S_f$$

Comparing the derived momentum equation and pressure interface condition with the mixture momentum equation (6.10), the pressure jump condition appears in right-hand-side of mixture momentum equation as density gradient. The surface tension which is neglected in stress balance is given in mixture momentum equation.

6.2 Interface modeling

The Level-Set (LS) function for interface modeling which is categorized as an Eulerian method is used in the present study. LS function is the signed distance function from the interface defined by

$$\psi(\mathbf{x}) = \begin{cases} -d, & \text{if} \quad \mathbf{x} \in \Omega_a, \\ 0, & \text{if} \quad \mathbf{x} \quad \text{on the interface } S_f, \\ d, & \text{if} \quad \mathbf{x} \in \Omega_w \end{cases} \tag{6.18}$$

where d denotes the distance from interface. Ω_a and Ω_w represent air and water fluid domains, respectively. The LS function has a positive value when the cell is submerged. The volume fraction α can be calculated from LS function as

$$\alpha(\mathbf{x}) = \frac{1}{2} \left[\text{sgn} \left\{ \psi(\mathbf{x}) \right\} + 1 \right]. \tag{6.19}$$

The above equation results in α field having a sudden change across the interface, which is not desirable when the continuous viscosity effects need to be accounted for in the simulation. VOF with user-defined interface thickness (ϵ_{inter}) can be introduced to smooth change of the α field near the interface

$$\alpha(\mathbf{x}) = \frac{1}{2}\left\{\tanh\left(\frac{\psi(\mathbf{x})}{\epsilon_{inter}\sqrt{2}}\right) + 1\right\}. \tag{6.20}$$

Mixture density and viscosity are calculated from the equation 6.5. The LS function transport equation is written by

$$\frac{\partial \psi}{\partial t} + \mathbf{u} \cdot \nabla \psi = 0. \tag{6.21}$$

The signed distance function is not bounded, the LS function after solving the above transport equation is not bounded. Therefore, conservation of fluid mass should be checked during the entire simulation.

After solving the LS function transport equation, redistancing of LS function in the entire fluid domain is used to keep a sharp interface (Chang et al., 1996; Sussman et al., 1998; Di Mascio et al., 2007). Re-distancing of LS function is usually conducted to make LS function satisfy the Eikonal equation

$$|\nabla \psi| = 1.$$

A pseudo-time τ is introduced to get the steady state solution of Eikonal equation as

$$\frac{\partial \tilde{\psi}}{\partial \tau} + \mathrm{sgn}(\psi)\left(\left|\nabla \tilde{\psi}\right| - 1\right) = 0.$$

Solving the Eikonal equation needs extra sub-iteration within the time step.

In the present study re-distancing of LS function in the entire fluid domain is done by re-calculating the distance from the nearest interface in equation 6.18 at each time step.

6.3 Functional decomposition

A variant version of the Navier-Stokes equations which is called Spectral Wave Explicit Navier-Stokes Equations (SWENSE) has been introduced for wave-structure interaction problem (Ferrant et al., 2003). The SWENSE method is based on the hypothesis that the functional quantity of total flow can be decomposed into incident and complementary parts as

$$\chi = \chi_I + \chi_C \tag{6.22}$$

where χ, χ_I and χ_C are quantities from respectively total, incident and complementary flows.

It is assumed that the incident flow is already available from a nonlinear potential flow model for incident waves. The incident flow components are subtracted from original Navier-Stokes equations by supposing that the incident flow satisfies Euler equations. Then, equations for the complementary flow can be reconstructed. In this way, a numerical (CFD) computation is performed for the complementary flow only, the total flow being reconstructed from (6.22). Thus procedure has numerical advantages:

- The incident flow components are not affected by the viscous flow solver.
- The absorption of complementary waves is easier.
- The computational mesh needs to be refined in the vicinity of the body only, savings in computer resources.

The SWENSE method has been validated for single phase flows by Luquet et al. (2003); Gentaz et al. (2004); Monroy (2010); Reliquet (2013). Recently, Vukčević (2016) applied SWENSE method to decompose fluid velocity and LS function. Li (2018) decomposed velocity and pressure in a two-phase flow solver with the original VOF equation.

The present work aims at decomposing the fluid velocity, pressure and LS function into the incident and complmentary flow components by combining the ideas of Vukčević (2016) and Li (2018). The fluid velocity, pressure and LS function are decomposed as

$$\mathbf{u} = \mathbf{u}_I + \mathbf{u}_C, \qquad \Leftrightarrow \qquad \mathbf{u}_C = \mathbf{u} - \mathbf{u}_I, \tag{6.23}$$

$$p = p_I + p_C, \qquad \Leftrightarrow \qquad p_C = p - p_I, \tag{6.24}$$

$$\psi = \psi_I + \psi_C, \qquad \Leftrightarrow \qquad \psi_C = \psi - \psi_I, \tag{6.25}$$

where $\mathbf{u}$, p and ψ are fluid velocity, pressure and LS function, respectively. Subscripts $_I$ and $_C$ denote quantities of incident and complementary flows, respectively.

6.3.1 Governing equations

The decomposition of the continuity equation is written as

$$\nabla \cdot \mathbf{u}_C = -\nabla \cdot \mathbf{u}_I = 0. \tag{6.26}$$

Vukčević (2016) remarked that though the divergence of the incident velocity field is theoretically zero, it does not vanish when it is mapped into finite volume discretization. To keep the order of the numerical discretization, he kept the term $(-\nabla \cdot \mathbf{u}_I)$ in his formulation. In the present study, only $\nabla \cdot \mathbf{u}_C = 0$ is kept. because $-\nabla \cdot \mathbf{u}_I$ is thought to give an extra error source in the pressure equation.

Euler equations for incident flow are written as

$$\frac{\partial \mathbf{u}_I}{\partial t} + \nabla \cdot (\mathbf{u}_I \mathbf{u}_I) = -\frac{1}{\rho} \nabla p_I + \mathbf{g}. \tag{6.27}$$

Nonlinear potential flow models for incident flow explained in Chapter 3 are limited to the water domain. Incident flow needs to be extended up to the air domain to apply multi-phase flow. The incident fluid velocity and pressure can be extended by using hyperbolic function used in the potential flow model for incident waves. However, the extrapolation of incident pressure with hyperbolic function results in large values in the air zone which can lead to numerical instability during simulation. To overcome this, Li (2018) scaled the incident pressure by mixture density

$$p_I^* = \frac{\rho}{\rho_w} p_I, \tag{6.28}$$

where p_I^* is pseudo mixture incident pressure. Euler equations can be rewritten with p_I^* as

$$\frac{\partial \mathbf{u}_I}{\partial t} + \nabla \cdot (\mathbf{u}_I \mathbf{u}_I) = -\frac{1}{\rho}\nabla p_I^* + \frac{p_I}{\rho_w}\frac{\nabla \rho}{\rho} + \mathbf{g}, \tag{6.29}$$

The second term in right-hand-side, $\frac{p_I}{\rho_w}\frac{\nabla \rho}{\rho}$, is equal to zero in both water and air regions, it only has a non-zero value on the interface. The momentum equations for complementary flow can be given by (Li, 2018)

$$\frac{\partial \mathbf{u}_C}{\partial t} + \nabla \cdot (\mathbf{u}\mathbf{u}_C) + \mathbf{u}_C \cdot \nabla \mathbf{u}_I = -\frac{1}{\rho}\nabla p_C - \frac{p_I}{\rho_w}\frac{\nabla \rho}{\rho} + \nabla \cdot \left(\nu \left(\nabla \mathbf{u}_C + \nabla \mathbf{u}_C^T\right)\right). \tag{6.30}$$

The transport equation for complementary LS function is given by

$$\frac{\partial \psi_C}{\partial t} + \nabla \cdot (\mathbf{u}\psi_C) = -\frac{\partial \psi_I}{\partial t} - \nabla \cdot (\mathbf{u}\psi_I). \tag{6.31}$$

The re-distancition of the complementary LS function is calculated by subtracting the incident wave LS function from distance as

$$\psi_C = \mathrm{sgn}(d) - \psi_I. \tag{6.32}$$

6.3.2 Interface conditions

Interface boundary conditions need to be formulated with respect to complementary terms. The kinematic free surface boundary condition is given by

$$[\![\mathbf{u}]\!] = [\![\mathbf{u}_I + \mathbf{u}_C]\!] = 0, \qquad \text{on} \qquad \mathbf{x} \in S_f. \tag{6.33}$$

Assuming that the incident velocity is continuous across the interface by Wheeler stretching, e.g., $[\![\mathbf{u}_I]\!] = 0$. The kinematic free surface boundary condition for complementary velocity is given by

$$[\![\mathbf{u}_C]\!] = 0, \qquad \text{on} \qquad \mathbf{x} \in S_f. \tag{6.34}$$

The pressure jump condition is given by

$$[\![p]\!] = [\![p_I + p_C]\!] = 0, \qquad \text{on} \qquad \mathbf{x} \in S_f. \tag{6.35}$$

The incident pressure p_I is replaced by pseudo incident pressure given in equation (6.28). The jump condition for complementary pressure is given by (Li, 2018)

$$[\![p_C]\!] = -[\![p_I^*]\!] = -p_I \frac{[\![\rho]\!]}{\rho_w} = p_I \frac{\rho_w - \rho_a}{\rho_w}. \tag{6.36}$$

The pressure jump term is shown in the right-hand-side term. Compared to Vukčević (2016), pressure jump condition in the present study incorporates the incident wave pressure, including hydrostatic pressure. For the calm water case, the same pressure jump condition is obtained $p_I = \rho_w \mathbf{g} \cdot \mathbf{x}$.

6.3.3 Summary of functional decomposition

Govening equations for complementary flow are summarized as below:

- Continuity equation for complementary flow

$$\nabla \cdot \mathbf{u}_C = 0.$$

- Momentum equations for complementary flow

$$\frac{\partial \mathbf{u}_C}{\partial t} + \nabla \cdot (\mathbf{u}\mathbf{u}_C) + \mathbf{u}_C \cdot \nabla \mathbf{u}_I = -\frac{1}{\rho}\nabla p_C - \frac{p_I}{\rho_w}\frac{\nabla \rho}{\rho} + \nabla \cdot \left(\nu \left(\nabla \mathbf{u}_C + \nabla \mathbf{u}_C^T\right)\right).$$

- LS function transport equation for complementary flow

$$\frac{\partial \psi_C}{\partial t} + \nabla \cdot (\mathbf{u}\psi_C) = -\frac{\partial \psi_I}{\partial t} - \nabla \cdot (\mathbf{u}\psi_I).$$

- Redistancing ψ_C

$$\psi_C = \mathrm{sgn}(d) - \psi_I,$$

  where d is the distance from nearest interface.

Interface boundary conditions for complementary flow are summarized as below:

- Kinematic interface condition for complementary flow

$$[\![\mathbf{u}_C]\!] = 0.$$

- Pressure jump condition for complementary flow

$$[\![p_C]\!] = p_I \frac{\rho_w - \rho_a}{\rho_w}.$$

6.4 Domain decomposition: Relaxation

Relaxation scheme described in section 2.3.1 is used to relax the complementary LS function and velocity into target quantities. Explicit relaxation scheme which blends computed complementary quantities and target quantities with weight function in the relaxation zone is adopted. Complementary flow is relaxed as

$$\chi_C = (1 - w)\chi_C + w\chi_C^{Target}, \tag{6.37}$$

where χ_C is the complementary quantity, χ_C^{Target} is the target quantity and w is a weight function. In the literature, the target quantity has been set to zero due to the lack of solution (Jacobsen et al., 2012; Seng, 2012; Vukčević, 2016; Li, 2018).

In present study, Poincaré's velocity representation is used to calculate target complementary quantities in the relaxation zone. Complementary fluid velocity and LS function are relaxed as

$$\mathbf{u}_C = (1 - w)\mathbf{u}_C + w\mathbf{u}_C^{\text{Poincaré}}, \tag{6.38}$$

$$\psi_C = (1 - w)\psi_C + w\psi_C^{\text{Poincaré}}. \tag{6.39}$$

where $\mathbf{u}_C^{\text{Poincaré}}$ and $\psi_C^{\text{Poincaré}}$ are the target complementary fluid velocity and LS function computed by Poincaré's velocity representation.

6.5 Extrapolation of flows up to air zone

The SWENSE method in multi-phase flow requires the evaluation of incident flows in air zone which is not available in potential flow model. Wheeler stretching can be used to extrapolate incident flow, however hyperbolic characteristics of waves in vertical direction generates large velocity and pressure for large z. It causes undesirable results in numerical discretization especially for discretizing the incident wave quantities in air zone. Li (2018) set constant values for incident flow above limited height to prevent numerical errors due to large value. Nevertheless, their gradients still have the discontinuities at limited height.

In the present study, incident wave quantities are extrapolated by using cubic polynomials to prevent discontinuities of incident flow and its gradient in the air zone.

6.5.1 Extrapolation by cubic polynomials

Let the flow quantity and its gradient are given at $z = \Xi + h_{ref}$ and $z = \Xi + h_{ref} + h_{thickness}$ as

$$f(\Xi + h_{ref}) = f_0, \qquad \frac{df(\Xi + h_{ref})}{dz} = f_0', \tag{6.40}$$

$$f(\Xi + h_{ref} + h_{thickness}) = f_1 \qquad \frac{df(\Xi + h_{ref} + h_{thickness})}{dz} = f_1'. \tag{6.41}$$

where h_{ref} is a reference height from interface to start extrapolation. $h_{thickness}$ is the height interval for cubic polynomials. Introducing cubic polynomials with normalized coordinate $\tilde{\zeta}$ defined between $\tilde{\zeta} \in [0, 1]$ as

$$g(\tilde{\zeta}) = a\tilde{\zeta}^3 + b\tilde{\zeta}^2 + c\tilde{\zeta} + d, \tag{6.42}$$

where a, b, c and d are coefficients. $\tilde{\zeta}$ is a normalized coordinate defined by

$$\tilde{\zeta} = \frac{z - \Xi + h_{ref}}{h_{thickness}}. \tag{6.43}$$

Boundary conditions for cubic polynomials $g(\tilde{\zeta})$ can be given as

$$g(0) = f_0, \qquad \frac{dg(0)}{d\tilde{\zeta}} = g_0' = h_{thickness} f_0', \tag{6.44}$$

$$g(1) = f_1 \qquad \frac{dg(1)}{d\tilde{\zeta}} = g_1' = h_{thickness} f_1'. \tag{6.45}$$

Using boundary conditions, coefficients of cubic polynomials are determined as

$$a = \left\{2(g_0 - g_1) + (g_0' + g_1')\right\}, \tag{6.46}$$

$$b = -\left\{3\left(g_0 - g_1\right) + 2\left(g_0' + g_1'\right) - g_1'\right\}, \tag{6.47}$$

$$c = g_0', \tag{6.48}$$

$$d = g_0. \tag{6.49}$$

6.5.2 Application to flow properties and discussion

Boundary conditions for incident velocities are given by

$$\mathbf{u}_0 = \mathbf{u}_I(\Xi_I + h_{ref}), \qquad \mathbf{u}'_0 = \frac{d\mathbf{u}_I(\Xi_I + h_{ref})}{dz} \tag{6.50}$$

$$\mathbf{u}_1 = \mathbf{u}(\Xi_I + h_{ref} + h_{thickness}) = \mathbf{u}_{wind}, \qquad \mathbf{u}'_1 = \frac{d\mathbf{u}_I(\Xi_I + h_{ref} + h_{thickness})}{dz} = 0. \tag{6.51}$$

The dynamic part of the incident pressure is defined by subtracting the hydrostatic pressure as

$$p_{I,d} = p_I - \rho \mathbf{g} \cdot \mathbf{x}, \tag{6.52}$$

where $p_{I,d}$ is the dynamic incident pressure and $\rho \mathbf{g} \cdot \mathbf{x}$ is the hydrostatic pressure. Boundary conditions for the dynamic incident pressure are given by

$$p_0 = p_{I,d}(\Xi_I + h_{ref}), \qquad p'_0 = \frac{dp_{I,d}(\Xi_I + h_{ref})}{dz}, \tag{6.53}$$

$$p_1 = 0, \qquad p'_1 = \frac{dp_{I,d}(h_{ref})}{dz} = 0, \tag{6.54}$$

If vertical gradients of incident velocity and dynamic pressure are available from the incident potential flow model, extrapolations of fluid velocity and dynamic incident pressure are straightforward.

Extrapolated fluid velocity by cubic polynomials does not satisfy mass conservation in the air zone. If horizontal fluid velocity and its horizontal gradient at $z = \Xi_I + h_{ref}$ are slowly varying, the total continuity error due to extrapolation can be estimated as

$$\begin{aligned} \frac{\epsilon_{continuity}}{\Delta x \Delta y} &\approx \int_{\Xi_I + h_{ref}}^{\Xi_I + h_{ref} + h_{thickness}} \nabla \cdot \mathbf{u}(z) dz \\ &\approx \int_{\Xi_I + h_{ref}}^{\Xi_I + h_{ref} + h_{thickness}} \frac{d\mathbf{u}(z)}{dz} dz \\ &= \left| \mathbf{u}_{wind} - \mathbf{u}_I(\Xi_I + h_{ref}) \right|. \end{aligned} \tag{6.55}$$

The estimated continuity error is constant with respect to $h_{thickness}$ and proportional to the difference of fluid velocity between incident waves and wind. The local continuity error on the local cell therefore decreases as $h_{thickness}$ increases. Extrapolation improves numerical stability and prevents large flux in the air zone due to discontinuity of velocity.

Buffer zone with thickness h_{ref} is introduced to have a distance from interpolation region to interface because of mentioned continuity error in air. Extrapolated velocity is shown in figure 6.1. Velocity fields with air extrapolation for nonlinear regular waves are shown in figure 6.2. No discontinuity of fluid velocity is seen when the extrapolation is applied.

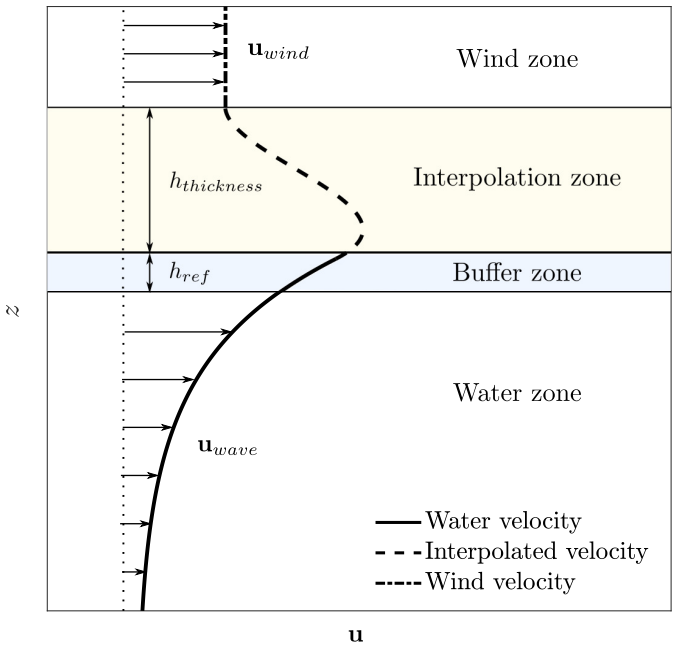

Figure 6.1. Velocity extrapolation up to air zone with cubic polynomials.

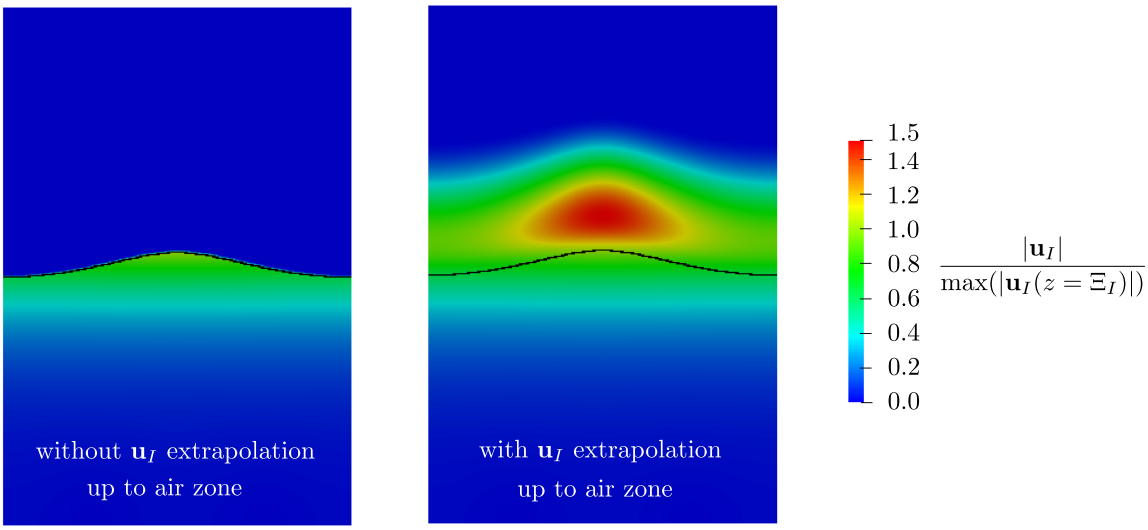

Figure 6.2. Comparison of $|\mathbf{u}_I|$ field with/without velocity extrapolation up to air zone by cubic polynomials(black line denotes the interface).

6.6 Finite volume discretization

The numerical discretization of governing equations for two-phase interface flows is presented in this section. Collocated Finite Volume (FV), second-order discretization on the arbitrary polyhedral (unstructured) grid is used (Jasak, 1996). Computational domain is discretized into computational cells and each of these cells is treated as a control volume having averaged quantities within cell. The geometrical description of computational cell with owner index P is shown in figure 6.3. Computational cell has its own volume (V_P) and has the faces connected with

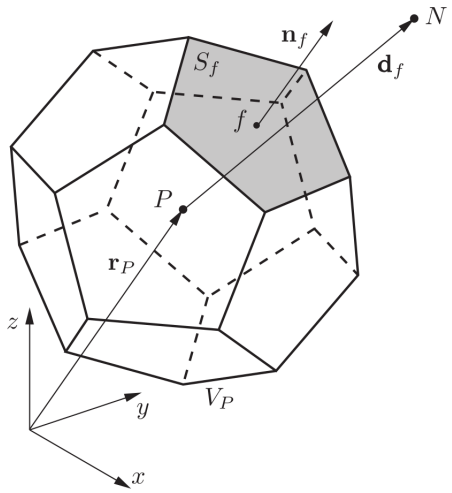

Figure 6.3. Finite volume cell in polyhedral shape, (Tukovic and Jasak, 2012).

neighbor cells (cell index; N) or boundary surfaces. The surface area vector ($\mathbf{s}_f$) is defined as a vector normal to the corresponding face with its magnitude equal to the surface area. The distance vector ($\mathbf{d}_f = \mathbf{x}_N - \mathbf{x}_P$) is defined as the distance from owner cell P to neighbor cell N. General FV discretization on collocated grids is well described in Jasak (1996). Special FV discretization considering the pressure conditions on the interface is also given by Vukčević (2016). These pressure conditions need a special FV discretization technique, which is called Ghost Fluids Method (GFM).

Numerical discretization of governing equations and terms related to pressure proposed by Vukčević (2016) is briefly reproduced in this section.

6.6.1 Discretization of momentum equations

Momentum equations given in (6.30) are rearranged as

$$\frac{\partial \mathbf{u}_C}{\partial t} + \nabla \cdot (\mathbf{u}\mathbf{u}_C) - \nabla \cdot (\nu \nabla \mathbf{u}_C) = -\frac{1}{\rho}\nabla p_C - \frac{p_I}{\rho_w}\frac{\nabla \rho}{\rho} - \mathbf{u}_C \cdot \nabla \mathbf{u}_I + \nabla \mathbf{u}_C \cdot \nabla \nu,$$

Following the discretization notation of Rusche (2002), momentum equations without pressure gradient are discretized by

$$\left\{ \frac{\partial \mathbf{u}_C}{\partial t} + \nabla \cdot (\mathbf{u}\mathbf{u}_C) - \nabla \cdot (\nu \nabla \mathbf{u}_C) \right\}^i = \left\{ -\frac{p_I}{\rho_w}\frac{\nabla \rho}{\rho} - \mathbf{u}_C \cdot \nabla \mathbf{u}_I + \nabla \mathbf{u}_C \cdot \nabla \nu \right\}^e, \tag{6.56}$$

where $\{\cdot\}^i$ and $\{\cdot\}^e$ denote the implicit and explicit discretization, respectively. The discretization of momentum equations in FV grid is given by

$$a_P \left(\mathbf{u}_C\right)_P + \sum_f a_N \left(\mathbf{u}_C\right)_N = \mathbf{s}_{\mathbf{u}_C}, \tag{6.57}$$

where $(\cdot)_P$ and $(\cdot)_N$ denote averaged quantities at owner (P) and neighbor (N) cells, respectively. a_P and a_N represent the diagonal and off-diagonal terms of momentum equations, respectively. $\mathbf{s}_{\mathbf{u}_C}$ is the source term of the momentum equations which includes:

- The old time contribution of local term in momentum equations.
- Nonlinear deffered correction of convection term.
- Non-orthogonal correction of FV discretization.
- Incident flow terms coming from SWENSE method.

Deferred correction of convection terms and non-orthogonal correction are well explained in (Jasak, 1996; Moulkalled et al., 2015).

6.6.2 Discretization of pressure equation

To satisfy the continuity equation, complementary pressure and velocity are coupled (Patankar and Spalding, 1972). Predicted complementary velocity from the momentum equation is written as

$$\left(\mathbf{u}'_C\right)_P = \frac{1}{a_P}\mathbf{H}\left\{\left(\mathbf{u}_C\right)_P\right\} = -\frac{1}{a_P}\left\{\sum_f a_N \left(\mathbf{u}_C\right)_N - \mathbf{s}_{\mathbf{u}_C}\right\} \tag{6.58}$$

The pressure gradient, excluded from previous discretization of momentum equations, is now added to predicted velocity as

$$\left(\mathbf{u}_C\right)_P = \left(\mathbf{u}'_C\right)_P - \frac{1}{a_P}\left(\frac{1}{\rho}\nabla(p_C)_P\right), \tag{6.59}$$

Right-hand side term is called pressure corrected velocity. Complementary velocity should satisfy the continuity equation as

$$\nabla \cdot \left(\mathbf{u}_C\right)_P = 0, \tag{6.60}$$

Therefore, the equation for complementary pressure is given by

$$\nabla \cdot \left[\frac{1}{a_P}\left(\frac{1}{\rho}\nabla(p_C)_P\right)\right] = \nabla \cdot \left[\frac{1}{a_P}\mathbf{H}\left\{\left(\mathbf{u}_C\right)_P\right\}\right], \tag{6.61}$$

Applying FV discretization and Gauss's divergence theorem of volume integral over V_P above equation gives

$$\sum_f \left(\frac{1}{a_P}\left(\frac{1}{\rho}\nabla(p_C)_P\right)\right)_f \cdot d\mathbf{s}_f = \sum_f \left(\frac{1}{a_P}\mathbf{H}\left\{\left(\mathbf{u}_C\right)_P\right\}\right)_f \cdot d\mathbf{s}_f. \tag{6.62}$$

where $(\cdot)_f$ denotes the quantity at face center. When the computational cell is small, the quantity at face center is interpolated from adjacent cell centers as

$$\sum_f \overline{\left(\frac{1}{a_P}\right)}_f \left(\frac{1}{\rho}\nabla(p_C)_P\right)_f \cdot d\mathbf{s}_f = \sum_f \overline{\left(\frac{1}{a_P}\mathbf{H}\left\{(\mathbf{u}_C)_P\right\}\right)}_f \cdot d\mathbf{s}_f. \tag{6.63}$$

where $\overline{(\cdot)}_f$ is interpolated at face center from cell centered value. The above equation gives the algebraic equations for complementary pressure at cell center. After solving the pressure equation, the complementary velocity is corrected by equation (6.58) and the total flux is also calculated by

$$F_f = \mathbf{s}_f \cdot (\mathbf{u}_C + \mathbf{u}_I)_f = \mathbf{s}_f \cdot \left\{ \overline{\left(\frac{1}{a_P}\mathbf{H}\left\{(\mathbf{u}_C)_P\right\}\right)}_f - \overline{\left(\frac{1}{a_P}\right)}_f \left(\frac{1}{\rho}\nabla(p_C)_P\right)_f + (\mathbf{u}_I)_f \right\}. \tag{6.64}$$

The incident velocity should be also evaluated at face centers to give the total flux.

6.6.3 Discretization of LS function transport equation

The complementary LS function transport equation is discretized using implicit and explicit operators by

$$\left\{\frac{\partial \psi_C}{\partial t} + \nabla \cdot (\mathbf{u}\psi_C)\right\}^i = \left\{-\frac{\partial \psi_I}{\partial t} - \nabla \cdot (\mathbf{u}\psi_I)\right\}^e, \tag{6.65}$$

and it gives the discretized equation for complementary LS function as

$$a_P^{\psi} (\psi_C)_P + \sum_f a_N^{\psi} (\psi_C)_N = \mathbf{s}_{\psi}, \tag{6.66}$$

where a_P^{ψ} and a_N^{ψ} are diagonal and off-diagonal terms. The total LS function is calculated after solving the above equation as

$$(\psi)_P = (\psi_I)_P + (\psi_C)_P, \tag{6.67}$$

Interface location is calculated from total LS function ($\psi = 0$). The distance from the interface to the cell center (P) is calculated for each computational cell. Re-distancing of complementary LS function is computed by subtracting incident LS function from signed distance by

$$(\psi_C)_P = \operatorname{sgn}\left\{(d)_P\right\} - (\psi_I)_P. \tag{6.68}$$

6.6.4 Extrapolation of pressures by Ghost Fluid Method

The FV discretization of pressure terms appears in momentum and pressure equations. Interface boundary conditions for complementary pressure are considered by using Ghost Fluid Method (GFM). Layout of finite volume cells with the interface is depicted in figure 6.4. Interface between water and air is plotted with blue dashed line. Red colored lines denote interface faces. Interface cells are denoted with red cross at center. Interface cells are determined by

$$(\psi)_P (\psi)_N < 0. \tag{6.69}$$

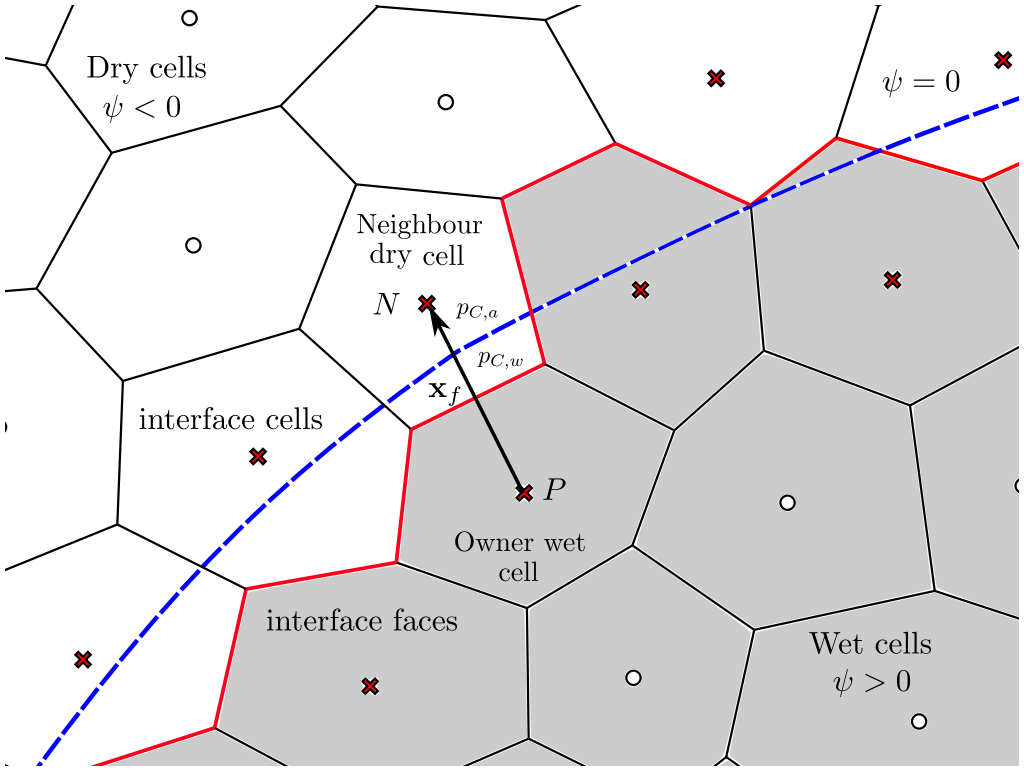

Figure 6.4. Finite volume cells and interface crossing the computational domain.

Wet cell P and dry cell N share an interface face $\mathbf{s}_f^f$. The dimensionless distance parameter defining the interface location by LS function is given by

$$\lambda_f = \frac{(\psi)_P}{(\psi)_P - (\psi)_N}, \tag{6.70}$$

The location of the interface is defined by using the dimensionless distance parameter (λ_f) as

$$\mathbf{x}_f = (\mathbf{x})_P + \lambda_f \mathbf{d}_f. \tag{6.71}$$

The pressure jump condition on the interface is given by

$$\begin{aligned} [\![(p_C)_P]\!] &= p_{C,a} - p_{C,w} = p_I \frac{\rho_w - \rho_a}{\rho_w} \\ &= \mathcal{H}_I \end{aligned} \tag{6.72}$$

where $p_{C,a}$ and $p_{C,w}$ are the complementary pressures near the interface at air and water sides. $\mathcal{H}_I = p_I \frac{\rho_w - \rho_a}{\rho_w}$ is the pressure jump on the interface. The complementary pressure values near the interface at each fluid domain are expressed with jump conditions

$$p_{C,w} = \frac{\rho_a}{\rho_w} p_{C,a} - \frac{\mathcal{H}_I}{\rho_w}, \tag{6.73}$$

$$p_{C,a} = \frac{\rho_w}{\rho_a} p_{C,w} + \frac{\mathcal{H}_I}{\rho_a}. \tag{6.74}$$

The relation of pressure gradient for extrapolation

The pressure boundary condition is imposed on the air/water interface. Because the interface between two fluids is not always located on a computational cell or face center, the pressure extrapolation from the computational cell or face center to the position of interface is necessary. Applying the kinematic boundary condition on the momentum equations gives

$$\left[\!\left[\frac{D\mathbf{u}}{Dt}\right]\!\right] = \left[\!\left[-\frac{1}{\rho}\nabla p + \nabla\cdot(\nu\nabla\mathbf{u}) + \nabla\mathbf{u}\cdot\nabla\nu + \mathbf{g}\right]\!\right] = 0, \qquad \text{on} \qquad \mathbf{x}\in S_f \tag{6.75}$$

It states that the acceleration of two fluid particles on the interface is equal to each other. After neglecting the viscosity terms, the jump condition for pressure gradient is derived as

$$\begin{aligned}\left[\!\left[\frac{1}{\rho}\nabla p\right]\!\right] &= \left[\!\left[\nabla\cdot(\nu\nabla\mathbf{u}) + \nabla\mathbf{u}\cdot\nabla\nu\right]\!\right], \qquad \text{on} \qquad \mathbf{x}\in S_f \\ &= 0.\end{aligned} \tag{6.76}$$

The pressure is decomposed into incident and complementary parts as in equation (6.23). Density scaling of incident pressure gives the continuous $\nabla p_I/\rho$ across the interface (Li, 2018). Therefore, the jump condition for complementary pressure gradient is given by

$$\left[\!\left[\frac{1}{\rho}\nabla p_C\right]\!\right] = 0, \qquad \text{on} \qquad \mathbf{x}\in S_f. \tag{6.77}$$

The pressure extrapolation using above relations is proposed by Vukčević (2016) in the procedure of Finite Volume (FV) discretization.

Pressure extrapolation from wet owner cell (P) to the dry neighbor cell (N)

When owner cell is wet and neighbor cell is dry, pressure gradient condition on the interface is given by

$$\begin{aligned}\left[\!\left[\frac{\nabla p_C}{\rho}\right]\!\right] &= \frac{\nabla p_{C,a}}{\rho_a} - \frac{\nabla p_{C,w}}{\rho_w} \\ &= \frac{1}{\rho_a}\frac{(p_C)_N - p_{C,a}}{1-\lambda_f} - \frac{1}{\rho_w}\frac{p_{C,w} - (p_C)_P}{\lambda_f} = 0,\end{aligned} \tag{6.78}$$

Using equations (6.73), (6.74) and (6.78), pressure near the interface can be expressed with pressure values at cell centers with pressure jump term as

$$p_{C,w} = \lambda_f\frac{\rho_a}{\tilde{\rho}_w}(p_C)_N + (1-\lambda_f)\frac{\rho_a}{\tilde{\rho}_w}(p_C)_P - \lambda_f\frac{\mathcal{H}_I}{\tilde{\rho}_w}, \tag{6.79}$$

$$p_{C,a} = \lambda_f\frac{\rho_w}{\tilde{\rho}_w}(p_C)_N + (1-\lambda_f)\frac{\rho_w}{\tilde{\rho}_w}(p_C)_P + (1-\lambda_f)\frac{\mathcal{H}_I}{\tilde{\rho}_w}, \tag{6.80}$$

with

$$\tilde{\rho}_w = \lambda_f\rho_w + (1-\lambda_f)\rho_a. \tag{6.81}$$

Extrapolated pressure at ghost dry cell center N from wet cell center P can be given by

$$\begin{aligned}(p_{C,w})_N^{GC} &= p_{C,w} + \frac{1-\lambda_f}{\lambda_f}\{p_{C,w} - (p_C)_P\} \\ &= \frac{\rho_a}{\tilde{\rho}_w}(p_C)_N + \left(1 - \frac{\rho_w}{\tilde{\rho}_w}\right)(p_C)_P - \frac{\mathcal{H}_I}{\tilde{\rho}_w}.\end{aligned} \tag{6.82}$$

Pressure extrapolation from dry owner cell (P) to the wet neighbor cell (N)
Similar to the previous case, when owner cell is dry and neighbor cell is wet, the pressure gradient condition on the interface is given by

$$\left[\!\left[\frac{\nabla p_C}{\rho}\right]\!\right] = \frac{1}{\rho_a}\frac{p_{C,a} - (p_C)_P}{\lambda_f} - \frac{1}{\rho_w}\frac{(p_C)_N - p_{C,w}}{1-\lambda_f} = 0, \tag{6.83}$$

Substituting the equations (6.73) and (6.74) into (6.83) yields the pressures near the interface as

$$p_{C,a} = \lambda_f \frac{\rho_w}{\tilde{\rho}_a}(p_C)_N + (1-\lambda_f)\frac{\rho_w}{\tilde{\rho}_a}(p_C)_P + \lambda_f \frac{\mathcal{H}_I}{\tilde{\rho}_a}, \tag{6.84}$$

$$p_{C,w} = \lambda_f \frac{\rho_a}{\tilde{\rho}_a}(p_C)_N + (1-\lambda_f)\frac{\rho_a}{\tilde{\rho}_a}(p_C)_P - (1-\lambda_f)\frac{\mathcal{H}_I}{\tilde{\rho}_a}, \tag{6.85}$$

with

$$\tilde{\rho}_a = \lambda \rho_a + (1-\lambda)\rho_w. \tag{6.86}$$

Similarly to the previous case, the extrapolated pressure on the ghost wet cell center (N) from dry cell center (P) is given by

$$\begin{aligned}(p_{C,a})_N^{GC} &= p_{C,a} + \frac{1-\lambda_f}{\lambda_f}\{p_{C,a} - (p_C)_P\} \\ &= \frac{\rho_w}{\tilde{\rho}_a}(p_C)_N + \left(1 - \frac{\rho_a}{\tilde{\rho}_a}\right)(p_C)_P + \frac{\mathcal{H}_I}{\tilde{\rho}_a}.\end{aligned} \tag{6.87}$$

The procedure of pressure extrapolation is well explained in Vukčević (2016).

6.6.5 FV discretization with extrapolated pressures

The gradient of the complementary pressure at cell center P is calculated by Gauss's divergence theorem

$$(\nabla p_C)_P = \frac{1}{V_P}\sum_f \mathbf{s}_f (p_C)_f, \tag{6.88}$$

Each of face components contributes to the pressure gradient. At face center, the complementary pressure is calculated by linear interpolation based on distance as

$$(p_C)_f = f_x (p_C)_P + (1-f_x)(p_C)_N, \tag{6.89}$$

where $f_x = \overline{fP}/|\mathbf{d}_f|$ is a distance weight. $\overline{fP}$ is the distance from cell center P to face center f.

When the owner cell is wet and the neighbour cell is dry, the complementary pressure at neighbour is replaced by the extrapolated complementary pressure obtained by GFM

$$(p_C)_f^{GC} = f_x (p_C)_P + (1-f_x)(p_{C,w})_N^{GC}. \tag{6.90}$$

where $(p_{C,w})_N^{GC}$ is the extrapolated pressure from wet cell by the GFM defined in equation (6.82).

When the owner cell is dry and the neighbour cell is wet, the complementary pressure at the neighbour cell is replaced by the extrapolated complementary pressure by GFM as

$$(p_C)_f^{GC} = f_x (p_C)_P + (1-f_x)(p_{C,a})_N^{GC}. \tag{6.91}$$

where $(p_{C,a})_N^{GC}$ is the extrapolated pressure from dry cell by the GFM defined in equation (6.87).

The pressure gradient of interface cell is evaluated by replacing the complementary pressure at face center by the extrapolated complementary pressure by GFM

$$(\nabla p_C)_P = \frac{1}{V_P}\left\{\sum_f \mathbf{s}_f (p_C)_f - \sum_{fs_f} \mathbf{s}_f (p_C)_f + \sum_{fs_f} \mathbf{s}_f (p_C)_f^{GC}\right\}. \tag{6.92}$$

The same procedure can be applied for other gradient discretization by replacing complementary pressure at interface face. Laplacian operator in pressure equation also requires special FV discretization considering interface condition. Interpolated density $\left(\frac{1}{\rho}\right)_f$ is necessary to construct the pressure equation in (6.63). Continuous $\frac{\nabla p_C}{\rho}$ across interface enables us to extrapolate density by GFM

$$\left(\frac{1}{\rho}\right)_f^{GC} = \begin{cases} \dfrac{1}{\rho_w}, & \text{when the owner cell } P \text{ is wet, } (\psi)_P \geq 0. \\ \dfrac{1}{\rho_a}, & \text{when the owner cell } P \text{ is dry, } (\psi)_P < 0. \end{cases} \tag{6.93}$$

The pressure Poisson equation is rewritten with interpolated density at face center as

$$\sum_f \overline{\left(\frac{1}{a_P}\right)}_f \left(\frac{1}{\rho}\right)_f (\nabla p_C)_f \cdot d\mathbf{s}_f = \sum_f \overline{\left(\frac{1}{a_P}\mathbf{H}\left\{(\mathbf{u}_C)_P\right\}\right)}_f \cdot d\mathbf{s}_f, \tag{6.94}$$

The left-hand side is divided into orthogonal and non-orthogonal components (Jasak, 1996)

$$\begin{aligned}\sum_f \overline{\left(\frac{1}{a_P}\right)}_f \left(\frac{1}{\rho}\right)_f (\nabla p_C)_f \cdot d\mathbf{s}_f = &\sum_f \overline{\left(\frac{1}{a_P}\right)}_f \left(\frac{1}{\rho}\right)_f \Delta_f \cdot (\nabla p_C)_f \\ &+ \sum_f \overline{\left(\frac{1}{a_P}\right)}_f \left(\frac{1}{\rho}\right)_f \mathbf{k}_f \cdot (\nabla p_C)_f\end{aligned} \tag{6.95}$$

where the surface vector $\mathbf{s}_f$ is divided into two vectors

$$\mathbf{s}_f = \Delta_f + \mathbf{k}_f. \tag{6.96}$$

The vector Δ_f is taken to be parallel with $\mathbf{d}_f$. $\mathbf{k}_f$ is a non-orthogonal vector component $\mathbf{k}_f = \mathbf{s}_f - \Delta_f$. The choice and effects of non-orthogonal correction are well discussed in Jasak (1996). The non-orthogonal correction term is calculated by previous outer iteration or time step by deferred correction and it is taken into account as the source term. Rewritten complementary pressure equation is given as

$$\begin{aligned}\sum_f \overline{\left(\frac{1}{a_P}\right)}_f \left(\frac{1}{\rho}\right)_f \Delta_f \cdot (\nabla p_C)_f = &\sum_f \overline{\left(\frac{1}{a_P}\mathbf{H}\left\{(\mathbf{u}_C)_P\right\}\right)}_f \cdot d\mathbf{s}_f \\ &- \sum_f \overline{\left(\frac{1}{a_P}\right)}_f \left(\frac{1}{\rho}\right)_f \mathbf{k}_f \cdot (\nabla p_C)_f^o .\end{aligned} \tag{6.97}$$

Left-hand side is given by complementary pressures at neighbor N and owner P center

$$\sum_f \overline{\left(\frac{1}{a_P}\right)}_f \left(\frac{1}{\rho}\right)_f \Delta_f \cdot (\nabla p_C)_f = \sum_f \overline{\left(\frac{1}{a_P}\right)}_f \left(\frac{1}{\rho}\right)_f \frac{|\mathbf{s}_f|}{|\mathbf{d}_f|}\left\{(p_C)_N - (p_C)_P\right\} \tag{6.98}$$

On the interface face, complementary pressure at neighbor cell center N is replaced by extrapolated pressure

$$\begin{aligned}\sum_f \overline{\left(\frac{1}{a_P}\right)}_f \left(\frac{1}{\rho}\right)_f \frac{|\mathbf{s}_f|}{|\mathbf{d}_f|}\left\{(p_C)_N - (p_C)_P\right\} &= \sum_f \overline{\left(\frac{1}{a_P}\right)}_f \left(\frac{1}{\rho}\right)_f \frac{|\mathbf{s}_f|}{|\mathbf{d}_f|}\left\{(p_C)_N - (p_C)_P\right\} \\ &- \sum_{fs_f} \overline{\left(\frac{1}{a_P}\right)}_f \left(\frac{1}{\rho}\right)_f \frac{|\mathbf{s}_f|}{|\mathbf{d}_f|}\left\{(p_C)_N - (p_C)_P\right\} \\ &+ \sum_{fs_f} \overline{\left(\frac{1}{a_P}\right)}_f \left(\frac{1}{\rho}\right)_f^{GC} \frac{|\mathbf{s}_f|}{|\mathbf{d}_f|}\left\{(p_{C,i})_N^{GC} - (p_C)_P\right\}, \qquad i = w, a.\end{aligned} \tag{6.99}$$

Above equation constructs the system matrix with respect to pressure at each cell center. The diagonal contribution of interface face S_f is given by interface cell P as,

$$a_P^{p_C} = -\begin{cases}\left(\frac{1}{a_P}\right)_f \frac{|\mathbf{s}_f|}{|\mathbf{d}_f|}\frac{\rho_w}{\tilde{\rho}_w}, & \text{if the owner cell } P \text{ is wet, neighbor cell } N \text{ is dry,} \\ \left(\frac{1}{a_P}\right)_f \frac{|\mathbf{s}_f|}{|\mathbf{d}_f|}\frac{\rho_a}{\tilde{\rho}_a}, & \text{if the owner cell } P \text{ is dry, neighbor cell } N \text{ is wet.}\end{cases} \tag{6.100}$$

and the off-diagonal contribution

$$a_{PN}^{p_C} = \begin{cases}\left(\frac{1}{a_P}\right)_f \frac{|\mathbf{s}_f|}{|\mathbf{d}_f|}\frac{\rho_a}{\tilde{\rho}_w}, & \text{if the owner cell } P \text{ is wet, neighbor cell } N \text{ is dry,} \\ \left(\frac{1}{a_P}\right)_f \frac{|\mathbf{s}_f|}{|\mathbf{d}_f|}\frac{\rho_w}{\tilde{\rho}_a}, & \text{if the owner cell } P \text{ is dry, neighbor cell } N \text{ is wet.}\end{cases} \tag{6.101}$$

The pressure jump terms appear as the extra source term as

$$Q_P^{p_C} = \begin{cases}-\left(\frac{1}{a_P}\right)_f \frac{|\mathbf{s}_f|}{|\mathbf{d}_f|}\frac{\mathcal{H}_I}{\tilde{\rho}_w}, & \text{if the owner cell } P \text{ is wet, neighbor cell } N \text{ is dry,} \\ \left(\frac{1}{a_P}\right)_f \frac{|\mathbf{s}_f|}{|\mathbf{d}_f|}\frac{\mathcal{H}_I}{\tilde{\rho}_a}, & \text{if the owner cell } P \text{ is dry, neighbor cell } N \text{ is wet.}\end{cases} \tag{6.102}$$

Vukčević (2016) showed that the off-diagonal contributions of pressure equation are symmetric but the extra source term arising from pressure jump is antisymmetric. The details on the FV discretization with interface condition is well described in Vukčević (2016) with different notation on the inverse density $\beta = \frac{1}{\rho}$.

6.7 Boundary conditions

Solving the Navier-Stokes equation requires initial and boundary conditions. For the wave-structure problem, the initial conditions are set to be incident wave fields without scattering waves. There are several types of boundaries (1) body/wall(bottom) (2) inlet/outlet and (3) atmosphere.

On the body surface

- The boundary condition for scattering fluid velocity is set to

$$\mathbf{u}_C = \mathbf{u}_b - \mathbf{u}_I \tag{6.103}$$

  where $\mathbf{u}_b$ is the velocity of the body surface. The impermeable no-slip body boundary condition is achieved.

- The `fixedFluxPressure` boundary condition is imposed on the pressure. The pressure gradient is adjusted by velocity flux which is specified with velocity boundary condition. Complementary fluid velocity on the boundary face is written by

$$(\mathbf{u}_C)_f = \overline{\left(\frac{1}{a_P}\mathbf{H}(\mathbf{u}_C)\right)}_f - \overline{\left(\frac{1}{a_P}\right)}_f (\nabla p_C)_f \tag{6.104}$$

  Applying the inner product with the surface vector $\mathbf{s}_f = |\mathbf{s}_f|\,\mathbf{n}_f$ gives

$$(\mathbf{u}_C)_f \cdot \mathbf{s}_f = \overline{\left(\frac{1}{a_P}\mathbf{H}(\mathbf{u}_C)\right)}_f \cdot \mathbf{s}_f - \overline{\left(\frac{1}{a_P}\right)}_f (\nabla p_C)_f \cdot \mathbf{s}_f \tag{6.105}$$

  Therefore, the pressure boundary condition is given in

$$\begin{aligned}(\nabla p_C)_f \cdot \mathbf{n}_f &= \frac{\overline{(a_P)}_f}{|\mathbf{s}_f|}\left(\overline{\left(\frac{1}{a_P}\mathbf{H}(\mathbf{u}_C)\right)}_f \cdot \mathbf{s}_f - (\mathbf{u}_C)_f \cdot \mathbf{s}_f\right) \\ &= \frac{\overline{(a_P)}_f}{|\mathbf{s}_f|}\left(F_f^{H/A} - F_f\right)\end{aligned} \tag{6.106}$$

  where

$$F_f^{H/A} = \overline{\left(\frac{1}{a_P}\mathbf{H}(\mathbf{u}_C)\right)}_f \cdot \mathbf{s}_f, \qquad F_f = (\mathbf{u}_C)_f \cdot \mathbf{s}_f. \tag{6.107}$$

  $F_f^{H/A}$ is the flux predicted by momentum equation and F_f is the flux calculated by the velocity boundary condition.

- Zero gradient condition is imposed to complementary LS function to prevent extra LS function flux.

$$\frac{\partial \psi_C}{\partial n} = 0. \tag{6.108}$$

inlet/outlet zones

Relaxation to total waves represents that the quantities computed by viscous flow model are relaxed to total waves including nonlinear incident waves with linear complementary waves. Linear complementary waves are computed by Poincaré's velocity representation.

- Complementary velocity is blended with zero or values of potential theory if it is available.

$$\mathbf{u}_C = \begin{cases} (1-w)\mathbf{u}_C, & \text{relaxation to nonlinear incident waves,} \\ (1-w)\mathbf{u}_C + w\mathbf{u}_C^{\text{Poincaré}}, & \text{relaxation to total waves} \end{cases} \tag{6.109}$$

- The `fixedFluxPressure` boundary condition is imposed on the pressure that determined by velocity boundary condition, likewise body boundary condition.

$$(\nabla p_C)_f \cdot \mathbf{n}_f = \frac{\overline{(a_P)}_f}{|\mathbf{s}_f|}\left(F_f^{H/A} - F_f\right) \tag{6.110}$$

- Complementary LS function is blended with zero or complementary wave elevation computed by potential theory.

$$\psi_C = \begin{cases} (1-w)\psi_C, & \text{relaxation to nonlinear incident waves,} \\ (1-w)\psi_C + w\psi_C^{\text{Poincaré}}, & \text{relaxation to total waves} \end{cases} \tag{6.111}$$

Atmostphere

- The `pressureInletOutlet` boundary condition which is a combined boundary condition imposing a zero normal gradient for outflow and velocity obtained from boundary cell–center for inflow is imposed for complementary velocity.

$$\begin{aligned} \mathbf{n} \cdot \nabla \mathbf{u}_C &= 0, && \text{for outflow.} \\ \mathbf{u}_C &= (\mathbf{u}_C)_{BC}, && \text{for inflow.} \end{aligned} \tag{6.112}$$

  where $(\mathbf{u}_C)_{BC}$ is the velocity obtained from boundary cell–center.

- Following pressure condition is imposed at atmosphere boundary as

$$p_C = p_0 - 0.5\rho\left|\mathbf{u_C}\right|^2 \tag{6.113}$$

  where the reference pressure, p_0 is set to zero.

- At atmosphere boundary surfaces normal to z-plane, $\nabla\psi \approx \nabla\psi_I \approx 1$. Boundary condition for complementary LS function at atmosphere is given by

$$\mathbf{n} \cdot \nabla \psi_C = 0. \tag{6.114}$$

6.8 Comparison with Vukčević (2016) and Li (2018)

The present study is based on the previous works of Vukčević (2016) and Li (2018). Previous and present works can be summarized as:

Vukčević (2016)

- Fluid velocity and interface quantity are decomposed in incident and complementary parts in framework of SWENSE.
- Pressure is not decomposed and is coupled with complementary velocity.
- All incident wave terms survive in FV discretization to keep the order of the numerical discretization.
- Transport equation for Level-Set (LS) function is derived from Phase-Function (PF) transport equation. Self-adjusting terms controlling the diffusion and compression of interface are considered.

Li (2018)

- Fluid velocity and pressure are decomposed into incident and complementary parts in the framework of SWENSE.
- Incident flow terms appearing in Euler equations are canceled in momentum equations, therefore they do not appear in FV discretization.
- Volume Of Fluid (VOF) is used for interface modeling. Boundedness of VOF is kept, however VOF is not decomposed into incident and complementary parts.

Present work

- Fluid velocity, pressure, and interface quantity are decomposed in incident and complementary parts in framework of SWENSE.
- Incident flow terms appearing in Euler equations are canceled in momentum equations, therefore they do not appear in FV discretization.
- Transport equation for Level-Set (LS) function is used for interface modeling. However, incident LS function terms are not canceled but given as the source terms of complementary LS function transport equuation. Re-distanding of complementary LS function is applied by calculating the distance from nearest interface.
- Incident fluid velocity and pressure are extrapolated up to air zone using cubic polynomials. Incident fluid velocity and pressures and their gradient have smooth profiles in the computational domain for multi-phase flow.

6.9 Validation and discussion

6.9.1 Wave propagation in NWT

Incident wave propagation in a numerical wave tank is considered as benchmark test case. The same computational mesh and wave conditions as described in the section 2.2 are used. Relaxation zones of length 1.5λ are defined at ends of computation domain as the inlet and outlet for generation and absorption of waves. Length and height of total computational domain are 10λ and $2H$. Mean free surface is located on $z = 0$.

Extrapolation of incident wave velocity and pressure above free surface

Incident velocity in the air by Li (2018) is evaluated by putting the height limit ($1.5\Xi_I$) as

$$\mathbf{u}_I(x, y, z; t) = \begin{cases} \mathbf{u}_I(x, y, z; t), & \text{for} \quad z \leq 1.5\Xi_I, \\ \mathbf{u}_I(x, y, 1.5\Xi_I; t), & \text{for} \quad z > 1.5\Xi_I. \end{cases} \tag{6.115}$$

The same principle is applied for p_I/ρ_w. In the present study, the incident fluid velocity and pressure are extrapolated up to air zone by combining Wheeler stretching and cubic polynomials. The magnitude of the incident wave velocity field with extrapolation by cubic polynomials is compared in figure 6.5. Air velocity without extrapolation by cubic polynomials is fixed to the constant velocity above the certain height ($z = 1.5\Xi_I$). Incident velocity at $z = 1.5\Xi_I$ is calculated by applying Wheeler stretching on the incident wave model. Meanwhile, the extrapolation by cubic polynomials permits incident velocity up to air to have a smooth transition from water velocity to the wind velocity.

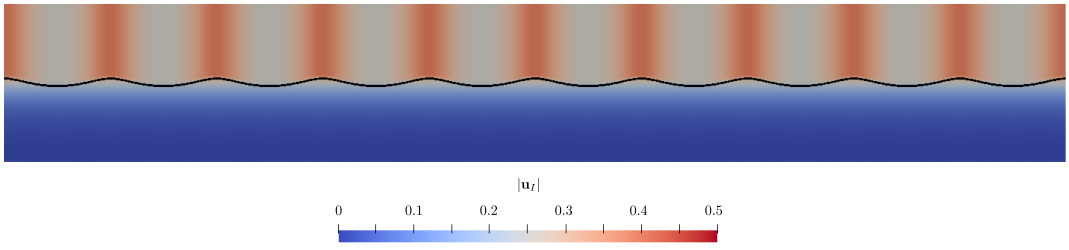

(a) $|\mathbf{u}_I|$ field without extrapolatation by cubic polynomials

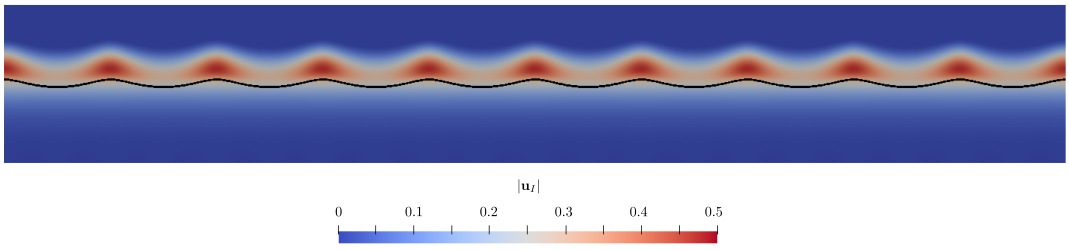

(b) $|\mathbf{u}_I|$ field with extrapolatation by cubic polynomials

Figure 6.5. Magnitude of incident wave field ($\mathbf{u}_I$) with and without extrapolation by cubic polynomials up to air, Black line denotes $\psi \in [-0.01, 0.01]$.

Figures 6.6 shows $|\mathbf{u}_C|$ fields in the middle of the computational domain at the simulation time $t = 1T$. Spurious air velocity appears in both fields but the air velocity without extrapolation reaches large values in the at atmosphere, near the upper limit of the domain. A sudden change of complementary velocity is observed at $z = 1.5\Xi_I$ when the air velocity is fixed to the constant velocity. As the vertical gradient of the incident wave velocity $\frac{\partial \mathbf{u}_I}{\partial z}$ is not continuous at $z = 1.5\Xi_I$, the complementary velocity has an extra velocity at $z = 1.5\Xi_I$ to satisfy the continuity equation. This sudden change of $\mathbf{u}_C$ gives a large velocity flux when solving the complementary LS function transport and momentum equations. As large flux exists near the interface, the complementary LS function are affected by $\mathbf{u}_C$. The air velocity field with the extrapolation by cubic polynomials has also extra velocity above the interface, however its value and gradients change smoothly along the vertical direction. Therefore, computed LS function field is reliable when the extrapolation by cubic polynomials is applied.

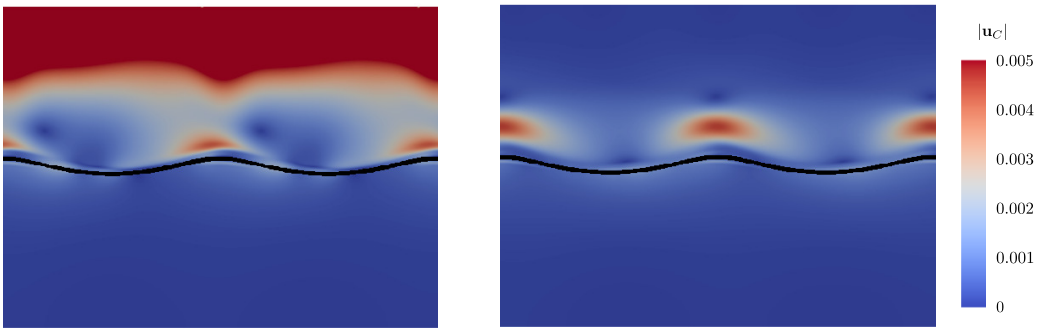

(a) $|\mathbf{u}_C|$ field without cubic polynomials extrapolation

(b) $|\mathbf{u}_C|$ field with cubic polynomials extrapolation

Figure 6.6. Magnitude of complementary velocity field ($\mathbf{u}_C$) with and without extrapolation by cubic polynomials up to air at $t = 1T$, $T/\Delta T = 400$, Black line denotes $\psi \in [-0.01, 0.01]$.

Redistancing Level-set

Complementary LS function (ψ_C) fields without and with redistancing are plotted in figure 6.7. ψ_C-fields should be zero theoretically for propagating waves in NWT, however ψ_C-fields without redistancing have errors near to interface, and errors evolve as the simulation time goes. Generated errors appear in the total computational domain not from the relaxation zones. When the FV discretization is applied to the ψ_C-transport equation

$$\left\{\frac{\partial \psi_C}{\partial t} + \nabla \cdot (\mathbf{u}\psi_C)\right\}^i = \left\{-\frac{\partial \psi_I}{\partial t} - \nabla \cdot (\mathbf{u}\psi_I)\right\}^e,$$

Numerical time differential and convection schemes are applied to the incident wave terms in the right-hand-side terms. Time and spatial discretizations of incident wave terms have numerical discretization errors and they are given as extra source terms in the ψ_C-transport equation. It has been tried with complementary LS function transport equation without incident wave terms given by

$$\left\{\frac{\partial \psi_C}{\partial t} + \nabla \cdot (\mathbf{u}\psi_C)\right\}^i = \{-\nabla \cdot (\mathbf{u}_C\psi_I)\}^e,$$

However, the combination of complementary flux with incident LS function $-\nabla\cdot(\mathbf{u}_C\psi_I)$ induces large extra source on near to interface, the simulation becomes unstable.

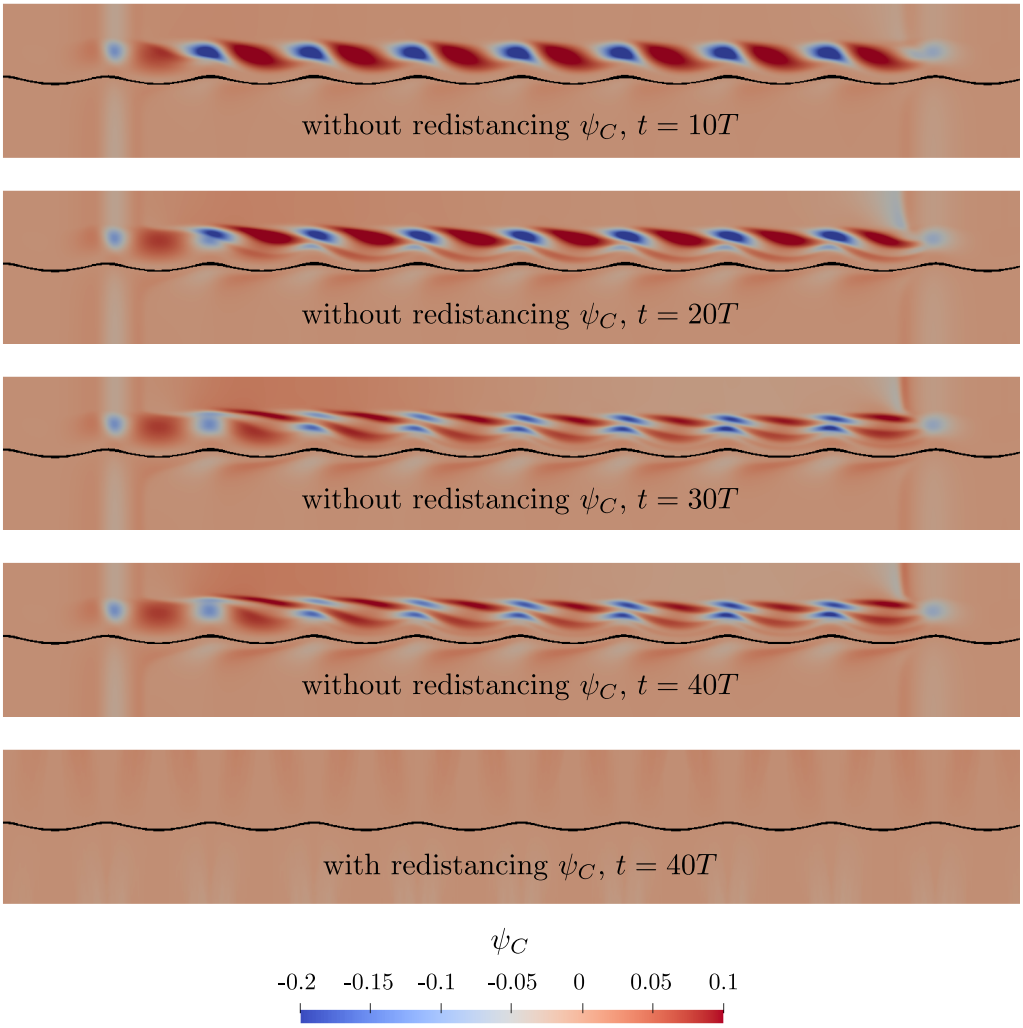

Figure 6.7. Complementary LS function fields with/without redistancing ψ_C, the black line denotes $\psi \in [-0.01, 0.01]$.

Futhermore, the extrapolated incident wave velocity above the interface is non-physical and has large values. The combination of opposite signed large velocities near crest and trough and the convection scheme makes ψ_C above the interface unstable. Measured time series and first-harmonics of wave elevation at the middle of the computational domain are compared in figure 6.9. The first harmonic amplitude without redistanding ψ_C show fluctuating behaviors for simulation time. On the contrary, the first harmonic amplitude with redistancing ψ_C show consistent results during the simulation. Numerical discretization errors can be listed as the below:

- Discretization of equation for incident LS function by low order numerical scheme may not satisfy the incident LS function transport equation.
- When the incident LS function is calculated from the wave theory, the signed distance

function is calculated as the vertical distance from wave elevation $\psi_I = -z + \Xi_I$. As the incident LS function is defined to be the signed distance from the nearest interface, it may generate extra errors.

- Numerical FV discretization of the pressure jump and continuous p_C/ρ across the interface conditions is considered by GFM. However, the numerical discretization of the pressure jump condition generates an extra flux due to the pressure jump on the interface. This extra flux can affect the complementary LS function transport equation.

These error sources appear in right-hand-side terms and they are cumulated during the simulation. Redistancing of LS function is thought to cancel the cumulated error sources during the simulation.

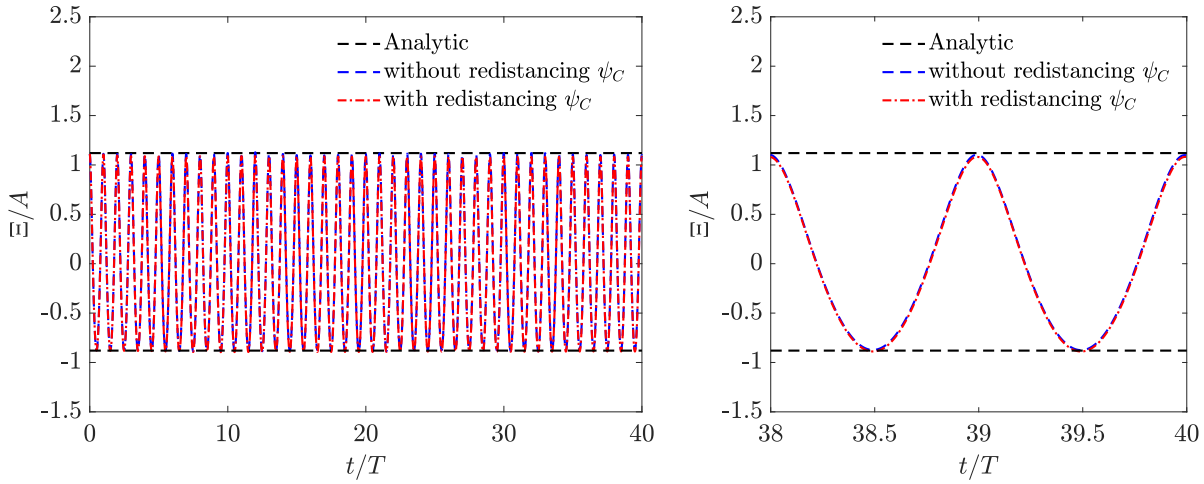

Figure 6.8. Wave elevation time series at the middle of computational domain with/without redistancing ψ_C.

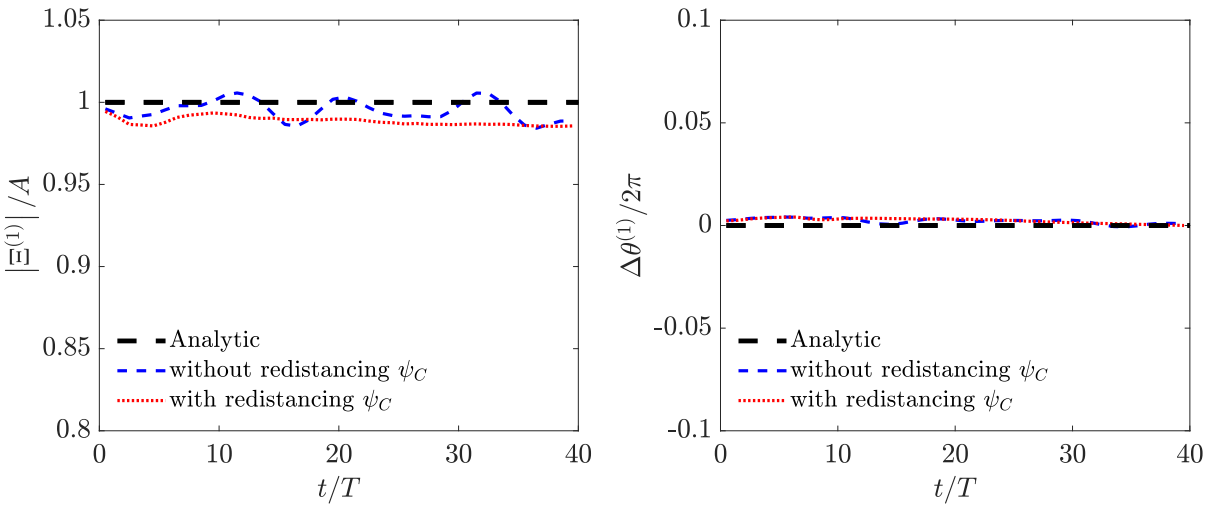

(a) First-harmonic amplitude

(b) First-harmonic phase difference

Figure 6.9. First-harmonic amplitudes and phase differences of wave elevation with/without redistancing ψ_C.

Mesh and time convergence tests

Spatial and temporal discretizations given in Table 6.1 are tested. Representative Courant(Co) and Reynolds numbers (Re_Δ) are defined in equation 2.5. A Crank-Nicolson time scheme with $c_{CN} = 0.95$ is used for all local terms. Convection terms of LS function transport equations are discretized by van Leer scheme (van Leer, 1974). A first-order upwind scheme is used to discretize the convection terms in momentum equations.

Table 6.1. Spatial and temporal discretization for SWENSE-LS convergence test.

Case	$\lambda/\Delta x$	$H/\Delta z$	$T/\Delta t$	Co	Re_Δ
Mesh025-dt100	25	5	100	0.171	8,836
Mesh030-dt120	30	6	120	0.171	7,363
Mesh040-dt160	40	8	160	0.171	5,523
Mesh050-dt200	50	10	200	0.171	4,418
Mesh100-dt400	100	20	400	0.171	2,209
Mesh200-dt800	200	40	800	0.171	1,105
Mesh100-dt200	100	20	200	0.684	2,209
Mesh100-dt800	100	20	800	0.086	2,209
Mesh100-dt1600	100	20	1600	0.043	2,209

Wave elevation time series measured at the center of computational domain are compared in figures 6.10 and 6.11 with respect to Co and Re_Δ discretizations. The results show that the measured wave elevation converges to the analytic solution, and the wave amplitudes are well preserved with respect to Co and Re_Δ discretizations.

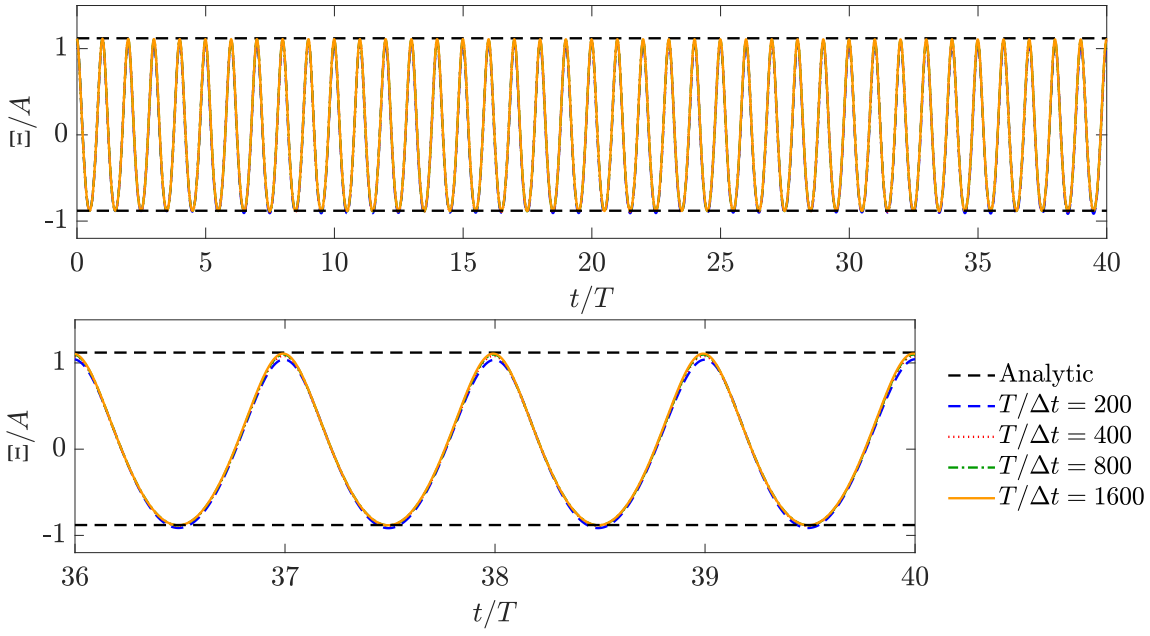

Figure 6.10. Wave elevation time series with respect to Co discretization.

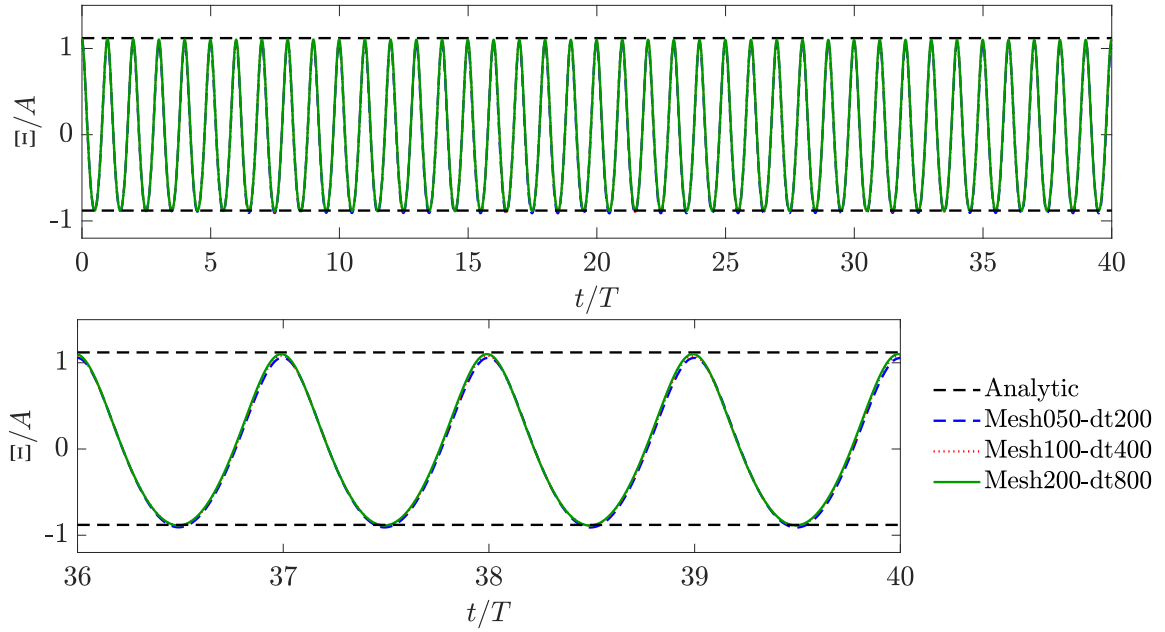

Figure 6.11. Wave elevation time series with respect to Re discretization.

First-harmonic amplitudes and phase differences of wave elevation with respect to Co and Re_Δ discretizations are shown in figures 6.12 and 6.13. When coarse time and space discretization are used, the first-harmonic amplitudes of wave elevation show unstable results compared to the simulation case with a fine discretization.

Figure 6.14 shows the convergence of first-harmonic amplitudes during $t \in [25T, 40T]$ with respect to Co and Re_Δ discretizations. The procedure of Eça and Hoekstra (2014) is applied to estimate the order of convergence (p). The obtained convergence orders for Co and Re_Δ discretization are $p = 1.2$ and 2.0, respectively.

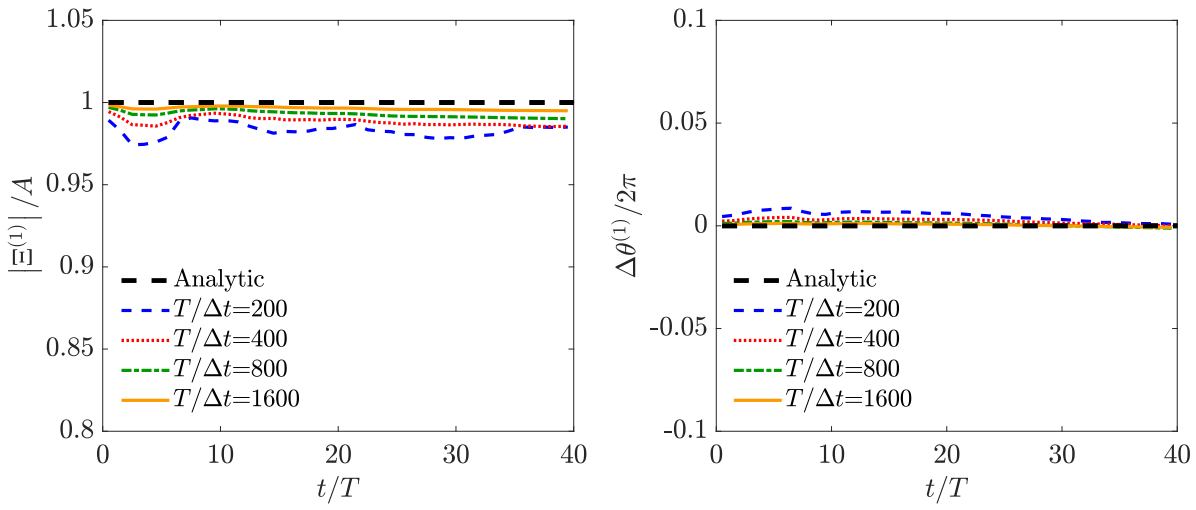

(a) First-harmonic amplitudes

(b) First-harmonic phase differences

Figure 6.12. First-harmonic wave amplitudes and phase differences with respect to Co discretization.

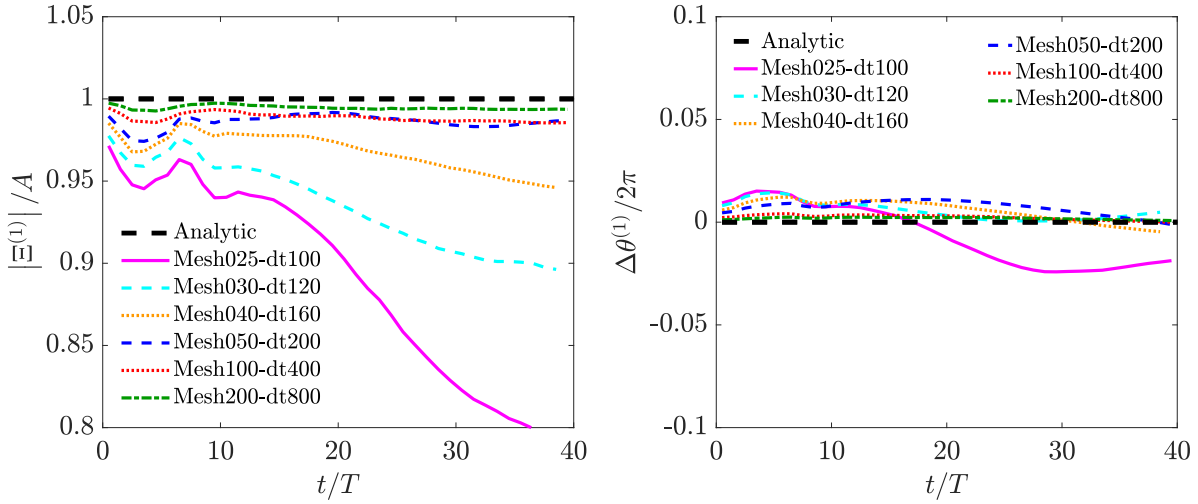

(a) First-harmonic amplitudes **(b)** First-harmonic phase differences

Figure 6.13. First-harmonic wave amplitudes and phase differences with respect to Re_Δ discretization.

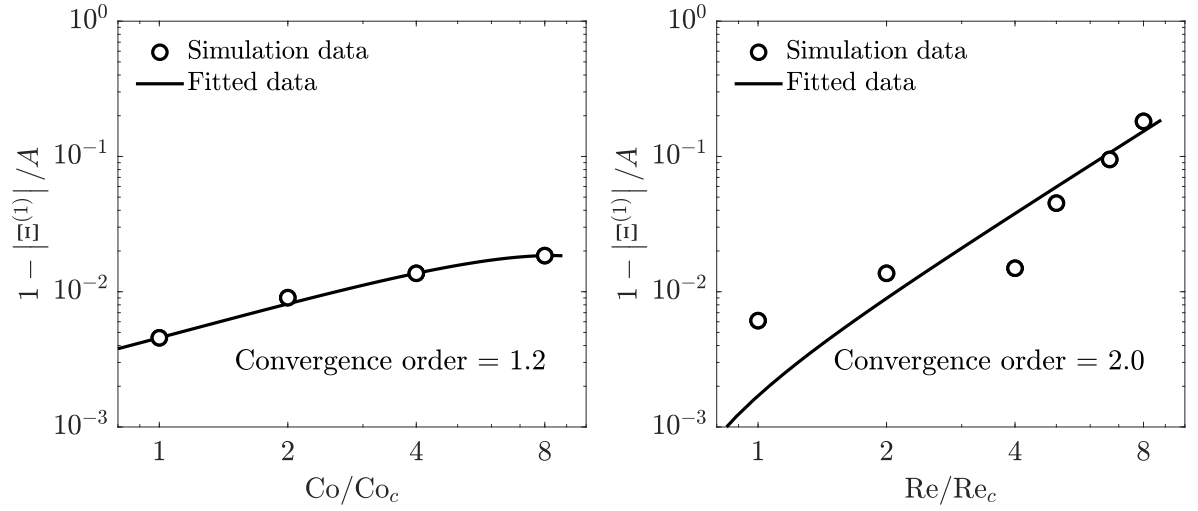

(a) First-harmonic amplitude **(b)** First-harmonic phase difference

Figure 6.14. Convergence of first-harmonic wave amplitude with respect to Co and Re_Δ discretizations.

A non-zero mean shift of the wave elevation is observed during the simulation. Moving averages of wave elevation time series for one wave period are shown in figure 6.15. Results show that redistancing ψ_C can generate a mean shift of wave elevation compared to the simulation case without redistancing ψ_C. It it thought to be due to a mass loss when redistancing the LS function. The mass loss due to redistancing Level-Set function have been reported by Sussman et al. (1994).

The mean shift of wave elevation decreases as time and space discretizations are refined. Redistancing technique adopted in present study is based on the calculation of the distance from the nearest interface.

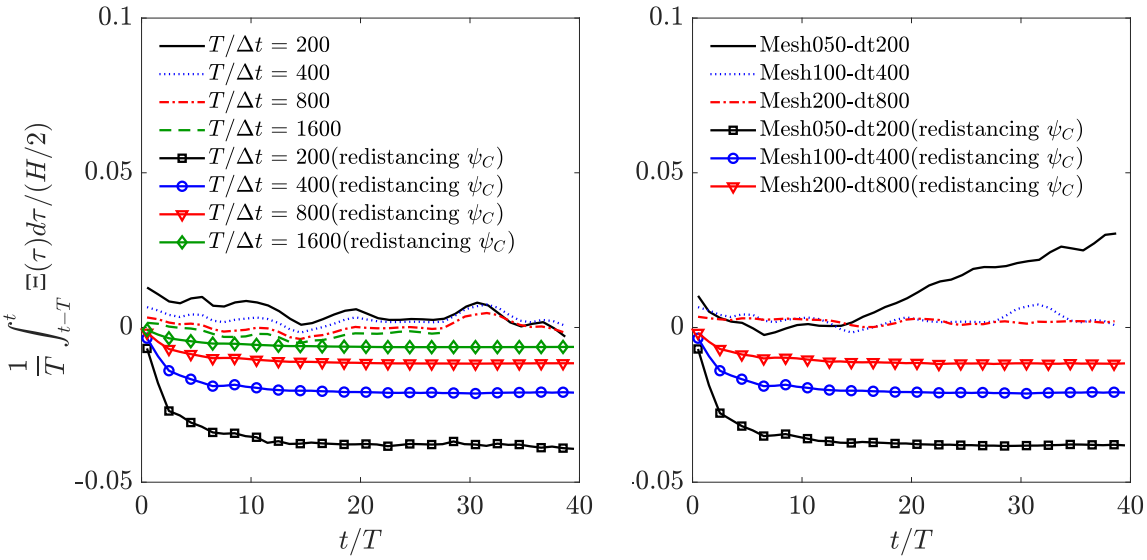

(a) Co discretization **(b)** Re discretization

Figure 6.15. Moving averages of wave elevation with respect to Co and Re_Δ discretization and ψ_C redistancing.

Comparison with other viscous flow solvers

Viscous flow solvers based on Navier-Stokes (NS) with VOF interface modeling (`foamStar`) and SWENSE with VOF interface modeling by Li (2018) are considered for comparison. An artificial compression term is commonly added to the VOF-transport equation in order to counteract the interface smearing

$$\frac{\partial \alpha}{\partial t} + \nabla \cdot (\mathbf{u}\alpha) + c_\alpha \nabla \cdot (\mathbf{u}_n \alpha(1-\alpha)) = 0, \tag{6.116}$$

where c_α is an interface compression coefficient and $\mathbf{u}_n$ is the fluid velocity normal to the interface. The VOF compression term $c_\alpha \nabla \cdot (\mathbf{u}_n \alpha(1-\alpha))$ only acts when $\alpha \in (0,1)$.

Wave elevation time series at the center of the computational domain are compared in figure 6.16. Wave elevation calculated by solving Navier-Stokes equations with VOF interface modeling show a decaying behavior for simulation time, and a small phase shift is seen. Wave elevations simulated by solving SWENSE with VOF interface modeling depend on artificial VOF compression term. When a small VOF compression coefficient $c_\alpha = 0.3$ is used, wave elevations show a decaying behavior with a large phase shift. Meanwhile, wave elevations computed by the present method show consistent results compared to other viscous flow solvers.

First-harmonic amplitudes and phase difference between analytical solution are compared in figure 6.17. Wave amplitudes computed by solving Navier-Stokes equations with VOF interface modeling show decaying behavior during simulation time. Results simulated by solving SWENSE with VOF interface modeling with $c_\alpha = 0.3$ are poor compared to the other viscous flow solvers. When $c_\alpha = 1.0$ is used for SWENSE with VOF interface modeling, first-harmonic amplitudes larger than 1 are obtained until $t < 32T$ and decay after $t = 32T$. First-harmonic amplitudes and phase differences calculated by solving SWENSE with LS function for interface modeling show a good and consistent behaviour compared to other viscous flow models.

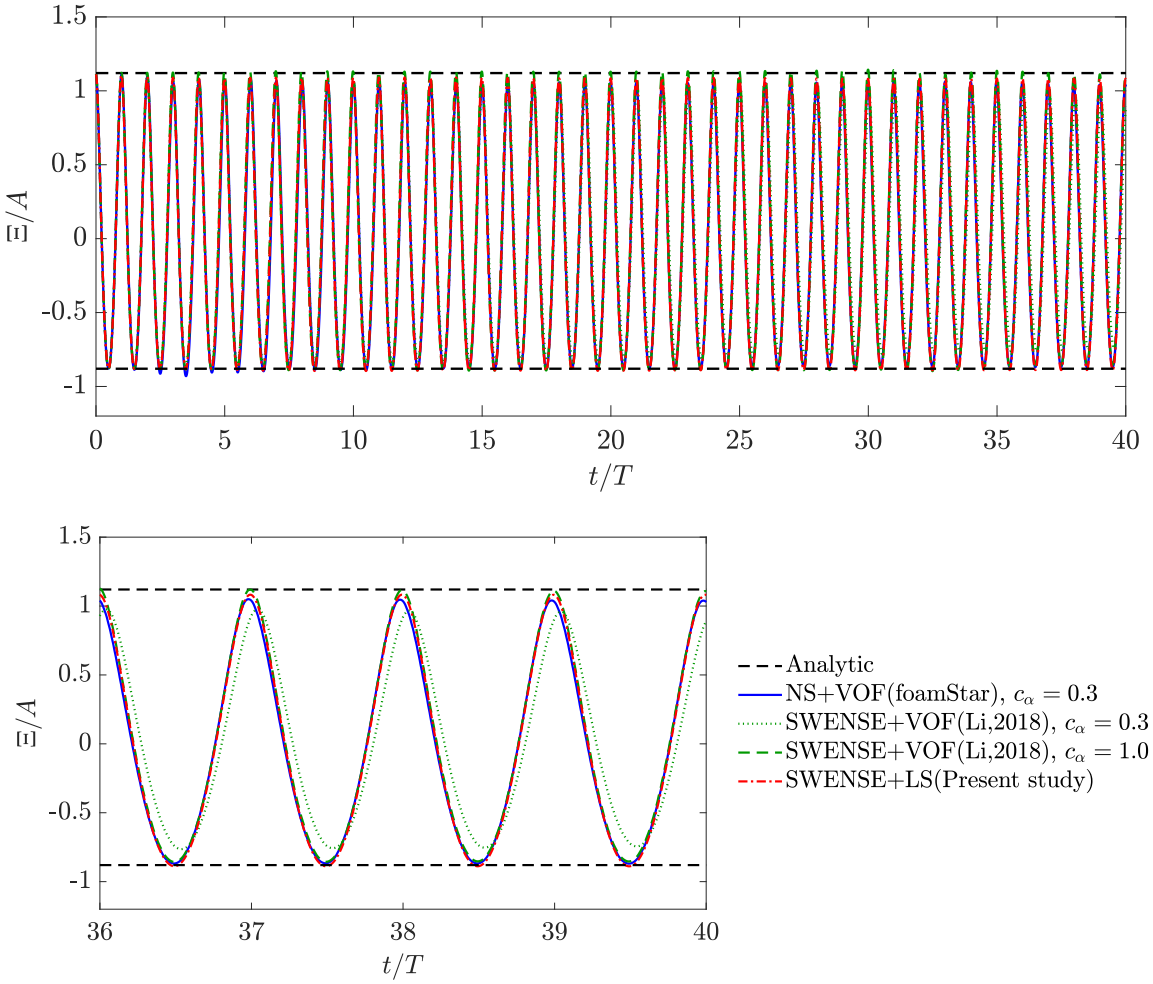

Figure 6.16. Comparison of wave elevation time series with other viscous solvers.

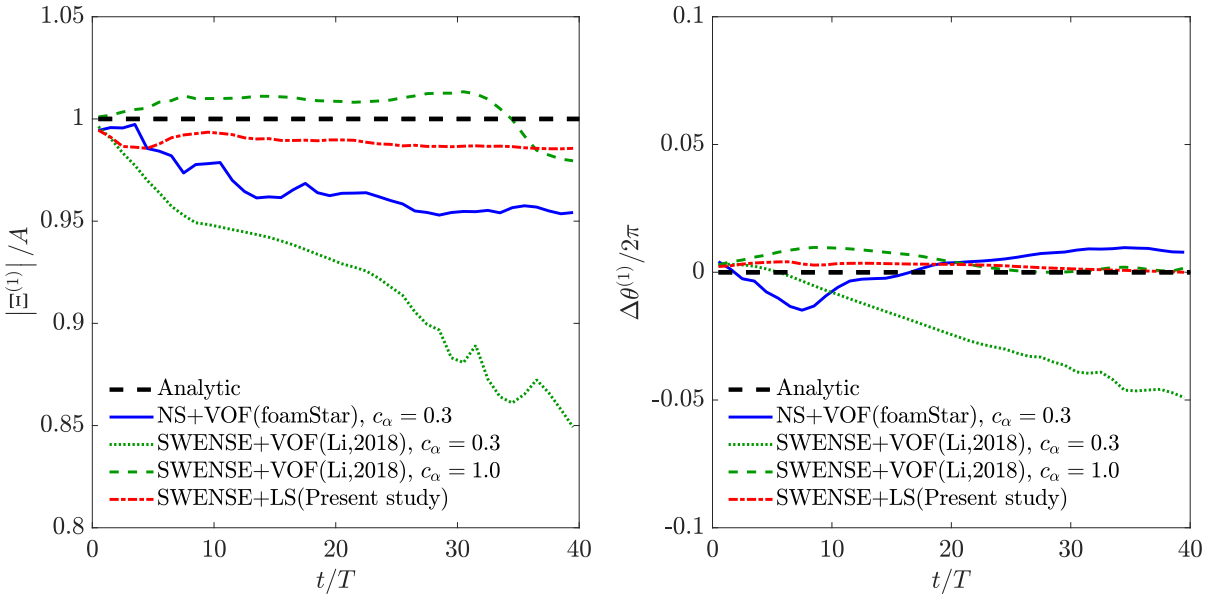

(a) First-harmonic amplitude **(b)** First-harmonic phase difference

Figure 6.17. Comparision of wave elevation first harmonics with other viscous solvers.

6.9.2 Regular wave diffraction by a vertical circular cylinder

Experiments on a vertical circular cylinder in regular wave are considered. The configuration of experiments conducted by Huseby and Grue (2000) is depicted in figure 6.18. A thin cylinder with radius $r = 0.03m$ is fixed in wave tank of depth $H = 0.6m$. Incident regular waves of frequency $f = \frac{\omega}{2\pi} = 1.425$ Hz with various wave height (H) are generated by a wavemaker.

In the present study, simulations are conducted in wave steepness range $kH \in [0.12, 0.48]$. A cylindrical computation mesh with radius of $2\lambda = 1.537m$ and height $0.8m$ is considered. A relaxation zone with the length of 1.5λ is defined from the far-field boundary. The pure CFD zone is 0.5λ from cylinder wall to relaxation zone following previous work (Li, 2018). The computational domain is discretized with cell length ratio in the radial direction by $\Delta R_{\max}/\Delta R_{\min} = 40$. The number of cells in the radial direction is $N_R = 40$. The mesh is discretized uniformly in θ-direction with $N_\theta = 30$. Three mesh blocks are considered in the vertical direction. The underwater block is defined in $z \in [-0.6H, -0.75H]$ with cell height ratio $\Delta z_{\max}/\Delta z_{\min} = 50$, and number of cells $N_{z1} = 25$ is used. The free surface block is defined in $z \in [-0.75H, 0.75H]$. This part of the domain is discretized uniformly with $N_{z2} = 40$. The air block is defined in $z \in [0.75H, 0.2m]$. Here the mesh uses a cell height ratio $\Delta z_{\max}/\Delta z_{\min} = 12$ with number of cells $N_{z3} = 15$. The computational mesh used for the simulation case $kH = 0.48$ is shown in figure 6.19. The time step is set to $T/\Delta t = 800$. Total number of cells used for computation is $N_{cell} = 190,000$.

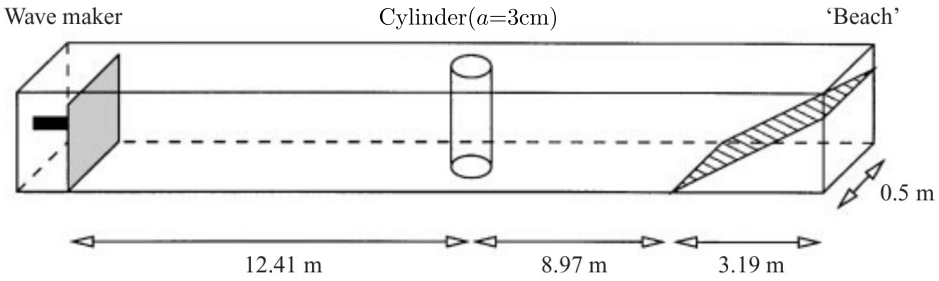

Figure 6.18. Configuration of experiments for thin cylinder in regular waves by Huseby and Grue (2000).

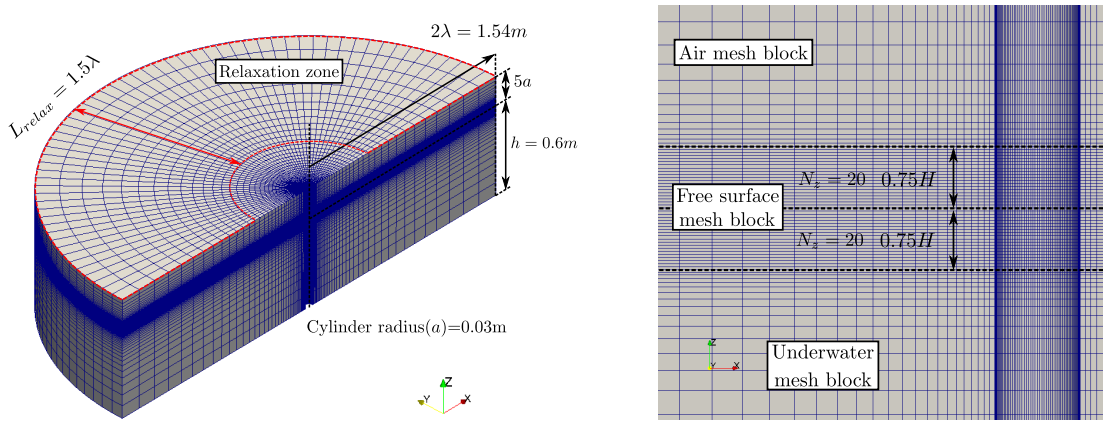

Figure 6.19. Computational mesh used for thin cylinder in regular waves, $kH = 0.48$.

Figure 6.20 shows the force time series with respect to different wave steepnesses. Magnified force time series shows that nonlinear components increase with wave steepness. Total wave fields around cylinder at the simulation time $t = 30T$ are compared in figure 6.21 with respect to different wave steepnesses. This figure shows that complementary waves around cylinder increase with wave steepness.

Figure 6.22 shows total wave elevations around cylinder for simulation time. Complementary waves generated by a vertical cylinder are clearly verified.

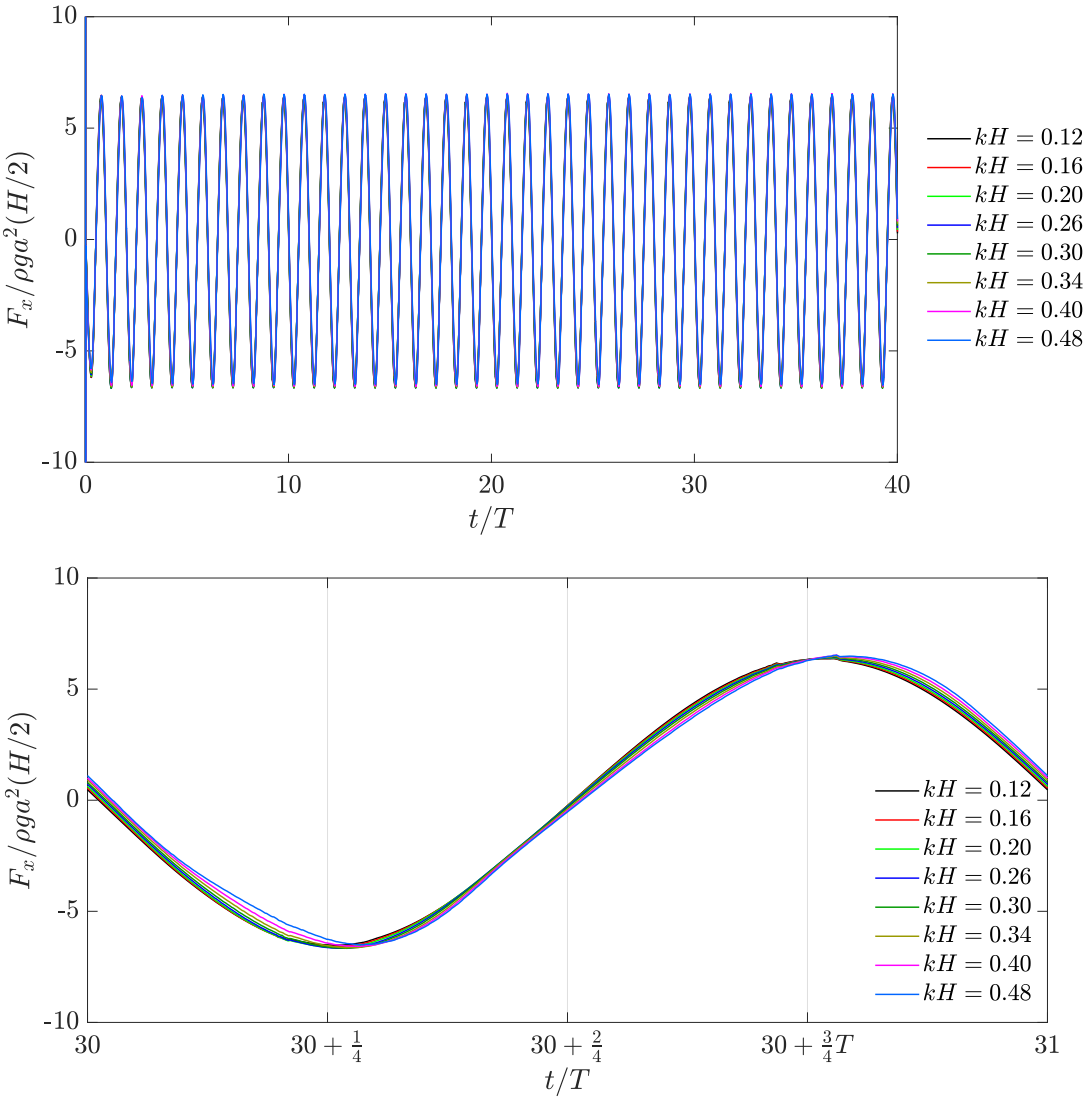

Figure 6.20. Time series of horizontal force acting on the cylinder for different wave steepness (kH).

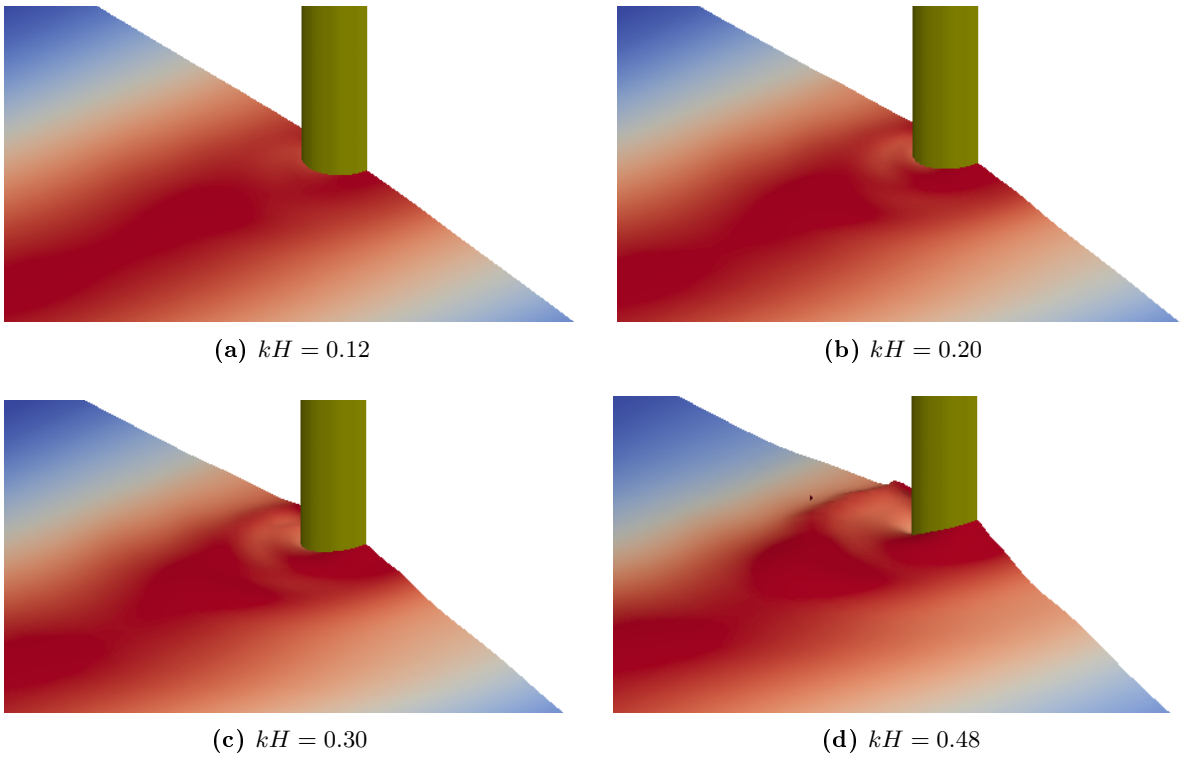

(a) $kH = 0.12$ **(b)** $kH = 0.20$

(c) $kH = 0.30$ **(d)** $kH = 0.48$

Figure 6.21. Total wave field around cylinder at $t = 30T$ for different wave steepness (kH).

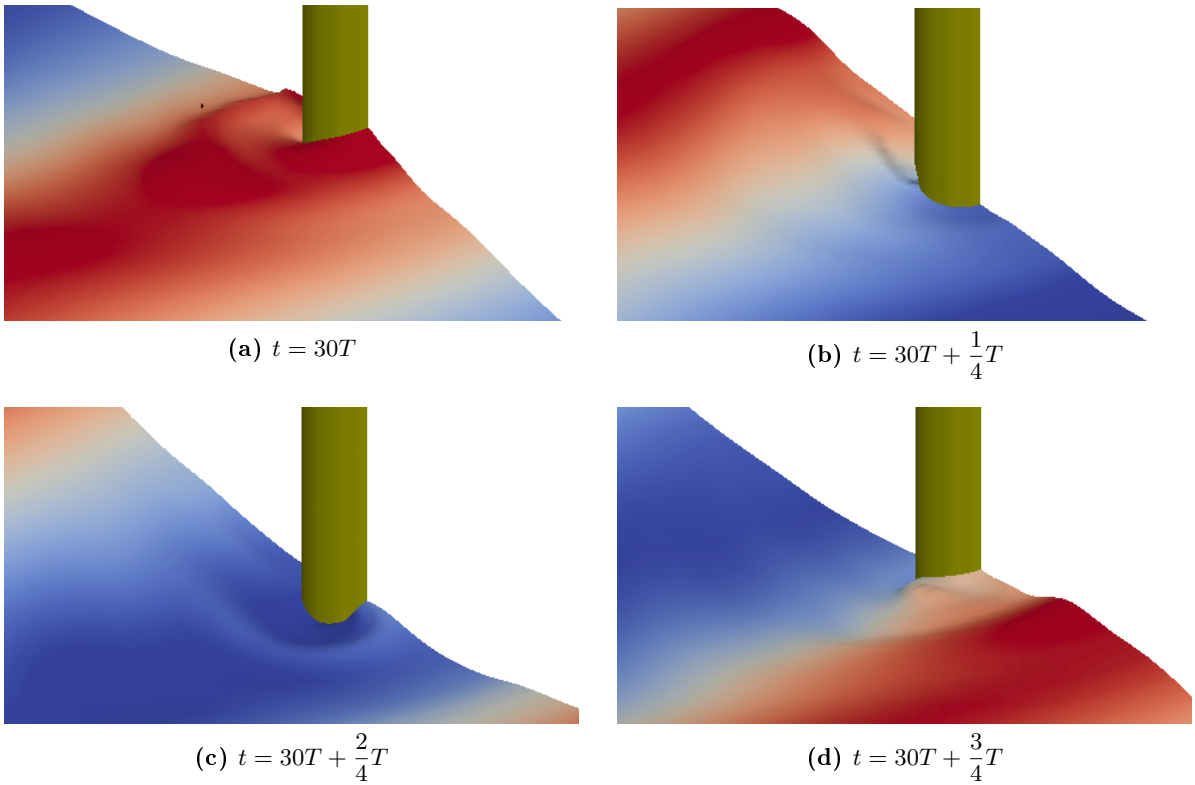

(a) $t = 30T$ **(b)** $t = 30T + \frac{1}{4}T$

(c) $t = 30T + \frac{2}{4}T$ **(d)** $t = 30T + \frac{3}{4}T$

Figure 6.22. Total wave field around cylinder at 4 instants, $kH = 0.48$.

First and higher harmonics of the horizontal force acting on cylinder are compared in figure 6.23. Analytical solution on the vertical circular cylinder in regular waves is available up to third-order. McCamy and Fuchs (1954) introduced linear theory based on the eigenfunction expansion, Kim and Yue (1989) presented the second order velocity potential on the vertical circular cylinder and Chau and Taylor (1992) suggested the complete expression for second order problem. Malenica and Molin (1995) extended the eigen-function expansion up to third-order problem. Huseby and Grue (2000) conducted the experiments with different cylinder radii (a=3cm, 4cm). Special attention was given to remove the second-order free waves due to the wave maker. Measurement is taken before high-harmonic free waves reach the cylinder. They compared the force harmonics amplitudes ($\left|F^{(n)}\right|$) and phases ($\vartheta(F^{(n)})$), where $^{(n)}$ denotes the harmonic order. Amplitudes of force harmonics are normalized as follows:

$$\frac{\left|F^{(n)}\right|}{\rho g a^3}\left(\frac{a}{H/2}\right)^n. \tag{6.117}$$

Horizontal force harmonics calculated by present method is compared with others (Ferrant, 1998; Shao and Faltinsen, 2014; Li, 2018). Shao and Faltinsen (2014) evaluated the force harmonics by Harmonic Polynomial Cell (HPC) method and Li (2018) calculated forces by finite vomume method based on multi-phase SWENSE and VOF procedure for interface modeling. Computed force harmonics by present study show good results with others.

First-harmonic amplitudes and phases have similar tendencies with what shown in Li (2018). However, small amplitude differences are observed for small kH that should have the similar value with analytical solution. Second-harmonic amplitudes and phases show similar results with Li (2018). Third-harmonic amplitudes and phases are slightly different for small kH compared to others and analytic solution. Fourth-hamonic amplitude and phase show similar results with Ferrant (1998) and Shao and Faltinsen (2014).

Force harmonics calculated by proposed method show good results even if a relative coarse discretization ($N_{cell} = 190,000$) is used.

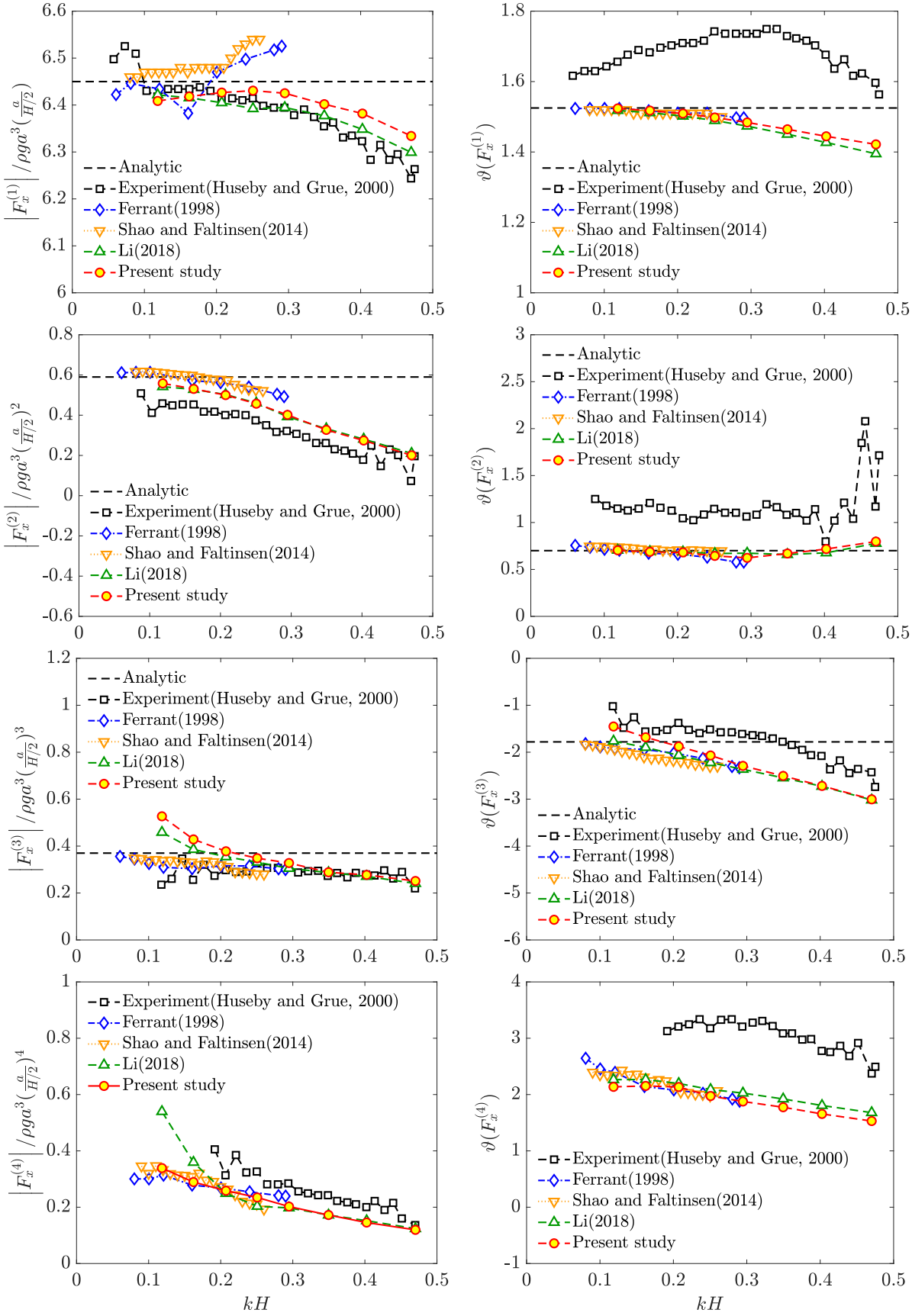

Figure 6.23. Harmonics of horizontal force acting on the cylinder.

6.10 Conclusion

The SWENSE method is applied to multi-phase flow with Level-Set function for the interface modeling. Kinematic and dynamic interface boundary conditions in multiphase flow are reviewed. Navier-Stokes equations and interface boundary conditions are reformulated with respect to the complementary flow by combining previous works by Vukčević (2016) and Li (2018).

Pressure related terms are discretized by considering the interface boundary conditions in the framework of Finite Volume (FV). A FV discretization procedure based on Ghost Fluid Method (GFM) proposed by Vukčević (2016) is used to consider the pressure boundary conditions on the interface. The incident pressure including the dynamic pressure of incident waves and hydrostatic pressure is used for the pressure jump condition (Li, 2018). Both pressure jump conditions proposed by Vukčević (2016) and Li (2018) are same for calm water case.

The extrapolation of incident velocity and dynamic part of incident wave pressure with cubic polynomials is proposed in the present work. It provides smooth transitions of incident wave quantities up to air zone without any complex algorithm and with fast computation. Nevertheless, the extrapolation with cubic polynomials generates mass continuity error in the air zone. Numerical simulations showed that the extrapolation of the incident flow up to air zone is necessary for multi-phase flow simulation based on the SWENSE approach.

Redistancing Level-Set (LS) function by calculating the distance from the nearest interface is used in the present study. The numerical discretization of incident flow terms in LS equation generates errors which are cumulated in simulation time. Redistancing LS is thought to remove cumulated errors due to the discretization of incident flow terms. Then, a negligible mass loss is observed during the simulation.

Spatial and time discretization tests were conducted to check the order of convergence. Furthermore, a comparison with other viscous flow solvers was conducted for wave propagation. Results showed that the proposed viscous flow solver gives better results during simulation compared to others.

At last, a benchmark test on the wave diffraction by a thin cylinder is conducted. Amplitudes and phase of force harmonics are compared with analytical solution, experiments and other numerical computations. Although a small number of computation cells is used for the simulation, the results calculated by the proposed viscous flow solver show similar results compared with other computations.

7 Two-way coupling of potential and viscous flows

The computational algorithm solving a problem of wave-structure interaction by considering the two-way coupling between potential and viscous flow models are introduced. It is based on the hypothesis that total flow can be decomposed into the incident and complementary is assumed. In the present study, the following principles are used:

- Total flow can be decomposed into the incident and complementary parts.
- The incident parts are calculated from the nonlinear potential flow models for incident waves in a whole computational domain.
- The complementary parts in the vicinity of a structure are solved by viscous flow model based on SWENSE method.
- The complementary parts in the far-field are modeled by Poincaré's velocity representation based on linear potential theory.

Based on the above principle, the functional decomposition (FD) and domain decomposition (DD) are applied as the coupling methodology as:

- **Functional decomposition (FD)** is applied for both potential and viscous flow models. Because the nonlinear potential flow model for incident waves is available in a whole fluid domain, the complementary parts are considered as the main concerns for the computation. The governing equations and boundary conditions for potential and viscous flow models are reformulated for complementary flow. Poincaré's velocity representation is used for potential flow and SWENSE method is applied for viscous flow.
- **Domain decomposition (DD)** is considered to decompose the computational domain of potential and viscous flow models for complementary parts. The viscous flow model based on SWENSE with LS function for interface modeling calculates the complementary waves in the vicinity of a structure. The complementary waves in the region of far-field are modeled by Poincaré's velocity representation based on linear potential theory.

Two-way coupling between potential and viscous flow models for complementary flow assumed that the fluid velocity and wave elevation across the flow models are continuous. Each of the flow models is updated as follows:

- **Viscous flow model to potential flow model**

  The complementary fluid velocity and wave elevations on the matching surface are obtained from the viscous flow model. Fourier-Laguerre and Fourier coefficients of complementary velocity and wave elevation are calculated, respectively. The complementary velocity and wave elevation fields in the relaxation zones are constructed by using Poincaré's velocity representation.

- **Potential flow model to viscous flow model**

  The target values of complementary velocity and Level-Set function in the relaxation zone are calculated from the complementary velocity and wave elevation fields by using Poincaré's velocity representation. The relaxation scheme, which blends the calculated quantity with the target quantity, is used to update the viscous flow model.

7.1 Computation algorithm

A segregated algorithm is used to solve the wave-structure interaction problem considering coupling viscous and potential flow models. The fluid velocities and wave elevations computed by potential and viscous solvers are coupled and they are imposed as the boundary conditions of each flow model at the same computational time.

Figure 7.1 shows the computation algorithm solving the wave-structure interaction problem. Viscous flow model and potential flow model are initialized at the beginning of the algorithm.

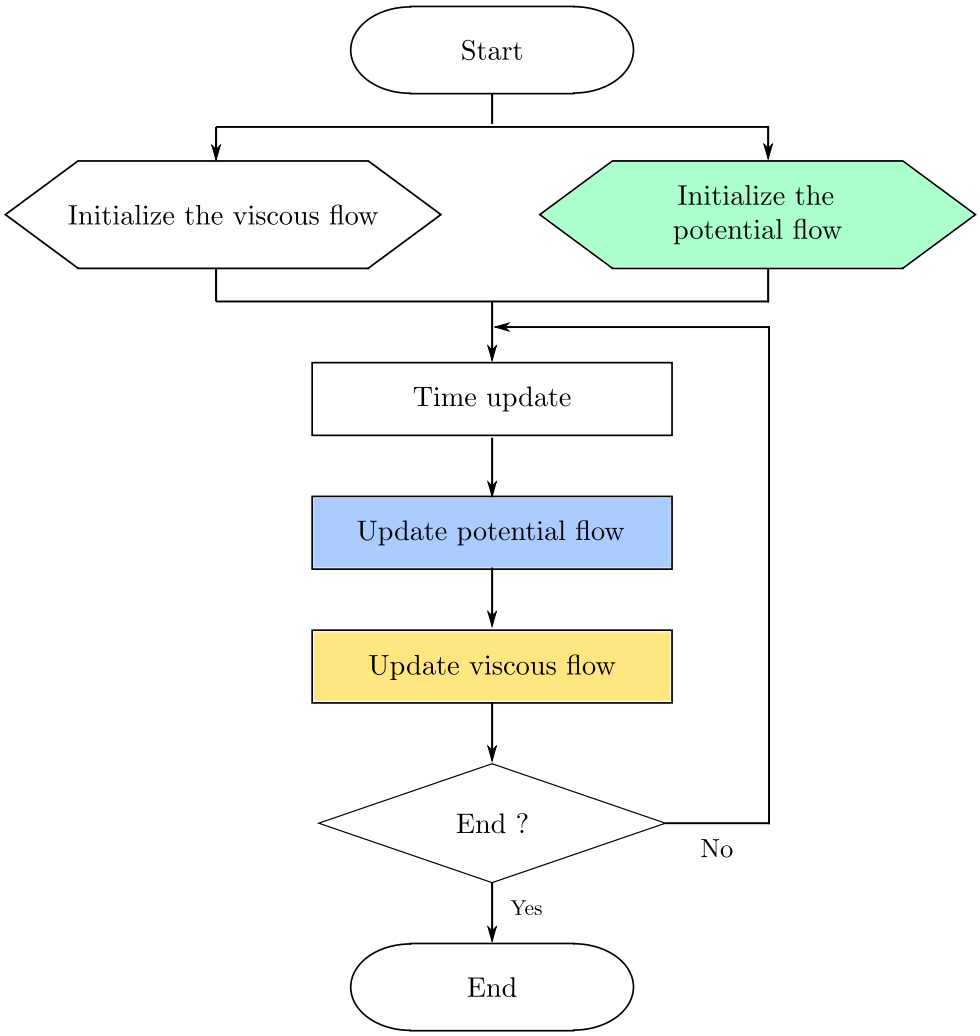

Figure 7.1. Global computational algorithm of two-way coupling between potential and viscous flows.

7.1.1 Initialization of the potential flow

Figure 7.2 shows the initialization procedure of potential flow model. The nonlinear potential flow model for different incident waves is initialized:

- Regular waves: Stream function theory is used. The modal amplitudes for fluid velocity and wave elevation of regular waves are computed in this step.
- Irregular waves/Propagating waves in NWT: HOS model is used. The input parameters and numerical results of HOS wave simulation are read. Initial 3D wave field for interpolation is constructed.

Potential flow model for complementary waves is initialized by computing the elementary functions of source, image source, harmonic terms and waterline. After calculating the elementary functions necessary for Poincaré's velocity representation, 3D cylindrical grid is constructed for the interpolation of complementary velocity and wave elevation in the relaxation zone.

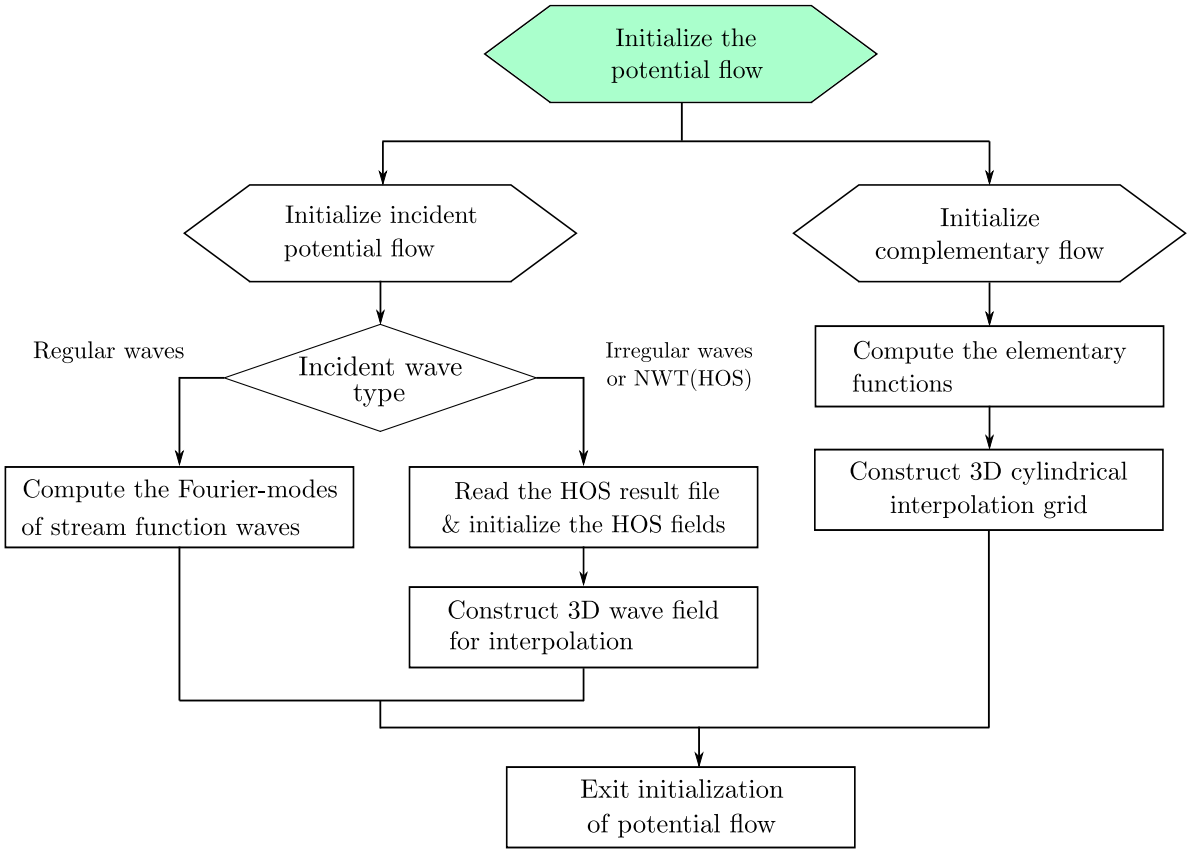

Figure 7.2. Initialization of incident and complementary potential flows.

7.1.2 Update of potential flow

Figure 7.3 shows the update procedure of the potential flow model in the time loop.

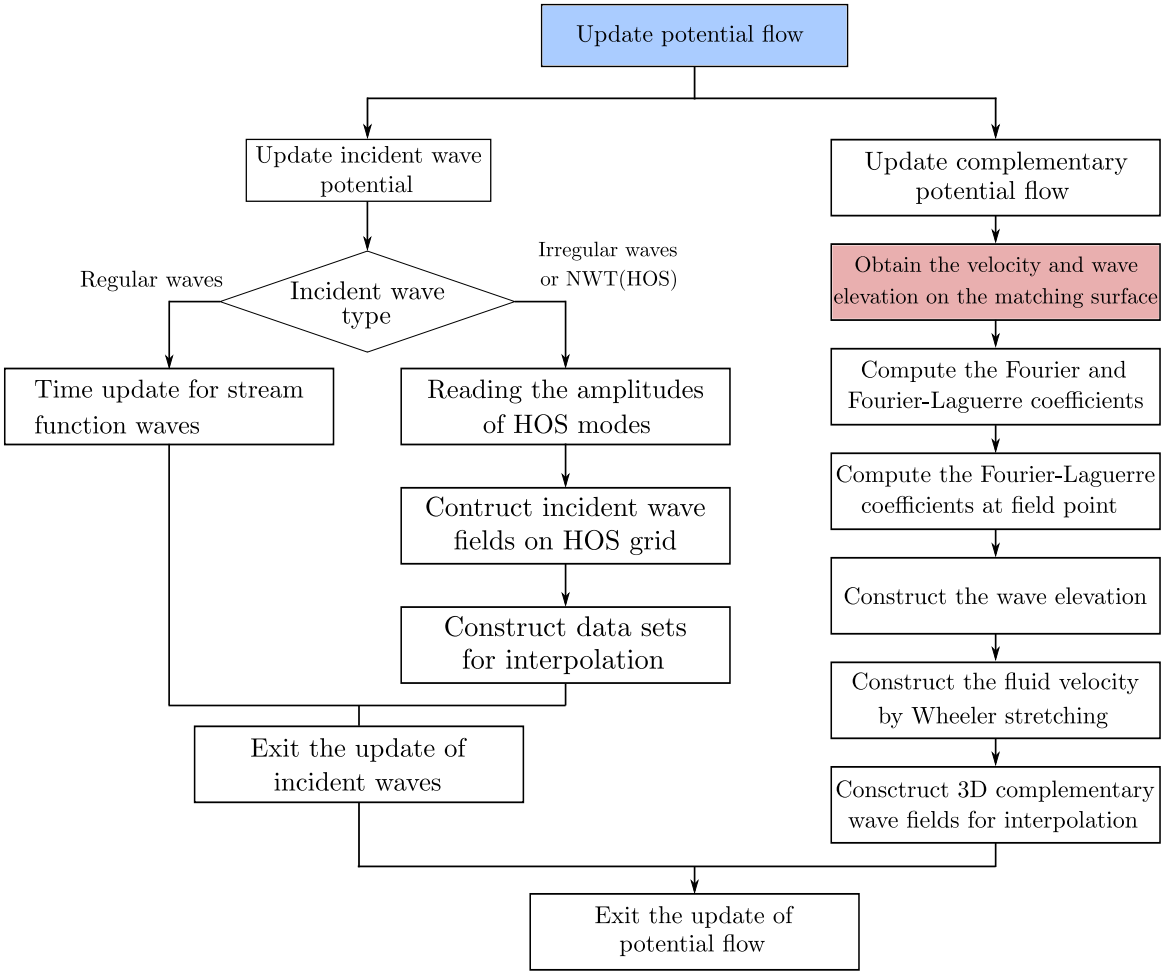

Figure 7.3. Update procedure of the potential flow models for the incident and complementary waves in the time loop.

Updating the potential flow model for incident waves depends on the wave type. The following procedures are used to update regular or irregular incident waves.

- Regular waves: Time is updated to change the phase function of the stream function theory. Fluid velocity, wave elevation and dynamic pressure of incident waves are updated by new phase function. Wave elevation and stream function of regular waves were given in equations (3.3) and (3.4) as

$$\Xi_I(x;t) = \eta_I(x)e^{-\mathrm{i}\omega t}, \qquad \Psi_I(x,z;t) = \psi_I(x,z)e^{-\mathrm{i}\omega t}.$$

  where t is time, and it is updated with new simulation time.

- Irregular waves/Propagating waves in NWT: Time-varying mode amplitudes of HOS wave model are updated by the results of HOS simulation. The velocity potential for Open-ocean

was given in equation (3.16) as

$$\Phi_I(x,y,z;t) = \sum_{m=0}^{\infty}\sum_{n=0}^{\infty} A_{mn}^I(t)\phi_{I,mn}(x,y,z)$$

and the velocity potential for NWT was given in equation (3.32) as

$$\Phi_I(x,y,z;t) = \Phi_H(x,y,z;t) + \Phi_L(x,y,z;t)$$

where Φ_H and Φ_L are the harmonic and local velocity potentials given in (3.36) and (3.41) as

$$\Phi_H(x,y,z';t) = \sum_{m=0}^{M_x}\sum_{n=0}^{N_y} B_{mn}^{\Phi}(t)\phi_{H,mn}(x,y,z'),$$
$$\Phi_L(x,y,z';t) = \sum_{n=0}^{N_y}\sum_{p=0}^{N_{add}} B_{np}^{add}(t)\phi_{L,mn}(x,y,z')$$

where $A_{mn}^I(t)$, $B_{mn}^{\Phi}(t)$ and $B_{np}^{add}(t)$ are time-varying mode amplitudes of HOS wave model. Fluid velocity, wave elevation and dynamic pressure of incident waves are reconstructed on the computational grid by applying inverse Fourier transform. The reconstructed 3D wave fields are used to construct 3D incident wave field in the viscous flow model by using cubic spline interpolation.

The complementary fields obtained by the potential flow solver are updated by following procedure:

- Fluid velocities and wave elevations of complementary waves on the matching surface and waterline are obtained from the viscous flow model. The principle of Wheeler stretching is applied to obtain the fluid velocity of complementary waves on the matching surface because the wave elevations of viscous flow model are not calculated on the mean position. The vertical position of Gauss point (ζ_i) is given in case of calm water, the vertical position of Gauss point is moved with respect to total wave elevation

$$\zeta_i' = \zeta_i - \Xi, \tag{7.1}$$

  where ζ_i' is a new vertical position of Gauss point adapted to the total wave elevation (Ξ). Fluid velocities of complementary waves at Gauss points are interpolated from fluid velocities on the matching surface. It should be noted that the weight of Gauss-Laguerre quadrature is not changing, but the vertical location of the Gauss point is moved with respect to total wave elevation.

- Fourier-Laguerre coefficients of complementary fluid velocity are computed on the matching surface. Fourier coefficients of complementary wave elevation are computed on the matching waterline.

- Poincaré's velocity representation is used to calculate Fourier-Laguerre coefficients of the complementary fluid velocity at the field point. The elementary functions and Fourier-Laguerre coefficients of complementary fluid velocity and Fourier coefficients of complementary wave elevations are used.

- The vertical component of the complementary fluid velocity is computed at the field point on the free surface. Complementary wave elevation at field point is computed by integrating the vertical complementary fluid velocity.
- The complementary fluid velocity at the field points is computed by applying Wheeler stretching and Fourier-Laguerre series.
- Constructed complementary fluid velocity and wave elevation at the field points are used to interpolate the complementary flows for viscous flow model.

7.1.3 Update of viscous flow

Figure 7.4 shows the computational procedure to update the viscous flow model. The PIMPLE algorithm, which is a combination of PISO (Pressure Implicit with Splitting of Operator) and SIMPLE (Semi-Implicit Method for Pressure-Linked Equations), is used to solve the segregated equations for an unsteady problem.

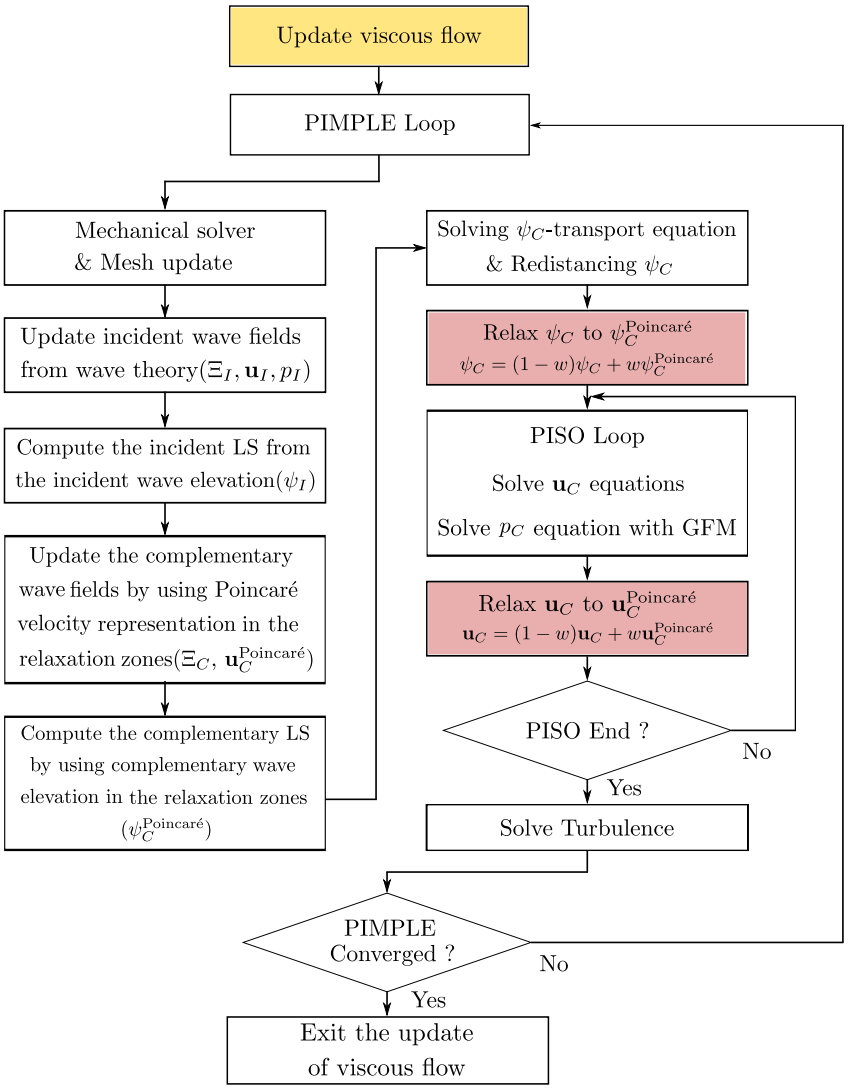

Figure 7.4. Updating the viscous flow in time loop.

The viscous flow model is updated by following the computational procedure:

- The dynamics of the body is solved by using a mechanical solver if a floating body is considered. The computational mesh of the viscous flow model is updated from the displacement of the body surface.
- Flow quantities related to the incident waves are updated. Fluid velocity, wave elevation and dynamic pressure of incident waves are updated from the incident wave model.
- The incident Level-Set (LS) function (ψ_I) is calculated by using wave elevation (Ξ_I) as

$$\psi_I(x, y, z; t) = -z + \Xi_I(x, y; t).$$

- Flow quantities related to the complementary waves in the relaxation zone are updated from Poincaré's velocity representation. The complementary fluid velocity and wave elevation in the relaxation zones are updated.
- The complementary LS function in the relaxation zone is calculated by using the complementary wave elevation as

$$\psi_C^{\text{Poincaré}}(x, y, z; t) = \Xi_C(x, y; t).$$

  where $\psi_C^{\text{Poincaré}}$ is the complementary LS function obtained from Poincaré's velocity representation.
- The transport equation of complementary LS function (ψ_C), as given below, is solved in the computational mesh of the viscous flow model.

$$\frac{\partial \psi_C}{\partial t} + \nabla \cdot (\mathbf{u}\psi_C) = -\frac{\partial \psi_I}{\partial t} - \nabla \cdot (\mathbf{u}\psi_I)$$

  After solving ψ_C-transport equation, the complementary LS function is re-distanced by

$$(\psi_C)_P = \text{sgn}((d)_P) - (\psi_I)_P,$$

  where d is the distance from the nearest interface(free surface) to cell center(P).
- The relaxation scheme is applied to the complementary LS function in the relaxation zones as

$$\psi_C = (1 - w)\psi_C + w\psi_C^{\text{Poincaré}},$$

  where $w \in [0, 1]$ is the weight function defined in the relaxation zones.
- PISO loop is used to solve $\mathbf{u}_C$ and p_C equations with interface conditions. The governing equations for $\mathbf{u}_C$ and p_C are given by

$$\frac{\partial \mathbf{u}_C}{\partial t} + \nabla \cdot (\mathbf{u}\mathbf{u}_C) - \nabla \cdot (\nu_{eff} \nabla \mathbf{u}_C) = -\frac{p_I}{\rho_w}\frac{\nabla \rho}{\rho} - \mathbf{u}_C \cdot \nabla \mathbf{u}_I + \nabla \mathbf{u}_C \cdot \nabla \nu_{eff},$$

  and

$$\nabla \cdot \left\{ \frac{1}{a_P} \left(\frac{1}{\rho} \nabla (p_C)_P \right) \right\} = \nabla \cdot \left[\frac{1}{a_P} \mathbf{H} \left\{ (\mathbf{u}_C)_P \right\} \right].$$

  The interface conditions are given by

$$[\![\mathbf{u}_C]\!] = 0, \qquad [\![p_C]\!] = p_I \frac{\rho_w - \rho_a}{\rho_w}, \qquad \left[\!\!\left[\frac{1}{\rho} \nabla p_C \right]\!\!\right] = 0.$$

  The Ghost Fluid Method is applied to solve the equations for $\mathbf{u}_C$ and p_C by considering the interface boundary conditions.

- The relaxation scheme is applied to the complementary fluid velocity in the relaxation zones as

$$\mathbf{u}_C = (1-w)\mathbf{u}_C + w\mathbf{u}_C^{\text{Poincaré}}.$$

- Turbulence model is solved after the PISO loop. In the present study, the turbulence model is not considered. In other words, a laminar flow is assumed.
- If the solutions are converged in the PIMPLE loop, the update of viscous flow is done.

7.2 Benchmark test 1: A vertical circular cylinder in regular waves

7.2.1 Description

A bottom-mounted vertical circular cylinder in regular waves is considered for the benchmark test case. Different wave frequencies are used for incident regular waves. The magnitude of waves diffracted by the cylinder increases as the wavelength of incident waves becomes shorter. The test cases are selected from the previous study on the wave diffraction theory by Malenica and Molin (1995) (M&M theory). They calculated the third-order harmonic forces acting on a vertical circular cylinder. Perturbation series with respect to wave steepness is applied to the velocity potential and wave elevation. The third-hamonic component magnitude of horizontal forces acting on the vertical circular cylinder are compared with experimental results (Moe, 1993). Nevertheless, the third harmonic components measured in experiments show a scattered distribution, that is why the first, second and third harmonic components of horizontal forces calculated from M&M theory can be used as reference values (Malenica, 1994).

The horizontal forces on the bottom-mounted vertical circular cylinder in regular waves can be decomposed into the harmonic components as (Malenica and Molin, 1995)

$$F_x(t) = \Re\left[F_x^{(1)}e^{-\mathrm{i}\omega t} + F_x^{(2)}e^{-2\mathrm{i}\omega t} + F_x^{(3)}e^{-3\mathrm{i}\omega t}\right] + \bar{F}_x^{(2)} + \cdots, \tag{7.2}$$

where $F_x^{(1)}$, $F_x^{(2)}$ and $F_x^{(3)}$ are the first harmonic, second harmonic(sum-frequency) and third harmonic components of horizontal force. $\bar{F}_x^{(2)}$ is a mean drift force which corresponds to a second order different-frequency component. Analytical solution of force harmonics can be found in the literature: the first harmonic by McCamy and Fuchs (1954), the second harmonic by Kim and Yue (1989); Chau and Taylor (1992) and the third harmonic by Malenica and Molin (1995). Mean drift force acting on the structure is given by Pinkster (1980). In the present study, the mean drift forces are calculated by using Higher-Order Boundary Element Method(HOBEM) (Hong et al., 2005).

The conditions of regular waves considered in the present study are given in Table 7.1. The modal wave number (k_0) is selected to be in the range $k_0 a_{cylinder} \in [0.5, 2.0]$ satisfying a deep water condition that the half of wavelength is smaller than the water depth. The modal wave number is calculated by using a linear dispersion relationship as

$$\omega^2 = k_0 h \tanh(k_0 h) \tag{7.3}$$

where $\omega = \frac{2\pi}{T}$ is wave frequency, T is wave period. $\lambda_0 = \frac{2\pi}{k_0}$ is the modal wavelength. Wave height is selected to keep the wave steepness, $\frac{k_0 H}{2} = 0.25$.

Table 7.1. Wave conditions for a vertical circular cylinder in regular wave.

$k_0 a_{cylinder}$	Wave period (T)	Wave height ($H = 2A$)	Wavelength ($\lambda_0 = \frac{2\pi}{k_0}$)	Wave steepness ($\frac{k_0 H}{2}$)
[-]	[s]	[m]	[m]	[-]
0.50	2.837	1.000	12.566	0.25
0.75	2.316	0.667	8.376	0.25
1.00	2.006	0.500	6.283	0.25
1.25	1.794	0.400	5.027	0.25
1.50	1.638	0.333	4.189	0.25
1.75	1.516	0.286	3.590	0.25
2.00	1.419	0.250	3.142	0.25

The force harmonics and mean drift components of horizontal force are extracted from the CFD solution by applying moving window FFT. The force harmonics and mean drift forces are nondimensionalized by:

$$\frac{F_x^{(m)}}{\rho g a_{cylinder}^3 (A/a_{cylinder})^m} \tag{7.4}$$

where m is the order of force harmonics. A is wave amplitude.

7.2.2 Computational domain

Figure 7.5 shows the configuration of the benchmark test case. A bottom-mounted vertical circular cylinder having a radius of $a_{cylinder} = 1m$ is located in regular waves. Water depth is $h = 10a_{cylinder} = 10m$. The computational domain of the viscous flow solver is defined surrounding the vertical circular cylinder, as colored grey in figure 7.5. The radius and height of the computational domain of the viscous flow solver are L_{CFD} and $h + h_{air}$, respectively. The relaxation zone is defined from the far-field boundary with its length L_{relax}. The pure zone where no relaxation scheme is applied has a length $L_{pure} = L_{CFD} - L_{relax}$. The computational domain of the potential flow model for complementary waves is constructed to cover at least the relaxation zone of viscous flow model, as outlined with a solid black line in figure 7.5. The complementary fluid velocity and wave elevation are obtained from viscous flow model at Gauss points colored red in figure 7.5.

With two-way coupling, the viscous solver needs the target solution for each nodes of the relaxation zone. The potential solver based on Poincaré's velocity representation computes the complementary flows on the interpolation grid. Therefore, the interpolation grid should cover the whole relaxation zone of the viscous flow domain. The schematic view of the interpolation grid for potential flow model is depicted in Figure 7.6.

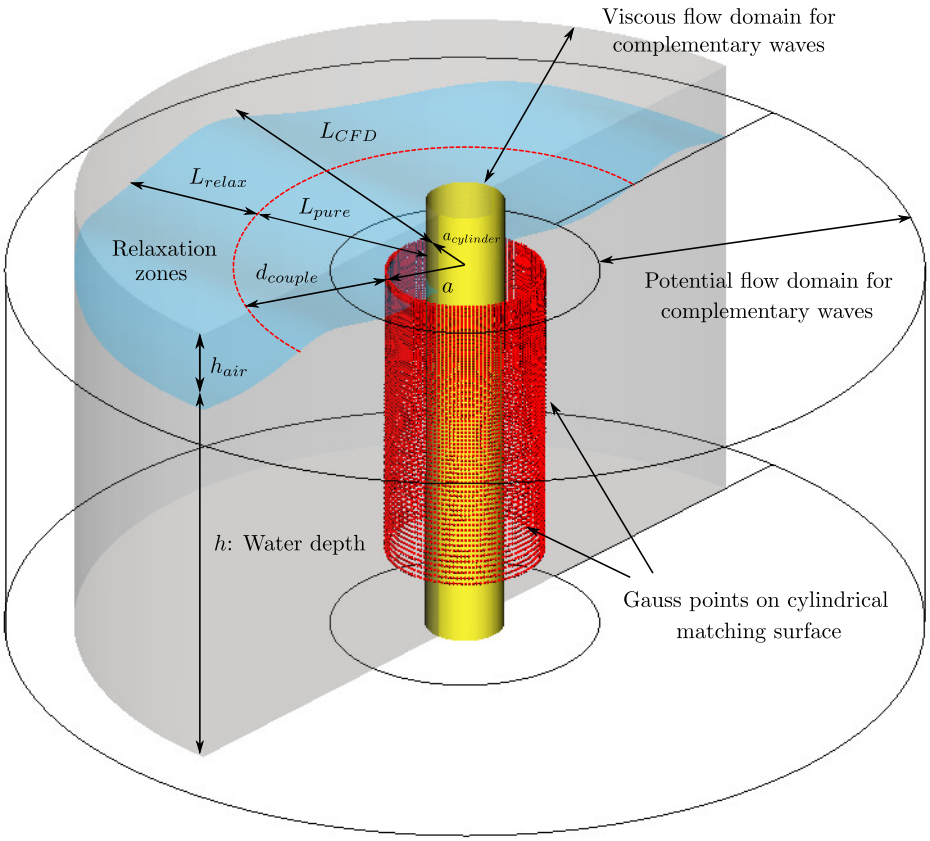

Figure 7.5. Computational domain of viscous and potential flow models for benchmark test case on a vertical circular cylinder in regular waves.

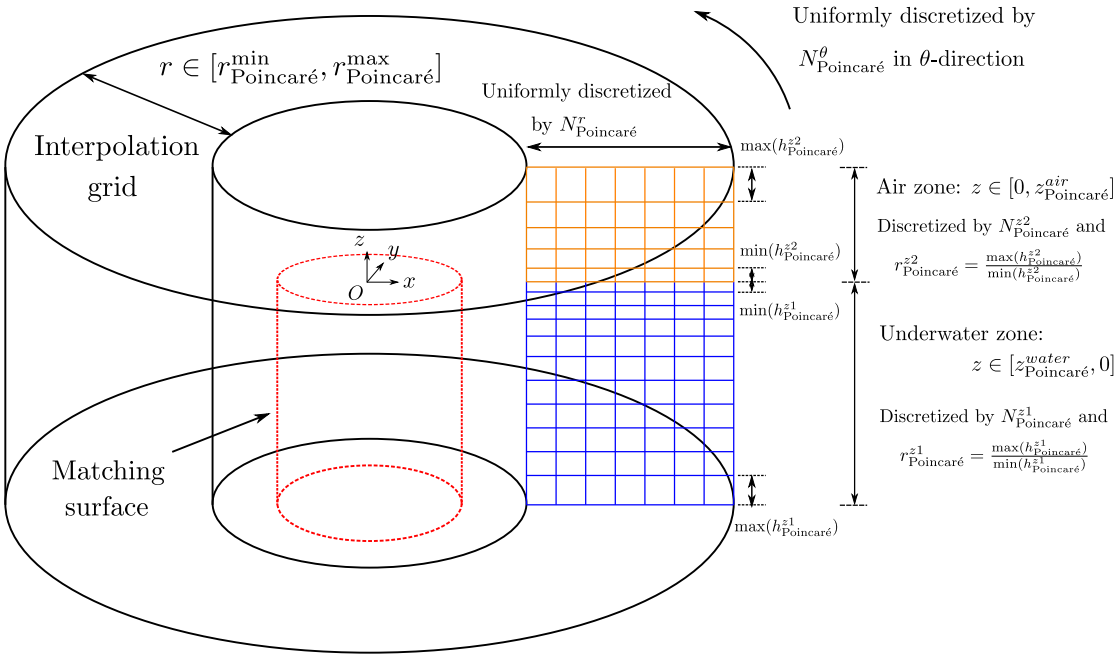

Figure 7.6. Interpolation grid of Poincaré's velocity representation for complementary flows.

The cylindrical-shaped interpolation grid is defined in $r \in [r^{\min}_{\text{Poincaré}}, r^{\max}_{\text{Poincaré}}]$, $z \in [z^{water}_{\text{Poincaré}}, z^{air}_{\text{Poincaré}}]$ and $\theta \in [0, 2\pi]$. The interpolation grid is discretized uniformly in a radial direction with discretization number ($N^r_{\text{Poincaré}}$). In the vertical direction, the grid is decomposed into the underwater zone ($z \leq 0$) and the air zone ($z > 0$). The underwater zone is discretized with the number of N^{z1} with a cell height ratio r^{z1} in the vertical direction. The air zone is also discretized in the vertical direction with the number of $N^{z2}_{\text{Poincaré}}$ with a cell height ratio r^{z2}. The cell height ratios are defined as

$$r^{z1}_{\text{Poincaré}} = \frac{\max(h^{z1}_{\text{Poincaré}})}{\min(h^{z1}_{\text{Poincaré}})}, \qquad r^{z2}_{\text{Poincaré}} = \frac{\max(h^{z2}_{\text{Poincaré}})}{\min(h^{z2}_{\text{Poincaré}})}. \tag{7.5}$$

where $h^{z1}_{\text{Poincaré}}$ and $h^{z2}_{\text{Poincaré}}$ are the cell height of the underwater and air zone, respectively. The cells having the minimum height are located on the mean free surface to give a dense mesh distribution near to the free surface. Interpolation grid is uniformly distributed in θ-direction with the number of $N^{\theta}_{\text{Poincaré}}$.

7.2.3 Coupling between viscous flow solver based on SWENSE with LS function and potential flow solver

Numerical setting

The viscous flow solver based on SWENSE with LS function for interface modeling is used. Results with and without two-way coupling are compared. Two computational meshes are used for the viscous flow solver and relative information is given in Table 7.2.

Table 7.2. Computational domains of viscous flow model based on SWENSE with LS function for the vertical circular cylinder in waves.

Item	Mesh1	Mesh2
L_{CFD}	$a_{cylinder} + 2.5\lambda_0$	$a_{cylinder} + 1.5\lambda_0$
L_{relax}	$2\lambda_0$	$1\lambda_0$
L_{pure}	$a_{cylinder} + 0.5\lambda_0$	$a_{cylinder} + 0.5\lambda_0$
N_{cell}	360,000	360,000
a	$2a_{cylinder}$	$2a_{cylinder}$
Interpolation grid	$r \in [a + 0.3\lambda_0, L_{CFD} + 0.2\lambda_0]$, $z \in [-H - 1m, 3.5m]$	$r \in [a + 0.3\lambda_0, L_{CFD} + 0.2\lambda_0]$, $z \in [-H - 1m, 3.5m]$
$N^r_{\text{Poincaré}}$ and $N^{\theta}_{\text{Poincaré}}$	120 and 128	80 and 128
$N^{z1}_{\text{Poincaré}}$ and $N^{z2}_{\text{Poincaré}}$	300 and 50	300 and 50
$r^{z1}_{\text{Poincaré}}$ and $r^{z2}_{\text{Poincaré}}$	5 and 3	5 and 3
d_{couple}	$0.5\lambda_0$	$0.5\lambda_0$

The domain lengths are set to be $L_{CFD} = a_{cylinder} + 2.5\lambda_0$ and $L_{CFD} = a_{cylinder} + 1.5\lambda_0$ for Mesh1 and Mesh2, respectively. A relaxation zone is defined in the far-field region, as colored yellow in figure 7.7. The length of relaxation zones are set to be $L_{relax} = 2\lambda_0$ and $L_{relax} = 1\lambda_0$

for Mesh1 and Mesh2 respectively. The pure zone has same length in Mesh1 and Mesh2. The computational meshes of viscous flow solver for the case of $k_0 a_{cylinder} = 1.0$ are shown in figure 7.7. The same number of computational cells, $N_{cell} = 360,000$, is used for mesh refinement.

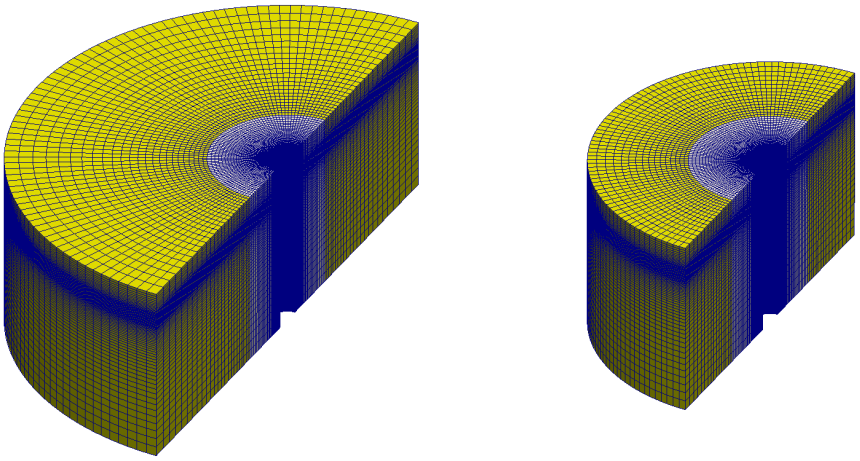

(a) Mesh1 **(b)** Mesh2

Figure 7.7. Computational meshes of viscous flow model based on SWENSE with LS function for the case of $ka_{cylinder} = 1.0$.

The radius of the matching surface used to update the potential flow model is set to be $a = 2a_{cylinder}$. The information of interpolation grid used in the benchmark test are summarized in Table 7.2. The number of Fourier and Laguerre modes used for Poincaré's velocity representation are $N_{fourier} = 6$ and $N_{laguerre} = 3$, respectively. Distance between matching surface and relaxation zone is $d_{couple} = 0.5\lambda_0$.

In the relaxation zone, the complementary flows are relaxed to zero when no coupling is applied or to the complementary flows calculated by potential flow solver when the coupling is considered.

Complementary wave field

Figure 7.8 shows the complementary wave elevations in the computational domain of the viscous flow model at simulation time $t = 12T, 12.4T$ and $12.8T$. Incident waves are propagating from left to right. Relaxation zone is defined in the far-field region of the computational domain, from red-circle to the ends of domain in figure 7.8. The matching surface of radius $a = 2.5a_{cylinder}$ is is located at blue circle in figure 7.8.

The complementary wave elevation fields without considering the two-way coupling between potential and viscous flows are shown in figures 7.8a, 7.8c and 7.8e. The complementary wave elevations only exist in the vicinity of the circular cylinder where no relaxation scheme is applied. In the relaxation zone, the complementary wave elevation is relaxed to zero. Therefore no complementary waves are propagating up to the region of far-field.

The complementary wave elevation fields when the two-way coupling is considered are shown in figures 7.8b, 7.8d and 7.8f. The complementary waves exist both in the vicinity of the circular cylinder and the region of far-field. A smooth transient of complementary wave elevation between pure and relaxation zone is shown in the figures.

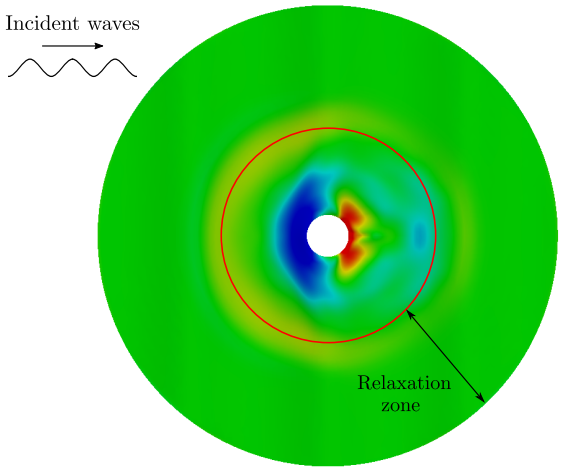

(a) without coupling, $t = 12T$

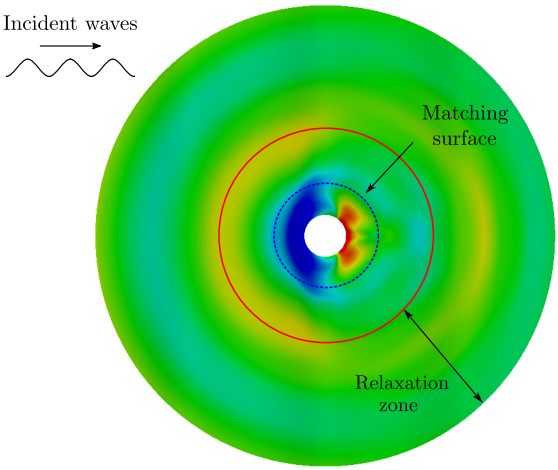

(b) with coupling, $t = 12T$

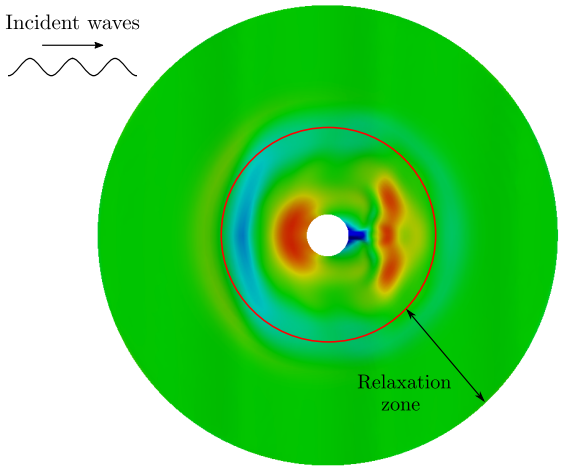

(c) without coupling, $t = 12.4T$

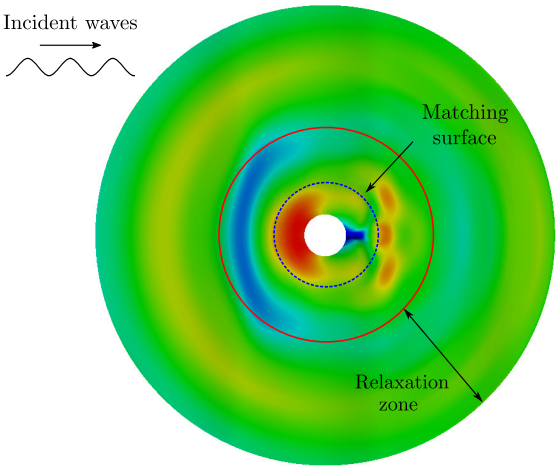

(d) with coupling, $t = 12.4T$

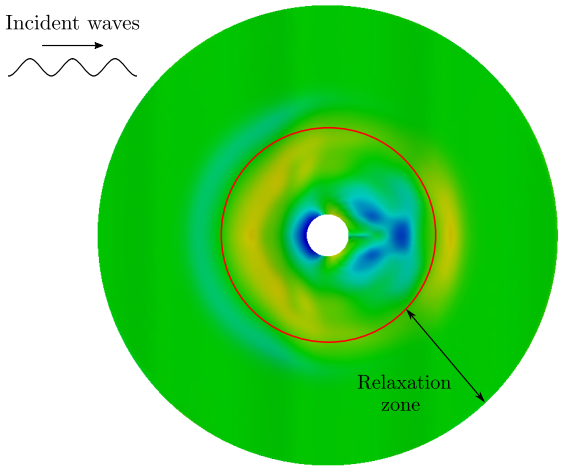

(e) without coupling, $t = 12.8T$

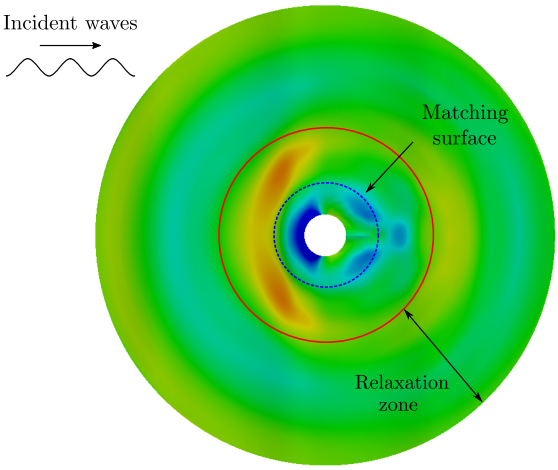

(f) with coupling, $t = 12.8T$

Figure 7.8. Complementary wave elevation fields with respect to application of two-way coupling for the case of $k_0 a_{cylinder} = 1.0$ (Left: without coupling, right: with coupling).

The horizontal force acting on the vertical circular cylinder

Figure 7.9 shows the time series of horizontal forces acting on the vertical circular cylinder. The horizontal forces are compared with respect to the different computational meshes of viscous flow model and two-way coupling between viscous and potential flows. The magnitude of total forces and behaviours are not changed significantly with respect to the computational meshes and two-way coupling. The time series of forces are slightly changed when the different computational meshes are used for the case of large wavenumber, $k_0 a_{cylinder} \geq 1$. Two-way coupling between potential and viscous flows also slightly affects the time series of forces.

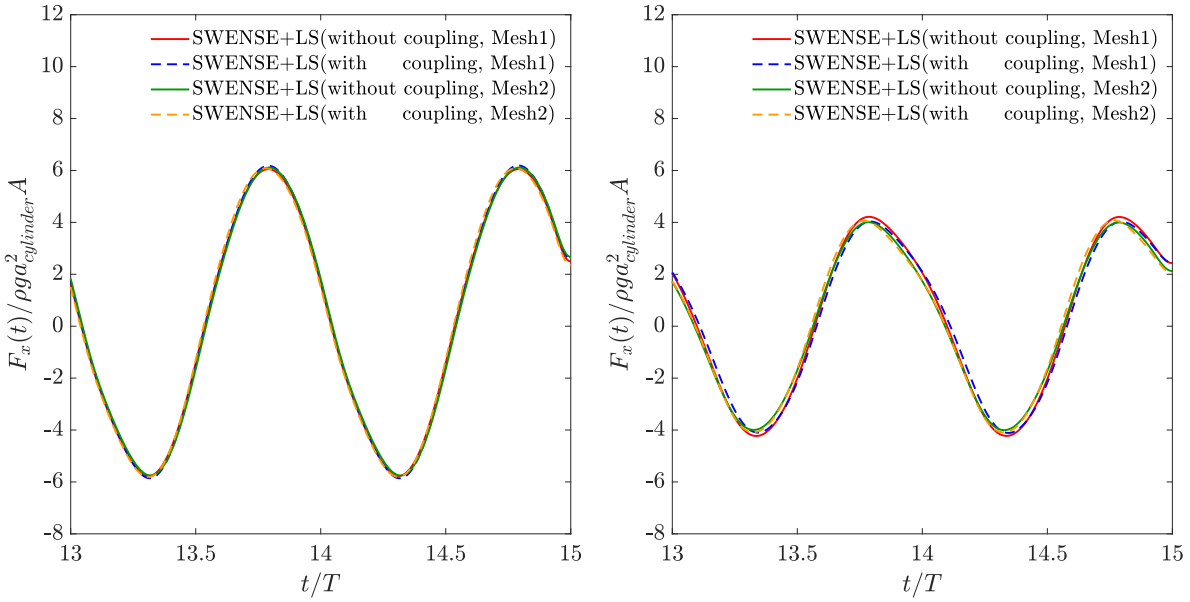

(a) $k_0 a_{cylinder} = 0.5$ **(b)** $k_0 a_{cylinder} = 1.0$

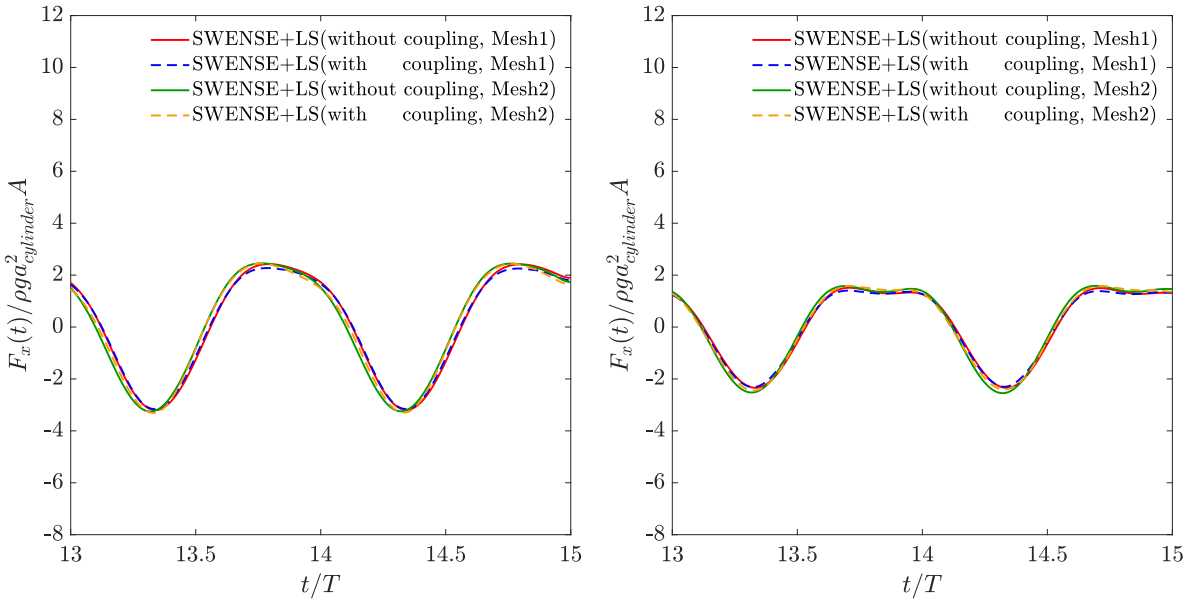

(c) $k_0 a_{cylinder} = 1.5$ **(d)** $k_0 a_{cylinder} = 2.0$

Figure 7.9. Horizontal force time series with respect to the computational meshes and the application of two-way coupling (Viscous flow model based on SWENSE with LS function and Poincaré's velocity representation is used for two-way coupling).

Force harmonics and mean drift forces are extracted by using moving window FFT. They are compared in figure 7.10 with respect to different computational meshes of viscous flow model and two-way coupling between potential and viscous flows. The analytical values for the first , second and third harmonics of horizontal forces are obtained from potential flow theory based on perturbation series (Malenica, 1994), as given by black lines in figures 7.10a, 7.10c and 7.10d. Reference values for the mean drift forces are calculated by using HOBEM (Hong et al., 2005), as given by black line in figure 7.10b.

Figure 7.10a shows the first harmonic of horizontal forces compared with the analytical solution. The first harmonics show good agreements with the analytical solution obtained from the potential flow theory. When no coupling is applied, the first harmonics obtained from different computational meshes are slightly different for the cases of $k_0 a_{cylinder} \geq 0.75$. The first harmonics obtained from different computational meshes by applying two-way coupling show consistent values for the cases of $k_0 a_{cylinder} \leq 1.25$.

Figure 7.10b shows the mean drift force in the horizontal direction. They are similar compared with the results of HOBEM(numerics) except the case with small computational domain and without two-way coupling. It seems that the two-way coupling helps to assess the mean drift force on the structure in a small computational domain.

Figure 7.10c shows the second harmonic of horizontal forces. The second harmonics show similar behaviour with the analytical solution from potential flow theory. With two-way coupling, the second harmonics are slightly better compared to the simulation results without two-way coupling.

Figure 7.10d shows the third harmonic of horizontal forces. The third harmonics of horizontal forces for all simulations have similar tendencies with the analytical solution, but the poor results are obtained on the magnitude of forces for all simulations. Especially for the cases of large wavenumbers $k_0 a_{cylinder} > 1$, the simulation results are different.

The following things are summarized from the results.

- SWENSE with LS function for interface modeling with a relatively large computational domain gives good results up to second-order forces.
- Two-way coupling between viscous and potential flow model gives slightly better results for the first- and second harmonics and mean drift forces in a small computational domain. However, poor results are obtained for third-order harmonics.
- Nevertheless, the third harmonics obtained from the simulation have tendencies similar to the analytical solution, the large differences between analytical solution and simulation results are shown.

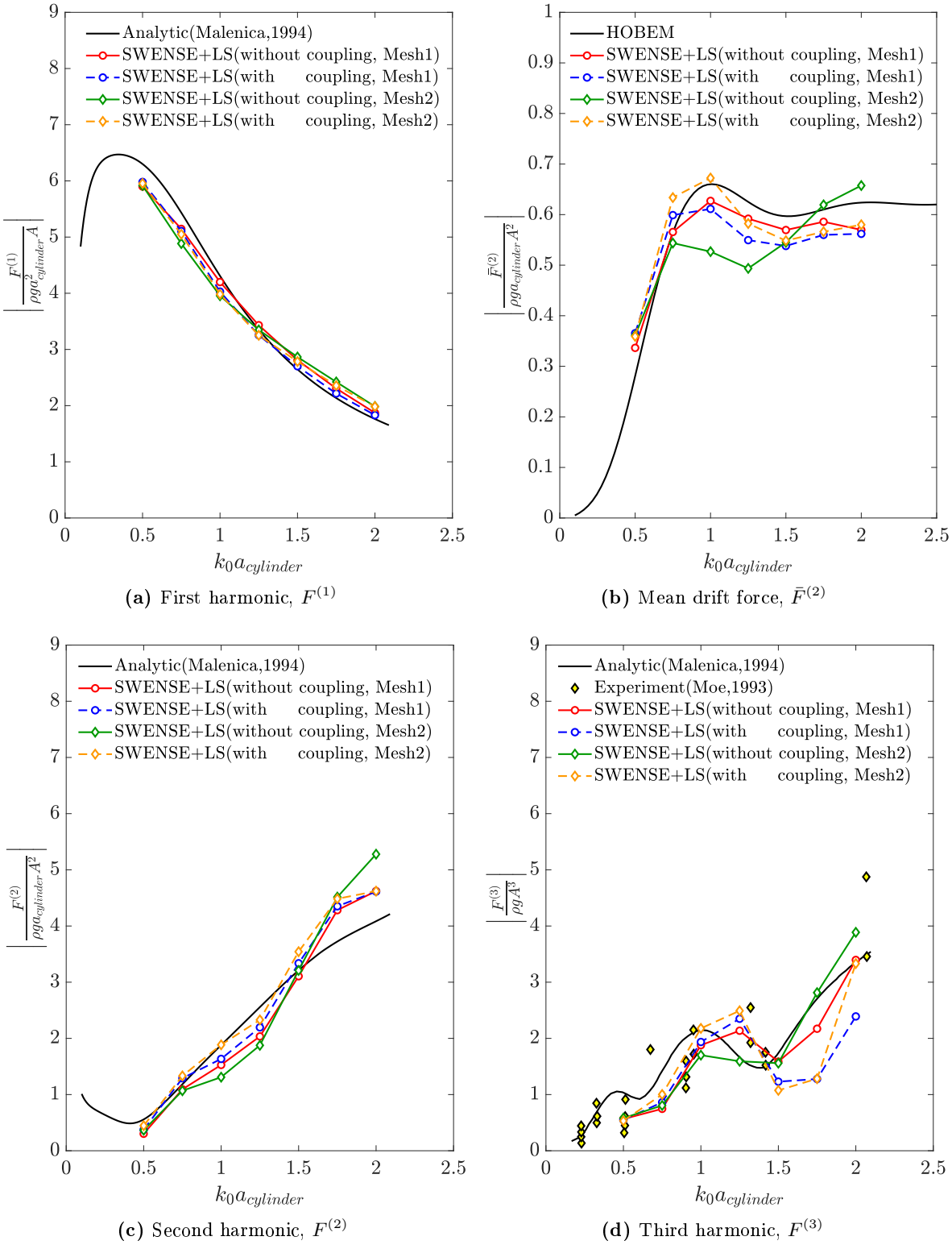

(a) First harmonic, $F^{(1)}$ **(b)** Mean drift force, $\bar{F}^{(2)}$

(c) Second harmonic, $F^{(2)}$ **(d)** Third harmonic, $F^{(3)}$

Figure 7.10. Harmonics of horizontal force acting on vertical circular cylinder. Horizontal forces are calculated by viscous flow model based on SWENSE with LS function. Poincaré's velocity representation is used for two-way coupling.

7.2.4 Comparison and discussion

Considered computations

The viscous flow solvers with and without two-way coupling are applied. The computations considered are listed as below:

- **Viscous flow solver based on NS+VOF with and without two-way coupling**

  Viscous flow solver based on Navier-Stokes equations and VOF interface modeling is used. In the relaxation zone, the functional quantities of total flows are relaxed to the target functional quantities as quantities calculated by incident waves as

  $$\mathbf{u} = (1-w)\mathbf{u} + w\mathbf{u}^{Target}, \tag{7.6}$$
  $$\alpha = (1-w)\alpha + w\alpha^{Target}, \tag{7.7}$$

  where $\mathbf{u}^{Target}$ and α^{Target} are the target fluid velocity and VOF.

  When the coupling is not applied, the target fluid velocity and VOF are set to be the functional quantities of incident waves as

  $$\mathbf{u}^{Target} = \mathbf{u}_I, \qquad \alpha^{Target} = \alpha^{Target,I}, \tag{7.8}$$

  where $\mathbf{u}_I$ is the fluid velocity computed by incident waves, $\alpha^{Target,I}$ is VOF calculated by using the wave elevation of incident waves.

  Meanwhile, the target fluid velocity and VOF changes when the two-way coupling is applied as

  $$\mathbf{u} = (1-w)\mathbf{u} + w(\mathbf{u}_I + \mathbf{u}_C^{\text{Poincaré}}), \tag{7.9}$$
  $$\alpha = (1-w)\alpha + w\alpha^{Target,Total}, \tag{7.10}$$

  where $\mathbf{u}^{\text{Poincaré}}$ is complementary fluid velocity computed by Poincaré's velocity representation, $\alpha^{Target,Total}$ is VOF calculated by using total wave elevation(Ξ). Total wave elevation in the relaxation zone is given by a superposition of incident wave and complementary waves

  $$\Xi = \Xi_I + \Xi_C^{\text{Poincaré}}, \tag{7.11}$$

  To update the potential flow solver, the complementary fluid velocity and wave elevation on the matching surface are obtained by subtracting the incident flow parts as

  $$\begin{aligned} \mathbf{u}_C &= \mathbf{u} - \mathbf{u}_I, \\ \Xi_C &= \Xi - \Xi_I, \end{aligned} \quad \text{at Gauss points on matching surface and waterline,} \tag{7.12}$$

  where $\mathbf{u}_I$ and Ξ_I are fluid velocity and wave elevation calculated by incident waves at Gauss points, respectively.

- **Viscous flow solver based on SWENSE+LS with and without two-way coupling**

  Viscous flow model based on SWENSE with LS function for interface modeling is used. In the relaxation zone, the complementary flows are relaxed to the complementary flows

computed by Poincaré's velocity representation as

$$\mathbf{u}_C = (1-w)\mathbf{u}_C + w\mathbf{u}_C^{\text{Target}},$$
$$\psi_C = (1-w)\psi_C + w\psi_C^{\text{Target}},$$

The target complementary fluid velocity and LS functions are determined by application of two-way coupling as

$$\mathbf{u}_C^{\text{Target}} = \begin{cases} 0 & \text{without coupling} \\ \mathbf{u}_C^{\text{Poincaré}} & \text{with coupling} \end{cases}, \qquad \psi_C^{\text{Target}} = \begin{cases} 0 & \text{without coupling} \\ \psi_C^{\text{Poincaré}} & \text{with coupling} \end{cases}$$

where $\mathbf{u}_C^{\text{Poincaré}}$ and $\psi_C^{\text{Poincaré}}$ are the complementary fluid velocity and LS function calculated by using Poincaré's velocity representation.

Computational domain

Some information of computational domains are summarized in Table 7.3. The radius of viscous flow domains is $L_{CFD} = a_{cylinder} + 3.0\lambda_0$ and $a_{cylinder} + 1.5\lambda_0$ for MeshL and Mesh2, respectively. The relaxation zone is defined in the far-field region with its length $L_{relax} = 1.5\lambda_0$ and $1\lambda_0$ for MeshL and Mesh2, respectively. The numbers of computational cells are in the range of 3millions and 0.36millions for MeshL and Mesh2, respectively. The simulation time step is $T/\Delta t = 1600$ and 1000 for MeshL and Mesh2, respectively. Figure 7.11 show the computational grid of MeshL for the simulation case of $ka_{cylinder} = 1.0$. The computational grid for Mesh2 is already shown in figure 7.7b.

The radius of matching surface is $a = 2a_{cylinder}$. Some information of interpolation grid is given in Table 7.3. Two-way coupling is only applied when Mesh2 is used in the viscous flow solver. The distance between the matching surface and relaxation zone is $d_{couple} = 0.5\lambda_0$. The numbers of Fourier and Laguerre modes are $N_{fourier} = 6$ and $N_{laguerre} = 3$, respectively.

Table 7.3. Computational domains used for the comparison of two-way coupling with various viscous flow models.

Item	MeshL	Mesh2
L_{CFD}	$a_{cylinder} + 3.0\lambda_0$	$a_{cylinder} + 1.5\lambda_0$
L_{relax}	$1.5\lambda_0$	$1\lambda_0$
L_{pure}	$a_{cylinder} + 1.5\lambda_0$	$a_{cylinder} + 0.5\lambda_0$
N_{cell}	2,808,000 - 3,132,000	360,000
a	$2a_{cylinder}$	$2a_{cylinder}$
Interpolation grid	-	$r \in [a + 0.3\lambda_0, L_{CFD} + 0.2\lambda_0]$, $z \in [-H - 1m, 3.5m]$
$N^r_{\text{Poincaré}}$ and $N^\theta_{\text{Poincaré}}$	-	80 and 128
$N^{z1}_{\text{Poincaré}}$ and $N^{z2}_{\text{Poincaré}}$	-	300 and 50
$r^{z1}_{\text{Poincaré}}$ and $r^{z2}_{\text{Poincaré}}$	-	5 and 3
d_{couple}	-	$0.5\lambda_0$

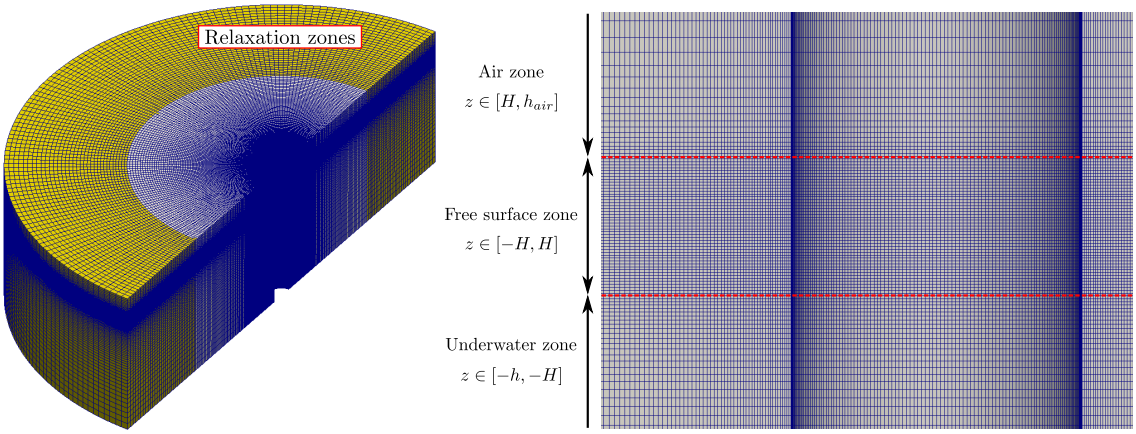

Figure 7.11. Computational grid of MeshL for the simulation case of $ka_{cylinder} = 1.0$

Total wave field

Total wave elevation fields in the vicinity of the circular cylinder are compared in figure 7.12. Incident waves are propagating from left to right. The relaxation zone is defined in the far-field, from red circle to the end. The matching surface is given as the blue circle.

Figure 7.12a shows total wave elevation field computed by solving Navier-Stokes (NS) equations and VOF interface modeling in MeshL without coupling. In the figure, the total waves diffracted by the vertical circular cylinder are propagating to the far-field. The amplitudes of total wave elevation in the vicinity of the vertical circular cylinder are smaller than the simulation case with Mesh2 due to numerical dissipation.

Figures 7.12b and 7.12d show the total wave elevation fields calculated by viscous flow solvers without two-way coupling in Mesh2, Figure 7.12b by viscous flow solver based on NS equations with VOF interface modeling and Figure 7.12d by viscous flow solver based on SWENSE with LS function for interface modeling. They show that the total wave elevations in the relaxation zone are blended to the incident waves.

Figures 7.12c and 7.12e show the total wave elevation fields calculated by viscous flow models with two-way coupling in Mesh2, Figure 7.12c by viscous flow model based on NS equations and VOF interface modeling, and Figure 7.12e by viscous flow model based on SWENSE with LS function. The total waves diffracted by the cylinder are propagating in the relaxation zone and a smooth transient of wave elevation across the pure and relaxation zone are presented.

The results can be summarized as follows:

- Total wave fields in the vicinity of the vertical circular cylinder are similar.
- The viscous flow solver based on NS equations and VOF interface modeling needs more refined mesh than the computational mesh used in the present study.
- When the two-way coupling is used, the waves diffracted by the structure are propagating up to far-field. A smooth transition of complementary waves across the relaxation and pure zone are presented.

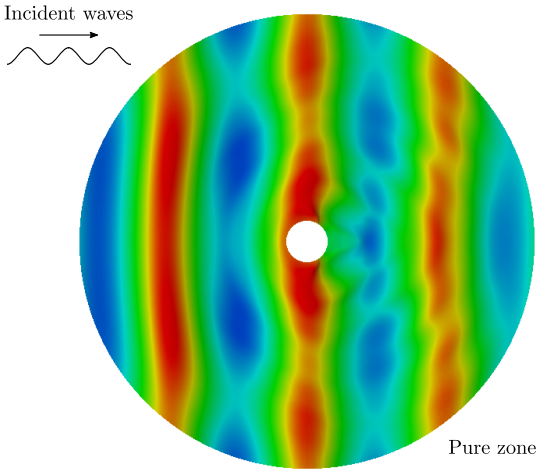

(a) NS and VOF without two-way coupling(Large domain), large domain

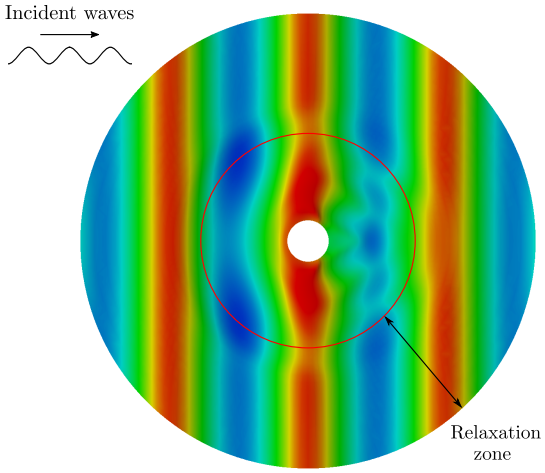

(b) NS and VOF without two-way coupling, small domain

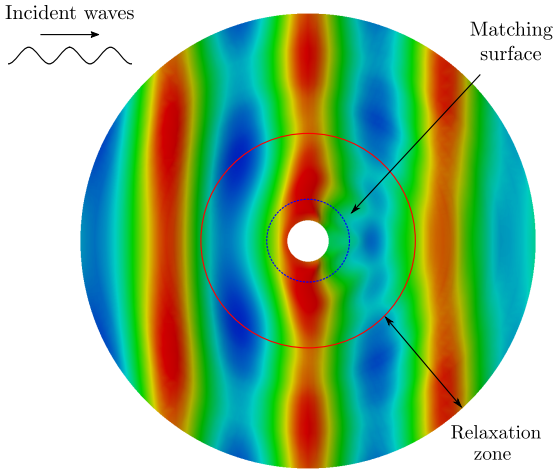

(c) NS and VOF with two-way coupling, small domain

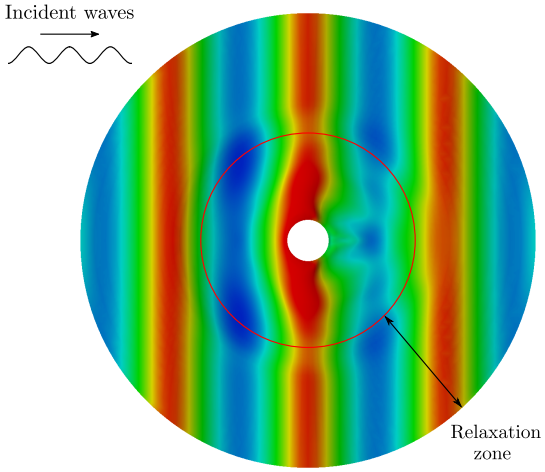

(d) SWENSE and LS without two-way coupling, small domain

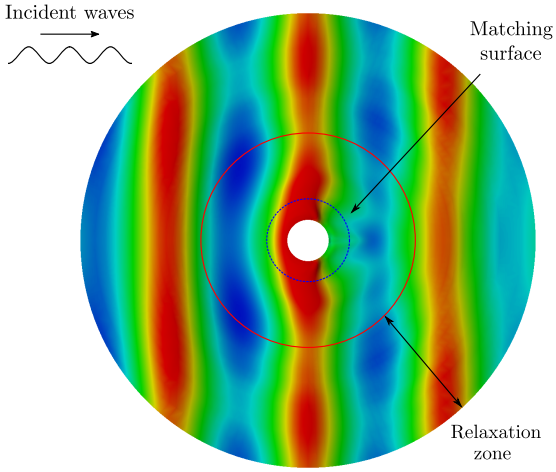

(e) SWENSE and LS with two-way coupling, small domain

Figure 7.12. Total wave elevation fields with respect to two-way coupling for the case of $k_0 a_{cylinder} = 1.0$.

Horizontal force acting on the vertical circular cylinder

Horizontal force harmonics and mean drift forces acting on the vertical circular cylinder are compared in figure 7.13 with respect to the two-way coupling for different viscous flow models.

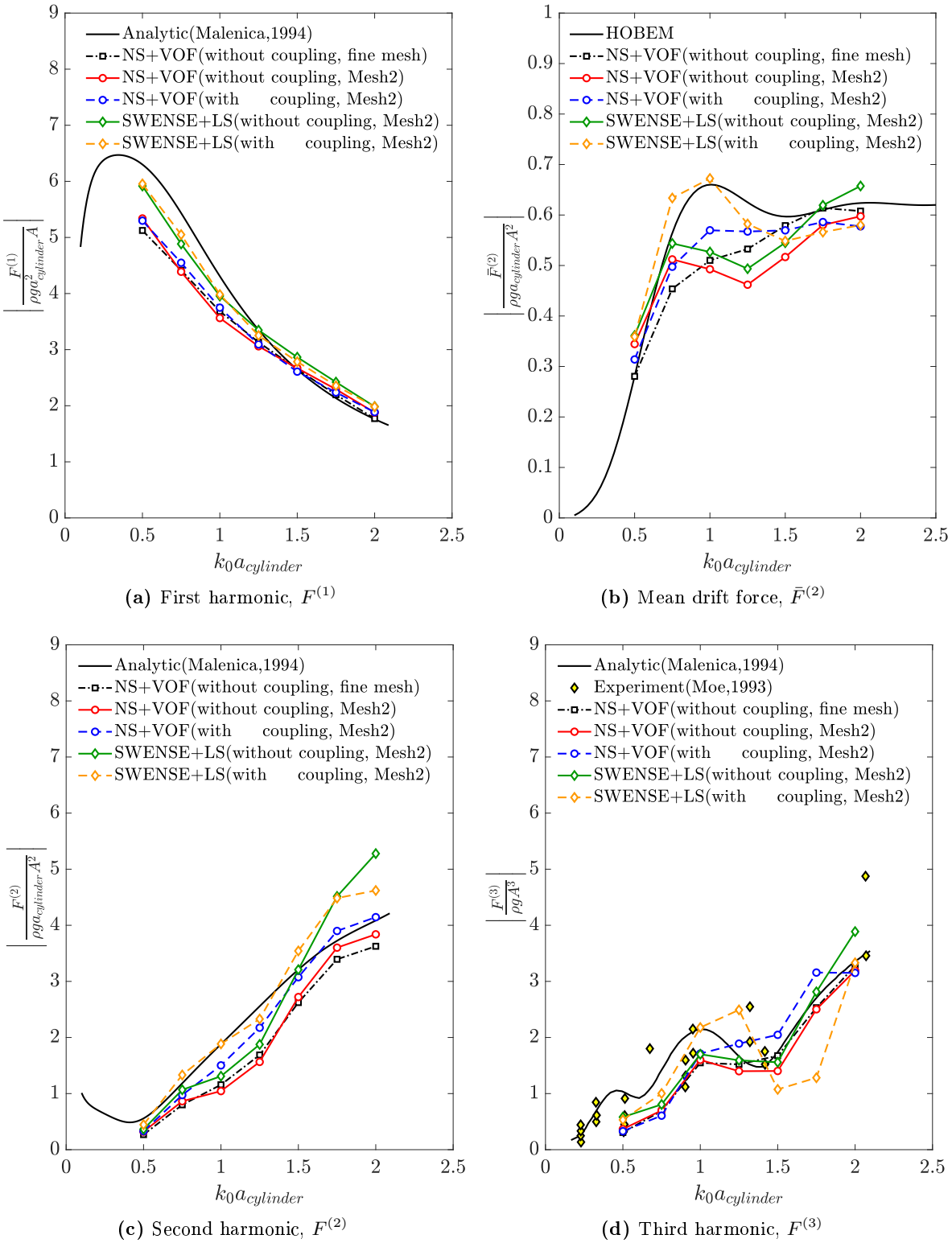

(a) First harmonic, $F^{(1)}$ **(b)** Mean drift force, $\bar{F}^{(2)}$

(c) Second harmonic, $F^{(2)}$ **(d)** Third harmonic, $F^{(3)}$

Figure 7.13. Horizontal force harmonics and mean drift forces with respect to the two-way coupling for different viscous flow models.

Figure 7.13a shows the first harmonics of horizontal forces. The first harmonics calculated by solving SWENSE with LS function show better results for small wavenumbers than the simulation solving NS equations and VOF interface modeling. Nevertheless, the effects of two-way coupling on the first harmonics are small, the first harmonics approach to the analytical solution when the two-way coupling is considered.

Figure 7.13b shows the horizontal mean drift forces. The mean drift forces calculated by viscous flow models without two-way coupling show big differences, especially for the simulation cases of $k_0 a_{cylinder}$=1,1.25. When the two-way coupling is considered, the mean drift forces show better results than the simulation without considering two-way coupling.

Figure 7.13c shows the second harmonics of horizontal forces. The second harmonics obtained from all simulations follow the analytical solution. When the two-way coupling is considered, the second harmonics show better results than the simulation cases without considering two-way coupling.

Figure 7.13d shows the third harmonics of horizontal force. Third harmonics by SWENSE and NS viscous flow models without considering two-way coupling show similar tendency. When the two-way coupling is applied, the results are more divergent than the simulation cases without considering two-way coupling for large wavenumbers.

Differences of force harmonics and mean drift forces are summarized in Table 7.4. Relative differences of horizontal force with the solution potential flow model are defined by

$$\epsilon_{F_{x,i}^{(m)}} = \frac{1}{N_{k_0 a_{cylinder}}} \left[\sum_{i=1}^{N_{k_0 a_{cylinder}}} \left(\frac{F_{x,i}^{(m)} - F_{x,i,potential}^{(m)}}{F_{x,i,potential}^{(m)}} \right)^2 \right]^{\frac{1}{2}}, \tag{7.13}$$

where $\epsilon_{F_{x,i}^{(m)}}$ is a relative difference of $m-$th harmonics of horizontal force with respect to potential flow result. $N_{k_0 a_{cylinder}}$ is the number of simulated wavenumbers. $F_{x,i}^{(m)}$ is m-th harmonic component of horizontal force obtained by simulation with i-th $k_0 a_{cylinder}$. $F_{x,i,potential}^{(m)}$ is m-th harmonic components calculated by potential flow theory at i-th $k_0 a_{cylinder}$.

When the two-way coupling is applied, the relative differences of force harmonics are reduced for first- and second harmonics and mean drift forces. Meanwhile, the relative differences of third harmonics increases when the two-way coupling is considered.

Table 7.4. Relative differences of force harmonics acting on vertical circular cylinder with respect to viscous flow models and two-way coupling.

Simulations / Force harmonics	$\epsilon_{F_x^{(1)}}$	$\epsilon_{\bar{F}_x^{(2)}}$	$\epsilon_{F_x^{(2)}}$	$\epsilon_{F_x^{(3)}}$
NS+ VOF without coupling (large domain)	0.0443	0.0481	0.2814	0.1317
NS + VOF without coupling (small domain)	0.0449	0.0662	0.1133	0.1285
NS + VOF with coupling (small domain)	0.0410	0.0363	0.0736	0.1368
SWENSE + LS without coupling (small domain)	0.0355	0.0605	0.0928	0.0972
SWENSE + LS with coupling (small domain)	0.0300	0.0485	0.0522	0.1425

Computational cost

Computational costs for simulating the wave diffraction by the vertical circular cylinder are compared. The computational costs are defined by computational time multiplied by the number of processors used for computation as

$$\text{Cost} = t_{proc} \times N_{proc}, \tag{7.14}$$

where t_{proc} is a computational time, N_{proc} is the number of processors used for parallel computation. In the present study, $N_{proc} = 12$ is used for both viscous flow solvers based on NS equations and SWENSE in the small computational domain. In the large domain, the number of processor $N_{proc} = 120$ is used for computation. Figure 7.14 shows the normalized computational costs by the computational cost of the viscous flow solver based NS equations and VOF interface modeling without two-way coupling in the small computational domain.

The computational cost of the viscous flow solver based on the NS equation and VOF interface modeling in the large computational domain is about 21.6 times of reference case. Viscous flow solver based on SWENSE with LS function is faster than the viscous flow solver based on NS equations and VOF interface modeling. VOF transport equation is solved by an algorithm called `MULES`, which solves the transport equation by using FCT-scheme (Boris and Book, 1973; Zalesak, 1979), in OpenFOAM framework. `MULES` needs the nonlinear iteration for calculating the flux limiter on each internal faces. Therefore, the computational costs are larger than solving the LS-transport equation.

Computational costs are increased when the two-way coupling is applied. Extra computational costs for two-way coupling are listed as below:

- Computation of convolution integrals in Poincaré's velocity representation needs extra computational time. It can be reduced by applying parallel computation.
- Interpolating the complementary fluid velocity and wave elevation in the relaxation zone are computational burden.
- Approximation of complementary flows on the matching surface by Fourier-Laguerre series and Fourier series needs a short computational time compared to other procedures.

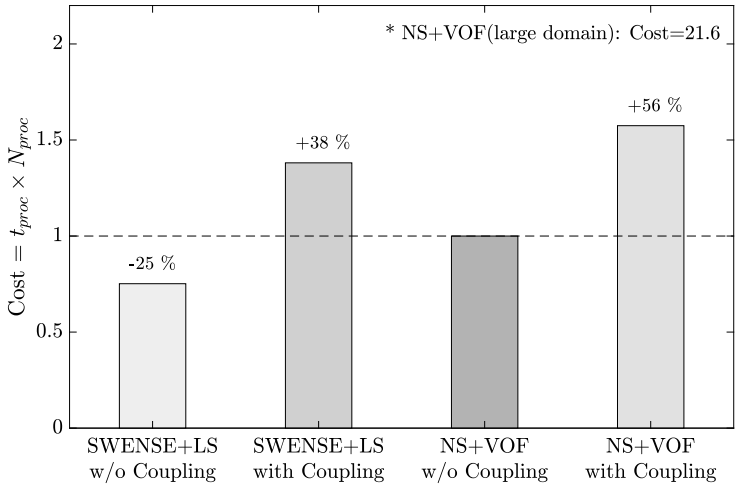

Figure 7.14. Computational cost.

7.2.5 Summary of benchmark test 1

Two-way coupling strategy between viscous and potential flows is applied for a problem of wave diffraction by a bottom mounted vertical circular cylinder in regular waves. Two-way coupling strategy is also applied for the viscous flow solver based on SWENSE with LS function. The simulations are conducted for various regular wave frequency keeping the wave steepness.

The complementary waves diffracted by the vertical circular cylinder propagates up to far-field with two-way coupling. Total wave fields obtained from the simulations with two-way coupling shows that the diffracted waves are propagating in the relaxation zone that are similar to the total wave fields obtained from the simulation in the large computational domain.

Horizontal forces acting on the vertical circular cylinder are compared by extracting its harmonics and mean drift forces. The simulations by considering two-way coupling give good results for the first harmonics, second harmonics and mean drift forces which correspond to the second-order component. In the potential theory, the linear wave distribution along the waterline contributes mainly on the second order forces (Pinkster, 1980). When the two-way coupling is applied the differences of first and second order forces with the solution potential flow model are reduced because the linear parts of complementary waves in the relaxation zone are well treated.

However, the third harmonics obtained from the simulation by considering two-way coupling are worst than those obtained without two-way coupling. The potential flow model for complementary flows based on linear theory may not appropriate to obtain the third order components which are given by the combination of second and first order components.

The two-way coupling strategy is applied also for the viscous flow solver based on NS equations and VOF and the results are compared. The same conclusion is drawn from the simulation results.

The computational costs are increased when the two-way coupling is applied. The computational costs are increased by 84% (=1.38/0.75) for the viscous flow solver based on SWENSE with LS function. When the viscous flow solver based on NS equations and VOF is used, the computational costs are increased by 56%.

7.3 Benchmark test 2: Calm buoy in waves

A Catenary Anchor Leg Mooring (CALM) buoy is considered to demonstrate the ability of coupling methodology between the viscous flow model based on SWENSE with LS interface modeling and the potential flow model Poincaré velocity representation.

7.3.1 Description

The experiments on a fixed Catenary Anchor Leg Mooring (CALM) buoy in regular and irregular waves were carried out in 3D ocean wave tank in Ecole Centrale de Nantes (Rousset and Ferrant, 2005; Monroy et al., 2011; Li, 2018). Specifications of wave basin in Ecole Centrale de Nantes

was given in section 3.3. The buoy is a truncated vertical circular cylinder with a thin skirt near to the bottom. The buoy model and the picture of the installed buoy in the wave basin are shown in figure 7.15. Geometrical dimensions of the buoy are given in Table 7.5. The horizontal and vertical forces acting on the buoy and the wave elevations are measured in experiments.

The conditions of regular and irregular waves are given in Table 7.6. Stream function theory is used to generate regular waves. The irregular waves are re-generated in the simulation by using the reconstruction procedure of HOS wave model explained in section 3.2. HOS-NWT model for 2D propagating waves is used for HOS wave model.

(a) Buoy model

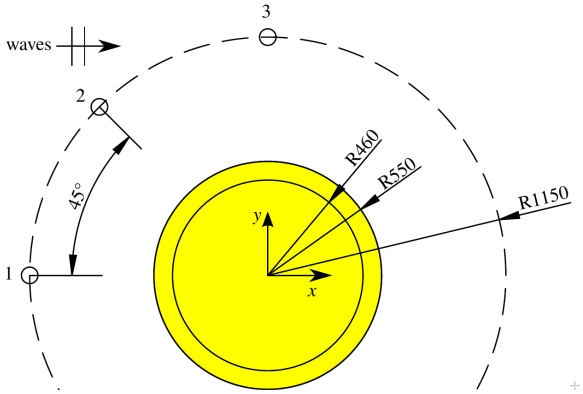

(b) Wave gauge position

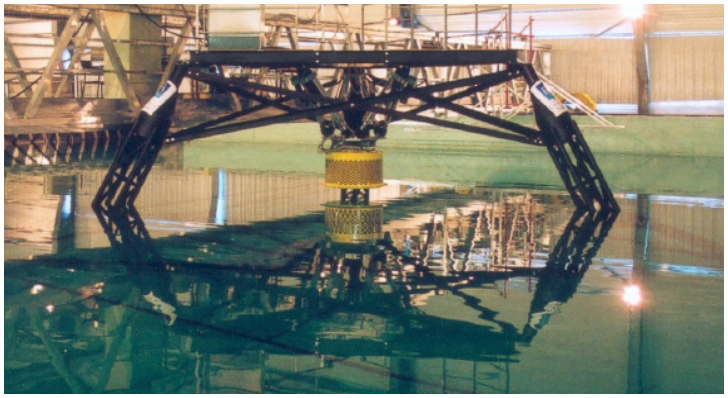

(c) Buoy model installed in the wave basin

Figure 7.15. A CALM Buoy model.

Table 7.5. Geometrical dimensions of the CALM buoy model.

Item	Value
Calm buoy radius (a_{buoy})	0.460m
Height overall	0.560m
Skirt radius (a_{skird})	0.550m
Skirt thickness	0.004 m
From bottom to the skirt	0.04 m
Draft	0.25 m

Table 7.6. Wave conditions considered in the experiments on the CALM buoy model.

Wave Type			
Regular waves		Irregular waves	
Item	Value	Item	Value
Wave height(H)	0.16 m	Significant wave height(H_s)	0.12 m
Wave period(T)	1.80 s	Peak wave period(T_p)	2.00 s
-	-	Peak enhancement factor(γ)	3.0
-	-	Wave spectrum	JONSWAP

Figure 7.16 shows a configuration of the computational domain of viscous and potential flow models for complementary waves. The same configuration of the previous benchmark test is used. The body in the computational domain of the viscous flow model is only replaced.

The computational domain of viscous flow model is composed of relaxation and pure zones. The relaxation and pure zones are colored yellow and grey in figure 7.16, respectively. In the relaxation zone, the complementary flow is relaxed to the complementary flows calculated by Poincaré's velocity representation when the two-way coupling is considered.

The matching surface is located at $a = 2.5a_{skirt}$. The complementary fluid velocity and wave elevations at Gauss points are obtained from the viscous flow model to update the complementary waves in the relaxation zones. Gauss points are shown as red points in figure 7.16.

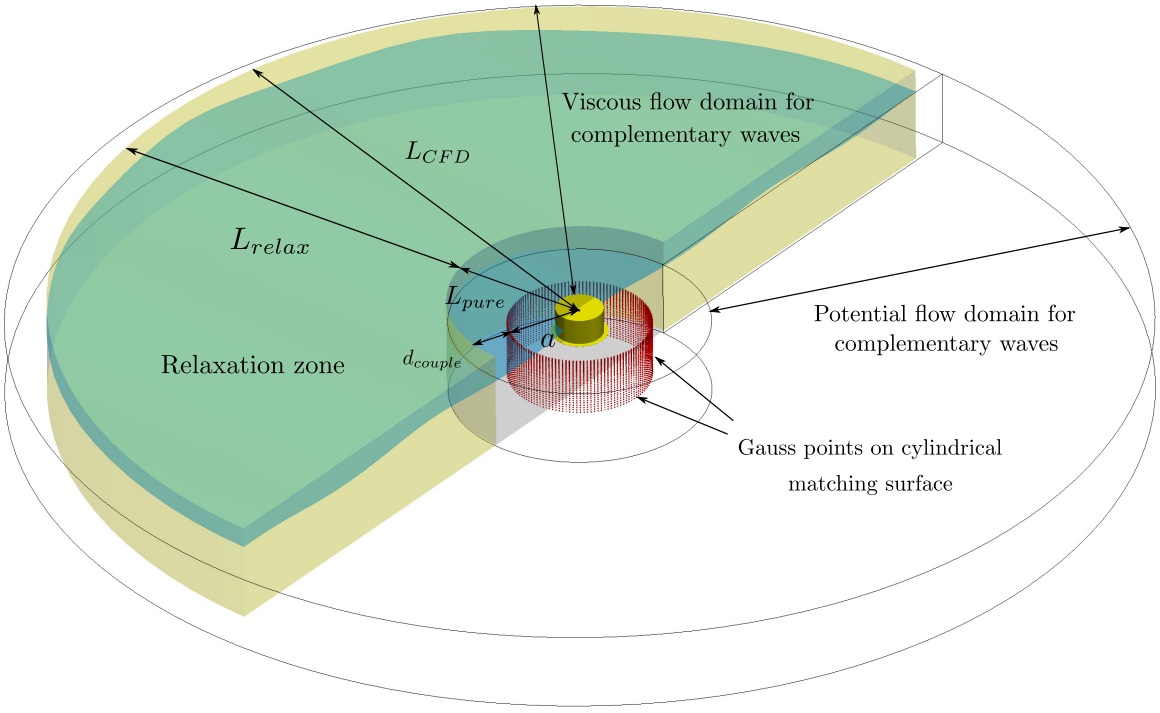

Figure 7.16. Computational domain of viscous and potential flow models for CALM buoy.

7.3.2 Regular waves

Numerical setup

Figure 7.17 shows the computational mesh for viscous flow model. The relaxation zone is defined in the region of far-field, as colored grey in figure 7.17a. The computational mesh is refined in the vicinity of buoy model, as shown in figure 7.17b. The boundary faces of buoy model are shown in figure 7.17c.

Information of computational domain is given in Table 7.7. The length of computional domain for the viscous flow model is $L_{CFD} = a_{skirt} + 2\lambda$. The relaxation zone is defined from far-field boundary with its length $L_{relax} = 1.5\lambda$. The pure zone, where relaxation scheme is not applied, has a length $L_{pure} = a_{skirt} + 0.5\lambda$. The computational cells of $N_{cell} = 473,136$ is used for simulation.

The matching surface to update the potential flow model is located with its radius $a = 2.5a_{skirt}$. The same configuration of interpolation grid for Poincaré's velocity representation, as explained in section 7.2.1, is used. The information of interpolation grid is given in Table 7.7. The numbers of Fourier and Laguerre modes used for Poincaré's velocity representation are $N_{fourier} = 6$ and $N_{laguerre} = 3$, respectively. The distance from the matching surface to the relaxation zone is $d_{couple} = 1.15m$.

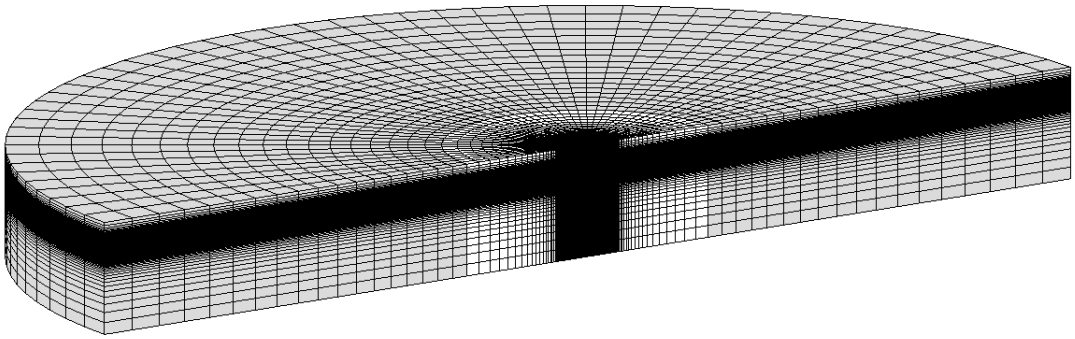

(a) Global view

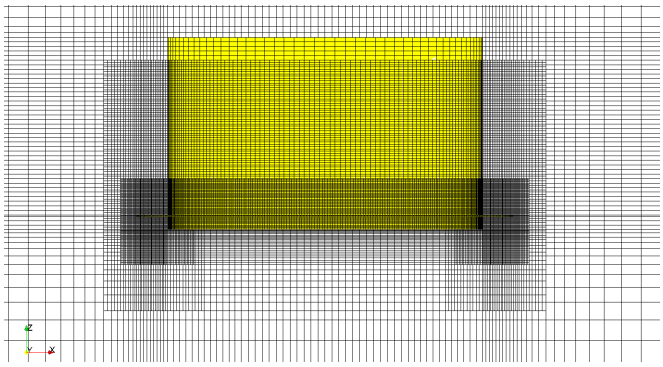

(b) Side view

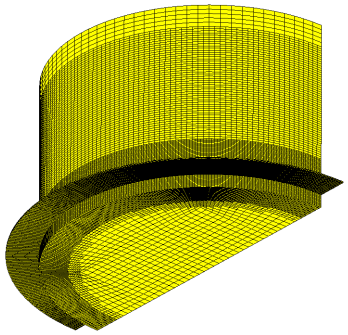

(c) Discretized boundary faces of buoy model

Figure 7.17. Computational mesh used for the viscous flow model.

Table 7.7. Computational domain of the buoy model in regular waves.

Item	Value	Remarks
L_{CFD}	10.1 m	$a_{skirt} + 2\lambda$
L_{relax}	7.575 m	1.5λ
L_{pure}	2.525 m	$a_{skirt} + 0.5\lambda$
N_{cell}	473,136	-
a	1.375 m	$2.5a_{skirt}$
Interpolation grid	$r \in [2.4m, 11.0m]$, $z \in [-1.6m, 0.6m]$	Cover whole relaxation zone.
$N^{r}_{\text{Poincaré}}$ and $N^{\theta}_{\text{Poincaré}}$	80 and 128	-
$N^{z1}_{\text{Poincaré}}$ and $N^{z2}_{\text{Poincaré}}$	300 and 100	-
$r^{z1}_{\text{Poincaré}}$ and $r^{z2}_{\text{Poincaré}}$	3 and 3	-
d_{couple}	1.15 m	$0.5\lambda - 1.5a_{skirt}$

Wave fields

Figure 7.18 shows complementary wave elevation fields with respect to the application of two-way coupling. Relaxation zone is defined in outer-region of red-circle. Matching surface is located inside of relaxation zone, as plotted red circle in figure 7.18. Complementary waves propagate up to far-field and smooth transient across the relaxation and pure zones are shown when the coupling is applied.

Figure 7.19 shows the total wave elevations measured at wave gauge positions in simulation and experiment. Total wave elevation computed by considering two-way coupling shows better agreements with experimental results comparing with the simulation without considering coupling.

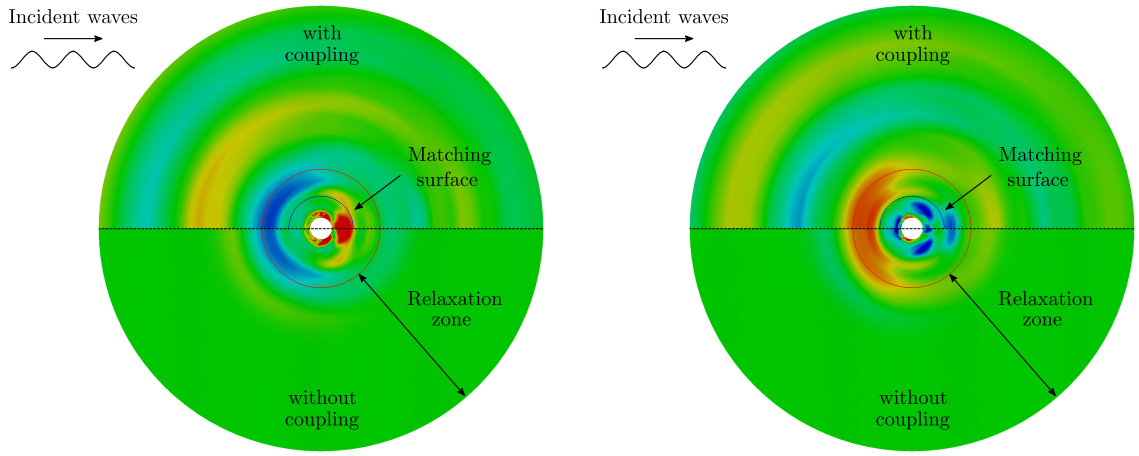

(a) $t = 10T$ **(b)** $t = 10.5T$

Figure 7.18. Complementary wave fields with respect to two-way coupling for the calm buoy in regular wave.

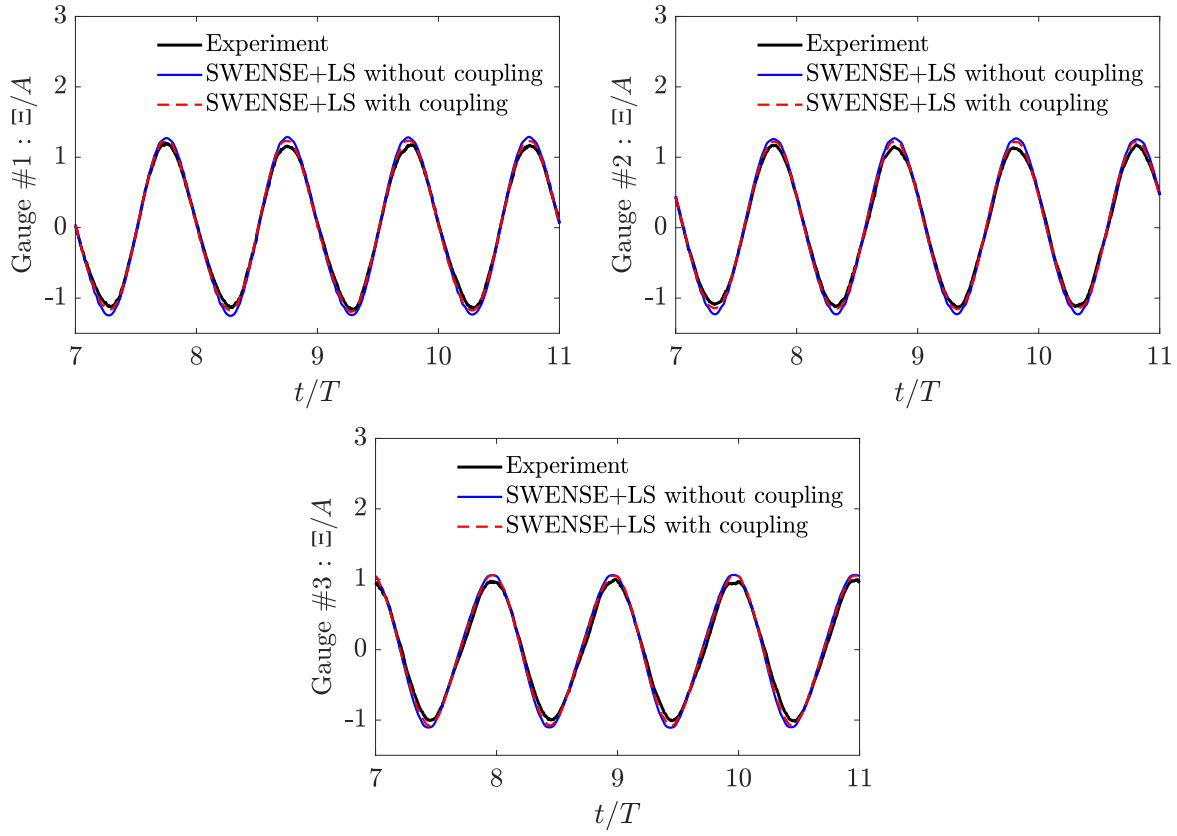

Figure 7.19. Wave elevations measured at the positions of wave gauges for the buoy model in regular wave

The magnitudes of first-harmonics obtained from simulations are compared with the experiment in Table 7.8 with results of Li et al. (2019b). When the two-way coupling is applied, the diffrences between simulation and experiments are reduced. Even if a small number of cell (N_{cell}) is used, the coupling gives good results compared with results of Li et al. (2019b).

Table 7.8. Harmonics of wave elevation measured at wave gauges.

Case	Gauge #1 ($\Xi^{(1)}/A$)	Gauge #2 ($\Xi^{(1)}/A$)	Gauge #3 ($\Xi^{(1)}/A$)	Average Difference
Experiment	1.140 ± 0.0032	1.122 ± 0.0027	0.969 ± 0.0040	-
ISIS-CFD-IWG (Li et al. (2019b), $N_{Cell} = 2.4M$)	1.201 (5.33%)	1.189 (5.93%)	1.009 (4.12%)	5.13 %
SWENSE+VOF w/o coupling (Li et al. (2019b), $N_{Cell} = 0.72M$)	1.196 (4.89%)	1.180 (5.13%)	1.013 (4.54%)	4.85 %
SWENSE+LS w/o coupling (Present study, $N_{Cell} = 0.47M$)	1.240 (8.71%)	1.226 (9.25%)	1.062 (9.58%)	9.18 %
SWENSE+LS with coupling (Present study, $N_{Cell} = 0.47M$)	1.184 (3.80%)	1.174 (4.62%)	1.035 (6.77%)	5.06 %

Forces acting on the buoy model

Figure 7.20 shows horizontal and vertical forces acting of buoy model. The forces obtained by considering two-way coupling show better agreements with experimental results than the simulation results without considering two-way coupling.

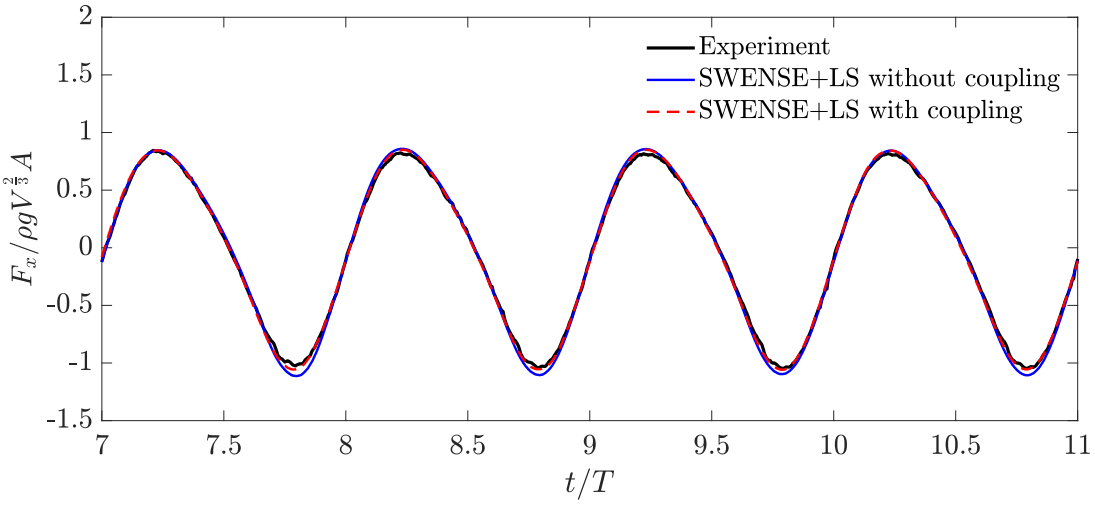

(a) Horizontal force F_x

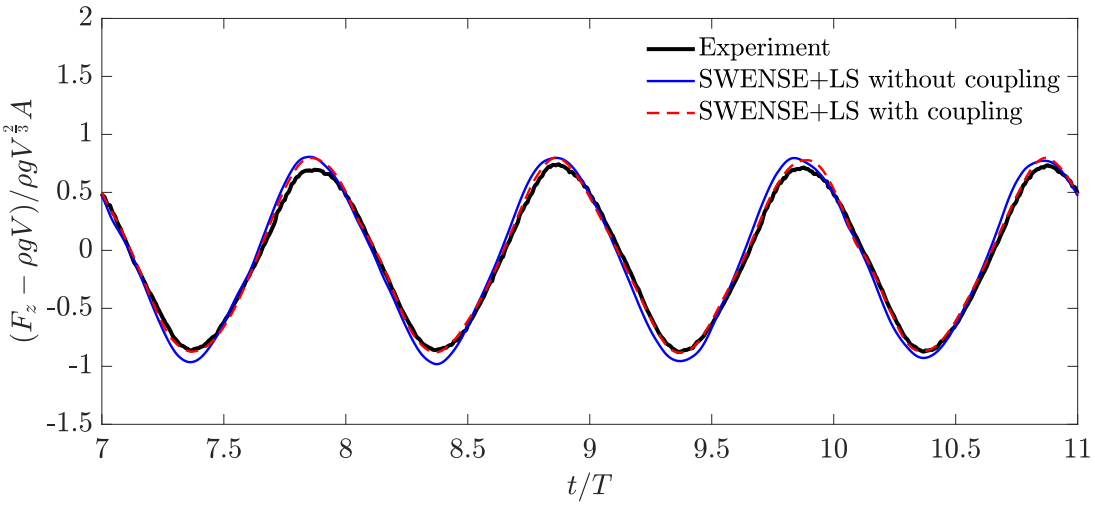

(b) Vertical force F_z

Figure 7.20. Horizontal and vertical forces acting on buoy model in regular waves

Force-harmonics and horizontal mean drift force are extracted by applying moving window FFT, as given in Table 7.9 with results of Li et al. (2019b).

First-harmonic components of horizontal forces obtained from simulations have differences of less than 5%. When the two-way coupling is applied, the difference between simulation and experiment is reduced.

Horizontal mean drift force obtained from the simulation without considering two-way coupling has an difference of 16.8% with respect to the result of the experiment. When the two-way coupling is considered in simulation, the difference of 4.17% is obtained. It reconfirms the results

of benchmark case on the vertical cylinder discussed in section 7.2.4 that the two-way coupling helps to assess horizontal mean drift forces acting on the structure.

Second-harmonic components of horizontal forces calculated by simulations have differences of less than 9%. An difference obtained by applying two-way coupling is smaller than the simulation without considering two-way coupling.

First-harmonic components of vertical forces computed by simulations have large differences compared with horizontal force. The difference between experiments and simulation is also reduced when the two-way coupling is considered.

Table 7.9. Harmonics of forces acting on buoy model.

Case	$\frac{F_x^{(1)}}{\rho g A V^{\frac{2}{3}}}$	$\frac{\bar{F}_x^{(2)}}{\rho g A^2 V^{\frac{1}{3}}}$	$\frac{F_x^{(2)}}{\rho g A^2 V^{\frac{1}{3}}}$	$\frac{F_z^{(1)}}{\rho g A V^{\frac{2}{3}}}$
Experiment	0.907	0.302	0.802	0.779
ISIS-CFD-IWG	0.939	0.289	0.887	0.758
(Li et al. (2019b), $N_{Cell} = 2.4M$)	(3.55%)	(-4.24%)	(10.6%)	(-2.66%)
SWENSE+VOF w/o coupling	0.921	0.313	0.817	0.765
(Li et al. (2019b), $N_{Cell} = 0.72M$)	(1.53%)	(3.48%)	(1.84%)	(-1.70%)
SWENSE+LS w/o coupling	0.952	0.360	0.877	0.857
(Present study, $N_{Cell} = 0.47M$)	(5.02%)	(19.08%)	(9.27%)	(10.01%)
SWENSE+LS with coupling	0.926	0.314	0.774	0.818
(Present study, $N_{Cell} = 0.47M$)	(2.17%)	(3.89%)	(-3.56%)	(5.04%)

Computational cost

The computational times spent for the simulations are summarized in Table 7.10. The buoy model in regular waves is simulated for 15 wave periods $t \in [0, 15T]$. The same number of processors are used for the simulations.

The computational time is increased by 80.4% when the two-way coupling is considered. The increased percentage of computational time is similar to the increased percentage of the benchmark test on the vertical circular cylinder. In the previous benchmark test, the computational time increases by 84% with viscous solver based on SWENSE and LS interface modeling.

Table 7.10. Computational cost for the simulation of CALM buoy in regular waves.

Case	Computational time
SWENSE+LS without coupling	129,394s
SWENSE+LS with coupling	233,397s (1.804)

7.3.3 Irregular waves

Numerical setup

The computational mesh of viscous flow model is shown in figure 7.21. Relaxation zone is defined in far-field region of computational domain, as colored grey in figure 7.21a. The computational mesh is refined near to the buoy model. The side view near to the buoy model is shown in figure 7.21b. The boundary faces of the buoy model is shown in 7.21c.

The computational domain of viscous flow model has a length $a_{skirt} + 1.92\lambda_p$ where λ_p is a wavelength of peak wave period of wave spectrum in Table 7.6. Length of relaxation zone is $L_{relax} = 1.5\lambda_p$.

When the two-way coupling is considered, the matching surface has a radius of $a = 2.5a_{skirt}$. The information of interpolation grid for Poincaré's velocity representation is summarized in Table 7.6. Distance from the matching surface to the relaxation zone is $d_{couple} = 1.823m$. The number of Fourier and Laguerre modes used for Poincaré's velocity representation are $N_{fourier} = 6$ and $N_{laguerre} = 3$, respectively.

Numerical simulation starts at the simulation time $t = 25T$ to observe extreme event. The irregular waves in computational domain of viscous flow is generated by using the reconstruction procedure in section 3.2.4.

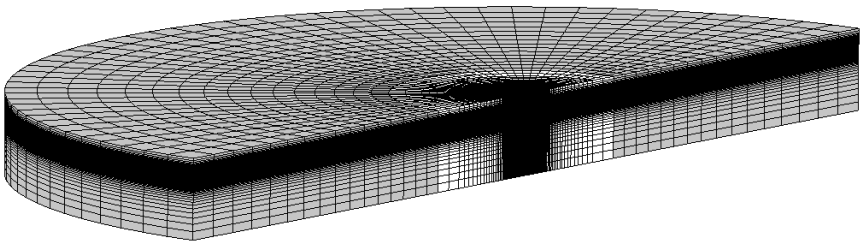

(a) Global view

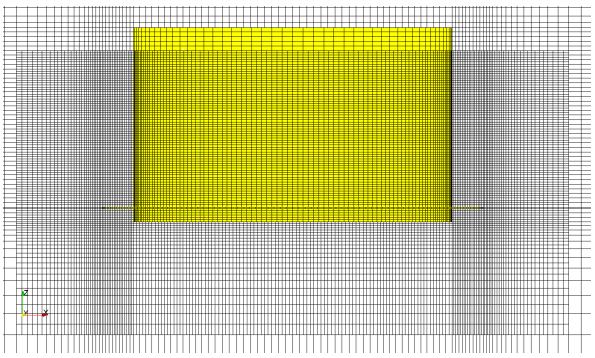

(b) Side view

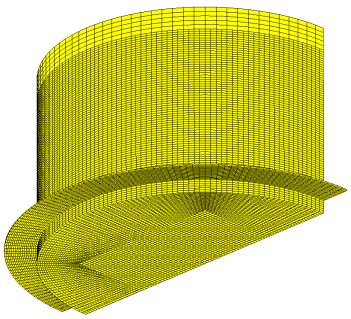

(c) Discretized boundary faces on buoy surface

Figure 7.21. Computational mesh of viscous flow model for the buoy model in irregular waves.

Table 7.11. Computational domain of the buoy in irregular waves.

Item	Value	Remarks
L_{CFD}	12.5664 m	$a_{skirt} + 1.92\lambda_p$
L_{relax}	9.368 m	$1.5\lambda_p$
L_{pure}	3.198 m	$a_{skirt} + 0.42\lambda_p$
N_{cell}	644,016	-
a	1.375 m	$2.5a_{skirt}$
Interpolation grid	$r \in [3.0m, 13.0m]$, $z \in [-1.6m, 0.6m]$	Cover whole relaxation zone.
$N^r_{\text{Poincaré}}$ and $N^\theta_{\text{Poincaré}}$	80 and 128	-
$N^{z1}_{\text{Poincaré}}$ and $N^{z2}_{\text{Poincaré}}$	300 and 100	-
$r^{z1}_{\text{Poincaré}}$ and $r^{z2}_{\text{Poincaré}}$	3 and 3	-
d_{couple}	1.823 m	$0.42\lambda_p - 1.5a_{skirt}$

Wave fields

Figure 7.22 shows total wave elevation measured at the positions of wave gauges in simulations and experiment. The wave elevations calculated by simulations have small differences with respect to the application of two-way coupling. The wavelength of peak wave period is relatively longer than the size of the buoy model. Therefore the complementary waves generated by the buoy model is small. The wave elevations at the positions of wave gauges have small differences because the complementary waves are small.

Total wave elevations obtained from simulations are following the behaviour of wave elevation measured in the experiments. The time series of wave elevation near to the time of the extreme event ($t \approx 31.2T$) are magnified on the right. The wave elevations are globally similar to the wave elevations measured in the experiment, but the differences are shown.

The differences between simulations and experiment can be listed as

- The incident waves simulated by HOS-NWT model have small discrepancies with the incident waves generated in the experiments.
- Transfer function of wavemaker in HOS simulation is based on linear theory and minor compensation is applied for second order component.
- Wave reflections exist at the wavemaker and absorbing beach in the wave tank. HOS-NWT model also uses a numerical beach model to absorb propagating waves. Wave reflections both in experiment and simulation may give the difference, especially when the size of the wave tank is limited. Experiment on the irregular waves needs a long measurement time. Therefore the wave reflections exist in the experiment.

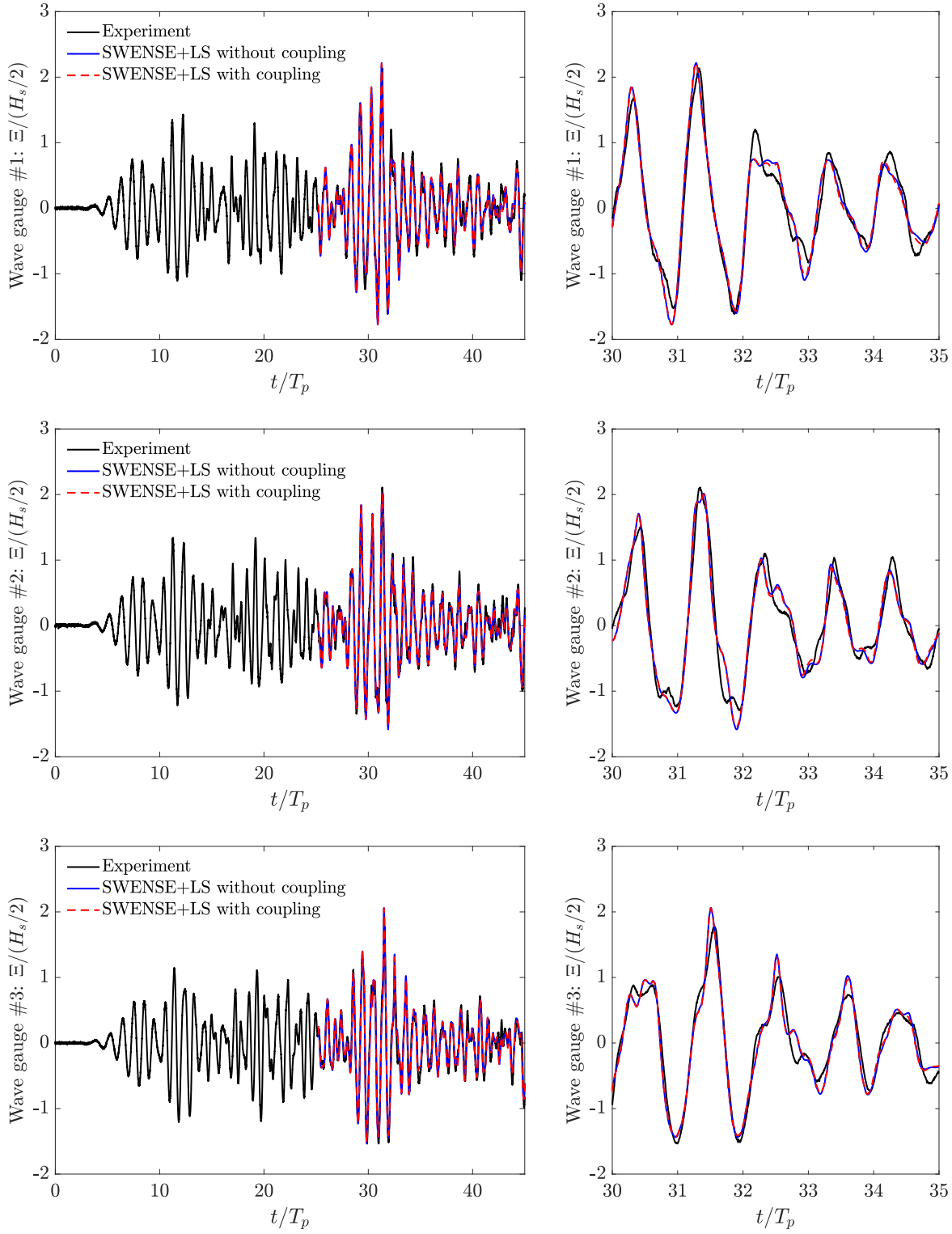

Figure 7.22. Wave elevations measured from wave gauges for the buoy model in irregular waves.

Forces acting on the buoy model

Figure 7.23 shows the horizontal and vertical forces acting on the buoy model. The force time series obtained from simulations are globally following the behaviours of experimental measurements. Forces near to the time of the extreme event are magnified in the sub-figures located at the right. When the two-way coupling is considered, the force time-series are slightly different from the results of the simulation without two-way coupling after the extreme event. Nevertheless, the difference exists after the extreme event. The force time series obtained from both simulation are similar. It is understood that the generated complementary waves are relatively small. They show similar behavior in global simulation time.

The main difference between simulation and experiments come from incident waves.

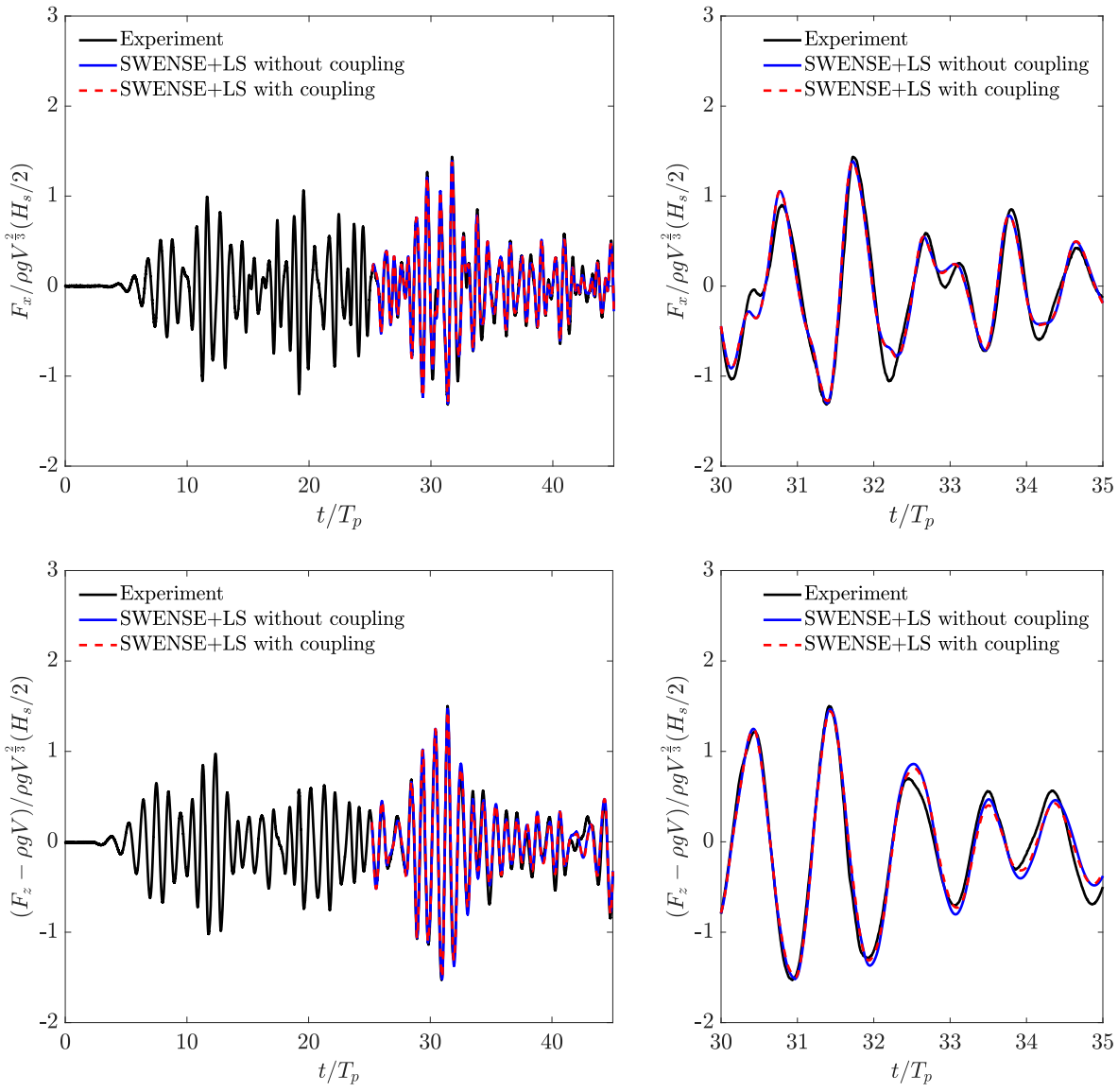

Figure 7.23. Horizontal and vertical forces acting on buoy model in regular waves

Computational cost

Computational times for simulating the buoy model in irregular waves are summarized in Table 7.12. The number of processors, $N_{proc} = 22$, is used for simulations. When the two-way coupling is applied, the computational time is increased by 48.5%.

Table 7.12. Computational cost for the simulation of CALM buoy in irregular waves.

Case	Computational time
SWENSE+LS without coupling	202,972s
SWENSE+LS with coupling	301,424s (1.485)

7.3.4 Summary of benchmark test 2

A CALM buoy model in regular and irregular waves is simulated by considering the two-way coupling between potential and viscous flows. The SWENSE and LS interface modeling is used for viscous flow model and Poincaré's velocity representation based on linear theory is used for the potential flow model.

When the two-way coupling is applied the first harmonics of horizontal and vertical forces acting on the buoy model show better results than the simulation without considering two-way coupling. The second-harmonic and horizontal mean drift forces obtained by considering two-way coupling have smaller differences than the simulation without two-way coupling.

The complementary waves generated due to the existence of structure is small, the two-way coupling affects small on the wave elevations and forces acting on the structure.

The computational costs are increased by 80% for the simulation of structure in the regular wave, and 49% for the simulation of structure in the irregular wave.

7.4 Closure

The computational algorithm solving a problem of wave-structure interaction by considering the two-way coupling between potential and viscous flow models has been introduced.

Fully nonlinear potential flow models compute the flow quantities related to incident waves. The stream function theory is used for regular wave. HOS wave model is used for irregular waves. The reconstruction based on cubic-spline interpolation is used to generate irregular waves in the viscous flow model.

The complementary waves in the far-field region are modeled by Poincaré's velocity representation based on linear potential theory. The complementary fluid velocity and wave elevations on the matching surface are obtained from the viscous flow model to update the complementary wave field in the relaxation zone.

The viscous flow model based on SWENSE with LS function for interface modeling calculates the complementary waves in the vicinity of a structure. The complementary fluid velocity and

LS function are relaxed to the corresponding target quantities calculated by Poincaré's velocity representation in the relaxation zone defined in the region of far-field.

The benchmark test on the bottom-mounted vertical circular cylinder was conducted. Two viscous flow models and two-way coupling are considered. Another viscous flow model is based on Navier-Stokes equations and VOF interface modeling. The wave fields computed by considering the two-way coupling show that the diffracted waves are going out in the relaxation zone that is shown in the calculation with a large computational domain.

Harmonic components of force acting on the vertical circular cylinder are compared. When the two-way coupling is applied, the errors of first- and second-order forces are reduced. The distribution of linear wave elevation along the waterline contributes mainly on the second-order forces. The complementary waves are well treated in the relaxation zones by linear potential flow theory. Therefore the errors of second-order forces can be reduced.

However, the third-harmonics obtained by considering two-way coupling are poor than the case without considering two-way coupling. The potential flow model for complementary flows based on linear theory may not appropriate to obtain the third-order components.

Finally, the benchmark test on the CALM buoy model in regular and irregular waves are conducted. In the regular wave test, the errors of wave elevation and forces are reduced when the two-way coupling is applied. Notably, the horizontal mean drift force shows a good result. In the irregular wave test, the generated complementary waves by buoy model are small. The two-way coupling has little effects on the numerical results. The incident wave model in numerical simulation gives the main difference between experiment and numerical simulation.

The computational cost increases when the two-way coupling is applied. When the viscous flow model based on SWENSE with LS function for interface modeling is used, the computational times are increased about 80% for the case of regular wave and 40% for the case of irregular waves. The computational time increases 56% for the case of regular wave when the viscous flow model based on Navier-Stokes with VOF interface modeling is considered.

8 Conclusion and perspectives

In the present work a numerical model is developped to solve the wave-structure interaction problem by considering a two-way coupling between potential and viscous flow models, the latter being considered only in the vicinity of the body.

Flow quantities are decomposed into incident and complementary parts. In the functional decomposition used, the incident waves are computed without considering the structure and once it is known only the complementary flow need to be solved both in the potential and viscous flow models. The potential flow models for nonlinear incident waves is detailed.

A domain decomposition strategy is applied for the complementary flow. In the vicinity of structure the viscous flow model is based on a two-phase Spectral Wave Explicit Navier-Stokes Equation (SWENSE) method, with a Level-Set function introduced for interface modeling. In the far-field, the complementary flow is calculated by using a linear potential flow model based on Poincaré's velocity representation. This is done with new theoretical developments with respect to the existing literature. The complementary fluid velocity and wave elevation are used to couple potential and viscous flow models. The matching surface for potential flow model and the relaxation scheme for viscous flow model are applied to update each flow solver.

During the PhD various software package were updated or developped for the broad subject of numerical computations about wave structure interaction.

- **Grid2Grid** (newly developped from exisiting package): Fast library for reconstrusting HOS flow field in CFD grid (Choi et al., 2018)
- **POIVRE** (newly developped): Library for calculating the complementary flow based on the Poincaré's velocity representation
- **foamStar** (updated): Multiphase flow model based on Navier-Stokes and VOF
- **foamStarSWENSE** (Level-Set version is newly introduced): Multiphase flow model based on SWENSE and LS function

On each separated subject, improvements have been documented and quality results were achieved. However in the final applications involving functional and domain decompositions with a 2-way coupling approach, the complexity of the algorithm is increased and it is still to be understood how efficient this will be in practical case.

8.1 Summary

8.1.1 Literature survey on the coupling methodology in a marine application

Literature survey on potential and viscous flow models in marine application is proposed. A focus is given on the coupling between potential and viscous flows. One- and two-way couplings are distinguished. The methodology of coupling are categorized into Functional Decomposition (FD) and Domain Decomposition (DD). Associated research on coupling is explained by way of coupling and coupling methodology.

8.1.2 Preliminary study on the coupling of potential and viscous flows

The preliminary study on the two-way coupling was conducted to investigate the feasibility of coupling between potential and viscous flow models. OpenFOAM based multi-phase viscous flow solver is used. The viscous flow model is based on the Navier-Stokes equations and the Volume Of Fluid (VOF) method for interface modeling. The parametric tests on the viscous flow model were conducted to set the proper parameters for propagating waves.

The benchmark tests are devised by using multiple outlet conditions. The outlets considered in the present study are the *stretched mesh*, *increased viscosity in the outlet*, *linear momentum source*, and *relaxation schemes with different target flows*. The relaxation scheme blends the viscous flows with the target flows in the relaxation zone. The target flows for propagating waves are *no waves*, *incident wave* and *modified incident wave*. The modified waves are an adaptation of incident waves by measuring the wave elevation in front of the outlet.

The benchmark tests were carried out for propagating waves in numerical wave tank (NWT) and a swaying 2D Lewis form. The results show that the *relaxation to the propagating waves* in the outlet zone gives good results compared to others. The size of the computational domain and simulation time both can be reduced when the two-way coupling is applied. An efficient potential flow model with good relaxation schemes are necessary for two-way coupling.

8.1.3 Potential flow: Incident waves

The nonlinear incident wave models on the regular and irregular waves are summarized. The stream function theory for regular waves (Rienecker and Fenton, 1981) and HOS wave models for irregular waves and waves in NWT (Ducrozet et al., 2007, 2012) are briefly reviewed.

The reconstruction procedure of nonlinear waves simulated by HOS wave model is proposed in the present study. B-spline interpolation on HOS grid is used to compute nonlinear waves at the arbitrary space and time. The generation of nonlinear HOS waves in viscous flow solver is validated with numerical simulation for various HOS wave models.

The nonlinear irregular waves corresponding to the 1000 year return period waves in the Gulf of Mexico (GOM) are regenerated in viscous flow solver. The simple wave breaking model is used to capture the extreme event during HOS simulation. The viscous flow model is used to simulate the extreme event with limited computational domain and simulation time. The simulation results show good agreements with the results of HOS simulation and experiments.

8.1.4 Potential flow: Complementary waves

A new Poincaré's velocity representation for unsteady free surface flow in deep water is proposed based on linear potential theory. The contribution of dipoles in the Boundary Integral Equation (BIE) is replaced by an equivalent source contribution with tangential velocity on the boundary surface. The complementary fluid velocity at field point can be obtained by the distribution of

fluid velocity on the matching surface and wave elevation on the waterline of matching surface. It is proved that two expressions of the time-domain Green function for deep water in velocity representation are the solutions of Clément's 4-th order Ordinary Differential Equation(ODE) (Clément, 1998). The computational algorithm based on time-marching Frobenius method proposed by Chuang et al. (2007) is used to calculate the time-domain Green function. Proposed velocity representation can be applied for the arbitrary matching surface with a heaving hemisphere. However, the singular behaviour is observed when the field point moves towards the mean free surface due to diverging behavior of time-domain Green functions.

A circular cylindrical matching surface is introduced to remedy the singular behavior. Coordinates transformation from Cartesian to circular cylindrical coordinates are applied to the velocity components and Green function. A pseudo-spectral method using the Fourier-Laguerre and Fourier series is applied. Fluid velocity at the field points is expressed by a combination of Fourier and Fourier-Laguerre coefficients and elementary functions. The elementary functions are the resultants of surface or line integral of the Green function with modal function. Two numerical algorithms evaluating the elementary functions are proposed. Benchmark tests validate the velocity representation with the circular cylindrical matching surface on the heaving hemisphere and wave diffraction by a vertical circular cylinder.

8.1.5 Viscous flow: Multi-phase SWENSE with Level-set

The methodology of spectral wave explicit Navier-Stokes equations (SWENSE) is applied for the multi-phase flow with Level-set interface modeling. The method of SWENSE for multi-phase flows have been studied by Vukčević (2016) and Li (2018). Vukčević (2016) applied the functional decomposition on the fluid velocity and LS function to reconstruct the governing equations with respect to complementary flows. However, the terms corresponding to the Euler equation are saved. He used Ghost Fluid Method (GFM) to solve the multi-phase flow problem by considering the pressure jump condition on the interface. Li (2018) introduced an extended mixture pressure up to air zone to cancel the terms related to the Euler equation. He presented many versions of SWENSE for multi-phase flow with a method of Volume Of Fluid (VOF) for interface modeling.

In the present study, the works done by Vukčević (2016) and Li (2018) are combined. The Navier-Stokes equations are reformulated into SWENSE by using the extended mixture pressure proposed by Li (2018). The interface between two fluids is modeled by LS function. Functional decomposition is applied to the LS function (Vukčević, 2016). The original LS function transport equation with a simple re-distancing the LS function is used instead of using the LS function equation in Vukčević (2016). The numerical discretization by GFM is applied to solve the multiphase flow problem with a pressure jump condition (Vukčević, 2016).

The benchmark tests ware conducted to validate the viscous flow model. The viscous flow model gives good results for propagating waves in Numerical Wave Tank (NWT) compared to other viscous flow models. Nevertheless, a small loss of mass is observed when the coarse mesh and large time difference are used for simulation. The mass loss is reduced as the mesh and time difference are refined.

The wave diffraction by a vertical circular cylinder is considered for second benchmark test (Huseby and Grue, 2000). The proposed viscous flow model gives good results on the force-harmonics when coarse computational meshes are used.

8.1.6 Two-way coupling of potential and viscous flows

A segregated computational algorithm is suggested to solve the problem of wave-structure interaction by considering the two-way coupling between potential and viscous flow models. The domain and functional decompositions are applied for coupling methodology.

Functional decomposition (FD) is applied to decompose the flow quantities of potential and viscous flow models into the incident and complementary parts. The incident waves are calculated by nonlinear potential flow model. Poincaré's velocity representation based on linear potential theory is used to calculate the complementary waves in the far-field. The SWENSE method is applied in a viscous flow model to solve the complementary flows in the vicinity of the structure.

Domain decomposition (DD) is used to couple complementary flows calculated by potential and viscous flow models. The complementary fluid velocity and wave elevation on the matching surface are obtained from the viscous flow model. The obtained flows are used to update the complementary flows in the relaxation zone by using Poincaré's velocity representation. In the relaxation zone, the complementary fluid velocity and LS function of viscous flow model are relaxed to the target values which are updated by using potential flow model.

The coupling strategy is applied for a vertical circular cylinder in regular waves and the CALM buoy model in waves. Simulations with two-way coupling between potential and viscous flow models give better results on the wave elevations, first-order and second-order forces acting on the structure. The computational time increases when the two-way coupling is applied.

8.2 Conclusion

Two-way coupling between potential and viscous flow models are proposed in the present study. The potential flow models for the incident and complementary flows and the viscous flow model based on SWENSE and LS interface modeling are explained. Benchmark tests validate each flow models and show good agreements. It is assumed that the wave elevation and fluid velocity across the flow models are continuous. To couple the potential and viscous flow models, the methodologies of functional decomposition (FD) and domain decomposition (DD) are applied for potential and viscous flows.

Functional decomposition (FD) is applied for potential and viscous flow models. The functional quantities of the total flow into the incident and complementary parts. The nonlinear potential flow for incident waves is assumed to be available in a whole fluid domain and satisfies the Euler equations. The linear potential flow model based on Poincaré's velocity representation for complementary flow is proposed. The availability of nonlinear incident waves leads to use of a

Spectral Wave Explicit Navier-Stokes Equations (SWENSE) method as the viscous flow model only to consider the complementary flow.

Domain decomposition (DD) is used to decompose the computational domain. The nonlinear incident waves from the nonlinear potential flow model are available in the whole computational domain. It makes us divide the computational domain of potential and viscous flow models only for complementary waves. In the vicinity of structure, the viscous flow model based on SWENSE is used. The linear potential flow model for complementary flow is applied in the far-field region.

To couple potential and viscous flow models, the continuous wave elevation and fluid velocity across the computational domain are assumed. In the matching surface, the complementary fluid velocity and wave elevation are used to update the complementary flow field in the far-field region by using Poincaré's velocity representation. In the far-field, the relaxation scheme is used to blend the computed complementary flow with the target flow calculated from Poincaré's velocity representation.

A segregated algorithm solving the wave-structure problem by considering two-way coupling is presented. The benchmark tests are carried out for a bottom-mounted vertical circular cylinder in regular waves and a fixed buoy model in regular and irregular waves. Results of the benchmark tests show that the two-way coupling can improve the wave elevations and the forces acting on the structure. Especially, the horizontal mean drift forces acting on the structure are enhanced significantly when the two-way coupling is adopted. However, the two-way coupling gives poor results on the third-harmonics of forces. When the complementary waves are small, the two-way coupling does not affect the results. When the two-way coupling is applied, the computational costs are increased by 80% for regular wave simulation and 40% for irregular wave simulation.

8.3 Proposals for future work

8.3.1 Poincaré's velocity representation for unsteady free surface flow with forward speed

Poincaré's velocity representation in a marine application has been studied for steady and time-harmonic problems by Noblesse et al. (1997); Noblesse (2001); Noblesse and Yang (2004). The velocity representation is extended to the unsteady free surface problem without forward speed in the present study. The velocity representation for unsteady wave-structure interaction problem with forward speed may be derived with Neumann-Kelvin free surface boundary condition. It can be used to couple viscous flow model for evaluating the added resistance of ship in waves.

8.3.2 Coupling between linear potential flow model and other flow models

The proposed velocity representation may be used to couple with the viscous flow model based on SWENSE and VOF interface modeling by Li (2018). The elementary function introduced in the present study can be applicable for boundary integral equation. The flow model used to solve

wave-structure interaction in the vicinity of structure can be replaced by nonlinear potential flow models such as Rankine Panel Method (RPM) or Finite Element Method (FEM).

8.3.3 Evaluation of mean drift forces acting on blunt body

Two-way coupling between potential and viscous flow models show good results on the horizontal mean drift forces acting on the structure. The mean drift forces on the blunt body such as shuttle tanker and FPSO are significant and important to design a mooring system. The proposed two-way coupling strategy can enhance the simulation based on the viscous flow model to assess mean drift forces, especially for the blunt body in beam sea condition.

References

Abramowitz, M. and Stegun, I. A. (1965). *Handbook of mathematical functions: With Formulas, Graphs, and Mathematical Tables*. Applied mathematics series. Dover Publications.

Airy, G. B. (1845). Tides and waves. In *Encyclopaedia Metropolitana, Tom. V*. William Clowes and Sons.

Arfken, G. B., Weber, H. J., and Harris, F. E. (1995). *Mathematical methods for physicists (Seventh Edition)*. Academic Press.

Babarit, A. and Delhommeau, G. (2015). Theoretical and numerical aspects of the open source BEM solver NEMOH. In *Proc. of the 11th European Wave and Tidal Energy Conference (EWTEC2015), Nantes, France*.

Bai, K. J. (1981). A localized finite-element method for three dimensional ship motion problems. In *The 3rd Int. C. on Numerical Ship Hydrodynamics, Paris, France*.

Bai, K. J., Kim, J. W., and Kim, Y. H. (1989). Numerical computations for a nonlinear free surface flow problem. In *Th 5th Int. C. on Numerical Ship Hydrodynamics, Hiroshima, Japan*.

Bai, K. J. and Yeung, R. W. (1974). Numerical solutions to free surface flow problems. In *The 10th Symp. on Naval Hydrodynamics*. Office of Naval Research, MIT.

Barthelemy, X., Banner, M. L., Peirson, W. L., Fedele, F., Allis, M., and Dias, F. (2018). On a unified breaking onset threshold for gravity waves in deep and intermediate depth water. *Journal of Fluid Mechanics*, 841:463–488.

Beck, R. F. and Liapis, S. (1987). Transient motions of floating bodies at zero forward speed. *Journal of Ship Research*, 31(3):164–176.

Bingham, H. B. (1994). *Simulating ship motions in the time domain*. PhD thesis, Massachusetts Institute of Technology(MIT).

Bingham, H. B. (2016). A note on the relative efficiency of methods for computing the transient free-surface Green function. *Ocean Engineering*, 120:15 – 20.

Blackemore, M., Evans, G. A., and Hyslop, J. (1976). Comparison of some methods for evaluating infinite range oscillatory integrals. *Journal of Computational Physics*, 22(3):352–376.

Boettinger, W., Warren, J., Beckermann, C., and Karma, A. (2002). Phase-field simulation of solidification 1. *Annu. Rev. Mater. Res*, 32:163–94.

Bonnefoy, F., Ducrozet, G., Le Touzé, D., and Ferrant, P. (2009). Time-domain simulation of nonlinear water waves using spectral methods. In *Advances in Numerical Simulation of Nonlinear Water Waves*. World Scientific.

Boris, J. P. and Book, D. L. (1973). Flux-corrected transport. I. SHASTA, a fluid transport algorithm that works. *Journal of Computational Physics*, 11(1):38 – 69.

Brard, R. (1948). Introduction à l'étude théorique du tangage en marche. *Bulletin de l'ATMA*, pages 455–471.

Brown, J. W. and Churchill, R. V. (2004). *Complex variables and applications*. Brown-Churchill series. McGraw-Hill Higher Education.

Campana, E. F., Di Mascio, A., Esposito, P. G., and Lalli, F. (1992). Viscous-inviscid coupling in ship hydrodynamics. In *11th Australasian Fluid Mech. Conf., Australia*.

Campana, E. F., Di Mascio, A., Esposito, P. G., and Lalli, F. (1995). Viscous-inviscid coupling in free surface ship flows. *International Journal for Numerical Methods in Fluids*, 21(9):699–722.

Carmigniani, R. A. and Violeau, D. (2018). Optimal sponge layer for water waves numerical models. *Ocean Engineering*, 163:169 – 182.

Carrica, P. M., Wilson, R. V., and Stern, F. (2007). An unsteady single-phase level set method for viscous free surface flows. *International Journal for Numerical Methods in Fluids*, 53(2):229–256.

Chang, Y. C., Hou, T. Y., Merriman, B., and Osher, S. (1996). A level set formulation of Eulerian interface capturing methods for incompressible fluid flows. *Journal of Computational Physics*, 124(2):449 – 464.

Chau, F. P. and Taylor, R. E. (1992). Second-order wave diffraction by a vertical cylinder. *Journal of Fluid Mechanics*, 240:571–599.

Chen, H.-C., Yu, K., and Chen, S.-Y. (2005). Simulation of wave runup around offshore structures by a chimera domain decomposition approach. In *Sixth Int. C. on Civil Engineering in the Oceans*, pages 267–280.

Chen, X. and Li, R. (2019). Reformulation of wavenumber integrals describing transient waves. *Journal of Engineering Mathematics*, 115(1):121–140.

Chen, X. B. (1991). Free surface Green function and its approximation by polynomial series. *In Bureau Veritas' research report No 641 DTO/XC*.

Chen, X. B. (2004). Hydrodynamics in offshore and naval applications - Part I. In *6th Intl. Conf. HydroDynamics*.

Chen, Y. and Maki, K. J. (2017). A velocity decomposition approach for three-dimensional unsteady flow. *European Journal of Mechanics - B/Fluids*, 62:94 – 108.

Choi, Y., Gouin, M., Ducrozet, G., Bouscasse, B., and Ferrant, P. (2018). Grid2Grid: HOS wrapper program for CFD solvers. *ArXiv e-prints*.

Chuang, J. M., Qui, W., and Peng, H. (2007). On the evaluation of time-domain Green function. *Ocean Engineering*, 34(7):962–969.

Clément, A. H. (1998). An ordinary differential equation for the Green function of time-domain free surface hydrodynamics. *Journal of Engineering Mathematics*, 33(2):201–217.

Clément, A. H. (2013). A second order ordinary differential equation for the frequency domain Green function. In *28th International workshop on water waves and floating bodies (IWWWFB2013), Marseille, France.*

Colicchio, G., Greco, M., and Faltinsen, O. M. (2006). A BEM-level set domain-decomposition strategy for non-linear and fragmented interfacial flows. *International Journal for Numerical Methods in Engineering*, 67(10):1385–1419.

Corana, A., Marchesi, M., Martini, C., and Ridella, S. (1987). Minimizing multimodal functions of continuous variables with the "Simulated Annealing" algorithm. *ACM Trans. Math. Softw.*, 13(3):262–280.

Damián, S. M. (2013). *An extended mixture model for the simultaneous treatment of short and long scale interfaces.* PhD thesis, Universidad Nacional del Litoral.

Davis, P. J. and Rabinowitz, P. (1988). *Methods of Numerical Integration.* Academic Press, 2nd edition.

Dawson, C. W. (1977). A practical computer method for solving ship-wave problems. In *2nd Int. Conf. Numerical Ship Hydrodynamics, Berkely, USA.*

De, S. C. (1955). Contributions to the theory of Stokes waves. *Mathematical Proceedings of the Cambridge Philosophical Society*, 51(4):719–736.

De Boor, C. (1978). *A practical guide to splines.* Springer-Verlag, New York.

Dean, R. and Dalrymple, R. (1991). *Water wave mechanics for engineers and scientists.* Advanced series on ocean engineering. World Scientific.

Delhommeau, G. (1989). Amélioration des performances des codes de calcul de diffraction-radiation au premier ordre. In *Proc. Deuxièmes Journées de l'Hydrodynamique*, pages 69–88. Ecole Nationale Supérieure de Mécanique de Nantes.

Desjardins, O., Moureau, V., and Pitsch, H. (2008). An accurate conservative level set/ghost fluid method for simulating turbulent atomization. *Journal of Computational Physics*, 227(18):8395 – 8416.

Di Mascio, A., Broglia, R., and Muscari, R. (2007). On the application of the single-phase level set method to naval hydrodynamic flows. *Computers & Fluids*, 36(5):868 – 886.

Dommermuth, D. G. and Yue, D. K. P. (1987). A high-order spectral method for the study of nonlinear gravity waves. *J . Fluid Mech*, 184:267–288.

Ducrozet, G., Bonnefoy, F., Le Touzé, D., and Ferrant, P. (2007). 3-D HOS simulations of extreme waves in open seas. *Natural Hazards and Earth System Sciences*, 7(1):109–122.

Ducrozet, G., Bonnefoy, F., Le Touzé, D., and Ferrant, P. (2012). A modified high-order spectral method for wavemaker modeling in a numerical wave tank. *European Journal of Mechanics - B/Fluids*, 34:19 – 34.

Ducrozet, G., Bonnefoy, F., Le Touzé, D., and Ferrant, P. (2016). HOS-ocean: Open-source solver for nonlinear waves in open ocean based on high-order spectral method. *Computer Physics Communications*, 203:245 – 254.

Ducrozet, G., Bouscasse, B., Gouin, M., Ferrant, P., and Bonnefoy, F. (2019). CN-Stream: Open-source library for nonlinear regular waves using stream function theory. *arXiv:1901.10577 [physics.flu-dyn]*.

Eça, L. and Hoekstra, M. (2014). A procedure for the estimation of the numerical uncertainty of CFD calculations based on grid refinement studies. *J. of Comp. Physics*, 262:104 – 130.

Edmund, D. O. (2012). *A velocity decomposition method for efficient numerical computation of steady external flows*. PhD thesis, University of Michigan.

Elhay, S. and Kautsky, J. (1987). Algorithm 655: IQPACK, FORTRAN subroutines for the weights of interpolatory quadrature. *ACM Transactions on Mathematical Software*, 13(4):399–415.

Engsig-Karup, A. P. (2006). *Unstructured nodal DG-FEM solution of high-order Boussinesq-type equations*. PhD thesis, Technical University of Denmark, Kgs. Lyngby.

Engsig-Karup, A. P., Bingham, H. B., and Lindberg, O. (2009). An efficient flexible-order model for 3D nonlinear water waves. *Journal of Computational Physics*, 228(6):2100 – 2118.

Fenton, J. D. (1988). The numerical solution of steady water wave problems. *Computers and Geosciences*, 14(3):357–368.

Ferrant, P. (1998). Fully nonlinear interactions of long-crested wave packets with a three dimensional body. In *Proc. 22nd ONR symposium on Naval Hydrodynamics*, pages 403–415.

Ferrant, P., Gentaz, L., Alessandrini, B., and Le Touzé, D. (2003). A potential/RANSE approach for regular water wave diffraction about 2-D structures. *Ship Technology Research*, 50(4):165–171.

Fredriksen, A. G. (2015). *A numerical and experimental study of a two-dimensional body with moonpool in waves and current*. PhD thesis, Norwegian University of Science and Technology (NTNU).

Frigo, M. and Johnson, S. G. (2005). The design and implementation of FFTW3. *Proceedings of the IEEE*, 93(2):216–231. Special issue on "Program Generation, Optimization, and Platform Adaptation".

Fuhrman, D. R. (2004). *Numerical solutions of Boussinesq equations for fully nonlinear and extremely dispersive water waves*. PhD thesis, Technical University of Denmark, Kgs. Lyngby.

Gatin, I., Vukčević, V., and Jasak, H. (2017). A framework for efficient irregular wave simulations using Higher Order Spectral method coupled with viscous two phase model. *Journal of Ocean Engineering and Science*, 2(4):253 – 267.

Gentaz, L., Luquet, R., Alessandrini, B., and Ferrant, P. (2004). Numerical simulation of the 3D viscous flow around a vertical cylinder in non-linear waves using an explicit incident wave model. In *23rd Int. C. on Offshore Mechanics and Arctic Eng., OMAE2004-51098*.

Goda, Y. (1983). Analysis of wave grouping and spectra of long-travelled swell. Technical report, Rep. Port and Harbour Tech. Res. Inst.

Goda, Y. (1999). A comparative review on the functional forms of directional wave spectrum. *Coastal Engineering Journal*, 41(01):1–20.

Gradshteyn, I. S. and Ryzhik, I. M. (2007). *Table of Integrals, Series, and Products*. Elsevier Science, 7th edition.

Greco, M., Colicchio, G., Lugni, C., and Faltinsen, O. (2013). 3D domain decomposition for violent wave-ship interactions. *International Journal for Numerical Methods in Engineering*, 95(8):661–684.

Guillerm, P. E. (2001). *Application de la méthode de Fourier-Kochin au problème du couplage fluide visqueux-fluide parfait*. PhD thesis, Ecole Centrale de Nantes.

Hamada, T. (1965). The secondary interactions of surface waves. Technical report, Rep. Port and Harbour Tech. Res. Inst.

Hamilton, J. A. and Yeung, R. W. (2011). Viscous and inviscid matching of three-dimensional free-surface flows utilizing shell functions. *Journal of Engineering Mathematics*, 70(1):43–66.

Harlow, F. H. and Welch, J. E. (1965). Numerical calculation of time-dependent viscous incompressible flow of fluid with free surface. *The Physics of Fluids*, 8(12):2182–2189.

Hasselmann, K., Barnett, T., Bouws, E., Carlson, H., Cartwright, D., Enke, K., Ewing, J., Gienapp, H., Hasselmann, D., Kruseman, P., Meerburg, A., Mller, P., Olbers, D. J., Richter, K., Sell, W., and H., W. (1973). Measurements of wind-wave growth and swell decay during the joint north sea wave project (JONSWAP). *Ergnzungsheft zur Deutschen Hydrographischen Zeitschrift Reihe*, 8(12).

Hirt, C. W. and Nichols, B. D. (1981). Volume of fluid (VOF) method for the dynamics of free boundaries. *Journal of Computational Physics*, 39:201–225.

Hong, S., Kim, J., Cho, S., Choi, Y., and Kim, Y. (2005). Numerical and experimental study on hydrodynamic interaction of side-by-side moored multiple vessels. *Ocean Engineering*, 32(7):783 – 801. Deepwater Mooring Systems; Design, Analysis and Materials.

Huang, J., Carrica, P. M., and Stern, F. (2007). Coupled ghost fluid/two-phase level set method for curvilinear body-fitted grids. *International Journal for Numerical Methods in Fluids*, 55(9):867–897.

Hulme, A. (1982). The wave forces acting on a floating hemisphere undergoing forced periodic oscillations. *Journal of Fluid Mechanics*, 121:443–463.

Hunt, B. (1980). *The mathematical basis and numerical principles of the boundary integral method for incompressible potential flow over 3-D aerodynalic configurations, Numerical methods in applied fluid dynamics*. London and New York, Academic Press.

Huseby, M. and Grue, J. (2000). An experimental investigation of higher-harmonic wave forces on a vertical cylinder. *Journal of Fluid Mechanics*, 414:75–103.

Iafrati, A. and Campana, E. F. (2003). A domain decomposition approach to compute wave breaking (wave-breaking flows). *International Journal for Numerical Methods in Fluids*, 41(4):419–445.

Israeli, M. and Orszag, S. (1981). Approximation of radiation boundary conditions. *J. of Comp. Physics*, 41(1):115–135.

Issa, R. I. (1986). Solution of the implicitly discretised fluid flow equations by operator-splitting. *Journal of Computational Physics*, 62:40–65.

Jacobsen, N. G., Fuhrman, D. R., and Fredsøe, J. (2012). A wave generation toolbox for the open-source CFD library: OpenFoam®. *International Journal for Numerical Methods in Fluids*, 70(9):1073–1088.

Jasak, H. (1996). *Error analysis and estimation for the finite volume method with applications to fluids flows*. PhD thesis, Imperial College.

Joseph, D. D. (2006). Potential flow of viscous fluids: Historical notes. *Int. J. of Multiphase Flow*, 32(3):285 – 310.

Kang, M., Fedkiw, R. P., and Liu, X. D. (2000). A boundary condition capturing method for multiphase incompressible flow. *Journal of Scientific Computing*, 15(3):323–360.

Kashiwagi, M. (2003). *Hydrodynamics of floating body (in Japanese)*. The Japan Society of Naval Architects and Ocean Engineers.

Kim, J., O'Sullivan, J., and Read, A. (2012). Ringing analysis of a vertical cylinder by Euler overlay method. *31st Int. C. on Ocean, Offshore and Arctic Eng.*, pages OMAE2012–44915.

Kim, K., Sirviente, A. I., and Beck, R. F. (2005). The complementary RANS equations for the simulation of viscous flows. *International Journal for Numerical Methods in Fluids*, 48(2):199–229.

Kim, K. T. (2011). Hydroelastic analysis of three dimensional floating structures. Master's thesis, Korea Advanced Institute of Science and Technology (KAIST), Daejeon, Korea.

Kim, M.-H. and Yue, D. K. P. (1989). The complete second-order diffraction solution for an axisymmetric body Part 1. Monochromatic incident waves. *Journal of Fluid Mechanics*, 200:235–264.

Kim, Y., Kim, K.-H., Kim, J.-H., Kim, T., Seo, M.-G., and Kim, Y. (2011). Time-domain analysis of nonlinear motion responses and structural loads on ships and offshore structures: development of WISH programs. *International Journal of Naval Architecture and Ocean Engineering*, 3(1):37–52.

Kraaiennest (2009). Le Méhauté's diagram. `https://commons.wikimedia.org/wiki/File:Water_wave_theories.svg`. [Online; accessed April 30, 2019].

Kring, D. C. (1994). *Time domain ship motions by a three-dimensional Rankine panel method.* PhD thesis, Massachusetts Institute of Technology.

Lamb, H. (1945). *Hydrodynamics.* Dover Books on Physics. Dover publications.

Le Méhauté, B. (1976). *An introduction to hydrodynamics and water waves.* Springer.

Lee, C.-H. (1995). *WAMIT Theory Manual.* Massachusetts Institute of Technology.

Lervåg, K. Y. (2008). *Simulation of two-phase flow with varying surface tension.* PhD thesis, Norwegian University of Science and Technology (NTNU).

Li, R., Chen, X. B., and Duan, W. Y. (2019a). Numerical study on integrals involving the product of Bessel functions and a trigonometric function arising in hydrodynamic problems. submitted.

Li, R. P. and Chen, X. B. (2018). Fast algorithm on the interaction of transient Green function on the cylindrical surface. *8th Green function Seminar.*

Li, Z. (2018). *Two-phase spectral wave explicit Navier-Stokes equations method for wave-structure interactions.* PhD thesis, École Centrale de Nantes.

Li, Z., Deng, G., Queutey, P., Bouscasse, B., Ducrozet, G., Gentaz, L., Le Touzé, D., and Ferrant, P. (2019b). Comparison of wave modeling methods in CFD solvers for ocean engineering applications. *Ocean Engineering*, 188:106237.

Li, Z.-F., Ren, H.-L., Tong, X.-W., and Li, H. (2015). A precise computation method of transient free surface Green function. *Ocean Engineering*, 105:318 – 326.

Liang, H. and Chen, X.-B. (2017). A new multi-domain method based on an analytical control surface for linear and second-order mean drift wave loads on floating bodies. *Journal of Computational Physics*, 347:506 – 532.

Liang, H., Chen, X.-B., and Feng, X. (2018). Wave-making problem by a vertical cylinder:Neumann-Kelvin theory versus Neumann-Michell theory. *The 33th of Int. Workshop on Water Waves and Floating Bodies (IWWWFB33).*

Longuet-Higgins, M. S., Cartwright, D. E., and Smith, N. D. (1963). Observations of the directional spectrum of sea waves using the motions of a floating buoy. In *Ocean Wave Spectra, Proc. Conf., Easton, Md., May 1–4, 1961, Prentice-Hall, N.J., 111–132.*

Lucas, S. K. (1995). Evaluating infinite integrals involving products of Bessel functions of arbitrary order. *Journal of Computational and Applied Mathematics*, 64(3):269–282.

Lucas, S. K. and Stone, H. A. (1995). Evaluating infinite integrals involving Bessel functions of arbitrary order. *Journal of Computational and Applied Mathematics*, 64(3):217–231.

Luquet, R., Alessandrini, B., Ferrant, P., and Gentaz, L. (2003). RANSE analysis of 2D flow about a submerged body using explicit incident wave models. In *NUmerical Towing Tank Symposium (NUTTS Symposium)*.

Lyness, J. (1985). Integrating some infinite oscillating tails. *Journal of Computational and Applied Mathematics*, 12-13:109–117.

Malenica, Š. (1994). *Diffraction de troisième ordre et interaction houle-courant pour un cylindre vertical en profondeur finie*. PhD thesis, Universite Paris VI.

Malenica, Š. and Molin, B. (1995). Third-harmonic wave diffraction by a vertical cylinder. *Journal of Fluid Mechanics*, 302:203–229.

Mayer, S., Garapon, A., and Sørensen, L. S. (1998). A fractional step method for unsteady free-surface flow with applications to non-linear wave dynamics. *Int. J. for Num. Methods in Fluids*, 28:295–315.

McCamy, R. C. and Fuchs, R. A. (1954). Wave forces on piles: A diffraction theory. Tech. Memo No. 69, U.S. Army Corps of Engrs.

Moe, G. (1993). Vertical resonant motions of TLP's(final report). Technical report, NTH Rep. R-1-93.

Monroy, C. (2010). *Simulation numérique de l'interaction houle-structure en fluide visqueux par décomposition fonctionnelle*. PhD thesis, École Centrale de Nantes.

Monroy, C., Ducrozet, G., Bonnefoy, F., Babarit, A., Gentaz, L., and Ferrant, P. (2011). RANS simulations of a calm buoy in regular and irregular seas using the SWENSE method. *International Journal of Offshore and Polar Engineering*, 21.

Monroy, C., Seng, S., and Malenica, Š. (2016). Développements et validation de l'outil CFD OpenFOAM pour le calcul de tenue à la mer. In *15ès journées de l'hydrodynamique*.

Moulkalled, F., Mangani, L., and Darwish, M. (2015). *The finite volume method in computational fluid dynamics*. Springer Publishing Company, Incorporated, 1st edition.

Muzaferija, S. and Peric, M. (1999). Computation of free-surface flows using interface-tracking and interface-capturing methods. In *Nonlinear water wave interaction*. Computational Mechanics Publication.

Nakos, D. E. (1990). *Ship wave patterns and motions by a three dimensional Rankine panel method*. PhD thesis, Massachusetts Institute of Technology.

Nam, B. W. (2015). *A numerical study on berthing problem between two floating bodies in waves.* PhD thesis, Seoul National University.

Newman, J. N. (1985). Algorithms for free-surface Green function. *Journal of Engineering Mathematics*, 19(1):57–67.

Newman, J. N. (1992). Approximation of free-surface Green functions. In Martin, P. and Wickham, G., editors, *Wave asymptotics*. Cambridge University Press.

Noblesse, F. (2001). Velocity representation of free-surface flows and Fourier-Kochin representation of waves. *Applied Ocean Research*, 23:41–52.

Noblesse, F. and Yang, C. (2004). Weakly singular boundary-integral representations of free-surface flows about ships or offshore structures. *Journal of Ship Research*, 48(1):31–44.

Noblesse, F., Yang, C., and Xiao-Bo, C. (1997). Boundary-integral representation of linear free-surface potential flows. *Journal of Ship Research*, 41(1):10–16.

Ochi, M. and Hubble, E. (1976). Six-parameter wave spectra. *Coastal Engineering Proceedings*, 1(15).

Osher, S. and Sethian, J. A. (1988). Fronts propagating with curvature-dependent speed: Algorithms based on Hamilton-Jacobi formulations. *Journal of Computational Physics*, 79(1):12 – 49.

Park, J.-C., Kim, M.-H., and Miyata, H. (1999). Fully non-linear free-surface simulations by a 3D viscous numerical wave tank. *Int. J. for Num. Methods in Fluids*, 29(6):685–703.

Patankar, S. and Spalding, D. (1972). A calculation procedure for heat, mass and momentum transfer in three-dimensional parabolic flows. *International Journal of Heat and Mass Transfer*, 15(10):1787 – 1806.

Paulsen, B. T., Bredmose, H., and Bingham, H. B. (2014). An efficient domain decomposition strategy for wave loads on surface piercing circular cylinders. *Coastal Engineering*, 86:57 – 76.

Pawlowski, J. (1992). Nonlinear theory of ship motion in wave. In *19th Symp. Naval Hydro., Seoul, Korea*.

Perić, R. and Abdel-Maksoud, M. (2015). Assessment of uncertainty due to wave reflections in experiments via numerical flow simulations. In *The Twenty-fifth International Ocean and Polar Engineering Conference*, pages 530–537.

Perić, R. and Abdel-Maksoud, M. (2016). Reliable damping of free-surface waves in numerical simulations. *Ship Tech. Research*, 63(1):1–13.

Perić, R., Vukčević, V., Abdel-Maksoud, M., and Jasak, H. (2018a). absorbing-layer-for-free-surface-waves. `https://github.com/wave-absorbing-layers/absorbing-layer-for-free-surface-waves`.

Perić, R., Vukčević, V., Abdel-Maksoud, M., and Jasak, H. (2018b). Tuning the case-dependent parameters of relaxation zones for flow simulations with strongly reflecting bodies in free-surface waves. *ArXiv e-prints*.

Pierson, W. and Moskowitz, L. A. (1964). Proposed spectral form for fully developed wind seas based on the similarity theory of s. a. kitaigorodskii. *Journal of Geophysical Research*, 69:5181–5190.

Pierson, W., Neumann, G., and James, R. W. (1955). Practical methods for observing and forecasting ocean waves by means of wave spectra and statistics. *U. S. Dept. Commerce. Hydrographic Office Publ.*, 603.

Pinkster, J. A. (1980). *Low frequency second order wave exciting forces on floating structures*. PhD thesis, TU Delft.

Prandtl, L. (1904). über flüssigkeitsbewegung bei sehr kleiner reibung. *Verhandl III, Intern. Math. Kongr. Heidelberg, Auch: Gesammelte Abhandlungen*, 2:484 – 491.

Raven, H. C. (1995). *A solution method for the nonlinear wave resistance problem*. PhD thesis, TU Delft, Delft University of Technology.

Reliquet, G. (2013). *Simulation numérique de l'interaction houle/carène par couplage d'une méthod spectral HOS avec un algorithme de capture d'interface*. PhD thesis, École Centrale de Nantes.

Rienecker, M. M. and Fenton, J. D. (1981). A Fourier approximation method for steady water waves. *Journal of Fluid Mechanics*, 104:119–137.

Roenby, J., Bredmose, H., and Jasak, H. (2016). A computational method for sharp interface advection. *Royal Society Open Science*, 3(11).

Rosemurgy, W. J. (2014). *A velocity decomposition approach for lifting and free-surface flows*. PhD thesis, University of Michigan.

Rousset, J.-M. and Ferrant, P. (2005). Model tests for principia R&D. CTR1-JIP Calm Buoy 2. Technical report, Laboratoire de Mécanique des Fluids de l'Ecole Centrale de Nantes(UMR CNRS 6598).

Rusche, H. (2002). *Computational fluid dynamics of dispersed two-phase flows at high phase fractions*. PhD thesis, Imperial College.

Schwartz, L. (1974). Computer extension and analytic continuation of Stokes' expansion for gravity waves. *Journal of Fluid Mechanics*, 62(3):553–578.

Seiffert, B. R. and Ducrozet, G. (2018). Simulation of breaking waves using the high-order spectral method with laboratory experiments: wave-breaking energy dissipation. *Ocean Dynamics*, 68(1):65–89.

Seiffert, B. R., Ducrozet, G., and Bonnefoy, F. (2017). Simulation of breaking waves using the high-order spectral method with laboratory experiments: Wave-breaking onset. *Ocean Modelling*, 119:94 – 104.

Seng, S. (2012). *Slamming and whipping analysis of ships*. PhD thesis, Technical University of Denmark (DTU), Lyngby.

Shanks, D. (1955). Non-linear transformations of divergent and slowly convergent sequences. *Journal of Mathematics and Physics*, 34(1-4):1–42.

Shao, Y.-L. and Faltinsen, O. M. (2014). A harmonic polynomial cell (HPC) method for 3D Laplace equation with application in marine hydrodynamics. *Journal of Computational Physics*, 274:312 – 332.

Shen, Z. and Wan, D. (2016). An irregular wave generating approach based on naoe-FOAM-SJTU solver. *China Ocean Eng.*, 30(2):177–192.

Sidi, A. (1988). A user-friendly extrapolation method for oscillatory infinite integrals. *Mathematics of Computation*, 51:249–266.

Stokes, G. (1847). On the theory of oscillatory waves. *Transactions of the Cambridge Philosophical Society*, 8:441–455.

Sun, Y. and Beckermann, C. (2007). Sharp interface tracking using the phase-field equation. *Journal of Computational Physics*, 220(2):626 – 653.

Sussman, M., Fatemi, E., Smereka, P., and Osher, S. (1998). An improved level set method for incompressible two-phase flows. *Computers & Fluids*, 27(5):663 – 680.

Sussman, M., Smereka, P., and Osher, S. (1994). A level set approach for computing solutions to incompressible two-phase flow. *Journal of Computational Physics*, 114(1):146 – 159.

Tahara, Y., Stern, F., and Rosen, B. (1992). An interactive approach for calculating ship boundary layers and wakes for nonzero Froude number. *Journal of Computational Physics*, 98(1):33 – 53.

Tasai, F. (1960). Formula for calculating hydrodynamic force on a cylinder heaving in free surface (N-parameter family). Technical Report 31, Research Institute for Applied Mechanics, Kyushu University.

Tasai, F. (1961). Hydrodynamic force and moment produced by swaying and rolling osciilation of cylinders on the free surface. Technical Report 35, Research Institute for Applied Mechanics, Kyushu University.

Telste, J. and Noblesse, F. (1986). Numerical evaluation of the Green function of water-wave radiation and diffraction. *Journal of Ship Research*, 30:69–84.

Tian, Z., Perlin, M., and Choi, W. (2010). Energy dissipation in two-dimensional unsteady plunging breakers and an eddy viscosity model. *Journal of Fluid Mechanics*, 655:217–257.

Tian, Z., Perlin, M., and Choi, W. (2012). An eddy viscosity model for two-dimensional breaking waves and its validation with laboratory experiments. *Physics of Fluids*, 24(3):036601.

Tick, L. J. (1963). *Nonlinear probability models of ocean waves.* Prentice-Hall.

Tukovic, Z. and Jasak, H. (2012). A moving mesh finite volume interface tracking method for surface tension dominated interfacial fluid flow. *Computers & Fluids*, 55:70–84.

Ubbink, O. (1997). *Numerical prediction of two fluid systems with sharp interfaces.* PhD thesis, Imperial College of Science, Technology and Medicine.

Unverdi, S. O. and Tryggvason, G. (1992). A front-tracking method for viscous, incompressible, multi-fluid flows. *Journal of Computational Physics*, 100(1):25 – 37.

Ursell, F. (1949). On the heaving motion of a circular cylinder on the surface of a fluid. *Quaterly J. of Mechanics and Applied Mathematics*, 2:218–231.

Ursell, F. (1953). The long-wave paradox in the theory of gravity waves. *Proceedings of the Cambridge Philosophical Society*, 49:685.

van Leer, B. (1974). Towards the ultimate conservative difference scheme. II. Monotonicity and conservation combined in a second-order scheme. *Journal of Computational Physics*, 14(4):361 – 370.

Vukčević, V. (2016). *Numerical modelling of coupled potential and viscous flow for marine applications.* PhD thesis, University of Zagreb.

Wehausen, J. V. and Laitone, E. V. (1960). *Surface waves. In: Handbuch der Physik.* Springer, New York, USA.

West, B. J., Brueckner, K. A., Janda, R. S., Milder, M., and Milton, R. L. (1987). A new numerical method for surface hydrodynamics. *J. Geophys. Res.*, 92:11803–11824.

Wheeler, J. D. (1970). Method of calculating forces produced by irregular waves. *Journal of Petroleum Technology*, 22:359–367.

Williams, J. (2018). bspline-fortran. Open source program. Available at Github "https://github.com/jacobwilliams/bspline-fortran".

Wilton, J. R. (1914). On deep water waves. *The London, Edinburgh, and Dublin Philosophical Magazine and Journal of Science*, 27(158):385–394.

Wynn, P. (1956). On a device for computing the $e_m(S_n)$ transformation. *Mathematical Tables and Other Aids to Computation*, 10(54):91–96.

Xie, C. (2019). *An efficient method for the calculation of the free-surface Green function using ordinary differential equations.* PhD thesis, Ecole Centrale de Nantes.

Xie, C., Choi, Y.-M., Rongère, F., Clément, A. H., Delhommeau, G., and Babarit, A. (2018). Comparison of existing methods for the calculation of the infinite water depth free-surface Green function for the wave–structure interaction problem. *Applied Ocean Research*, 81:150 – 163.

Zalesak, S. T. (1979). Fully multidimensional flux-corrected transport algorithms for fluids. *Journal of Computational Physics*, 31(3):335 – 362.

Résume étendu

Introduction générale

Un modèle numérique prenant en compte le couplage bidirectionnel entre les modèles de fluide parfait potentiel loin de la structure et de fluide visqueux au voisinage de celle-ci est présenté pour résoudre le problème de l'interaction houle-structure.

L'écoulement total est décomposé en un écoulement incident et un écoulement complémentaire (diffracté). En pratique, les variables (vitesses, pression) du problème sont la somme d'un terme incident et d'un terme complémentaire. Pour les ondes incidentes, le modèle d'écoulement potentiel utilisé est non-linéaire et peut être utilisé dans l'ensemble du domaine fluide. Pour l'écoulement complémentaire le domaine de calcul est divisé en deux parties distinctes. Au voisinage de la structure, cet écoulement complémentaire est résolu en utilisant un modèle fluide réel basé sur la méthode SWENSE (Spectral Wave Explicit Navier-Stokes Equation) qui consiste à écrire les équations RANS (Reynolds Averaged Navier-Stokes) pour les variables complémentaires, les termes incidents apparaissant alors comme des termes de forçage. Loin de la structure, l'écoulement complémentaire est traité avec un modèle de fluide parfait potentiel basé sur la représentation de Poincaré.

La présente étude se résume comme suit :

- Les modèles de fluide parfait potentiel et de fluide visqueux utilisés dans les applications marines sont brièvement passés en revue. Les couplages existants pour ces modèles sont également présentés. Une étude préliminaire est réalisée pour étudier la faisabilité du couplage entre les modèles d'écoulement potentiel et visqueux. Les premiers résultats montrent que le couplage bidirectionnel avec un bon schéma de relaxation peut améliorer les résultats numériques.
- Les modèles de fluide parfait potentiel pour les ondes incidentes non-linéaires sont présentés. Une nouvelle procédure de reconstruction des ondes non-linéaires définies via une méthode fluide parfait potentiel HOS (High Order Spectral) sur un maillage de domaine fluide adapté à un modèle de fluide visqueux via une interpolation B-spline est présentée et validée à l'aide de comparaison entre simulation numérique et expérience.
- Un nouveau modèle potentiel linéarisé basé sur la représentation de Poincaré est proposé pour l'écoulement complémentaire instationnaire loin de la structure. La vitesse complémentaire du fluide au point considéré peut être explicitement calculée avec la fonction de Green instationnaire par des combinaisons de vitesses de fluide et d'élévations de surface libre. Un algorithme de calcul pour différents types de fonction de Green dans le domaine temporel est également présenté. La représentation de Poincaré proposée est validée avec une solution analytique et montre un bon accord lorsque le point de calcul est situé sous la surface libre. Cependant, un comportement singulier est observé lorsque le point du calcul est situé sur la surface libre moyenne.
- Une surface de couplage cylindrique circulaire à axe vertical avec une méthode pseudo-

spectrale basée sur la série de Fourier-Laguerre est introduite pour remédier au comportement singulier constaté précédemment. La vitesse complémentaire du fluide au point considéré est donnée par les coefficients de Fourier-Laguerre de la vitesse du fluide et les coefficients de Fourier de l'élévation de la houle avec les fonctions élémentaires correspondantes. Les fonctions élémentaires représentent les intégrales de surface de la fonction de Green et de la fonction de forme. Les procédures numériques pour calculer les fonctions élémentaires sont présentées. La vitesse complémentaire du fluide et l'élévation de la houle sont reconstruites en utilisant l'étirement de Wheeler. La méthode proposée est validée avec une solution analytique et montre un bon accord y comprsi sur la surface libre moyenne.

- Un modèle d'écoulement de fluide visqueux basé sur la méthode SWENSE pour un écoulement multi-phase avec une fonction Level-set pour la mise à jour de l'interface est présenté. Ce modèle combine les développements numériques spécifiques proposés par Vukčević (2016) et Li (2018). Il s'agit d'une part de la décomposition de la vitesse du fluide, la pression et de la fonction Level-set en composantes incidentes et complémentaires ainsi que la prise en compte des conditions aux limites sur l'interface air-eau à l'aide de la méthode Ghost Fluid (GFM pour Ghost Fluid Method). Une procédure simple d'extrapolation de la vitesse de l'écoulement incident et de la pression dynamique est introduite pour assurer la stabilité numérique. Les résultats de la simulation de propagation de houle seule et d'un cylindre circulaire vertical en houle régulière montrent un bon accord avec les résultats expérimentaux correspondants.
- La procédure de calcul du couplage bidirectionnel entre les modèles d'écoulements de fluide potentiel et visqueux est finalement testée. Un cylindre circulaire vertical soumis à une houle régulière et une bouée fixe soumise à des houles régulières et irrégulières sont utilisés pour étudier les effets du couplage entre les modèles d'écoulements de fluide potentiel et visqueux. Les résultats de la simulation montrent que le couplage bidirectionnel peut améliorer les résultats, notamment pour les forces de dérive.

Résumé par chapitre

1. Introduction

L'intérêt du couplage entre les modèles d'écoulements de fluide potentiel et visqueux est expliqué pour le problème d'interaction houle-structure. Les modèles d'écoulements de fluide potentiel et visqueux couramment utilisés pour des applications en ingénierie navale et offshore sont passés en revue. Les méthodologies des couplages fluide visqueux-fluide potentiel existants sont également présentées et expliquées. Ces méthodologies se répartissent entre décomposition fonctionnelle (FD ; functional decomposition) et décomposition de domaine (DD ; domain decomposition).

Dans le travail présenté, les méthodologies FD et DD sont utilisées pour coupler des modèles d'écoulement potentiel et visqueux. Sur la base de l'hypothèse selon laquelle la houle totale peut être décomposée en houle incidente et houle complémentaire, les quantités d'intérêt des modèles d'écoulements de fluide potentiel et visqueux sont décomposées en une somme de termes incident

et complémentaire. Etant donné que le modèle d'écoulements en fluide parfait potentiel non-linéaire pour les ondes incidentes est disponible pour l'ensemble du domaine fluide, la méthode DD est appliquée uniquement aux parties complémentaires des modèles de fluides potentiel et visqueux. Au voisinage de la structure, le modèle d'écoulement visqueux basé sur la méthode SWENSE est utilisé et le modèle d'écoulement potentiel basé sur la représentation de Poincaré est introduit pour décrire les ondes complémentaires dans le champ lointain.

Les équations qui régissent chacun des deux modèles de fluide sont résumées et le contexte général de l'étude expliqué.

2. L'étude préliminaire sur le couplage des écoulements potentiel et visqueux

Une étude préliminaire sur le couplage entre les modèles d'écoulements de fluide potentiel et visqueux est menée. Le modèle d'écoulement de fluide visqueux basé sur les équations de Navier-Stokes (approche RANS) avec une modélisation d'interface Volume Of Fluid (VOF) est considéré. Une série d'études paramétriques avec ce modèle est réalisée pour trouver une configuration numérique appropriée au problème de propagation de houle. Cette étude montre que le schéma d'intégration en temps du problème de propagation de houle devrait avoir au moins une précision de second ordre pour conserver l'amplitude et la phase de la houle. Les schémas de convection affectent l'ordre de convergence et la stabilité de la simulation. Les schémas de convection d'ordre élevé donnent de bons résultats mais conduisent à une instabilité de la simulation.

La propagation de la houle en bassin (sans interaction avec une structure) et le problème de radiation pour une forme de Lewis 2D sont considérés comme des essais préliminaires pour le couplage. Les tests sont effectués en modifiant le traitement numérique dans la zone extérieure du domaine fluide. Les cas considérés sont l'étirement horizontal des mailles, l'augmentation de la viscosité, l'utilisation de coefficients d'amortissement dans les équations de quantité de mouvement ou d'un schéma de relaxation. Dans la zone extérieure du domaine fluide ou zone de relaxation, le schéma de relaxation fait tendre progressivement les quantités d'intérêt calculées vers les quantités cibles souhaitées (pas de houle, houles incidente ou totale calculées par le modèle potentiel ...).

Les résultats numériques montrent que le schéma de relaxation avec des quantités cibles similaires aux ondes sortantes donne des résultats stables et satisfaisants par rapport aux autres. En outre, le temps de simulation nécessaire pour obtenir la solution convergée diminue lorsque le schéma de relaxation est considéré avec des quantités cibles correctement définies. Cela confirme que le couplage entre les modèles d'écoulement potentiel et visqueux peut réduire à la fois le domaine de calcul et le temps de simulation. En conclusion, une évaluation efficace des ondes sortantes par un modèle d'écoulement potentiel et un schéma de relaxation amélioré sont nécessaires pour réussir le couplage entre les deux modèles d'écoulement.

3. L'écoulement potentiel : Houle incidente

Les modèles de houle incidente non-linéaire pour des houles régulières et irrégulières sont résumés.

Pour la houle régulière, le modèle adopté (Rienecker and Fenton, 1981) s'appuie sur la fonction de courant développée en série de Fourier. La librairie open-source pour les ondes régulières non-linéaires appelé `CN-Stream` développé par Ducrozet et al. (2019) est utilisé pour la génération d'ondes incidentes régulières.

La méthode HOS pour les houles irrégulières en mer ouverte (HOS-ocean) ou en bassin limité (HOS-NWT) est ensuite rappelée (Ducrozet et al., 2007, 2012, 2016).

La librairie open-source pour la reconstruction des houles HOS sur un maillage quelconque est publiée sous licence GPL (Choi et al., 2018)

La procédure de reconstruction proposée est validée avec un modèle d'écoulement de fluide visqueux basé sur la modélisation des équations RANS par des schémas discrets de type volumes finis ainsi qu'une résolution découplée en vitesses-pression et la mise à jour de l'interface par une procédure VOF. Les ondes HOS sont générées dans le modèle à écoulement visqueux et validées par simulation HOS pour différents modèles HOS. Ceux-ci montrent un bon accord les uns avec les autres. De plus, un cas de vagues extrêmes correspondant à la période de retour de 1000 ans dans le Golfe du Mexique (GOM ; Gulf of Mexico) est pris en compte pour validation. Un événement de déferlement est prédit à l'aide d'un modèle simple inclus dans le modèle HOS. L'événement extrême simulé dans le modèle à écoulement visqueux est validé avec la simulation et les expériences HOS. L'accord entre ces différents résultats est satisfaisant.

4. L'écoulement potentiel : Houle complémentaire sur une surface arbitraire

Une nouvelle représentation de la vitesse de Poincaré pour un écoulement à surface libre en profondeur infinie est proposée dans le cadre de la théorie de fluide parfait potentiel linéarisé. La contribution des dipôles dans l'équation intégrale de frontière (BIE ; Boundary Integral Equation) est remplacée par une contribution source équivalente avec une vitesse tangentielle à la surface de la frontière. La vitesse du fluide complémentaire au point du calcul peut être calculée par la distribution de la vitesse du fluide sur la surface correspondante et de l'élévation de la houle sur la ligne de flottaison de la surface correspondante.

Deux types de fonction de Green dans le domaine temporel doivent être évaluées pour la représentation de la vitesse de Poincaré pour un écoulement de surface libre instable. Il est prouvé que les deux types de la fonction de Green dans le domaine temporel et leurs dérivées spatiales sont les solutions de l'équation différentielle ordinaire (ODE ; Ordinary Differential Equation) du 4ème ordre de Clément (Clément, 1998). Ces éléments (fonctions de Green et leurs dérivées) sont calculés en utilisant une méthode de Frobenius à avance temporelle proposée par Chuang et al. (2007).

La représentation de vitesse proposée est validée avec la solution analytique de l'écoulement

autour d'un hémisphère perçant la surface libre et en mouvement forcé (Hulme, 1982). La vitesse du fluide et l'élévation de la vague sur la surface correspondante ainsi que la fonction de Green dans le domaine temporel sont utilisées pour reconstruire la vitesse complémentaire à partir de la représentation de la vitesse de Poincaré. La vitesse complémentaire reconstruite par la représentation de vitesse de Poincaré est comparée à la solution analytique.

Lorsque le point de champ est situé sous la surface libre moyenne, les tests de référence suivants sont effectués :

- L'étude de convergence en temps montre que les vitesses complémentaires reconstruites convergent correctement avec la diminution du pas de temps. Lorsque la discrétisation est suffisante, la vitesse relative reconstituée a une erreur relative inférieure à 1%.
- Lorsque le point où on évalue le champ complémentaire est fixe, la fréquence de mouvement de l'hémisphère est modifiée. Les résultats montrent un bon accord avec la solution analytique. Lorsque la discrétisation est suffisante, la vitesse complémentaire reconstruite présente des erreurs relatives inférieures à la valeur de 1%.
- Différentes surfaces de couplage, telles que un hémisphère, un cylindre circulaire ouvert par le bas, un ellipsoïde ou un cube fermé sur sa partie inférieure sont utilisées pour vérifier la sensibilité de la représentation de vitesse proposée à la géométrie de la surface de couplage. Après calcul, la vitesse complémentaire reconstruite a des erreurs relatives inférieures 1%. Il est vérifié que la représentation de vitesse proposée fonctionne même lorsque la surface inférieure est suffisamment ouverte pour une surface correspondante suffisamment profonde.

Cependant, un comportement singulier apparaît lorsque le point de calcul de la vitesse est situé sur la surface libre moyenne ($z = 0$). Deux contributions de vitesse sont identifiées pour générer ce comportement singulier :

- La contribution de la composante harmonique a un profil de vitesse hautement instable lorsque l'intégrale de convolution est partiellement évaluée avec un intervalle de type fenêtre glissante.
- La contribution de la composante de surface libre a un profil de vitesse hautement oscillant lorsque l'intégrale de convolution est partiellement évaluée avec un intervalle de type fenêtre glissante.

Ce comportement singulier est dû au comportement divergent de la fonction de Green lorsque les points de calcul et de la source sont situés sur la surface libre moyenne ($z = \zeta = 0$). En effet, le comportement hautement oscillant de la vitesse du fluide ne peut être corrigé en raffinant la discrétisation de la ligne de flottaison. Pour finir, la nécessité d'intégrer la représentation de Poincaré le long de la surface de couplage cylindrique verticale est expliquée.

5. L'écoulement potentiel : Houle complémentaire sur une surface de couplage cylindrique circulaire verticale

La représentation de vitesse de Poincaré est formulée avec une surface de couplage cylindrique circulaire. La vitesse complémentaire et l'élévation de surface libre sont approximées respectivement par les séries de Fourier-Laguerre et de Fourier. Après avoir intégré la représentation de

la vitesse de Poincaré le long de la surface de couplage cylindrique circulaire avec la vitesse du fluide et l'élévation de la houle multipliées par la fonction de Green dans le domaine temporel, la vitesse complémentaire au point d'intérêt peut être calculée par les coefficients des séries de Fourier-Laguerre et de Fourier de la vitesse complémentaire et de l'élévation de la houle sur la surface de couplage multipliée par des fonctions élémentaires.

Les fonctions élémentaires sont dérivées de l'intégrale de surface des séries de Fourier-Laguerre et de Fourier avec la fonction de Green dans le domaine temporel. Elles impliquent l'intégrale utilisant les fonctions de Bessel multipliées par une fonction sinus ou cosinus. Des algorithmes numériques adaptés sont présentés pour calculer les fonctions élémentaires. Après avoir calculé l'intégrale oscillante jusqu'à la borne d'intégration définie, deux approches permettent d'évaluer l'intégrale semi-infinie de cette borne à l'infini. Les détails des deux approches s'expliquent comme suit :

- **Division des fonctions oscillantes**

  L'idée d'évaluer l'intégrale impliquant les fonctions de Bessel proposée par Lucas and Stone (1995); Lucas (1995) est développée ici. Les fonctions oscillantes irrégulières sont divisées en fonctions oscillantes elles-mêmes transformées en une somme infinie de sous-intégrales avec des zéros. Cette somme infinie est calculée à l'aide de l' ϵ-algorithme de Wynn (Wynn, 1956).

- **Méthode à directions de descente**

  Les intégrales semi-infinies sont évaluées en appliquant une méthode à directions de descente Liang et al. (2018); Li et al. (2019a). Les fonctions oscillatoires sont transformées dans le plan complexe. L'intégrale le long du contour fermé dans le plan complexe est obtenue en appliquant le théorème de Cauchy. Le chemin d'intégration le plus efficace est trouvé en prenant les parties imaginaires de l'argument exponentiel à zéro. Finalement, les intégrales le long du chemin de descente le plus efficace impliquent les facteurs exponentiels ayant des arguments réels négatifs qui permettent de faire tendre l'intégrand rapidement vers zéro.

Les fonctions élémentaires sont évaluées en utilisant les approches proposées. Deux approches montrent un bon accord entre elles.

L'élévation de houle complémentaire au point considéré est reconstruite en utilisant la condition cinématique à la surface libre. La vitesse verticale sur la surface libre moyenne est intégrée en fonction du temps pour calculer l'élévation de la houle complémentaire. Un pseudo-étirement de Wheeler est appliqué sur la fonction de Laguerre pour l'extrapolation de la vitesse au-dessus de la surface libre moyenne ($z > 0$). La valeur de la fonction de Laguerre au-dessus de la surface libre moyenne est limitée afin d'empêcher de trop fortes valeurs de la vitesse dans l'air.

La reconstruction de la vitesse complémentaire et de l'élévation de surface libre en un point donné est obtenue en utilisant une interpolation B-spline. Après avoir reconstitué la vitesse complémentaire du fluide et l'élévation de surface libre sur la grille cylindrique circulaire 3D, l'interpolation B-spline est utilisée pour calculer la vitesse complémentaire du fluide et l'élévation de surface libre en un point donné.

L'approximation de Fourier-Laguerre de la vitesse complémentaire sur la surface de couplage est testée. Les vitesses complémentaires approximées sont en bon accord avec la solution analytique.

Un hémisphère perçant la surface libre en mouvement forcé et la diffraction d'une houle incidente régulière par un cylindre circulaire vertical sont utilisés comme tests de validation. Les vitesses complémentaires reconstruites et les élévations de houle montrent un bon accord avec la solution analytique. Aucun comportement singulier n'apparaît dans les résultats.

6. L'écoulement visqueux : Multi-phase SWENSE avec fonction Level-set

La méthodologie SWENSE est appliquée pour l'écoulement multi-phase avec une modélisation d'interface de type Level-set (LS). Le modèle utilisé dans ce travail de thèse combine les travaux antérieurs de Vukčević (2016) et de Li (2018). Vukčević (2016) a appliqué la décomposition fonctionnelle sur les variables de vitesse du fluide et fonction LS pour reconstruire les équations du problème relatives aux écoulements complémentaires. De plus, les termes incidents ne sont pas simplifiés par le fait que l'écoulement incident vérife les équations d'Euler mais recalculés systématiquement. Il a utilisé la méthode GFM pour résoudre le problème d'écoulement multi-phase en prenant en compte la condition de saut de pression sur l'interface. Li (2018), pour sa part, introduit une pression de mélange étendue jusqu'à la zone occupée par l'air, au-dessus de l'interface, pour annuler les termes liés au champ incident. Il a présenté différentes versions de SWENSE pour l'écoulement multi-phase avec une méthode de Volume Of Fluid (VOF) pour la modélisation de l'interface.

Dans la présente étude, les équations RANS sont reformulées en SWENSE en utilisant la pression de mélange étendue proposée par Li (2018). L'interface entre deux fluides est modélisée par la fonction LS. Une décomposition fonctionnelle est appliquée à la fonction LS suivant (Vukčević, 2016). Par conséquent, la vitesse du fluide, la pression et la fontion LS sont décomposées en parties incidentes et complémentaires.

Les termes liés à la pression sont discrétisés en considérant les conditions sur l'interface dans le cadre d'une approche de type Volumes Finis (FV ; Finite Volume). La procédure de discrétisation FV basée sur la méthode GFM proposée par Vukčević (2016) est utilisée pour prendre en compte la condition de pression sur l'interface. La pression incidente, y compris la pression dynamique de la houle incidente et la pression hydrostatique, est utilisée pour définir le saut de pression Li (2018). Les conditions de saut de pression proposées par Vukčević (2016) et Li (2018) sont identiques pour les cas d'écoulements en eau calme.

L'équation de transport de la fonction LS d'origine avec une simple redistanciation est utilisée dans la présente étude. La discrétisation numérique des termes de l'écoulement incident dans l'équation de la fonction LS génère des sources d'erreur qui se cumulent au cours des simulations mais que la redistanciation de la fonction LS permet de diminuer largement. Finalement, la perte de masse observée est négligeable.

L'extrapolation de la vitesse incidente et de la partie dynamique de la pression de la houle incidente avec des polynômes cubiques est proposée dans les travaux actuels. Elle permet des

transitions en douceur des quantités relatives à la houle incidente jusqu'à la zone au-dessus de l'interface sans algorithme complexe et avec un calcul rapide. Même si cette technique ne satisfait pas la continuité de masse dans la zone aérienne, la simulation multi-phase SWENSE devient stable.

Les houles qui se propagent dans le bassin numérique (NWT ; Numerical Wave Tank) sont prises en compte dans le cas de référence. Le modèle d'écoulement de fluide visqueux proposé donne de bons résultats par rapport à d'autres modèles de fluide visqueux. Néanmoins, une faible perte de masse est observée lorsqu'un maillage grossier et un pas de temps important utilisés pour la simulation. La perte de masse est réduite à mesure que le maillage est raffiné et le pas de temps diminué.

La diffraction de la houle incidente par un cylindre circulaire vertical est considérée pour le deuxième test (Huseby and Grue, 2000). Les amplitudes et les harmoniques en amplitude et en phase pour les efforts sont comparés à la solution analytique, aux expériences et à d'autres calculs numériques. Les résultats calculés par le modèle d'écoulement visqueux proposé montrent des résultats similaires à ceux d'autres calculs.

7. Couplage bidirectionnel des écoulements potentiel et visqueux

L'algorithme de calcul résolvant un problème d'interaction houle-structure en considérant le couplage bidirectionnel entre les modèles d'écoulement potentiel et visqueux est introduit. Il repose sur l'hypothèse selon laquelle le l'écoulement total peut être décomposé en incident et supposé complémentaire. Dans la présente étude, les principes suivants sont utilisés :

- L'écoulement total peut être décomposé en parties incidentes et complémentaires.
- Les parties incidentes sont calculées à partir des modèles d'écoulement potentiel non-linéaire pour les houles incidentes dans l'ensemble du domaine fluide considéré.
- Les parties complémentaires au voisinage d'une structure sont résolues par un modèle d'écoulement visqueux basé sur la méthode SWENSE.
- Les parties complémentaires dans le champ lointain sont modélisées par la représentation de vitesse de Poincaré basée sur la théorie d'écoulement potentiel linéarisé.

Sur la base du principe ci-dessus, la décomposition fonctionnelle (FD) et la décomposition de domaine (DD) sont appliquées en tant que méthodologie de couplage :

- **La décomposition fonctionnelle (FD)** est appliquée à la fois aux modèles d'écoulement potentiel et visqueux. Parce que le modèle d'écoulement potentiel non-linéaire pour les ondes incidentes est disponible dans l'ensemble du domaine fluide entier, les parties complémentaires constituent le coeur du problème à résoudre. Les équations principales et les conditions aux limites pour les modèles d'écoulement potentiel et visqueux sont reformulées pour un écoulement complémentaire. La représentation de la vitesse de Poincaré est utilisée pour un écoulement potentiel et la méthode SWENSE est utilisée pour un écoulement visqueux.

- **La décomposition domaine (DD)** est considéré comme décomposant le domaine de calcul des modèles d'écoulement potentiel et visqueux pour les parties complémentaires. Le modèle d'écoulement visqueux basé sur la modélisation d'écoulement de fluide visqueux SWENSE et de la fonction LS calcule les ondes complémentaires au voisinage d'une structure. Les ondes complémentaires dans la région du champ lointain sont modélisées par la représentation de vitesse de Poincaré basée sur la théorie du potentiel linéaire.

Le couplage bidirectionnel entre les modèles d'écoulement potentiel et visqueux pour un écoulement complémentaire suppose que la vitesse du fluide et l'élévation de la houle soient des fonctions continues au passage d'un modèle à l'autre. Chacun des modèles est mis à jour comme suit :

- **Modèle d'écoulement visqueux vers modèle d'écoulement potentiel**

  La vitesse du fluide complémentaire et les élévations des vagues sur la surface de couplage correspondante sont obtenues à partir du modèle d'écoulement visqueux. Les coefficients de Fourier-Laguerre et de Fourier pour, respectivement, la vitesse complémentaire et l'élévation de la houle sont calculés. Les champs complémentaires de vitesse et d'élévation des vagues dans les zones de relaxation sont construits à l'aide de la représentation de vitesse de Poincaré.

- **Modèle d'écoulement potentiel vers modèle d'écoulement visqueux**

  Les valeurs cibles de la vitesse complémentaire et de la fonction Level-set dans la zone de relaxation sont calculées à partir des champs complémentaires de vitesse et d'élévation de la vague en utilisant la représentation de vitesse de Poincaré. Le schéma de relaxation, qui associe la quantité calculée à la quantité cible, est utilisé pour mettre à jour le modèle d'écoulement visqueux.

Deux cas de test de référence sont considérés pour validation :

- **Un cylindre circulaire vertical en houle régulière** est simulé en considérant le couplage entre les modèles d'écoulement potentiel et visqueux. Le couplage bidirectionnel est appliqué à divers modèles d'écoulement visqueux. L'un est basée sur la modélisation multiphase SWENSE avec la fonction LS pour la gestion de l'interface proposée dans la présente étude. L'autre est basé sur le modélisation des équations RANS avec un modèle VOF pour la gestion de l'interface. La comparaison est faite en comparant le champ d'élévation de houle, les harmoniques des amplitudes des efforts et le coût de calcul.

  Les ondes complémentaires générées par le cylindre se propagent jusqu'à la fin de la zone de relaxation lorsque la méthode de couplage est prise en compte. Il est montré que les harmoniques en amplitude des efforts au premier et second ordre sont légèrement améliorées si le couplage est appliqué. En particulier, les forces de dérive moyennes horizontales agissant sur le cylindre sont améliorées. Cependant, les coûts de calcul augmentent lorsque le couplage est appliqué. Le coût de calcul augmente d'environ 84% pour SWENSE avec la modélisation d'interface LS et de 56% pour RANS avec la modélisation d'interface VOF.

- **Une bouée fixe en houle régulière et irrégulière** est ensuite considérée. Les résultats de la simulation sont comparés aux résultats expérimentaux. Dans le test de bouée dans la houle régulière, les élévations de surface libre obtenues pour différentes sondes à houle

et comparées aux expériences montrent des erreurs moins importantes lorsque le couplage est appliqué. Les harmoniques en amplitude des efforts au premier et deuxième ordre et les forces de dérive moyennes sont améliorées lorsque le couplage est appliqué. Dans le test de la houle irrégulière, un effet de couplage négligeable est observé car les houles complémentaires sont de faible amplitude. Les coûts de calcul augmentent lorsque le couplage est appliqué d'environ 80% et 49% pour les cas de simulation de houle régulière et irrégulière, respectivement.

En conclusion, le couplage bidirectionnel entre les modèles d'écoulement potentiel et visqueux fonctionne lorsque les houles complémentaires sont suffisamment importantes. L'élévation de la houle et les efforts aux premier et deuxième ordres -en particulier les forces de dérive- agissant sur la structure peuvent être améliorées si l'on considère le couplage bidirectionnel. Cependant, les coûts de calcul augmentent d'environ 80% pour les cas de houle régulière et de 50% pour les cas de houle irrégulière.

8. Conclusion et perspectives

Le couplage bidirectionnel entre les modèles d'écoulement de fluide parfait potentiel et visqueux est proposé dans la présente étude. Les modèles d'écoulement potentiel pour des écoulements incidents et complémentaires ainsi que le modèle d'écoulement visqueux basé sur SWENSE avec la fonction LS pour la modélisation de l'interface sont expliqués. Les tests de référence valident chaque modèle d'écoulement et montrent un bon accord avec les résultats de référence disponibles. On suppose que l'élévation de surface libre et la vitesse du fluide dans les modèles d'écoulement sont continues. Pour coupler les modèles des écoulements potentiels et visqueux, les méthodologies de décomposition fonctionnelle (FD) et de décomposition de domaine (DD) sont appliquées.

La décomposition fonctionnelle (FD) est appliquée aux modèles d'écoulement potentiel et visqueux. Les quantités d'intérêt totales sont décomposés en parties incidente et complémentaire. L'écoulements potentiel non-linéaire pour les houles incidentes est supposé disponible dans tout le domaine fluide et satisfait les équations d'Euler. Le modèle potentiel linéarisé basé sur la représentation de la vitesse de Poincaré pour un écoulement complémentaire est proposé. D'autre part, le fait de disposer d'un modèle de houle incidente non-linéaire conduit à l'utilisation de la méthode SWENSE pour prendre en compte l'écoulement complémentaire dans le cadre d'un modèle de fluide visqueux.

La décomposition de domaine (DD) est utilisée pour décomposer le domaine de calcul. Les ondes incidentes non-linéaires du modèle d'écoulement de potentiel nonlinéaire sont disponibles dans tout le domaine de calcul. Cela nous oblige à diviser le domaine de calcul des modèles d'écoulement potentiel et visqueux uniquement pour les ondes complémentaires. Au voisinage de la structure, le modèle d'écoulement visqueux basé sur SWENSE est utilisé et le modèle d'écoulement potentiel linéarisé pour un écoulement complémentaire est appliqué dans la région du champ lointain.

Pour coupler les modèles d'écoulement potentiel et d'écoulement visqueux, on accepte l'hypothèse

de l'évolution continue de l'élévation de surface libre et de la vitesse du fluide dans le domaine de calcul. Sur la surface de couplage considérée, la vitesse du fluide complémentaire et l'élévation de la houle sont utilisées pour mettre à jour le champ d'écoulement complémentaire dans la région du champ lointain à l'aide de la représentation de la vitesse de Poincaré. Dans le champ lointain, le schéma de relaxation est utilisé pour fusionner le champ complémentaire calculé avec le champ cible calculé à partir de la représentation de la vitesse de Poincaré.

Un algorithme résolvant le problème d'interaction houle-structure en considérant un couplage bidirectionnel est présenté. Les tests de référence sont effectués pour un cylindre circulaire vertical soumis à une houle incidente régulière et une bouée fixe soumis à des houles incidentes régulière et irrégulière. Les résultats des tests de référence montrent que le couplage bidirectionnel peut améliorer les élévations de surface libre et les efforts agissant sur la structure. En particulier, les efforts de dérive moyennes horizontales agissant sur la structure sont considérablement améliorés lorsque le couplage bidirectionnel est adopté. Cependant, le couplage bidirectionnel donne des résultats médiocres sur la troisième harmonique des efforts. Lorsque les houles complémentaires sont ptites, le couplage bidirectionnel n'affecte pas les résultats. Lorsque le couplage bidirectionnel est appliqué, les coûts de calcul sont augmentés de 80 % pour la simulation en houle régulière et de 40 % pour la simulation en houle irrégulière.

Pour les travaux futurs, les sujets de recherche suivants peuvent être mentionnés :

- **Représentation de la vitesse de Poincaré pour un écoulement de surface libre pour le navire avec vitesse d'avance**

  La représentation de la vitesse de Poincaré dans une application marine a été étudiée pour résoudre des problèmes stationnaires et périodiques par Noblesse et al. (1997); Noblesse (2001); Noblesse and Yang (2004). La représentation de la vitesse pour le problème d'interaction houle-structure avec vitesse d'avance peut être réalisée avec la condition limite de surface libre de Neumann-Kelvin. Un tel modèle peut être utilisé pour coupler un modèle d'écoulement visqueux afin d'évaluer la résistance ajoutée du navire dans la houle.

- **Couplage entre le modèle d'écoulement potentiel linéaire et d'autres modèles d'écoulement**

  La représentation de vitesse proposée peut être utilisée pour coupler le modèle d'écoulement visqueux basé sur la modélisation d'interface SWENSE et VOF par Li (2018). La fonction élémentaire introduite dans la présente étude peut être applicable à l'équation intégrale de frontière. Le modèle d'écoulement utilisé pour résoudre l'interaction houle-structure au voisinage de la structure peut être remplacé par des modèles d'écoulement à potentiel non-linéaire tels que la méthode des singularités de type Rankine (RPM ; Rankine Panel Method) ou la méthode des éléments finis (FEM ; Finite Element Method).

- **Evaluation des efforts de dérive moyennes agissant sur un corps non-profilé**

  Le couplage bidirectionnel entre les modèles d'écoulement potentiel et visqueux donne de bons résultats sur les forces de dérive moyennes horizontales agissant sur la structure, forces qui sont importantes dans la conception des systèmes d'amarrage pour des navires-citernes ou des FPSO. Il serait donc intéressant d'étudier le comportement à la mer de telles structures via le couplage bidirectionnel mis en place dans ce travail.

Titre : Couplage bidirectionnel entre des écoulements de potentiel et visqueux pour une application marine

Mots clés: Interaction houle-structure ; Génération et absorption de houle; Couplage des écoulements en fluide potentiel et visqueux; représentation de la vitesse par modèle de Poincaré; équations SWENS ; logiciel OpenFOAM

Résumé: Ce travail propose une méthodologie de couplage bidirectionnel entre un modèle Navier-Stokes et un modèle fluide parfait potentiel pour des applications d'ingénierie marine et particulièrement d'interaction houle-structure.
Les quantités d'intérêt sont décomposées comme la somme d'un terme d'écoulement incident et un terme d'écoulement complémentaire. Un modèle potentiel non-linéaire (HOS : High-Order Spectral) est utilisé pour l'écoulement incident. L'écoulement complémentaire est traité par des modèles de fluide visqueux et de fluide parfait potentiel. Le modèle fluide visqueux est basé sur les équations SWENS (Spectral Wave Explicit Navier-Stokes) et une formulation de type Level-Set pour la prise en compte de l'interface; ce modèle est utilisé dans un domaine proche de la structure marine étudiée. Le modèle de fluide potentiel est un modèle linéarisé basé sur une description de Poincaré. Cette description est utilisée pour effectuer de nouveaux développements où la surface de couplage est un cylindre circulaire, ce qui permet de résoudre les problèmes de divergence numérique rencontrés initialement sur la surface libre. Les variables utilisées pour le couplage entre les deux modèles sont la vitesse du fluide et l'élévation de surface libre.
Le couplage proposé est validé pour des cas de diffraction-radiation et l'accord avec les résultats de référence est bon. En particulier, les efforts du 1er et du 2ème ordre sont bien restitués.

Title : Two-way coupling between potential and viscous flows for a marine application

Keywords: Wave-structure interaction; Wave generation and absorption; Potential and viscous flow coupling; Poincaré's velocity representation; SWENSE; OpenFOAM

Abstract: The present study proposes a two-way coupling methodology between potential and viscous flow models for a marine application. A hypothesis that the functional quantities of total flow can be decomposed into the incident and complementary parts is assumed. The nonlinear potential flow model for incident flow is available. Therefore the complementary flow is only concerned in the potential and viscous flow models. The computational domain for complementary flow is decomposed. In the vicinity of structure, the viscous flow model based on Spectral Wave Explicit Navier-Stoke Equations (SWENSE) is used. A linear potential flow model based on Poincaré velocity representation is applied to simulate the complementary wave in the far-field. The fluid velocity and wave elevation are used to couple the potential and viscous flow models.
A preliminary study on the coupling is conducted and the necessity to a fast evaluation of potential flow is raised. The nonlinear potential flow models for incident waves are summarized and the reconstruction procedure in the viscous flow solver is proposed and validated with the simulation and experiments. A new Poincaré's velocity representation for time domain free surface flow is introduced with a circular cylindrical matching surface. The proposed representation is validated with the linear radiation-diffraction problem and the results show good agreements. The viscous flow solver based on SWENSE method with Level-Set interface modeling is proposed. The potential and viscous flow models are coupled and the results show that the coupling can enhance the first- and second-order forces acting on the structure.